Étude multi-approches des voiles bactériens du Paléoprotérozoïque (2,1 Ga, Gabon) : Biogénicité, minéralogie et biogéochimie

Jérémie Aubineau

To cite this version:

Jérémie Aubineau. Étude multi-approches des voiles bactériens du Paléoprotérozoïque (2,1 Ga, Gabon) : Biogénicité, minéralogie et biogéochimie. Sciences de la Terre. Université de Poitiers, 2019. Français. NNT : 2019POIT2278 . tel-02619041

HAL Id: tel-02619041
https://theses.hal.science/tel-02619041

Submitted on 25 May 2020

THESE

Pour l’obtention du Grade de

DOCTEUR DE L’UNIVERSITE DE POITIERS

Institut de chimie des milieux et matériaux de Poitiers - IC2MP

Faculté des Sciences Fondamentales et Appliquées

Diplôme National - Arrêté du 25 mai 2016

Ecole Doctorale :

Chimie Ecologie Géosciences Agrosciences « *Théodore Monod* »

Secteur de Recherche : Terre solide : géodynamique des enveloppes supérieures, paléobiosphère

Présentée par

Jérémie AUBINEAU

****

Étude multi-approches des voiles bactériens du Paléoprotérozoïque (2,1 Ga, Gabon) : Biogénicité, minéralogie et biogéochimie

****

Directeur de Thèse : Abderrazak El Albani

****

Soutenue le 27 septembre 2019 devant la Commission d’Examen

****

JURY

Rapporteur	Olivier Rouxel	Docteur, IFREMER, Brest
Rapporteur	Bénédicte Ménez	Professeur, IPGP, Paris
Directeur de thèse	Abderrazak El Albani	Professeur, Université de Poitiers
Examinateur	Laurent Caner	Professeur, Université de Poitiers
Examinateur	Claude Geffroy	Maître de conférence, Université de Poitiers
Examinateur	Claire Rollion-Bard	Ingénieur de recherche CNRS, IPGP, Paris
Examinateur	Timothy Lyons	Professeur distingué, Université de Riverside
Examinateur	Ernest Chi Fru	Professeur associé, Université de Cardiff

A mon grand-père Michel,

Résumé

La Série sédimentaire du Francevillien âgée de 2,1 milliards d’années du Gabon a fait l’objet de plusieurs investigations notamment à des fins économiques en lien avec les gisements uranifère et manganésifère. Ceci a également promu de nombreuses recherches pour reconstruire les paléoenvironnements et la paléobiodiversité du bassin de Franceville. Les sédiments abritent les plus anciens macrofossiles de tailles et de formes variées, ainsi que les traces laissées par des organismes mobiles, mettant en valeur l’enregistrement grandissant des formes primitives complexes et organisées au Paléoprotérozoïque. Cependant, le style de vie microbien, qui a émergé plus d’un milliard et demi d’années avant la sédimentation du Francevillien, a été peu décrit. Une étude multi-approches et pluridisciplinaire a révélé une grande diversité de structures liées aux voiles (MRS). Ces communautés microbiennes étaient principalement construites par des Cyanobactéries oxyphototrophiques qui ont prospéré dans des environnements peu profonds et dans la zone photique. Etant donné que ces bactéries peuvent avoir produit de grandes quantités d’oxygène très localement, ceci explique à priori la présence rependue de formes de vie avancées à proximité des MRS. Les structures fragiles bactériennes ont ensuite été analysées d’un point de vue minéralogique et géochimique. Les analyses montrent un assemblage minéralogique argileux riche en potassium (K) localisé dans les MRS mais inexistant dans les sédiments encaissants sous-jacents constitués de grès et d’argiles riches en matière organique (black shales). Cela suggère un piégeage des cations K^+ par les MRS. Ce K, qui provient de l’eau de mer, a été ensuite relargué dans l’espace interstitiel pendant la dégradation de la matière organique, permettant ainsi la néoformation argileuse riche en K. Ceci confirme l’enrichissement potassique induit par des microbes. En ce qui concerne la teneur en éléments traces (TE) dans les MRS, aucun enrichissement en lien avec les microorganismes a été observé. La concentration de certains TE dans les MRS est plus élevée que celle du sédiment encaissant, mais des facteurs physiques environnementaux et non biologiques pourraient avoir causé ces enrichissements. Les données du redox local de l’eau de mer pour le sédiment encaissant montrent que le milieu de dépôt se traduit par des fluctuations des conditions redox (oxiques/suboxiques). Les signaux isotopiques du carbone organique et de l’azote de la roche totale sont similaires dans les structures bactériennes et le sédiment encaissant. La composition des isotopes du carbone suggère l’occurrence d'un recyclage secondaire d’un matériel carboné dérivé de la photosynthèse. Par ailleurs, les isotopes de l’azote indiquent une limitation azotée où les fixateurs de l’azote n’ont pas efficacement compensé la perte de ce dernier. La fixation de l’azote dans la colonne d’eau aurait été passagère et potentiellement contrôlée par la structure redox de l’océan, tandis que cette voie métabolique associée aux MRS est vraisemblablement commune au royaume des voiles benthiques à travers l’histoire de la Terre. L’ensemble de

ces résultats soulignent la manifestation fréquente du mode de vie bactérien dans la série du Francevillien et révèlent si les microbes ont laissé des biosignatures spécifiques. La conservation exceptionnelle des MRS en association avec les macrofossiles du Gabon représente un écosystème marin unique à la suite de la première montée significative de la teneur en oxygène dans l’atmosphère terrestre.

Abstract

The 2.1-billion-year old (Ga) Francevillian Series in Gabon has been intensively studied because of economic interests in their uranium and manganese ore deposits. This also promoted numerous scientific investigations to reconstruct the palaeoenvironments and palaeobiodiversity of the Francevillian basin. The sediments host the oldest reported macrofossils of various sizes and shapes, and traces left by motile organisms, highlighting the growing record of early complex forms in the Palaeoproterozoic. However, the microbial lifestyle, which emerged more than a billion and a half years before the Francevillian deposition, has been poorly described. Through a combination of analytical technics, a large diversity of mat-related structures (MRS) has been observed. These microbial communities were mainly built by oxyphototrophic Cyanobacteria that thrived in shallow water environments within the photic zone. Considering that these bacteria may have locally produced higher amount of oxygen than in the oxygen-stressed water column, this likely explained the widespread presence of advanced forms of life in the vicinity of MRS. The delicate bacterial structures were then analyzed for their mineralogical and geochemical compositions. A distinct potassium (K)-rich clay assemblage characterizes the MRS, but not the underlying host sandstone and black shale sediments. It suggests that the MRS trapped K^+ from the seawater and released it into the pore-waters during degradation of organic matter, resulting in K-rich clay neoformation. This confirms the microbially induced K enrichment in the geological rock record. However, the trace element (TE) content in the MRS does not reveal particular microbially mediated enrichments. The concentration of some TE in the MRS is higher relative to that of the host sediments, but physical environmental factors may overwhelm any potential biological signal. The local seawater redox data for the host sediments show that the depositional setting reflects fluctuations in redox conditions (oxic/suboxic). The organic carbon and bulk nitrogen isotopes between the bacterial structures and host sediments are mostly similar. The carbon isotope composition suggests the occurrence of secondary recycling of photosynthetically derived carbonaceous material, while the nitrogen systematic points to a nitrogen limitation by which the N_2 fixers did not sufficiently replenish the nitrogen loss. The nitrogen fixation in the water column would have been transient and likely controlled by the ocean redox structure, whereas this metabolic pathway in the MRS is likely common to the realm of benthic mats over Earth's history. Combined, these results underline the common occurrence of bacterial lifestyle in the Francevillian Series and reveal whether the microorganisms left typical biosignatures. The exceptional conservation of the MRS in association with the Gabonese macrofossils represents a unique marine ecosystem in the aftermath of the first significant rise of oxygen content in Earth's atmosphere.

REMERCIEMENTS

Avant de commencer, je tiens à exprimer ma gratitude au Ministère de l'Education Nationale, de l'Enseignement et de la Recherche, à la région Nouvelle-Aquitaine, à l'Université de Poitiers, au Centre National de Recherche Scientifique (CNRS), à l'école doctorale Théodore Monod, et enfin le laboratoire IC2MP qui ont contribué directement et indirectement à ce travail de thèse.

Trois années viennent de s'écouler : DEJA ! On se dit « 3 ans, j'ai le temps de tout faire » mais en fait pas vraiment. Je voudrais remercier dans un premier temps Abder qui m'a fait confiance dès le début il y a maintenant 6 ans. En effet, notre collaboration a débuté lorsque je rangeais et classais des échantillons de roches avec d'autres étudiants pendant un simple stage de licence. J'ai donc pu effectuer ce doctorat dont l'aventure humaine et intellectuelle fut particulièrement enrichissante. J'ai également eu la possibilité de visiter d'autres laboratoires à travers de nombreuses collaborations nationales et internationales, toutes riches en expérience. Pour tout cela merci à toi Abder.

Je tiens à remercier mon jury de thèse, Olivier Rouxel, Bénédicte Ménez, Laurent Caner, Claude Geffroy, Claire Rollion-Bard, Ernest Chi Fru et Timothy Lyons, qui m'a fait l'honneur de lire et de juger mes travaux.

Un grand, grand merci à Alain Meunier qui malgré son statut de retraité était là tous les matins (ou presque) pour nous préparer le café. Au-delà de cela, c'est avec Alain que j'ai échangé le plus durant cette thèse et je pense que je lui dois ma gratitude car sans son aide précieuse ce doctorat n'aurait pas la même valeur.

Merci à tous les membres de l'équipe HydrASA et à l'ensemble du service technique pour leur accueil chaleureux et leur soutien humain et analytique durant cette thèse. Un grand merci également aux filles du service administratif de l'IC2MP pour leur aide, leur disponibilité et leur réactivité. Je souhaite également remercier chaleureusement François Leconte, Olabode Bankole et « papa » Claude qui ont toujours su se montrer disponible et généreux à bien des égards durant ces trois longues années.

Je suis très reconnaissant envers mes collègues Andrey Bekker et Ernest Chi Fru qui m'ont accueilli avec plaisir chez eux. Je n'oublierai pas nos longues discussions scientifiques, parfois tardives, mais toutes enrichissantes. Je souhaite exprimer ma gratitude à Kurt Konhauser qui m'a fourni une aide incroyable dans l'ensemble de nos collaborations et que j'ai finalement rencontré dans un cadre idéal pour la recherche : Banff (Canada).

Petit détour par le Nord… Malgré le fait que le soleil ne soit pas tout le temps au rendez-vous, j'ai pu compter sur le soutien indéfectible de mes nombreux collègues et amis lillois. Je tiens à remercier tout particulièrement Kévin Lepot, Philippe Recourt, Jean-Yves Reynaud, Armelle Riboulleau, Alain Trentesaux et Nicolas Tribovillard pour les nombreux conseils et moments partagés depuis mon Master 2. C'est toujours un plaisir de se rendre à Lille pour travailler, échanger et éventuellement boire quelques bières avec Alexis Caillaud, Martin Jovillet Castelot et Fabio Francescangeli.

Une pensée amicale pour mes amis géologues de longue date, Romain Beuzeval, Gaël Cherfallot, Maxime Comby, Nicolat Tricot, Héloïse Verron sans oublié l'inévitable Christophe Ronez avec lequel j'ai partagé de très bons moments, surtout à Los Angeles (une histoire incroyable).

Ce doctorat n'aurait pas eu la même valeur sans eux. Je souhaite remercier mes collègues post-docs, doctorants géologues, paléontologues et de l'association Pictasciences qui m'ont permis de voir sous un autre angle le travail de thèse, surtout autour d'un verre. A ce titre, merci à Marine Bonnet, Grâce Guiyelegou, Thomas Dabat, André Somavilla, Génia Soldatenko, Anastasia Chupryna, Emilie Berlioz, Marion Corbé, Corentin Gibert, Florian Martin, Laurent Pallas et Gislain Thiery. Une pensée également pour l'ensemble des anciens collègues, actuels stagiaires et étudiants extérieurs qui étaient de passage dans nos locaux. Tout de même, mention spéciale à Christopher Sevin et Axelle Walker pour leur caractère atypique et leur sens hors du commun à épater la galerie.

Un grand merci à mes amis lycéens avec qui nous avons su prolonger notre nostalgie. Malgré leur manque d'intérêt pour la recherche fondamentale, j'ai pu compter sur le soutien plus que précieux de Bruno, Catherine, Léa, Jérémy, Mélanie, Jordan et Norine. Pour finir, je tiens à remercier mon amie Véronique, mon frère, mes parents et grands-parents, qui m'ont toujours rassuré dans les périodes difficiles et soutenu, ce qui n'a jamais été aussi important à mes yeux.

Merci à vous tous.

TABLE OF CONTENTS

LIST OF FIGURES

LIST OF TABLES

LIST OF APPENDICES

INTRODUCTION (FRANÇAIS)

Les microbes, connus pour leur grande diversité morphologique, écologique et phylogénique, sont les plus anciennes formes de vie sur Terre et englobent les êtres vivants procaryotiques tels que les archées et les bactéries. Les biofilms et les voiles bactériens font référence à une association fructueuse de microorganismes qui s'est développée au début de l'histoire de la Terre, il y a 3,5 – 3,8 milliards d'années (Ga). Ce mode de vie fournit une large gamme de propriétés émergentes comparé à celui observé des cellules bactériennes isolées. Ces propriétés spécifiques incluent une sorption améliorée pour le piégeage de ressources, une rétention enzymatique, des interactions sociales pour un remodelage dynamique des microorganismes, et des gradients physico-chimiques localisés (Flemming *et al.*, 2016). Les biofilms et les voiles bactériens ont largement été étudiés, cependant la terminologie est souvent confuse sans définition globalement acceptée (Krumbein *et al.*, 2003). Néanmoins, un biofilm peut renvoyer à un groupe de cellules intégré dans une matrice organique dont la structure est monocouche, tandis qu'un voile bactérien définit une distribution multicouche de communautés bactériennes. Ainsi, les voiles bactériens peuvent être perçus comme des biofilms améliorés. Considérant cette terminologie controversée, le terme 'structures liées aux voiles' (MRS; Eriksson *et al.*, 2010) a été choisi pour inclure toutes les structures fossilisées induites et/ou préservées par des microorganismes.

Il est largement reconnu que les microbes ont joué un rôle important dans l'évolution du climat et des cycles biogéochimiques de notre planète (Lyons *et al.*, 2014). L'un des plus frappants exemples repose sur le fait que les Cyanobactéries oxyphototrophiques sont capables de produire une grande quantité d'oxygène (O_2) à travers la photosynthèse. Bien que le timing de leur émergence reste débattu, elles sont considérées comme les premiers producteurs d'O_2 sur la surface de la Terre. Ainsi, du fait de leur activité, l'ère du Paléoprotérozoïque (2,5–1,6 Ga) fut marquée par la première augmentation significative d'O_2 atmosphérique, communément appelée l'événement de la grande oxygénation (GOE; Holland, 2002), il y a 2,4 Ga. Cet évènement géochimique répandu sur l'ensemble de la surface terrestre a facilité l'apport de nouveaux composés oxydés dans l'océan, ce qui a vraisemblablement boosté la vie microbienne et déclenché une vie eucaryotique (*i.e.*, complexe).

La série du Francevillien au Gabon âgée de *ca*. 2,1 Ga s'est déposée dans des conditions environnementales principalement oxygénées, en plus d'héberger l'assemblage le plus ancien de fossiles macroscopiques (El Albani *et al.*, 2010, 2014, 2019). Ces macroorganismes coloniaux auraient pu être multicellulaires et fortement organisés du fait de leur grande diversité de taille et morphologie. Quelques preuves d'une activité microbienne ont été soulignées dans les roches du Gabon, incluant des structures ressemblant à des bactéries (Dubois *et al.*, 2015), des filaments de Cyanobactéries (Lekele Baghekema *et al.*, 2017), et des stromatolithes (Bertrand-Sarfati & Potin, 1994), mais il est encore incertain si une vie microbienne prospéra durant le vivant des macroorganismes complexes. De plus, de nombreuses études dans des environnements actuels et anciens ont mis l'accent sur le rôle clé des voiles bactériens dans le développement et la préservation d'animaux primitifs. Les communautés bactériennes peuvent fournir des « oasis à oxygène » localisés et stabiliser la surface du sédiment (*e.g.*, Gingras *et al.*, 2011; Buatois *et al.*, 2014). Dans ce sens, il semble concevable que des microbes auraient pu prospérer en association étroite avec les premiers organismes coloniaux connus pendant le moyen âge de la Terre.

Bien que les MRS ont largement été rapportées de roches sédimentaires archéennes (4,0–2,5 Ga) et du Mésoprotérozoïque (1,6–1,0 Ga) (Davies *et al.*, 2016), la diversité microbienne du Paléoprotérozoïque est peu connue. Peu de sédiments de ces âges sont non métamorphisés, ce qui explique le manque d'enregistrement des MRS. Néanmoins, les dépôts du Francevillien sont bien préservés avec un effet minimal de la température d'enfouissement et de la diagenèse tardive (Gauthier-Lafaye & Weber, 1989, 2003; Ngombi-Pemba *et al.*, 2014), ce qui a promu d'abondantes recherches sur la sédimentologie, pétrographie, minéralogie et géochimie, principalement publiées dans des thèses de doctorat (Weber, 1968; Azziley Azzibrouck, 1986; Gauthier-Lafaye, 1986; Pombo, 2004; Ossa Ossa, 2010; Ngombi Pemba, 2014; Bankole, 2015; Onanga Mavotchy, 2016; Dubois, 2017; Lekele Baghekema, 2017). Enfin, les minéraux argileux ont fait l'objet d'études approfondies pour élargir la compréhension (i) des conditions de dépôts dans lesquelles les macroorganismes vécurent, il y a 2,1 Ga (Ossa Ossa *et al.*, 2013; Ngombi-Pemba *et al.*, 2014; Bankole *et al.*, 2018) et (ii) du degré des transformations diagénétiques dans les sédiments.

Objectifs

La série du Francevillien a potentiellement abrité une vie microbienne. Tandis que les conditions environnementales (*i.e.*, abondance de nutriments, faible profondeur) ont vraisemblablement favorisé l'émergence d'une vie complexe, il est possible que le style de vie bactérien se soit également épanoui. En effet, des structures ressemblant à des MRS ont été récemment identifiées et collectées sur des grès et des argiles riches en matière organique (black shales). C'est pourquoi, le but de cette thèse est de déterminer leurs morphologies et textures, jusqu'à une échelle micrométrique, à travers une combinaison d'observations et d'une variété de techniques analytiques. Particulièrement, l'étude d'une supposée diversité microbienne dans des roches de 2,1 Ga serait unique. Par conséquent, ce travail vise à :

(i) Documenter la vie microbienne et décrire le schéma organisationnel et écologique du biota francevillien ;

(ii) Caractériser la minéralogie des minéraux argileux des MRS et du sédiment encaissant ainsi que de distinguer si les différences sont liées à des processus biologiques ;

(iii) Déterminer la distribution des éléments traces (TE) dans les MRS et le sédiment encaissant pour établir si un enrichissement biocontrôlé est enregistré ;

(iv) Investiguer les compositions isotopiques des MRS et du sédiment encaissant tout en contraignant les conditions locales du redox dans lesquelles les MRS se sont développées.

Structure de la thèse

L'agencement du manuscrit est organisé en quatre parties thématiques distinctes. Les techniques analytiques requises pour chaque investigation sont détaillées dans les sections concernées.

La partie 1 présente l'actuelle connaissance scientifique des voiles bactériens modernes ainsi que les caractères d'identification de telles structures organiques dans l'enregistrement géologique. Par la suite, l'histoire du Paléoprotérozoïque et le contexte géologique du Francevillien sont décrits. L'évolution sédimentaire et stratigraphique de la série du Francevillien avec l'apport des MRS est également mentionnée (Reynaud *et al.*, 2017; associated works §1). Pour finir, l'échantillonnage et la zone d'étude sont succinctement décrits.

La partie 2 met l'accent sur les résultats des analyses macroscopiques et des microtextures des MRS du Francevillien pour confirmer la biogénicité de ces structures. De plus, l'observation d'analogues actuels et fossiles est détaillée pour caractériser l'environnement de dépôt dans lequel les microorganismes prospérèrent. Cette section décrit également l'association entre les MRS et l'assemblage des macrofossiles du biota francevillien (El Albani *et al.*, 2019; associated works §2). La partie 2 est principalement dédiée à l'article publié dans le journal *Geobiology* :

Aubineau J, El Albani A, Chi Fru E, Gingras M, Batonneau Y, Buatois LA, Geffroy C, Labanowski J, Laforest C, Lemée L, Mángano MG, Meunier A, Pierson-Wickmann A-C, Recourt P, Riboulleau A, Trentesaux A, and Konhauser KO (2018) Unusual microbial mat-related structural diversity 2.1 billion years ago and implications for the Francevillian biota. Geobiology 16, 476–497.

La partie 3 présente les analyses géochimiques de la roche totale et *in situ* des éléments majeurs ainsi que la caractérisation minéralogique des MRS et du sédiment encaissant. Ensuite, l'interaction entre les microbes et les minéraux et le possible impact sur le climat de la Terre primitive sont discutés. Cette partie reproduit l'article publié dans le journal *Nature Communications*.

Aubineau J, El Albani A, Bekker A, Somogyi A, Bankole OM, Macchiarelli R, Meunier A, Riboulleau A, Reynaud J-Y, and Konhauser KO (2019) Microbially induced potassium enrichment in Paleoproterozoic shales and implications for reverse weathering on early Earth. Nature Communications 10: 2670.

La partie 4 détaille toutes les données géochimiques acquises pour les MRS et le sédiment encaissant. Tout d'abord, cette partie expose principalement les données géochimiques de la roche totale des éléments traces afin de vérifier si les MRS et le sédiment encaissant peuvent être différenciés. Le rôle des facteurs environnementales et la chimie de la colonne d'eau sur la distribution des TE ont fait l'objet d'une discussion détaillée. De plus, l'investigation du cycle de l'arsenic à travers le GOE (Chi Fru *et al.*, 2019; associated works §3) permet de discuter de l'émergence probable de communautés microbiennes adaptées en réponse à l'arrivée de composés oxydants et toxiques dans la série du Francevillien. Un article soumis dans le journal *Chemical Geology* constitue cette première partie. Deuxièmement, cette partie porte également sur la spéciation de fer pour contraindre les conditions locales du redox dans lesquelles les MRS se développèrent. Les isotopes stables du carbone et de l'azote des MRS et du sédiment encaissant ont été explorés afin d'évaluer les processus géomicrobiologiques impliqués dans l'environnement de dépôt. Cette deuxième section sous la forme d'un article en préparation complète la partie 4.

INTRODUCTION

Microbes, known for their large diversity in morphology, ecology, and phylogeny, are the Earth's oldest life forms, comprising archaeal and bacterial prokaryotic living beings. Biofilms and microbial mats, referring to a fruitful association of a variety of microbial communities, formed at the beginning of the Earth's history 3.5 to 3.8 billion years (Ga) ago. This microbial lifestyle provides a wide array of emergent properties compared of free-living bacterial cells. These particular properties encompass an enhanced sorption for resource capture, enzyme retention, social interactions for a dynamic remodeling of microorganisms, and localized physicochemical gradients (Flemming *et al.*, 2016). Biofilms and microbial mats have been extensively studied, however the terminology is often confusing without widely accepted definitions (Krumbein *et al.*, 2003). Nonetheless, a biofilm may refer to a cluster of cells embedded in an organic matrix and the structure is monolayer, while a microbial mat is defined by a multilayered distribution of bacterial communities. Thus, microbial mats may be seen as advanced biofilms. Considering the controversial terminology, the term 'mat-related structures' (MRS; Eriksson *et al.*, 2010) is chosen to encompass all fossilized features induced and/or preserved by microorganisms.

It is broadly recognized that microbes have played a major role in our planet's biogeochemical cycles and climates (Lyons *et al.*, 2014). One of the most striking examples relies on the fact that oxyphototrophic Cyanobacteria are able to produce a large amount of free oxygen (O_2) through photosynthesis. Although the timing of their emergence remains controversial, they are considered as the earliest O_2 producers on Earth's surface. Thus, due to their biological activity, the Palaeoproterozoic Era (2.5–1.6 Ga) was marked by the first significant rise of atmospheric O_2, known as the "Great Oxidation Event" (GOE; Holland, 2002) some 2.4 Ga ago. This globally extended geochemical event facilitated the delivery of oxidized compounds to seawater, likely triggering the microbial diversity and eukaryotic (*i.e.*, complex) life.

The *ca*. 2.1 Ga-old Francevillian Series in Gabon was primarily deposited in oxygenated environments (Canfield *et al.*, 2013), in addition to hosting the oldest macroscopic fossil assemblage (El Albani *et al.*, 2010, 2014, 2019). The colonial macroorganisms could have been multicellular and highly organized due to their large size and shape. A few evidence of microbial activity have been highlighted in the Gabonese rocks, including bacterial-like features (Dubois *et al.*, 2015), filamentous Cyanobacteria (Lekele Baghekema *et al.*, 2017), and stromatolites (Bertrand-Sarfati & Potin, 1994), but it remains unclear whether a microbial life flourished during the living of complex macroorganisms (El Albani *et al.*, 2014). Moreover, numerous studies from modern and ancient environments have stressed the key role of microbial mats in the development and preservation of early animals by proving localized "oxygen oases" and stabilizing the sediment surface (*e.g.*, Gingras *et al.*, 2011; Buatois *et al.*, 2014). In this regard, it seems plausible that microorganisms would have thrived in close association with the first known colonial organisms during Earth's middle age.

Although MRS have been widely reported from Archaean (4.0–2.5 Ga) and Mesoproterozoic (1.6–1.0 Ga) sedimentary rocks (Davies *et al.*, 2016), little is known about the Palaeoproterozoic microbial diversity. Few Palaeoproterozoic-aged sediments are unmetamorphosed, explaining the lack of MRS record. Nonetheless, the Francevillian deposits are well-preserved with a minimal effect of burial temperature and late diagenesis (Gauthier-Lafaye & Weber, 1989, 2003; Ngombi-Pemba *et al.*, 2014), which has promoted abundant investigations on sedimentology, petrography, mineralogy, and geochemistry, mostly in PhD thesis (Weber, 1968; Azziley Azzibrouck, 1986; Gauthier-Lafaye, 1986; Pombo, 2004; Ossa Ossa, 2010; Ngombi Pemba, 2014; Bankole, 2015; Onanga Mavotchy, 2016; Dubois, 2017; Lekele Baghekema, 2017). Particularly, clay minerals were extensively studied for widening the understanding of (i) depositional conditions in which the macrofossils lived, 2.1 Ga ago (Ossa Ossa *et al.*, 2013; Ngombi-Pemba *et al.*, 2014; Bankole *et al.*, 2018), and (ii) the degree of diagenetic transformations in the sediments.

Objectives

The Francevillian Series may have putatively hosted a microbial life. While environmental conditions (*i.e.*, abundance of nutrients, shallow depth) likely favored the emergence of complex life, a bacterial lifestyle may have also flourished. Indeed, MRS-like features have been recently identified and collected from sandstone and black shale facies. Therefore, the purpose of this thesis is to determine their morphology and texture down to the micrometric scale through a combination of field observations and means of analytical techniques. Importantly, the study of a putative microbial diversity in 2.1 Ga-old rocks is unique. Consequently, this work is designed to:

(i) Document the microbial life and describe the organizational and ecological pattern of the Francevillian biota;

(ii) Characterize the clay mineralogy of MRS and host sediments and distinguish whether differences are linked to biological processes;

(iii) Determine the distribution of trace elements (TE) of MRS and host sediments to establish whether a biocontrolled enrichment is recorded;

(iv) Investigate the isotope compositions of MRS and host sediments, and constrain redox conditions in which the Francevillian biota flourished.

Thesis structure

The layout of this manuscript is organized into four distinct thematic parts. The analytical techniques, required to the specific investigations, are detailed in sections concerned.

Part I presents the current scientific background on modern microbial mats and how identify such organic features in the geological record. Then, the Palaeoproterozoic history and Francevillian geological background are given. The newly documented stratigraphic and sedimentary evolution of the Francevillian Series with the contribution of MRS is then mentioned (Reynaud *et al.*, 2017; associated works §1). Lastly, the studied area and sampling are succinctly described.

Part II focuses on the results of the macroscopic, and microtexture analyses of Francevillian MRS to confirm the biogenicity of these structures. In addition, an examination with modern and fossil equivalents is detailed for characterizing the depositional setting in which the microorganisms thrived. This section also describes the association of MRS with the macroscopic fossil assemblage of the Francevillian biota (El Albani *et al.*, 2019; associated works §2). Part II is mainly dedicated to the published article in *Geobiology* journal:

Aubineau J, El Albani A, Chi Fru E, Gingras M, Batonneau Y, Buatois LA, Geffroy C, Labanowski J, Laforest C, Lemée L, Mángano MG, Meunier A, Pierson-Wickmann A-C, Recourt P, Riboulleau A, Trentesaux A, and Konhauser KO (2018) Unusual microbial mat-related structural diversity 2.1 billion years ago and implications for the Francevillian biota. Geobiology 16, 476–497.

Part III provides the bulk-rock and *in situ* geochemical analyses of major elements and clay characterization of MRS and host sediments. Then, it discusses the microbe-mineral interactions and the possible impact on early Earth's climate. This part reproduces the published article in the journal *Nature Communications*.

Aubineau J, El Albani A, Bekker A, Somogyi A, Bankole OM, Macchiarelli R, Meunier A, Riboulleau A, Reynaud J-Y, and Konhauser KO (2019) Microbially induced potassium enrichment in Paleoproterozoic shales and implications for reverse weathering on early Earth. Nature Communications 10: 2670.

Part IV presents the overall geochemical analyses of the MRS and their host sediments. First, this part outlines the whole-rock and *in situ* geochemical data of trace elements to ascertain whether the MRS and host sediments can be distinguished. It also discusses the role of environmental factors and water column chemistry on the TE distribution. In addition, the investigation of arsenic cycling across the GOE (Chi Fru *et al.*, 2019; associated works §3) allows to discuss of the likely emergence of adapted microbial communities in response to the rise of toxic, oxidized arsenic species in the Francevillian Series. A submitted article in the journal *Chemical Geology* constitutes this section. Second, this part also deals with iron speciation to constrain local redox conditions in which the MRS developed. The stable isotopes of carbon and nitrogen in both the MRS and host sediments were explored in order and to establish the geomicrobiological processes that have been involved in the depositional setting. This second section under the form of an article in preparation completes the part 4.

PART 1. STATE OF THE ART

1.1. Introduction to microbial life

1.1.1. Terminology

Microbial mats can be perceived as an ecosystem due to the occurrence of essential trophic levels and a specific organization of communities (Figure 1A) (Stolz *et al.*, 1989). A classic view of a microbial mat consists of an uppermost community of oxygenic photosynthetic Cyanobacteria (green layer) overlying a mixed phototrophic-chemolithoautotrophic population (purple layer). Respirers (*i.e.*, heterotrophs) and fermenters dominate the lowermost domain in anoxic conditions, resulting in black layers (Nisbet & Sleep, 2001; Des Marais, 2010). Microbes secrete a cohesive organic matrix, referred to as extracellular polymeric substances (EPS), which provides an attachment to the sediment surface, protective coating and growth optimization (Decho, 1990, 2000). Moreover, lithification predominantly due to calcium carbonate ($CaCO_3$), oxide and silicate precipitations, may arise in the organic structure, facilitating their preservation in the rock record (Dupraz & Visscher, 2005). The chemical requirements and processes leading to the precipitation of carbonates have been extensively reviewed by Dupraz & Visscher (2005) and Dupraz *et al.* (2009). The alkalinity engine and the nature of EPS are the main parameters controlling the mineralization. Following lithification, microbial mats form organosedimentary structures widely regarded as stromatolites or microbialites (Riding, 2011).

Kalkowsky (1908) first introduced the term “stromatolite”—from Greek *stromat* “to spread out”, *lithos* “stone” (Riding, 2000)—and stated that “all stromatolites show distinct layering in vertical section”. Besides, he was convinced that microbes were somehow involved. However, it raised the question of whether stromatolites are biogenic or abiogenic formations. After decades of research, stromatolites was defined as “megascopic organosedimentary structures produced by sediment trapping, binding and/or precipitation as a result of growth and metabolic activity of organisms, primarily blue-green algae” by Awramik & Margulis (1974), but the biogenicity of this statement was difficult to solve when applied to fossilized remnants. Semikhatov *et al.* (1979) bypassed the biogenicity requirement by describing stromatolites as “laminated, lithified, sedimentary growth structures that accrete away from a point or limited surface of attachment”. In this regard, stromatolites are abiogenic and/or biogenic deposits. Riding (2011) reconciled all available definitions by proposing that “stromatolites are macroscopically layered authigenic microbial sediments with or without interlayered abiogenic precipitates” (Figure 1B). In addition, authigenesis does not necessarily imply a carbonate neoformation, but silica (Jones *et al.*, 2005) and evaporates (Pope *et al.*, 2000) may compose the stromatolites.

Following Awramik & Margulis (1974)'s definition, a stromatolite does not require a laminated structures, instead a microbial view prevails. Thus, the term "microbialite" was introduced to compensate the gap between a layered macrofabric and a bacterial origin (Burne & Moore, 1987). Microbialites are "organosedimentary deposits that have accreted as a result of a benthic microbial community trapping and binding detrital sediment and/or forming the locus of mineral precipitation" (Figure 1C). Regardless of the macrofabric, microbialites encompass all biologically derived organosedimentary structures. Hence, laminated (stromatolite) and non-laminated (*e.g.*, clotted) microbial deposits coexist.

Figure 1: Microbial structures. (**A**) A modern non-lithified microbial mat from Cayo Coca lagoon, Cuba. Modified from Pace (2016). (**B**) A 2.72 Ga-old stromatolites from Tumbiana Formation, Australia. Modified after photo published in Lepot *et al*. (2009). (**C**) A modern microbialite from Cayo Coca lagoon, Cuba. Modified from Pace (2016).

1.1.2. Modern microbial mats

The occurrence of microbial mats is globally reported from hypersaline and tidal depositional environments due to the light-dependent requirement of photosynthetic microorganisms and favorable ecological parameters (Noffke *et al.*, 2002; Mata & Bottjer, 2009). However, a diversity of chemolithoautotrophic microorganisms may also thrive in deep marine settings, but the growth and generation times are limited (Jørgensen & Boetius, 2007). Bacterial mats even colonize extreme environmental conditions such as acidic geothermal springs (Beam *et al.*, 2016) and subglacial lakes in Antarctica (Christner *et al.*, 2014; Sumner *et al.*, 2015). A recent study on metagenomics analyses have shown that more than 7,300 species compose the microbial diversity within biofilms (Zhang *et al.*, 2019).

The wide range of microbial metabolisms affects biogeochemical cycles of Earth’s surface by oxidizing or reducing chemical compounds. The biologically mediated carbon (C) cycle is intimately linked to the cycling of oxygen, nitrogen, and sulfur, as the latter provide electron donors/acceptors (Canfield & Des Marais, 1993; Dupraz *et al.*, 2009). This has direct implications for the evolution of biosphere and climate.

a. Formation and organizational pattern

There is a vast amount of literature pertaining to the formation of microbially induced sedimentary structures (MISS; Noffke *et al.,* 1996), features attributed to microbial mats of filamentous bacteria, such as Cyanobacteria, trapping siliciclastic sediments in energetic tidal flat settings (*e.g.*, Schieber, 2007; Noffke, 2010). Indeed, the hydraulic pattern must be moderated because waves and currents in such conditions are strong enough to prohibit huge settlement of fine-grained particles (Schieber, 1998; Noffke, 2009). The filamentous bacteria trapped and bound sediments with their EPS secretions as they grew upward, and this biostabilization method helped them withstand erosion by waves and currents. The distinctive sedimentary characteristics of MISS can also be found in mats forming in modern tidal flats (*e.g.*, wrinkle structures, roll-up structures, and laminated textures) where fossilized equivalents are made up of carbon and iron oxide minerals such as hematite (Fe_2O_3) and siderite ($FeCO_3$). Further, Cyanobacteria are able to move through sand upward, but they cannot go across mud (Noffke, 2009, 2010).

An assemblage of microbial communities often consists of multiple trophic levels (*i.e.*, primary producers, consumers, and decomposers). Steep physical and chemical gradients (*i.e.*, light, pH, oxygen, and sulfide) with diel fluctuations characterize these biological structures (Figure 2), resulting in distinct microenvironments (Dupraz & Visscher, 2005; Dupraz *et al.*, 2009; Gingras *et al.*, 2011). The metabolic stratification displays a relationship with the thermodynamic yield, resulting from oxido-reduction reactions of organic and inorganic compounds. Indeed, the microbial metabolism with the highest energetic yield is found in the uppermost part of the mat. As such, a vertically laminated arrangement of microbes takes place in which bacterial species interact each other. Thus, six major groups of microorganisms primarily compose a microbial mat (Visscher & Stolz, 2005): (i) oxygenic photosynthetic Cyanobacteria are the major primary producers (Jørgensen, 2001) and provide organic compounds and O_2, (ii) aerobic heterotrophic bacteria have the highest energetic yield by respiring oxygen and organic carbon, (iii) Sulfur-based chemolithotrophic bacteria coupled to C fixation oxidized sulfur compounds with different electron acceptors, (iv) anoxygenic photosynthetic green and purple sulfur bacteria generate carbonaceous material and sulfate or iron oxides instead of O_2, (v) anaerobic heterotrophic bacteria gain energy from respiration of inorganic and organic compounds in the absence of O_2, and (vi) methanogens produce methane (CH_4) by consuming carbon dioxide (CO_2) and methanogenesis is energetically the least favorable respiration metabolism (Lovley & Klug, 1983).

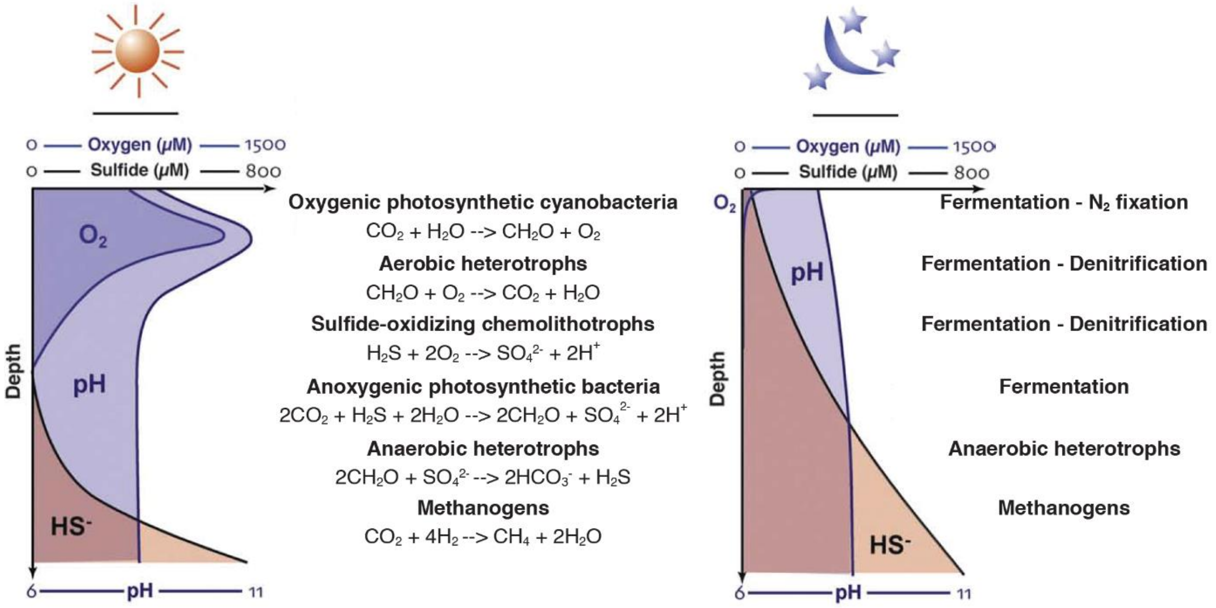

Figure 2: Diel fluctuations of vertical geochemical gradients in microbial mats that are composed of six major metabolic pathways. Daytime and nighttime metabolic and geochemical reactions lead to distinct microenvironments. Modified from Dupraz *et al*. (2009).

During daytime, the partial pressure of O_2 within cyanobacterial layers is higher than in the overlying water column, and decreases dramatically to meaningless levels with increasing depth in the sulfate-rich layers of the microbial mat (Gingras *et al.*, 2011). Thus, the microbial carpet starts to be anoxic, and then sulfidic in the deepest part due to the activity of sulfate-reducing bacteria. At night, photosynthesis ceases and microbial mats rapidly become anoxic and sulfidic close to the mat-water interface because of O_2 consumption by aerobic respirers. Cyanobacteria may also fix nitrogen—the reduction of molecular nitrogen (N_2) to ammonium

(NH_4^+)—through the nitrogenase enzyme (Glass *et al.*, 2009), leading to the production of bioavailable nitrogen that is essential to all life forms. However, nitrogenase is inhibited with high oxygen concentrations and Cyanobacteria lack O_2-protection mechanism. Thus, the enzyme activity mainly occurs during nighttime to counter the oxygen sensitivity (Stal, 2001). In addition, methanogenesis depends on the Cyanobacteria-driven flux of H_2 (Hoehler *et al.*, 2001) resulting from N_2 fixation and fermentation (Fay, 1992; Stal & Moezelaar, 1997). Regardless of the diel fluctuation, fermentation, in which the same organic compound acts as electron donor and acceptor, degrades large organic molecules to low-molecular weight matter (Dupraz *et al.*, 2009). In the absence of O_2, this metabolic process is widespread among microorganisms (Visscher & Stolz, 2005).

b. Nature and role of EPS

The EPS, which surround cells, can be perceived as an extension of microbial cells (Costerton *et al.*, 1995). The EPS matrix consists of high molecular weight polysaccharides, low molecular weight dissolved organic carbon (*e.g*. lactate, acetate), and even extracellular DNA (Sutherland, 2001; Decho *et al.*, 2005). A large range of microorganisms secretes EPS, such as photoautotrophic and heterotrophic bacteria, but the most important EPS producers are undoubtedly oxygenic Cyanobacteria and to a lesser extent sulfate-reducing bacteria (Richert *et al.*, 2005; Braissant *et al.*, 2007). The production and secretion of an organic mucus fulfill fundamental functions within microbial mats, especially for promoting growth (Decho, 1990, 2000). First, the anchoring of microbial cells to sediments is intense, and the microbially mediated geochemical gradients are maintained. Second, EPS stabilize depositional surfaces and help microbial communities to resist to moderate hydrodynamic conditions, such as waves and tidal currents. Third, EPS act as a shield against desiccation, UV exposure, and nutrient shortages. Fourth, the organic matrix creates a physical boundary between microbes and antimicrobial agents, predators, and toxic metals by diffusion-reaction inhibition, leading to a tolerance (Flemming *et al.*, 2016).

The EPS matrix is known for its high cation-binding capacity due to the presence of negatively charged macromolecules, such as carboxyl/hydroxyl, sulfate, and amino groups that strongly chelate divalent cations (De Philippis *et al.*, 2001). Moreover, the mucus is a template for crystal nucleation via a rearrangement of macromolecules during diagenesis (Trichet & Défarge, 1995). The EPS matrix of microbial mats is a key player in the carbonate precipitation and subsequent formation of microbialites, but strict requirements (saturation index and nature of biomass) must be met (Arp *et al.*, 1999; Dupraz & Visscher, 2005; Visscher & Stolz, 2005; Dupraz *et al.*, 2009; Pace, 2016). Microbial metabolisms as well as diel fluctuations influence the carbonate precipitation and dissolution.

c. Biomineralization

Extracellular polymeric substances remove Ca^{2+} and Mg^{2+} cations from surrounding environment and strongly bind them in the matrix, inhibiting the carbonate precipitation. This process is referred to as “anticalcification” (Westbroek *et al.*, 1994). Even in alkaline environments, the lack of free Ca^{2+} in microbial mats has been observed (Dupraz & Visscher, 2005). Regardless of the microbial metabolism involved in the secreted mucus, the calcium binding capacities range from ~50 to 180 mg Ca/g EPS (Perry *et al.*, 2005; Ortega- Morales *et al.*, 2007). The reduction of the Ca-binding capacity in the EPS matrix leads to $CaCO_3$ precipitation via three different pathways (Figure 3). Thus, the biologically induced and biologically influenced mineralization that accomplished through diagenetic organomineralization *s.s.* (Trichet & Défarge, 1995) or saturation of the cation binding capability (Arp *et al.*, 2003) involve the alteration of mucus (Dupraz & Visscher, 2005; Dupraz *et al.*, 2009). The biologically induced mineralization refers to interactions between a biological activity and their environment, leading to a precipitation from an inorganic solution (Frankel & Bazylinski, 2003), whereas the biologically influenced mineralization results in passive mineralization of EPS matrix where environmentally driven parameters promote precipitation (Dupraz *et al.*, 2009). Organisms are also capable of creating an extra- or intracellular mineral phase by actively regulating their biomineral formation. The mechanism is known as the biologically controlled mineralization (Bazylinski & Frankel, 2003). This process is radically different, and therefore it will not be described in this section.

The organic mucus is used as C source for the respiration of heterotrophic bacteria. When EPS are rapidly consumed over the production rate, Ca^{2+} and other cations are liberated from the polymers, increasing the saturation index (Dupraz & Visscher, 2005; Visscher & Stolz, 2005). In addition, the pH fluctuates as a consequence of the coupled microbial-geochemical reactions. For instance, sulfate reducers increase the alkalinity, promoting $CaCO_3$ precipitation, while aerobic heterotroph decrease it, leading to the $CaCO_3$ dissolution. Accounting for more than 80% of organic carbon oxidation, anaerobic respiration is therefore a fundamental process in the microbial EPS degradation and subsequent $CaCO_3$ precipitation (Canfield *et al.*, 1993). Both increase in calcium concentration and alkalinity result in biologically induced mineralization.

Trichet & Défarge (1995) defined the organomineralization *s.s.* as a diagenetic rearrangement of Ca-hosting acidic groups in order to promote a template for $CaCO_3$ precipitation. The alignment of these groups that allow nucleation sites to be organized is somehow theoretical. A continuous supply of cations can lead to the saturation of the cation-binding capacity of EPS, together with the presence of free Ca^{2+} and alkaline conditions, would force the EPS mineralization (Arp *et al.*, 1999). The strong abundance of calcium ions may occur in evaporitic or upwelling settings (Arp *et al.*, 2003). Both diagenetic alteration of EPS matrix and saturation of the binding capacity enhance precipitation, known as the biologically influenced mineralization.

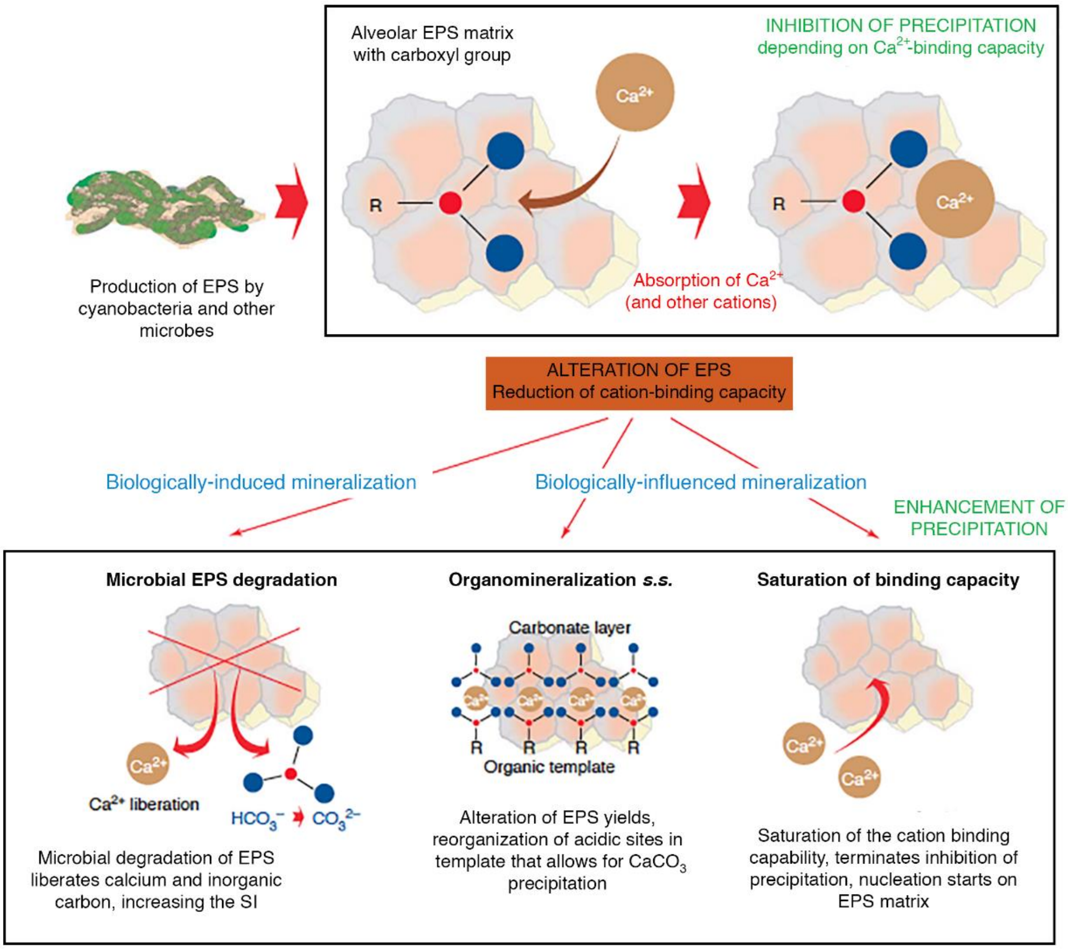

Figure 3: The role of EPS in calcium (and other cations) uptake and liberation. Biologically induced and/or biologically influenced mineralization may promote carbonate precipitation following three main pathways, including (i) anaerobic microbial respiration, (ii) diagenetic alteration, and (iii) environmentally driven saturation of binding capacity. Modified from Dupraz & Visscher (2005).

1.1.3. Evidence for microbial activity at the beginning of Earth's history

The organic carbon constitutes the fossil residue of primary biogenic substances. Hence, numerous investigations were conducted to the quest of evidence for life and microbial metabolisms in Archaean and Palaeoproterozoic deposits. This challenge is even more difficult because these old rocks are poorly preserved or transformed by diagenesis or metamorphism. In addition, contaminated and/or degraded organic matter predominantly composes the Archaean fossil record, but the preservation of biological structures and/or biogeochemical by-products (*e.g.*, light C isotopes, biomarkers) may arise (see section 1.1.4). The

Palaeoproterozoic sediments show abundant and diagnostic biological activities (Javaux *et al.*, 2013), highlighting the biosphere evolution and indicating that the Palaeoproterozoic Era has been a crucial period in Earth and life history.

a. Stromatolites

Stromatolites are one of the most widespread, shallow-water palaeobiological features in ancient rocks due to the dominant occurrence of light-driven bacterial metabolisms. The different stromatolite morphotypes also indicate physical and chemical interactions with the environmental conditions (Dupraz & Visscher, 2005; Jahnert & Collins, 2012; Suosaari *et al.*, 2016). Indeed, the distribution and morphological textures of modern stromatolites across tidal flats depend on bathymetry, hydrodynamic regime, sedimentological parameters, and intrinsic microbial proprieties (*e.g.*, growth rate, microbial communities).

A rapid emergence of life has been proposed (Nutman *et al.*, 2016), resulting from the observation of 3.7 Ga-old stromatolite-like structures from metacarbonate rocks of Isua supracrustal belt, southwest Greenland. Through a three-dimensional analysis, these putative biological structures are, however, highly challenged (Allwood *et al.*, 2018). The latter authors have indicated that an abiotic origin and post-depositional deformations would have led to their formation. Walter *et al.* (1980) have reported the Earth's earliest convincing evidence of stromatolites from the *ca*. 3.48 Ga-old Warrawoona Group, Pilbara craton, Western Australia. These strata also host newly observed stromatolite fabrics from terrestrial hot spring deposits (Djokic *et al.*, 2017), suggesting an early colonization of microbes on land surfaces. The Archaean Eon war marked by the prosperity of stromatolites, as indicated by at least >40 known occurrences (Schopf *et al.*, 2007). For instance, well-developed Archaean fossil stromatolites have been reported from the 3.43 Ga-old Warrawoona Group, Pilbara craton, Western Australia (Allwood *et al.*, 2006), the 2.98 Ga-old Insuzi Group, Kaapvaal craton, Eastern South Africa (Beukes & Lowe, 1989), the *ca*. 2.73-2.72 Ga-old Fortescue Group, Pilbara craton, Western Australia (Lepot *et al.*, 2008, 2009; Flannery *et al.*, 2016), the 2.7 Ga-old Platberg Group, Kaapvaal craton, Northern South Africa (Wilmeth *et al.*, 2019), and the *ca*. 2.6-2.5 Ga-old Cambell Group, Kaapvaal craton, South Africa (Altermann & Schopf, 1995; Sumner & Grotzinger, 2004).

Considering that the lack of microfossils is relatively common in Archaean stromatolites, non-biological processes have been raised for interpreting these structures (Lowe, 1994; Grotzinger & Knoll, 1999). That said, the recognition of distinct laminated morphotypes that are heterogeneous in size and shape and broadly extended in space, as well as the specific relationships within their environmental setting argue for strong biogenic indicators in the geological record (Allwood *et al.*, 2006). Besides, diagnostic microtextures must be demonstrated for verifying the biogenicity of such structures. Specific criteria, including comparisons with modern equivalents, high resolution of organo-mineral interactions, bubble-like features inferred to a microbial gas production (Figures 4A, B), and/or more generally the presence of organic laminae, are consistent with biologically influenced formations (Lepot *et al.*, 2008; Bosak *et al.*, 2009, 2013).

b. Microbial mat remnants

The inherent cohesiveness of mat layers can lead to a wide range of sedimentary features in tidal depositional environments during a physical destruction of mat-bound surfaces. Strong currents and active wave motion lead to the formation of detached, torn, and reworked microbial mats. Eroded mat surfaces, redeposition of deformed mat layers, and mat fragments form well-known structures identified as flipped-over edges, rolled-up features, and microbial sand chips, respectively (Eriksson *et al.*, 2007; Noffke, 2010). Upon a long time of subaerial exposure, desiccation of microbial mats leads to shrinkage cracks. The mat margin is curled up because the mat structure atop the depositional surface shrinks significantly more than the underlying substrate. Hence, these sedimentary structures that are unlikely to arise in rocks without biological mediation are used to infer the presence of microbial mats in ancient rocks, assuming that ancient mat layers had similar or near similar physicochemical properties as today.

Stinking examples of Archaean fossil mat fragments come from the *ca*. 3.48 Ga-old Warrawoona Group, Pilbara craton, Western Australia (Noffke *et al.*, 2013), the *ca*. 3.42 Ga-old Buck Reef Chert, Barberton Greenstone Belt, South Africa (Figure 4C) (Tice & Lowe, 2004, 2006a; Tice, 2009), the 3.33 Ga-old Moodies Group, Kaapvaal craton, Northeastern South Africa (Westall *et al.*, 2015), and the 2.9 Ga-old Mozaan Group, Kaapvaal craton, Northeastern South Africa (Noffke *et al.*, 2008). These observations also allow to refine palaeodepositional conditions in which the microbial mats flourished. Combined with the isotopes analyses, the involvement of one or more microbial communities in the construction of mat layers can be deduced. Diverse phototrophic, chemolithotrophic, and/or chemo-organotrophic bacterial metabolisms have been invoked in Archaean-aged sediments (Tice & Lowe, 2004, 2006b; Westall *et al.*, 2015), suggesting an early microbial diversification.

c. Microfossils

Microfossils may express various morphologies, comprising spherical, rod- to starlike, and filamentous shapes that can be similar to microfossil-like artefacts produced in natural environments (Wacey, 2009). It is, thus, heavily difficult to distinguish them from inorganic structures that could mimic biological processes. Moreover, Archaean rocks have experienced long and complex histories, decreasing the preservation potential of their primary signature.

The organic matter is highly subjected to hydrothermal alteration of younger fluid circulation (Buick, 1990), but the crystal morphology surrounding microfossils may be relevant for verifying whether the host rocks have undergone post-depositional processes.

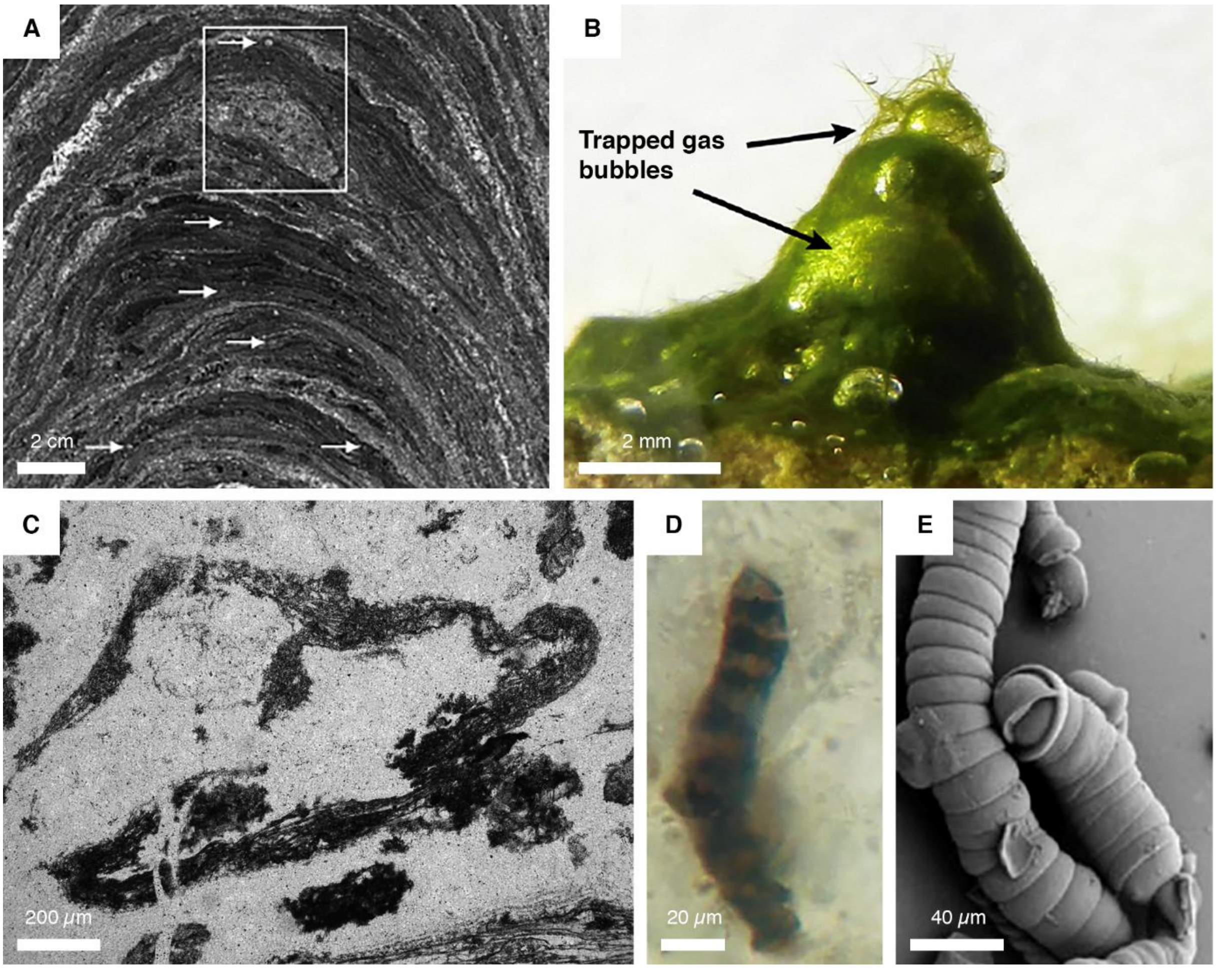

Figure 4: Examples of evidence for the earliest signs of life. (**A**) Optical photomicrographs of a stromatolite. Inset shows a fossilized bubble that likely suggests a mat-related gas production. Arrows point to tiny bubble-like features. Modified after photo published in Bosak *et al*. (2009). (**B**) Modern analogue of microbial mat producing and trapping O_2-rich bubbles. Modified after photo published in Homann *et al*. (2015). (**C**) Rolled-up mat fragment. Modified after photo published in Tice (2009). (**D**) Controverted bacterial filament. Modified after photo published in Schopf *et al*. (2002). (**E**) Synthetic inorganic filaments mimicking biogenic filaments. Modified after photo published in Garcia-Ruiz *et al*. (2003).

To avoid mistaking contaminants, the syngenicity of the biological material must be well constrained (Javaux *et al.*, 2010). For instance, spectroscopy Raman combined with other proxies (*e.g.*, minerals formed during metamorphism and O isotopes) provide crucial information on organic matter maturity. The originally carbonaceous cellular structures coupled to biominerals and diagenetic mineral replacements indicate the true biogenicity of microfossils (see review in Javaux & Lepot, 2018). Other important challenges in recognizing the true antiquity of microfossils include taxonomic identification. Based on the analysis of cell morphology and structure, prokaryotic and eukaryotic microfossils can be distinguished.

The *ca*. 3.465 Ga-old Apex chert of northwestern Australia putatively hosts the oldest known assemblage of microfossils (Figure 4D) (Schopf, 1993; Schopf *et al.*, 2002, 2007). It consists of preserved morphologically diverse microscopic fossils. Over the last two decades, numerous investigations were conducted for demonstrating their origin, in consequence of their controversy. The Apex microfossils are challenged because they were reported from a metalliferous hydrothermal vein chert, which would have favored the formation of non-syngenetic structures (Brasier *et al.*, 2002, 2005). Moreover, these microfossil-like forms would derive from amorphous graphite. The morphology of pseudo-microfossils also mimics the abiotic reorganization of organic material during silica recrystallization. Some other researches have highlighted the fact that synthetic silica-coated carbonate crystals generate biological-like forms (Figure 4E) (Garcia-Ruiz *et al.*, 2003), strongly similar to those of Apex microfossils. Recently, high resolution *in situ* geochemical analyses would confirm the biogenicity of the oldest known Archaean microbes, stimulating new debates on the earliest life forms (Schopf *et al.*, 2018).

Convincing evidence of a distinctive cluster of microfossils—subsequently called Gunflint-type assemblages—was primarily found in the Palaeoproterozoic Gunflint Iron Formation, Canada (Figure 5) (Barghoorn & Tyler, 1965). Stromatolitic cherts associated with iron-rich deposits commonly host these Gunflint-type assemblages in various Palaeoproterozoic rocks (*e.g.*, Walter *et al.*, 1976; Yun, 1984; Knoll *et al.*, 1988; Amard & Bertrand-Sarfati, 1997; Lekele Baghekema *et al.*, 2017). The remarkable preservation of Gunflint-type assemblages in the geological rock record were used as a benchmark for the search of the earliest signs of life in Archaean deposits. The Gunflint-type assemblages host microfossils, among which the dominant bacterial species could represent possible oxygenic photosynthesizers, Mn- /Fe- / S-oxidizing bacteria, and/or heterotrophs (Barghoorn & Tyler, 1965; Cloud Jr., 1965; Strother & Tobin, 1987; Knoll *et al.*, 1988; Lepot *et al.*, 2017). Although environmental conditions were certainly stressful for most of the domain of life (see section 1.2), the wide range of metabolic participation observed in Gunflint-type assemblages provide key information on the Palaeoproterozoic microbial biosphere.

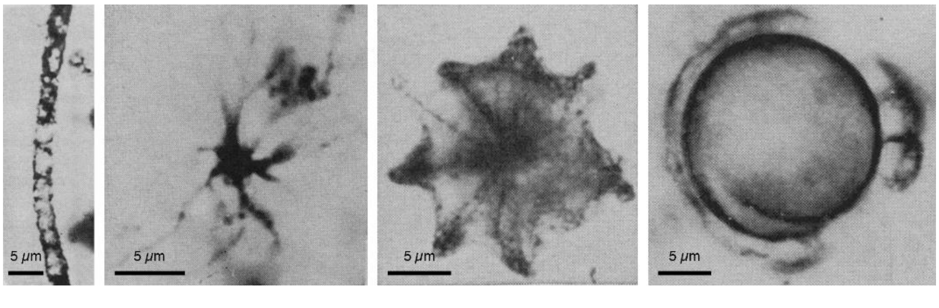

Figure 5: A Gunflint-type assemblage from the earliest discovery of Gunflint Iron Formation. Filamentous, star-shaped, umbrella-like, and spheroidal morphologies (from left to right) are the most abundant features. Modified after photos published in Barghoorn & Tyler (1965).

1.1.4. Recognition of biosignatures in Archaean and early Proterozoic sediments

Biological structures are crucial for identifying early life, however taphonomical processes may have not been suitable for most of samples. Besides, pieces of rocks that are collected from drill cores may not exhibit the specific morphological textures. Therefore, other analytical technics are used. A robust assessment for ancient signs of life relies on convergent evidence from different disciplines such as palaeobiology, organic and inorganic geochemistry, and geology. In agreement with these fields of study, Wacey (2009) listed several biogenicity criteria, including one that takes into account the recognition of biologically mediated products (*e.g.*, minerals, carbonaceous compounds). In this section, I outline the most abundant working tools that facilitate the search of such organic signatures and former bacterial metabolisms in the geological rock record.

a. Hydrocarbons biomarkers

The cyclic terpenoids—steranes, hopanes and cheilanthanes—usually constitute a small amount of the soluble fraction of organic matter (*i.e.*, bitumen) (Figure 6). These compounds widely promote the search for a palaeobiological source. Although cheilanthanes are detected in Precambrian rocks, there is no known bacterial synthesis responsible of their generation (Brocks *et al.*, 2003). However, hopanes and steranes are unambiguously biogenic features. These hydrocarbon biomarkers are molecular fossils of cell membrane lipids of all living organisms. They provide pertinent information of the presence and abundance of major taxonomic groups due to their specific structure and organic partitioning (Buick, 2008). Hopanes are derived from hopanoids, which are produced by bacterial biosynthesis, while steranes are derived from sterols, which are ubiquitous features of domain Eukarya (Summons *et al.*, 2006). In addition, the synthesis of steranes requires the presence of O_2. Thus, the occurrence of steranes in sediments not only indicates eukaryotic organisms, but also aerobic microbial metabolisms. These key evidence might give rise to elucidate the timing of advent of biological oxygen cycling (*e.g.*, Brocks *et al.*, 2003). Besides, the relative abundance of steranes in sediments supports major shifts in the evolution of eukaryotes through time (Grantham & Wakefield, 1988). Finally, the ratio of steranes to hopanes records the balance of eukaryotic *vs*. bacterial inputs into ancient marine deposits (Brocks *et al.*, 2017).

Lipid biomarkers have been detected in Archaean sedimentary rocks (Brocks *et al.*, 1999, 2003; Waldbauer *et al.*, 2009), but their syngenetic origin is controversial. Anthropogenic contaminants are largely the cause of post-depositional contamination either by infiltration of younger organic molecules or subaerial exposure (Illing *et al.*, 2014; Leider *et al.*, 2016). Brocks *et al.* (2003) reported steranes from 2.7 to 2.5 Ga-old shales in the Pilbara Craton, Western Australia, suggesting that oxygenic photosynthesizers and eukaryotes arose before the permanent rise of oxygen on Earth's surface, at the Archaean-Proterozoic boundary (see section 1.2.2). Nonetheless, French *et al.* (2015) analyzed ultraclean Archaean drill cores from the same location, and subsequently demonstrated and reassessed these steranes as overmature hydrocarbons and contaminants. Most of Archaean strata, if not all, have experienced high and prolonged burial temperatures, suggesting that these rocks overpassed the appropriate thermal maturity window for recording syngenetic lipid molecular fossils.

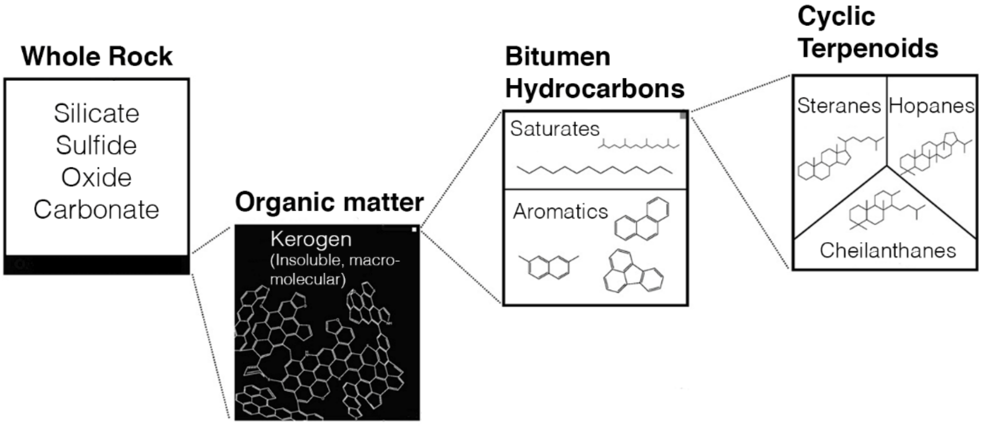

Figure 6: Schematic model of biomarker distribution in organic matter of ancient rocks. Modified from Waldbauer *et al*. (2009).

Supporting evidence of biomarkers from Archaean rocks should be taken with considerable cautions, but the molecular clock study helped to constrain the dynamic of sterol synthesis (Gold *et al.*, 2017). The latter authors predicted that the presence of a simple sterol (*i.e.*, protosterol) synthesis, inferred as the divergence time between the bacterial domain and stem group of eukaryotes, would have been close to the Archaean-Palaeoproterozoic boundary. If this is correct, the protosterol production is, thus, consistent with the widespread availability of free O_2 in oceans and atmosphere at that time. So far, the oldest convincing evidence of biologically derived steranes comes from the Cryogenian Period (Brocks *et al.*, 2017). The mid-Proterozoic rocks have shown the absence of organic biomarker fingerprints of eukaryotes, which is an accepted consensus after numerous investigations (Blumenberg *et al.*, 2012; Jarrett *et al.*, 2019; Nguyen *et al.*, 2019).

b. Stable isotopes

The isotope ratio of any element, which is revealed by "light" and "heavy" reservoirs of fractionated molecules, is an effective tool for recognizing biological signatures. Life preferentially takes advantage of light isotopes, creating an isotopic disequilibrium possibly preserved in ancient rocks. Post-depositional abiotic processes may modify the primary signature, but geological and geochemical evidence must confirm or refute such assertions.

The isotopic fractionation is mass-dependent, meaning that kinetic processes yield compounds isotopically different from the precursor substances. In this section, I document the most commonly used stable isotopes (carbon, nitrogen, and sulfur) to detect microbial activities.

The stable isotope compositions are reported in the δ-notation (per mil, equation 1), which describes the deviation of the isotope ratio of a sample relative to that of a known standard for a chemical element (E):

$$\delta^{heavy}E\ (‰) = \left[\frac{\left(\frac{heavyE}{lightE}\right)sample}{\left(\frac{heavyE}{lightE}\right)standard} - 1\right] \times 1000 \tag{1}$$

Carbon: Nier & Gulbransen (1939) published a pioneer work about the redistribution of carbon isotopes after the conversion of inorganic C into biogenic material. It is now firmly established that autotrophic organisms are the primary producers since they fix inorganic CO_2. Because of the kinetic isotope effect during the enzymatic CO_2-fixing reactions, autotrophs take up the light ^{12}C over heavy ^{13}C isotopes (Schidlowski, 1987). Heterotrophs use a ^{12}C-enriched, autotrophically derived carbonaceous material for their own metabolic pathway, but heterotrophy leads to a slight ^{13}C enrichment (Hayes *et al.*, 1990). Thus, all forms of biogenic organic matter consist of a preferential accumulation of ^{12}C, while the other inorganic C pools (*e.g.*, atmosphere, oceans, and marine carbonates) remain weakly fractionated. The $\delta^{13}C$ (deviation from Vienna-Pee Dee Belemnite standard) of organic substances are highly negative (< -10‰), which provides evidence for biological signals, whereas the inorganic C pools display $\delta^{13}C$ values around 2 and -7‰ (Figure 7). The C fixers assimilate either CO_2 or CH_4 into living biomass, resulting in a wide range of C isotope fractionations (Schidlowski, 2001; Zerkle *et al.*, 2005; Berg *et al.*, 2010).

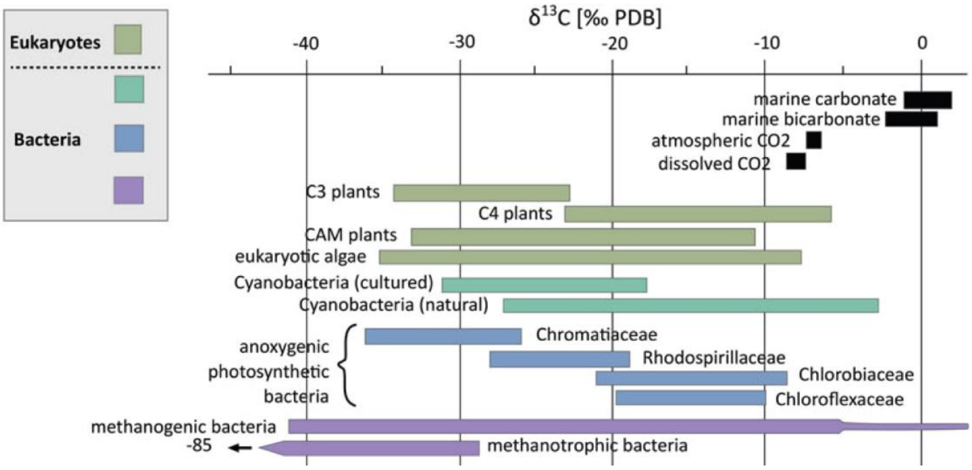

Figure 7: $\delta^{13}C$ composition of inorganic carbon reservoirs and autotrophs (both bacterial and eukaryotic domains). Modified from Schirrmeister *et al*. (2016).

Nitrogen: Nitrogen (N) is one of the most essential nutrients to all organisms on Earth, required for the formation of nucleic acids, lipids, proteins. Its bioavailable reduced form (ammonium, NH_4^+) is the primary source to the biosphere (Stüeken *et al.*, 2016), while the oxidized N species are strongly oxidizing redox compounds. The latter may yield a large amount of electrochemical energy for metabolic activity (Schoepp-Cothenet *et al.*, 2013).

Nitrogen isotope geochemistry ($\delta^{15}N$, deviation from air standard) is affected by the kinetic effect of various biogeochemical processes that drive the N cycle (Figure 8), fractionating by several per mil the $^{15}N/^{14}N$ ratio from the reactant to the product (Sigman *et al.*, 2009). The microbial N fixation (*i.e.*, diazotrophy) is the reduction of atmospheric N_2 to NH_4^+ that imparts small negative fractionations (Zerkle *et al.*, 2008). The use of Mo-containing nitrogenase enzyme or V- and Fe-based alternative nitrogenase enzymes during N fixation imparts different isotopic fractionations (Zhang *et al.*, 2014). In the presence of O_2, the assimilated NH_4^+ into organic matter becomes oxidized and subsequently forms nitrite (NO_2^-) and ultimately nitrate (NO_3^-) via nitrification. This mechanism produces a ^{15}N-depleted nitrate reservoir (Casciotti *et al.*, 2003; Casciotti, 2009). These newly bioavailable N compounds are returned to the atmosphere as $^{14}N_2$ gas through the anaerobic ammonium oxidation (anammox, the oxidation of ammonium coupled to nitrite reduction) and denitrification (the reduction of NO_3^- to N_2), leaving a ^{15}N-enriched nitrate residual pool (Sigman *et al.*, 2009). In modern oceans, these metabolic reactions are the main sinks for bioavailable nitrate and nitrite (Canfield *et al.*, 2010).

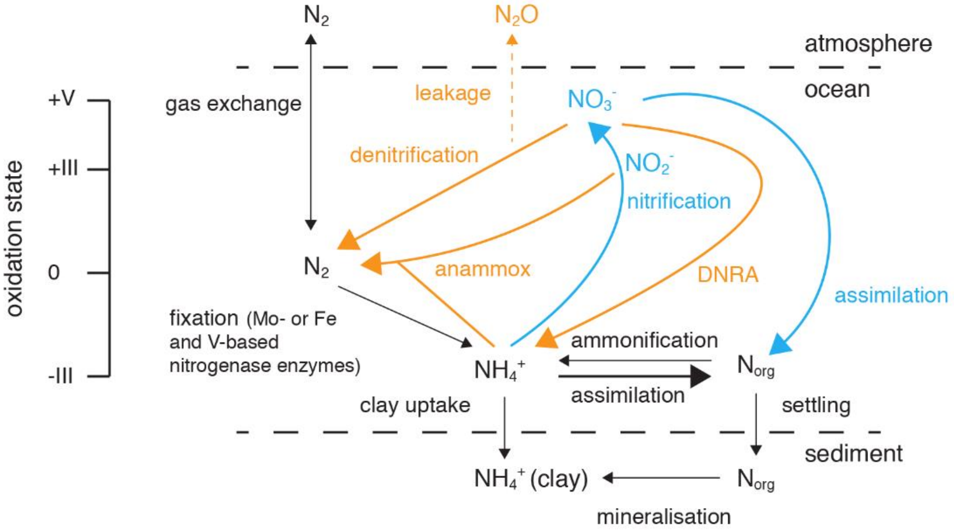

Figure 8: Nitrogen cycling. Black, orange and blue metabolic pathways show the anaerobic N cycle, suboxic and oxic processes, respectively. Arrow size represents the intensity of fractionation. Adapted from Stüeken *et al*. (2016). Anammox: anaerobic ammonium oxidation; DNRA: dissimilatory nitrate reduction to ammonium.

The large fractionations induced by nitrification and biological assimilation do not leave specific signatures in modern sediments, since the recycling of N compounds is rapid and quantitatively comparable (Hoch *et al.*, 1992).

Nitrogen is also a redox-sensitive element, meaning that the presence of molecular oxygen (O_2) drives the evolution of its biogeochemical cycle. Given that, nitrogen is a useful proxy for O_2 abundance, thus documenting the dominance of either N_2-fixing prokaryotes in anaerobic conditions or nitrate-using organisms (prokaryotes or eukaryotes) in more oxic conditions.

It is thought that the Mesoarchaean (3.5–2.8 Ga) was dominated by a global anaerobic N cycle through diazotrophy and ammonification (Ader *et al.*, 2016; Stüeken *et al.*, 2016). Convincing isotopic evidence for biological N fixation with very limited O_2 production are reported from 3.2 Ga-old deposits (Stüeken *et al.*, 2015a) and 2.95- to 2.85 Ga-old rocks (Ossa Ossa *et al.*, 2019). Then, the late Archaean rocks have recorded moderately high $\delta^{15}N$ values above the range of microbial fixation (*e.g.*, Garvin *et al.*, 2009), interpreted as evidence of a restricted or transient aerobic N cycle—so-called "oxygen oases". Molecular O_2 became permanent in Earth's atmosphere across the Archaean-Palaeoproterozoic transition (see section 1.2.2), which has triggered the onset of a pervasive aerobic N cycle with elevated $\delta^{15}N$ signatures (Zerkle *et al.*, 2017; Kipp *et al.*, 2018). Since eukaryotes preferentially assimilate oxidized N compounds (Karl *et al.*, 2001), it remains elusive whether the long-lived aerobic N cycle allowed for their emergence and proliferation after the accumulation of free atmospheric O_2.

Sulfur: The identification of microbial sulfate reduction (MSR) in Precambrian rocks relies on the sulfur (S) isotopic composition of sulfides and sulfates in sedimentary deposits (Johnston, 2011). Sulfur is composed of four stable isotopes (^{32}S, ^{33}S, ^{34}S, and ^{36}S). The S isotopic ratios are always related back to ^{32}S as it is the most abundant isotope (95.04 %, Coplen *et al.*, 2002). Moreover, the $^{34}S/^{32}S$ ratio is the most widely used S isotopic ratio, providing information on biological activity and sulfate-related environmental conditions. Large negative fractionations, reported as $\delta^{34}S$ (deviation from the Vienna-Canyon Diablo Troilite standard), found in S-containing minerals are imparted to the MSR (Canfield & Thamdrup, 1994). This microbial pathway also leads to a ^{32}S-depleted sulfate reservoir. However, the size of the marine sulfate pool and sulfate concentrations strongly impact the magnitude of the isotopic fractionation (Habicht *et al.*, 2002; Crowe *et al.*, 2014). Besides, sulfide oxidation may yield similar $\delta^{34}S$ signatures, making difficult the recognition of one or more S-utilizing microorganisms. Given that, multiple sulfur isotope geochemistry has recently helped researchers to discriminate the wide range of S-based microbial metabolisms (see review in Johnston, 2011).

The S biogenic fractionation emerged very early on Earth, in the Palaeoarchaean Era, with evidence from 3.47 Ga-old barites, Northern Australia (Shen *et al.*, 2001), and from 3.22 Ga-old pyrite (FeS_2), Northeastern South Africa (Nabhan *et al.*, 2016). Moreover, the MSR was actively developed at least 300 million years (Ma) before the rise of free atmospheric O_2 (Thomazo *et al.*, 2013; Marin-Carbonne *et al.*, 2018). In a closed system with respect to sulfate, the occurrence of ^{34}S-enriched pyrite rims (positive δ^{34}S values) may account for the Rayleigh distillation. With the increasing ^{32}S depletion of the residual sulfate pool, the MSR starts to incorporate heavy S isotopes.

Finally, significant amounts of atmospheric O_2 is tracked by the disappearance of sedimentary sulfur isotope mass-independent (S-MIF) anomaly via Δ^{33}S proxy (equation 2; Johnston *et al.*, 2007; Farquhar *et al.*, 2010) (see section 1.2.2.c). This Δ-notation reflects the deviation of a measured ^{33}S/^{32}S ratio from a known relationship between ^{34}S/^{32}S and ^{33}S/^{32}S ratios. The S-MIF forms by photodissociation of sulfur dioxide (SO_2) by ultraviolet light in the absence of ozone (O_3) layer (Farquhar *et al.*, 2001).

$$\Delta^{33}S(‰) = \delta^{33}\mathrm{S} - 1000\ \times \left[\left(1 + \frac{\delta^{34}\mathrm{S}}{1000}\right)^{0.515} - 1\right] \tag{2}$$

Similarly, whiffs of atmospheric O_2 and “oxygen oases” in the Archaean that are linked to the oxygenic photosynthesis (Kasting & Siefert, 2002) can be supported by Cr, Fe, Mn, and Se isotope fractionations (Anbar *et al.*, 2007; Frei *et al.*, 2009; Planavsky *et al.*, 2014a; Satkoski *et al.*, 2015; Stüeken *et al.*, 2015b).

c. Biominerals

The biologically controlled mineralization is the ability of living organisms to mineralize extracellular or intracellular inorganic compounds through regulated processes, which results from the genome expression. The most striking example is the external (calcareous) envelop of numerous metazoans (*e.g.*, corals, lamellibranches), whereby these organisms actively pump ions from seawater for building their own mineral phase. Biominerals can also derive from the biologically induced mineralization, a secondary event generated by microbe-environment interactions. Widespread mechanism in the bacterial realm, it only occurs with favorable conditions. According to Pósfai *et al.* (2001), the crystal size distribution of biologically mediated Fe-bearing minerals is an effective tool for identifying processes that have led to the crystal repartition. The authors showed that a Gaussian crystal size distribution is typical of biologically controlled mineralization, while a lognormal crystal size distribution represents a biologically induced mineralization. Regardless of the type of biomineralization, the authenticity of biological activities in former rocks can be thus asserted.

The recognition of biominerals in ancient sedimentary deposits requires high resolution technics and favorable taphonomical processes. Overall, the formation of biologically controlled and biologically induced Fe-containing crystals is one of the most described biomineralization in nature (Figures 9A, B) (Konhauser & Ferris, 1996; Konhauser, 1997). In the search of biologically controlled mineralization, the bacterial cellular structure is essential for demonstrating the site at which a mineral forms. For instance, some modern Cyanobacteria and eukaryotes are capable of generating the biosynthesis of Fe-containing minerals in their intracellular structures. This mechanism underpins the strategy for iron storage by Fe-dependent microorganisms (*e.g.*, Brown *et al.*, 2010; Brayner *et al.*, 2012). Moreover, non-tolerant Cyanobacteria may mineralize internal Fe compounds to cope with Fe intracellular oxidative stress (Shcolnick *et al.*, 2009). Similarly, perfectly preserved microfossils from the 1.88 Ga-old Gunflint Iron Formation, Canada, have shown intracellular Fe biomineralization (Figure 9C) (Lepot *et al.*, 2017). This mineral signature, together with the morphological study of cellular structures, allowed to infer the occurrence of Fe-mineralizing Cyanobacteria during the Palaeoproterozoic.

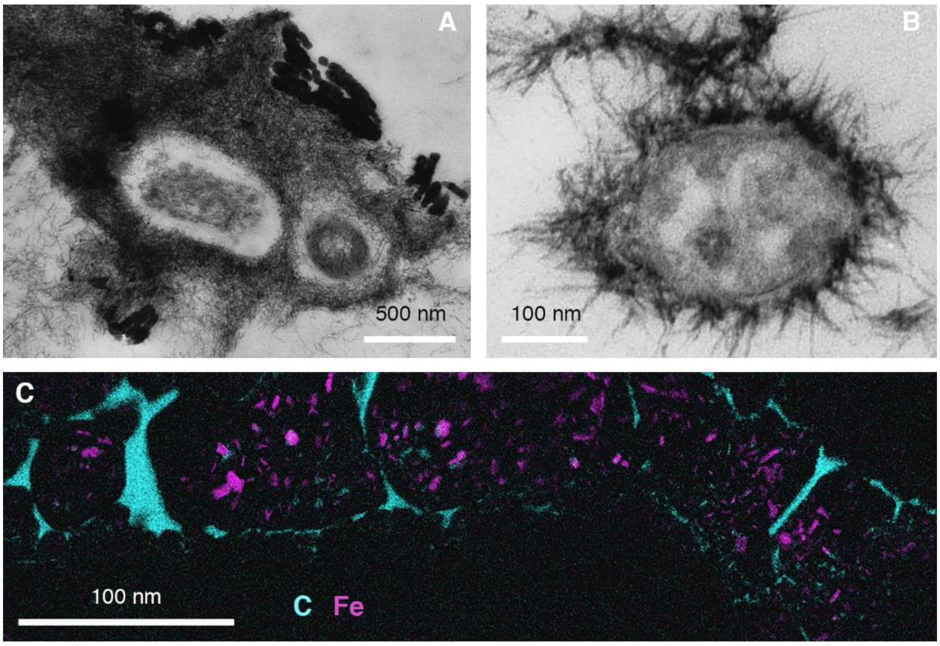

Figure 9: Modern and fossilized microorganisms that performed the biologically controlled or biologically induced mineralization. (**A**) Complete encapsulation of modern microbial cells by iron-rich minerals. Modified after photo published in Konhauser & Ferris (1996). (**B**) Precipitation of iron oxides on modern bacterial cell walls. Modified after photo published in Konhauser & Ferris (1996). (**C**) Intracellular Fe biomineralization from 1.88 Ga-old cyanobacterial filaments. Modified after photo published in Lepot *et al*. (2017).

Banded Iron Formation (BIF) and biologically mediated pyritization are the most common mineral phases linked to biological activities in the Precambrian geological record. The former results from an important precipitation of iron (oxyhydr)oxides formed through the direct oxidation of ferrous iron with O_2-producing photosynthesizers (Cloud Jr., 1965). The anaerobic photosynthetic oxidation of Fe^{2+}, whereby Fe^{2+} is the electron donor in this microbial metabolism, may also lead to the precipitation of iron (oxyhydr)oxides. (*e.g.*, Kappler *et al.*, 2005). Sedimentary pyrite is the stable end product of the MSR, during which reactive Fe reacts with hydrogen sulfide (H_2S), the latter is generated by sulfate-reducing microorganisms in reduced sediments (Berner, 1984). Although pyrite grains can directly precipitate from hydrothermal systems and euxinic water columns, these iron sulfides are mostly biologically induced in low-temperature environments (Trudinger *et al.*, 1985).

It is widely thought that microbial communities, especially Cyanobacteria, play a major role in the extracellular carbonate precipitation, as secondary by-products, under favorable pH conditions (see section 1.1.2.c). Besides, intracellular calcification of cyanobacterial species has been recently documented (Couradeau *et al.*, 2012; Benzerara *et al.*, 2014; Cam *et al.*, 2018), providing new interests for the search of biomineral-producing Cyanobacteria. The role of intracellular carbonate biomineralization remains elusive, but it might suggest that the carbonate precipitation buffers intracellular pH without specific biological function (Couradeau *et al.*, 2012). Despite the widely accepted implication of cyanobacterial communities in the carbonatogenesis, Cyanobacteria forming carbonates intracellularly induce a negative feedback on extracellular carbonate precipitation (Cam *et al.*, 2018).

Recent attempts to constrain mechanisms by which microbes mediate the authigenesis of clay minerals in laboratory-cultured bacteria have arisen new perspectives in the recognition of ancient biological signatures. As a result of their high surface reactivity and metabolic activity, microbes are capable of transforming and precipitating a wide variety of phyllosilicates (Fortin *et al.*, 1998; Konhauser & Urrutia, 1999; Kim *et al.*, 2004; O'Reilly *et al.*, 2005; Zhang *et al.*, 2007; Vorhies & Gaines, 2009; Wacey *et al.*, 2014; Pace *et al.*, 2016). Among them, Fe-, Mg- and K-rich clay minerals are by-products of a biologically induced mineralization. In addition, the dissolution of clays by microorganisms is energetically favorable, as indicated by the well-known microbial reduction of structural Fe(III) in smectite via dissimilatory iron reduction (Kim *et al.*, 2004; O'Reilly *et al.*, 2005; Zhang *et al.*, 2007; Vorhies & Gaines, 2009).

In all cases, there is a vast amount of biominerals used as proxy for documenting the presence of microorganisms in Precambrian sediments.

d. Bioessential (trace) elements

Bioessential elements (BE) are crucial compounds found in oxidoreductase enzymes across the three domains of life (Figure 10). These enzymes are nanomolecules where electron-transfer reactions take place, then giving energy to the organisms (Falkowski *et al.*, 2008). The majority of these BE are transition metals such as V, Mn, Fe, Co, Ni, Cu, Zn, Mo, and W, but metals (Mg) and non-metals (P and Se) also exert control over biological evolution (see reviews in Robbins *et al.*, 2016; Moore *et al.*, 2017). The BE requirement differs between metabolic pathways and has changed with the fluctuation of metal availability though time.

Particularly, the decrease of Ni and Co was inferred to the diminution of Ni- and Co-containing ultramafic rocks, resulting from a cooling upper-mantle temperatures (Konhauser *et al.*, 2009; Gregory *et al.*, 2015). Other BE (*e.g.*, Mn, Se, and Mo) accumulated with the increasing levels of molecular O_2 over the course of the Earth's history (Large *et al.*, 2014). Moreover, Mo, which is involved in a wide range of oxidoreductase enzymes in N-utilizing organisms (Williams & Fraústo da Silva, 2002), would have been a limiting component for evolution of complex life in mid-Proterozoic (Anbar & Knoll, 2002). Molybdenum is readily scavenged from sulfur-rich seawater that became developed in ocean continental margins during the Proterozoic (see section 1.2.2). Hence, the biogeochemical cycling of a large number of BE is connected to the evolution of ancient environments on Earth, highlighting the relationships between the geosphere and biosphere.

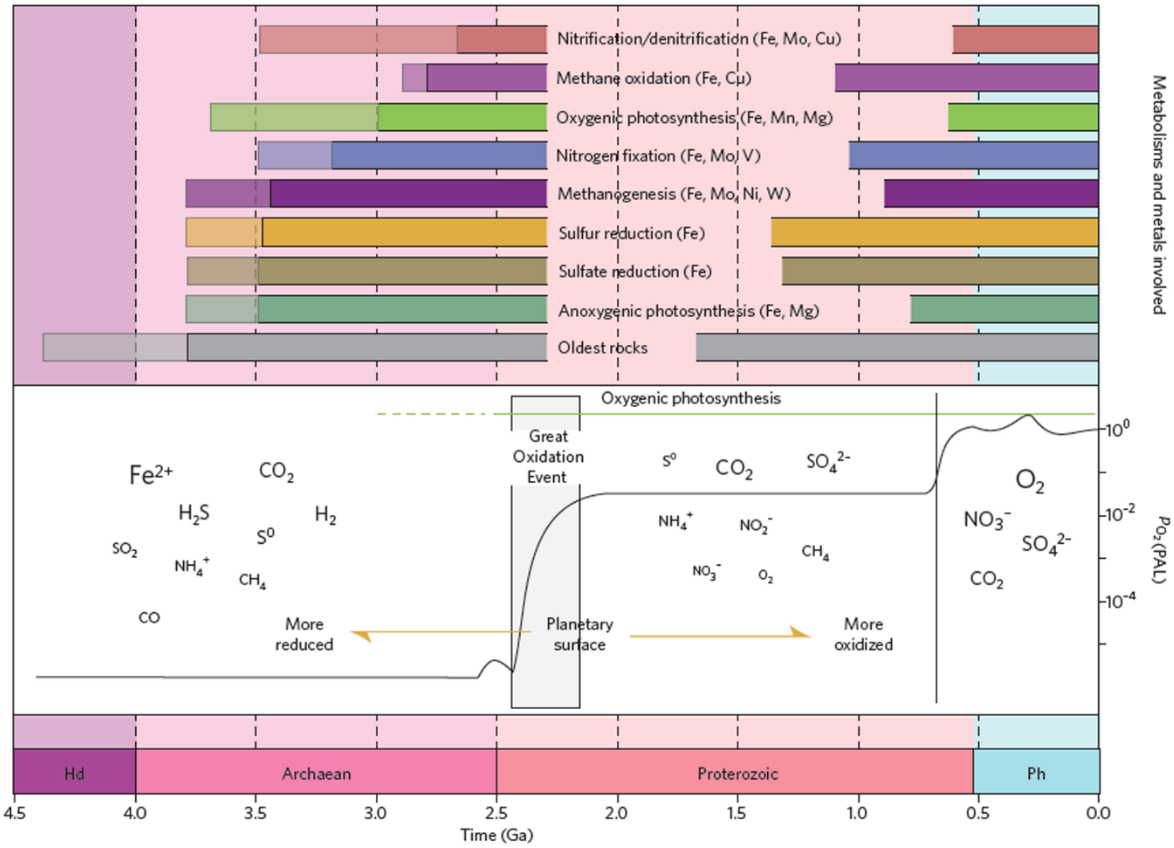

Figure 10: Synthesis of the evolution of both microbial metabolism and atmospheric oxygen throughout Earth's history. The oxidoreductase enzymes are associated with each metabolism. PAL, present atmospheric level; Hd, Hadean; Ph, Phanerozoic. Reproduced from Moore *et al*. (2017).

Zerkle *et al.* (2005) modelled the amount of BE required to the expression of metalloenzymes in multiple microbial genomes through time to track whether metals could be used as biosignatures. Some variations are imparted to the microbial metabolisms, while other are connected to seawater chemistry. The most convincing biosignature of metabolic pathways is seen through Ni and W biological requirements, characterizing the methanogenesis. The authors also proposed a global pattern in the biological use of BE: Fe ≫ Zn > Mn ≫ Mo, Co, Cu ≫ Ni > W, V. A major change in the composition of metallocofactors is the occurrence of Cu-containing oxidoreductase enzymes in numerous aerobic metabolisms as the planet became oxygenated (Moore *et al.*, 2017). The appropriation of Cu allows access to high energy redox potentials (Ochiai, 1983; Ridge *et al.*, 2008).

The composition of chemical sedimentary rocks (Fe-rich and Si-rich deposits) appears as robust palaeomarine proxies because it likely indicates the trace element abundance at the time of mineral precipitation (Bekker *et al.*, 2010). In addition, organic matter-rich shale sediments offer pertinent information on primary palaeoproductivity and bottom-water redox conditions. Indeed, shales preferentially incorporate trace metals and redox-sensitive elements that are efficiently bound to organic matter and/or removed in anoxic conditions but soluble in oxic seawater (Tribovillard *et al.*, 2006). Since the last decade, the interest of sedimentary to early diagenetic pyrite has grown for reconstructing the availability of trace elements in the geological archives (Large *et al.*, 2014, 2015; Gregory *et al.*, 2015, 2017). The authors have suggested that the elemental composition of seawater or pore-waters may be recorded in syngenetic to early diagenetic pyrite. Collectively, these sedimentary rocks and minerals allow to track the evolution of ancient microbial metabolisms and redox conditions on early Earth.

1.2. The Palaeoproterozoic rock record

1.2.1. Palaeogeographic reconstruction

The presence of at least 35 cratonic fragments constitutes the global Archaean record (Figure 11; Bleeker, 2003). Nonetheless, the reconstruction of putative Archaean-Proterozoic supercontinents (or supercratons) is a challenge given the scarcity of available palaeomagnetic record (Evans, 2013). The palaeogeographic reconstructions for those times remain unclear, mostly because of the absence of information of palaeomagnetic poles. Besides, several cratons do not display the same age of stabilization.

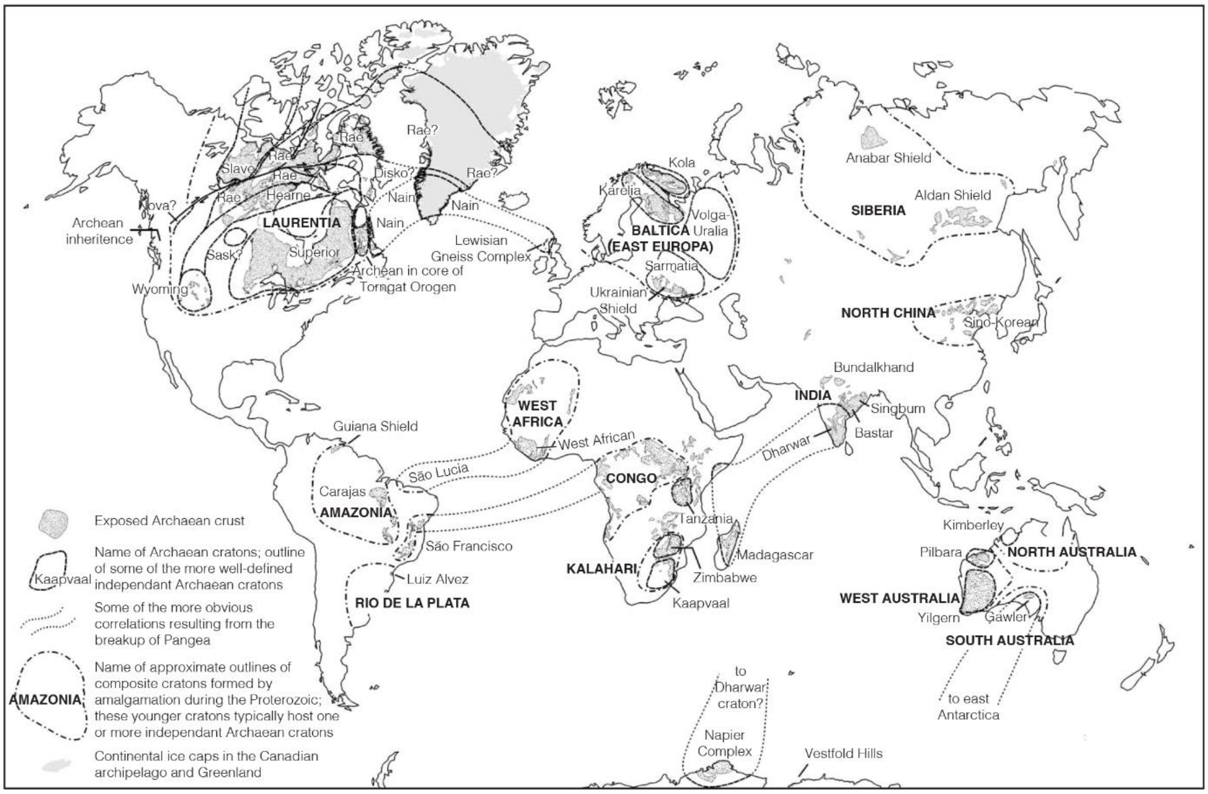

Figure 11: The record of exposed Archaean cratonic blocks. Adapted from Bleeker (2003).

It was suggested that Archaean cratonic fragments might have formed two major crustal assemblies at *ca*. 2.8–2.6 Ga, referred to as Kenorland and Zimvaalbara supercontinents (Aspler & Chiarenzelli, 1998). According to the latter authors, Kenorland would have comprised parts of Baltica, Laurentia, and Siberia supercratons, while Zimvaalbara would have possibly included Kaapval, Pilbara, Zimbabwe, and perhaps Indian, and São Francisco cratonic blocks. Bleeker (2003) also posited that three large independent supercratons (Slavia, Superia, and Vaalbara) distinguished by their age of cratonization would have occurred in the Neoarchaean. A fourth speculative family of “clan” of cratons (Zimgard) has been reported (Smirnov *et al.*, 2013). Possible Archaean-Proterozoic palaeogeographic reconstructions of supercratons are primarily based upon geometries of radiating dykes and sills (Figure 12A; Evans, 2013; Gumsley *et al*., 2017, and references therein).

Regardless of the number of supercratonic landmasses, the conceptual model of Palaeoproterozoic geodynamic first consists of a protracted breakup of supercratons extended over 300–400 Ma, resulting from mantle plumes and subsequent intraplate rifting (Aspler & Chiarenzelli, 1998). This has led to the fragmentation and dispersion of cratonic blocks to high latitudes (Figure 12B). Continental landmasses positioned at low latitudes, together with the emplacement of widespread large igneous provinces generated by mantle plumes in the early Palaeoproterozoic, would have played a role in the drastic change of Earth's redox conditions (see section 1.2.2) (Gumsley *et al.*, 2017). In addition, a rapid growth of subaerial landmasses likely occurred at the same time, influencing global climate by increasing Earth's albedo, subaerial weathering, and continental margins (Bindeman *et al.*, 2018). After a minimal tectonic activity driven by a magmatic shutdown between 2.4 to 2.2 Ga (Condie *et al.*, 2009), continents ultimately amalgamated by a global-scale collisional orogeny at *ca*. 2.1–1.8 Ga, forming the Nuna (Columbia) supercontinent (Rogers & Santosh, 2002; Zhao *et al.*, 2002; D'Agrella-Filho & Cordani, 2017).

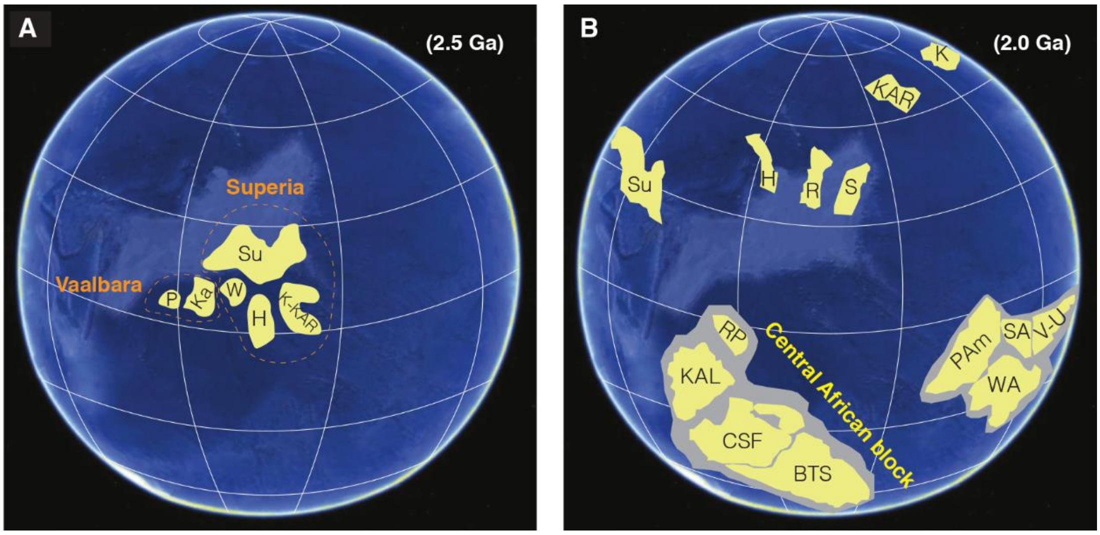

Figure 12: Possible palaeogeographic reconstructions. Abbreviations: Su, Superior; P, Pilbara; Ka, Kaapvaal; W, Wyoming; H, Hearne; K, Kola; KAR, Karelia; R, Rae; S, Slave; RP, Rio de la Plata; KAL, Kalahari; CSF, Congo/São Francisco; BTS, Borborema/Trans-Sahara; Pam, Proto-Amazon; WA, West Africa; SA, Sarmatia; V-U, Volgo-Uralia. (**A**) Assembly of supercratons during the Neoarchaean-Palaeoproterozoic transition. Adapted from Gumsley *et al*. (2017) and references therein. (**B**) Breakup of supercontinents followed by the gathering of cratons (Nuna cycle) during the late Palaeoproterozoic. The most recent plate reconstruction for this time (after D'Agrella-Filho & Cordani, 2017).

1.2.2. The "Great Oxidation Event"

a. General information

The Palaeoproterozoic Era was marked by profound changes in chemistry of Earth's oceans and atmosphere—commonly named the "Great Oxidation Event" (GOE; Holland, 2002)—in association with a global atmospheric cooling, which has led to worldwide Snowball Earth conditions (Kirschvink *et al.*, 2000). The GOE consists of the first measurable accumulation of atmospheric oxygen at $pO_2 > 10^{-5}$ present atmospheric level (PAL), as shown by the disappearance of S-MIF anomalies (Farquhar *et al.*, 2001). The newly oxygenated environments in surface seawater and atmosphere occurred right after the Neoarchaean-Palaeoproterozoic transition. The onset of the GOE roughly became apparent elsewhere between 2.45 and 2.32 Ga (Figure 13) (Bekker *et al.*, 2004; Luo *et al.*, 2016; Gumsley *et al.*, 2017).

Oxygen-producing photosynthesizers, which evolved several hundred million years before the GOE (Schirrmeister *et al.*, 2016), have likely triggered the rise of molecular O_2 on Earth (Kasting & Siefert, 2002). Favorable tectonic and magmatic constraints may also have played a key role in our planet's oxygenation. Although the atmospheric O_2 content is uncertain, the O_2 accumulation after the GOE is estimated higher than 0.1% PAL (Lyons *et al.*, 2014) and putatively up to 20% PAL (Blättler *et al.*, 2018), which was sufficiently high enough to oxidize untapped reservoirs. It was widely accepted that the GOE was a rapid and synchronous global event (Hoffman, 2013; Luo *et al.*, 2016), but recent studies have suggested that the Earth's oxygenation was rather protracted, asynchronous, and characterized by oscillations (Gumsley *et al.*, 2017; Philippot *et al.*, 2018; Chi Fru *et al.*, 2019).

The surface seawater became globally oxygenated, whereas anoxic (ferruginous) conditions persisted in the deep oceans (Lyons *et al.*, 2014). In addition, euxinia (*i.e.*, sulfide-rich conditions) developed in ocean continental margins, resulting from high biological productivity (Poulton & Canfield, 2011). Indeed, the oxidation of sulfide-containing rocks released sulfate to seawater that is used as energy source by MSR. The latter microbial pathway ultimately produces sulfide-rich conditions.

The protracted oxygenation lasted over ~200 Ma, primarily sustained by a high burial rate of organic matter, the so-called "Lomagundi Event" (see section 1.2.3) that occurred between 2.22 and 2.06 Ga (Karhu & Holland, 1996). A precipitous collapse of O_2 concentrations towards much lower levels was possibly linked to an abrupt shift of biogeochemical cycles, inhibiting primary productivity (Bekker & Holland, 2012). Long after the GOE, atmospheric O_2 quantities were likely very low thought the late Palaeoproterozoic, near or even below 0.1% PAL

(Planavsky *et al.*, 2014b; Bellefroid *et al.*, 2018), but oxygenation to higher levels may have been transiently recorded (Planavsky *et al.*, 2018).

The shift of redox environmental conditions have had drastic consequences on global biological and geochemical cycles, because of newly available redox potentials. A wide range of geological and organic and inorganic geochemical proxies allowed to detect changes of Earth's physicochemical conditions.

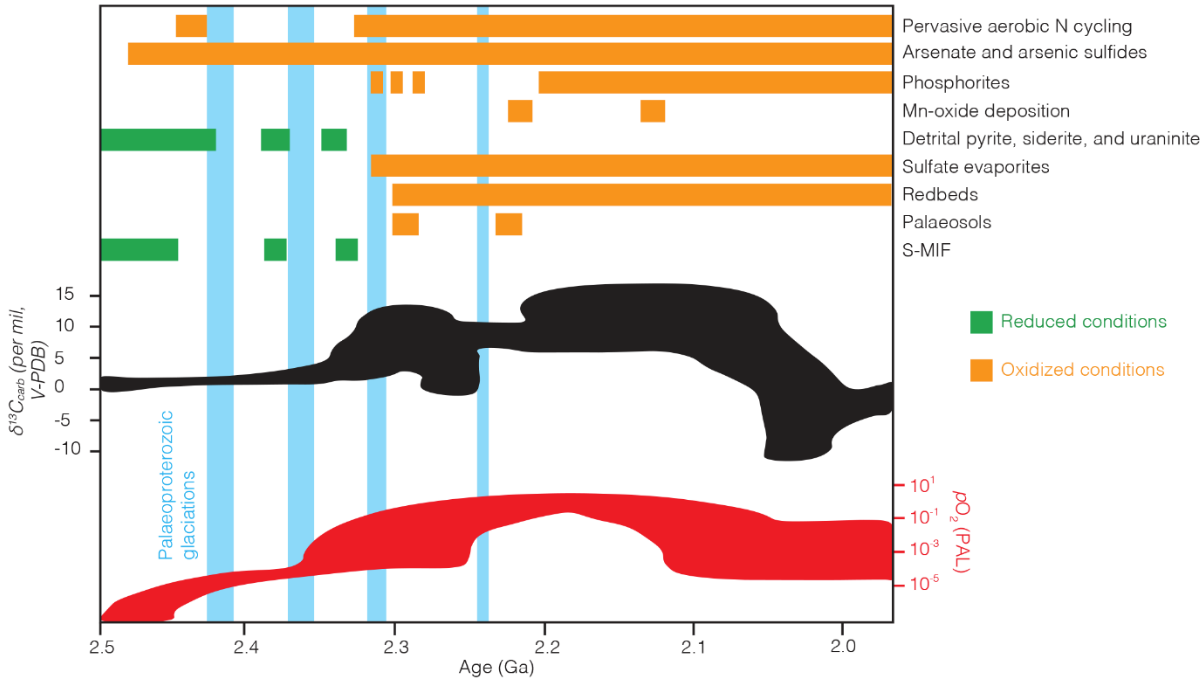

Figure 13: Schematic representation of redox indicators for the Earth's oxidation state combined with the secular carbon isotopic composition and pO_2 variations across Archaean-Proterozoic boundary. Modified from Farquhar *et al*. (2011) and Bekker & Holland (2012), and references therein. Timelines of arsenic dynamic (after Chi Fru *et al*., 2019), nitrogen aerobic cycling (after Zerkle *et al*., 2017; Kipp *et al*., 2018), and phosphorites (after Papineau, 2010; Soares *et al*., 2019) are added. Black and red curves show the evolution of carbon isotopes and oxygenation (present atmospheric level; PAL), respectively (after Lyons *et al*., 2014).

b. Sedimentary evidence

A number of geological lithologies have recorded drastic changes in the redox state of atmosphere-ocean system following the GOE transition (Figure 13), including palaeosols, red beds, sulfate evaporites, manganese oxide deposits, phosphorites, and detrital minerals. The appearance/disappearance of these proxies in early Palaeoproterozoic is thus a good geological record of our planet's oxygenation.

Palaeosols and red beds: The increase in the retention of Fe(III) in palaeosols and sedimentary rocks (*i.e.*, referred to as red beds) is related to the precipitation of insoluble ferric iron as oxy(hydr)oxides under oxidizing conditions. The distinctive red color is inferred to the occurrence of disseminated hematite (Turner, 1980). Moreover, red beds are typically formed in depositional environments close to the atmosphere-hydrosphere interface, including lacustrine, fluviatile, and aeolian settings. These iron oxide-bearing sedimentary rocks appeared around 2.3 Ga and were common for the rest of the Proterozoic (Chandler, 1980), suggesting the persistence of oxidized conditions.

Sulfate evaporites: The chemically precipitation of sulfate evaporite minerals (*e.g.*, gypsum, anhydrite) has implied an increase in seawater sulfate concentrations, indisputably connected to substantial amounts of Earth's surface oxidant. Thus, the sulfate evaporites are unknown before the rise of atmospheric O_2 (Bekker *et al.*, 2006; Schröder *et al.*, 2008). They are exclusively younger than 2.32 Ga and are relatively common in shallow water, open-marine settings deposited between 2.3 and 2.0 Ga (Melezhik *et al.*, 2005; Schröder *et al.*, 2008; Blättler *et al.*, 2018). A 2.0 Ga-old, 800 m thick stratigraphic interval of evaporites in Russian Karelia provides further support to an extensive marine sulfate reservoir in the wake of the GOE (Blättler *et al.*, 2018). Importantly, the variation in seawater sulfate concentrations is characterized by the temporal distribution of $CaSO_4$-bearing evaporites (Bekker & Holland, 2012).

Manganese oxide deposits: Economically Mn-oxide deposits are recorded in *ca*. 2.22 and 2.1 Ga-old sedimentary rocks in South Africa and Gabon, respectively (Weber, 1968; Tsikos & Moore, 1997). Their deposition has required exceptional levels of atmospheric oxygen (Maynard, 2010), making these sedimentary rocks a robust proxy of Earth's oxygenation.

Phosphorites: Major phosphorus (P) deposits appeared near the end of the GOE, at around 2.2–2.0 Ga (Papineau, 2010), although older P-enriched sediments have been recently described (Soares *et al.*, 2019). Sedimentary phosphorites witnessed the accumulation of free O_2 as well as positive feedbacks between oxygen and phosphorus productions (Bekker & Holland, 2012). The phosphogenesis is related to a series of events, during which the increase of chemical weathering of continental crust first resulted in abundant P inputs to seawater (Papineau, 2010). Then, the significant source of newly bioavailable P allowed to sustain productivity and, as consequence, primary producers gave rise to large production of P-bearing organic matter. This sequence has promoted higher burial rate of carbonaceous material, leading to a more oxygenated water column in the early Palaeoproterozoic (Bekker & Holland, 2012). During the early or late diagenesis, the decay of organic matter would cause the precipitation of authigenic P-containing minerals, expressed as concretions, nodules, clasts, or peloids, although mechanisms are not well constrained (Notholt, 1980).

Detrital pyrite, siderite and uraninite: Well-rounded detrital minerals, such as pyrite, siderite, and uraninite (UO_2), are only stable in unoxygenated conditions. Thus, before the rise of Earth oxidized conditions, they are relatively common in the geological rock record, especially in conglomerates deposited in fluvial to shallow-marine depositional environments (Rasmussen & Buick, 1999; Hofmann *et al.*, 2009). Their disappearance after 2.3 Ga suggested a drastic shift in mineralogical composition of riverine delivery under more oxidized conditions.

c. Geochemical evidence

Several lines of geochemical evidence also indicate a progressive accumulation of atmospheric oxygen some 2.4 Ga ago (Figure 13, and reference therein among others). One of the most reliable working tools giving support to the GOE is the disappearance of the mass-independent fractionation of S isotopes, expressed in terms of $\Delta^{33}S$ (equation 2) (Farquhar *et al.*, 2000, 2010), although some researchers have shown recently the persistence of S-MIF after 2.31 Ga (Philippot *et al.*, 2018). Generally, the rate at which isotopes fractionate each other depends on their mass, but if other factors strongly influence the reaction, the fractionation is no longer mass-dependent. Sulfur-containing minerals older than 2.45 Ga record anomalous $\Delta^{33}S$ values, varying between -3‰ to +11‰, while sulfides and sulfates in younger sedimentary rocks display $\Delta^{33}S$ signatures close to 0‰ (Figure 14A) (Farquhar *et al.*, 2010). Typically, the photodissociation of SO_2 by UV light into elemental and water-soluble S compounds in an oxygen-free atmosphere is the only known mechanism capable of producing highly variable $\Delta^{33}S$ values (Farquhar *et al.*, 2001). The depositional environment in which sulfide-bearing minerals formed has also affected the composition of S-MIF. In other words, the oxygen buildup (>10^{-5} PAL) allowed to permanently prevent this photochemical reaction, by creating an ozone shield in the atmosphere.

The O_2 accumulation following the GOE caused drastic changes in the geochemical cycle of some redox-sensitive elements. The oxidation state of these elements reflects that of oceans. The redox-sensitive elements are soluble under oxic conditions and insoluble under suboxic to anoxic conditions, which may trigger their enrichment in the O_2-lean water column or at the water-sediment interface (Tribovillard *et al.*, 2006). Thus, the oxidative weathering of exposed upper continental crust led to the rise of oxygen-sensitive tracer contents, including V, Cr, As, Se, Mo, Re, and U (*e.g.*, Tribovillard *et al.*, 2006; Large *et al.*, 2014; Gregory *et al.*, 2017; Chi Fru *et al.*, 2019), in chemical and sedimentary rocks. For instance, uranium and chromium are widely recognized as powerful proxies to track the increase of atmospheric O_2 (Figures 14B, C) (Konhauser *et al.*, 2011; Partin *et al.*, 2013a). As U and Cr can be associated with iron formations and detrital input, respectively, U/Fe and Cr/Ti ratios allowed to assess authigenic enrichments. Moreover, Chi Fru *et al.* (2019) recently showed that the rise of arsenic content, especially arsenate and arsenic-sulfide, overlaps with the GOE (Figure 14D). Importantly, the concentration of these oxygen-sensitive tracers dramatically increased by several orders of magnitude during the GOE.

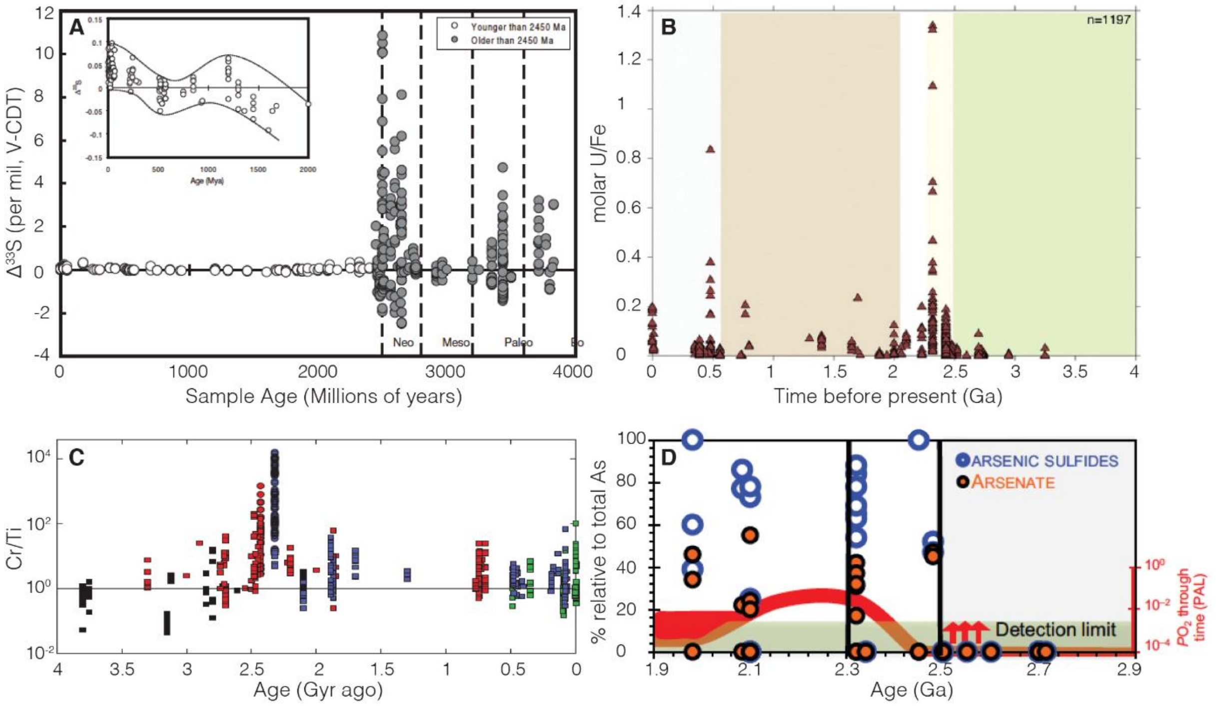

Figure 14: Geochemical evidence for ocean-atmosphere redox evolution following the GOE transition. (**A**) Disappearance of S-MIF. Modified from Farquhar *et al*. (2010). (**B**) Uranium content in iron-rich rocks. Modified from Partin *et al*. (2013b). (**C**) Chromium dynamic in iron formations. Each symbol denotes a type of analysis and each color represents a depositional setting. Cr/Ti ratios have been normalized to the evolving Cr/Ti ratio of upper continental crust (solid line). Modified from Konhauser *et al*. (2011). (**D**) Dynamic of arsenic species in shales. Modified from Chi Fru *et al*. (2019).

1.2.3. The “Lomagundi” Event

Contemporaneous with the worldwide appearance of O_2-indicating sedimentary rocks and O_2-sentitive geochemical tracers is the evidence of one of the greatest fluctuation of carbon cycle (Karhu & Holland, 1996). This unprecedented perturbation represents the longest and most extreme positive carbon isotope excursion in seawater composition, known as the “Lomagundi” Event (LE; Schidlowski *et al.*, 1976). The carbon isotope variations in the marine carbonates, deposited during this δ^{13}C excursion, are best defined between 2.22 and 2.06 Ga (Figure 13) (Karhu & Holland, 1996). Martin *et al*. (2013) assessed that the LE was synchronous worldwide, with a duration of between 128 and 249 Ma. These Lomagundi-aged marine carbonates record carbon isotopic compositions commonly between +5‰ and +16‰ (Karhu & Holland, 1996; Melezhik *et al.*, 2005) with maximum values at around +28‰ (Bekker *et al.*, 2003). Compared to other older and younger marine limestones and dolostones, the δ^{13}C compositions usually fall within a narrow range close to 0‰.

A widely accepted scenario is that the positive $\delta^{13}C$ excursion in marine carbonates reflects an increase in the proportion of ^{12}C-enriched organic carbon that was buried (Karhu & Holland, 1996). To elucidate the cause of the high rate of organic carbon deposition, Bekker & Holland (2012) posited that positive feedbacks between the O_2 accumulation and the rise of terrestrial phosphate flux to seawater were likely responsible for the LE. The extreme phosphate flux stimulated the production of primary productivity, leading to elevated burial rate of organic matter. The oxidation of organic carbon is a potent sink for O_2, thus the burial of organic matter is a source of oxygen to the atmosphere. As long as organic matter were permanently isolated from subsequent oxidation, higher concentrations of atmospheric O_2 were reached in the wake of GOE. In addition, the siderite oxidation followed by photosynthetically mediated CO_2 fixation may have led to a substantial O_2 buildup (Bachan & Kump, 2015).

The termination of LE no later than 2.06 Ga (Martin *et al.*, 2013) was marked by an abrupt swing to low (positive) $\delta^{13}C$ values in marine carbonates (Karhu & Holland, 1996). The decrease in the terrestrial phosphate flux, decreasing the rate of organic carbon burial, may have caused the end of the most extreme positive carbon isotope excursion (Bekker & Holland, 2012). Hence, the rate of oxidative weathering exceeded that of organic carbon deposition, which ultimately led to low O_2 levels.

1.2.4. The Shunga-Francevillian excursion

The aftermath of the LE started with a negative shift in the $\delta^{13}C$ signature of the inorganic fraction. The values, down to -14‰, were only observed in the *ca*. 2-0 Ga-old Zaonega Formation (shungite deposits), Karelia craton, Russia (Figure 13) (Kump *et al.*, 2011). The latter authors have shown that extremely low $\delta^{13}C_{org}$ values in the shungite deposits and the Francevillian Series of Gabon also accompanied this negative excursion in carbonates. Thus, the Shunga-Francevillian event, which possibly results from an intense oxidative weathering of the Lomagundi-aged organic matter, has been interpreted as global in extant (Kump *et al.*, 2011). However, lithological observations in the shungite deposits indicate that local thermogenic CH_4 and seepage formed due the magmatic intrusions, fueling CH_4-based microbial metabolisms (Qu *et al.*, 2012). The organic carbon isotopic composition may also reflect the incorporation of ^{12}C-enriched methanotroph-derived carbonaceous material in the Francevillian sediments (Weber & Gauthier-Lafaye, 2013). This interpretation relies on the fact that the $\delta^{13}C$ relationship between marine carbonates and organic matter is insignificant. Collectively, the Shunga-Francevillian anomaly would hint the influence of episodic methanotrophic biomass rather than a global oxidative process.

1.3. Geological background

1.3.1. General information

The *ca*. 2.1 Ga-old Palaeoproterozoic Booué, Lastourville, Okondja, and Franceville domains are a family of four intracratonic sub-basins located in the southeastern part of the Republic of Gabon (Figure 15). The Ondili and Amieni basement horsts separate these domains from each other. The Francevillian Series, hosted in these sub-basins, is composed of unmetamorphosed and weekly folded siliciclastic and volcanic deposits. Moreover, it unconformably overlies Archaean rocks, known as the East-Gabonian block within the Congolese craton (Figure 15A) (Weber, 1968; Gauthier-Lafaye & Weber, 1989; Thiéblemont *et al.*, 2009). Granitoids mixed with greenstone belts mainly constitute this Archaean crystalline basement (Bouton *et al.*, 2009a; Préat *et al.*, 2011). The Francevillian Series, referred to as the Francevillian basin, covers an area of 35,000 km^2 between 1° to 2° S and 13° to 13°44’E (Préat *et al.*, 2011). The basin fill is 4,000 m thick in the deepest part (Weber, 1968) with a thinning to 1,000–2,500 m thick towards the edge (Thiéblemont *et al.*, 2009). The lithostratigraphic sequence is organized into five major formations, labelled FA to FE from the oldest to youngest. In addition, the occurrence of the oldest uranium ore deposits that have acted as natural fission reactors, and large manganese deposits have promoted important geological surveys and drilling campaigns (Gauthier-Lafaye & Weber, 1989; Gauthier-Lafaye, 2006).

The Archaean basement of the West Congolese craton is mainly composed of 3.2–2.8 Ga-old rocks and was emplaced during successive magmatic events (Feybesse *et al.*, 1998; Bouton *et al.*, 2009a; Thiéblemont *et al.*, 2009; Préat *et al.*, 2011). The Ogooué complex and Cenozoic continental sediments lie in the western and eastern parts of the Francevillian basin, respectively (Figure 15A). The mobile zone of Ogooué is a fold-and-thrust belt containing metasedimentary formations that have undergone high-grade metamorphism (Gauthier-Lafaye & Weber, 1989; Weber *et al.*, 2016). The establishment of the Ogooué complex occurred during the accretion of the Central African Eburnean Orogenic Belt, extending from Cameroon, Gabon to Congo, elsewhere between 2.5 and 2.12 Ga ago (Feybesse *et al.*, 1998; Weber *et al.*, 2016). The strike-slip Ikoy-Ikobé fault separates the Ogooué orogenic belt from the West-Gabonian block (Figure 15A). The latter consists of 2.45 Ga-old (pre-Eburnean) migmatites formed from a partial melting of Archaean basement, and of 2.08–2.04 Ga-old calco-alkaline plutons emplaced from an intensive granitization during the Eburnean Orogeny (Thiéblemont *et al.*, 2009; Weber *et al.*, 2016).

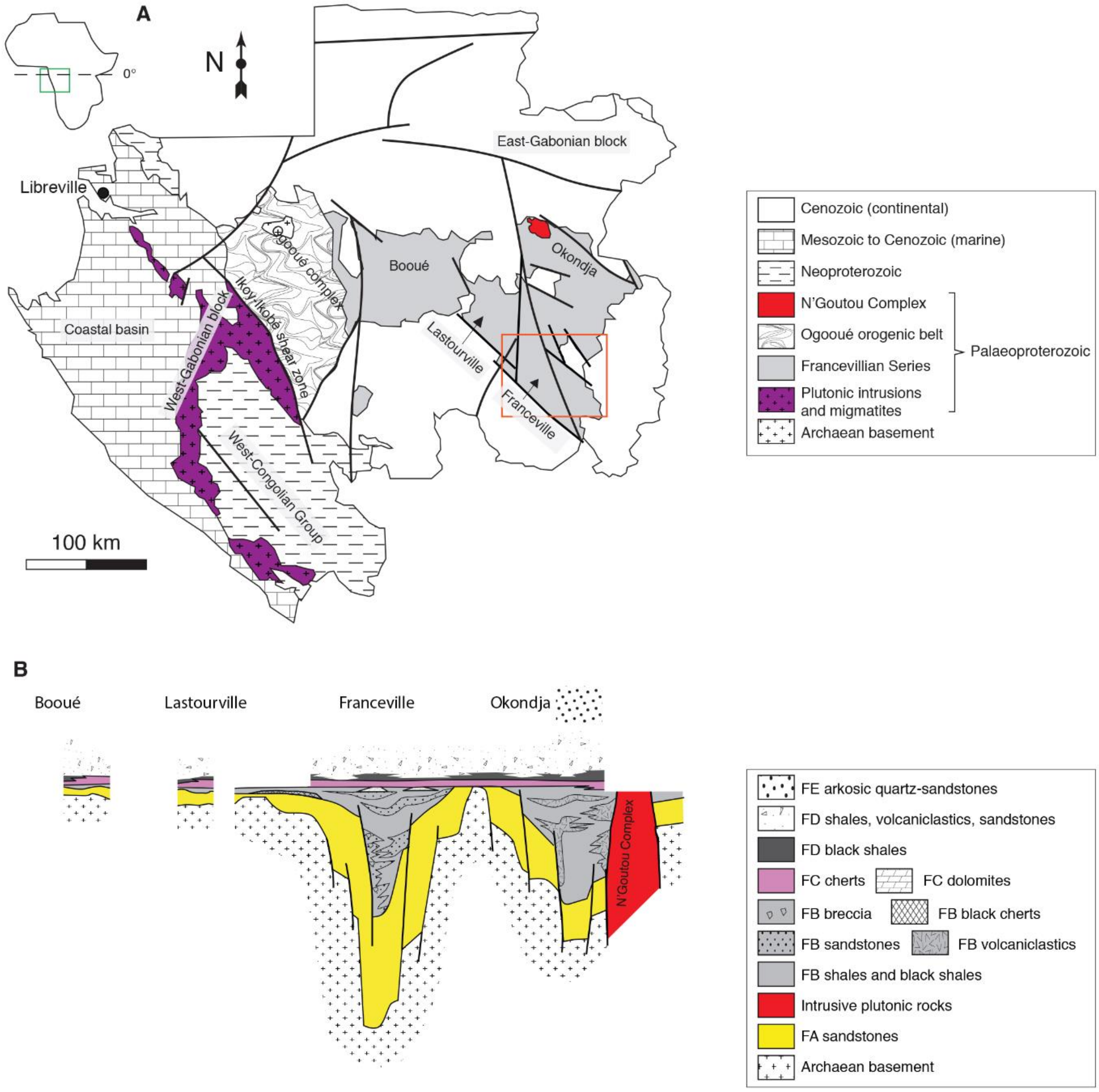

Figure 15: Simplified geological map of Gabon and cross-section across the four intracratonic sub-basins. (**A**) Geological map showing the major lithostructural domains. The orange inset box shows the geological map of Franceville sub-basin in Figure 18. Modified from Thiéblemont *et al*. (2009). (**B**) Schematic basin fill architecture of Francevillian basin. Modified from Bouton *et al*., (2009a).

1.3.2. Geodynamic

The regional geodynamic setting of the Francevillian basin is controversial, however the Palaeoproterozoic Era was marked by the gathering of continental masses that subsequently formed the Nuna supercontinent, 2.1–1.8 Ga ago (Zhao *et al.*, 2002).

The Gabon block was emplaced during the 2.2 to 2.0 Ga-old Transamazonian—Eburnean orogens, resulting from the continental collision between the West Congolese and São Francisco cratons (Figure 16) (Feybesse *et al.*, 1998; Zhao *et al.*, 2002; Thiéblemont *et al.*, 2009; Weber *et al.*, 2016). Weber *et al.* (2016) have recently reviewed the geodynamic evolution of the Francevillian Series by attributing three main syn-sedimentary tectonic events, including (i) rifting after the continental breakup of the Archaean basement at 2.45 Ga, combined with the creation of an oceanic crust, resulted in the occurrence of pre-Eburnean migmatites and a transgressive system of sedimentary deposits, (ii) west-directed subduction of oceanic crust, at the origin of the Ogooué orogenic belt, with ocean closure at 2.2 to 2.1 Ga, and (iii) continental collision at 2.04 to 2.0 Ga. In addition, a sinistral rotational movement during the collision process has likely involved strike-slip movements, leading to the opening of pull-apart intracratonic basins. Matabenonites or K-bentonites of the Francevillian Series added new insights on geodynamic setting, by which their deposition in distal part of a pro-foreland basin is expected (Bankole *et al.*, 2018).

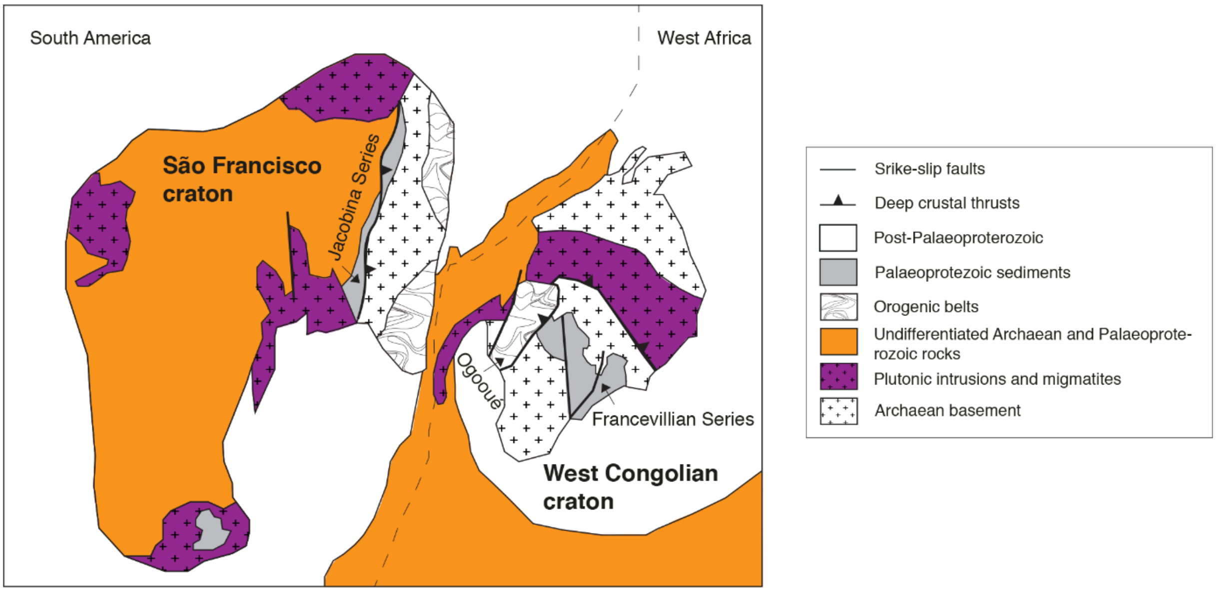

Figure 16: Palaeoreconstruction of West Congolese and São Francisco cratons during the 2.2–2.0 Ga-old Transamazonian–Eburnean orogens. Adapted from Zhao *et al*. (2002).

1.3.3. Lithostratigraphy

Weber (1968) was the first to recognize five lithostratigraphic formations, known as the Francevillian FA, FB, FC, FD, and FE formations from the bottom to the top (Figure 17). The lithostratigraphy of the Francevillian Series is most complete in Franceville and Okondja sub-basins. However, the presence of FE Formation in the Francevillian Series is controversial due to its low geographical scope (Thiéblemont *et al.*, 2014). In addition, FA, FC, and FD formations are continuous across the Francevillian basin, whereas the fault-controlled subsidence in the Franceville and Okondja sub-basins constrained the FB Formation.

a. FA Formation

The basal FA Formation unconformably rests on the Archaean crystalline basement and is predominantly composed of fluvial to fluvio-deltaic, coarse- to fine-grained quartz arenites conglomerate with minor interlayered mudstones, indicating a progressive marine invasion (Gauthier-Lafaye, 1986; Gauthier-Lafaye & Weber, 1989; Bankole *et al.*, 2015). The thickness of the FA Formation ranges from 100 to >1000 m, from the proximal to the distal part of the Francevillian basin. Based on the complex lithofacies variations in the central area of the basin, five distinct zones corresponding to different depositional settings have been distinguished (Gauthier-Lafaye, 1986; Gauthier-Lafaye & Weber, 1989). Zone 4 is composed of poorly-sorted, coarse-grained sandstones and conglomerates, suggesting fluviatile deposits. Moreover, red radioactive conglomerates locally occur. The overlying Otobo series is a coarsening-upward sequence, and consists of alternating mudstones and fine- to coarse-grained sandstones, which indicates a progradation of a plain deltaic environment. Zone 3 is dominated by thick bedded, fine-grained sandstones, and interlayered mudstones with medium to coarse-grained sandstones, reflecting a tidal palaeoenvironment. Zone 2 is predominantly made up of fluvial fine- to coarse-grained sandstones. At last, Zone 1 is composed of fine- to coarse-grained sandstones interbedded with mudstones in a coarsening-upward sequence, indicating a deltaic sedimentation. A typical feature of FA siliciclastic sediments is the variation in color from red alternating with green to grey from bottom to the top, respectively (Gauthier-Lafaye & Weber, 1989). A change in the composition of diagenetic fluids would be linked to this pattern.

The upper part of the formation has revealed the occurrence of uranium ore deposit in association with bitumen (Gauthier-Lafaye & Weber, 2003; Gauthier-Lafaye, 2006). The natural nuclear fission reaction zones are located at Oklo-Okelobondo and Bangombé sites.

b. FB Formation

The marine FB Formation sedimentary rocks discordantly overly the fluviatile to deltaic FA Formation. It consists of a 400–1000 m thick sequence characterized by the predominance of fine-grained sediments (black shales and siltstones) with interbedded debris flows, dolomites, iron-rich levels, and sandstones (Gauthier-Lafaye, 1986; Gauthier-Lafaye & Weber, 1989). This formation was deposited during a synsedimentary tectonic activity that induced important facies lateral variations and thickness changes. Besides, the black shales are characterized by high contents of organic carbon, up to 15 wt.% (Canfield *et al.*, 2013). The FB Formation is classically subdivided into FB_1 (a, b, and c) and FB_2 (a and b) members based on lithological variations (Weber, 1968; Azziley Azzibrouck, 1986). The FB_1 Member is dominated by greenish, silty to sandy shales, heterolithic beds that are composed of shales interbedded with dolomite-cemented siltstones, and manganese-rich black shales (Azziley Azzibrouck, 1986; Pombo, 2004; Reynaud *et al.*, 2017). At the top of the FB_1 Member, the manganese ore deposits rest on a thin iron-rich interval (up to 5-10 m thick; Gauthier-Lafaye & Weber, 2003), and formed by the weathering of Mn-rich carbonate layers known as protore (Weber, 1968; Pombo, 2004). The overlying FB_2 Member is composed of numerous 1- to 5 m-thick beds of coarse-grained "Poubara" sandstones in which few sedimentary structures are recorded. Black shales interbedded with thin layers of siltstones rest on the latter sedimentary package (Weber, 1968). The upper part of FB_2 Member hosts the well-known large colonial macrofossils and organisms motility (El Albani *et al.*, 2010, 2014, 2019).

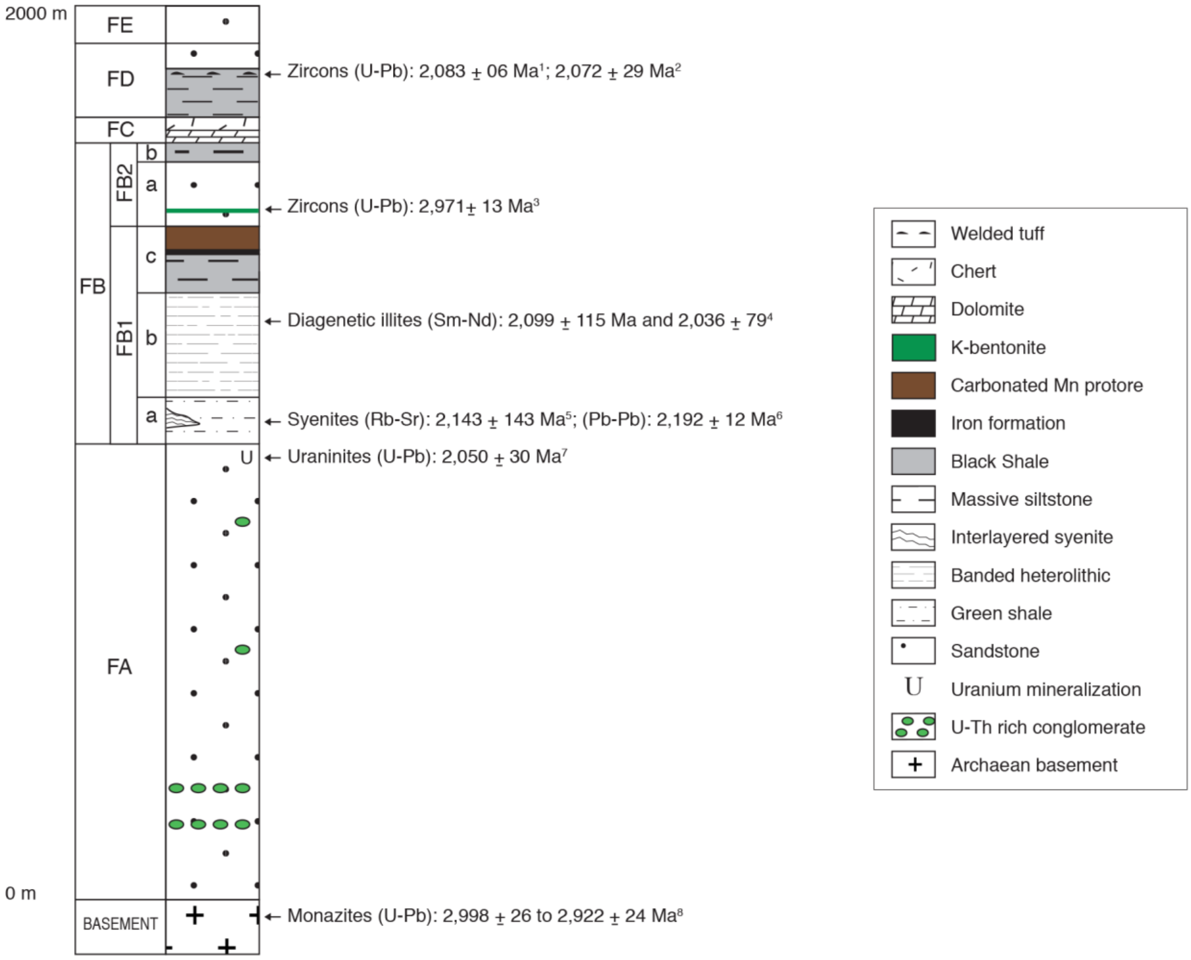

Figure 17: Synthetic lithostratigraphic column of Francevillian Series ([1]Horie *et al*., 2005; [2]Thiéblemont *et al*., 2009; [3]Bankole *et al*., 2018; [4]Bros *et al*., 1992; [5]Bonhomme *et al*., 1982; [6]Sawaki *et al*., 2017; [7]Gancarz, 1978; [8]Mouélé *et al*., 2014).

The N'Goutou Complex has intruded the northern part of Okondja sub-basin during the deposition of FB Formation (Gauthier-Lafaye & Weber, 1989). The emplacement of alkaline granite and syenite in this domain is related to high extension rates, resulting from major strike-slip movements (Moussavou & Edou-Minko, 2006; Thiéblemont *et al.*, 2014; Weber *et al.*, 2016).

c. FC Formation

The FC Formation consists of massive dolomite layers formed in an evaporitic system, and stromatolitic cherts with interlayered black shales (Weber, 1968; Bertrand-Sarfati & Potin, 1994; Préat *et al.*, 2011). The silica-rich horizons (*i.e.*, cherts) are diagenetic replacements of carbonates and sulfates, likely connected to hydrothermal fluids or volcanic origins (Weber, 1968; Préat *et al.*, 2011). This formation varies between 5 and 40 m in thickness (Bouton *et al.*, 2009a) and is ubiquitous in the Francevillian basin. Therefore, it is perceived as a lithostratigraphic marker, although it was secondary formed (Thiéblemont *et al.*, 2014). The FC deposition seals the synsedimentary tectonic activity (Bouton *et al.*, 2009a). In addition, an exceptionally preserved, Gunflint-type microfossil assemblage was recently documented, giving support to the occurrence of filamentous Cyanobacteria in the Francevillian basin (Lekele Baghekema *et al.*, 2017).

d. FD Formation

The FD Formation ranges from 200 to 400 m in thickness and is mainly formed by black shales interbedded with volcanic tuffs and fine- to medium-grained sandstones (Bouton *et al.*, 2009a; Thiéblemont *et al.*, 2014). Thus, it does not really differ from the FB Formation, however the occurrence of underlying silica-rich FC rocks allows us to distinguish the FB rocks from the FD deposits. These sediments were settled in near-continental margin, sulfidic conditions during a transgressive phase (Canfield *et al.*, 2013; Chi Fru *et al.*, 2019). These rocks are organic-rich shales (up to 10 wt.%) and highly depleted in ^{13}C, suggesting the incorporation of methanotroph-derived organic matter (Weber & Gauthier-Lafaye, 2013).

e. FE Formation

The topmost FE Formation consists of ~400 m of medium-grained arkose with interlayered shales (Gauthier-Lafaye & Weber, 1989; Thiéblemont *et al.*, 2014). The sediments show a restricted geographical extension and are merely identified in the northwestern part of the Okondja sub-basin. Thiéblemont *et al.* (2014) considered that the FE Formation has filled local depressions through weathering of the Ogooué orogenic belt.

1.3.4. Biomarkers

Despite the exceptional preservation of the Francevillian Series, this sedimentary package is likely overmature (see section 1.3.5). Hence, little investigations have been conducted for analyzing organic geochemistry. Dutkiewicz *et al.* (2007) published the only available record of molecular fossils in the Francevillian basin, consisting of lipid biomarkers inside fluid inclusion oils. The latter authors described hopanes and steranes in the FA basal sediments and indicated that the organic matter is derived from bacterial and eukaryotic organisms, respectively. This is in agreement with the prediction of molecular clock studies by which a protosterol biosynthesis evolved around 2.31 Ga (Gold *et al.*, 2017). Nonetheless, the timing of the deposition of hydrocarbon biomarkers inside oil-bearing fluid inclusions may not be well constrained (Brocks *et al.*, 2017).

1.3.5. Diagenetic history

Based on fluid inclusions in quartz overgrowth, the unmetamorphosed FA siliciclastic rocks have reached an estimated burial depth of about 4,000 m, a maximum temperature <200 °C, and a pressure gradient ranging from 150 to 200 bars/km (Gauthier-Lafaye & Weber, 1989; Dutkiewicz *et al.*, 2007). The diagenetic effect is also recorded through the authigenesis of various phylosillicates. The neoformation of chlorite, $1M_t$ polytype of illite, and illite/smectite mixed-layer minerals (I-S MLMs) predominantly characterizes the assemblage of diagenetic clays in the Francevillian Series (Ossa Ossa *et al.*, 2013; Ngombi-Pemba *et al.*, 2014; Bankole *et al.*, 2015). The remnant of smectite layers of I-S MLMs over a long period of time required a minimal burial temperature, probably lower than the one estimated by the fluid inclusion method, and a lack of potassium supply (Ngombi-Pemba *et al.*, 2014).

The FB and FD black shales contain a large amount of organic matter and, therefore, have been investigated for their properties of potential petroleum source rock (Gauthier-Lafaye & Weber, 1989; Cortial *et al.*, 1990). Cortial *et al.* (1990) have shown that the organic matter of Francevillian basin has reached high thermal maturity with corresponding low H/C (<0.5 %) and O/C (<0.3 %) ratios. This has been confirmed from the carbonaceous nature of microfossils in the FC Formation by using the Raman spectroscopy (Lekele Baghekema *et al.*, 2017). Indeed, the latter authors estimated a burial temperature of 296 ± 30 °C, but this result is not concordant with the occurrence of early diagenetic clay minerals (Ngombi-Pemba *et al.*, 2014). In fact, the organic matter reacts kinetically faster than the clay neoformation (Velde & Lanson, 1993), and a prolonged time of thermal exposure affects the organic geothermometer (Schiffbauer *et al.*, 2012). The kerogen of the Francevillian Series has not experienced the true anthracite stage, indicating the absence of metamorphism overprint (Cortial *et al.*, 1990). Hydrocarbons were generated in the FB Formation when black shales passed through the oil window, and the compaction and tectonic activity have induced their migration into petroleum-type structural traps in the Upper FA Formation (Gauthier-Lafaye & Weber, 1989; Mossman *et al.*, 2001). The organic matter is now preserved as a solidified hydrocarbon (pyrobitumen) that fills the primary and the secondary porosity of FA sandstones (Gauthier-Lafaye, 1986; Cortial *et al.*, 1990; Nagy *et al.*, 1993).

Both lithology and basin structure have controlled the uranium mineralization process in the upper part of FA Formation (Gauthier-Lafaye & Weber, 1989, 2003; Gauthier-Lafaye, 2006).

The pore space of sandstones host the uranium ore deposits. The migration of liquid hydrocarbons, derived from the overlying organic matter-rich FB Formation, into the uranium-free FA reservoir and the specific tectonic structure of basin have led to the subsequent specific localization of uranium ores. Then, oxidized basinal uranium-bearing fluids have migrated upwardly and interacted with the reduced hydrocarbons at the boundary of FA and FB formations, resulting in uranium precipitation (Gauthier-Lafaye & Weber, 1989; Bankole *et al.*, 2016). Iron geochemistry constrained changes in redox conditions in the sandstone-hosted uranium mineralization during diagenesis (Bankole *et al.*, 2016). It is highlighted that the Fe redistribution under middly oxidizing conditions would have involved the shift in color of facies from red (oxidized) to green (reduced) during late diagenesis. Thus, the circulation of oxidized fluids along faults led to the loss of uranium and its enrichment in the lower and upper part of FA Formation, respectively.

Post-collisional movements induced deformations in the Francevillian basin, 1.95 Ga ago (Weber *et al.*, 2016), but the overall sedimentary sequence is slightly deformed and the basin remains stable until successive Palaeozoic uplifts (Linol *et al.*, 2015). Finally, dolerite dykes have intruded the whole Francevillian Series oriented NNW-SSE and ENE-WSW, and yield a K-Ar isotopic age of 970 ± 30 Ma (Bonhomme *et al.*, 1982).

1.3.6. Radiometric dating

Several radiometric ages have been obtained for the Francevillian basin (Table 1), but the timing of deposition of the Lower Francevillian Series (FA and FB formations) is still controversial and unresolved. U-Pb ages from 2,998 ± 25 Ma to 2,922 ± 24 Ma on monazites are reported for Archaean plutonic rocks (Mouélé *et al.*, 2014). Uranium mineralization in the FA Formation provided U-Pb age of 2,050 ± 30 Ma that delineates early diagenesis (Gancarz, 1978). Interlayered syenites of the N'goutou volcanic Complex intruding the FA and FB formations have been imprecisely dated at 2,143 ± 143 Ma using the Rb-Sr method (Bonhomme *et al.*, 1982). A new dating of zircons for the N'Goutou Complex yields a Pb-Pb age of 2,192 ± 12 Ma, although some zircons are complex in nature and produce highly discordant ages (Sawaki *et al.*, 2017). Diagenetic illites in the Upper FB_1 Member yield an Sm-Nd isotopic ages of 2,099 ± 115 Ma and 2,036 ± 79 Ma on <0.4 μm and <0.2 μm clay fractions, respectively (Bros *et al.*, 1992). Recent dating of zircons from K-bentonites in the Lower FB_2 Member produced a U-Pb age of 2,971 ± 13 Ma, consistent with the age of the underlying Archaean basement (Bankole *et al.*, 2018). Finally, the depositional age of FD Formation is well constrained with ignimbrite tuffs and sandstones, providing U-Pb ages of 2,083 ± 06 Ma (Horie *et al.*, 2005) and 2,072 ± 29 Ma (Thiéblemont *et al.*, 2009), respectively.

Table 1: Summary of radiometric ages in the Francevillian basin.

Lithostratigraphy	Method	Age (Ma)	Age significance	Reference
Ignimbrite tuffs (FD)	U-Pb on zircons	2,083 ± 06	Heritage	Horie *et al.* (2005)
Sandstones (FD)	U-Pb on zircons	2,072 ± 29	Heritage	Thiéblemont *et al.* (2009)
K-bentonites (FB)	U-Pb on zircons	2,971 ± 13	Archaean heritage	Bankole *et al.* (2018)
Black shales (FB)	Sm-Nd isotope on 0.4 µm clay fraction	2,099 ± 115	Diagenesis	Bros *et al.* (1992)
Black shales (FB)	Sm-Nd isotope on 0.2 µm clay fraction	2,036 ± 79	Diagenesis	Bros *et al.* (1992)
Granite (FA-FB)	Pb-Pb on interlayered syenites	2,192 ± 12	Intrusion	Sawaki *et al.* (2017)
Granite (FA-FB)	Rb-Sr on interlayered syenites	2,143 ± 143	Intrusion	Bonhomme *et al.* (1982)
U mineralization (FA)	U-Pb on uraninites	2,050 ± 30	Diagenesis	Gancarz (1978)
Archaean basement	U-Pb on monazites	2,998 ± 25 to 2,922 ± 24	Intrusion	Mouélé *et al.* (2014)

1.3.7. Synthesis of depositional conditions with evidence for microbial activity in the Francevillian basin

The depositional conditions of the FB_2 Member, within which the macrofossils were found, were controversial because sedimentary features are not abundant and weakly indicative. Several authors proposed various palaeoenvironmental interpretations, ranging from shallow-water settings (El Albani *et al.*, 2010; Ngombi-Pemba *et al.*, 2014) to a deep-sea turbiditic setting (Parize *et al.*, 2013).

A reassessment of the sedimentary and stratigraphic evolution of the Francevillian FB and FC formations, together with the occurrence of bacterial communities interpreted as photosynthesizers, confidently argue for a depositional setting within the photic zone and during a regressive system (Reynaud *et al.*, 2017; associated works §1).

1.4. Studied area and sampling

Our investigation occurred in the fossil-rich quarry where the assemblage of macrofossils has been documented in the Franceville sub-basin (El Albani *et al.*, 2010, 2014, 2019). Thus, our observations and field sampling were conducted in the Moulendé Quarry that belongs to the Upper FB Formation—the FB_2 Member (Figure 18). The FB2a unit consists of a 15 m-thick coarse-grained sedimentary package in the quarry, commonly known as Poubara sandstones. The latter facies is overlain by 5 m-thick laminated black shales, which forms the FB2b unit. Outcrop exposures of FB2b black shales are scarce in the Francevillian basin likely due to basin configuration where the organic-rich sediments have been deposited in a mud "pool" between thicker packages of sandstones (Reynaud *et al.*, 2017). However, the Moulendé

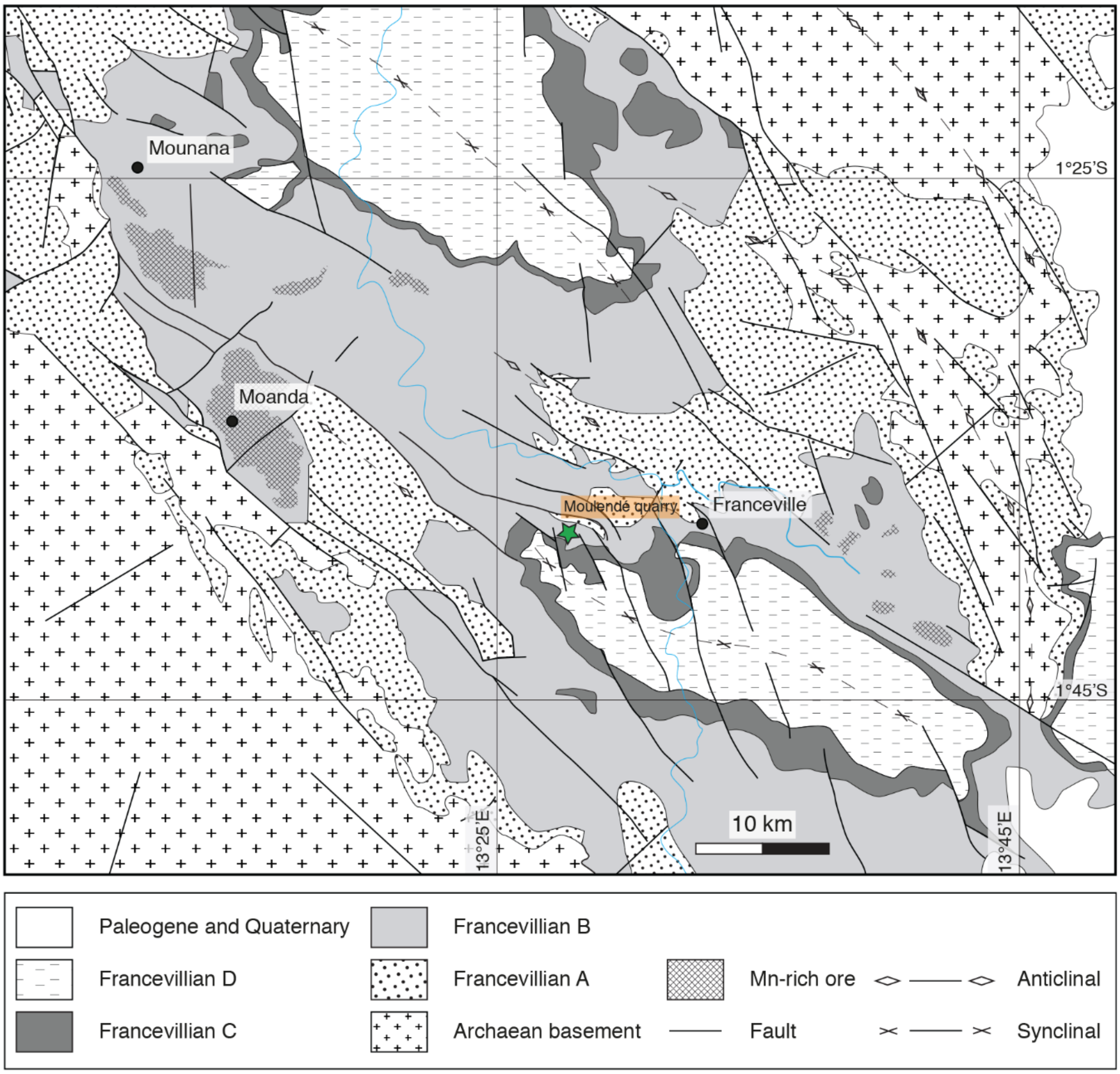

Figure 18: General geological map of Franceville sub-basin. The Moulendé quarry is shown by the green star. Modified from Bouton *et al*. (2009b).

quarry is a well-preserved locality with a non-erosional contact between FB2a and FB2b units, providing high-quality information.

Our petrological, mineralogical, geochemical investigations were carried out on more than 50 samples (both MRS-like and host rocks). The lithology and texture were first taken into account for selecting the most representative specimens. Then, they were described and logged on a synthetic lithostratigraphic column (Figure 19). The samples were subsequently prepared for different analyses.

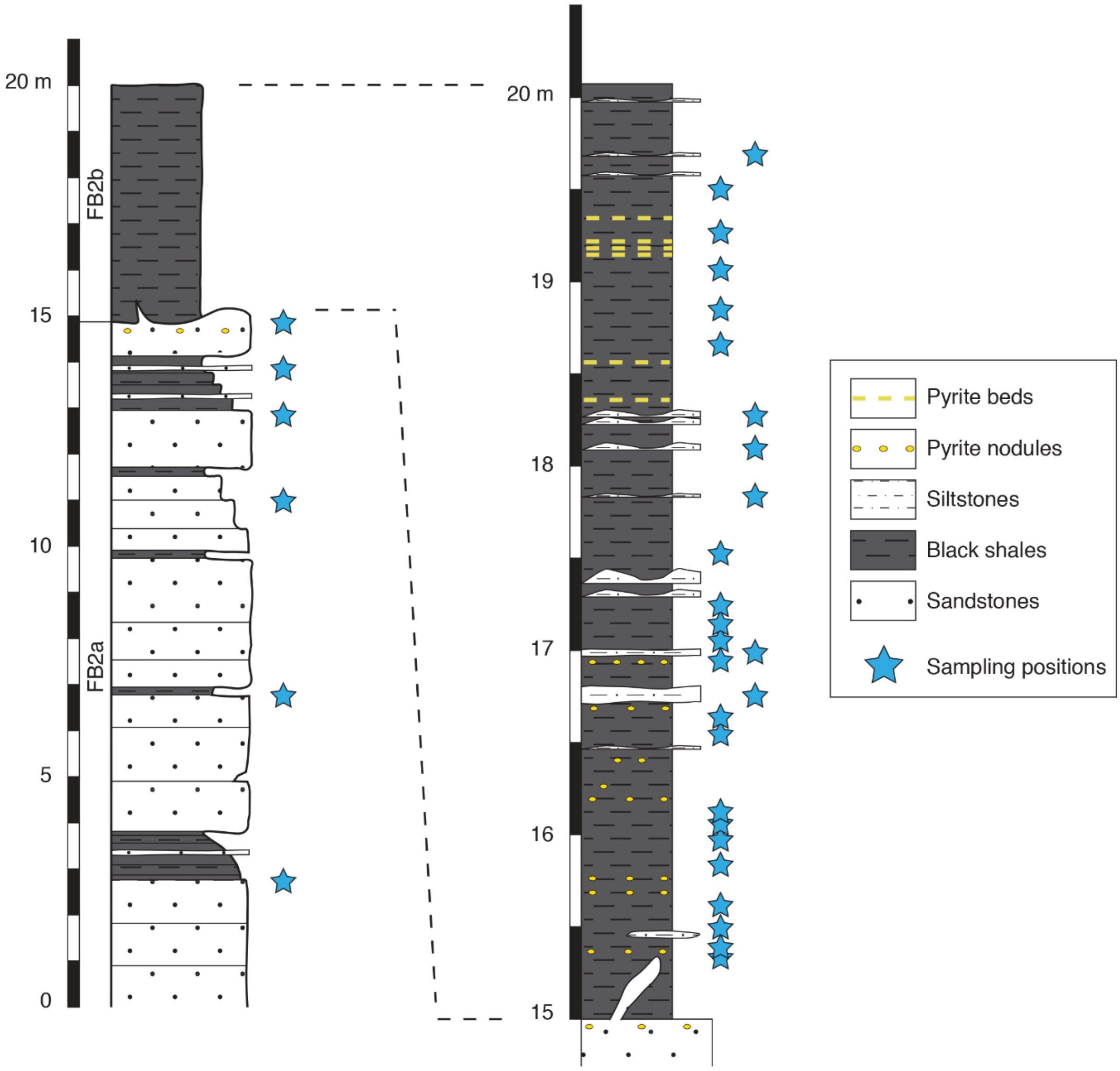

Figure 19: Synthetic stratigraphic column of the Moulendé quarry in the FB_2 Member.

1.5. Methodology

1.5.1. Sample preparation

The MRS-like samples with their underlying host rocks (sandstone and black shale) were slabbed for visual inspections of cut surface. A ZEISS Discovery.V8 stereoscope combined with Axio Cam ERc 5s microscope camera were used to observe the polished slab section. Twenty µm-thick thin sections of approximately 25 x 35 mm were produced perpendicular to the upper surface of polished slabs using standard technics.

After painstaking investigations, the MRS-like samples from the Moulendé quarry were gently removed from their host rocks. A blade was used to extract these delicate specimens to prevent as much as possible contaminations. Directly below the putative MRS features, the host sediments were collected for comparative analyses. For bulk mineralogical and geochemical analyses, small amount of the sample was gently hand crushed in an agate mortar with pestle. The material was systematically cleaned with deionized water and ethanol between each sample preparation to avoid contamination.

For scanning electronic microscopy and X-ray Fluorescence spectroscopy, a specific sample preparation has been conducted. A piece of the sample (less than 2 cm in width) was placed in a plastic tube of 2.5 cm diameter and mounted in epoxy resin. After 24 to 48h of polymerization, the plastic tube was removed. Then, the mounted sample was polished with a series of decreasing coarseness diamond polishing compounds until a perfectly smooth surface was obtained.

The sample preparations were carried out at the University of Poitiers.

1.5.2. Petrographic and mineralogical analyses

a. Optical microscopy

Thin sections were studied for textural relationships and mineralogical examinations. They were examined under plane and cross polarized transmitted light, and reflected light using a Nikon ECLIPSE E600 POL microscope equipped with a Nikon Digital Sight DS-U1 camera and NIS-Element D software at the University of Poitiers.

b. Raman spectroscopy

The Raman spectroscopy analysis is a complementary method for examining the mineralogical composition. This analytical tool identifies mineral phases (*e.g.*, polytypes) that cannot be distinguished with the optical microscopy, and especially, it provides a wide array of information on the carbonaceous material. The Raman spectra of organic matter show representative changes with increasing burial temperature (Kouketsu *et al.*, 2014), indicating that the Raman spectroscopy might be used as a geothermometer.

The analyses were mainly performed on small pieces of polished slab sections for documenting the carbonaceous material in both the MRS-like and host sediment samples. The Raman spectra were obtained with a HORIBA JOBIN YVON Labram HR8OOUV, an integrated Olympus confocal microscope connected to a CCD detector using a Peltier-cooled charge at the University of Poitiers. All analyses were performed by means of 514.5 nm Ar^+ laser of 1 mW, 200 µm confocal hole, 1800 grooves/mm grating, and 5 mm spatial resolution. LabSpec 5 software was used to data recording and treatment.

c. X-ray diffraction (XRD)

The XRD is a convenient method for the identification and analysis of mineralogical composition of rocks.

Sample preparation: This section describes the sample preparations of MRS-like and host rock samples following the standard procedures outlined by Brindley & Brown (1980) and Moore & Reynolds Jr (1997).

Small amount of the powdered sample was mounted into a cavity mount for bulk qualitative mineralogical analyses. The preparation of bulk sample needed to be specific during which the powders were randomly oriented to avoid preferential detection of some minerals. In addition, the < 2 µm clay fraction was extracted from bulk rock samples for a detailed clay mineralogy. The clay size fraction was obtained by dispersion of gently hand-crushed small-sized particles in deionized water with an Elma S60 ultrasonic agitation device without any chemical pre-treatment (Moore & Reynolds Jr, 1997). The dispersed particles were let to settle under gravity in a cylindrical bottle according to Stoke's law at a controlled room temperature of 20 °C, and centrifuged to obtain the <2 µm clay fraction with GR 4 22 centrifuge. Then, the suspensions of clay size fraction were concentrated by evaporation in the oven at 60 °C over night. Oriented mounts were obtained from ~1 mL of the prepared clay-sized suspensions that were pipetted on glass slides. They were subsequently analyzed after drying at room temperature (AD) and ethylene glycol (EG) treatment. The <2 µm fraction of some samples were also Ca-saturated after three dispersions in a 1 M calcium chloride ($CaCl_2$) solution followed by several washings with deionized water. This specific preparation homogenizes the sheets of swelling clays to ascertain whether the interlayer properties are stable. Finally, the randomly oriented clay size fraction was mounted into a cavity mount for examining the diagenetically formed particles through the study of illite polytypes.

Acquisition: The mineralogical composition of bulk powders and <2 µm clay fraction were determined with a Bruker D8 ADVANCE diffractometer at the University of Poitiers using a CuKα radiation operated at 40 kV and 40 mA. Bulk samples were analyzed over an angular range of 2–65° 2θ with a step size of 0.025° 2θ per 3 s counting time, while the analysis of <2 µm clay fraction was performed over 2–30° 2θ angular range with a step size of 0.02° 2θ per 3 s counting time. Finally, illite polytypes were analyzed over an angular range of 19–33° 2θ with a step size of 0.01° 2θ per 2 s counting time.

Treatment: Bruker Eva software was used for background stripping, indexing of diffraction peaks, and identification of mineral phase by comparing with International Centre for Diffraction Data (ICDD) files. The XRD patterns were also compared with reference data published in Brindley & Brown (1980).

XRD profile modelling: The NEWMOD 2.0 program simulation (Reynolds Jr & Reynolds III, 1996) was used for determining the proportion of each clay mineral phase in both MRS-like and host sediment samples. The fit was done on experimental Ca-saturated samples in AD and EG states over 2–30° 2θ angular range. A special attention was given to the stacking mode (R, Reichweite ordering parameter) of illite-smectite mixed layer minerals as well as the proportion of smectite and illite layers in such minerals. The fit is thought to be acceptable when the same solution is obtained for the AD and EG states. The experimental and instrumental factors such as length and thickness of the oriented slides, horizontal and vertical beam divergences, and goniometer radius were introduced as suggested by Drits & Tchoubar (1990). The mass absorption coefficient (μ^*) and sigmastar (degree of orientation of the clay particles on the slide) were set to 45 cm^2/g and to 12° and 18°, respectively, as recommended by Moore & Reynolds Jr (1997). The profile-fitting process does not include angular domains containing non-clay mineral reflections.

d. Electron microscopy

Representative thin sections and polished slabs coated with carbon were examined with a FEI Quanta 200 scanning electron microscope (SEM) equipped with an energy dispersive X-ray spectrometer (EDX) at the University of Lille. The selected samples were observed in both secondary electron (SE) and back-scattered electron (BSE) imaging modes operated at 15 kV accelerating voltage, 1 nA beam current, and a working distance of 10.5 mm. Morphological habits and documentation of textural relationships were acquired in both SE and BSE imaging modes, respectively. The mineral chemistry was obtained through the EDX. The coupled SEM/EDX analyses allowed to characterize chemically the zones of interest with elemental maps and semi-quantification. Varying resolutions and magnifications were used for examining the large set of samples.

The transmission electron microscopy provides a significantly higher resolution for documenting the particle micromorphology. Thus, the <2 µm clay fraction of selected samples (MRS-like and sandstone) was examined with a JEOL 2100 UHR transmission electron microscope (TEM) working at 200 kV accelerating voltage with a LaB6 emitter and equipped with a JEOL EDX detector at the University of Poitiers. Samples were prepared by suspending ~1 mg of each sample in distilled water. A droplet of diluted suspension after ultrasonic treatment was deposited on a C-coated Au grid. In addition, selected-area electron diffraction (SAED) patterns were collected to image the hexagonal net pattern of the analyzed particles in (*hk*0) reflections (Kumai, 1976; Veblen *et al.*, 1990; Whitney & Velde, 1993). The SAED patterns reveal the stacking arrangement of the layers (Veblen *et al.*, 1990; Whitney & Velde, 1993; Kim *et al.*, 2004). A turbostratic ring pattern is typical of turbostratic smectite structure (random rotations between layers), while non-turbostratic (*i.e.*, coherent) stacking pattern is commonly observed in illite crystal structure (*hk*0 dots), forming a hexagonal pattern (Kumai, 1976).

1.5.3. Geochemical analyses

a. Whole-rock elemental analyses

Whole-rock geochemical analyses of major (Si, Al, Fe, Mn, Mg, Ca, Na, K, P, and Ti), trace (As, Ba, Be, Bi, Cd, Co, Cr, Cs, Cu, Ga, Ge, Hf, In, Mo, Nb, Ni, Pb, Pr, Rb, Sb, Se, Sc, Sn, Sr, Ta, Th, U, V, W, Y, Zn, and Zr), and rare earth elements (La, Ce, Pr, Nd, Sm, Eu, Gd, Tb, Dy, Ho, Er, Tm, Yb, and Lu) were carried out at Service d'Analyse des Roches et des Mineraux (SARM) of the Centre des Recherches Pétrographiques et Géochimiques (CRPG), Nancy, France. Major elements were analyzed by inductively coupled plasma atomic emission spectrometry (ICP-AES), while trace and rare earths elements concentrations were measured by inductively-coupled plasma mass spectrometry (ICP-MS). Each powdered sample was fused with lithium metaborate ($LiBO_2$), followed by digestion in dilute nitric acid (HNO_3).

For major elements, the uncertainties are 1% for concentrations higher than 10%, 5% for concentrations between 0.5 and 10%, and 10% for concentrations between 0.1 and 0.5%. According to the analyzed trace element concentration, the uncertainty is lower than 5–10% for elemental concentrations > 50 ppm, lower than 5–20% for elemental concentrations between 10 and 1 ppm, and higher than 25% for elemental concentrations near the detection limit (see Carignan *et al.* (2001) for a detailed description of uncertainties in measurements according to the elemental concentration and related limits of determination).

b. Organic elemental analyses

Fundamental elemental components (carbon, hydrogen, nitrogen, and sulfur) were analyzed on powdered MRS-like samples and their host rocks at the University of Poitiers. The CHNS investigation provides primarily information on elemental content and these compounds are of considerable interest as they are involved in biological cycling. The analyses were carried out with a FlashEA 1112 (ThermoFisher Scientific) CHNS analyzer for flash dynamic combustion at 970 °C under a constant helium flow. Small aliquots of bulk-rock powders (between 5 and 20 mg) were weighed into tin cups depending on how organic-rich the sample was. Data acquisition was done with an Eager 300 software. A calibration curve was performed with aspartic acid and nicotinamide before each analysis when sulfur was not analyzed. In the other case, the calibration curve was obtained with sulphanilamide and BBOT—2,5-Bis(5-tert-butyl-benzoxazol-2-yl)thiophene.

c. Isotopic geochemistry

The carbon isotope composition of organic matter ($\delta^{13}C_{org}$) was first analyzed in 15 samples of MRS-like and black shales at the University of Rennes to ascertain the biogenicity and provide information on the nature of microbial carbon fixation. Then, carbon and nitrogen isotope compositions were completed and measured on MRS-like and host sediment (both sandstone and black shale) samples at the University of California, Riverside.

<u>Sample preparation:</u> For carbon isotope analyses, about 200 mg of each powdered sample were weighed and placed in glass tube. The whole-rock powders were twice decarbonated with 6 M hydrochloric acid (HCl) for one hour at 70 °C. The solid residue was rinsed four times with deionized water by centrifugation and dried in a clean hood overnight. Finally, small aliquots of decarbonated residues (mostly less than 10 mg) were weighed into tin cups.

For nitrogen isotope composition of bulk rock ($\delta^{15}N_{bulk}$), powdered bulk samples (between 20 and 50 mg) were directly weighed into tin cups.

<u>Acquisition:</u> The $\delta^{13}C_{org}$ and $\delta^{15}N_{bulk}$ measurements were measured by flash combustion on an isotope ratio mass spectrometer (IRMS), operated under a constant helium flow, and coupled to an elemental analyzer (EA). All data have been standardized using in-house standards and the isotope data are relative to V-PDB (Vienna Pee Dee Belemnite) and Air-N_2 for $\delta^{13}C$ and $\delta^{15}N$, respectively. Duplicate analyses were performed on approximatively half of the analyzed samples. Total organic carbon (TOC) and bulk nitrogen (TN) concentrations were calculated from peak CO_2 and N_2 areas, respectively.

d. Iron speciation

Iron speciation analysis was performed on MRS-like and black shale samples at the University of Cardiff for assessing the depositional redox conditions. The laboratory procedure for sample preparation is described in details in Canfield *et al.* (1986) and Poulton & Canfield (2005). The total iron (Fe_T) is characterized by three dominant iron pools. First, highly reactive iron (Fe_{HR}) consists of four iron phases that could react with hydrogen sulfide to form pyrite in the diagenetic sequence: iron-bearing carbonate (Fe_{Carb}) + ferric oxides (Fe_{Ox}; including hematite and goethite), + magnetite (Fe_{Mag}) + pyrite iron (Fe_{py}). Second, poorly reactive Fe (Fe_{PRS}) refers to the fraction of some Fe from sheet silicate minerals. Third, unreactive silicate Fe (Fe_U) consists of residual silicate Fe, which is essentially unreactive towards dissolved sulfide. Total Fe extraction were already measured by ICP-AES. Samples containing low total Fe and organic carbon (less than 0.5 wt.%) contents were removed to ensure of the robustness of values, as recommended by Clarkson *et al*. (2014).

Replicate analysis was performed on a third of the studied samples.

Sequential iron extraction: The iron phases (Fe_{Carb}, Fe_{Ox}, Fe_{Mag}, and Fe_{PRS}) were extracted using the sequential extraction procedure (Poulton & Canfield, 2005). Prior the iron extracts, ~50 mg of bulk samples were weighed and placed in 30 mL plastic vial. The Fe_{Carb} was first extracted with 10 mL of sodium acetate buffer at pH 4.5 and 50 °C for 48 hours, followed by Fe_{Ox} using 10 mL of sodium dithionite at pH 4.8 and room temperature for 2 hours, and finally Fe_{Mag} using ammonium oxalate at pH 3.2 and room temperature for six hours. After each extraction, the solution was centrifuged for 5 minutes. Then, I took out 250 µL sample and diluted it to 10 mL with MilliQ water in a new plastic vial, resulting in a dilution factor of 40. I poured out the rest of the buffer and kept the bottom residue for the following extraction. For the final step, I let the residue dried over a weekend in room temperature. Then, Fe_{PRS} was extracted by boiling for 2 min in 5 mL of 12 M HCl. I added 15 mL of MilliQ water before to take out 250 µL and dilute it to 10 mL, which means that the dilution factor for this step is 600.

Iron concentrations were determined using atomic absorption spectrometer after the ferrozine test. Standardization was achieved using 0.1–10 $\mu g.mL^{-1}$ $FeCl_3$ solution in 10^{-2} $mol.L^{-1}$ HCl.

Chromous chloride ($CrCl_2$) distillation: Fe_{Py} was extracted using the standard chromium reduction method (Canfield *et al.*, 1986). First, a larger mass of powdered bulk sample (between 200 and 2000 mg) was weighed into a digestion flask. Then, 10 mL of ethanol, 20 mL of concentrated HCl, and 40 mL of $CrCl_2$ solution were slowly added in a N_2-flushed system for at least 90 minutes. The reaction produced hydrogen sulfide that was collected in trapping vessels where a copper (II) chloride ($CuCl_2$) solution was introduced. Hydrogen sulfide reacted with the working solution and subsequently formed CuS precipitate. The $CuCl_2$ remaining solution is transferred to a flask with a filtration system that collects the precipitate in a filter paper. Titration of the $CuCl_2$ remaining solution was conducted, and was initiated by the addition of 70 mL of sodium acetate trihydrate buffer and 3 to 5 drops of indicator (glycine cresol red). Titrant (0.1 M EDTA) was added from a microburette inserted into the second hole of the stopper. The end-point arose when the solution turns green permanently. Assuming FeS_2 stoichiometry, Fe_{Py} was calculated from the weight percentage of sulfur extracted.

e. X-ray Fluorescence (XRF) microscopy

The synchrotron-based XRF microscopy is a high sensitivity analytical technique and provides elemental maps with a micron-scale spatial resolution. Synchrotron-based XRF analyses were focused on representative MRS-like and black shale samples. The XRF investigations were performed on several areas within the studied polished slabs at the Nanoscopium hard X-ray nanoprobe beamline (Somogyi *et al.*, 2015) of Synchrotron Soleil, L'Orme des Merisiers Saint-Aubin, France. The monochromatic X-ray beam with 12 keV energy was focused on the sample by a Kirckpatrick-Baez nano-focusing mirror. A fast continuous scanning (FLYSCAN) technic was used to obtain micrometer resolution for elemental maps of mm^2-sized sample areas (Medjoubi *et al.*, 2013). The solid angle of detection was increased by means of two Si-drift detectors (VITUS H50, KETEK GmbH) to collect full XRF spectra in each pixel of the scans. The XRF spectra of S, K, Ca, Ba, Mn, Fe, Ni, Cu, Zn, Ga, Ge, and As were obtained, but the distributions of S, K, Fe, Ni, and As are only provided in this manuscript. Each elemental map was normalized to 10 ms/pixel exposure time.

1.5.4. Descriptive statistic and statistical treatment

R software (R version 3.5.1; R Core Team, 2018) was used to carry out descriptive treatment and statistical tests with “FactoMineR”, “factoextra”, and “PMCMR” packages as well as “ggplot2” for drawing plots. Descriptive statistic by means of boxplot is an easy way to show the dataset according to a variable (*i.e.*, elemental concentration and elemental ratio). The box represents 50% of the data and whiskers extend to 1.5 times the interquartile range. The mean, the median, and outliers are often displayed. In addition, principal component analysis (PCA) allows to explore graphically relationships among independent individuals and quantitative variables. PCAs are often realized before statistical tests. Prior to the statistical analysis, the assumption of normality and the homogeneity of variances were tested to perform parametric tests. If such conditions were violated for parametric tests, then non-parametric tests were used. However, the latter return a pvalue less accurate.

PART 2. THE FRANCEVILLIAN BIOTA

2.1. Introduction

Although the distribution of MRS-bearing rocks shows a continuous record throughout much of Earth's history, there are more reported MRS in Phanerozoic rocks (Davies *et al.*, 2016). This may be attributed to potential bias coming from different aims of the personal research interests. The description and interpretation of microbial mats for palaeoenvironmental reconstructions, and/or taphonomical implications are the main purposes of MRS-specific publications (Davies *et al.*, 2016). For instance, Neoproterozoic and Permian-Triassic sedimentary deposits have received a particular interest of researchers because these strata recorded major climatic fluctuations, and significant biological evolution or turnover. In this regard, the Palaeoproterozoic Era fulfils these conditions, but surprisingly was overlooked (Davies *et al.*, 2016). In addition, it is frequently argued that the MRS were more widespread on tidal flats before the Cambrian explosion due to the lack of grazing and bioturbating metazoans (*e.g.*, Gehling, 1999; Bottjer *et al.*, 2000). Nonetheless, complex organisms and benthic microbial communities are capable of prospering together in oxygen-stressed environments, as observed in modern settings (Gingras *et al.*, 2011) and Cambrian equivalents (Buatois *et al.*, 2014).

According to the recent work of Reynaud *et al*. (2017), some MRS were described as a phototrophic ecosystem in the fossiliferous Moulendé quarry, but their structural diversity and organizational pattern with the large colonial macrofossils have not yet been explored. Thus, this second part aims at extending the known record of microbial diversity in the Palaeoproterozoic. Finally, the relationship between bacterial communities with the more complex organism is underlined.

2.2. A study of Palaeoproterozoic microbial mats from the Francevillian Series in Gabon

This section is dedicated to the published article in *Geobiology* journal.

Unusual microbial mat-related structural diversity 2.1 billion years ago and implications for the Francevillian biota

Jérémie Aubineau[1], Abderrazak El Albani[1*], Ernest Chi Fru[2], Murray Gingras[3], Yann Batonneau[1], Luis A. Buatois[4], Claude Geffroy[1], Jérôme Labanowski[1], Claude Laforest[1], Laurent Lemée[1], M. Gabriela Mángano[4], Alain Meunier[1], Anne-Catherine Pierson-Wickmann[5], Philippe Recourt[6], Armelle Riboulleau[6], Alain Trentesaux[6] & Kurt Konhauser[3]

[1]UMR CNRS IC2MP 7285, University of Poitiers, 86073 Poitiers, France. [2]Cardiff University, Main Building, Room 2.15B Park Place Cardiff, CF10 3AT, UK. [3]Department of Earth and Atmospheric Sciences University of Alberta Edmonton, Alberta, T6G 2E3 Canada. [4]Department of Geological Sciences, University of Saskatchewan, Saskatoon, SK S7N 5A5, Canada. [5]Department Geosciences, UMR 6118, University of Rennes 1, 35042 Rennes, France. [6]UMR 8187 LOG CNRS, University of Lille, ULCO, 59655, Villeneuve d'Ascq, France.

*corresponding author: abder.albani@univ-poitiers.fr

Abstract

The 2.1-billion-year-old (Ga) Francevillian series in Gabon hosts some of the oldest reported macroscopic fossils of various sizes and shapes, stimulating new debates on the origin, evolution and organization of early complex life. Here, we document ten representative types of exceptionally well-preserved mat-related structures, comprising “elephant-skin” textures, putative macro-tufted microbial mats, domal buildups, flat pyritized structures, discoidal microbial colonies, horizontal mat growth patterns, wrinkle structures, “kinneyia” structures, linear patterns and nodule-like structures. A combination of petrographic analyses, scanning electron microscopy, Raman spectroscopy and organic elemental analyses of carbon-rich laminae and microtexture, indicate a biological origin for these structures. The observed microtextures encompass oriented grains, floating silt-sized quartz grains, concentrated heavy minerals, randomly oriented clays, wavy-crinkly laminae and pyritized structures. Based on comparisons with modern analogues, as well as an average $\delta^{13}C$ organic matter (C_{org}) composition of –32.94 ± 1.17‰ (1 standard deviation, SD) with an outlier of –41.26‰, we argue that the mat-related structures contain relicts of multiple carbon pathways including heterotrophic recycling of photosynthetically derived C_{org}. Moreover, the relatively close association of the macroscopic fossil assemblages to the microbial mats may imply that microbial communities acted as potential benthic O_2 oases linked to oxyphototrophic cyanobacterial mats and grazing grounds. In addition, the mat's presence likely improved the preservation of the oldest large colonial organisms, as they are known to strongly biostabilize sediments. Our findings highlight the oldest community assemblage of microscopic and macroscopic biota in the aftermath of the "Great Oxidation Event," widening our understanding of biological organization during Earth's middle age.

Keywords

Bacterial mats, Gabon, geochemistry, geomicrobiology, palaeoenvironment, Palaeoproterozoic

1 | INTRODUCTION

The Palaeoproterozoic Era hosted one of the most important geochemical events in Earth's history, marked by a measurable accumulation of atmospheric oxygen, the so-called "Great Oxidation Event" (GOE) between 2.45 and 2.32 billion years ago (Ga). Evidence for the GOE comes from the disappearance of detrital pyrite, uraninite and siderite from fluvial and deltaic deposits, an increase in the retention of iron in palaeosols, an enrichment of Cr and U in iron formations, and perhaps most importantly, the disappearance of sedimentary sulfur isotope mass-independent (S-MIF) anomalies indicative of atmospheric SO_2 processing in the absence of appreciable ozone (Holland, 2002; Bekker *et al.*, 2004; Farquhar *et al.*, 2011; Konhauser *et al.*, 2011; Partin *et al.*, 2013b; Lyons *et al.*, 2014). In the wake of the GOE, large positive excursions in the $\delta^{13}C$ of marine inorganic carbon, during the "Lomagundi Event" *ca.* 2.22–2.1 Ga (Karhu & Holland, 1996), are believed to reflect large-scale burial of organic matter in marine sediments (Berner, 2004; Bekker & Holland, 2012). New evidence suggests that the "Lomagundi Event" ended with a drastic drop in Earth's oxygen content (*e.g.*, Partin *et al.*, 2013a), perhaps related to large-scale oxidation of organic carbon (Canfield *et al.*, 2013) and/or changes in ocean biogeochemical processes that may have inhibited primary productivity (Chi Fru *et al.*, 2015).

The Francevillian sedimentary rocks *ca.* 2.1 Ga record these biogeochemical fluctuations in Earth's oxygen accumulation dynamics through extreme excursions in the carbon cycle, in addition to hosting the oldest large colonial macroorganisms (El Albani *et al.*, 2010, 2014). Major elements, trace metals, organic carbon and isotope analyses offer constraints on the basin geochemistry, revealing variations from the base to the top that are linked to sea level changes (Canfield *et al.*, 2013; Bankole *et al.*, 2016). The Lower Francevillian fluviatile rocks were deposited in oxygenated waters (Bankole *et al.*, 2016), whereas the Upper Francevillian marine rocks were deposited in oxic, ferruginous and euxinic waters (Canfield *et al.*, 2013). The large macrofossils are highly variable in terms of size, shape and pyritization process being represented by lobate, elongated, rod-shaped, and disc-shaped morphotypes. The pyritization process did not fully occur in the circular discs, indicating that their organic composition differs from that of pyritized specimens (El Albani *et al.*, 2010, 2014). In addition, some carbonaceous spheroidal microstructures have also been reported as organic-walled acritarchs that might have a planktonic origin.

Of late, microbial fossils were found in the Francevillian sequence, including putative bacteriomorphous structures (Dubois *et al.*, 2015) and a Gunflint-type assemblage of microfossils in the stromatolitic units (Lekele Baghekema *et al.*, 2017). The presence of colonial macroorganisms and microfossils makes the Francevillian biota unique, but interestingly, evidence of microbial mats has never been demonstrated. In this work, we describe for the first time ever microbial mat-related structures (MRS) from 2.1 Ga siliciclastic sandstones and black shales from the FB_2 Member of the Francevillian basin, Gabon. MRS are physical remains of destroyed mats and structures associated with decay, instead of well-preserved mat growth features (Eriksson *et al.*, 2010). Their sedimentary features are preserved because microbes secrete extracellular polymeric substances (EPS), an adhesive mucilage (Decho, 2000), that provide a coherent and protective coating that is unlikely to arise in sediments without a biological input (Gerdes *et al.*, 1993, 2000; Porada & Bouougri, 2007; Noffke, 2010).

Microbial life in the Palaeoproterozoic has been poorly described (Davies *et al.*, 2016) even though existing palaeontological and biogeochemical evidence points towards the existence of significant microbial diversity previously in the Archaean. Through a combination of macroscopic and microtexture analyses, petrographic, geochemical, organic elemental analyses and stable carbon isotope composition of bulk organic matter, we compare modern and fossil mat-related structures, to characterize the marine palaeoenvironment in which the putative microbial mats formed. The data reveal the biogenicity of these structures, adding new insights into the origins of the Francevillian biota (El Albani *et al.*, 2010, 2014; Ossa Ossa, 2010; Parize *et al.*, 2013; Ngombi Pemba, 2014; Reynaud *et al.*, 2017). It is important that, we assessed and described the organizational, ecological and taphonomical processes that led to the development and preservation of the unique Francevillian biota.

2 | GEOLOGICAL BACKGROUND

The Francevillian basin, located in the southeastern part of the Republic of Gabon (Figure 20A), is a 35,000 km² depression comprising 2.2–2.0 Ga marine sedimentary rocks that unconformably overly an Archaean basement (Weber, 1968). Petrographic and geochemical analyses indicate that the Francevillian sediments were not affected by metamorphic transformation (maximum temperature 100 °C; Gauthier-Lafaye & Weber, 1989; Ngombi-Pemba *et al*., 2014), resulting in the preservation of seawater composition at the time when deposition took place. Moreover, carbon isotopic and redox sensitive element compositions suggest that the “Lomagundi Event” was a global event (Canfield *et al.*, 2013).

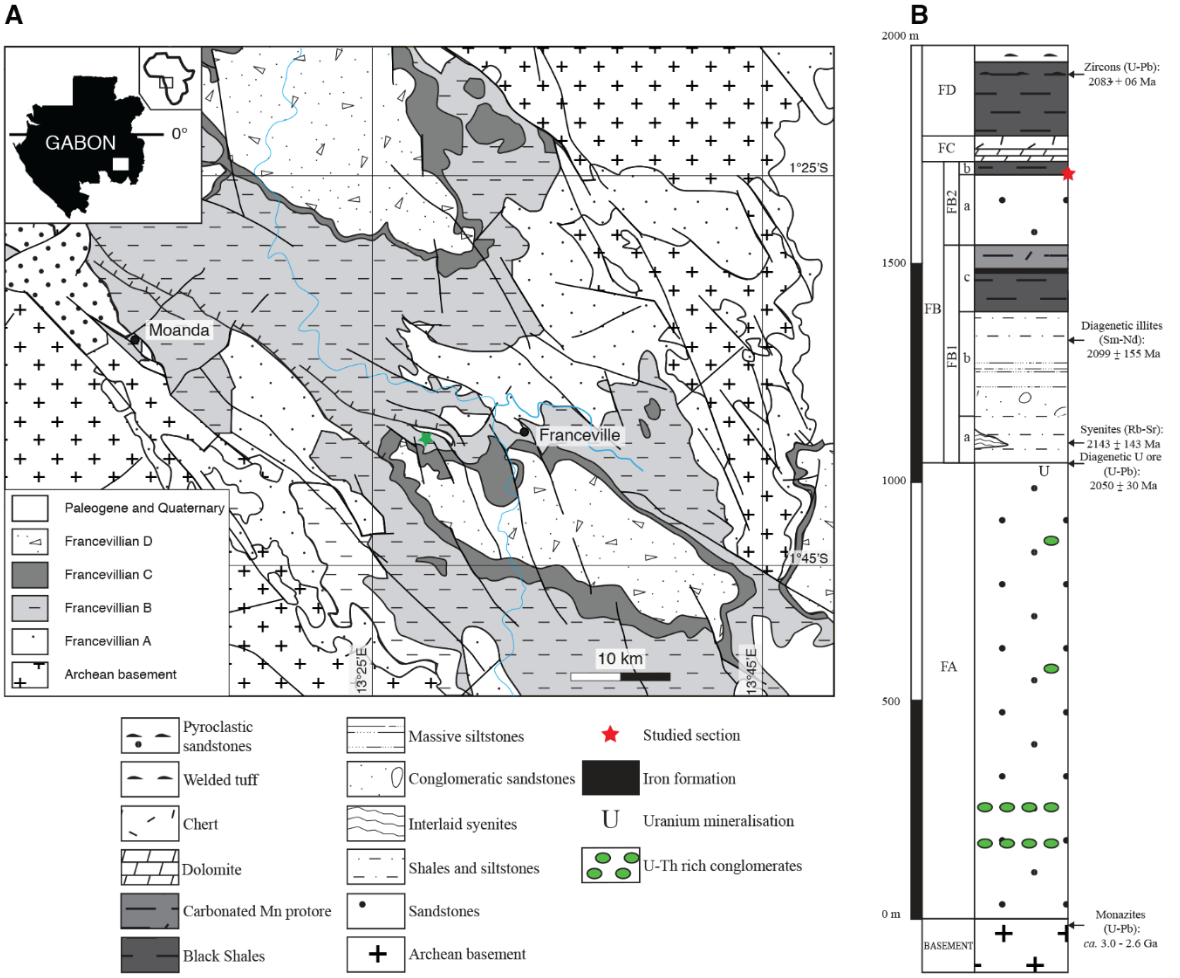

Figure 20: Geological map and lithostratigraphic column. (**A**) Geological map of the Francevillian basin. The studied quarry is Moulendé (green star). Geological map adopted from Bouton *et al.* (2009b). (**B**) Synthetic lithostratigraphy of the Francevillian series. Four sedimentary units rest unconformably on Archean rocks. The red star indicates the detailed lithostratigraphic column observed in the Moulendé quarry (Figure 21).

The basin fill, composed of siliciclastic fluvial and marine deposits that are 1,000–2,500 m thick, is subdivided into four major lithostratigraphic formations, FA to FD (Figure 20B; Weber, 1968; Gauthier-Lafaye & Weber, 1989; Gauthier-Lafaye, 2006; El Albani *et al.*, 2010, 2014, 2014). Fluviatile to deltaic conglomeratic sandstones, overlain by marine sandstones deposited in a tidal environment (*i.e.*, syntectonic filling), make up the FA Formation, with the overlying sediments hosting diagenetic uranium ore deposits and the natural nuclear fission reactors of Oklo (Gauthier-Lafaye & Weber, 1989, 2003). The marine-dominated FB sequence rests unconformably on FA. The former was deposited below storm wave base during basin deepening and is subdivided into the FB1 (a, b and c) and FB2 (a and b) subunits. The FB1a and FB1b subunits are composed of interbedded shales, sandstones and conglomerate, stacked into fining upwards packages, while the overlying FB1c subunit mainly consists of black shales with a thin iron formation, likely corresponding to a maximum flooding surface. This is then overlain by thick Mn-rich carbonates. Massive sandstone beds of the FB2a subunit, probably deposited in channels near the fair-weather wave base, are capped by thinly laminated black shales that are 5 m thick, and interbedded with thin siltstone layers (FB2b), presumably deposited by waning storm surges. Outcrops of the FB2b subunit are scarce but host the well-known colonial macroorganisms described in El Albani *et al*. (2010, 2014). The overlying FC Formation consists of dolomite and thickly-banded stromatolitic cherts that were deposited under shallow water conditions (Bertrand-Sarfati & Potin, 1994). The uppermost FD Formation consists mainly of black shales, with pyroclastic material at the top deposited in a deep marine environment (Gauthier-Lafaye & Weber, 2003).

The Francevillian basin has been intensively studied because of economic interests in their uranium and manganese ore content (Gauthier-Lafaye & Weber, 1989, 2003). Therefore, various ages have been obtained for the Francevillian sediments. For example, monazites contained in Archaean plutonic rocks from the Chaillu massif close to the FA Formation transition provided U-Pb ages of 2,998 ± 25 Ma to 2,621 ± 30 Ma (Mouélé *et al.*, 2014). A U-Pb age of 2,050 ± 30 Ma reported for uranium mineralization, delineates early diagenesis at the FA-FB boundary (Gancarz, 1978). Coarse-grained syenites of the N'Goutou volcanic complex, in the northern part of the Republic of Gabon, that are interlayered with rocks at the base of the FB1 sequence, yield an Rb-Sr age of 2,143 ± 143 Ma (Bonhomme *et al.*, 1982). It is considered that these volcanic rocks were formed simultaneously with the sedimentary rocks. Diagenetic illites from the top of the FB1b subunit have been dated at 2,099 ± 115 Ma using the Sm-Nd method (Bros *et al.*, 1992). At last, recent dating of zircons from welded tuffs near the top of the FD Formation produced a U-Pb age of 2,083 ± 6 Ma (Horie *et al.*, 2005).

The Palaeoproterozoic Francevillian MRS were discovered in the Moulendé quarry, the same fossiliferous quarry where large colonial organisms have been reported (El Albani *et al.*, 2010, 2014). MRS are heterogeneously distributed in the Upper FB2a subunit, as well as in the overlying laminated black shale. The latter is 5 m thick and forms the FB2b subunit (Figure 21), covering a ~20 m thick host interval.

3 | METHODS

3.1 | Sampling and sample preparation

About one hundred samples were collected in order to describe large-scale variability in morphology, structural organization and diversity from outcrops localized in one locality over several years (Figure 20). All samples were logged to provide information on their spatial and time repartitions of the studied area (Figure 21), and then photographed at the University of Poitiers using a Nikon Europe D610 digital single-lens reflex camera equipped with a Nikon AF-S 24–120 mm f/4G ED VR lens. Polished slabs were observed using a ZEISS Discovery.V8 stereoscope combined with Axio Cam ERc 5s microscope camera. Based on this pre-screening analysis, representative samples were selected and powdered in an agate mortar for elemental and carbon isotope systematics.

3.2 | Petrographic and mineralogical analysis

Petrographic and mineralogical examinations were performed by transmitted and reflected light on eight polished thin sections using a Nikon ECLIPSE E600 POL microscope equipped with a Nikon Digital Sight DS-U1 camera and NIS-Element D software for scanning observations. Seven thin sections were carbon coated and examined for textural and compositional analyses using a FEI Quanta 200 scanning electron microscope (SEM) at the University of Lille 1. The SEM, coupled to Rontec energy-dispersive spectra (EDS) for semi-quantitative mineral analysis in backscattered electron mode (BSE), was operated at 15 kV accelerating volts and a 1 nA beam current at a working distance of 10.5 mm.

3.3 | Carbon analysis

Raman spectroscopy was used to determine the composition of carbon preserved within the MRS on two representative samples. Analyses were carried out at the University of Poitiers with a HORIBA JOBIN YVON Labram HR800UV, an integrated Olympus confocal microscope coupled to a Peltier-cooled CCD detector. All analyses were performed by means of 514.5 nm Ar^+ laser of 1 mW, 200 µm confocal hole, 1,800 grooves/mm grating. Data recording and treatment were done with LabSpec 5 software.

Ten representative samples, composed of five mat samples and five associated surrounding sediments, were crushed for the determination of the elemental content of associated organic matter, as well as carbon and sulfur composition, at the University of Poitiers. Analyses were performed using a CHNS analyzer, model FlashEA 1112 (Thermofisher Scientific) by flash dynamic combustion at 970 °C under a constant flow of helium. Data were recorded using Eager 300 software. A calibration curve was obtained with sulfanilamide and BBOT—2,5-Bis(5-tert-butyl-benzoxazol-2-yl) thiophene—before each analysis. The results of carbon contents include both inorganic and organic carbon, but petrographic analyses showed that calcium carbonate and dolomite concentrations were low.

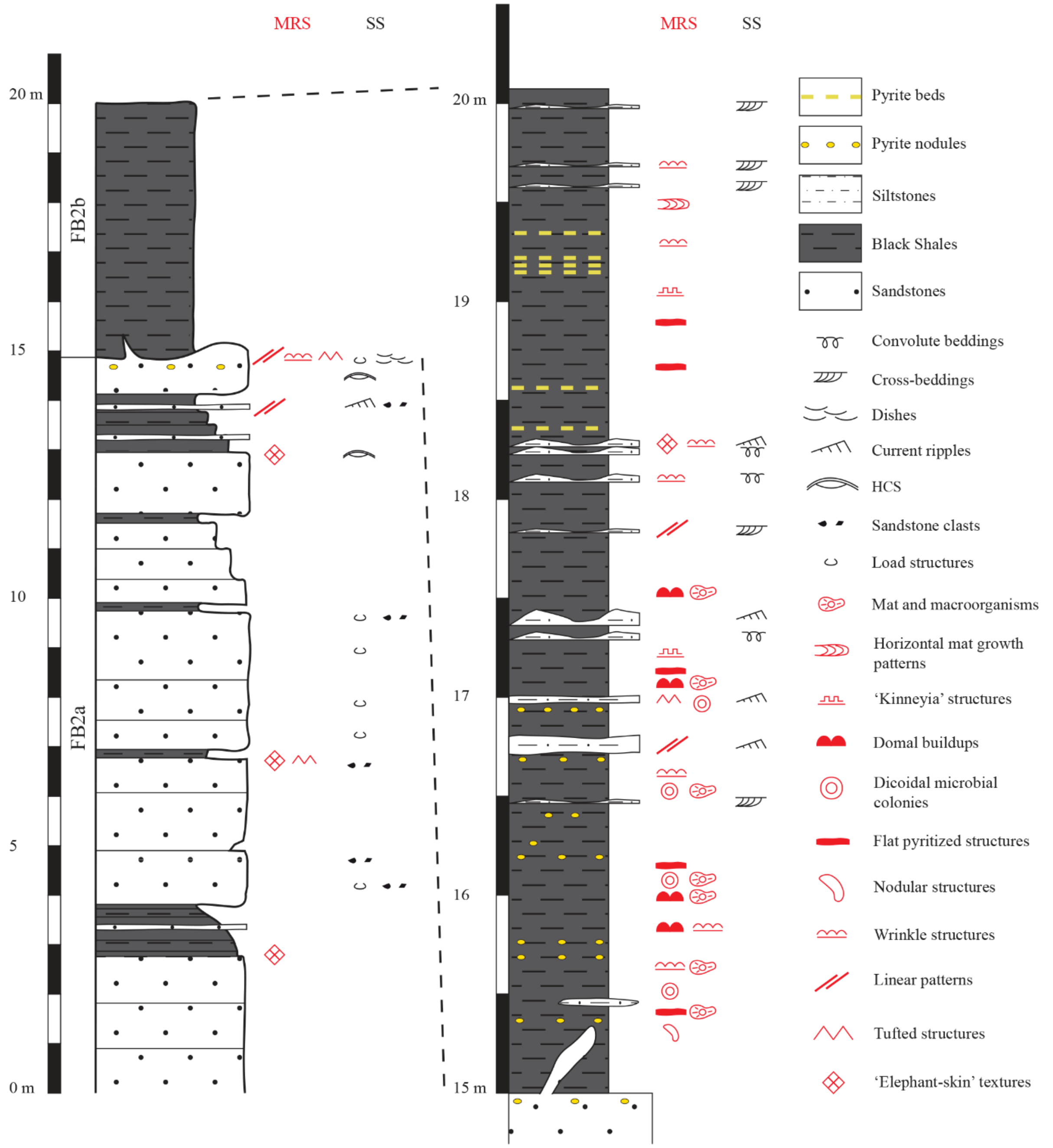

Figure 21: Detailed lithostratigraphic column. Composite columnar section of the Moulendé quarry in the FB$_2$ Member showing the vertical distribution of ten representative types of mat-related structures (MRS) and sedimentary structures (SS).

Stable carbon isotope measurements (^{12}C, ^{13}C) of organic matter from 14 mat samples (from both FB2a and FB2b subunits) were conducted at the Stable Isotopes Laboratory of UMR Pegase (INRA Rennes, France), using an elemental analyzer coupled with an isotope ratio mass spectrometer (IRMS; VG Isoprime; UMR PEGASE—INRA Rennes). More than 500 mg of fine-grained powders were analyzed and loaded in tin capsules for each sample. IAEA-C6 (sucrose ANU, $\delta^{13}C$ = −10.63‰), USGS-24 (graphite, $\delta^{13}C$ = −15.98‰), USGS-40 (glutamic acid, $\delta^{13}C$ = −26.32‰) and Urea Isotopic Working Standard ($\delta^{13}C$ = −38.3‰) were used as reference standards. Data are expressed as delta values (‰) relative to Vienna Pee Dee Belemnite (V-PDB). No correction was added to the measured values, and the analytical uncertainty is estimated to be lower than 0.2‰.

4 | FACIES ANALYSIS OF THE MOULENDÉ QUARRY

The Moulendé quarry has been examined over an area of ~5 ha, for a total of nine studied outcrops (Figure 22A). Among them, the F8 outcrop (Figures 22A-C) was logged in detail because of its well-exposed strata and sedimentary structures. It is the only outcrop where the FB2a-FB2b transition is observed with accompanying black shale deposits. Lithological composition, vertical facies relationships and sedimentary features allow recognition of two depositional facies from the MRS-bearing strata.

4.1 | Facies 1

Thick-bedded, coarse-grained sandstones represent the main facies of the Moulendé quarry. These deposits are commonly referred to the Poubara sandstones (FB2a subunit; Figures 21, 22A-C). This facies is 15 m thick in the quarry, as well as in the closest drill core (GR5; Azziley Azzibrouck, 1986), but could be up to 100 m thick elsewhere in the basin (Weber, 1968). Interbedded thin-bedded, coarse-grained sandstones and laminated black shales form heterolithic beds. The uppermost massive sandstone bed is laterally heterogeneous in thickness, and its bedding surface is undulatory. At the top of several massive sandstone beds, sedimentary features, including load structures, sandstone clasts and water escape structures, such as dishes, are present. These beds occasionally contain dm-scale hummocky cross-stratification (HCS), restricted to the upper part of the succession (Figures 21, 22D; Reynaud *et al.*, 2017).

4.2 | Facies 2

Numerous thin-bedded, parallel-laminated black shales with interbeds of siltstones lie conformably upon Facies 1. They form stacks of variable thickness in the upper part of the studied succession and are about 5 m thick. Connected to the underlying facies and approximately 0.4 m in height, a sandstone dyke cross-cuts these multilayered black shales (Figures 21, 22E). There is no evidence of fracturing along the dyke, indicating that the sediments were not consolidated prior to injection. The main component of facies 2 is characterized by rhythmic successions of mm-scale light and dark laminae of siltstones and shales. Small-scale cross-laminae are found within mm-thick interbedded siltstones. Load-shaped and flame-shaped structures forming convolute bedding (Figures 21, 22F) are observed in interbedded medium-to-coarse-grained siltstone beds ranging from 2 to 5 cm in thickness. Interference ripples are also observed, indicating palaeowaves coming from two directions (Figures 21, 22G). At last, a dm-scale bed containing dark-colored convex laminae associated with cm-scale current ripples comprise the thickest interbedded coarse-grained siltstones (Figures 21, 22H).

Figure 22: Plane view and outcrop pictures of sedimentary facies in the Moulendé quarry. (**A**) Representation of the quarry from plane view. Red box indicates the main studied outcrop in B (F8).F = outcrops. (**B**) Details of the bedding geometry at the transition between massive sandstone beds and thinly laminated black shales. (**C**) Closer view of B. (**D**) Cross-section view of decimeter scale hummocky cross-stratifications (HCS), FB2a subunit. (**E**) Sandstone dyke, FB2a—FB2b transition. Coin diameter: ~2 cm. (**F**) Cross-section view of convolute structures, FB2b subunit. (**G**) Bedding plane view of interference ripples, FB2b subunit. (**H**) Longitudinal view of dark-colored convex laminae associated with cm-scale foreset beds, FB2b subunit.

4.3 | Interpretations

The variation in thickness of the uppermost massive sandstone level (at ~15 m in the stratigraphy) may be related to detachment folds and troughs later infilled by overlying sediments (Reynaud *et al.*, 2017). Sudden and rapid deposition of coarse-grained sediments produce load and dish structures by immediate dewatering (Reineck & Singh, 1980). Rapid sedimentation also results in sandstone dykes formed by elevated pore pressures leading to fluidization of the unconsolidated sediment. In addition, conditions that are favorable for the formation of HCS are commonly found between the fair-weather and storm wave base (Immenhauser, 2009). Various interpretations have been proposed for the palaeoenvironmental setting of the FB2a subunit. They range from a deltaic palaeoenvironment subjected to tidal influence (El Albani *et al.*, 2010; Ossa Ossa, 2010), to a shoreface palaeoenvironmental setting (Ngombi Pemba, 2014), to a turbidite lobe setting in waters deeper than 200 m (Parize *et al.*, 2013). Reynaud *et al*. (2017) showed that the Poubara sandstones are composed of high-density sediment gravity flow deposits, emplaced during a forced regressive system tract. These authors underline that the Francevillian basin was likely isolated because of the absence of wave deposits. They also noticed the presence of linguoid and interference ripples that is consistent with shallow water settings. Thinly laminated black shales are deposited in a relatively quiet water setting but interrupted by quickly deposited supplies of millimeter-to-centimeter-scale siltstones. These laminae host many sedimentary structures that indicate a strong current. Reynaud *et al*. (2017) suggest that these sediments were deposited close to the maximum regressive surface whereas Parize *et al*. (2013) argue for the deposition of turbidites on an upper slope setting.

5 | MAT-RELATED STRUCTURES (MRS) IN THE FB$_2$ MEMBER

The MRS documented here come from a 20 m thick interval of the FB$_2$ sequence (Figure 21). Some specimens are entirely or partially pyritized, while others display a few isolated pyrite grains within the mat layers. Following the classification scheme by Sarkar *et al.* (2008) the Francevillian MRS are divided into two major categories: (a) mat-layer structures, representing potential in situ growth of a microbial mat (Figures 23, 24; Appendix 1) and (b) mat-protected structures (Figure 25), possibly formed by abiotic processes but requiring the protection of a microbial mat (Davies *et al.*, 2016).

5.1 | Mat-layer structures

This group of MRS represents the “mat-layer itself that may be intact, deformed or rafted” (Sarkar *et al.*, 2008). In this work, we interpret well-preserved, intact mat growth according to the following criteria.

5.1.1 | “Elephant-skin” textures

Description

“Elephant-skin” textures (Runnegar & Fedonkin, 1992) encompass quasi-polygonal, geometrically distinct reticulate patterns, ranging from the millimeter to centimeter scale, and bearing bulges or ridges (Figures 23A-C). They are both identified at the top of the massive Poubara sandstones and the interbedded siltstones in the black shales (Figure 21). Individual polygons are 0.3–1.3 cm in diameter, with a maximum relief of 0.2 cm.

Microscopic analyses show reticulate patterns preserved as non-homogenous dark laminae above a light, coarser material 200–600 μm thick (Figures 26A, F). The overlying layer consists of abundant wavy-crinkly laminae entangling 20–50 μm quartz grains and heavy minerals (*e.g.*, titanium oxides, apatites and monazites); the latter suggested by the relative proportions of the elements found through SEM-EDS analysis (Appendix 2), as well as transmitted and reflected light microscopy. Most of the grains in the wavy-crinkly laminae are randomly arranged within a clayey matrix and are dominated by O, Al, Si, Mg, K and Fe (Appendices 2, 3). Reticulate patterns are also C-rich (up to 8.52%) compared to the underlying sandstone bed, as evident from the Raman (Figures 27A-C) and organic elemental analyses (Appendix 4). The carbonaceous layer is punctuated by tufted microstructures, either on bulge rims or within the bulges, with similar striking morphologies to each other and where clay layers are almost vertically oriented (Figures 26F, 28A, B). Based upon the description by Noffke *et al*. (2013), the height/base index is 30/100 to 120/220 μm long, separated at regular distances of 150–230 μm from each other.

Interpretation

“Elephant-skin” textures are formed by a specific arrangement of tufts, pinnacles, bulges and smaller-scale bulges arranged into ridges. Tufts, often arising in ridge junctions or at the intersection of microbial bulges, are proposed as a particular type-feature of cyanobacterial mat filaments growing vertically towards a light source (phototaxis; Gerdes *et al.*, 2000; Porada & Bouougri, 2007; Bose & Chafetz, 2009). These textures are known in modern supratidal environments (Gerdes *et al.*, 2000; Gerdes, 2007; Bose & Chafetz, 2009; Taj *et al.*, 2014), but have also been recorded and described in some ancient shallow water environments from the terminal Proterozoic (Runnegar & Fedonkin, 1992; Gehling, 1999), and perhaps even the Archaean (Flannery & Walter, 2012). However, Shepard & Sumner (2010) debated the role of phototaxis in the formation of reticulate patterns and tufted structures. They investigated whether filamentous Cyanobacteria were influenced by light to form polygonal structures or whether they were related to their own morphotype. Thus, reticulate patterns may result from an undirected motility of filamentous bacteria without the influence of light.

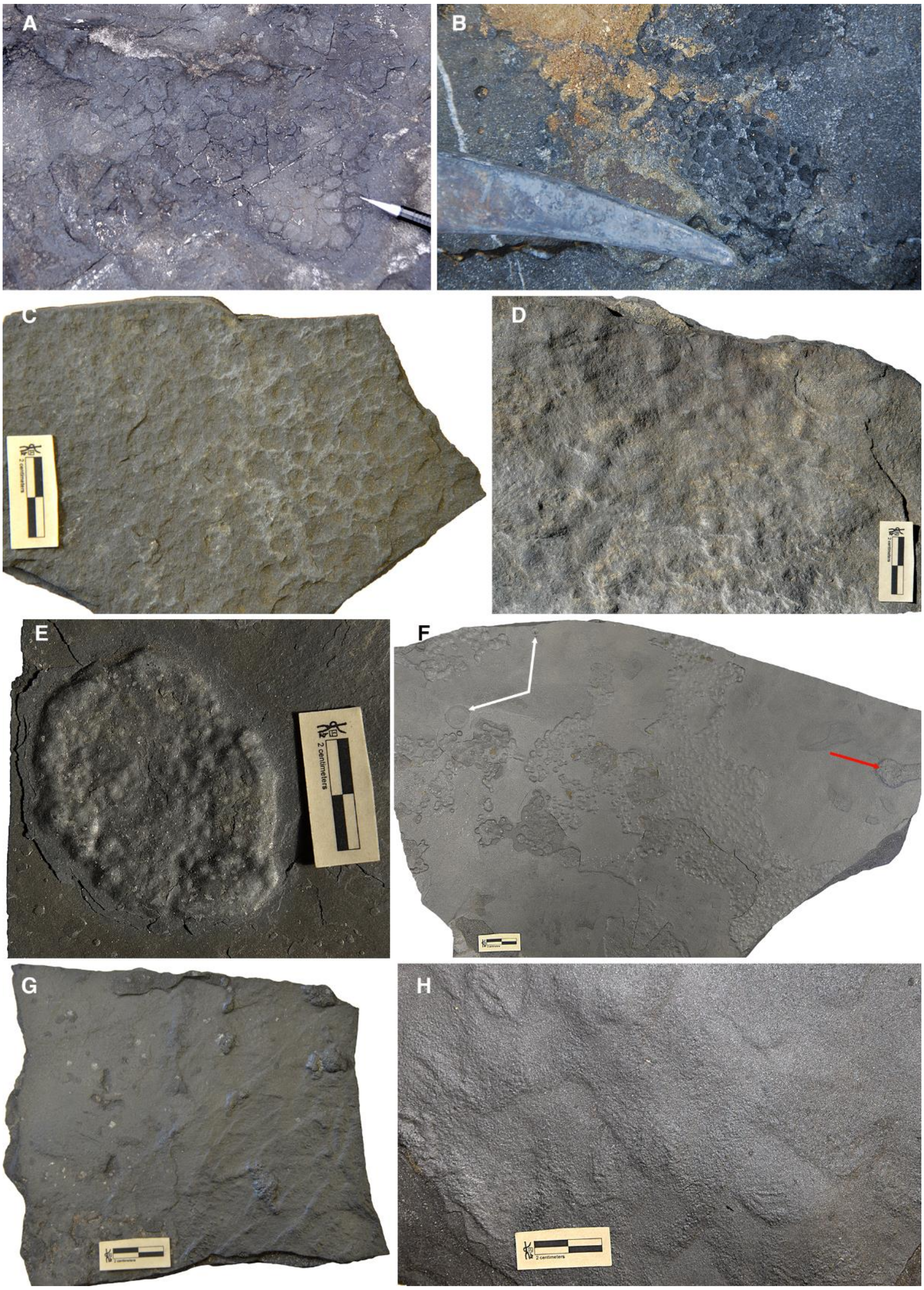

Figure 23: Microbial mat structures in the Francevillian B Formation (FB$_2$): Mat-layer structures. (**A**-**C**) “Elephant-skin” textures. (**D**) Putative macro-tufted microbial mat. (**E**, **F**) Clustered domal buildups and flat pyritized microbial structure (red arrow). Macrofossil specimens (white arrows). (**G**) Isolated domal buildups. (**H**) Wrinkle marks.

5.1.2 | Putative macro-tufted microbial mat structures

Description

The putative macro-tufted microbial mats are preserved as positive epireliefs that display patches of vertical bump-like structures protruding 0.05–0.2 cm on the upper surface of interbedded, coarse-grained siltstones (Figures 21, 23D).

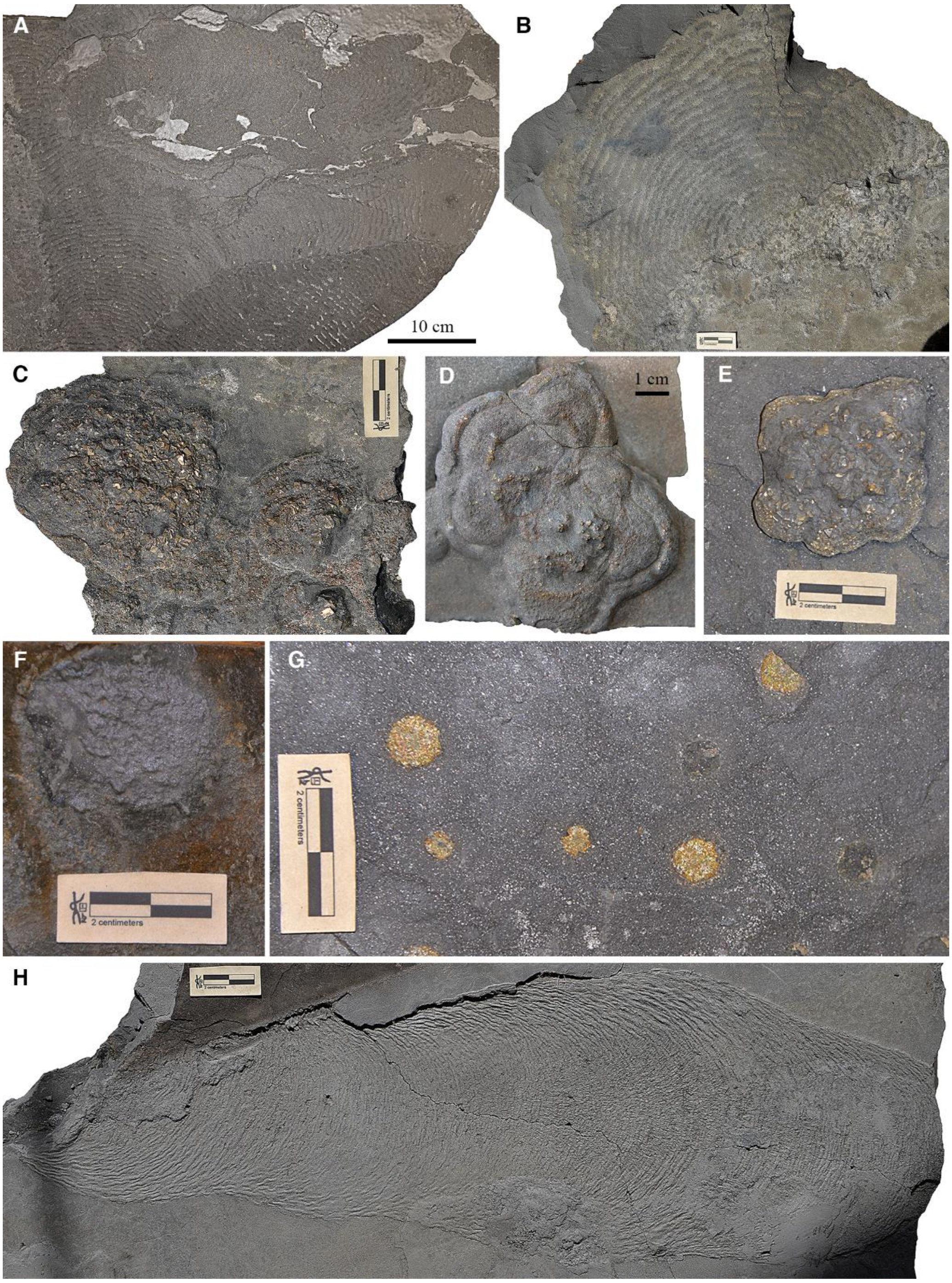

Figure 24: Microbial mat structures in the Francevillian B Formation (FB$_2$): Mat-layer structures. (**A**, **B**) Discoidal mats likely representing “fairy ring” structures. (**C**-**E**) Disc-shaped mats that display a cauliflower-like pattern. (**F**) Disc-shaped mat with internal wrinkle structures. (**G**) Small pyritized circular bodies. (**H**) Horizontal mat growth pattern.

Microscopic features seen in longitudinal thin sections reveal that the coarse-grained siltstone is draped by a 50–500 µm thin, dark, clay-rich layer with floating quartz grains (Figures 26B, G, H). These grains are clearly different in size compared to the coarser grains in the underlying sediment. Some clay particles are micaceous and oriented more or less parallel to the bedding plane. Furthermore, it can be noted that the thickness of this overlying dark layer varies along the longitudinal section. The thinner dark-colored layer is found at the top of the microtopography, whereas the thicker one overlies the troughs.

SEM imaging reveals that the dark lamina encompasses heterogeneously-sized, 5–40 µm quartz grains and heavy minerals (Figure 28C), while clay minerals are positioned subvertically. In addition, EDS analyses suggest that these laminated minerals are mainly made of O, Si, Al, K elements, with minor Mg, Fe and Na (Appendix 3), consistent with the elemental composition of mica and illite minerals (*e.g.*, Velde & Meunier, 2008).

Interpretation

A similar macro-tufted microbial mat was recorded from a 2.0 Ga palaeodesert environment where 0.2 cm high mound-like structures are randomly arranged on a fine-grained sandstone (Simpson *et al.*, 2013). The mechanism behind the development of this feature in the sedimentary rock record remains unclear. However, by changing the polarity of their filamentous structure, the growth of a microbial biofilm is able to produce similar bump-like structures in modern sedimentary environment (Gerdes *et al.*, 2000; Gerdes, 2007; Bose & Chafetz, 2009; Taj *et al.*, 2014). This pattern may also result from the direct filling of the pre-existing microtopography by mat-building organisms as they grow and expand (Simpson *et al.*, 2013). The smooth but bumpy morphology is likely enhanced by synsedimentary loading and post-depositional compaction, and so this bio-sedimentary expression could be viewed as a combined microbial and compaction feature.

5.1.3 | Domal buildups

Description

Domal buildups are preserved as positive bed-top features on bedding surfaces of black shales (Figure 21). They are characterized by 0.1–0.4 cm convex, domal structures projecting upwards from the bedding plane. Distinctive features include a cluster of low mound-shaped structures, 0.4 cm in diameter, nearly equal in all instances and without any central depressions (Figures 23E, F). In an alternative manner, they can be isolated structures with a diameter ranging from 0.7 to 1.5 cm that seem to reveal a cauliflower-like texture associated with extensive positive relief, wrinkled structures (Figure 23G). Circular discs belonging to the oldest large colonial organisms (El Albani *et al.*, 2014) seem closely associated with these specific structures. Both isolated and clustered domal structures have been shown to be pyritized (Appendix 4). Bulk sulfur level of up 22.16% within the domal structures is associated with a carbon content <0.53%. There are also flat, pyritized mat-related structures without any particular distinctive features that tend to develop close to the clustered domes (Figure 23F; Appendix 1).

Thin sections reveal a well-defined alternation of clay and silt layers beneath the domal structures (Figure 26C). Most of the quartz particles from the underlying sediment are laminated and/or have a length of grain-to-grain contact of mostly 20–80 µm. None of these grains were found in the topmost dark, clay layer. Furthermore, the domal structures typically show an indication of internal convex lamination between all pyrite grains (Figure 26I), which reflects the position of the domes in epirelief.

Interpretation

Domal buildups have been reported from fluvial and fluvio-deltaic settings in Mid-Proterozoic (Garlick, 1988; Schieber, 1998, 1999; Sheldon, 2012; Wilmeth *et al.*, 2014) to shallow water settings in Late Cambrian times (Bottjer & Hagadorn, 2007). The latter authors proposed that they “may represent different life histories, biological affinities, and/or histories of interaction with the physical environment”. Previous studies have also invoked a distinct mat growth pattern (Wilmeth *et al.*, 2014) and inferred that domal structures are built by an upward growth of microbial mats. This might reflect competition for light (Garlick, 1988; Schieber, 1999). The $\delta^{13}C_{org}$ isotopic signatures of Mesoproterozoic domal-like structures in Copper Harbor Conglomerate (Upper Peninsula of Michigan) are attributed to photosynthesis (Sheldon, 2012).

Extracellular polymeric substances possess chemical properties that protect cells by creating sharp geochemical gradients (Decho, 2000), while the anaerobic decay of the buried mat material facilitates the precipitation of diagenetic minerals such as pyrite, depending on sulfate and iron bioavailability. If this diagenetic mineralization follows individual layers within the EPS demarcated boundaries, or if it is associated with specific features, the former presence of microbial mats is overprinted and preserved as a mineralized signature (Schieber, 1999). Thus, sulfate-reducing microorganisms probably used the carbonaceous material from the domal buildups as their electron donor, thereby releasing hydrogen sulfide to react with available iron. This mechanism is supported by the recurrent low carbon to high sulfur contents in the materials. Analyses of the sulfur isotope contained in pyrite from the Francevillian series measured by Secondary Ion Mass Spectrometry (SIMS) further revealed negative $\delta^{34}S$ values associated with widespread microbial decay, linked to the activities of the sulfate-reducing microorganisms (El Albani *et al.*, 2014).

5.1.4 | Discoidal microbial colonies

Description

A discoidal microbial colony (Grazhdankin & Gerdes, 2007) is a term for a mat layer that includes disc-shaped, internal, centimeter-scale features (Figures 24A-G). Two major distinct discoidal microbial colony-like morphologies occur on bedding planes in the black shale unit (Figure 21). The first is characterized by centimeter to the decimeter scale clusters of outward-convex, rod-shaped structures with internal pyritized concentric bands, possessing a series of ~0.4 cm wide light and dark zones (Figures 24A, B). This specific feature does not exhibit any relief. The second variety is made up of well-marked circular bodies represented by sharp outlines separating the specimens from the surrounding black shale (Figures 24C-G). The disc-shaped colonies display slight internal concentric zonations, wrinkle features or a lack of any specific morphological characteristics. A variety of the specimens have a 1.1–1.7 cm high disc-shaped relief with concentric rims restricted to the edges, which may present themselves as cauliflower-like patterns varying between 3.3 and 8.2 cm in diameter (Figures 24C-E). There are numerous distinct large euhedral pyrite crystals on these structures. Less common are disc-shaped bodies of 2.3 cm in diameter and represented by a minor relief, internal millimeter-scale wrinkles, and devoid of sharp outlines (Figure 24F). Other observable discoidal structures are relatively small (~0.5 cm diameter) that do not have particular features (Figure 24G). However, these are the only structures that are entirely pyritized by tiny pyrite crystals.

Interpretation

Previous studies have shown that a wide range of variability exists in the morphology and organization of modern discoidal microbial colonies in natural environments (Gerdes *et al.*, 1993; Banerjee *et al.*, 2014; Sarkar *et al.*, 2014) as well as under laboratory conditions (Matsushita *et al.*, 2004). Concentric zonations with a series of light and dark bands represent a particular variety of discoidal microbial colony known as “fairy rings.” Modern “fairy ring” structures are ubiquitous in salt marshes (Gerdes *et al.*, 1993; Gerdes, 2007) and in shallow water environments (Banerjee *et al.*, 2014). The concentric ring-shaped structures of the Francevillian series discoidal structures clearly display the same striking morphologies. All modern examples indicate that filamentous Cyanobacteria and diatoms, which are embedded in EPS and crowned by micro-pinnacles, form these concentric ring-shaped structures. This arrangement is likely not random but represents an oriented behavior that might be triggered by external environmental factors (Gerdes, 2007). So far, the generally accepted mechanism of formation involves escaping gas bubbles from the substrate, which may cause concentric wave propagation (Gerdes *et al.*, 1994). In a subsequent way, chemotactic responses initiated by adapted filamentous Cyanobacteria may form the concentric organizational patterns. At present, the oldest discoidal microbial colonies that have been described are from Mesoproterozoic and Neoproterozoic shallow submarine environments (Grazhdankin & Gerdes, 2007; Banerjee *et al.*, 2010, 2014; Sarkar *et al.*, 2014), where pyritized filamentous structures are sometimes preserved (Grazhdankin & Gerdes, 2007).

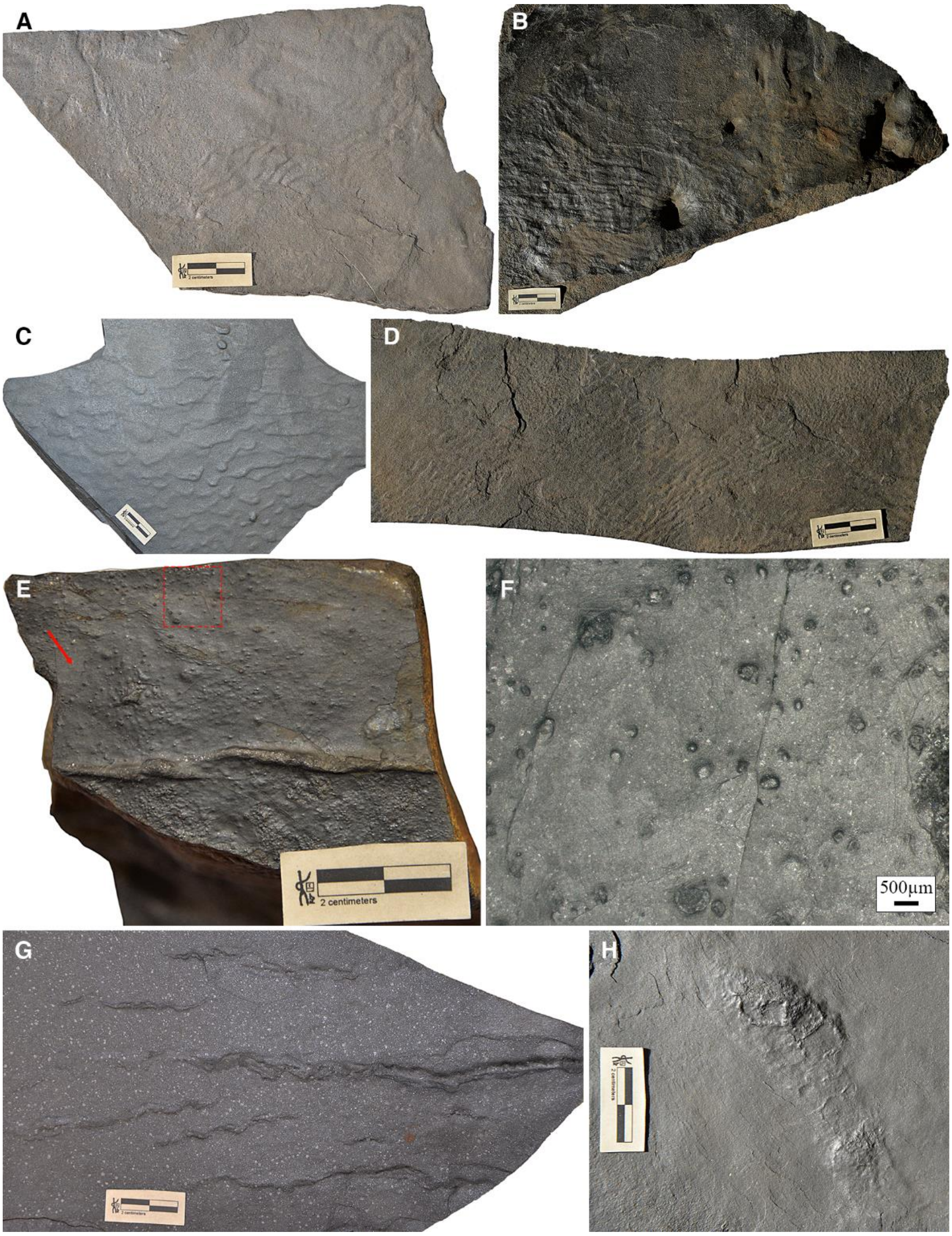

Figure 25: Mat-related structures in the Francevillian B Formation (FB$_2$): Mat-protected structures. (**A**, **B**) Parallel wavy wrinkle structures. (**C**) Cross-cutting wrinkle structures. (**D**) "Kinneyia" structure. (**E**) Linear pattern. Dashed red box indicates the position of the magnification in F. Red arrow shows the location where the Raman spectroscopy was performed. The Raman spectra are visible in Figure 27D. (**F**) Micrometric spots interpreting as oriented grains. (**G**) Linear patterns with several parallel ridges. (**H**) Nodular-like structure.

5.1.5 | Horizontal mat growth pattern

Description

A unique, outward-convex, spindle-shaped structure extending over 34 cm is developed on the bedding plane surface of the black shale unit (Figures 21, 24H). The structure appears similar to the spindle-shaped “fairy ring” structures described above. However, this structure is represented by tiny, 0.1 cm tall, arched ridges, rising horizontally, following a well-defined geometric pattern. These sharp-crested ridges of 0.15 cm in width are regularly spaced, commonly dissected and slightly undulated. It appears that the laminae convexity of the whole structure is unevenly distributed, ranging from 55 to 86 degrees.

Interpretation

The horizontal mat growth pattern could be related to “fairy ring” structures with which the pattern shares some similarities (*e.g.*, outward-convex, spindle-shaped, sharp-crested ridges). Nevertheless, there are no alternations of light and dark zones. Processes implicated in the formation of “fairy ring” structures may be involved here, but topography is added. The orientation of the wave propagation and subsequent millimeter-sized ripples may be induced by gravity. Then, pinnacle-forming organisms would interact with the nutrient front by chemotactic responses to colonize the substratum, producing the distinct morphology preserved in the sedimentary record. In an alternative way, localized mat failure and strain induced by gravity, waves or currents could also explain the morphology as a mechanical deformation of biogenically stabilized sediment. Although it has not been suggested in other studies, morphological features including a point of origin, persistent “growth” in one vector, and sharp boundaries could also be explained by an underwater seep that is confined by a biomat and promotes mat growth in a downslope direction. In any case, the parallel arrangement of ridges, as well as the regularity of components in the horizontal mat growth pattern, suggests a biotic origin.

5.2 | Mat-protected structures

This category of mat-related structures arises from structures that probably require mats for their preservation, the excepting being wrinkle marks.

5.2.1 | Wrinkle structures

Description

Based on morphology, three types of wrinkle structures are categorized here: wrinkle marks, parallel wavy wrinkle structures and cross-cutting wrinkle structures. Wrinkle marks are represented as laterally continuous or discontinuous, slight, outward-convex positive relief on bedding plane of the black shales (Figures 21, 23H).

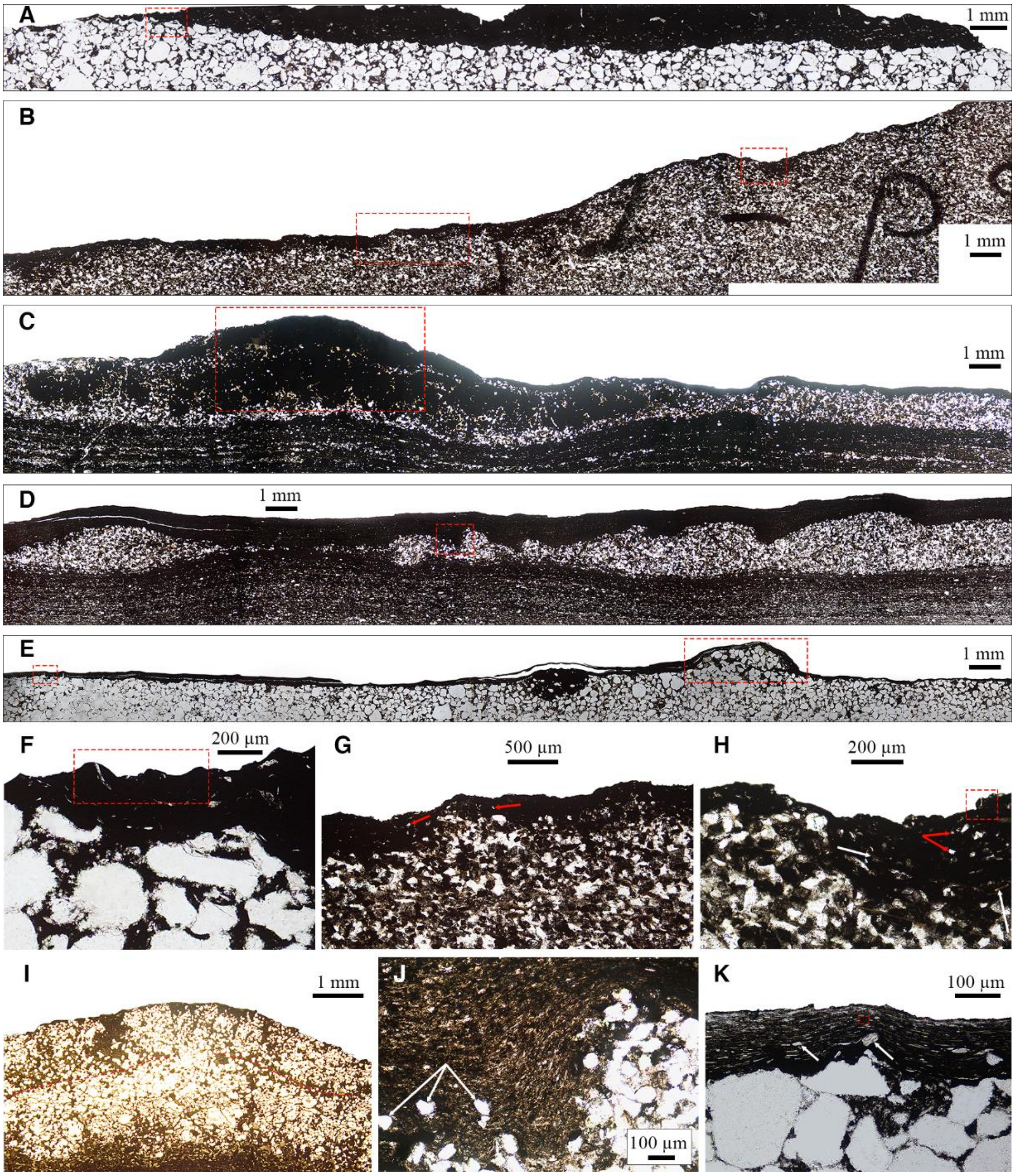

Figure 26: Optical photomicrographs of mat-related structures. (**A**) Transmitted thin section of “elephant-skin” texture. Dashed red box denoting area magnified in F. (**B**) Transmitted thin section of putative macro-tufted microbial mat. Dashed red boxes denoting areas magnified in G and H. (**C**) Transmitted thin section of an isolated domal buildup. Dashed red box denoting area magnified in I. (**D**) Transmitted thin section of parallel wavy wrinkle structures. Dashed red box denoting area magnified in J. (**E**) Transmitted thin section of a linear pattern. Dashed red boxes denoting areas magnified in K and Figure 28E. (**F**) Tufted microstructures and wavy-crinkly laminae. Dashed red box denoting area magnified in Figure 28A. (**G**, **H**) Thickness variation across the mat layer with floating grains embedded by clays (red arrows). Mica (white arrows). Dashed red box denoting area magnified in Figure 28C. (**I**) Reflected magnified thin section of an entirely pyritized dome. An internal convex lamination is indicated by dashed red lines. (**J**) Clay laminae do not onlap the rippled siltstone bed but rather well follow its topography. Oriented grains (arrows). (**K**) High amount of quartz particles (arrows as example) within dark-coloured laminae. Dashed red box denoting area magnified in Figure 28D.

Parallel wavy wrinkle structures are preserved as sinuous, continuous ridges separated by parallel, narrow valleys extending for <10 cm on bedding surfaces of sandstones and interbedded thin-to-medium-bedded siltstones (Figures 21, 25A, B). The ridges have rounded tops and steep sides, with an individual ridge elevation of 0.1 cm and a spacing of 0.4 cm. Organic elemental analysis of one sample from the black shale unit does not reveal significant differences in carbon content between the parallel wavy wrinkle structures and the surrounding sediment (Appendix 4). However, microscopic analysis of thin sections, cut perpendicularly through the wrinkles, indicates that a dark-colored layer caps the coarse, silt-sized rippled structures. Further down, the sediment displays quasi-planar laminations (Figure 26D). Oriented quartz grains trapped within the carbonaceous layer (Figure 26J) appear to have the same grain size as those found in the rippled structure. Tiny floating grains are also embedded in the clay-sized fractions. Sheets of various clay particles entangle several heavy minerals, mainly titanium oxides (Appendix 3).

Cross-cutting wrinkle structures (Banerjee & Jeevankumar, 2005) are characterized by bifurcating and frequently interconnected asymmetric ridges with intervening subparallel troughs on the bedding surface of black shales (Figures 21, 25C). The rounded ridges are 0.1–0.2 cm high, 0.4–0.5 cm wide, and their spacings vary from 0.4 to 1 cm. A few dome-like structures of 0.5–0.6 cm are close to these cross-cutting wrinkle structures (Figure 25C).

Interpretation

Wrinkle structures are one of the most common sedimentary features related to microbial mats. They are found over a large palaeogeographic range, including the deep-sea (Buatois & Mángano, 2003; Flood *et al.*, 2014), shallow marine (Hagadorn & Bottjer, 1997; Banerjee & Jeevankumar, 2005; Sarkar *et al.*, 2006, 2014, 2016; Porada & Bouougri, 2007; Mata & Bottjer, 2009; Banerjee *et al.*, 2014; Buatois *et al.*, 2014; Yang *et al.*, 2017), fluvial and lacustrine (Chu *et al.*, 2015, 2017), and even continental environments (Simpson *et al.*, 2013). Some researchers claimed that relative microbial community growth correlates to with irregular surface of wrinkle structures (Hagadorn & Bottjer, 1997; Banerjee & Jeevankumar, 2005; Sarkar *et al.*, 2006, 2014).

Loading and dewatering processes have also been proposed for wrinkle generation (Noffke *et al.*, 2002). A recent study has proposed that abiotic mechanisms are unable to create millimeter-scale ripples (3–15 mm wavelengths) because waves with small orbital amplitudes are not strong enough to mobilize sand and silt grains (Mariotti *et al.*, 2014). In wave tank experiments, millimeter-scale ripples were perfectly reproduced by means of microbial aggregates rolling along the substrate and transporting grains. The preservation of such structures requires burial by fine material that may be represented by the biostabilization of a bacterial community. The dark-colored layer overlapping the silt-sized rippled structures (Figures 26D, J) is probably induced by EPS that acts as a trap for particles from the surrounding environment (Hagadorn & Bottjer, 1997). Oriented grains are result of a growing biofilm that envelops, lifts, rotates and orientates the grains (Noffke *et al.*, 1997, 2001). By combining morphological description and petrographic study, it appears that wrinkle structures are polygenic. Both mat-layer and mat-protected structures are therefore most likely represented in this case.

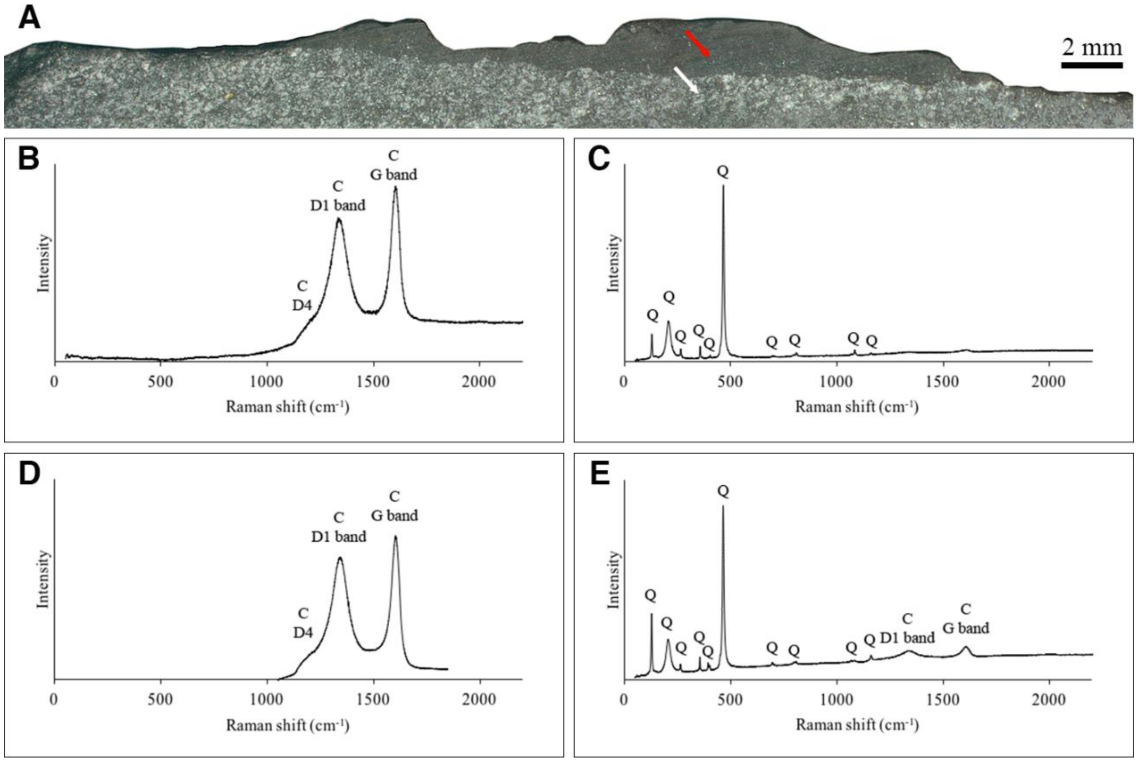

Figure 27: Polished slab of "elephant-skin" texture and Raman spectra of both "elephant-skin" texture and linear pattern. (**A**) Polished slab in cross-section perpendicular to bedding plane. Non-homogenous dark layer preserved above a pronounced boundary. Red arrow and white arrow indicate Raman spectra in B and C, respectively. (**B**) Representative Raman spectra of the microbial mat within bulges. It shows the presence of three carbon peaks ("C") at ~1202 cm^{-1} ("D4" disordered peak), 1,336 cm^{-1} (the "D1" disordered peak) and 1,603 cm^{-1} (the "G" graphite peak). (**C**) Typical Raman spectra of sandstone with quartz ("Q") peaks. (**D**) Representative Raman spectra of mat layers of linear pattern indicated in Figure 25E. It shows the presence of three carbon peaks ("C") at ~1,170 cm^{-1} ("D4" disordered peak), 1,344 cm^{-1} (the "D1" disordered peak) and 1,603 cm^{-1} (the "G" graphite peak). (**E**) Typical Raman spectra of host sediment of linear pattern, with quartz (Q) peaks and very small intensities of "C" peaks.

5.2.2 | "Kinneyia" structures

Description

"Kinneyia" structures are characterized by clearly distinct, short, sinuous ridges and troughs of 0.2 cm in width and <0.1 cm in height on the bedding surface of the black shale unit (Figures

21, 25D). These structures fit with the definition of “Kinneyia” as proposed by Porada *et al.* (2008), that is, they are “comparatively short, curved, frequently bifurcating, flat-topped crests, 0.5–1 mm high and 1–2 mm wide, which are separated by parallel, round-bottomed depressions. The crests are usually steep sided and may run parallel”.

Interpretation

The origins of “Kinneyia” structures have long been among the most problematic to understand. From their initial description as fossil algae (Walcott, 1914) to the present day where the term is now used to describe MRS, they have been interpreted in various ways (Hagadorn & Bottjer, 1997; Noffke *et al.*, 2002; Porada & Bouougri, 2007; Porada *et al.*, 2008; Thomas *et al.*, 2013; Mariotti *et al.*, 2014). However, few hypotheses properly explain how the underlying sediment is affected (Davies *et al.*, 2016). Of late, “Kinneyia” structures were successfully reproduced in wave tank experiments using microbial aggregates (Mariotti *et al.*, 2014), although the sharply defined morphology of the depressions preserved might suggest that gas bubbles formed beneath the biomat could also be a possible mechanism (Pflüger, 1999). It has also been demonstrated that “Kinneyia” is a polygenetic texture (Davies *et al.*, 2016), but the Francevillian “Kinneyia” structures do not rule out formation by biotic mediators.

5.2.3 | Linear patterns

Description

Linear patterns are characterized by 0.1–0.3 cm high, parallel, linear ridges, slightly undulated on the bedding surfaces of massive sandstones and interbedded siltstones (Figures 21, 25E, G). They are of varying size, ranging from 2 to 8 cm in length and 0.3–0.7 cm in width. Around these linear ridges, the surface morphology is not uniformly flat but bears micrometric spots that seem to be embedded in the matrix (Figure 25F). Furthermore, Raman spectroscopy indicates this dark-colored layer is carbon-rich compared to the underlying sediments (Figures 27D, E).

Microscopic observations reveal that the 100–300 μm thick, carbon-rich layer lies on lighter, sand-sized quartz grains and consists of multiple, well-defined sheets of clay minerals (Figures 26E, K). SEM imaging shows that numerous small quartz grains and heavy minerals, such as apatite, titanium oxide and zircon, are embedded in the clay matrix (Figures 28D, E). This matrix is formed by O, Si, Al, Mg, Fe and K elements that is chlorite and illite, as expressed by EDS analyses (Appendix 3). Furthermore, sand-sized quartz grains are observed inside the ridges as well as the surrounding sediment but are separated by a clayish undulated layer (Figure 28E). The quartz grains inside the ridges and those from the host rock appear randomly oriented.

Interpretation

According to the identification of linear patterns in modern tidal flats by Porada & Bouougri (2007) “straight to irregular ridges are developed at distance of 1–2 cm and are locally interrupted or reduced to faint lines on the flat mat surface”. Towards the water line, oriented bacterial filaments dominate these structures. In experimental studies, Shepard & Sumner (2010) observed linear ridges of up to 15 cm long made of cyanobacterial filaments running parallel to the incident light. Moreover, it has been proposed that a faint rippled surface may imply a linear pattern because of the preferential microbial growth following slight ridges (Bouougri & Porada, 2007; Gerdes, 2007; Porada & Bouougri, 2007).

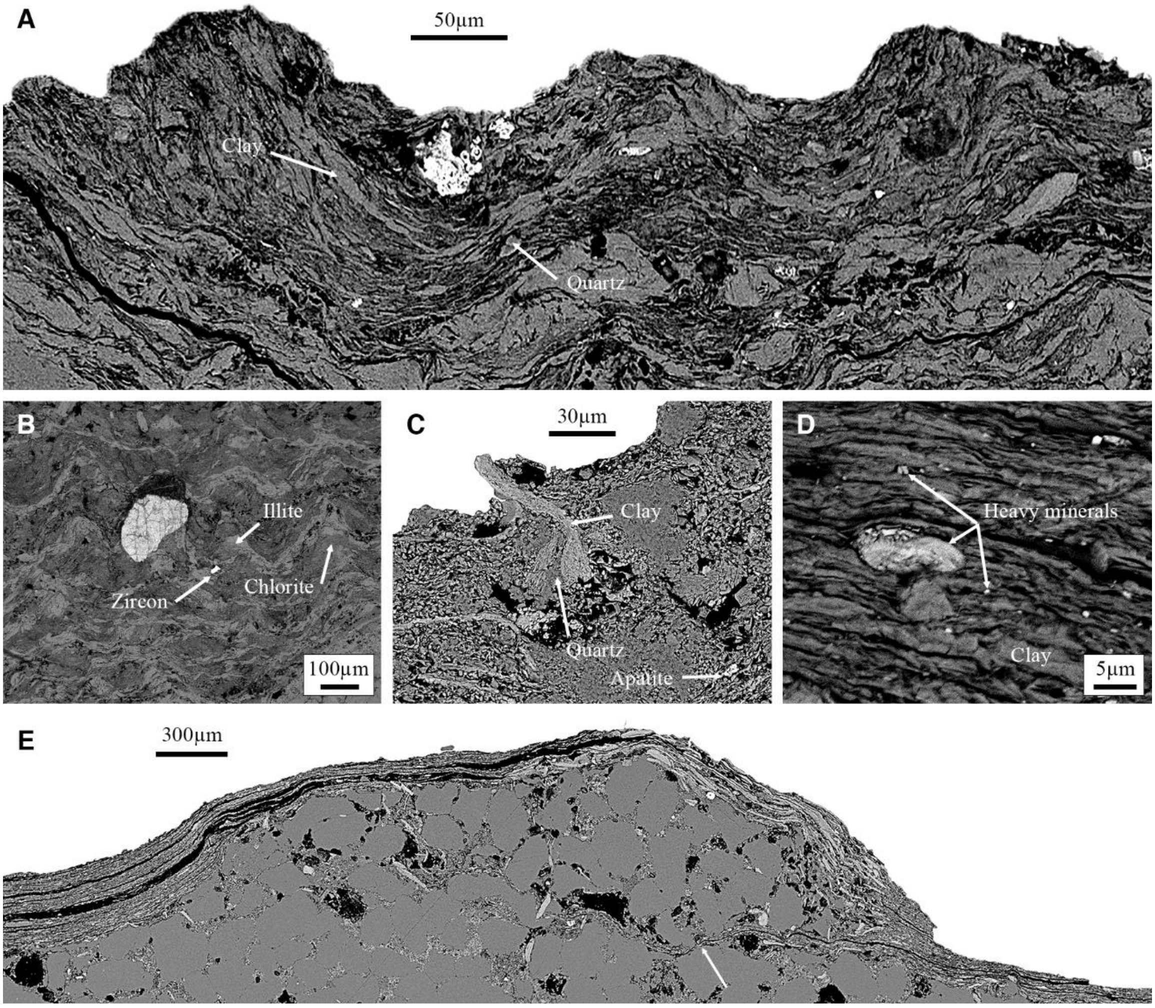

Figure 28: SEM imaging of mat-related structures. (**A**) Magnified view of box area in Figure 26F. Upward clay laminae within tufted microstructures and wavy-crinkly layers. (**B**). Tufted microstructures and heavy minerals constitute bulges of the “elephant-skin” texture. (**C**) Magnified view of box area in Figure 26H. Quartz grains, heavy minerals and randomly oriented clays constitute the dark-coloured mat layer. (**D**) Magnified view of box area in Figure 26K. Detrital particles wrapped by sheet clays. (**E**) Magnified view of box area in Figure 26E. Clay minerals above and throughout the ridge (arrow). No significant clue of liquefaction nor microbial shrinkage.

The presence of carbonaceous material within the dark-colored layer is congruent with a biotic origin. Microtextures, such as tiny quartz particles and heavy minerals embedded in the matrix, are caused by the trapping and binding processes related to microbial activity (Gerdes, 2007; Noffke, 2010). Individual grains bound in the organic matrix can be compared to those observed with laboratory-grown Cyanobacteria. These are described as oriented grains that are pushed upwards during their growths (Noffke *et al.*, 2001; Noffke, 2010).

On a macroscopic level, the Francevillian MRS strongly resemble the linear structures described above, commonly equivalent in shape but slightly smaller in size. However, no microscopic features were described until now. Taking microtextures into account, it seems unlikely that bacterial orientation is capable of mobilizing large amount of sediments to form ridges. Microbial shrinkage caused by a period of subaerial exposition, is also a possibility (*e.g.*, Chu *et al.*, 2017; Kovalchuk *et al.*, 2017), although the surface morphologies and microtextures are not consistent with this process. Also, dilational strain on a mildly dipping sediment surface could explain these features, but their orientations are irregular and their distributions are sporadic. Liquefaction underneath the microbial mat, due to a rise in pressure (*e.g.*, Porada *et al.*, 2007), could have been the cause of these particular ridges but neither sediment rising nor upward-facing microbial laminae beneath the ridges have been observed. At last, linear patterns may result from two growth periods interrupted by small and rippled sedimentary structures (Figure 28E). This condition might be the best explanation for microbial laminae throughout the linear ridges, and the second mat growth period may have followed the ridge orientation as previously thought (Bouougri & Porada, 2007; Gerdes, 2007; Porada & Bouougri, 2007). In some way, linear patterns are considered to be mat-protected structures.

5.2.4 | Nodule-like structures

Description

Nodule-like structures are characterized by an elongated shape approximately 10 cm long and an irregular surface topography on the bedding surfaces of black shales (Figures 21, 25H). The surfaces of nodule-like structures comprise several millimeter-scale, tiny, crinkled ridges that are randomly distributed. Composed of silt-sized grains and capped by a dark-colored wrinkle layer, the nodule-like structure was observed in a polished slab.

Interpretation

Similar nodular to biscuit-like surface structures have been observed in laboratory-cultured bacteria and in modern supratidal settings (Gerdes, 2007). This atypical morphology is thought to be produced by a relative abundance of coccoid Cyanobacteria. However, the Francevillian nodular structures possibly reflect mat-protected structures instead of mat growth structures since the internal part of the nodules is not composed of organic matter but rather of quartz particles.

5.3 | Isotopic analyses

The $\delta^{13}C$ values (V-PDB) of the organic fraction, measured on different mat morphologies in both sandstone and black shale facies range from –30.67‰ to –41.26‰ (Table 2). These values are similar to previous determinations on the bulk $\delta^{13}C$ of the organic matter within the FB_2 sequence, varying between ca. –35‰ and –30‰ (Gauthier-Lafaye & Weber, 2003; Canfield *et al.*, 2013).

Table 2: $\delta^{13}C$ values of organic matter in mat-related structures (MRS).

Subunits	Samples	$\delta^{13}C_{org}$ (‰)
FB2b Black shale	MRS_1	-34.92
	MRS_2	-34.41
	MRS_3	-32.45
	MRS_4	-41.26
FB2a Sandstone	MRS_5	-31.68
	MRS_6-1	-32.72
	MRS_6-2	-33.32
	MRS_7	-33.95
	MRS_8	-33.55
	MRS_9	-33.66
	MRS_10	-33.61
	MRS_11	-32.28
	MRS_12	-30.67
	MRS_13	-31.95
	MRS_14	-32.03

6 | DISCUSSION

6.1 | Biogenicity

The biogenicity criteria reviewed in Noffke (2009) and Wacey (2009) establishes the investigated mat-like structures to be of a microbial mat origin, having formed on the shallow marginal self-environment of the 2.1 Ga Francevillian basin (Reynaud *et al.*, 2017). The sedimentary facies on which the structures are identified must not have undergone metamorphism beyond greenschist grade (Noffke, 2009). This is in agreement with the absence of metamorphic overprint in the Francevillian facies (maximum temperature 100 °C; Gauthier-Lafaye & Weber, 1989; Ngombi-Pemba *et al*., 2014). In terms of shape and size, the

Francevillian MRS are a perfect match to those described in the Precambrian and the Phanerozoic (Appendices 5, 6) in accordance with the size distribution between modern and ancient MRS, which should be comparable (Noffke, 2009). In general, the taphonomic preservation window of MRS in the sedimentary record is valid, but not restricted by ecological setting (Davies *et al.*, 2016). Noffke (2009) suggested that most MRS are related to photoautotrophic mats formed in well-lit shallow marine environments, preferentially on fine sand deposits, even though recent studies argued that such features can also arise on deep marine sediments that do not receive light (Davies *et al.*, 2016). Regardless, our samples originated from a shallow marine setting associated with rapid sand flow deposits within a well-lit portion of the 2.1 Ga Francevillian continental shelf (Reynaud *et al.*, 2017).

Microtextural composition of the analyzed fabric further supports the biological trapping, binding (or "flypaper" effect) and orientation of grains induced by the growth and development of microbial mats and their hydrologically-controlled interaction with sediments. The Francevillian MRS express this biological process by containing clay particles, floating grains of silt-sized quartz and concentrated heavy minerals, as well as by wavy-crinkly laminae (Figures 26F-K, 28; Appendices 2, 3). These form well-defined organo-sedimentary structures caused by microbial baffling and trapping. The randomly oriented clay minerals in mat laminae suggest that they were trapped on the mat surface whereas laminated clay particles suggest a probable alignment by compaction (Schieber, 1998). Oriented grains reflect a particular microtexture (Figures 25F, 26J), while grain size matches that of the underlying substratum. It is commonly thought that these particles were dragged upwards by cyanobacterial mat growth (Noffke *et al.*, 1997, 2001).

In addition, geochemical evidence suggests bacterially induced biological processes characterized by carbonaceous material enriched in light carbon (Figure 27; Table 2) and pyritized structures (Figures 23E-G, 24A-E, G, 26C, I) that are depleted in heavy sulfur. The latter points to diagenetic mat destruction through burial decay (Noffke, 2009; Noffke *et al.*, 2013) and anaerobic respiration of that organic carbon by sulfate-reducing microorganisms (El Albani *et al.*, 2014; Hill *et al.*, 2016).

6.2 | Palaeoenvironmental interpretations and implications

Modern mat-related structures are mostly described in carbonate and siliciclastic environments but few have been described from shale deposits. The presence of black shales with large amounts of organic matter deposited in the photic zone may arise in restricted to isolated basins (Schwark & Frimmel, 2004). Some anoxygenic photosynthetic bacteria even prospered in these palaeoecological conditions and their high productivity may be related to the availability of essential nutrients. For any MRS-bearing rocks, the hydraulic pattern must be moderated with a low sedimentation rate to promote the development of microbial communities on a substrate (Schieber, 1999; Gerdes *et al.*, 2000; Gerdes, 2007; Noffke, 2009, 2010). As an indicator of palaeohydrological conditions, clay minerals and silt-sized grains within mat layers, are taken to represent currents strong enough to move thin particles but insufficient to transport sand-sized grains (Schieber, 1998; Noffke, 2009). Silt-sized sedimentary particles and heavy minerals can also be baffled and trapped by cyanobacterial filaments moving vertically upwards in order to escape being buried by the small-sized particles, as well as their need to reach optimal light conditions for growth (Noffke, 2009, 2010).

In this study, some of the mat-like structures, including the “elephant-skin” morphotypes, the tufted structures, and the linear patterns, tend to be associated with silty lenses (Figure 21), suggesting that the baffling and grain trapping processes were operating in potential microbial mat-dominated environments at 2.1 Ga. Further, the comparable association of several MRS to the distribution of modern and fossil analogues have been used to improve the reliability of palaeoenvironmental marine interpretations, including physical processes such as desiccation and erosion and biological activity (Bose & Chafetz, 2009; Noffke *et al.*, 2013; Banerjee *et al.*, 2014; Sarkar *et al.*, 2014). It is important that, the absence of desiccation and erosion-induced MRS in the Francevillian rocks suggest a quiet underwater environment from the time of deposition to when the sediments were lithified and buried.

The Palaeoproterozoic Francevillian MRS possess a wide spectrum of morphologies that can be related to photoautotrophic microbial assemblages. Indeed, discoidal microbial colonies in the modern environments and domal buildups in ancient settings are results of cyanobacterial chemotaxis or phototaxis behaviors (Gerdes, 2007). The biological mechanisms leading to oriented grains has been reproduced with cultures of Cyanobacteria (Noffke *et al.*, 2001). Reticulate patterns and tufted microbial mats have striking morphologies with modern analogues built by filamentous Cyanobacteria (Appendix 5A; Gerdes *et al.*, 2000; Gerdes, 2007; Bose & Chafetz, 2009; Taj *et al.*, 2014). It is thought that their formation implies a phototactic behavior (Gerdes *et al.*, 2000; Reyes *et al.*, 2013), whereas laboratory-cultured filamentous Cyanobacteria show a dependency on oxygen concentration (Sim *et al.*, 2012). It has also been proposed that the undirected gliding motility of filamentous bacteria species may form these structures (Shepard & Sumner, 2010). Therefore, all bacteria with highly motile filaments are believed to be able to display these morphologies. Filamentous sulfur-oxidizing bacteria may also have the ability to produce “elephant-skin”-like and tuft-like structures (Flood *et al.*, 2014). However, research by genomic comparisons reveals that these phenotypic traits were most likely inherited by horizontal gene transfers from the Cyanobacteria (Flood *et al.*, 2014). In other words, those aerobic chemolithoautotrophs may not have been in existence at 2.1 Ga. In addition, recent studies in a perennially ice-covered Antarctic lake have shown the specific assemblage of a photosynthetic microbial ecosystem (Sumner *et al.*, 2015; Jungblut *et al.*, 2016), with Cyanobacteria forming tuft-related structures exclusively found in the oxic zone where irradiance is at its highest, whereas flat bacterial mats of anoxygenic photoautotrophs are restricted to the deeper euxinic zone experiencing lower irradiance. Thus, “elephant-skin” and tufted structures may possibly have a link with oxygenic photoautotrophic microorganisms. It is important that, Flannery & Walter (2012) and Homann *et al.* (2015) thought that Cyanobacteria are the only microorganisms capable of producing vertical structures or tufts.

6.3 | Geomicrobiological implications

It is well established that carbon fixation by autotrophic organisms preferentially incorporates light ^{12}C over heavy ^{13}C isotopes in biomass (Schidlowski, 1988, 2001). In this regard, the $\delta^{13}C_{org}$ values ranging from –30.67‰ to –41.26‰ (average –32.94 ± 1.17‰) reported here are within the expected range for autotrophic carbon fixation (Schidlowski, 1988, 2001; Berg *et al.*, 2010). The typical $\delta^{13}C_{org}$ values generated by the widespread activity of ribulose 1,5-bisphosphate carboxylase/oxygenase (RuBisCo), common in oxyphototrophic Cyanobacteria have average values from –20‰ to –30‰. These values are less negatively fractionated than an—oxygenic phototrophs (Quandt *et al.*, 1977; McNevin *et al.*, 2007; Berg *et al.*, 2010), while more negative values <–30‰ are related to autotrophic carbon fixation in the reductive acetyl CoA pathway (*i.e.*, methanogenesis). In the case of the latter, acetoclastic methanogenesis diagenetically supplies isotopically light ^{12}C methane to anaerobic oxidation of methane (AOM), the latter often comprising a consortia of sulfate reducers and methanotrophs (Conrad *et al.*, 2010). Therefore, autotrophic carbon fixation via acetyl CoA pathway, combined with anaerobic oxidation of fixed C_{org}, would effectively lead to deposition of residual C_{org} enriched in light ^{12}C in the range found in this study. Such fixation of CO_2 coupled with diagenetic recycling of phototrophically derived C_{org} would have inevitably resulted in the sequential overprinting of light $\delta^{13}C$ in buried biomats. The bulk $\delta^{13}C_{org}$ signatures <–30‰ are, therefore, most parsimoniously interpreted to represent a mixed isotopic signal resulting from the activities of various primary producers and heterotrophs.

The FB2b subunit hosts the first known multicellular organisms closely associated with biomats (Figures 21, 29). Burrows, trails and resting traces of metazoans are often closely associated with biomats in the past, being interpreted as sophisticated feeding behaviors (*e.g.*, Buatois & Mángano, 2012; Pecoits *et al.*, 2012; Buatois *et al.*, 2014; Meyer *et al.*, 2014; Chu *et al.*, 2015). In modern environments, photosynthetic bacterial mats create thin O_2-rich layers, thus providing benthic O_2 oases for macroorganisms that may mine mat layers for unexploited nutrients and O_2 (Gingras *et al.*, 2011). It is perhaps not a coincidence then that the biomats and macroorganisms belong to the same strata. Moreover, the generation of microenvironments due to the chemical properties of EPS (Decho, 2000) may permit soft-tissue mineralization, providing further protection against degradation (Sagemann *et al.*, 1999). Thus, the biomats may have stabilized the depositional surfaces and sheltered the macroorganisms, allowing them to become imprinted into the rock record. In an interesting way, the large colonial organisms associated with bacterial communities are only known from the FB2b rocks. Although other black shale facies are recorded in the Francevillian basin (*e.g.*, the ~2.08 Ga FD black shale formation; Figure 20B), they were deposited in deeper environments beyond the euphotic zone.

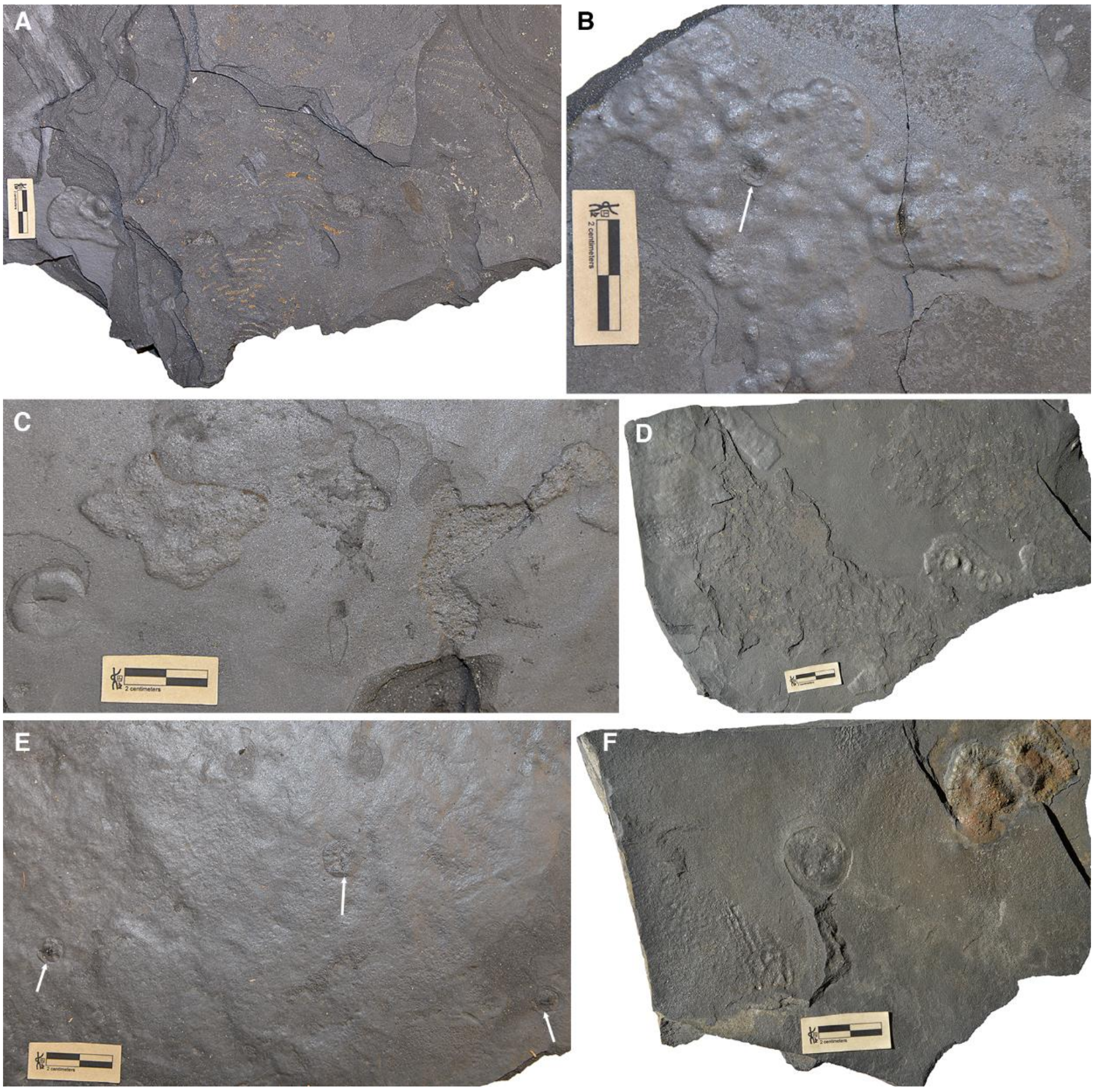

Figure 29: Examples of fossil macroorganisms associated with microbial mats. (**A**) Pyritized lobate form just beneath “fairy ring” structures. (**B**) Disc with radially striated core (arrow) lies on domal buildups. (**C**, **D**) Disc or lobate form and flat pyritized microbial structures on the same strata are closely associated. (**E**) Circular discs (arrows) rest on wrinkle marks. (**F**) Disc and lobate form are close to wrinkle marks on the same level or not.

7 | CONCLUSION

Mat-related structures of the 2.1 Ga Francevillian series exhibit ten types of surface morphologies, providing a new window into the highly diversified Palaeoproterozoic microbial life at that time. Mats are preserved in excellent conservation conditions from a 20 m thick interval of sandstone and black shale facies.

Microtexture analyses provide strong evidence in favor of mat-colonized sediment. Oriented grains, floating grains, heavy mineral concentrations, randomly oriented clays, pyritized structures and wavy-crinkly laminae all reflect the growth of microbial communities. Comparisons with ancient and modern analogues, as well as stable carbon isotope analyses, suggest growth within a palaeoenvironmental settings corresponding to the euphotic zone, likely <100 m deep. Associations between Palaeoproterozoic, large colonial organisms and mats may be similar to interactions of Ediacaran early metazoans and microbial carpets where O_2-producing cyanobacterial mats may explain this specific pattern. In addition, microbial mats may have played a major role in sediment biostabilization, fostering the preservation of complex macroorganisms that represent the first ecosystem comprising microbial biofilms and large colonial life forms.

ACKNOWLEDGMENTS

We thank the Gabonese government; National Center for Scientific Research of Gabon (CENAREST); Sylvia Bongo Foundation; Agence Nationale des Parcs Nationaux of Gabon for logistic supports; University of Masuku; French Embassy at Libreville; and Institut Français du Gabon, French Ministry for Foreign Affairs. We are grateful to Prof. P. Mouguiama Daouda for his support. ECF is funded by the European Research Council (ERC) Seventh Framework Program (FP7) grant No. 336092. Funding for KK and MG were provided by the Natural Sciences and Engineering Research Council (NSERC). For information and scientific discussion, we acknowledge O. Bankole, C. Fontaine and J-Y. Reynaud. For assistance, we thank N. Guignard (Raman microprobe analysis) and J. Laduranty (CHNS analysis). In France, we are grateful to the French CNRS, FEDER, the Universities of Poitiers and Lille 1, and the Nouvelle Aquitaine Region. All co-authors agree to the publication of this manuscript and declare no conflict of interest.

2.3. The role of Gabonese MRS closely associated with the advanced forms of life

The Francevillian sedimentary rocks shelter a large microbial diversity and exquisitely preserved macroorganisms displaying signs of coordinated growth (Figure 29). In the same location, newly discovered, biologically mediated string-shaped structures are also closely associated with the MRS (El Albani *et al.*, 2019; associated work §2), which adds unprecedented information to the uniqueness of the Palaeoproterozoic biosphere. A complex organism capable of migrating to reach food resources may have formed these specific structures. According to the authors, the producer may have been an amoeboidlike organism, since the aggregation of modern amoeboid cells into a migratory slug phase in cellular slime molds produces similar patterns. Collectively, the Francevillian Series hosts evidence for complex organisms using the mats as a food source. As mentioned in the previous section, the oxygenic photosynthesizers may have also provided “oxygen oases” for multicellular (eukaryotic?) organisms. It remains uncertain whether O_2 concentrations were significant at the time of Francevillian deposition or oxyphototrophic Cyanobacteria sufficiently enhanced O_2 levels to the surrounding environment for the rise of complex organisms.

The appearance of metazoans was firmly attributed to the accumulation of oxygen during the Neoproterozoic Oxidation Event (Och & Shields-Zhou, 2012), but the O_2 demand of early animals is not well established. Sperling *et al.* (2013) theoretically estimated the minimum O_2 requirement for the last common ancestor of bilaterians (advanced animal), varying between 0.14% and 0.36% PAL. Nonetheless, these theoretical values are a simplified view of complex organisms, as these did not incorporate metabolic and physiological requirements. The low atmospheric O_2 concentrations ($< 0.1\%$ PAL) during the mid-Proterozoic is well below the minimum O_2 demand and, therefore, may give support to the delayed rise of metazoans (Planavsky *et al.*, 2014b). Laboratory-cultured demosponges, perceived as ancient equivalents for early metazoans, have shown survival skills under low O_2 levels (0.5% PAL $< pO_2 < 4\%$ PAL; Mills *et al.*, 2014), but it remains unclear if such oxygenated conditions were met at the emergence of earliest animals. Thus, their origin and diversification may not have been triggered by a change of redox conditions.

Regardless of whether the emergence of complex macroorganisms is linked to the presence of molecular oxygen or other processes, either scenario can be questioned only if the Precambrian biological structures are preserved. Indeed, the fossilization of macroorganisms is likely enhanced by benthic matgrounds that biostabilize the substrate and delay the organic matter decomposition (Iniesto *et al.*, 2016, 2017). Subsequent mineralization processes can further protect the specimens during the burial stages.

2.4. Highlights of Part 2

- Optical and electron microscopies, Raman spectroscopy, and carbon isotopes were used to demonstrate the biogenic origin of the studied samples.
- The results show a large microbial diversity of more than ten representative morphotypes that are preserved as mat-growth and mat-protected structures.
- The inferred depositional setting is related to a shallow water palaeoenvironment within the euphotic zone with oxyphototrophic Cyanobacteria as the main constituent of MRS.
- The organizational pattern between the complex life forms and MRS clearly indicates the key role of microbial mats that likely sustained the development of macroorganisms in oxygen-lean conditions.
- The preservation of macroorganisms was enhanced by the intrinsic properties of microbes, the latter of which biostabilized the substrate and favored the mineralization process during early diagenesis.

PART 3: MICROBE-MINERAL INTERACTIONS

3.1. Introduction

The specific sorption properties of microbes enhance the trapping and binding of anionic and cationic compounds as well as fine- to coarse-grained mineral particles. Actually, suspended clay minerals can facilitate the encrustation of filamentous bacteria within days, which rises the idea that microbes may preserve the mineralogical fraction of the surrounding environments in which they prospered (Newman *et al.*, 2016, 2017). Then, the active sites around the cells and/or within the EPS can subsequently promote the nucleation and mineral precipitation of authigenic clays (Cuadros, 2017). It is frequently documented that microorganisms are capable of mediating the authigenesis of a large number of minerals such as clay particles (Wacey *et al.*, 2014 and references therein), iron oxides (Konhauser, 1998), and calcium carbonates (Brasier *et al.*, 2018).

The Francevillian Series hosts distinct evidence for benthic microbial communities that show a large variability in morphological textures (see section 2.2; Aubineau *et al.*, 2018). Despite their old age, the MRS display limited deformation and compaction processes. In this regard, their extraction from the underlying host sediments has been performed. Since the clay mineralogy in the Francevillian deposits has been extensively studied (*e.g.*, Ossa Ossa *et al.*, 2013; Ngombi-Pemba *et al.*, 2014; Bankole *et al.*, 2015, 2018), it seems relevant to examine clay minerals from the MRS and host sandstones and black shales. Therefore, the bulk and <2 µm clay fraction of both facies are presented in this part. Besides, the detrital and authigenic clay contributions can be evidenced. Because microbes have been widely recognized as a mediator for clay transformation (see review in Cuadros, 2017), this third part also aims at describing and discussing the microbe-mineral interactions in the 2.1 Ga-old Francevillian sedimentary rocks, if any. Finally, part 3 distinguishes the MRS into two different mat textures based on their sulfur content and lithostratigraphic position. The benthic microbial communities are described as non-pyritized MRS and pyritized MRS.

3.2. The link between biological processes and K-rich phyllosilicates

This section is dedicated to the published article in *Nature Communications*.

Microbially induced potassium enrichment in Paleoproterozoic shales and implications for reverse weathering on early Earth

Jérémie Aubineau[1], Abderrazak El Albani[1], Andrey Bekker[2], Andrea Somogyi[3], Olabode M. Bankole[1], Roberto Macchiarelli[4,5], Alain Meunier[1], Armelle Riboulleau[6], Jean-Yves Reynaud[6] & Kurt O. Konhauser[7]

[1]UMR 7285 CNRS IC2MP, University of Poitiers, Poitiers, France. [2]Department of Earth and Planetary Sciences, University of California, Riverside, CA, 92521, USA. [3]Nanoscopium beamline Synchrotron Soleil, BP 48, Saint-Aubin, 91192 GIF-sur-Yvette, France. [4]Department of Geosciences, University of Poitiers, Poitiers, France. [5]Department of Prehistory, UMR 7194 CNRS, National Museum of Natural History, Paris, France. [6]UMR 8187 CNRS LOG, University of Lille, ULCO, Villeneuve d'Ascq, France. [7]Department of Earth and Atmospheric Sciences, University of Alberta, Edmonton, Alberta, Canada.

*corresponding author: abder.albani@univ-poitiers.fr

Abstract

Illitization requires potassium incorporation into a smectite precursor, a process akin to reverse weathering. However, it remains unclear if microbes facilitate K^+ uptake to the sediments, and whether illitization was important in the geological past. The 2.1-billion-year-old Francevillian Series of Gabon has been shown to host mat-related structures (MRS), and, in this regard, these rocks offer a unique opportunity to test whether ancient microbes induced illitization. Here we show high K content confined to illite particles that are abundant in the facies bearing MRS, but not in the host sandstone and black shale. This observation suggests that microbial biofilms trapped K^+ from the seawater and released it into the pore-waters during respiration resulting in illitization. The K-rich illite developed exclusively in the fossilised MRS thus provides a new biosignature for metasediments derived from K-feldspar-depleted rocks that were abundant crustal components on ancient Earth.

1 | INTRODUCTION

The conversion of smectite to illite-smectite mixed-layer minerals (I-S MLMs) is a multistep process that takes place during diagenesis, and is mainly controlled by temperature, time, and K^+ availability (Perry Jr & Hower, 1970; Hower *et al.*, 1976; Środoń, 1984; Velde *et al.*, 1986).

The illitization process progressively converts hydrated smectite-rich layers to illite-rich layers, resulting in a common co-occurrence of smectite-rich, randomly interstratified I-S MLMs and long-range ordered I-S MLMs (Lanson *et al.*, 2009; Ferrage *et al.*, 2011). Two main mechanisms for smectite to illite transformation have been inferred, and these are likely linked to specific environmental conditions that are yet to be defined (Hower *et al.*, 1976; Nadeau *et al.*, 1985; Drits *et al.*, 1997; Lanson *et al.*, 2009; Ferrage *et al.*, 2011). A solid-state transformation characterized by a progressive replacement of smectite with illite via tetrahedral/octahedral Al substitutions and interlayer exchange has been proposed (Hower *et al.*, 1976; Drits *et al.*, 1997). The most likely mechanism involves the dissolution of the smectite lattice and growth of illite crystals due to the Ostwald ripening-like effect (Nadeau *et al.*, 1985; Lanson *et al.*, 2009; Ferrage *et al.*, 2011).

Microorganisms are capable of precipitating and transforming clay minerals as a result of their high surface reactivity and metabolic activity (Fortin *et al.*, 1998; Konhauser & Urrutia, 1999; Kim *et al.*, 2004; O'Reilly *et al.*, 2005; Zhang *et al.*, 2007; Vorhies & Gaines, 2009; Wacey *et al.*, 2014; Pace *et al.*, 2016; Cuadros, 2017). Perhaps one of the most striking examples is the transformation of hydrated smectite to illite through a process that involves the microbial release of structural Fe(III) from the smectite lattice via dissimilatory iron reduction (DIR) (Kim *et al.*, 2004; Zhang *et al.*, 2007; Vorhies & Gaines, 2009). This results in the negative charge of the octahedral sheet and K^+ uptake into the interlayer spaces to balance the structural charge imposed by DIR, thus enhancing the illitization process. In laboratory experiments, this clay transformation is enhanced by an abundant supply of K^+ cations to the medium (Kim *et al.*, 2004; Zhang *et al.*, 2007). In natural systems, K-rich fluids and dissolution of K-feldspar may also provide K^+ for this reaction to take place (Cuadros, 2017). A biologically controlled K^+ addition to sediments during diagenesis has not yet been described.

The Francevillian Formation B (FB) marine sedimentary rocks are exquisitely preserved within the Francevillian basin in southeastern Gabon (Bouton *et al.*, 2009b) (Figure 30A; Appendix 7A). The maximum burial depth is estimated to reach about 2 km with minimal burial temperature (Gauthier-Lafaye & Weber, 1989, 2003; Ngombi-Pemba *et al.*, 2014). An assemblage of diagenetic illite, chlorite, I-S MLMs, and K-bentonite characterizes the FB Formation (Ossa Ossa *et al.*, 2013; Ngombi-Pemba *et al.*, 2014; Bankole *et al.*, 2018). These sediments were deposited in an oxygenated environment (Canfield *et al.*, 2013) ~2.1 billion years ago (Horie *et al.*, 2005) during a transgression (FB_1 Member) followed by a sea-level fall (FB_2 Member). The shallowing brought the depositional site to the photic zone and allowed the formation of mat-related structures (MRS) under the dominant influence of Cyanobacteria (Reynaud *et al.*, 2017; Aubineau *et al.*, 2018). The marine FB_2 Member, which bears the MRS, is essentially a massive sandstone deposit (FB2a unit) overlain by black shales and diagenetic carbonates interbedded with thin siltstone layers (FB2b unit; Appendix 7B). Here, we present whole-rock and *in situ* geochemical analyses, bulk XRD, electron microscopy images, and synchrotron-based elemental distribution maps from MRS and their host sediments. We studied samples from a 15-m-thick, coarse-grained sandstone that conformably underlies a 5-m-thick, thinly-bedded black shale that hosts the oldest large colonial macrofossils with evidence for organism motility previously described from the FB_2 Member of the FB Formation (El Albani *et al.*, 2010, 2014, 2019) (Appendix 7B). This study highlights the K enrichments that are localized in illite particles within fossilized MRS, and, most crucially, it provides insight for the search of biosignatures in early Earth's sediments where stable isotope evidence are controversial. These findings have also important implications for Earth's climate and ocean chemistry in Palaeoproterozoic, which we discuss.

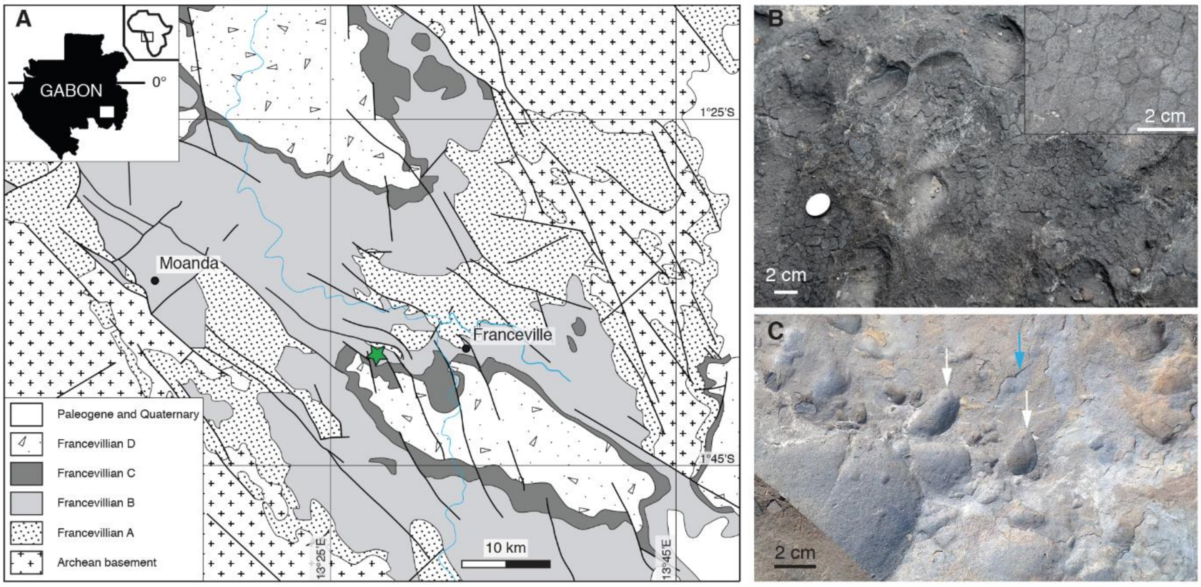

Figure 30: Geological map and field photographs of the FB_2 Member outcrops, Gabon. (**A**) Geological map of the Francevillian basin adapted from Bouton *et al*. (2009b). The studied area is the Moulendé Quarry (green star). (**B**) Elephant-skin texture on the bedding plane of coarse-grained sandstones. Inset box shows reticulate patterns. (**C**) Micrometer-thick microbial mat laminae (blue arrow) on the bedding plane of sandstones with rounded pits (white arrows).

2 | RESULTS

2.1 | Textures of mat-related structures

The investigated MRS exhibit a range of surface morphologies including those generated through mat propagation (mat-growth structures) and mat preservation/protection of structures formed independently from mat growth (mat-protected structures) (Sarkar *et al.*, 2008; Reynaud *et al.*, 2017; Aubineau *et al.*, 2018). The elephant-skin texture (Figure 30B) is one of the most common mat-growth morphologies showing evidence for biological activity (*i.e.*, undirected gliding motility, phototactic behavior), while wrinkle and kinneyia structures, linear ridges, and nodule-like structures point to the biostabilization of sediment (Shepard & Sumner, 2010; Reyes *et al.*, 2013). Mat laminae associated with irregular rounded pits (Figure 30C) provide evidence for biofilms that were capable of bioweathering the substratum onto which they were attached (Flemming *et al.*, 2016). Scanning electron microscopy - back-scattered electron imaging (SEM-BSE) coupled to energy-dispersive X-ray spectroscopy (EDX) displays textures and mineralogical compositions within the mat laminae that are different from host sediments (Figure 31; Appendices 8, 9) (Aubineau *et al.*, 2018).

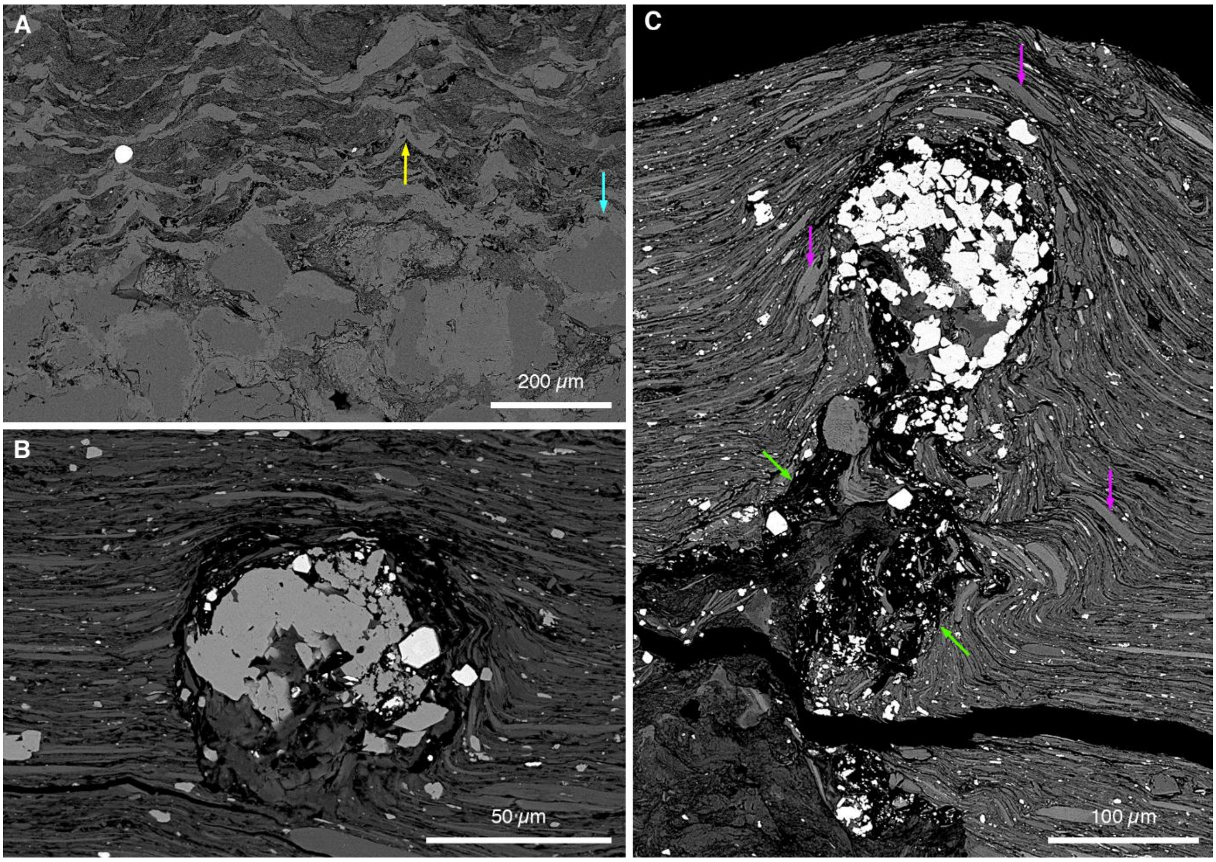

Figure 31: Biogenetic fabrics in the mat-related structures. The MRS textures are shown through SEM images. (**A**) Tufted microbial fabrics developed above the poorly-sorted quartz sandstone. Yellow and blue arrows point to tufts and quartz grains, respectively. (**B**) A void-filling titanium oxides that may have filled an oxygen bubble produced within the microbial mat. (**C**) Nearly-circular void filled with titanium oxides at the tip of a cone-like feature (green arrows). Detrital dioctahedral micas (*e.g.*, muscovite) are shown by purple arrows.

Laminated black shales host pyritized MRS that are primarily composed of 20 to 30 µm euhedral pyrite grains (Appendices 8C, D). The total sulfur content (higher than 6 wt%) within these MRS is associated with low total organic carbon content (Appendix 10). In addition, laminations between pyrite crystals, reflecting successive mat growth, were recently documented (Aubineau *et al.*, 2018). The non-pyritized MRS (with less than 4 wt% of S) comprise tufted microbial fabrics above coarse-grained sandstones (Figure 31A) with abundant nearly circular voids within the mat structures filled with titanium oxides, and they are typically enriched in heavy minerals, such as titanium oxides and zircons (Figures 31B, C; Appendices 8E, 9, 10). Inferred to be gas escape features, the voids show a pre-compactional formation whereby the clay particles are disorganized around the cone-like structures yet aligned above them.

2.2 | Potassium enrichment in the mat-related structures

Whole-rock geochemical analyses of major elements are presented in Appendix 10. Our data show higher K_2O/SiO_2 ratios for the MRS compared to the surrounding sediments, thus indicating a potassium-rich source specific to this lithology (Figure 32). The observed difference in the dataset is statistically significant (n= 41; Kruskal-Wallis test: $\chi^2 = 33.29$, df = 3, p-value < 10^{-7}). Pairwise comparisons show that the difference between all pairs of groups is also statistically significant (Appendix 11). The subtle, but significant difference in ratios between pyritized mats and black shales from the FB2b unit might be related to contamination of some black shale sediments during the extraction of pyritized mat structures (Figure 32). Binary plots of selected major elements were used to compare the MRS and host sediments (Supplementary Note 1; Appendix 12), as well as the likely control of mineral composition and the effect of quartz dilution on these sediments.

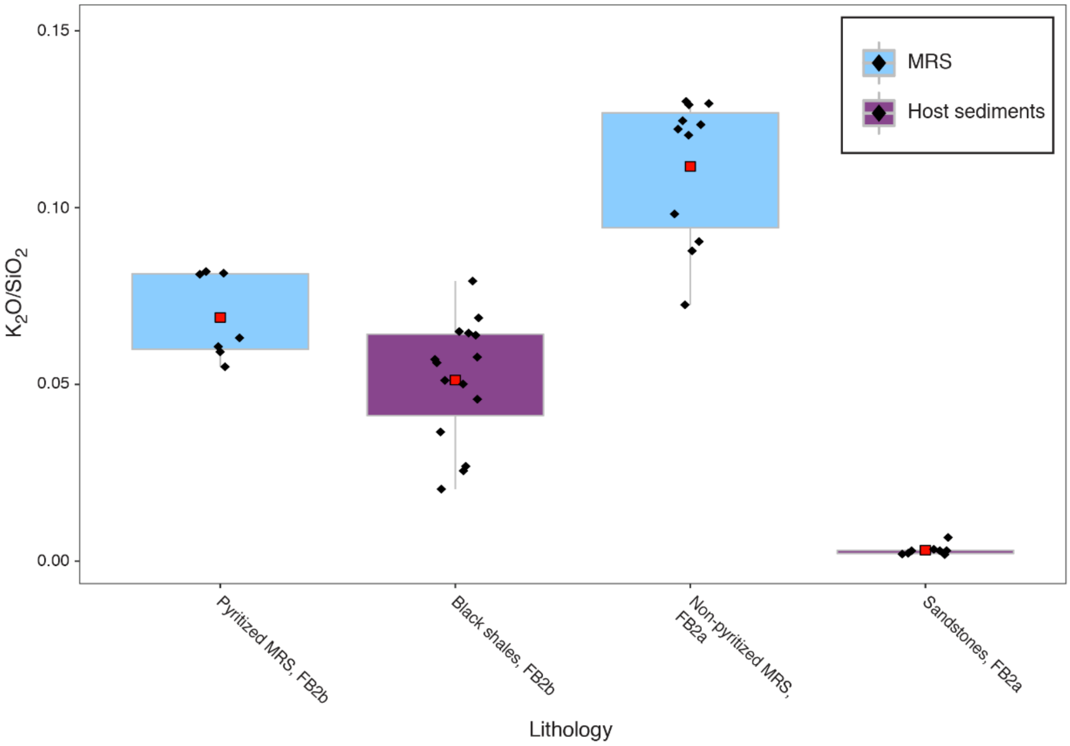

Figure 32: K_2O/SiO_2 ratios from mat-related structures and host sediments. Pyritized MRS are hosted by black shales and non-pyritized MRS are observed on bedding surface of sandstones. The data for each lithology are represented as box plots with a red square showing the mean, black diamonds corresponding to individual samples, 50% of the data are shown as a box and whiskers extend to 1.5 times the interquartile range.

Synchrotron-based scanning X-ray Fluorescence microscopy (XFM) study was performed on millimeter-sized areas of representative samples. This non-destructive, element-specific imaging technique provides the distribution of S, K, Ca, Ba, Mn, Fe, Ni, Cu, Zn, Ga, Ge, and As with micron-scale spatial resolution and high analytical sensitivity. The distributions of S and K were imaged in pyritized MRS (Figure 33A), black shale (Figure 33B), and non-pyritized MRS (Figure 33C). Sulfur is restricted to pyrite microcrystals (Figures 33A, C), highlighting the difference between pyritized and non-pyritized MRS. Pyrite crystals are not enriched in K. Potassium is homogeneously distributed throughout the MRS and black shales, without significant micro-scale heterogeneities. The K-distribution maps reveal a higher K content in the pyritized and non-pyritized MRS compared to that in the host sediments.

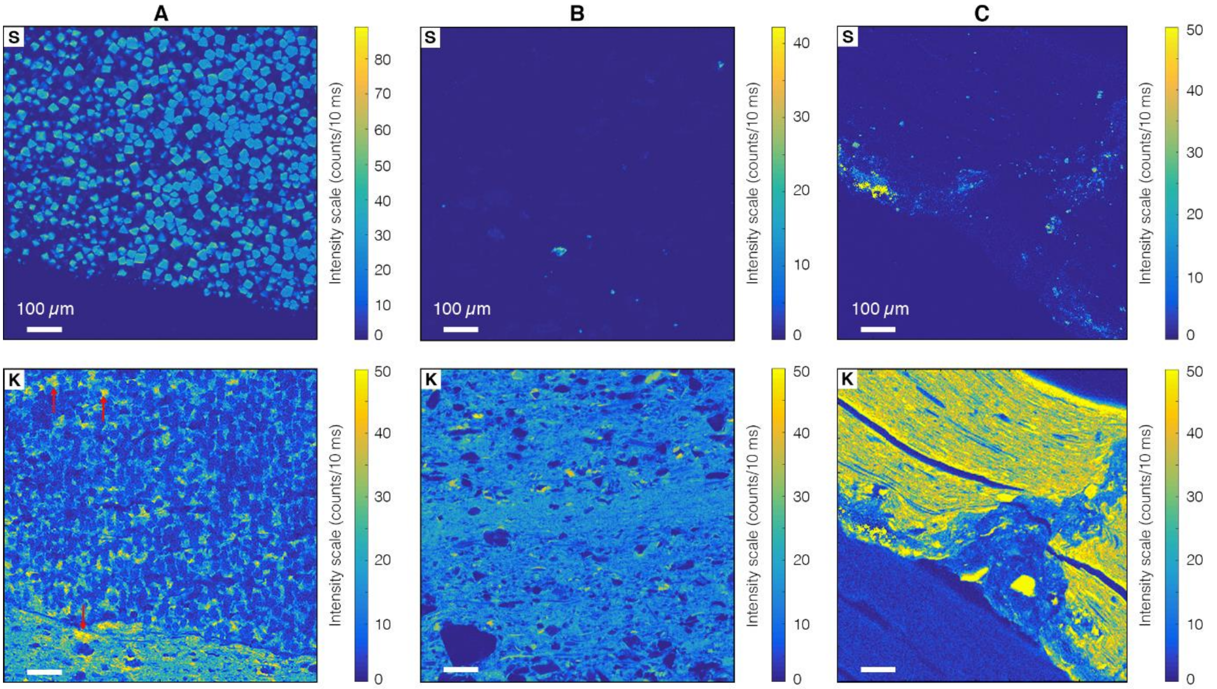

Figure 33: High-resolution sulfur and potassium distribution maps. (**A**) Pyritized MRS. Red arrows point to K enrichment between pyrite crystals and in the host sediment of MRS. (**B**) Black shales. (**C**) Non-pyritized MRS. Higher X-ray fluorescence (XRF) intensities correspond to higher S and K contents. For easier comparison, a common intensity scale was chosen for the K distribution maps.

2.3 | Potassium-rich clay assemblage patterns

Eleven representative samples, consisting of five MRS and six host sediments from the FB_2 Member, were further analyzed using the X-ray diffraction (XRD) technique (Figures 34A, D; Appendices 13-15). The stacking mode (R, Reichweite ordering parameter) of I-S MLMs, ranging from R0 (randomly interstratified) to R≥1 (long-range ordered) MLMs, was calculated (see Methods) to characterize the illite content with a higher R parameter corresponding to a higher illite content. The mineral assemblage of the MRS (both non-pyritized and pyritized types) includes quartz, mica, illite, chlorite, K-rich R3 I-S MLMs, and pyrite. In contrast, the host sediments contain quartz, mica, illite, chlorite, R0 I-S MLMs, and dolomite (Appendices 13-15). Notably, K-feldspars have been shown to be entirely absent, while plagioclase is present in the FB and FC formation lithologies, potentially reflecting provenance composition or depositional rather than climatic (via intense weathering) control (Ngombi-Pemba *et al.*, 2014; Bankole *et al.*, 2015). XRD patterns of the <2 µm fraction from the MRS show peaks at 10.56-10.37 Å in air-dried (AD) preparations splitting into 11.08-10.82 Å and ~9.9 Å peaks after ethylene glycolation (EG), consistent with characteristics of R3 I-S MLMs (Figure 34A; Appendices 14A, C). Smectite-rich R0 I-S MLMs, mixed with R3 I-S MLMs, in the host sediments are indicated by the shift of the 001 peak from around 14.35-14.1 Å in AD to 17.22-16.92 Å in EG (Figure 34D; Appendices 14B, D). The 002 peak of pure smectite close to 8.5 Å (Figure 34D) further characterizes the host sediments.

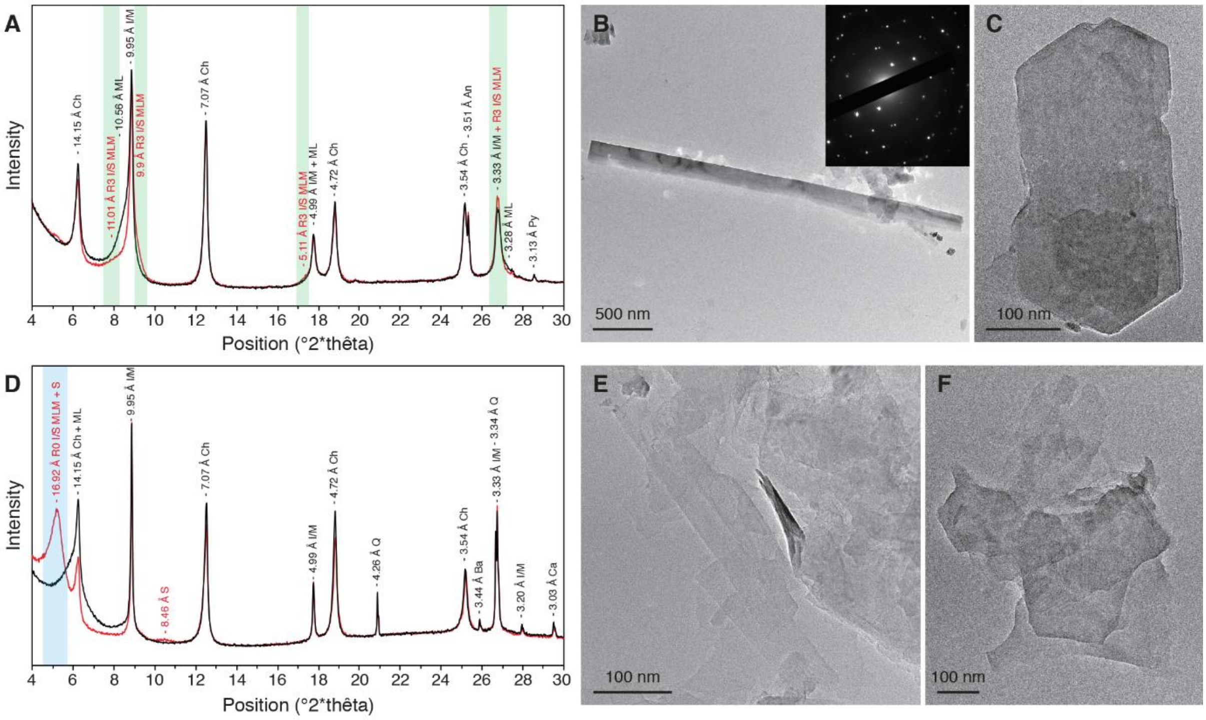

Figure 34: Mineralogical composition of the <2 µm clay-size fractions. X-ray diffraction profiles of oriented preparations after air-drying (black lines) and glycolation (red lines) and their transmission-electron images are given. (**A**) Microbial mat specimen. (**B**) Large, well-crystallized lath from microbial mat laminae. The inset shows selected area electron diffraction (SAED) pattern. *hk*0 pattern shows a hexagonal structure typical of phyllosilicates and coherently stacked crystals. (**C**) Hexagonal habit of illite from a mat sample. (**D**) Associated sandstone sediment. (**E**) Lathlike and poorly crystallized particles from the host sandstone. (**F**) Tiny hexagonal-shaped particles from the host sediment. [Green areas correspond to long-range ordered illite–smectite mixed- layer minerals (R3 I/S MLM); Blue areas represent randomly ordered illite–smectite mixed-layer minerals (R0 I/S MLM); smectite (S); chlorite (Ch); mixed-layer (ML); illite/mica (I/M); anatase (An); quartz (Q); pyrite (Py); barite (Ba); calcite (Ca)].

The modelling results by the NEWMOD program (Reynolds Jr & Reynolds III, 1996) for the MRS confirm the lack of R0 I-S MLMs. In contrast, the relative abundance of R3 I-S MLMs, together with a relative enrichment in detrital mica and chlorite, are higher than in the host sediments (Appendices 16-18), suggesting an intense dissolution of the reactive clay fraction and K input. In addition, smectite layers represent less than 12% of the R3 stacking in both the MRS and sediments, but are more abundant in the R0 I-S MLMs (S = 65%).

Transmission electron microscopy (TEM) was used to image the <2 µm clay-sized fraction and, specifically, the illite crystal habit. The illites form large laths, up to 10 µm long and 0.6 µm wide (Figure 34B; Appendices 19A-C), as well as hexagonal particles ~0.2 to 0.5 µm in size in the MRS (Figure 34C; Appendices 19D-F). The large lath-shaped particles indicate a well-crystallized illite growth through an Ostwald ripening-like process in which the small particles are dissolved, while large particles grow at their expense in order to minimize surface free energy (Nadeau *et al.*, 1985; Inoue *et al.*, 1988; Inoue & Kitagawa, 1994). The hexagonal particles represent steady-state growth during an advanced stage of illitization. The particle size of illite is much smaller in the host sediments than in the MRS. Illite in the host sediments predominantly forms lath-shaped particles ~0.15–0.4 µm long and 0.05 µm wide, with a few hexagonal particles up to 0.2 µm in size (Figures 34E, F; Appendices 19G, H). These tiny lath-shaped particles correspond to poorly crystallized illite (Inoue *et al.*, 1988; Meunier & Velde, 2004).

3 | DISCUSSION

The textural and geochemical observations of the pyritized MRS suggest that the organic carbon was oxidized via dissimilatory sulfate reduction (DSR) (El Albani *et al.*, 2014). This mechanism is also supported by the common diagenetic mineralization of individual mat layers, arguing for the former presence of organic carbon (Schieber, 1999). Moreover, if the earlier interpretation of the MRS in the FB_2 Member being cyanobacterial in origin is correct (Aubineau *et al.*, 2018), then the tufted appearance might be related to the escape of oxygen bubbles similar to that described in modern and ancient stromatolites (Bosak *et al.*, 2009, 2010; Sallstedt *et al.*, 2018). The differences between non-pyritized MRS and pyritized MRS might thus reflect a higher sedimentation rate and energy in the depositional setting of the non-pyritized MRS where a rapid burial would not have allowed sulfidic pore-waters to develop. Alternatively, this difference might be due to less reactive iron initially supplied to the depositional setting where the non-pyritized MRS were formed, consistent with the inferred shallow-water and high energy conditions.

The illitization process results in different abundances of illite and smectite, but points toward the association of the illite end-member with the MRS. The source of K^+ for diagenetic smectite-to-illite transformation is commonly linked to the dissolution of K-rich tuffs, K-feldspars, and micaceous minerals, as well as to migrating K-rich fluids (Meunier & Velde, 2004). Petrographic and XRD observations argue against significant contribution of K-rich tuffs to the composition of the FB_2 Member. The survival of R0 I-S MLMs (*i.e.,* smectite-rich) in both the sandstones and black shales lacking the MRS is consistent with incomplete illitization, attributed to the lack of K-feldspars in the FB Formation sediments (Ngombi-Pemba *et al.*, 2014; Bankole *et al.*, 2015). In our samples, dioctahedral micas (*e.g.,* muscovite) are only mechanically deformed (Figure 31C; Appendix 9), reflecting a limitation to no chemical alteration under diagenetic conditions (Bassett, 1960) and, therefore, they cannot be considered as a significant source of K^+. Moreover, it is unlikely that an external abiotic supply (*e.g.,* K-rich fluids or K-bearing minerals) would have provided K^+ only to the µm-thick microbial fabrics, but not to the host sediments. Organic matter could delay illitization by inhibiting exchange of interlayer cations (Li *et al.*, 2016); nonetheless non-pyritized MRS show both high organic carbon content (Appendix 10) and an advanced stage of illitization.

Our observations imply instead that microbes played two roles in the illitization process. First, the large mineral surface area of smectite may have helped to bind organic compounds within interlayer spaces (Kennedy *et al.*, 2002). The concentration of organic matter is critical because illitization is promoted via DIR, a process that oxidizes the sorbed organic carbon via reduction of Fe(III) minerals, and ultimately releases Fe(II) to the sediment pore-waters (Zhang *et al.*, 2007). Second, the microbes sequestered K^+ into the MRS of the FB_2 Member. In the case of the latter, potassium is one of the most essential cations for microorganisms to maintain their cellular machinery (Epstein, 2003), and, as a consequence, it is typically enriched in cells relative to seawater (Mulkidjanian *et al.*, 2012).

Biologically derived K could have been incorporated into MRS through the K^+ uptake into the living microbial cells, and/or K^+ absorption by reactive organic macromolecules – containing carboxyl, phosphate and hydroxyl groups – as part of the cell envelope or extracellular polymeric substances (EPS) of biofilms. In the first process, the structure of the K^+ channel (*e.g.*, proteins controlling K^+ transport across cell membranes) forms a selectivity filter that prevents Na^+ uptake, but works perfectly for incorporating K cations (Doyle, 1998). Thus, K^+ contributes to the regulation of osmotic pressure differences, the control of internal pH, and the activation of intracellular enzymes (Epstein, 2003); the thylakoid potassium channel (SynK) even promotes an optimal photosynthesis in Cyanobacteria (Checchetto *et al.*, 2012). As a result of K-dependent metabolic reactions, the intracellular concentration of K^+ in modern cells (100 mM) is one order of magnitude greater than that in the seawater (Williams & Da Silva, 2006; Mulkidjanian *et al.*, 2012), further supporting the ability of microbes to sequester this macronutrient. The second K^+ enrichment process involves the electrostatic binding of metal cations from solution to the cell wall and/or EPS, and in turn, the nucleation and mineral precipitation of authigenic mineral phases (Konhauser, 1998; Dupraz & Visscher, 2005).

Indeed, microbial cell surfaces have been shown to concentrate K^+ from solution (*e.g.*, Beveridge & Fyfe, 1985), and importantly, increased K^+ supply has been shown to stimulate the production of EPS by some bacterial strains (Wilkinson *et al.*, 1954). In addition, microbial respiration of EPS during early diagenesis could liberate adsorbed cations into the pore-waters, thus inducing K^+ supersaturation that can additionally promote mineral authigenesis (Dupraz *et al.*, 2009). Regardless of the path for K^+ uptake, biologically derived K^+ would have been required to facilitate the smectite-to-illite transformation during both decay of microbial mat organic matter and early diagenesis.

The proposed mechanism of bacterially enhanced illitization has important implications for the Palaeoproterozoic climate and ocean chemistry because the facilitated removal of K^+ from seawater into the clay fraction of sediments is akin to the modern reverse weathering process (Mackenzie & Garrels, 1966) to explain difference in the chemical composition of rivers and seawater. Formation of authigenic clays in the oceans involves (as an unbalanced reaction): $Si(OH)_4$ + cations (K^+, Mg^{2+}, Fe^{2+}, Al^{3+}) + HCO_3^- $\rightarrow$ clay mineral + CO_2 + H_2O. In the Amazon continental shelf, reverse weathering was estimated to account for a sink of ~10% of the annual riverine supply of K^+ to the oceans (Michalopoulos & Aller, 1995). Moreover, the release of CO_2 from bicarbonate consumption has been recently inferred to have helped maintain a warm Precambrian Earth at a time of lower solar luminosity and stabilized marine pH at lower values by releasing protons to seawater (Isson & Planavsky, 2018). While the conversion of smectite to illite is different (Boles & Franks, 1979): smectite + K^+ $\rightarrow$ illite + cations (Na^+, Ca^{2+}, Mg^{2+}, Fe^{2+}) + $Si(OH)_4$, its importance lies in the enforcing ultimate removal of K^+ from seawater with MRS, which would have strengthened the reverse weathering buffer on global climate during the Precambrian. Notably, in the absence of terrestrial vegetation and limited clay burial on landmasses in the Precambrian to consume K^+ released by chemical weathering, terrestrial K^+ fluxes to the oceans would have been significantly larger than in the Phanerozoic (McMahon & Davies, 2018). The K content in Precambrian seawater is highly uncertain with estimates ranging from those lower than that in the modern seawater to those that are higher (Holland, 1984; Weiershäuser & Spooner, 2005; Spear *et al.*, 2014; Marty *et al.*, 2018). Large land masses likely did not emerge until ~2.5 Ga (Bindeman *et al.*, 2018), thus the continental margin repository for marine evaporites was smaller with the correspondingly larger content of Na and K in seawater (Holland, 1984; Knauth, 1998, 2005). Regardless, the ability of bacteria to facilitate the incorporation of K^+ into illite at the time when microbial mats were likely more extensive in the oceans in the absence of grazing metazoans (Seilacher & Pflüger, 1994) provides a previously unrecognized biological feedback on the Earth surface system to control seawater pH and the atmospheric CO_2 content.

The recognition of ancient metabolic activity more specific than biogenic graphite is also of paramount importance in the search for Archean biosignatures. In this regard, we suggest that the process of illitization in association with the MRS might be evidence of biologically supplied K^+. Until now, this concept has not been tested because of the common abundance of K-feldspars in Phanerozoic and Precambrian sedimentary basins, which is related to the presence of felsic igneous rocks in the continental crust of all ages (Greber *et al.*, 2017). However, the predominance of mafic and ultramafic igneous rocks in the Archean and early Proterozoic greenstone belts (Arndt *et al.*, 2008; Moyen & Martin, 2012) requires a different mechanism to explain the K^+ enrichment with respect to host sediments that lack potassium-rich detrital minerals and illite-rich authigenic clays. Our finding of K-controlled mineral transformation during diagenesis in clay-rich shale deposits provides a new insight for seeking a potential biosignature in the early Earth's sedimentary environments that lacked granitoids in their provenance and where morphologic and carbon isotope evidence for MRS are often compromised.

4 | METHODS

4.1 | Sampling and sample preparation

We collected more than one hundred MRS with their associated host sediments from Moulendé Quarry, Francevillian basin, Gabon. The samples were photographed at the University of Poitiers using a Nikon Europe D610 digital single-lens reflex camera equipped with a Nikon AF-S 24-120 mm f/4G ED VR lens. Textural contrast between mat specimens and host sediments was investigated on polished slab sections with a ZEISS Discovery V8 stereoscope coupled with a Axio Cam ERc 5s microscope camera. Thirty samples covering all rock types were selected for mineralogical analyses. The µm-thick mat laminae (both non-pyritized and pyritized, defined according to petrographic analyses (Aubineau *et al.*, 2018) and their sulfur content) were carefully removed from their underlying host rocks by using a cutter blade to avoid contamination. Directly below the mat-bearing rocks, sandstone or black shale sediments were gently extracted with a hammer for mineralogical and geochemical analyses. MRS were carefully removed using spatula to extract and prepare <2 µm clay fraction and whole-rock powder for mineral and organic carbon analyses.

4.2 | X-ray diffraction

Approximatively the same quantity of the whole-rock powder and clay mineral fraction (<2 µm) from 11 samples were analyzed with a Bruker D8 ADVANCE diffractometer at the University of Poitiers using CuKα radiation operating at 40 kV and 40 mA. The <2 µm clay fraction was separated by dispersion of gently hand-crushed bulk samples in deionized water with an Elma

S60 ultrasonic agitation device without any chemical pre-treatment (Moore & Reynolds Jr, 1997). The dispersed particles were let to settle under gravity at a controlled room temperature of 20°C, and centrifuged to separate <2 µm clay fraction. Oriented slides were prepared by drying ~1 mL of suspension on glass slides at room temperature. The <2 µm fraction of some smectite-rich and illite-rich samples has been Ca-saturated after three dispersions in 1M $CaCl_2$ solution followed by several washings with deionized water. This cation exchange homogenizes the sheets of swelling clays to keep stable interlayer properties. Analysis of whole-rock powder samples was performed over an angular range of 2-65° 2θ with a step size of 0.025° 2θ per 3 s. Oriented slides of the <2 µm clay fraction were analyzed at a step size of 0.02° 2θ per 3 s counting time and over 2 to 30° 2θ angular range after successive air drying (AD) and ethylene glycol (EG) saturation. Oriented Ca-saturated samples were then prepared and analyzed in AD and EG states. Background stripping, indexing of peaks, and mineral identification were done using Bruker Eva software by comparing with International Centre for Diffraction Data (ICDD) files. Illite polytypes were observed on randomly oriented powders (<2 µm clay fraction) and analyzed at a step size of 0.01° 2θ per 2 s counting time and over 19 to 33° 2θ angular range. The results were compared with reference data (Bailey, 1980; Drits, 1993; Haines & Van Der Pluijm, 2008). Illite with $2M_1$ and $1M_t$ polytypes represent detrital and diagenetic illite, respectively (Grathoff *et al.*, 2001).

4.3 | X-ray diffraction profile modelling

The stacking mode (R, Reichweite ordering parameter) of I-S MLMs ranging from randomly interstratified (R=0) MLMs to long-range ordered MLMs (R= 1, 2 and ≥3) as well as the proportion of smectite and illite layers were determined by fitting experimental Ca-saturated samples in AD and EG states (over 2–30°2θ CuKα) using the NEWMOD 2.0 program simulation (Reynolds Jr & Reynolds III, 1996). When the same solution is obtained for the AD and EG states, we assumed the fit is acceptable. The instrumental and experimental factors such as horizontal and vertical beam divergences, goniometer radius, length and thickness of the oriented slides were introduced without further adjustment (Drits & Tchoubar, 1990). Sigmastar (degree of orientation of the clay particles on the slide) was set between 12 and 18° and the mass absorption coefficient (µ*) to 45 cm^2/g, as suggested by Moore and Reynolds (Moore & Reynolds Jr, 1997). Angular domains containing non-clay mineral reflections were not included in the profile-fitting process.

4.4 | Electron microscopy

Polished slab sections of selected samples were carbon coated and imaged with a FEI Quanta 200 scanning electron microscope (SEM) equipped with an energy dispersive X-Ray

Spectrometer (EDX) at the University of Lille. Mineral identification and documentation of textural relationships were acquired in back-scattered electron mode (BSE) operated at accelerating voltage of 15 kV, 1 nA beam current, and a working distance of 10.5 mm. Transmission electron microscopy (TEM) analysis of the <2 µm clay fraction was performed with a JEOL 2100 UHR microscope working at 200 kV accelerating voltage with a LaB6 emitter and equipped with a JEOL EDX detector at the University of Poitiers. Samples were prepared for TEM analysis by suspending ~1 mg of each sample in distilled water. A droplet of diluted suspension after ultrasonic treatment was deposited on a C-coated Au grid. Lath- and hexagon-shaped particles were selected from the grids because they only correspond to illitic minerals (Inoue *et al.*, 1988; Inoue & Kitagawa, 1994; Meunier & Velde, 2004). Selected-area electron diffraction (SAED) patterns were collected to image the hexagonal net pattern of the analyzed particles in (*hk*0) reflections (Kumai, 1976; Veblen *et al.*, 1990; Whitney & Velde, 1993).

4.5 | Whole rock analysis

Whole-rock geochemical analyses of major elements were carried out on 18 biofilms and 23 host sediments at *Service d'Analyse des Roches et Minéraux* (SARM) of the *Centre de Recherches Pétrographiques et Géochimiques* (CRPG), Nancy, France. Each sample was powdered in agate mortar and approximatively 1 g was fused with lithium metaborate ($LiBO_2$) and dissolved in nitric acid. Major element concentrations were obtained by inductively-coupled plasma atomic emission spectrometry (ICP-AES).

4.6 | Statistics

For descriptive treatment (boxplot) and statistical analyses, we used the R version 3.5.1 (R Core Team, 2018). The values for each group do not fulfil the assumption of normality and the Bartlett test of homogeneity of variances was computed prior statistical analyses. Our data returned a significant result (Bartlett test, $\chi^2 = 26.92$, df = 3, p-value < 10^{-6}), indicating overall inter-group heteroscedasticity of the dataset. According to these results, a multiple factor non-parametric test (*i.e.*, Kruskal-Wallis test) was used to calculate whether the difference in K_2O/SiO_2 ratios is statistically significant or not among lithologies. Finally, post hoc pairwise multiple comparison tests according to Conover were applied to figure out which pairs of groups (*i.e.*, lithologies) are different.

4.7 | Carbon analysis

MRS and their host sediments were powdered for the measurement of organic matter content. We used a FlashEA 1112 (ThermoFisher Scientific) CHNS analyser for flash dynamic combustion at 970°C under a constant helium flow. An Eager 300 software was used for data acquisition. A calibration curve was performed with aspartic acid and nicotinamide before each analysis. Carbon content includes both inorganic and organic carbon, but whole-rock geochemical data show that CaO content is low.

4.8 | Synchrotron-based scanning X-ray microscopy

Polished slab sections of representative samples were chosen for scanning XRM analysis. The XRM measurements were performed on several areas within the studied samples at the Nanoscopium hard X-ray nanoprobe beamline (Somogyi *et al.*, 2015) of Synchrotron Soleil (L'Orme des Merisiers Saint-Aubin, France). The monochromatic X-ray beam of 12 keV energy was focused on the sample area by a Kirckpatrick-Baez nano-focusing mirror. In order to obtain micrometre resolution for elemental maps of mm^2–sized sample areas, we used the fast continuous scanning (FLYSCAN) technique (Medjoubi *et al.*, 2013). Full XRF spectra were collected for each pixel of the scans by two Si-drift detectors (VITUS H50, KETEK GmbH) in order to increase the solid angle of detection. The XRF spectra of the two detectors were added and this sum was used for calculating the distributions of S, K, Ca, Ba, Mn, Fe, Ni, Cu, Zn, Ga, Ge and As in the measured sample regions. Each elemental map was normalized to 10 ms/pixel exposure time.

ACKNOWLEDGMENTS

We are grateful to the Gabonese Government, CENAREST, General Direction of Mines and Geology, and *Agence Nationale des Parcs Nationaux* of Gabon for logistic support. This work was supported by CNRS, the University of Poitiers, Nouvelle Aquitaine Region, and the French Embassy Libreville, Gabon. We would like to thank Prof. P. Mouguiama Daouda for his support. We also acknowledge E. Chi Fru, B. Dazas, F. Hubert, K. Medjoubi, and L. Pallas for scientific discussions and C. Fontaine, C. Laforest, S. Pronier, and P. Recourt for laboratory support at the Universities of Poitiers and Lille.

SUPPLEMENTARY NOTE 1

Geochemical comparisons of selected major elements between MRS and host sediments.

Al_2O_3 content reveals a negative relationship with SiO_2 in terms of clastic grain size (Appendix 12A), with shales being more aluminous than sandstone. This is to be expected, but surprisingly, non-pyritized MRS also have a higher SiO_2 content and K_2O/SiO_2 ratio than pyritized MRS (Figure 32), indicating that quartz dilution is unlikely. Moreover, the Francevillian FB_2 Member shales do not contain silica excess with respect to the average shale (Appendix 10) (Taylor & McLennan, 2001), inconsistent with extensive silicification during early diagenesis. Al_2O_3 displays a positive correlation with K_2O in pyritized MRS and host sediments, but shows no trend for non-pyritized MRS (Appendix 12B), suggesting the presence of K-poor clays. Lithologies show different K_2O and Na_2O relationships, but, on the average, K_2O and Na_2O contents co-vary (Appendix 12C), consistent with a similar relationship shown by chemical analyses of fine-grained illite (Środoń & Eberl, 1984). MgO exhibits no significant correlation with Al_2O_3 (Appendix 12D), indicating the presence of Mg-bearing carbonate and/or Mg-poor phyllosilicates. Collectively, these binary plots highlight that the variations in major element content are controlled by mineralogy (*e.g.*, type of detrital and/or authigenic clays present in lithologies).

3.3. Highlights of Part 3

- The potassium content in both the MRS and host sediments was measured by whole-rock analysis and synchrotron-based X-ray fluorescence.
- The X-ray diffraction profiles and transmission electron images show abundant and well-crystallized illite particles in the MRS, but not in the host rocks.
- The results point to a K enrichment confined to the MRS.
- The K was incorporated during the living of microbes and subsequently released after the decay of organic matter, enhancing the illitization process.
- The bacterially mediated illitization is akin to the reverse weathering process, which could have promoted feedbacks on seawater pH and climate, 2.1 Ga ago.
- The biologically derived K allows to recognize a new biosignature, providing new insights for seeking early life in Archaean rocks.

PART. 4: GEOCHEMICAL CHARACTERIZATION

4.1. Introduction

Part 4 now discriminates the MRS into three different mat textures described as pyritized MRS, poorly pyritized MRS, and unpyritized “elephant-skin” textures (EST). These are defined according to petrographic analyses (Aubineau *et al.*, 2018) and their sulfur content. The Francevillian MRS have shown to be characterized by K-rich phyllosilicates, while the host sediments are defined by K-poor clay minerals (see section 3.2; Aubineau *et al.*, 2019). This occurred from a biologically induced trapping of seawater K^+. In this regard, it seems likely that others cations would have been trapped in the microbial communities, especially because modern microbial cells tend to contain a measurable amount of trace elements important for the maintenance of cell function. This fourth part is intended to ascertain whether the MRS concentrate trace elements passively and/or actively. In addition, the interaction between toxic compounds and microbial communities is discussed through the following section. Indeed, the supply of toxicants (*e.g.*, oxidized arsenic species) to the Francevillian depositional environments in the wake of the GOE was recently documented by Chi Fru *et al.*, 2019 (associated works §3).

The carbon isotope compositions of MRS have been previously determined (see section 2.2; Aubineau *et al.*, 2018), but values from the different microbial morphotypes and host rocks have not yet been explored. Moreover, the investigation of nitrogen isotopes in the Francevillian MRS and host rocks is also undertaken for deciphering new microbial biogeochemical processes. The isotope analyses further characterize the studied samples and are reported in the last section of part 4. Lastly, Fe-based proxy analyses are provided to constrain the local redox conditions.

4.2. A biocontrolled trace element enrichment?

This section is dedicated to an article that is submitted in the journal *Chemical Geology*.

Trace element characterization of *ca*. 2.1-billion-year-old shallow-marine microbial mats from the Francevillian Series, Gabon

Jérémie Aubineau[1*], Abderrazak El Albani[1], Andrey Bekker[2], Ernest Chi Fru[3], Andrea Somogyi[4], Kadda Medjoubi[4], Armelle Riboulleau[5], Alain Meunier[1], & Kurt O. Konhauser[6]

[1]UMR 7285 CNRS IC2MP, University of Poitiers, Poitiers, France. [2]Department of Earth and Planetary Sciences, University of California, Riverside, CA, 92521, USA. [3]Centre of Geobiology and Geochemistry, School of Earth and Ocean Sciences, College of Physical Sciences and Engineering, Cardiff University, Cardiff CF10 3AT, Wales, UK. [4]Nanoscopium beamline Synchrotron Soleil, BP 48, Saint-Aubin, 91192 GIF-sur-Yvette, France. [5]UMR 8187 CNRS LOG, University of Lille, ULCO, Villeneuve d'Ascq, France. [6]Department of Earth and Atmospheric Sciences, University of Alberta, Edmonton, Alberta, Canada.

*corresponding author: jeremie.aubineau@univ-poitiers.fr

Abstract

The sedimentary fabrics of Precambrian mat-related structures (MRS) represent some of the oldest convincing evidence for early life on Earth. The *ca*. 2.1 billion-year (Ga) old MRS in the FB_2 Member of the Francevillian basin in Gabon has received considerable attention not only because they contain remnants of microbial mats that colonized large areas in oxygenated, shallow-marine settings, but also since they contain evidence for ancient multicellular organisms that thrived on these microbial mats using them as a food source. Despite these insights, what remains lacking is a full characterization of the geochemical composition of the MRS to test whether the bulk composition of fossilized MRS is distinct from the host sediments (sandstones and shales). Here, we show that the trace element (TE) content of microbial textures belonging to pyritized MRS, poorly pyritized MRS, and "elephant-skin" textures (EST) is highly variable and differs from that of the host sediments. The poorly pyritized MRS contain a unique matrix with embedded Ti- and Zr-rich minerals and syngenetically enriched in TE. The EST, some of which are developed along the same stratigraphic horizon as the poorly pyritized MRS, display a distinct distribution of TE-bearing heavy minerals, suggesting a local difference in physical conditions during sedimentation. Similarly, high chalcophile element (CE) content in pyrite-bearing MRS relative to the host sediments of the FB_2 Member further points to local bacterially influenced enrichments with high rates of microbial sulfate reduction during early diagenesis. The geochemical relationship between the MRS and the Francevillian sediments (*e.g.*, FB, FC, and FD formations) indicates that specific, biological pathways for CE enrichments (*i.e.*, microbially controlled accumulation) are not obvious. Our findings highlight bulk-rock TE distinction between the 2.1-billion-year-old MRS and their host sediments, but also indicate that environmental conditions, such as hydrodynamic regime and water-column redox chemistry, may simply overwhelm any potential biological signal. Our data imply that microbial activity played a role in the enrichment of local sediment TE content in the Francevillian Group, but suggest that bulk MRS TE concentrations are a poor example of a Paleoproterozoic biosignature.

Keywords

Microbial mats, trace element content, biological signal, environmental factors, Palaeoproterozoic

1 | INTRODUCTION

The *ca*. 2.1 billion-year-old Francevillian sedimentary rocks record significant changes in the Earth's ocean and atmosphere chemistry as they were deposited in the immediate aftermath of the first substantial rise of atmospheric oxygen (Holland, 2002; Bekker, 2015a) and coincident with Earth's longest and most extreme marine positive carbon isotope excursion (El Albani *et al.*, 2010; Canfield *et al.*, 2013; Bekker, 2015b). These sediments record the presence of cm-sized macroscopic fossils with a wide range of characteristics, including lobate, elongated, rod-shaped, and disc-shaped morphotypes (El Albani *et al.*, 2010, 2014), as well as diverse string-shaped structures that have been interpreted as evidence for ancient organism motility (El Albani *et al.*, 2019). In addition, benthic microbial mat communities prevailed in the Francevillian sedimentary deposits (Reynaud *et al.*, 2017; Aubineau *et al.*, 2018) and are now preserved as mat-related structures (MRS) with an exceptional diversity of mat growth patterns (*e.g.*, "elephant-skin" texture, "fairy rings") and mat-protected features (*e.g.*, wrinkle structures) (Aubineau *et al.*, 2018). Based on the observed tufted microtextures and comparison with modern analogues it has been suggested that shallow-marine conditions within the photic zone allowed the development of phototrophic microbial mats composed of oxygenic photosynthesizers such as cyanobacteria (Reynaud *et al.*, 2017; Aubineau *et al.*, 2018). Lastly, these MRS have been shown to record an ancient metabolic activity through a K-controlled mineral transformation that occurred during diagenesis (Aubineau *et al.*, 2019).

The observation of MRS in the Francevillian Group, therefore, offers us the opportunity to further ascertain whether specific chemical "biosignatures" unique to MRS might also be present. This is crucial because organic microbial remnants, preserved as graphite, are common features in early Archean rocks (Schidlowski *et al.*, 1979; Mojzsis *et al.*, 1996; Rosing, 1999; Nutman *et al.*, 2016; Dodd *et al.*, 2017), but these have been subjected to deep burial diagenesis or metamorphism, and as a consequence, without clear physical features of MRS, it is difficult to assess their biogenicity. Indeed, it has been suggested that carbonaceous matter may have been generated abiotically under hydrothermal conditions *via* a process similar to the Fischer–Tropsch synthesis (Brasier *et al.*, 2002; Van Zuilen *et al.*, 2002; Lindsay *et al.*, 2005). Therefore, seeking chemical biosignatures for ancient microbial mats is a sensible way forward because it is well documented that modern microbial mats, comprised of various bacterial species and their extracellular polymeric substances (EPS), are frequently enriched in metal cations in the nmol/g (Huerta-Diaz *et al.*, 2011, 2012; Petrash *et al.*, 2015) to µg/g (Webster-Brown & Webster, 2007; Sancho-Tomás *et al.*, 2018) range. This is a function of the EPS containing a variety of organic functional groups (*e.g.*, carboxyl, phosphate, and sulfhydryl) that deprotonate at circum-neutral pH conditions, thus making them anionic and prone to metal adsorption and potential authigenic mineral nucleation (Konhauser, 1997). The same functional groups are also responsible for the trapping and binding of detrital particles onto the surface of mats as they grow upward, including heavy mineral grains, such as titanium oxides and zircons (Homann *et al.*, 2015), or clays (Konhauser, 1998; Newman *et al.*, 2016, 2017; Playter *et al.*, 2017).

There is no reason to believe that Precambrian mats behaved differently from the modern so it stands to reason that fossilized mat fabrics should similarly show TE enrichments relative to host sediments. In this regard, we measured the bulk TE concentrations of the MRS and host sediments of sandstone and black shale from the *ca*. 2.1 Ga Francevillian FB_2 Member of the Francevillian Group in Gabon to ascertain whether potential biological TE enrichments are recorded. These sedimentary rocks were chosen because previous work has already demonstrated that they contain diverse microbial mat morphotypes (Aubineau *et al.*, 2018, 2019), previously described as pyritized MRS, poorly pyritized MRS, and unpyritized “elephant-skin” textures (EST). The rocks also possess geochemical record that tracks Earth’s oxygenation history and MRS with associated K enrichment (Canfield *et al.*, 2013; Aubineau *et al.*, 2019; Chi Fru *et al.*, 2019).

2 | GEOLOGICAL CONTEXT OF THE FRANCEVILLIAN SERIES

The unmetamorphosed and minimally deformed *ca*. 2.1 Ga old Francevillian Group in southeastern Gabon is a 1.0 to 2.5 km-thick succession that overlies an Archean crystalline basement (Figure 35A) (Gauthier-Lafaye & Weber, 1989; Weber *et al.*, 2016). Lithostratigraphically, the Francevillian Group has been divided into five formations, labelled FA to FE from the oldest to youngest (Figure 35B) (Weber, 1968). The Archean crystalline basement is mainly composed of granitoids and greenstone belts (Thiéblemont *et al.*, 2009) with ages *ca*. 3.0–2.9 Ga (Mouélé *et al.*, 2014). The basal FA Formation unconformably overlies the Archean basement and is predominantly composed of fluvial to fluvio-deltaic, coarse- to fine-grained quartz arenites, and conglomerates with minor interlayered mudstones. Collectively, this sedimentary sequence indicates a progressive transition to marine conditions (Gauthier-Lafaye & Weber, 1989; Bankole *et al.*, 2015).

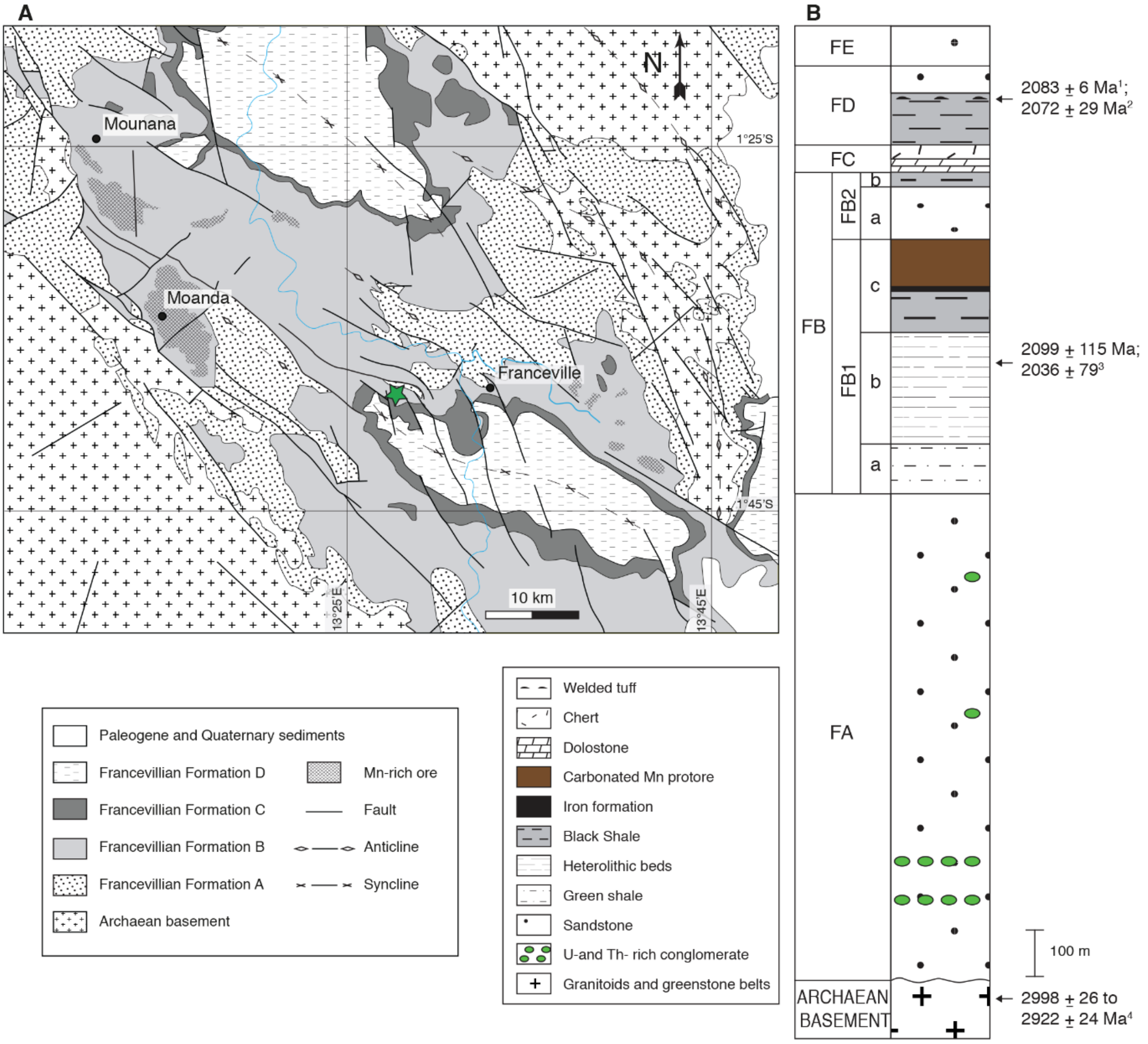

Figure 35: Geological map of the Paleoproterozoic Franceville sub-basin (**A**; modified from Bouton et al. (2009)) and general lithostratigraphic column of the Francevillian Series (**B**). The studied area (the Moulendé Quarry) is shown with the green star. [1Horie *et al*. (2005); 2Thiéblemont *et al*. (2009); 3Bros *et al*. (1992); 4Mouélé *et al*. (2014)].

The predominantly marine FB Formation sedimentary rocks conformably overlie the FA Formation and are characterized by fine-grained sediments with interbedded debris flows, dolostones, thin iron-rich horizons, manganese ore deposits, and sandstones (Gauthier-Lafaye, 1986; Gauthier-Lafaye & Weber, 1989). The FB Formation is classically subdivided into FB$_1$ (including a, b, and c units) and FB$_2$ (with a and b units) members based on lithological variations (Weber, 1968; Azziley Azzibrouck, 1986). The FB_1 Member is dominated by greenish, silty to sandy shales, heterolithic beds that consist of shales alternating with interbedded dolomite-cemented siltstones, and manganese-rich black shales (Azziley Azzibrouck, 1986; Pombo, 2004; Reynaud *et al.*, 2017). The FB_2 Member is essentially dominated by coarse-grained sandstones rapidly deposited from high-density gravity currents (FB2a unit) that formed largely structureless to dewatered beds (Reynaud *et al.*, 2017). The sandstones are overlain by black shales with thin interlayered siltstones (FB2b unit), deposited during a sea-level fall. Overall, the FB_2 sediments were deposited in a shallow-marine environment with an oxygenated water column (Canfield *et al.*, 2013; Ossa Ossa *et al.*, 2018). The overlying FC Formation consists of massive dolostone beds, and stromatolitic cherts interbedded with black shales (Weber, 1968; Bertrand-Sarfati & Potin, 1994; Amard & Bertrand-Sarfati, 1997; Préat *et al.*, 2011). Moreover, an exceptionally preserved, Gunflint-type microfossil assemblage was recently documented in cherts of the FC Formation, giving support to the diverse ecosystem in the Francevillian basin (Lekele Baghekema *et al.*, 2017). The FD Formation is mainly dominated by black shales alternating with volcanic tuffs and fine- to medium-grained sandstones (Thiéblemont *et al.*, 2014). The topmost FE Formation consists of medium-grained arkose with interlayered shales (Gauthier-Lafaye & Weber, 1989; Thiéblemont *et al.*, 2014).

A number of radiometric ages have been obtained for the Francevillian Group sediments, but the timing of deposition of the Lower Francevillian Group (FA and FB formations) is still controversial. Diagenetic illites in the FB1b unit yielded a Sm-Nd isotope ages of 2099 ± 115 Ma and 2036 ± 79 Ma on <0.4 μm and <0.2 μm clay fractions, respectively, which constrained the age of early diagenesis in this unit (Bros *et al.*, 1992). Finally, the depositional age of the FD Formation is well constrained with ignimbrite tuffs and sandstones that provided U-Pb ages of 2083 ± 6 Ma (Horie *et al.*, 2005) and 2072 ± 29 Ma (Thiéblemont *et al.*, 2009), respectively. Based on $\delta^{13}C_{carb}$ and $\delta^{13}C_{org}$ isotope compositions, the FB and FC formations also record the end of the Lomagundi carbon isotope excursion (El Albani *et al.*, 2010; Préat *et al.*, 2011; Canfield *et al.*, 2013), dated elsewhere between 2.11 and 2.06 Ga (Karhu & Holland, 1996; Martin *et al.*, 2013). Given these age constraints, the deposition of the Francevillian Group has likely occurred *ca*. 2.1 Ga ago, during a critical juncture when Earth's atmosphere underwent a critical transition towards modern oxygenated conditions.

3 | MATERIAL AND METHODS

3.1 | Materials

Highly diverse microbial mats and their host sediments were sampled from the Moulendé Quarry, Francevillian basin, Gabon. The mat layers were carefully separated from the underlying sediments with a blade, avoiding contamination with the underlying sediments. Directly from below the MRS, the host sediments were also sampled for geochemical analyses.

3.2 | Microscopy

Mineral composition and textural relationships were studied in polished and carbon-coated thin sections, using a FEI Quanta 200 scanning electron microscope (SEM) equipped with an energy-dispersive X-Ray Spectrometer (EDX) as previously described (Aubineau *et al.*, 2018).

3.3 | Major and trace element analyses

Whole-rock geochemical analyses of major and trace elements were performed on 7 pyritized MRS, 7 poorly pyritized MRS, 4 unpyritized “elephant-skin” textures, 7 sandstones, and 15 black shale samples. Major element concentrations were measured by inductively-coupled plasma atomic emission spectrometry (ICP-AES), while trace and rare earth element (REE) contents were analyzed by inductively coupled plasma mass spectrometry (ICP-MS) at *Service d’Analyse des Roches et Minéraux* (SARM) of the *Centre de Recherches Pétrographiques et Géochimiques* (CRPG), Nancy, France. Each sample was powdered in agate mortar and approximately 1 g was fused with lithium metaborate ($LiBO_2$) and dissolved in nitric acid. According to the analyzed trace element concentration, the uncertainty is lower than 5–10% for elemental concentrations > 50 ppm, lower than 5–20% for elemental concentrations between 10 and 1 ppm, and higher than 25% for elemental concentrations near the detection limit (Carignan *et al.*, 2001). Descriptive statistics for trace elements were performed with R software (version 3.5.1; R Core Team, 2018) to enhance data resolution relative to the number of individual samples within each lithology.

3.4 | X-ray fluorescence (XRF) microscopy

Scanning X-ray fluorescence microscopy analysis was performed on polished slab sections of representative MRS samples. The XRF elemental distribution maps were collected on several areas within the investigated samples at the Nanoscopium hard X-ray nanoprobe beamline (Somogyi *et al.*, 2015) of Synchrotron Soleil (L'Orme des Merisiers Saint-Aubin, France). The monochromatic X-ray beam with 12 keV energy was focused on the sample by a Kirckpatrick-Baez nano-focusing mirror. We used the fast continuous scanning (FLYSCAN) technique to obtain micrometer resolution for elemental maps of mm^2-sized sample areas (Medjoubi *et al.*, 2013). We have increased the solid angle of detection by the means of two Si-drift detectors (VITUS H50, KETEK GmbH) to collect full XRF spectra in each pixel of the scans. We provide the distribution of Fe, As, and Ni with micron-scale spatial resolution and high analytical sensitivity. Each elemental map was normalized to 10 ms/pixel exposure time.

4 | RESULTS

4.1 | Textural diversity of MRS

Mat-related structures, marine shales, and sandstones collected from across the FB_2 Member (Figure 36A) are different in their macroscopic and microscopic textures, mineralogy, and geochemistry (Figures 36B-G; Appendices 20, 21). Pyritized MRS are developed on top of thin bedded, parallel-laminated black shales. They range from 0.8 to 3 mm in thickness and contain euhedral pyrite crystals, 20 to 30 µm in size (Figures 36B, C). In this study, pyritized MRS refer to flat pyritized structures, domal buildups, and “fairy ring” features that were previously described by Aubineau *et al*. (2018) in the same rocks. The poorly pyritized MRS from the sandstone unit reflect mat growth or mat-protected (resulting from mat preservation of structures formed independently from mat growth) patterns (Sarkar *et al.*, 2008; Aubineau *et al.*, 2018). They vary between 0.2 and 0.5 mm in thickness (Figures 36D, E), and contain a large number of detrital minerals (Figure 36E; Appendix 22) (Aubineau *et al.*, 2018). Among them, randomly arranged zircons and titanium oxides, and clay particles up to 100 µm in size, are common. Numerous sub-euhedral to euhedral pyrite crystals with varying size, but generally smaller than those in the pyritized MRS, were observed at deeper levels in the poorly pyritized MRS (Appendix 23). In addition, interpreted gas escape and bubble-like structures, having clay minerals disorganized at the edges, but aligned around them, were likely formed before compaction (Figure 36E). The unpyritized EST, some of which developed on the same bedding plane in sandstones as the poorly pyritized MRS, is one of the most common mat morphologies, characterized by tufted microbial fabrics (Figures 36F, G) (Shepard & Sumner, 2010; Reyes *et al.*, 2013; Aubineau *et al.*, 2018). They reach up to 2 mm in thickness and lack embedded heavy minerals and putative gas escape structures.

4.2 | Provenance characterization

The host sediments have similar chondrite-normalized REE + Y patterns (Figure 37A; Appendix 21) (Schmitt *et al.*, 1964; Evensen *et al.*, 1978). The steep light-REE pattern with a flat heavy-REE profile in the post-Archaean shales reflects REE abundances in the upper continental crust exposed to weathering (Taylor & McLennan, 2001; Large *et al.*, 2018). REE contents decrease with increasing SiO_2 content, reflecting quartz dilution. The similar REE + Y patterns of sandstone and black shale lithologies suggest that the sediments on which the MRS formed had the same provenance. Furthermore, sandstones and black shales are interlayered (Figure 36A), indicating that they were deposited in the same general setting, but at different energy levels (Reynaud *et al.*, 2017).

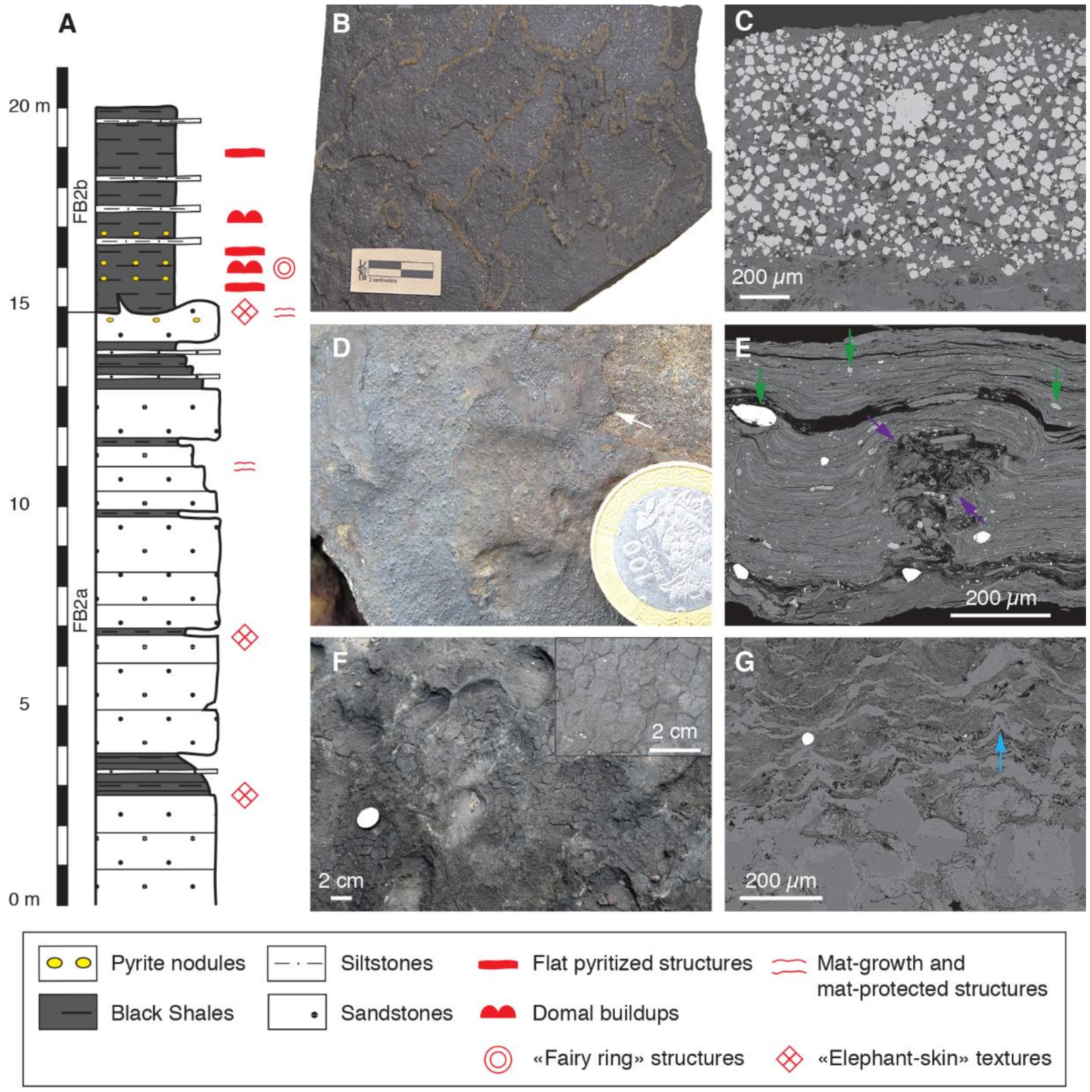

Figure 36: Lithostratigraphic column and representative mat-related structures (MRS) with their associated petrographic textures from both sandstone and black shale facies. (**A**) Composite lithostratigraphic section of the studied area in the FB2 Member showing the main microbial levels including pyritized MRS (flat pyritized, domal buildup, and 'fairy ring' structures), poorly pyritized MRS (mat-growth and mat-protected structures), and unpyritized MRS (EST: "elephant-skin" texture). (**B**) Flat pyritized MRS from the FB2b unit. (**C**) SEM image of pyritized MRS in cross-section perpendicular to the bedding plane. Pyrite grains and clay particles are developed within biofilms. (**D**) Mat-layer structures (white arrow) on the bedding surface of sandstone from the FB2a unit. (**E**) SEM image of micrometer-thick poorly pyritized MRS in cross-section perpendicular to the bedding plane. Green and purple arrows show trapped and bound heavy minerals and a gas escape structure, respectively. (**F**) "Elephant-skin" textures (EST) from the FB2a unit. Inset box shows reticulate pattern. (**G**) SEM image of tufted microbial fabrics from the EST above the poorly-sorted quartz sandstone. Blue arrow points to tufted microbial fabrics. Images in B and C, F, and G are modified from Aubineau *et al*. (2018) and Aubineau *et al*. (2019), respectively.

The REE abundances have also been normalized to the Post-Archaean Australian Shale (PAAS) average, a widely used reference for normalizing sedimentary lithologies, allowing easy comparison to previous works (Figure 37B). The PAAS-normalized REE + Y patterns of black shales from the FB$_2$ Member show moderately positive Eu anomalies (Eu/Eu*; see

Appendix 21 for method of calculation), ranging from 1.29 to 1.44. A strong positive Eu anomaly in sediments is usually interpreted to indicate high-temperature hydrothermal fluxes to the water column (Bolhar *et al.*, 2004; Planavsky *et al.*, 2010; Hiebert *et al.*, 2018). Moreover, the REE + Y patterns reveal a moderately steep trend with light-REE enrichments, as shown by shale-normalized Pr/Yb$_{(SN)}$ ratios ranging between 1.45 and 3.54 (Figure 37B; Appendix 21). In addition, the binary plot of Fe/Ti *vs*. Al/(Al+Fe+Mn), which resolves the influence of a hydrothermal *vs*. detrital source (Figure 37C; cf. Pecoits *et al.* 2009), suggests that the studied black shales predominantly reflect a detrital source, with limited hydrothermal influence. Similarly, the average Y/Ho value of 31.4 (Appendix 21) is lower than the seawater Y/Ho ratio that is >44 (Bolhar *et al.*, 2004), but above the invariable Y/Ho ratio of terrestrial materials (~26).

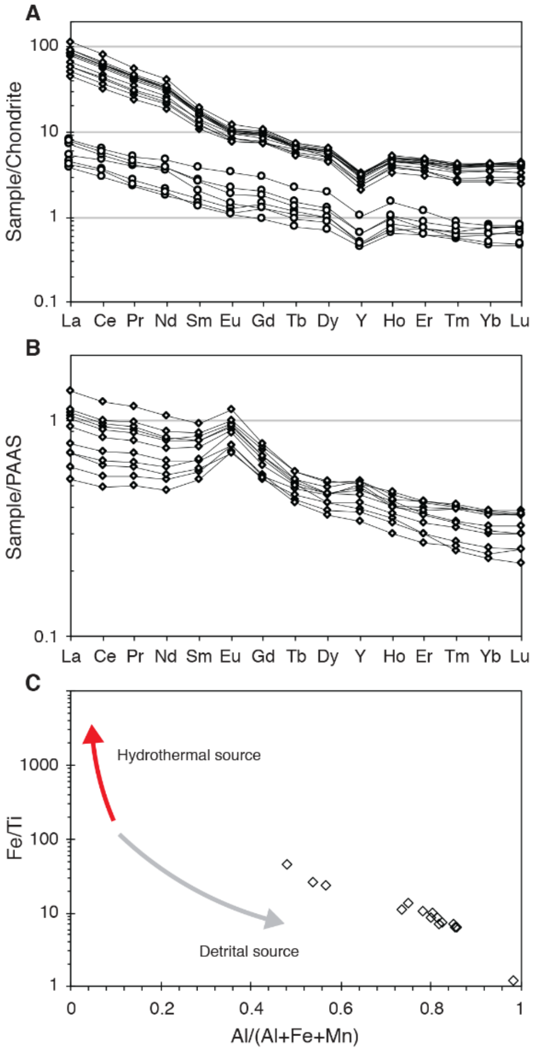

Figure 37: Geochemistry of the host rocks, black shales (diamonds) and sandstones (circles). (**A**) Chondrite-normalized REE + Y patterns. Chondrite values are from Schmitt *et al*. (1964) and Evensen *et al*. (1978). (**B**) PAAS-normalized REE + Y patterns. PAAS values are from Taylor & McLennan (1985). (**C**) Binary plot of Fe/Ti vs. Al/(Al+Fe+Mn).

4.3 | Chemical composition of host sediment and MRS

Descriptive statistical relationships among independent TE variables of MRS and individual sediment lithologies show the largest variation along the first and second Principal Components (PC) (Figure 38A). Collectively, both PC explain more than 78% of the total variance in the dataset (Appendix 24). According to the contribution of each variable along the PC1, the variation is induced by TE that are usually taken to be proxies of the detrital flux (Figure 38B; McLennan 1989, 2001; Tribovillard *et al.* 2006). Along the PC2, it appears that the metals enriched in pyrite, apart from Cd and Zn, are responsible for difference among lithologies. The PC1 accounts for 54.3% of the total variance, with the poorly pyritized MRS being different from the pyritized MRS, EST, and host sediments (Figure 38A). On the other hand, EST, pyritized MRS, and black shales do not cluster into distinctly separate groups. Their spread along the PC1 axis seems largely determined by the elements that are abundant in the heavy mineral fraction, as indicated by the large contribution of Zr and REE (Figure 38B). This is consistent with petrographic observations, which indicate the presence of detrital zircon and Ti-oxides in the poorly pyritized MRS. The PC2 contributes 24.4% to the total variance, with the pyritized MRS plotting above the poorly pyritized MRS, EST, and host sediments. The pyrite content likely controls their spread along the PC2 axis. One pyritized MRS sample has a signature similar to that of black shales, suggesting either a large contribution of the host sediment during sample separation or a depletion in metals enriched in pyrite compared to the other pyritized MRS (Figure 38A).

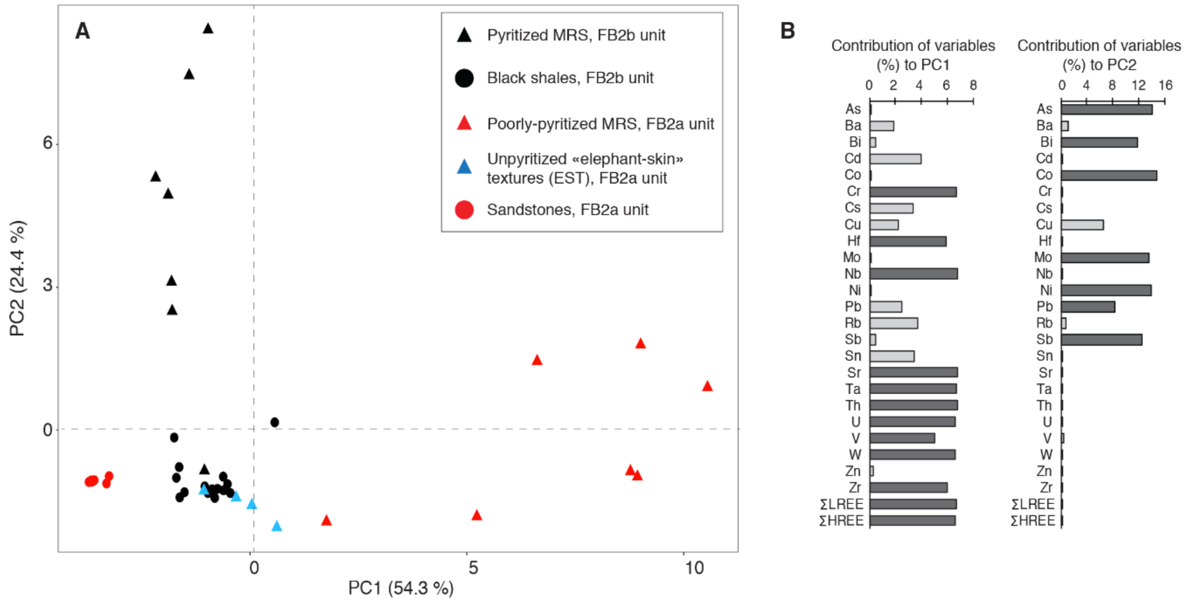

Figure 38: Descriptive statistical treatments. (**A**) Principal component analysis on 40 individuals representing the relationship among 3 MRS morphotypes and 2 host sediments (black shales and sandstones) and 26 independent variables (trace element concentrations). (**B**) Contribution of each variable (%) along PC1 (left) and PC2 (right). The stronger the contribution of TE, the darker the bar is.

Stratigraphic geochemical profiles of the FB_2 Member reveal dramatic difference in bulk composition among the three MRS morphotypes even on the same stratigraphic level, but also heterogeneous composition of the poorly pyritized and pyritized MRS (Figure 39). The enrichment factor The enrichment factor (EF; Tribovillard *et al.*, 2006) relative to the average shale (see Figure 39 for method of calculation; Taylor & McLennan (2001), Li & Schoonmaker (2003)) assesses whether an element was authigenically enriched or depleted. The EF are considered detectable and substantial when they are >3 and >10, respectively (Algeo & Tribovillard, 2009). In our samples, EF have a mean of 2.1 for Ti (EF_{Ti}) and 6.6 for Zr (EF_{Zr}) for the poorly pyritized MRS, which have both elements moderately to strongly enriched. These elements are predominantly depleted to moderately enriched in the EST (mean EF_{Ti} = 0.2; mean EF_{Zr} = 2.5) and in the pyritized MRS (mean EF_{Ti} = 0.3; mean EF_{Zr} = 0.5). Chalcophile elements (CE) are depleted to weakly enriched (mean EF_{As} = 0.1; mean EF_{Ni} = 1.1), weakly enriched (mean EF_{As} = 1.4; mean EF_{Ni} = 2.0), and strongly enriched (mean EF_{As} = 13.2; mean EF_{Ni} = 14.5) in the EST, the poorly pyritized MRS, and the pyritized MRS, respectively. The host sediments (both sandstone and black shale) show no to weak overall TE enrichment for most samples, with mean EFs for Ti, Zr, As, and Ni of 0.4, 1.5, 0.5, and 1.2, respectively (Appendix 25).

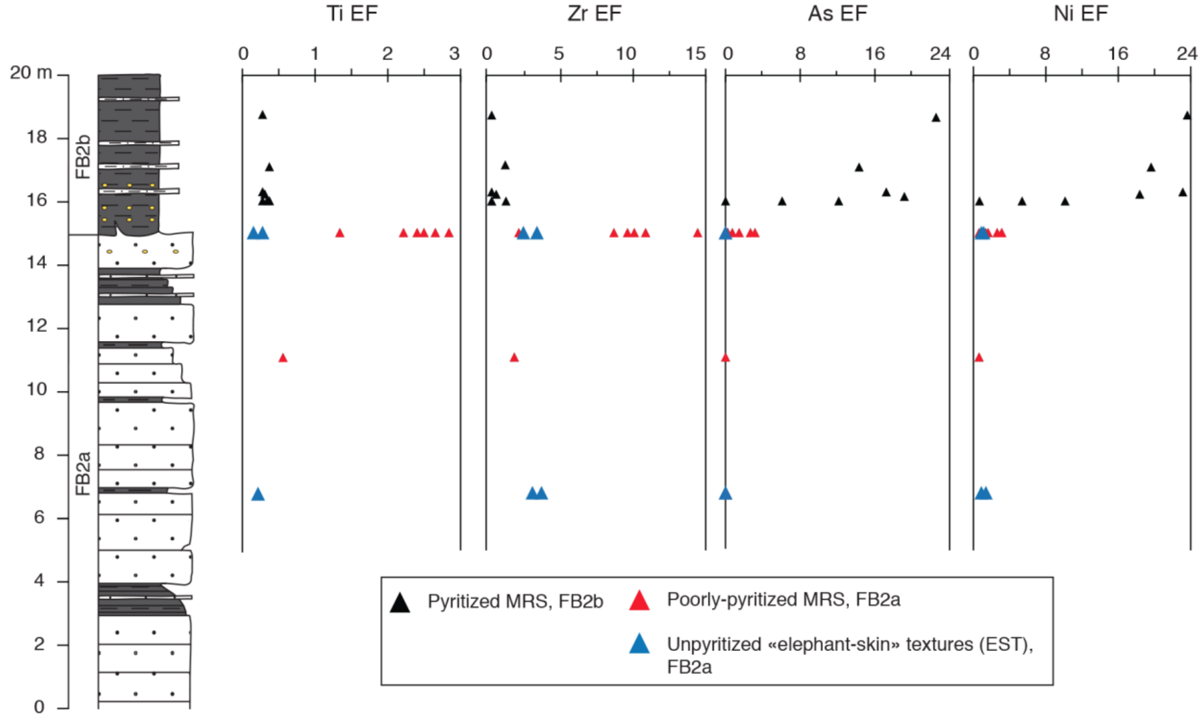

Figure 39: Stratigraphic profile of enrichment factors (EF) of selected detrital and chalcophile elements within MRS. EF relative to the average shale (Ti, Zr, Ni concentrations for the average shale are from Taylor & McLennan (2001) and As concentration for the average shale is from Li & Schoonmaker (2003)) were calculated as $(X/Al)_{sample}/(X/Al)_{average\ shale}$, where X stands for the element concentration.

Generally, CE are enriched within the sediment in association with S-bearing minerals, and when plotted against each other, show positive covariation. The trends found within the MRS and black shales from the FB$_2$ Member show the expected pattern for the preferential incorporation of CE into sulfide minerals (Figures 40A, B). The mixing trends among the poorly pyritized MRS, EST, and host shale reflect the variable content of CE-bearing pyrite. Nonetheless, the correlation trends of pyritized MRS differ from those of pyrite-poor MRS and

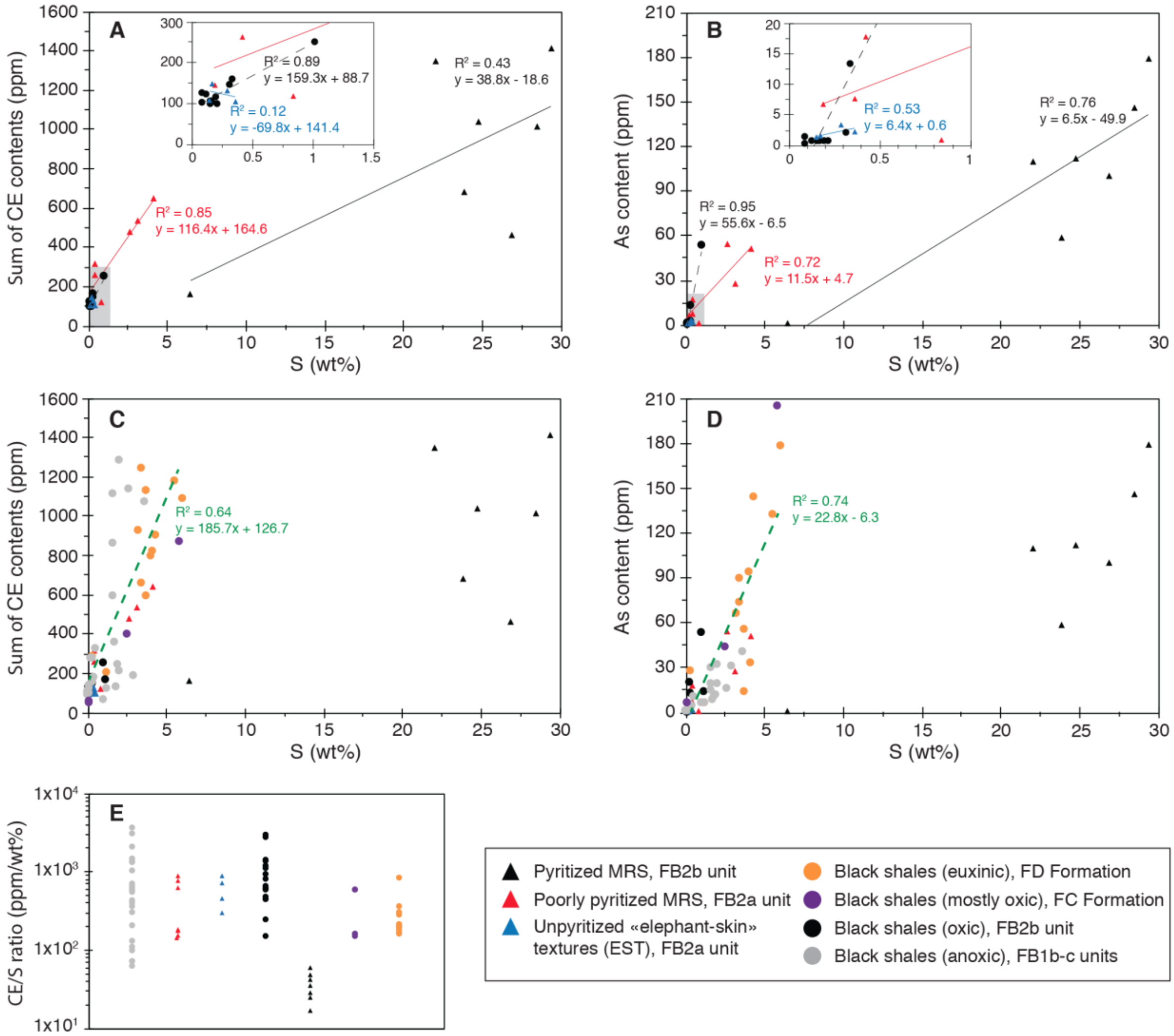

Figure 40: Relationships between chalcophile elements and sulfur for pyritized MRS, poorly pyritized MRS, unpyritized “elephant-skin” textures (EST), and Francevillian black shales (from the FB1b and FB1c units and the FD formation). (**A**) Cross plot of Σchalcophile element (As, Bi, Co, Cu, Mo, Ni, Pb, and Sb) contents *vs*. bulk S concentrations for MRS and host black shales. (**B**) Cross plot of As content vs. bulk S concentration for MRS and host black shales. Inset boxes (A and B) show covariations at low CE and S contents. (**C**) Cross plot of Σchalcophile (As, Bi, Co, Cu, Mo, Ni, Pb, and Sb) contents *vs*. bulk S concentration for MRS and all Francevillian Series black shales (green trend). (**D**) Cross plot of As content vs. bulk S concentration for MRS and all Francevillian Series black shales (green trend). (**E**) CE/S ratios for 3 MRS morphotypes and 2 host sediments (black shales and sandstones). CE and S contents for black shales of the Francevillian Series are from Canfield *et al*. (2013). Data for some samples are below the detection limit; in that case a value of half of the detection limit was used.

host sediments, indicating that either some intrinsic properties (*e.g.*, mineralogy, organic matter, or bacterial sulfate reduction) controlled incorporation of pyrite-hosted metals or the dynamic supply of CE fluctuated. Moreover, 43% (R^2=0.43) of total co-variation in the pyritized MRS between CE and S (Figure 40A) implies that CE are also associated with other components. We note that one pyritized MRS sample shows low CE contents by a factor of 10 to 100, with moderate S concentration, revealing a high heterogeneity in CE content in pyritized MRS.

Compiled data for CE and S contents of the Francevillian Series black shales (from the FB1b unit to FD Formation) illustrate an overall linear relationship (Figure 40C), suggesting that sulfide production controlled the enrichment in CE. The strong positive co-variation (R^2= 0.64) for black shales of the Francevillian Series suggests that CE contents are only moderately controlled by other mineral phases. The pyritized MRS show a different trend with higher S contents for the same CE concentrations. The same trend is also observed for As and S (Figure 40D), indicating that the As content was affected by the same processes that control CE enrichments. Finally, the CE/S ratios of pyrite-poor MRS and the Francevillian Series black shales are mostly within the same range from 10^2 to 10^3, whereas the pyritized MRS show the lowest ratios down to 17 (Figure 40E).

4.4 | High-resolution metal distribution in the MRS

Millimeter-sized areas of each MRS morphotype were analyzed by synchrotron-based scanning XFM. The distribution maps of Fe, As, and Ni are shown in Figures 41 and 42. Although some Fe is hosted in phyllosilicates, the highest abundance of iron is in pyrite grains, highlighting the difference among the MRS. EST have low As and Ni contents close to the detection limit (Figure 41A). These elements are unlikely to be associated with pyrite, since it is not present at detectable level, which is also consistent with the absence of a strong relationship between CE and S in the EST. The poorly pyritized MRS contain higher CE concentrations that are heterogeneously distributed in pyrite grains (Figure 41B). A few small, euhedral pyrite crystals display As-rich cores. Arsenic is preferentially located within the pyrite cores in the pyritized MRS with a variation in As content of ± 10% (1 SD), whereas Ni is mostly concentrated within the overgrowths (Figure 41C). This pattern suggests high As content in early pore-waters from which pyrite cores nucleated and higher Ni content during later diagenesis when the overgrowths were formed. The As distribution within individual pyrite crystals is heterogeneous, resulting from micrometer-thick As-rich rims around the cores and a decrease in As content toward the crystal surface (Figure 42). Ni also exhibits a highly variable abundance pattern often with a micrometer-thick Ni-rich zone at the pyrite crystal surface. CE appear to be enriched by a factor of 15 (As) and 6 (Ni) in pyritized MRS compared to poorly pyritized MRS.

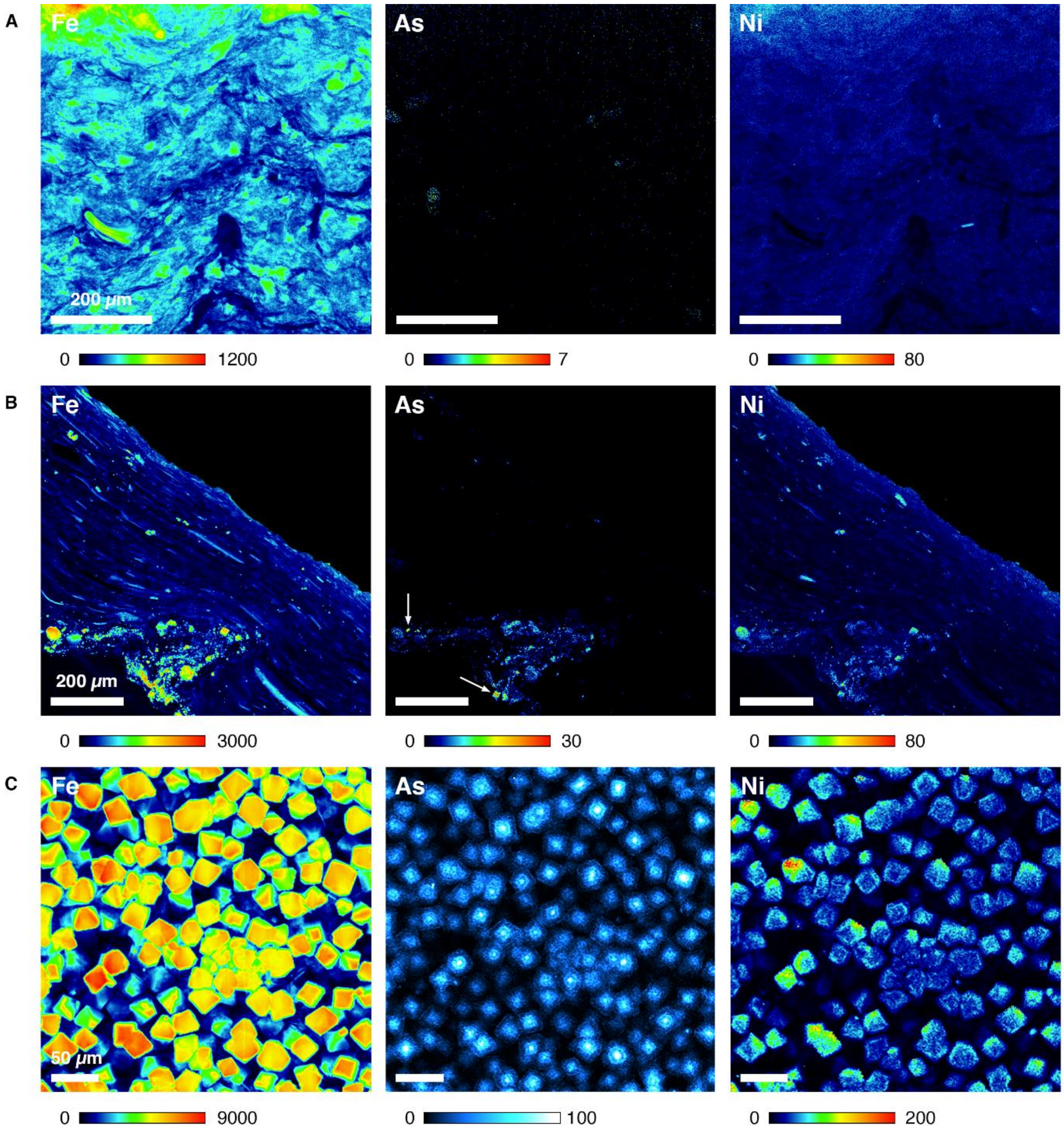

Figure 41: Synchrotron-based XFM showing the distribution of Fe, As, and Ni. (**A**) Unpyritized EST. (**B**) Poorly pyritized MRS. White arrow indicates As-rich pyrite core. (**C**) Pyritized MRS. The color bars indicate the intensity-scale of the metal X-Ray Fluorescence (XRF) distribution maps in counts/10 ms (black color, below detection limit). Higher XRF intensities correspond to higher metal contents.

5 | DISCUSSION

5.1 | Microbial fabric and response to the environment

At high concentrations of suspended material in the water column, laboratory-cultured cyanobacteria can become rapidly coated with clay minerals, which means that they may preserve the TE and mineralogical context of detrital input to the depositional setting in which they lived (Newman *et al.*, 2016, 2017; Playter *et al.*, 2017). The Francevillian poorly pyritized MRS and EST contain in a high abundance TE-bearing heavy minerals relative to the host sandstone facies. The absence of heavy mineral enrichment in the overlying pyritized MRS reflects a significant decrease in sedimentation rate and energy in the depositional setting (Figure 43A), consistent with a change in sediment supply from sand-rich high density flows to fine-grained black shales (Reynaud *et al.*, 2017). As such, the distribution of heavy minerals in the Francevillian Series MRS, or for that matter any MRS, is best explained by passive trapping and binding processes, rather than a selective and direct detrital entrapment (Sforna *et al.*, 2017).

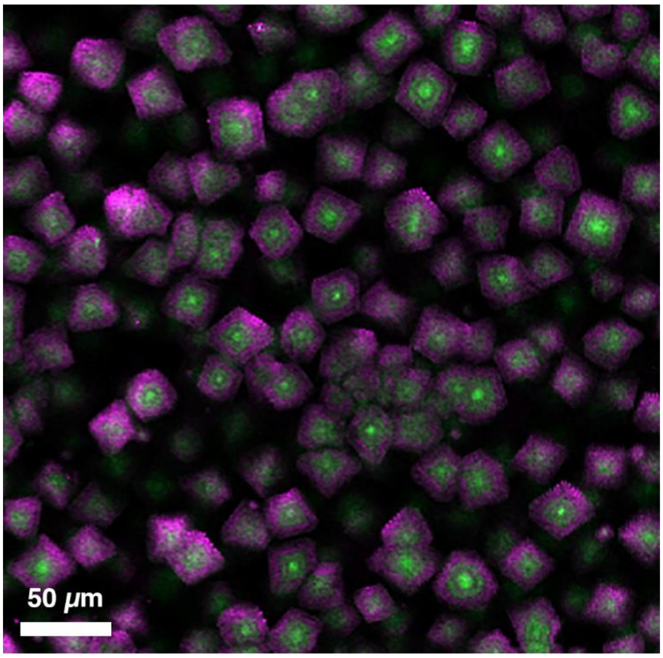

Figure 42: Combined As (green) and Ni (magenta) XRF maps for pyritized MRS.

Importantly, poorly pyritized MRS and EST developed along the uppermost and same stratigraphic horizon in coarse-grained sediments (Figure 43). Although the transition from sandstone to black shale might imply a transgressive surface, the sandstones of the FB Formation were deposited from pulses of high density flows into a depositional setting with a background mud sedimentation (Reynaud *et al.*, 2017). It is thus reasonable to assume that the poorly pyritized MRS and EST were formed under exactly the same depositional conditions. The variable abundance of Ti- and Zr-bearing heavy minerals in these mats only few meters apart likely reflects minor changes in environmental conditions under which the MRS flourished (*e.g.*, hydrodynamic regime or sediment delivery pattern) (Figure 43A). These changes appear to have impacted microbial growth patterns, resulting in a shift to different mat morphology (Figure 43A). Indeed, numerous observations on stromatolite morphology have shown active adaptation by the bacterial community to environmental conditions, such as water energy and the availability of light and nutrients (*e.g.*, Allwood et al., 2006; Jahnert and Collins, 2012). Similarly, distribution patterns of distinct microbial mat morphotypes across ancient tidal flats constrain palaeoenvironmental conditions (Bose & Chafetz, 2009; Sarkar *et al.*, 2014; Homann *et al.*, 2015).

The poorly pyritized MRS typically display the smallest mat thickness and planar morphologies that likely reflect a morphological adjustment to high energy hydrodynamic regime, while the EST and pyritized MRS show larger mat thicknesses and well-developed mat-growth fabrics (*i.e.*, tufted features, domal buildups), indicating optimal growth conditions (*e.g.*, Gerdes *et al.*, 2000). Difference in physical environmental conditions also likely led to highly variable abundance of TE-bearing heavy minerals in the Francevillian Group MRS and may have triggered ecologically controlled growth (Figure 43A). While mat morphology and thickness are linked to external environmental factors, it has been recently documented that the mat thickness may similarly influence the community structure (Suarez *et al.*, 2019). This leads to different redox profiles and internal carbon recycling styles among the microbial communities since thick mats contain a well-expressed anoxic area in the mat structure, whereas thin mats create only a limited anoxic region (Suarez *et al.*, 2019). However, effects of thickness on microbial architecture are difficult to quantify because the hydrodynamic regime (Battin *et al.*, 2003; Flemming *et al.*, 2016), water depth (Lydmark *et al.*, 2006), temperature (He *et al.*, 2016), and dissolved carbon to nitrogen ratios (Okabe *et al.*, 1996) also impact on the microbial community structure. Thus, in combination, these environmental parameters might have promoted the lack or poor expression of an anoxic zone in the thick unpyritized EST (Figure 43B).

5.2 | Microbial mineralization

Recent studies on transition metals and metalloids associated with present-day hypersaline mats (Huerta-Diaz *et al.*, 2012; Petrash *et al.*, 2015; Sforna *et al.*, 2017; Sancho-Tomás *et al.*, 2018) have revealed that TE can be trapped by and bound in the organic matrix, progressively accumulating with depth via incorporation into sulfides. The latter form as the original mat organic material is degraded by the activity of anaerobic heterotrophs (*e.g.*, sulfate-reducing microorganisms), eventually diminishing the cation-binding capacity of the EPS matrix (Dupraz & Visscher, 2005; Dupraz *et al.*, 2009). Then, as authigenic pyrite forms by the reaction of reactive Fe and biogenic H_2S, liberated from mats to pore-waters metals are scavenged into sulfidic microenvironments where pyrite crystals grow (Figure 43B), resulting in high spatial variability of metal distribution (Huerta-Diaz & Morse, 1992; Sforna *et al.*, 2017). The spatial restriction of pyrite grains to deeper levels in the mat in the poorly pyritized MRS or their

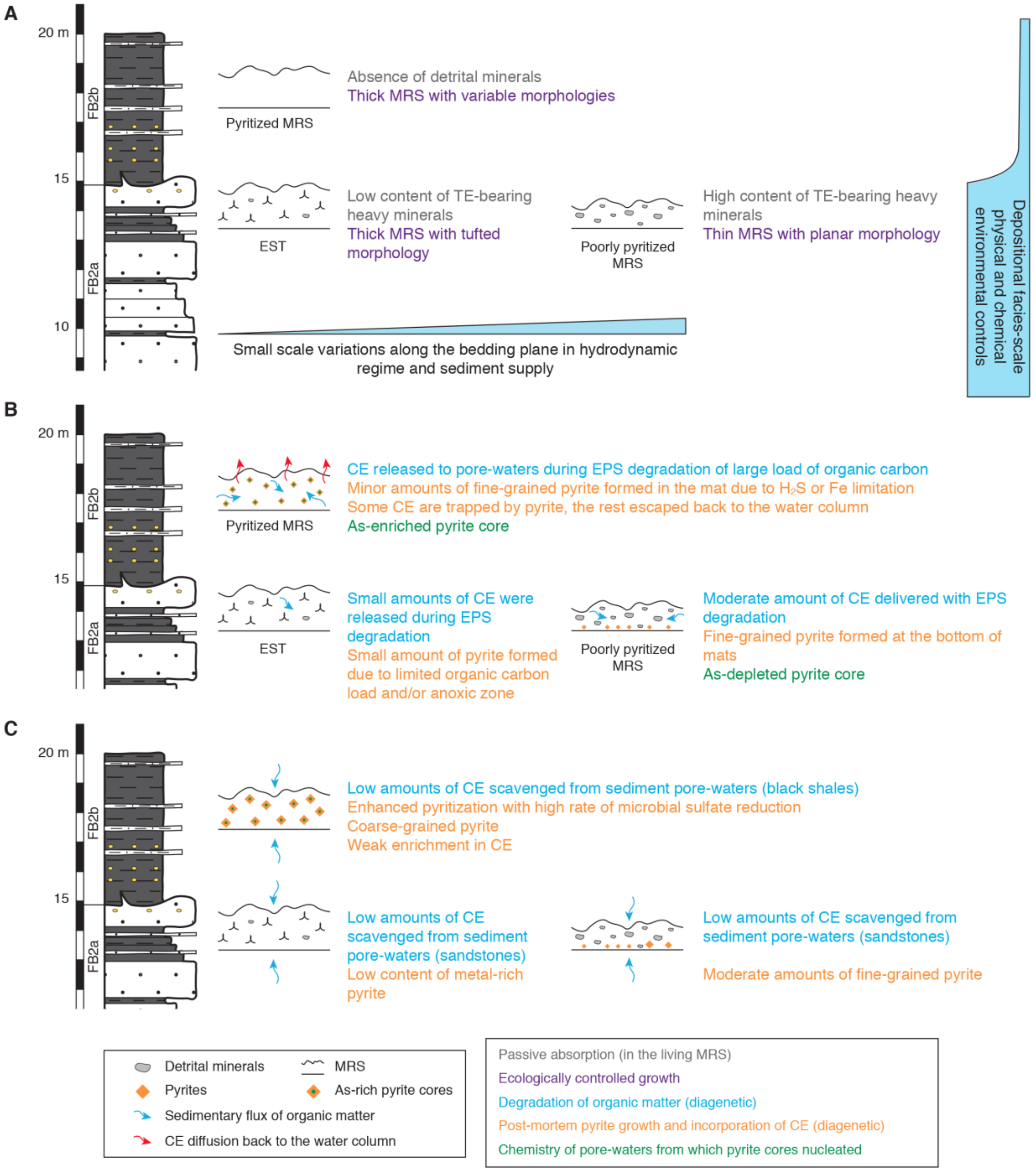

Figure 43: Conceptual model for the spatial and temporal TE variations in the Francevillian Group FB_2 unit MRS. (**A**) Processes that took place during the living stage of mats. Depositional local- to facies-scale environmental factors controlled the distribution of heavy minerals in the Francevillian MRS. The external mat morphologies provide information on local ecologic conditions. (**B**) Short-lived first stage of pyrite formation on the earliest phase of diagenesis. The EPS degradation resulted in the release of CE to pore-waters. The amount of CE delivered with EPS decay should be proportional to the organic carbon content that is buried. Depending of sulfur and Fe availability, CE were trapped by fine-grained pyrite or diffused back to the water column. (**B**) Long-lived second stage of pyrite formation as diagenesis progressed. The rest of organic matter was degraded with, thus, larger amounts of H2S and Fe released to pore-waters. High concentrations of biogenic H_2S were locally produced, but little CE were scavenged in coarse-grained pyrite.

development over the entire mat structure in the pyritized MRS likely reflects the extent of the anoxic region (Figure 43B).

The pyrite overgrowths in the MRS that formed later during diagenesis precipitated from pore-waters that were no longer enriched in As, but in Ni (Figure 43B). Alternatively, the preferential incorporation of As in the early pyrite phase and Ni in the later phase may simply suggest that these two elements have different kinetic behavior whereby As is more reactive towards H_2S than Ni (Huerta-Diaz & Morse, 1992). Hydrothermal fluids affecting sediments during diagenesis could produce CE-rich pyrite rims (Large *et al.*, 2009), but we have no evidence for migration of such fluids or late-stage remobilization that could account for strongly enriched CE in pyrite rims during late diagenesis. Variability in concentration of pyrite-hosted metals in the three microbial mat morphotypes is mainly linked to the sulfide production and concentration in pore-waters (Figures 43B, C). The relationship between CE and total S is, however, complicated since whole-rock data seem to reflect several host minerals. Some of these CE might be incorporated into clays, scavenged by organic matter, and/or absorbed onto the surface of Fe oxides (Nachtegaal *et al.*, 2005; Chappaz *et al.*, 2014; Chi Fru *et al.*, 2019), which might explain weak to moderate correlations within each MRS morphotype.

5.3 | Implication of weak enrichment in CE in the pyritized MRS

The CE enrichment is not unique to the MRS, but instead typical for the depositional setting of the Francevillian Group where seawater and pore-water sulfide levels controlled their incorporation in sediments. The provenance analysis reveals the weak influence of hydrothermal fluids on the depositional site, and rather suggests that CE were supplied by continental weathering, since large variations in CE/S ratios for the Francevillian Group shales (FB1b-c units, and FC and FD formations) are not observed. However, the absence of substantial CE enrichment in the pyritized MRS is unexpected because they contained appreciable amounts of carbonaceous materials to maintain extensive pyritization. The pyritized MRS samples with high bulk-rock S concentrations have lower CE/S ratios than the Francevillian Group sediments, which requires an explanation for the weak enrichment in CE.

Weak enrichment in CE in the pyritized MRS might reflect a change in fluxes to the ocean during the living stage of the MRS. However, this would not explain the similar range of CE content in the pyrite-poor MRS and the Francevillian Group black shales (FB1b-c units, and FC and FD formations). Similarly, different scavenging capabilities of planktonic (in the Francevillian Group black shales) and benthic (in MRS) organic matter is not likely to explain weak enrichment in CE in the pyritized MRS. Rather, low CE/S ratios recorded by the pyritized MRS could be related to profuse sulfide production in pore-waters in microenvironments with high content of easily degradable benthic organic matter. Highly negative $\delta^{34}S$ values of the pyritized Francevillian Group macrobiota point to bacterial sulfate reduction during early diagenesis with open connection to the overlying water column (El Albani *et al.*, 2010, 2019). In this regard, we suggest that the amount of CE delivered to the sediments was largely controlled by both the mat thickness and sedimentary flux of organic matter (Figures 43B, C). With high concentration of biogenic H_2S in the studied MRS, CE were not enriched to the same degree as in black shales from the Upper Francevillian Group, which were deposited under euxinic conditions where pyrite formed in the water column had access to a larger reservoir of CE.

We propose that the pyrite formation and CE trapping in the pyritized MRS followed a two-stage process, resulting in weak enrichment in CE (Figures 43B, C). First, the EPS degradation released to pore-waters CE, which were subsequently either incorporated into microcrystalline pyrite or returned to the water column (Figure 43B). As EPS degradation takes place immediately after deposition and last at most few days (Decho *et al.*, 2005), CE trapping at this stage was limited by sulfur and/or iron availability and, specifically, their reduction and release from the sediments. Hence, CE that were not trapped by pyrite diffused back to the water column, resulting in loss of co-variance between CE and S contents. On the second, protracted stage, most of organic matter in sediments was degraded under anoxic and, locally, massive sulfidic conditions resulted in the formation of coarse-grained, crystalline pyrite and overgrowths with low CE contents (Figure 43C). As this stage lasted longer, larger amounts of sulfide and iron were released to pore-waters, whereas pyrite formed was not enriched in CE since CE were either already trapped or lost from sediments during EPS degradation on the first stage.

The observed trend of weak enrichment in CE in the pyritized MRS thus reflects pyrite formation in pore-waters in the MRS and incorporation of CE, delivered to the sediments with organic matter, specifically with EPS, and released to pore-waters during EPS degradation rather than a specific, biologically controlled pathway for accumulation of CE. Diagenetic pyrite production within the MRS likely also enhanced the potential for preservation of the Francevillian Group macrobiota.

6 | CONCLUSION

Textural relationship and TE geochemistry argue for distinct biological signals in the Francevillian Group MRS relative to their host sediments, however no conclusive example of biologically controlled TE enrichment was found. Our results, summarized in Figure 43, indicate highly variable TE contents with environmental factors overprinting biologically controlled TE distribution.

A lack of accumulation of heavy minerals and pyrite-hosted CE characterizes the EST. The poorly pyritized MRS contain in high abundance Ti- and Zr-bearing minerals concentrated through passive absorption. External morphology of these two MRS could be a potential biogenicity indicator and provides information on local environmental and ecologic conditions, largely controlled by hydrodynamic regime and sediment supply. The CE concentrations in the poorly pyritized MRS co-vary with pyrite content, which indicates that the CE are largely hosted by pyrite. Abundant organic matter in the now pyritized MRS did not result in similar CE/S ratios as in the Francevillian Group black shales deposited in euxinic settings due to the limited trapping capacity of pore-waters close to the sediment-water interface immediately after sediment deposition when CE-enriched EPS degraded. Arsenic-rich pyrite cores indicate high As concentrations in the early diagenetic pore-waters, where it was likely supplied via decay of EPS.

In short, bulk-rock TE data provide additional evidence for biological activity during deposition of the *ca*. 2.1 Ga Francevillian Group, but there is no definitive biological signal since physical controls and water column redox chemistry overrode microbial influence on TE distribution in MRS. Recognition of the overprinting power of physical and chemical environmental conditions over microbially imprinted TE patterns in MRS further contributes to our understanding of interactions among ancient microbial life and the environmental and biological controls affecting TE contents in MRS, and their relationship to TE sinks in deep time.

ACKNOWLEDGMENTS

We are grateful to the Gabonese Government, CENAREST, General Direction of Mines and Geology, and Agence Nationale des Parcs Nationaux of Gabon for logistic support. This work was supported by CNRS-INSU, FEDER, the University of Poitiers, Nouvelle Aquitaine Region, and the French Embassy Libreville, Gabon. We would like to thank sincerely Prof. P. Mouguiama Daouda for his support. We also acknowledge F. Martin, L. Pallas, and P. Sardini for analytical advice and C. Fontaine, C. Laforest, and P. Recourt for laboratory support at the Universities of Lille and Poitiers. Participation of AB was supported by NSERC Discovery and Accelerator Grants.

SUPPLEMENTARY DISCUSSION

Interaction between MRS and toxicants

Given the high As content in the As-rich pyrite nuclei of some of the MRS, it is reasonable to question what impact if any this had on the once living microbial mats. It has recently been documented that the appearance of arsenate [As(V)] and As-S minerals in sediments was linked to the Great Oxidation Event (GOE) at *ca*. 2.48 Ga ago (Chi Fru *et al.* 2019). Although we did not measure As oxidation states in our samples, As(V) has been recorded in the Francevillian FB and FD formations (Chi Fru *et al.*, 2019). Arsenate is a well-known toxin to prokaryotes and eukaryotes even at nanomolar concentrations (Dyhrman & Haley, 2011). Thus, microbial cells of MRS would have needed to utilize an As detoxification system to pump out As that accumulated in the pore-waters. Arsenic methylation, linked to intensive detoxification in the modern ocean surface (Cullen & Reimer, 1989; Cutter & Cutter, 2006), likely had already evolved in Cyanobacteria by the Late Archean (Chen *et al.*, 2017). The ubiquitous nature of arsenic resistance genes (*ars* gene) in the three domains of life clearly illustrates their universal requirement for protection against As toxicity (Chen *et al.*, 2017; Ben Fekih *et al.*, 2018). A wide range of biogeochemical As cycling pathways is thought to have evolved in the Paleoproterozoic (Chi Fru *et al.*, 2019), but we have no evidence for demonstrating direct biological involvement in As cycling from our samples of MRS. Although As enrichment in pyrite from ancient MRS has never been reported so far, As-rich organic globules from Archean stromatolites (Sforna *et al.*, 2014) and modern microbial mats (Sforna *et al.*, 2017; Sancho-Tomás *et al.*, 2018) might be appropriate analogues. Furthermore, a recent study suggests that As co-precipitation with sulfide minerals strongly reduces As toxicity (Chi Fru *et al.*, 2018a), implying that there was an additional effective mechanism for reducing arsenic toxicity promoted by diagenetic activity of the sulfate-reducing bacteria in the Francevillian basin pore-waters.

4.3. Redox conditions in the FB_2 Member

This section is dedicated to an article in preparation.

A transient state of nitrogen fixation before the end of the Lomagundi Event

Abstract

Evidence for nitrogen-replete conditions in the Palaeoproterozoic Era come from a suite of shallow marine sediments that spans the Great Oxidation Event (GOE). The oldest reported macrofossils and traces of multicellular organisms able to migrate, together with mat-building Cyanobacteria, make the *ca.* 2.1-billion-years-old palaeobiological record unique in the Francevillian FB_2 Member, Gabon. The mat-related structures (MRS) have recently promoted numerous mineralogical and geochemical investigations for deciphering whether ancient MRS can be used to bring out biosignatures. However, a complete characterization of organic carbon and bulk nitrogen isotopes remains lacking in the FB_2 Member. Here, we document new carbon and nitrogen data from ancient mats and their host sandstone and black shale rocks, combined with bottom water redox proxies, to further constrain the microbial biogeochemical processes of both benthic and planktonic lifestyles. Our Fe-based proxies and redox-sensitive metals point to a bottom water column dominated by oxic/suboxic environmental conditions in the FB_2 Member. The C and N isotopes reveal slight distinctions between the MRS and host sediments, but unlikely characterize divergent microbial populations. The total fractionation of C isotopes ($\Delta^{13}C$), heavier in the MRS relative the host sediments and down to -44‰, supports multiple trophic levels involved in the cycling of photosynthetically derived C_{org}, including phototrophy, heterotrophy and methanotrophy. Nitrogen isotope values range from -3.5 to +1.9‰, which is consistent with nitrogen fixation and brings strong evidence for a restricted nitrate reservoir in the FB_2 Member. Modern microbial mats usually fix nitrogen due to high photosynthetic activity, revealing similar microbiogeochemical processes in the deep geological record. Considering that the first stage of deoxygenation in the Francevillian basin occurred during the deposition of the underlying sediments (Upper FB_1 Member), coupled with an enhanced denitrification at the chemocline driving nitrogen loss, our data support a nitrogen limitation modulated by the basin-scale ocean redox structure. Since the isotopic composition of aerobic nitrogen cycling is recorded in the overlying deposits (FC Formation), combined with a moderate phosphate flux fueled by upwelling or oxidative weathering in the studied sediments, the starvation of bioavailable nitrogen would have been transient in the aftermath of the GOE. Importantly, it is thus emphasized that diazotrophs would have sustained primary productivity in patterns similar to modern surface environments just downstream of upwelling systems. The nitrogen famine in the water column even transient would strengthen the explanation of the Francevillian complex life forms commonly present in the vicinity of the microbial mats.

Keywords

Microbial mats, upwelling, carbon recycling, nitrogen limitation, biogeochemistry, Palaeoproterozoic

1 | INTRODUCTION

The Palaeoproterozoic Francevillian Series from southeastern Gabon comprises five lithostratigraphic formations, referred to as the Francevillian FA, FB, FC, FD, and FE formations from the bottom to the top (Figure 17; Weber, 1968). Interestingly, the FB and FC formations were deposited at the end of the Lomagundi Event (LE) – the longest-lived positive carbon isotope excursion – (El Albani *et al.*, 2010; Préat *et al.*, 2011; Canfield *et al.*, 2013) that is bracketed between 2.11 and 2.06 billion years (Ga) (Karhu & Holland, 1996; Martin *et al.*, 2013). The deposition of the Lower FB rocks (FB_1 Member) was marked by the formation of iron and manganese sediments (Gauthier-Lafaye & Weber, 2003; Ossa Ossa *et al.*, 2018), during which episodic submarine volcanism and hydrothermal activity likely sourced the aqueous Mn(II) and Fe(II). Upwelling events brought the reductants into the oxic, shallow continental shelf (Gauthier-Lafaye & Weber, 2003; Canfield *et al.*, 2013), which would have driven to oxygen consumption and contributed to the first step of deoxygenation (Ossa Ossa *et al.*, 2018). The sulfur isotope compositions of authigenic pyrite in the overlying Upper FB rocks (FB_2 Member), however indicate that the water column was relatively oxygenated with abundant sulfate inventory (Canfield *et al.*, 2013; Ossa Ossa *et al.*, 2018).

In the last decade, the FB_2 Member provided tantalizing findings that comprise the first evidence for multicellular life (El Albani *et al.*, 2010, 2014) and organism motility (El Albani *et al.*, 2019). In addition, benthic microbial mats flourished in the vicinity of these advanced forms of life (Reynaud *et al.*, 2017; Aubineau *et al.*, 2018; El Albani *et al.*, 2019). The bacterial features, preserved as MRS, display a wide array of surface morphologies including mat-growth and mat-protected patterns. The former consists of the mat layer itself generated through mat propagation (*e.g.*, “elephant-skin” structures, domal buildups, discoidal microbial colonies), while the latter arises from structures that needed mats for their preservation/protection (*e.g.*, wrinkle and “kinneyia” structures). Morphological and microtexture observations have shown that the MRS were likely dominated by cyanobacterial communities (Aubineau *et al.*, 2018, 2019). In addition, some evidence suggest that the organic material in the Francevillian black shales possibly originated from planktonic algae (El Albani *et al.*, 2014), relying on the presence of acritarch-like microfossils and absence of filaments.

Modern microbial mat communities are capable of "fixing" atmospheric nitrogen gas (N_2), during which bioavailable ammonia (NH_3) is generated and subsequently consumed by microorganisms (Bebout *et al.*, 1994; Herbert, 1999). The nitrogen fixation (or diazotrophy) provides the nitrogen requirements for primary production, thus sustaining mat growth. Cyanobacterial mats exhibit high nitrogen fixation activity (from 0.8 to 76 g N m^{-2} $year^{-1}$), resulting from high rates of CO_2 reduction during photosynthesis (Herbert, 1999; Woebken *et al.*, 2015). The diverse microorganisms within the mat consume the whole bioavailable nitrogen that was produced by diazotrophs (Bebout *et al.*, 1994). The nitrogenase (*i.e.*, enzymatic complex responsible for the nitrogen fixation) is inactivated when high oxygen concentrations prevail. Given that, N_2 fixers have had to develop biological innovations to handle with this oxygen stress (see review in Stal, 2001). For instance, the highest N_2 fixation rates were observed during nighttime when the activity of O_2-producing photosynthesizers is at the lowest rates (Bebout *et al.*, 1994; Woebken *et al.*, 2015). Environmental constraints, including nutrient limitation, elevated ammonium concentration, temperature, pH, and light may also exert a control on nitrogen fixation (Paerl *et al.*, 1994).

Modern phytoplanktonic blooms of N_2-fixing photoautotrophs may also occur in surface waters just downstream of upwelling zones (Capone *et al.*, 1998; Deutsch *et al.*, 2007). Coastal upwelling systems correspond to wind-mediated movements of deep water to the surface during which the overlying water masses are pushed away from the coast. Upwelled waters usually exhale CO_2 and bring nutrients into the photic zone, enhancing blooms of phytoplankton productivity. Upwelling regimes enhance the oxygen consumption in the underlying water column due to high rates of aerobic bacterial respiration, which is supported by high sinking fluxes of organic matter (Helly & Levin, 2004). This leads to the nitrogen loss through microbial denitrification (the reduction of NO_3^- to N_2) and anaerobic ammonium oxidation (anammox; NH_4^+ oxidation coupled to NO_2^- nitrate reduction) (Dalsgaard *et al.*, 2005). During this process, NO_3^- is scarce relative to PO_4^3, resulting in the drawdown of the N:P ratio to a level much lower to the constant Redfield ratio of 16:1 (Redfield *et al.*, 1963). Therefore, the nitrogen limitation in surface waters along upwelling transect appears as a natural consequence of high primary productivity. It has been argued that residual nutrients in surface waters of coastal upwelling systems can support the activity of N_2-fixing Cyanobacteria (Deutsch *et al.*, 2007). Then, the input of nitrogen fixation strongly increases, allowing to restore the N:P ratio in a negative feedback (Tyrrell, 1999).

In order to provide further insights into the microbial biogeochemistry at the end of the LE, our study focuses on the MRS and their associated host sediments of the Francevillian FB_2 Member. Both have been previously described for their mineralogy (Aubineau *et al.*, 2019) and trace element contents (see section 4.2). Here, we present Fe-based analyses and redox-sensitive metals to constrain local redox conditions of the depositional setting. Furthermore, we measured organic carbon ($\delta^{13}C_{org}$) and bulk nitrogen ($\delta^{15}N_{bulk}$) isotopes in both the MRS and host rocks to highlight potential differences in microbial ecology (benthic *vs.* planktonic communities). In conjunction with published data (Kipp *et al.*, 2018; Ossa Ossa *et al.*, 2018), we explore the spatial and temporal trends in carbon and nitrogen isotopes in the Upper Francevillian Series to ascertain whether a typical signature of microbial mats and a stratified ocean redox structure are recorded.

2 | METHODS

2.1 | Sampling

All of our samples (both MRS and host sediments) come from outcrops in the Moulendé quarry. Before collecting outcrop material, we dug a few cm into the rock to remove the weathered outermost layers. Accordingly, sulfide-bearing sedimentary rocks were not typically oxidized in the outcrop samples.

2.2 | Scanning electron microscopy

Pyrite morphology of MRS and black shales was studied in carbon coated and polished slab sections, using a FEI Quanta 200 scanning electron microscope (SEM) equipped with an energy dispersive X-Ray Spectrometer (EDX), as previously described in section 4.2. Pyrite was specifically targeted for textural analysis to evaluate its morphology, as it can be readily affected by any potential oxidative weathering.

2.3 | Whole-rock analysis

Major and trace elements of powdered samples were analyzed by inductively-coupled plasma atomic emission spectrometry (ICP-AES) and inductively coupled plasma mass spectrometry (ICP-MS), respectively, as previously described in section 4.2.

2.4 | Iron speciation analysis

Iron speciation analysis (n = 14) was performed at the University of Cardiff, Walls. It provides palaeoredox information through a sequential extraction technique (Poulton & Canfield, 2005) followed by Fe analyses via atomic absorption spectroscopy. This allows to target the different pools of Fe that are considered “highly reactive” (Fe_{HR}) towards hydrogen sulfide in the diagenetic sequence. First, iron-bearing carbonate phases were extracted with a sodium acetate solution for 48 hours (Fe_{Carb}). Second, samples were treated via a sodium dithionite buffer for 2 hours to extract Fe-oxyhydroxides (Fe_{Ox}). The final step consists in a treatment with an ammonium oxalate solution for 6 hours that was used to extract mixed valence and/or highly crystalline Fe oxides, principally magnetite (Fe_{Mag}). Iron present as pyrite (Fe_{Py}) was extracted by weighing a CuS precipitate after an HCl and chromous chloride distillation, with Fe calculated assuming FeS_2 stoichiometry (Canfield *et al.*, 1986). Thus, the "highly reactive" pool of Fe is then calculated as follows: $Fe_{HR} = Fe_{Carb} + Fe_{Ox} + Fe_{Mag} + Fe_{Py}$. The total Fe ($Fe_T$) content was analyzed by ICP-AES as mentioned above. The latter is characterized by three dominant iron pools (Poulton & Canfield, 2005): (i) Fe_{HR}; (ii) poorly reactive sheet Fe silicates (Fe_{PRS}) that were extracted by boiling 12 N HCl for 2 minutes; and (iii) unreactive silicate Fe (Fe_U), calculated as $Fe_U = Fe_T – Fe_{HR} – Fe_{PRS}$. Replicated samples (n = 5) gave an average standard deviation of 0.11 wt.% for Fe_{Carb}, 0.19 wt.% for Fe_{Ox}, 0.004 wt.% for Fe_{Mag}, 0.07 wt.% for Fe_{PRS}, and 0.06 wt.% for Fe_{Py}.

Clarkson *et al.* (2014) have shown that the use of iron speciation is not appropriate for samples containing less than 0.5 wt% total Fe and organic carbon. Thus, we do not perform iron speciation analyses in such samples (mainly sandstones) to ensure of the robustness of values.

2.5 | Carbon and nitrogen isotope analyses

The carbon isotope analysis of organic matter ($\delta^{13}C_{org}$) and nitrogen isotope composition of bulk rock ($\delta^{15}N_{bulk}$) were performed on all lithologies (n = 34). The isotope values were measured by flash combustion on a Thermo Scientific DELTA V Advantage isotope ratio mass spectrometer (IRMS), operated under a constant helium flow, and coupled to a COSTECH 4010 elemental analyzer (EA) at the University of California, Riverside. For $\delta^{13}C_{org}$ analysis, ~200 mg of whole rock powders were decarbonized with 6 N HCl for one hour at 70 °C. The solid residue was thoroughly rinsed in deionized water and dried in a clean hood overnight. Small aliquots of decarbonated residues (mostly less than 10 mg) were weighed into tin cups. For $\delta^{15}N_{bulk}$ analysis, large quantity of powdered bulk samples (between 20 and 50 mg) were weighed into larger tin cups with a blank after each sample. All isotope data are reported in standard δ–notation relative to V-PDB and Air-N_2 for $\delta^{13}C$ and $\delta^{15}N$, respectively. UCM (acetinamide, $\delta^{13}C$ = -33.69‰, $\delta^{15}N$ = -0.75‰), glycine ($\delta^{13}C$ = -36.57‰, $\delta^{15}N$ = 11.25‰), SDO-1 ($\delta^{13}C$ = -30‰, $\delta^{15}N$ = -0.80‰), and SGR ($\delta^{13}C$ = -29.30‰, $\delta^{15}N$ = 17.40‰) in-house standards were used to calibrate isotope measurements. Replicated samples for $\delta^{13}C_{org}$ (n= 15) and $\delta^{15}N_{bulk}$ (n = 22) yielded an average standard deviation (1σ) better than 0.13 and 0.15‰, respectively. Total organic carbon (TOC) and total nitrogen (TN) abundances were calculated from peak CO_2 and N_2 areas, respectively. The $\delta^{15}N_{bulk}$ measurements with TN concentrations close to the detection limit were removed due the lack of repeatability.

3 | RESULTS

3.1 | Evaluating the addition/loss of sulfur

Although our samples come from outcrops, Fe (oxyhydr)oxide coatings were not found surrounding the pyrite crystals (Figure 44). Moreover, we have no evidence for corroded pyrite. The formation of iron monosulfides (AVS, pyrrhotite) during sediment maturation and metamorphic reactions, by which pyrite deteriorates, induces changes in Fe speciation (Reinhard *et al.*, 2013a; Slotznick *et al.*, 2016). Nonetheless, the assemblage of iron sulfides in the MRS and host sediments is dominated by the presence of pyrite, as indicated by the X-ray diffraction patterns (Appendix 13). We cannot exclude local redistribution of non-sulfidic Fe minerals during late diagenesis. Collectively, this suggests that Fe speciation systematic has not been compromised by secondary oxidative weathering.

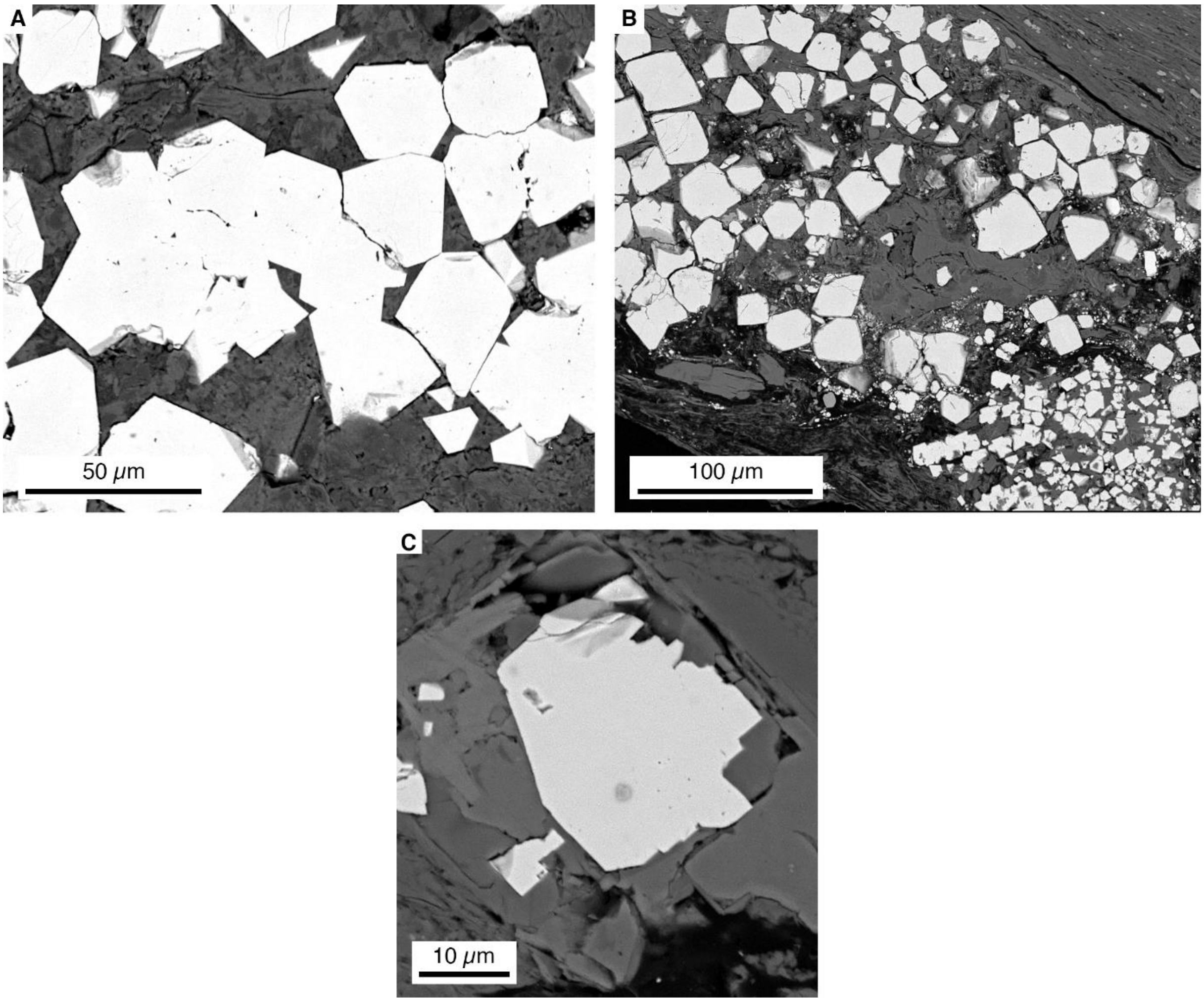

Figure 44: SEM images in backscatter mode of pyrite crystals. (**A**) Pyritized MRS. (**B**) Poorly pyritized MRS. (**C**) Black shales.

3.2 | Fe-based redox proxy analyses

Iron speciation analysis, preferentially in shale lithofacies, is by far the most widely used method to evaluate local modern and ancient water column redox conditions (Poulton & Raiswell, 2002; Planavsky *et al.*, 2011; Poulton & Canfield, 2011; Sperling *et al.*, 2013; Chi Fru *et al.*, 2018b). Sediments deposited under anoxic conditions are characterized by Fe_{HR}/Fe_T ratios higher than 0.38 driven by additional precipitation of Fe_{HR} minerals, while Fe_{HR}/Fe_T ratios are less than 0.22 under oxic conditions. Values between 0.22 and 0.38 are equivocal as they could reflect conditions when sedimentation rate is high or when the conversion of unsulfidized Fe_{HR} to less reactive minerals occurs during post-depositional transformation (Poulton & Canfield, 2011). Both mechanisms may mask Fe enrichments under anoxic water column conditions. If reactive Fe exceeds 38% of the Fe_T and if the Fe_{Py}/Fe_{HR} values are below 0.7-0.8, the deposition in ferruginous environments is expected (Poulton & Canfield, 2011). Values for Fe_{Py}/Fe_{HR} that indicate sulfide-rich (euxinic) conditions tend to be higher this threshold. Alternatively, the Fe_T/Al proxy also provides Fe enrichments that discriminate oxic/anoxic depositional environments (Lyons & Severmann, 2006; Clarkson *et al.*, 2014). This ratio is not affected by the possibility of a transfer of unsulfidized Fe_{HR} to Fe_{PRS} during diagenesis or metamorphism, providing a particular interest to pair Fe_T/Al and iron speciation (Raiswell *et al.*, 2018). Modern marine sediments deposited under oxic environments show an average Fe_T/Al ratio of 0.55±11, and this value can be applied to any siliciclastic rocks (Clarkson *et al.*, 2014). Thus, Fe_T/Al values rising above 0.66 (with a confidence threshold of 1σ) clearly indicate local Fe enrichments either under anoxic conditions or due to hydrothermal activity. Strong Fe enrichments ($Fe_T/Al > 2$) usually correspond to the addition of hydrothermal fluids into the depositional setting (Raiswell *et al.*, 2018).

Our Fe-based data were mainly obtained from the MRS and black shales, as iron speciation was not performed for sandstone samples (Figure 45; Table 3). The non-pyritized MRS samples (both poorly pyritized MRS and EST) are characterized by low Fe_T/Al ratios, a progressive increase in Fe_{HR}, and little Fe_{HR} converted to pyrite. Sandstones also indicate low Fe_T/Al values, but these results must be treated with caution because deposition of the FB2a unit arisen from high-density sand flows (Reynaud *et al.*, 2017). Thus, Fe enrichments could have been swamped at high siliciclastic sedimentation rate (Lyons & Severmann, 2006). Unsurprisingly, the pyritized MRS have high Fe_T/Al, Fe_{HR}/Fe_T, and Fe_{Py}/Fe_{HR} ratios. The anoxic (ferruginous and/or euxinic) conditions in the MRS are consistent with the activity of both dissimilatory iron reduction (DIR) and microbial sulfate reduction (MSR) during early diagenesis (Aubineau *et al.*, 2018, 2019). The black shales of the FB2b unit show a lack of Fe_T/Al enrichment, a predominance of Fe_{HR}/Fe_T and Fe_{Py}/Fe_{HR} lower than 0.38 and 0.7, respectively. However, abrupt swings are recorded with substantial increases in highly reactive Fe to total Fe.

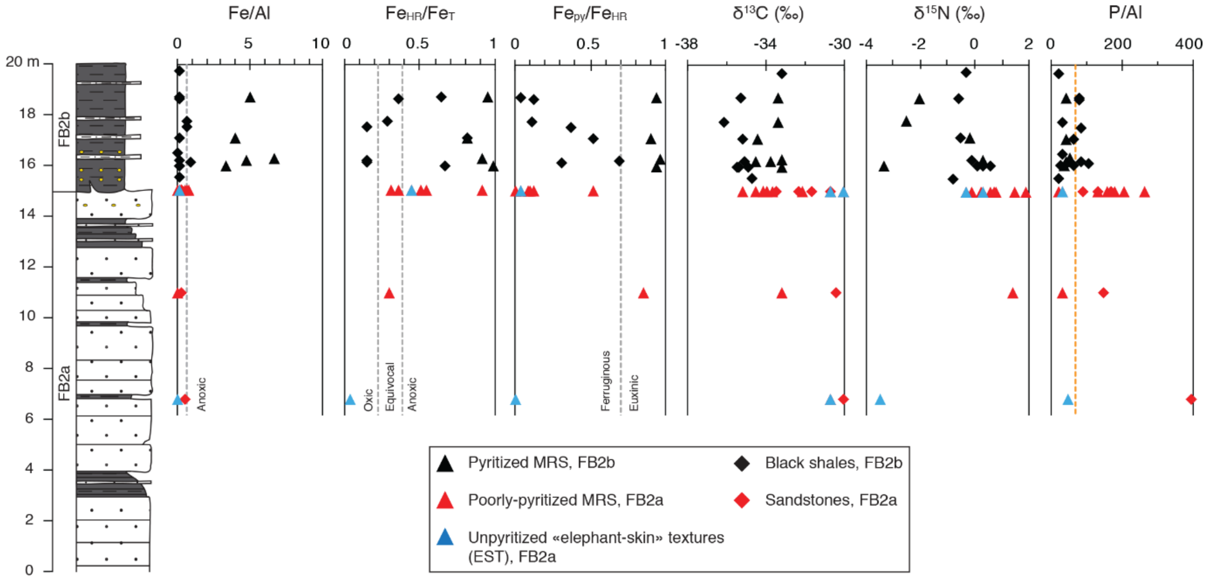

Figure 45: Geochemical data for the MRS and host sediments plotted along the lithostratigraphic profile of the studied sequence, FB_2 Member. Grey and orange vertical lines represent redox distinctions from Raiswell *et al*. (2018) and the average PAAS value from Taylor & McLennan (1985), respectively.

The potential conversion of unsulfidized Fe_{HR} to Fe_{PRS} in the Francevillian FB_2 sediments is unlikely since pyritized microbial laminae, macrofossils, and string-like structures are extensively preserved (El Albani *et al.*, 2010, 2019; Aubineau *et al.*, 2018). Thus, sulfide production was not limited, meaning that the incorporation of ferrous iron into clay minerals during diagenesis was likely negligible.

Table 3: Iron speciation data and whole-rock composition of major and minor elements for all measurements in this study.

Formation	Lithology	Sample ID	Height m	Fe_{Py} (wt. %)	Fe_{Carb} (wt. %)	Fe_{Ox} (wt. %)	Fe_{Mag} (wt. %)	Fe_{PRS} (wt. %)	Fe_{HR}/Fe_T	Fe_{Py}/Fe_{HR}	Al (wt. %)	Fe_T (wt. %)	Mn (wt. %)	K (wt. %)	P ppm	Cr ppm	Mo ppm	U ppm	V ppm	Fe/Al	Mn/Al* 90**	P/Al 70**	Cr/Al 11**	Mo/Al 0.1**	U/Al 0.31**	V/Al 15**
FB2b	Pyritized MRS	FPS_s5-mat	18.7	24.15	0.39	0.86	0.09	0.15	0.95	0.95	5.35	26.86	0.08	1.56	*218*	*2.50*	11.40	0.29	30.19	5.02	149	40.8	0.5	2.13	0.05	5.6
		DB_s4-mat	17.1	15.10	0.59	0.98	0.07	0.16	0.80	0.90	5.14	20.80	0.12	1.50	*218*	10.95	19.81	0.62	30.27	4.05	242	42.5	2.1	3.85	0.12	5.9
		FPS_s4-mat	16.3	25.17	0.33	0.64	0.07	0.29	0.90	0.96	4.37	29.02	0.07	1.11	*218*	*2.50*	13.94	0.30	23.48	6.64	151	49.9	0.6	3.19	0.07	5.4
		FPS_s3-mat	16.2	-	-	-	-	-	-	-	5.09	24.68	0.09	1.34	*218*	*2.50*	10.23	0.36	30.67	4.85	181	42.9	0.5	2.01	0.07	6.0
		DB_s3-mat	16.0	19.10	0.31	0.86	0.08	0.18	0.97	0.94	6.26	20.89	0.06	1.63	*218*	15.13	16.62	0.52	34.78	3.33	103	34.9	2.4	2.65	0.08	5.6
	Black shales	WS_s2-sed	19.7	-	-	-	-	-	-	-	10.40	1.90	1.85	3.34	*218*	48.71	*0.25*	1.02	53.37	0.18	1777	21.0	4.7	0.02	0.10	5.1
		FPS_s5-sed	18.7	0.05	0.43	0.51	0.07	0.73	0.64	0.05	8.85	1.67	0.37	2.63	699	31.64	*0.25*	1.32	48.28	0.19	413	78.9	3.6	0.03	0.15	5.5
		AFBSO-12#	18.6						0.35	0.13	9.87	2.41	0.05	3.01	742	54.76	0.76	1.21	52.97	0.24	55	75.2	5.5	0.08	0.12	5.4
		LP_s4-sed	17.8	0.18	0.24	0.97	0.06	0.57	0.29	0.12	7.61	5.05	0.10	1.40	*218*	-	-	-	-	0.66	128	28.7	-	-	-	-
		AFBSO-09#	17.5						0.14	0.37	6.38	4.55	0.57	1.22	524	40.61	0.76	1.08	32.39	0.71	898	82.1	6.4	0.12	0.17	5.1
		DB_s4-sed	17.1	0.83	0.26	0.45	0.06	0.09	0.81	0.52	9.04	1.96	0.34	2.75	568	36.33	*0.25*	1.24	49.54	0.22	379	62.8	4.0	0.03	0.14	5.5
		AFBSO-07#	16.5								7.03	0.25	*0.01*	2.36	*218*	42.50	0.63	1.03	34.45	0.04	8	31.1	6.0	0.09	0.15	4.9
		FPS_s3-sed	16.2	0.17	0.00	0.00	0.07	0.15	0.15	0.70	8.51	1.64	0.24	2.45	699	29.61	0.85	1.28	45.40	0.19	282	82.0	3.5	0.10	0.15	5.3
		AFBSO-06#	16.1						0.14	0.32	6.37	6.21	0.09	1.12	655	30.15	0.72	1.02	29.13	0.97	134	102.8	4.7	0.11	0.16	4.6
		DB_s2-sed	16.0	-	-	-	-	-	-	-	9.45	1.50	0.23	2.98	*218*	47.73	*0.25*	1.32	57.54	0.16	244	23.1	5.1	0.03	0.14	6.1
		FR_s1sed	16.0	0.33	0.33	0.37	0.06	0.06	0.66	0.30	9.98	1.65	0.19	3.14	611	33.21	*0.25*	1.24	50.73	0.17	189	61.2	3.3	0.03	0.12	5.1
		MLS_s9-sed	15.5	-	-	-	-	-	-	-	10.13	2.12	0.28	3.21	*218*	48.28	0.93	1.13	49.27	0.21	280	21.6	4.8	0.09	0.11	4.9
FB2a	Pyrite-poor MRS	MLS_s1-mat	15.0	-	-	-	-	-	-	-	11.96	9.17	0.25	3.46	2445	196.00	4.76	8.54	96.43	0.77	208	204.5	16.4	0.40	0.71	8.1
		MLS_s2-mat	15.0	1.89	0.29	1.35	0.06	0.00	0.54	0.53	12.34	6.61	0.08	3.36	1572	230.40	3.66	10.16	91.74	0.54	61	127.4	18.7	0.30	0.82	7.4
		EST_s3-mat	15.0	0.05	0.37	0.58	0.06	0.10	0.44	0.05	14.78	2.43	0.03	2.31	437	50.23	0.85	3.19	82.74	0.16	18	29.5	3.4	0.06	0.22	5.6
		MLS_s3-mat	15.0	-	-	-	-	-	-	-	10.94	9.33	0.12	2.87	2838	149.30	4.63	9.20	84.62	0.85	114	259.4	13.6	0.42	0.84	7.7
		MLS_s4-mat	15.0	0.16	0.05	1.15	0.07	0.27	0.36	0.11	12.59	3.98	0.08	3.68	2227	208.40	1.44	8.92	93.92	0.32	67	176.9	16.6	0.11	0.71	7.5
		MLS_s5-mat	15.0	0.20	0.35	1.62	0.07	0.20	0.50	0.09	12.99	4.48	0.07	3.56	2139	193.70	2.29	9.20	99.93	0.34	52	164.7	14.9	0.18	0.71	7.7
		MLS_s10-mat	15.0	0.00	0.28	0.43	0.08	0.05	0.91	0.00	12.54	0.86	0.01	3.22	*218*	-	-	-	-	0.07	5	17.4	-	-	-	-
		LP_s5-mat	15.0	0.12	0.00	0.78	0.06	0.32	0.30	0.13	15.18	3.17	0.12	4.76	2401	-	-	-	-	0.21	80	158.2	-	-	-	-
		MLS_s3-mat	11.0	0.43	0.00	0.00	0.07	0.07	0.29	0.86	16.82	1.74	0.02	4.16	524	87.81	*0.25*	2.92	77.14	0.10	14	31.1	5.2	0.01	0.17	4.6
		EST_s2-mat	6.8	0.00	0.00	0.00	0.07	0.07	0.04	0.00	16.63	1.74	0.01	4.76	742	36.63	0.57	3.51	75.49	0.10	8	44.6	2.2	0.03	0.21	4.5
	Sandstones	LP_s3-sed	15.0	-	-	-	-	-	-	-	1.30	0.46	0.05	0.26	*218*	*2.50*	*0.25*	0.16	4.88	0.36	414	167.4	0.2	0.12	3.74	0.3
		MLS_s1-sed	15.0	-	-	-	-	-	-	-	2.47	0.68	0.09	0.50	*218*	*2.50*	*0.25*	0.21	9.04	0.28	356	88.5	0.1	0.09	3.67	0.1
		MLS_s2-mat	15.0	-	-	-	-	-	-	-	1.70	0.56	0.21	0.22	*218*	*2.50*	*0.25*	0.20	6.23	0.33	1246	128.3	0.1	0.12	3.66	0.2
		MLS_s3-sed	11.0	-	-	-	-	-	-	-	1.51	0.47	0.02	0.18	*218*	5.57	*0.25*	0.27	4.93	0.31	129	144.6	0.2	0.18	3.27	0.2
		EST_s2-sed	6.8	-	-	-	-	-	-	-	0.78	0.44	0.002	0.15	306	9.62	0.80	0.34	2.64	0.56	22	391.9	1.0	0.44	3.39	0.7

FPS: flat pyritized structure; DB: domal buildup; WS: wrinkle structure; LP: linear pattern; FR: “fairy-ring” structure; MLS: mat-layer structure; EST: “elephant-skin” texture.
*: ppm/wt.% unit; **: average ratio for the PAAS (Taylor & McLennan, 1985); -: not measured; #: values from (Ossa Ossa, 2010). Italicized values: samples where half or more of the analyses were below detection limits for that element.

3.3 | Redox-sensitive metals

We investigated sedimentary Mn, Cr, Mo, U, and V concentrations (Figure 46; Table 3). The average Mn concentration in the Francevillian FB$_2$ Member is 0.18 wt.%, which is considerably higher than the Mn content of 0.085 wt.% for the Post-Archaean Australian Shales (PAAS; Taylor & McLennan, 1985). The Mn/Al ratios both in MRS and host sediments slightly increase upward, with values greater than the PAAS. On the other hand, the Cr/Al, Mo/Al, U/Al, and V/Al ratios remain low for most of samples, with values being lower than those for PAAS. The poorly pyritized MRS show higher values, but this is consistent with the presence of TE-containing heavy minerals (Figure 38). Moreover, pyrite-containing MRS samples display enrichment in Mo because of local sulfide-rich conditions that microbes imposed during MSR (see section 4.2).

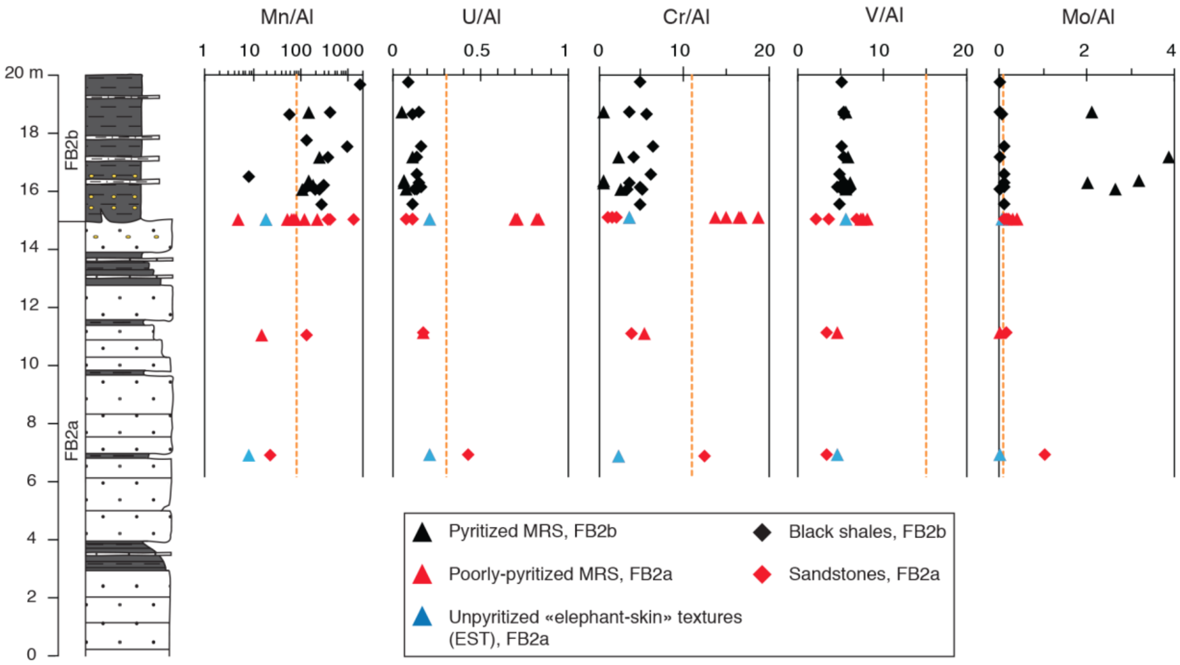

Figure 46: Data of redox-sensitive metals for the MRS and host sediments plotted along the lithostratigraphic profile of the studied sequence, FB$_2$ Member. Orange vertical lines correspond to average PAAS values from Taylor & McLennan (1985).

3.4 | Carbon, nitrogen, and phosphorus systematics

The studied stratigraphic interval shows equivalent $\delta^{13}C_{org}$ values relative to the previous determinations within the FB_2 Member (Gauthier-Lafaye & Weber, 2003; Canfield *et al.*, 2013), but our bulk-rock $\delta^{15}N$ profile (Figure 45; Table 4) differs from the one obtained recently in the FC Formation (Kipp *et al.*, 2018). The mean TOC for the sandstone facies is 0.28 wt.%, whereas that for the black shales is 2.21 wt.%. The TN contents for sandstones are close to the detection limit (~0.01 wt.%) and must be interpreted with caution, while those for black shales are nearly constant, with an average of 0.07 wt.%. This increase is accompanied by a decrease in the mean $\delta^{13}C_{org}$ value, which is -31.47 ± 1.17‰ (1σ, n = 6) for sandstones and -35.06 ± 0.76‰ (1σ, n = 9) for black shales. Thus, the FB2a-FB2b transition is marked by a shift toward negative $\delta^{13}C_{org}$ values. The mean $\delta^{15}N_{bulk}$ values for the fine-grained sediments are -0.17 ± 0.44‰ (1σ, n = 8; ranging from -0.79 to 0.55‰) without distinct compositional trend.

We also explored the carbon and nitrogen contents and isotopes of different microbial textures (Figures 45, 47; Table 4). TOC is strongly enriched in the poorly pyritized MRS and EST (mean of 6.85 wt.% and 9.78 wt.%, respectively), while TOC contents for pyritized MRS are systematically below 0.87 wt.%. TN is uniformly enriched in the poorly pyritized MRS and EST (mean of 0.13 wt.% and 0.12, wt.%, respectively), but shifts to lower values in pyritized MRS (mean of 0.06 wt.%). The $\delta^{13}C_{org}$ values average -33.89 ± 0.85‰ (1σ, n = 9), -30.52 ± 0.40‰ (1σ, n = 3), and -33.70 ± 0.53‰ (1σ, n = 7) for the poorly pyritized MRS, EST, and pyritized MRS, respectively. The average $\delta^{15}N_{bulk}$ compositions are 0.84 ± 0.62‰ (1σ, n = 9), -1.15 ± 2.04‰ (1σ, n = 3), and -1.53 ± 1.38‰ (1σ, n = 5) for the poorly pyritized MRS, EST, and pyritized MRS, respectively. Thus, it appears that the $\delta^{13}C_{org}$ values slightly discriminate the EST from the pyrite-containing MRS, while the $\delta^{15}N_{bulk}$ is similar between lithologies.

n the meantime, the area is characterized by a progressive decrease in the mean P/Al ratios (ppm/wt.%), ranging from 184, 121, 56, and 42 for sandstones, non-pyritized MRS, black shales, and pyritized MRS, respectively (Figure 45; Table 4). The average P/Al content in the FB2a unit is higher than that for PAAS, while P/Al ratios in the FB2b unit show values near the average P/Al for PAAS.

Table 4: Carbon and nitrogen data for all measurements in this study.

Formation	Lithology	Sample ID	Height m	$\delta^{13}C_{org}$ (‰, V-PDB)	TOC (wt. %)	$\delta^{15}N_{bulk}$ (‰, Air)	TN (wt. %)	$[C/N]_{bulk}$ (atomic)
FB2b	Pyritized MRS	FPS_s5-mat	18.7	-33.39	0.56	-2.01	0.06	8.64
		LP_s4-mat	17.8	-33.41	0.87	-2.47	0.10	9.84
		DB_s4-mat	17.1	-34.41	-	-0.21	0.07	-
		FPS_s4-mat	16.3	-33.17	0.23	nd	*0.04*	9.84
		FPS_s3-mat	16.2	-34.55	0.87	nd	*0.04*	25.47
		DB&FPS_s1-mat	16.2	-33.79	0.60	0.33	0.05	13.89
		DB_s3-mat	16.0	-33.17	0.50	-3.31	0.06	9.79
	Black shales	WS_s2-sed	19.7	-33.21	0.63	-0.31	0.08	9.69
		FPS_s5-sed	18.7	-35.27	3.67	-0.56	0.07	58.87
		LP_s4-sed	17.8	-36.17	0.67	nd	*0.05*	15.73
		DB_s4-sed	17.1	-35.22	2.81	-0.53	0.08	43.46
		FPS_s3-sed	16.2	-35.16	3.25	-0.14	0.06	63.20
		DB_s2-sed	16.0	-35.36	3.02	0.11	0.08	45.73
		FR_s1-sed	16.0	-34.91	1.73	0.55	0.08	26.02
		FR_s2-sed	16.0	-35.54	2.35	0.30	0.07	38.37
		MLS_s9-sed	15.5	-34.72	1.75	-0.79	0.08	26.06
FB2a	Pyrite-poor MRS	MLS_s1-mat	15.0	-34.51	4.85	0.21	0.12	47.61
		MLS_s2-mat	15.0	-33.68	8.13	0.72	0.15	63.67
		EST_s3-mat	15.0	-30.05	12.71	0.32	0.11	129.94
		MLS_s3-mat	15.0	-33.97	4.59	0.58	0.13	42.71
		MLS_s4-mat	15.0	-33.97	8.55	0.74	0.12	82.81
		MLS_s5-mat	15.0	-35.24	8.93	0.76	0.13	79.91
		WS_s3-mat	15.0	-34.13	4.32	1.44	0.14	35.35
		MLS_s10-mat	15.0	-32.17	18.24	1.85	0.16	136.33
		LP_s5-mat	15.0	-34.17	2.55	-0.09	0.14	21.78
		EST_s5-mat	15.0	-30.75	8.85	-0.28	0.10	100.40
		MLS_s3-mat	11.0	-33.21	1.45	1.38	0.10	16.77
		EST_s2-mat	6.8	-30.75	7.79	-3.48	0.13	69.69
	Sandstones	LP_s3-sed	15.0	-33.46	0.19	nd	*0.01*	22.66
		MLS_s10-sed	15.0	-31.68	0.34	nd	*0.01*	39.78
		MLS_s1-sed	15.0	-32.37	0.16	nd	*0.01*	18.94
		MLS_s2-sed	15.0	-30.76	0.29	nd	*0.01*	33.44
		MLS_s3-sed	11.0	-30.50	0.39	nd	*0.01*	45.21
		EST_s2-sed	6.8	-30.05	0.33	nd	*0.01*	38.44

-: not measured; nd: not detected. Italicized values: samples where analyses were close to detection limits. FPS: flat pyritized structure; LP: linear pattern; DB: domal buildup; WS: wrinkle structure; FR: "fairy-ring" structure; MLS: mat-layer structure; EST: "elephant-skin" texture.

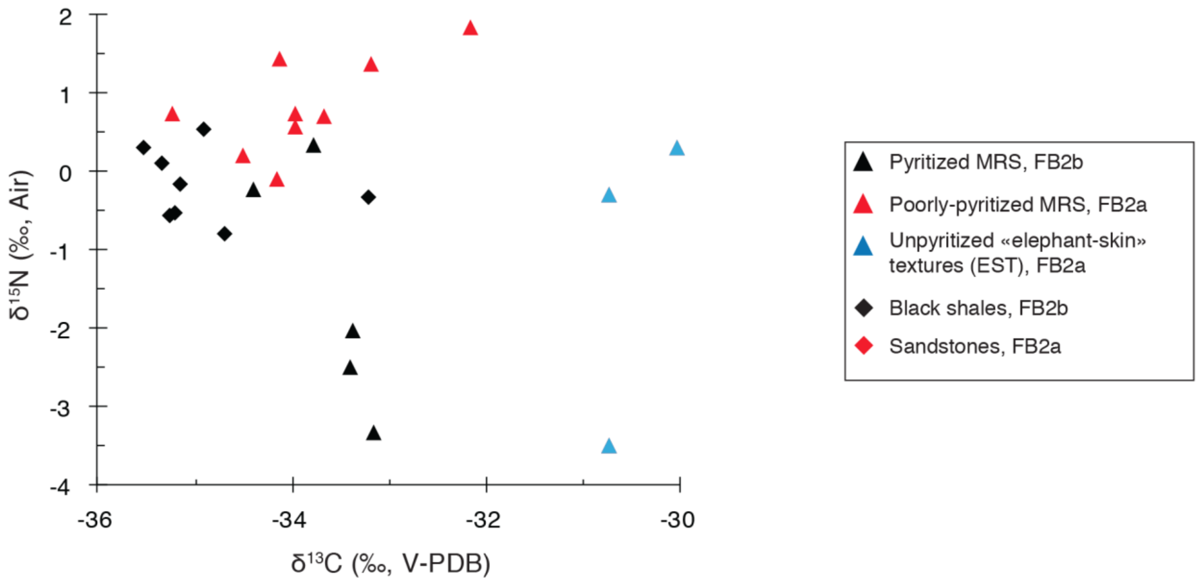

Figure 47: Cross plot of carbon and nitrogen isotopes.

4 | DISCUSSION

4.1 | Ocean chemistry reconstruction during deposition of the Francevillian FB$_2$ Member

To best evaluate confidently the redox of ancient water column, the Fe-based proxies must be coupled with other geochemical indicators. For instance, enrichments in redox-sensitive trace metals may be used to reconstruct bottom water redox conditions (Scott & Lyons, 2012). Some of these trace metals (*e.g.*, Mo, U, and V) are readily scavenged in and beneath anoxic or sulfide-rich waters. The sandstone sediments are not amenable to investigation via Fe speciation, but in this lithofacies we noted depletions in Cr, Fe, Mo, U, and V, which possibly indicate oxic bottom water conditions. The overlying black shales show evidence for oxic depositional settings likely in proximity to the chemocline, as suggested by the presence of intermittently ferruginous anoxic conditions. The lack of enrichment of redox sensitive trace elements provides further support for relatively oxygenated waters.

To explain the Fe- and Mn-enriched stratigraphic level in the Upper FB$_1$ Member, Ossa Ossa *et al.* (2018) suggested a progressive oxidation of Fe(II) and Mn(II) as deep-water upwelled across a chemocline towards shallow, oxygenated waters. The Fe and Mn deposits are derived from the precipitation Fe(III) and Mn(IV) (oxyhydr)oxides in the water column, followed by early diagenetic dissimilatory Fe and Mn reduction, respectively. According to Reynaud *et al.* (2017), the Upper FB and Lower FC formations were deposited during a continuous regressive track from deep marine (FB1c unit) to submergent sabkha environments (Lower FC Formation). Therefore, the moderate Mn enrichments in the studied sediments strongly argue for depositional settings just downstream of the upwelling zone (Figure 48). The simplest explanation for the lack of Fe enrichment in the FB_2 Member is that Fe was oxidized and removed deeper along the upwelling regime, an assumption consistent with the higher oxygen requirement for Mn(II) oxidation than Fe(II) oxidation. In support of the proposed model, upwelling systems would explain the moderate P enrichments in the studied sandstone and some black shale samples. Therefore, the relatively elevated TOC in the black shales would have resulted from high rates of primary productivity.

4.2 | Isotopic fidelity

The N isotope composition in sedimentary rocks can be affected by three main episodes of post-depositional process, including early and burial diagenesis, and metamorphism (Ader *et al.*, 2016). Therefore, before evaluating bulk-rock $\delta^{15}N$ signals, one must examine that the post-depositional alteration has had negligible impact on the primary signal (Appendices 26, 27A).

C/N values of the oceanic phytoplankton vary remarkably little, ranging from 4 to 10 (Gruber & Galloway, 2008; Ader *et al.*, 2016). The analyzed MRS and host sediment samples show TOC/TN ratios predominantly falling between 5 and 100 (Appendix 26), which is consistent with moderate diagenetic reworking of primary biomass. The Francevillian FB_2 Member has two MRS samples with TOC/TN values slightly above 100, suggesting that nitrogen may have been slightly lost during post-depositional thermal alteration. It has been shown that the transmission of $\delta^{15}N$ signal from primary producers to surface sediments under specific depositional settings does not imply isotopic fractionations (Robinson *et al.*, 2012). This conformity is confirmed in areas with minimal O_2 exposure time, high TOC content, and/or rapid sedimentation rate.

The occurrence of Fe- and Mn-bearing carbonate minerals after the microbial reduction of Fe- and Mn-oxyhydroxides (Ossa Ossa *et al.*, 2018), and the predominance of pyrite crystals suggest anoxic diagenetic conditions. Both early and late diagenesis under anoxic conditions can slightly modify the $\delta^{15}N_{bulk}$ values (Ader *et al.*, 2016). The first step in this process, is the degradation of organic-bound N (*i.e.*, remineralization), which releases N as NH_4^+ to pore-waters below the sediment-water interface. Then, NH_4^+ can become incorporated into the interlayers of phyllosilicates after substitution for potassium cations. The phyllosilicate-bound N phases represent up to half of TN content (Müller, 1977). Our samples show a strong positive covariation ($R^2 = 0.74$) between TN and K (wt.%), supporting NH_4^+ fixation in K-rich clays during the breakdown of organic matter (Appendix 27B). Nonetheless, there is no correlation between $\delta^{15}N_{bulk}$ and K (wt.%) ($R^2 = 0.11$), which is consistent with the fact that this diagenetic transfer did not affect the bulk $\delta^{15}N$ signal.

With increasing burial depth and metamorphism, organic matter undergoes the thermal maturation, resulting in the preferential loss of ^{14}N relative to ^{15}N. Thus, the $\delta^{15}N_{bulk}$ values slightly increase of <1‰ at lower greenschist facies, 1 to 2‰ at greenschist facies, and up to 4‰ at amphibolite facies (Bebout & Fogel, 1992; Ader *et al.*, 1998). The Francevillian basin was not affected by metamorphic transformation (Gauthier-Lafaye & Weber, 1989; Ngombi-Pemba *et al.*, 2014), suggesting a maximum increase in bulk $\delta^{15}N$ signal of 1‰. In addition, strong positive covariations between $\delta^{15}N_{bulk}$ and TN, $\delta^{15}N_{bulk}$ and C/N, $\delta^{13}C_{org}$ and TOC, as well as $\delta^{13}C_{org}$ and C/N would indicate a metamorphic alteration, as light isotopes are more mobile than heavier ones and N is more mobile than C (Bebout & Fogel, 1992). In contrast, these correlations are not observed across our Francevillian samples (Appendix 27A), indicating a minimal effect of post-depositional processes on primary $\delta^{15}N_{bulk}$ and $\delta^{13}C_{org}$ values.

4.3 | Interpretation of isotopic data in the FB$_2$ Member

4.3.1 | Carbon cycling

Autotrophic microorganisms preferentially incorporate ^{12}C from CO_2, CH_4, or other carbon-bearing gases into their biomass as a function of their carbon fixation pathways, resulting in large fractionation of carbon isotopes. The C isotope fractionation during primary productivity is also affected by a combination of other factors, including growth rates, dissolved CO_2 levels, and the ratio of volume to surface area (Hayes *et al.*, 1999). In the MRS and host sediments, the fractionation of C isotopes roughly fluctuates between 30 and 36‰, assuming near-to-modern marine dissolved inorganic carbon $\delta^{13}C$ values. Nonetheless, the $\delta^{13}C$ compositions for carbonate-containing rocks in the black shales average 6.6 ± 1.2‰ (1σ, n = 10; ranging from 5.5 to 9.6‰) (El Albani *et al.*, 2010), which reflects marine carbonates deposited during the LE (Bekker *et al.*, 2008). Accordingly, the total fractionation of C isotopes between carbonate and organic carbon ($\Delta^{13}C$) was probably between 35 and 44‰ (with a confidence threshold of 1σ).

Our samples show no obvious relationship between $\delta^{13}C_{org}$ values and TOC concentrations (Appendix 27A), which indicates an environmental influence on the isotopic data rather than post-depositional alterations. The $\Delta^{13}C$ values in the FB$_2$ host sediments may not result from the activity of photoautotrophs alone, instead they point to the contribution of organic matter derived from multiple carbon fixation pathways. Indeed, photosynthesizers yield $\delta^{13}C_{org}$ signatures typically between -20 and -35‰ through the Calvin–Benson–Bassham cycle (Schidlowski, 1987; Berg *et al.*, 2010), the most successful C fixation pathway over Earth history (Nisbet & Sleep, 2001). The shift towards more negative $\delta^{13}C_{org}$ values in the black shale facies likely reflects an enhanced secondary productivity in the water column and near the sediment–water interface (Hayes *et al.*, 1999). Particularly, the CO_2 fixation through the reductive acetyl-CoA pathway of strictly anaerobic microorganisms, including autotrophic and acetoclastic methanogens, and some sulfate reducers, renders $\delta^{13}C_{org}$ values down to around -42‰. Thus, this contributes to the deposition of residual organic carbon enriched in light ^{12}C (Schidlowski, 1987; Zerkle *et al.*, 2005; Stüeken *et al.*, 2017). However, CO_2 fixation pathways that generate a biomass lighter than –42‰ are unknown (Schidlowski, 1987; Zerkle *et al.*, 2005). Accordingly, the incorporation of isotopically “superlight” organic carbon into biomass is expected in our samples and it may be explained by the involvement of methanotrophy (Schidlowski, 1987; Zerkle *et al.*, 2005). Such microbial activity relies on the methane oxidation during which variable electron acceptors are used. Thus, both aerobic and anaerobic processes may promote the oxidation of methane. The large Francevillian seawater sulfate reservoir at that time (Canfield *et al.*, 2013; Ossa Ossa *et al.*, 2018), together with the relatively high pyritization degree of a small reservoir of Fe_{HR} in black shales (Figure 45), would suggest that the anaerobic oxidation of methane occurred with sulfate as the most plausible oxidant (*i.e.*, anaerobic oxidation of methane coupled to sulfate reduction). Collectively, negative $\delta^{13}C_{org}$ values beyond the range of phototroph-derived organic matter in the studied sediments argue for the addition of isotopically light biomass from the biological methane cycling below the sediment-water interface and during anoxic diagenesis (Figure 48).

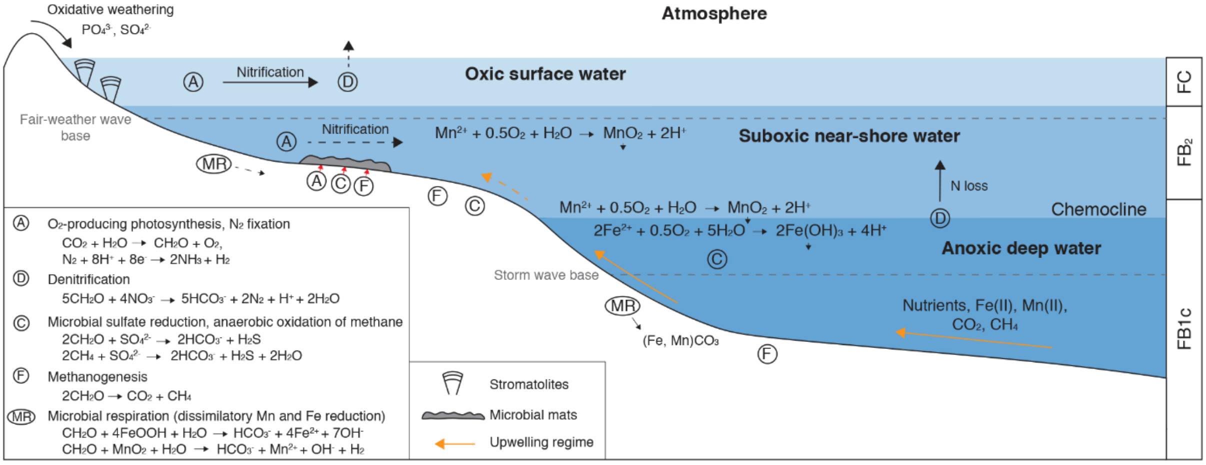

Figure 48: Proposed palaeoenvironmental reconstruction during deposition of the Francevillian Series at the end of the Lomagundi Event (from the FB1c unit to the Lower FC Formation). Ocean redox conditions and biogeochemical cycles are shown (modified from Ossa Ossa *et al*., 2018). Orange and black dotted arrows indicate the limited expression of upwelling system and microbial processes, respectively.

The presence of “elephant-skin” textures, “fairy ring” structures, tufted morphology, and oxygen-related gas bubbles suggest that filamentous Cyanobacteria were responsible for the establishment of Francevillian MRS (Aubineau *et al.*, 2018, 2019). However, the large $\Delta^{13}C$ fractionations higher than 35‰ in the MRS point to organic matter remineralization by sulfate reducers and CH_4-based metabolisms, as explained above (Figure 48). The oxidation of carbonaceous material via the activity of MSR in the pyritized MRS explains the low TOC contents (Aubineau *et al.*, 2018, 2019). Finally, the subtle difference in $\delta^{13}C_{org}$ values between the MRS morphotypes likely depends on the extent to which CO_2 fixation, methane production, and methanotrophy operate to control the carbon isotope composition. In this regard, the benthic microbial communities were unlikely ecologically stratified.

4.3.2 | Nitrogen cycling

Our geochemical data tend to indicate predominantly the occurrence of oxic, shallow-water depositional settings in the FB_2 Member. Well-oxygenated conditions were met in the overlying Lower FC Formation (Canfield *et al.*, 2013), in which a pervasive aerobic N cycle has been recorded (Kipp *et al.*, 2018). The latter is characterized by positive $\delta^{15}N$ values (from +4‰ to +7‰) that have been linked to rapid nitrification followed by non-quantitative denitrification in the water column. Such values clearly indicate the predominance of nitrate-using organisms that may comprise both prokaryotes and eukaryotes.

In contrast, the N isotope compositions of our samples are inconsistent with the occurrence of aerobic N cycling. The $\delta^{15}N$ values between -2‰ and +1‰ usually pertain to the biological N_2 fixation using the Mo-bearing nitrogenase that is performed by prokaryotes – mainly Cyanobacteria (Bauersachs *et al.*, 2009). At high Fe^{2+} concentrations, the fractionation driven by Mo-based diazotrophy can be more negative, by as much -4‰ (Zerkle *et al.*, 2008). Alternative nitrogenase enzymes, in which Fe or V replace Mo in the active site, generate a more ^{14}N-enriched biomass with $\delta^{15}N$ values as low as -8‰ (Zhang *et al.*, 2014; Stüeken *et al.*, 2016). The unchanged nitrogen isotope composition of the atmosphere over the last 3 Ga ($\delta^{15}N_{air} \approx 0‰$; Sano & Pillinger, 1990), together with minimal post-depositional alteration, suggest that the $\delta^{15}N_{bulk}$ values for the MRS and black shale samples correspond to the microbial N_2 fixation by Mo-nitrogenase (Figure 48). This global expression of the nitrogen limitation indicates the predominance of diazotrophy in benthic habitats and water column. In addition, some MRS samples show $\delta^{15}N$ values between -4‰ and -2‰, which is consistent with the fact that local Fe^{2+}-replete conditions may have been imposed by microbes during DIR (Aubineau *et al.*, 2019). The high TOC, TN, and P contents at least in the pyrite-poor MRS hint that the productivity was intense. Accordingly, the presence of active N_2 fixers in Palaeoproterozoic mat-building Cyanobacteria in ways similar to modern microbial mats (Herbert, 1999; Woebken *et al.*, 2015), point to the existence of analogous microbial drivers of biogeochemical nitrogen cycling in the Francevillian basin.

We may consider that the black shales are actually composed of microbial mats where their specific isotopic signatures of N_2 fixation would have been imposed to the black shale facies. However, the distinct morphological textures of microbial structures within the host sediment were not petrographically observed (Aubineau *et al.*, 2018). Furthermore, the presence of microbial mats can be inferred by the record of an advanced stage of illitization process, resulting from a biologically mediated K enrichment (Aubineau *et al.*, 2019). This biosignature is lacking in the host black shale facies. Given that, this leads to the assumption that (i) benthic communities did not occurred in the host black shales, and (ii) the carbonaceous material derived from the overlying water column was not enriched in K. Combined, these observations demonstrate the absence of microbial mat remnants in the fine-grained sediments. Modern analogue with an ecosystem dominated by N_2 fixers can be found in the Black Sea and Cariaco Basin (Thunell *et al.*, 2004; Fulton *et al.*, 2012). These environments have a limited connection to the global ocean, resulting in nutrient starvation. Our samples have higher C/S ratios than those for the modern normal marine sediments (Appendix 28; (Berner & Raiswel, 1983), however the present-day marine sulfate reservoir (28 millimolar; mM) is not as large as the estimated sulfate pool in the Palaeoproterozoic (1-10 mM; Fakhraee *et al.*, 2019). Hence, environmental signals of Francevillian FB_2 sediments do not reflect a restricted depositional setting.

Nitrogen isotopes along Mesoproterozoic cross-basinal transects usually recorded aerobic nitrogen cycling shoreward, while anaerobic nitrogen pathways were restricted to the anoxic deep basin (Stüeken, 2013; Koehler *et al.*, 2017). In contrast, the shallow depositional setting of Francevillian FB_2 rocks points to a nitrogen limitation. Given the high metabolic cost of biological N_2 fixation (16 ATP per molecule of N_2 fixed; Herbert, 1999), the $\delta^{15}N$ values near 0‰ suggest that fixed nitrogen was indeed scares in this environment. Considering that the redox potential of Mn(II) oxidation is higher than NH_4^+ oxidation, nitrifying microbes could have promoted the oxidation of NH_4^+ to NO_2^- or NO_3^- since the redox threshold was crossed, as indicated by the extensive Mn deposits along the upwelling zone (Ossa Ossa *et al.*, 2018). Although the Fe-based analyses, redox-sensitive trace elements and highly negative $\delta^{34}S_{pyrite}$ values indicate a relatively oxygenated water column with significant sulfate concentrations, our data rather suggest that the buildup of nitrate reservoir was not high enough to leave the positive isotopic fingerprint (*i.e.*, residual NO_3^- isotopically heavy) via non-quantitative denitrification (Figure 48). In modern oceans, bioavailable P and Fe are the main nutrients for biological productivity in coastal upwelling systems (Capone & Hutchins, 2013). Their scarcity could have been the main limiting factors in the production of bioavailable nitrogen. Under widespread ferruginous conditions, it is accepted that phosphorus availability is restricted (Bekker & Holland, 2012; Reinhard *et al.*, 2017), hampering rates of primary productivity and, thus, limiting the biological oxygen production. In contrast, we observe high to moderate P contents in the Francevillian sediment samples, which implies that diazotrophy may have kept pace with upwelling of phosphorus. In modern surface water of upwelling zones, a shortage of iron induces low nitrogen fixation rates (Sohm *et al.*, 2011). Petrographic and geochemical observations argue against a significant Fe limitation in the FB_2 Member. Molybdenum, one of the essential constituents of the nitrogenase enzyme (Williams & Fraústo da Silva, 2002), would have been a limiting component for biological activity throughout the mid-Proterozoic (Anbar & Knoll, 2002). Particularly, Mo is scavenged from sulfur-rich seawater that became developed in ocean continental margins during the Proterozoic. We cannot completely rule out the possibility of Mo limitation in the FB_2 Member, since low Mo contents have been predicted for Proterozoic oceans (Reinhard *et al.*, 2013b). However, given that Mo-nitrogenase has been operating at Earth's surface since ~3.2 Ga (Stüeken *et al.*, 2015a), when Mo was likely much scarcer in the marine environment, it is perhaps unlikely that widespread Mo limitation occurred in the Paleoproterozoic, particularly during the "oxygen overshoot" interval during which marine trace metal inventories are thought to have expanded (Bekker & Holland, 2012; Partin *et al.*, 2013b).

The threshold at which nitrification outpaces denitrification is modeled at low micromolar (>4.5 to 11 µM) dissolved oxygen concentrations (Fennel *et al.*, 2005; Kipp *et al.*, 2018). The relatively large sulfate reservoir in the FB_2 Member could have reached 10 mM dissolved sulfate contents, which are typical values observed during the LE (Planavsky *et al.*, 2012). Estimates of O_2 levels based on sulfur isotopes and seawater sulfate indicate contents of between 50 and 75 µM (Fakhraee *et al.*, 2019). Although these values may have been lower due to the oxygen removal by an overwhelming supply of aqueous Fe(II) and Mn(II) along the upwelling transect, it is likely that oxygen was present at levels high enough to sustain a dissolved nitrate reservoir during deposition of the FB_2 Member. Thus, if the observed $\delta^{15}N$ values are indicative of basinal- or global-scale, this would have likely been a transient state that ultimately yielded to more oxygenated and nitrate-replete conditions. In addition, high rates of primary production in the black shales, the lack of evidence of biolimiting elements, and combined with an aerobic nitrogen cycle of stable nitrate pool in the overlying sediments (Kipp *et al.*, 2018), are consistent with the short-lived N scarcity.

In this regard, we invoke that the nitrogen limitation was likely modulated by the ocean redox structure (Figure 48). A rapid nitrogen removal due to nitrification and subsequent denitrification has been proposed to be a dominant feature at the oxic/anoxic transition (Fennel *et al.*, 2005). Intense denitrification leads to severe loss of fixed nitrogen, which may promote surface activity of N_2 fixers (Deutsch *et al.*, 2007). This model has been highlighted in Cambrian settings whereby eustatic fluctuations and input of P through upwelling would have enhanced nitrogen fixation in shallow depositional environments (Chang *et al.*, 2019). In addition, the nitrate reservoir would have been severely depleted by denitrification or anammox if the chemocline was relatively shallow, particularly within the photic zone (Ader *et al.*, 2014). Accordingly, the significant amount of fixed nitrogen lost via denitrification and anammox at the chemocline during a sea level fall would have led to the drawdown of the reservoir of bioavailable nitrogen, and then, in turn, promoted diazotrophy.

4.4 | Implications for primary productivity and the development of complex life forms in the Upper FB Formation

Our results provide evidence for high N_2 fixation rates both in MRS and the water column. The N_2 fixation in microbial mats is a typical signature, however, benthic communities do not contribute to the N budget of the overlying water column (Bebout *et al.*, 1994; Herbert, 1999). Rather, cyanobacterial blooms in the water column may replenish the bioavailable nitrogen. Under nitrate-depleted and P-replete conditions, diazotrophic photoautotrophs sustain primary productivity since phosphate is in excess relative to nitrogen requirements (Tyrrell, 1999). A modelling approach has indicated that high phosphate flux, derived from crustal weathering and/or upwelling regime (Bekker & Holland, 2012), leads to the rise of N_2 fixation flux and inventory, which in turn invigorates oxygen production and accumulation (Fennel *et al.*, 2005). This assumption was recently evidence in Palaeoproterozoic rocks in the aftermath of GOE (Luo *et al.*, 2018). The latter authors proposed that the loss of bioavailable nitrogen was efficiently balanced by its replenishment through high productivity of cyanobacterial diazotrophy. This has likely promoted the widespread proliferation of nitrate-assimilating organisms afterwards (Kipp *et al.*, 2018). Although the aerobic nitrogen cycling following the GOE may have been pervasive as predicted (Zerkle *et al.*, 2017; Kipp *et al.*, 2018), our data suggest that local fluctuations in redox conditions controlled the nitrogen dynamic in the Francevillian Series. To summarize, the short-lived N scarcity in the FB_2 Member suggests that the nutrient remaining in surface waters along the upwelling transect was capable of sustaining diazotrophy. The latter metabolic pathway could have allowed fixed nitrogen to accumulate, consistent with the buildup of a large dissolved nitrogen reservoir in oxygen-replete conditions in the overlying FC Formation.

The widespread occurrence of aerobic nitrogen cycling in the early Palaeoproterozoic indicates the prevalence of nitrate-assimilating organisms (Kipp *et al.*, 2018). This biomass could have hosted eukaryotes, although molecular fossils pertaining to such advanced life forms are lacking until the late Palaeoproterozoic (Brocks *et al.*, 2005). Assuming that the complex and highly organized organisms from the FB_2 Member comprised nitrate- and oxygen-dependent metabolic processes, in ways similar to eukaryotic metabolisms, the nitrogen limitation in the water column even transient may explain the relatively close association between these complex macrofossils and MRS. Thus, the shallow microbial mats here may have played two roles for the proliferation of multicellular macroorganisms of various sizes and shapes. First, the MRS would have alleviated the oxygen limitation by creating “oxygen oases” (Aubineau *et al.*, 2018). Indeed, oxygen concentrations in modern mats can be up to 4 times higher than in low oxygen settings, hinting the copious amounts of oxygen that are produced by oxyphototrophic Cyanobacteria (Gingras *et al.*, 2011). Second, the high nitrogen fixation activity in cyanobacterial mats, combined with the presence of nitrifying bacteria, would have offered a pervasive source of bioavailable fixed nitrogen for nitrate-fueled organisms. Thus, the ancient multicellular organisms used the mats as oxygen and nutrient resources in oceans that had yet to become fully oxygenated.

5 | CONCLUSION

The combined use of bottom water redox proxies and carbon and nitrogen isotopes in the Francevillian MRS and host sediments allowed us to better constrain redox conditions and microbial biogeochemical cycling at the end of the Lomagundi Event. Our results summarized in Figure 48, suggest a short-lived nitrate scarcity in the water column as well as a nitrogen fixation in benthic microbial communities. Importantly, the presence of multiple C pathways and N_2 fixers in Palaeoproterozoic microbial structures points to the existence of biogeochemical carbon and nitrogen cycling in patterns similar to modern microbial mats.

In short, the large marine sulfate reservoir and the relatively oxygenated water mass indicate that the nitrogen limitation was likely controlled by the ocean redox structure in upwelling zones. Nutrient supply from upwelled waters may have promoted cyanobacterial blooms in surface environments, replenishing the bioavailable nitrogen pool. This would have enhanced the development of nitrate-assimilating organisms in the FC Formation. Although worldwide oxic conditions prevailed at the end of the LE, our results show that basin-scale redox fluctuations would have driven nitrate consumption, explaining potentially the unique association between the large colonial organisms and the MRS.

ACKNOWLEDGMENTS

We acknowledge the support of the Gabonese Government, CENAREST, General Direction of Mines and Geology, and Agence Nationale des Parcs Nationaux of Gabon. This work was supported by CNRS, the University of Poitiers, Théodore Monod Doctoral School, Nouvelle Aquitaine Region and the French Embassy Libreville, Gabon. We would like to thank sincerely Prof. P Mouguiama Daouda, J.C. Balloche, L. White, and R. Oslisly for their support. For assistance, we acknowledge C. Laforest, L. Magad-Weiss, A. Oldroyd, P. Recourt, C. Reedman, X. Tang, and L. Ying.

4.4. Highlights of Part 4

- The trace element distribution in the MRS shows passive accumulation of heavy minerals during mat growth and passive absorption of chalcophile elements in pyrite during diagenesis.
- Differences of TE-containing heavy minerals are observed in the MRS morphotypes, but these are consistent with changes of physical sedimentological conditions.
- There is no evidence for a biocontrolled TE enrichment in the benthic mats.
- Biogeochemical carbon and nitrogen cycling in the 2.1 Ga-old Francevillian MRS are equivalent to those observed in modern microbial mats.
- The overall nitrogen limitation in the Upper FB_2 Member was likely transient and modulated by the basin-scale ocean redox structure.

CONCLUSION AND PERSPECTIVES

This work aims at documenting the microbial diversity in Palaeoproterozoic rocks from the Francevillian Basin, Gabon. It is subsequently studied the mineralogical and geochemical record of these bacterial mats to reveal putative microbially induced signatures. The studied area has been previously explored because of the occurrence of the oldest large colonial organisms. Hence, the description of the organizational, ecological and taphonomical processes of the unique 2.1 Ga-old ecosystem is of considerable interest for investigating evolutionary innovations in the wake of the first significant accumulation of oxygen in Earth's atmosphere.

General conclusions

Through a combination of macroscopic analyses, scanning electron microscopy to mineral identification and documentation of textural relationships, Raman spectroscopy, and organic elemental analyses, the first result of this work allows to assess the true biological antiquity of putative mat-like structures. The MRS display more than ten different morphotypes, filling the gap between the Archaean and Mesoproterozoic mat record. Moreover, the mat-related microtextures are distinct and comprise perfectly preserved tufted structures, fossilized gas bubbles, and concentrated heavy minerals, among others. Collectively, these results likely indicate the presence of biologically formed structures that are related to oxyphototrophic Cyanobacteria as the main mat-building microorganisms. Given that, palaeoenvironmental interpretations were inferred to strongly constrain the depositional setting in which the Francevillian biota thrived. Thus, the lack of microbial structures indicative of physical processes such as desiccation and erosion, combined with the light-dependent requirement of photosynthesizers, support a quiet shallow water environment within the photic zone. The relatively close association between the benthic microbial communities and the advanced forms of life may hypothesize that the MRS played a role for oxygen and food resources.

The mineralogical study of the MRS and underlying host sediments has been then considered, being one of the main purposes of this PhD work. The X-ray diffraction and transmission electron microscopy were used in rare studies for describing the clay-size fraction of microbial structures. These analytical techniques coupled with X-ray fluorescence microscopy reveal high K content localized in well-crystallized illite particles that are abundant in the MRS, but not in the host rocks. Considering the absence of K-feldspars in the FB Formation, the lack of K addition in the medium did not promote a complete illitization reaction in the Francevillian host sediments. This is consistent with the occurrence of K-feldspar-depleted tonalite-trondhjemite-granodiorites that are crustal components in the West Congolese block. The advanced stage of illitization in the µm-thick mats rather suggests that microbes trapped K^+ from the seawater and released it into the pore-waters during degradation and burial of organic matter. Thus, this study demonstrates that the illitization process through a biologically supplied K recorded an ancient metabolic activity in sedimentary environments. This work provides a new biosignature for investigating early life on Archaean sediments that lacked granitoids in their provenance.

Furthermore, the facilitated removal of K^+ from seawater into the clay fraction is a process akin to the reverse weathering. The latter leads to the release of carbon dioxide, which would have helped maintain warm conditions during the faint young sun paradox. Thus, the bacterially enhanced illitization is also linked to a biological feedback that controlled CO_2 concentration of Earth’s atmosphere and seawater pH.

With the aid of whole-rock geochemical analyses and XRF elemental distribution maps, discrepancies in trace element abundance between the MRS and host sediments have been described. The microbial mat laminae embed a large amount of Ti- and Zr-rich heavy minerals that are syngenetically enriched in TE. The observed differences in TE content between the mat morphotypes reflect both global and local variations of hydrodynamic regime and sediment supply. In addition, the chalcophile element distribution in pyrite-containing bacterial structures supports enrichments during early diagenesis in ways similar to those for modern microbialites. In our studied samples, there is no evidence for a biocontrolled CE enrichment, as indicated by the absence of higher CE/S ratios in the MRS. The apparent variations in CE concentration between the MRS and host sediments simply hint a large sulfide production that is imposed locally by high sulfate reduction rates. This first geochemical study highlights bulk-rock TE distinctions between the MRS and host rocks, but changes of environmental factors may simply overwhelm any potential biological signal. This leads to the assumption that the bulk TE data should not be used as a biological proxy in the deep rock record.

Finally, special attention was paid to determine the carbon and nitrogen isotope compositions of ancient MRS and sediments coupled with local seawater redox data. The carbon and nitrogen isotopes reveal slight distinctions between the mats and host sediments, but unlikely characterize diverse microbial populations. Thus, the organic carbon geochemistry supports multiple trophic levels involved in the cycling of photosynthetically derived C_{org}, including phototrophy, heterotrophy and methanotrophy. Both the mat and sediment facies show nitrogen isotope values best explained by nitrogen fixation. Considering the N composition of black shales, it brings strong evidence for a restricted nitrate reservoir in the Upper FB

Formation, which was likely modulated by the ocean redox structure. This nitrogen famine would have been transient because of the likely high denitrification rate at the chemocline in the underlying sediments (Upper FB_1 Member) and the fully operational aerobic N cycling in the overlying sediments (Lower FC Formation). The abundant nutrient supply in surface waters just downstream of upwelling systems would have allowed diazotrophs to keep pace by replenishing bioavailable nitrogen. Importantly, the presence of multiple C pathways and N_2 fixers in the Palaeoproterozoic MRS points to the occurrence of biogeochemical cycling in patterns equivalent to modern microbial mats. Thus, the isotope analyses allow unravelling the existence of analogous microbiogeochemical processes during the Palaeoproterozoic.

Collectively, these results show that the MRS have recorded a wide range of mineralogical and geochemical information. The geobiological study is of considerable interest as it may provide clues for identifying early life on Archaean sedimentary rocks. Moreover, interactions between the benthic microbial communities and the macroorganisms in the Francevillian FB_2 Member provide a unique ecological snapshot at the time of the first emergence of complex biosphere, 2.1 Ga ago.

Future works

In order to go beyond this PhD work, it would be interesting to interpret ancient biosignatures through molecular fossils in the studied rocks. The Francevillian organic matter is considered overmature, and, therefore, few analyses have been conducted. The lipid biomarker analysis by the way of infrared spectroscopy and gas chromatography-mass spectrometry could be of deep interests for investigating the organic functional groups that compose the carbonaceous material. For instance, these working tools are used for understanding organic-mineral interactions (Kebukawa *et al.*, 2019) or deciphering the predominance of algal *vs*. bacterial input in the depositional setting (*e.g.*, Pehr *et al.*, 2018; Riboulleau *et al.*, 2018). Moreover, the oldest lipid molecular fossils that indicate the presence of eukaryotes were found in 820-Ma-old sediments (Brocks *et al.*, 2017). A putative occurrence of eukaryotes in Gabonese rocks would be of paramount importance in the evolutionary history of life and allow to support the early emergence of those organisms in Palaeoproterozoic (*e.g.*, Gold *et al.*, 2017; Kipp *et al.*, 2018).

Whole-rock geochemical data were used in this work to ascertain the potential of such analyses for distinguishing biological structures from non-biological features. However, the geochemical study in relation to the provenance (*i.e.*, the detrital source origin) has not yet been treated. The provenance analysis is a convenient method as it is mainly applied on fine-grained sediments to explore their palaeotectonic and/or palaeogeographic settings (*e.g.*, McLennan *et al.*, 1983; McLennan, 1989; Armstrong-Altrin *et al.*, 2004). This study would constrain the basin-scale depositional setting in which the MRS flourished. Besides, some results obtained by this geochemical approach were reported from the FA (Bankole, 2015) and FB formations (Bankole *et al.*, 2018). Thus, it would be interesting to compare information from the different lithostratigraphic formations to better understand the evolution of provenance in the Franceville sub-basin.

The CE content via bulk-rock measurements in the MRS does not show biocontrolled metal enrichments. However, this could be explained by the fact that the whole-rock analysis reflects a wide range of host mineral fractions, which makes the relationships difficult to interpret. One way to avoid this would be to perform laser ablation-inductively coupled plasma-mass spectrometry (LA-ICP-MS) analyses on sedimentary pyrite in the MRS and sediments. This widely used approach shows a considerable range of CE compositions (Large *et al.*, 2014; Gregory *et al.*, 2015). Thus, variations of S to trace element ratio distribution between the MRS and Francevillian rocks, among the same pyrite texture, might indicate whether the CE is scavenged from a biocontrolled process or enriched via a secondary fluids.

In this work, the investigation of sulfur isotope composition of MRS is lacking. Although numerous S isotope data from the Francevillian multicellular organisms have been published (El Albani *et al.*, 2010, 2014, 2019), such analyses in the MRS would allow a complete understanding on the biogeochemical sulfur cycling in the Francevillian biota. Besides, the S isotope composition would explain the various pyritization degrees of MRS and elucidate their timing relationship during the diagenesis. Indeed, a slow burial of MRS would have not restricted the MSR from the large sulfate pool of seawater, leading to extensive pyritization and negative $\delta^{34}S$ values. In contrast, a rapid burial of MRS would have led to a reservoir effect, resulting in limited pyritization and positive $\delta^{34}S$ values.

CONCLUSION ET PERSPECTIVES (FRANÇAIS)

Ce travail vise à documenter la diversité microbienne dans des roches du Paléoprotérozoïque du bassin de Franceville au Gabon. L'enregistrement minéralogique et géochimique dans les structures bactériennes a ensuite été étudié pour révéler de possibles signatures biologiquement induites. La zone d'étude a déjà été explorée à cause de l'occurrence des plus anciens organismes coloniaux. Ainsi, la description des processus organisationnels, écologiques et taphonomiques de l'unique écosystème de 2,1 Ga est d'un intérêt considérable pour l'investigation des innovations évolutives dans la foulée de la première accumulation significative de l'oxygène dans l'atmosphère terrestre.

Conclusions générales

A travers une étude pluridisciplinaire et multi-échelle, les résultats de ce travail ont montré la véritable antiquité biologique des structures liées aux voiles bactériens. Les MRS présentent une dizaine de morphotypes différents, comblant ainsi l'écart de l'enregistrement de structures microbiennes entre l'Archéen et le Mésoprotérozoïque. De plus, les microtextures liées aux voiles sont distinctes et comprennent des structures touffetées parfaitement préservées, des bulles de gaz fossilisées et une forte concentration de minéraux lourds, parmi d'autres. Ces résultats indiquent à priori la présence de structures biotiques. Ces dernières sont vraisemblablement composées de Cyanobactéries oxyphototrophiques représentant les principaux microorganismes formant les voiles microbiens. Les interprétations paléoenvironnementales ont permis de mieux contraindre le milieu de dépôt dans lequel les macrofossiles du Francevillien prospérèrent. L'absence de structures microbiennes indiquant des processus physiques tels que la dessiccation et l'érosion ainsi que la dépendance à la lumière des phototrophes argumentent pour un environnement marin calme et peu profonde appartenant à la zone photique. L'association étroite des communautés microbiennes benthiques et des macrofossiles peut laisser supposer que les MRS ont joué un rôle dans l'apport d'oxygène et de ressources nutritives.

L'étude minéralogique des MRS et du sédiment encaissant sous-jacent a été également réalisée. Ce volet représente l'un des principaux objectifs de ce travail de thèse. La diffraction des rayons X et la microscopie électronique à transmission ont été peu utilisées pour décrire la fraction argileuse associée aux structures microbiennes. Ces techniques d'analyse couplées à la microscopie à fluorescence X révèlent des teneurs élevées en K localisées dans des particules bien cristallisées telles que les illites. Ces dernières sont abondantes dans les MRS, mais absente dans la roche encaissante. Compte tenu de l'absence de feldspaths potassiques dans la Formation FB, la carence d'une source potentielle de potassium a ainsi promu une réaction incomplète d'illitisation dans le sédiment encaissant du Francevillien. Ceci est cohérant avec la présence de tonalite-trondhjemite-granodiorites qui sont appauvries en feldspaths potassiques et sont des composés du socle cristallin du craton du Congo occidental. Le stade avancé d'illitisation dans les voiles d'une épaisseur micrométrique suggère plutôt que les microbes ont piégé le K^+ de l'eau de mer et l'ont libéré dans l'espace interstitiel pendant la dégradation et l'enfouissement de la matière organique. Ainsi, cette étude démontre que le processus d'illitisation à travers un apport biologique en K a enregistré une ancienne activité métabolique dans des environnements sédimentaires. Ce travail fournit une nouvelle biosignature pour investiguer la vie primitive dans les sédiments très anciens (archéens) qui ne doivent pas avoir pour origine détritique des granitoïdes.

De plus, l'incorporation du K^+ dérivé biologiquement dans la fraction argileuse est un processus semblable à l'altération inversée. Cette dernière entraîne une libération de dioxyde de carbone, ce qui aurait aidé à maintenir des températures chaudes pendant le paradoxe du jeune soleil faible. Ainsi, l'illitisation promue de manière biologique est liée à une rétroaction biologique qui a contrôlé la concentration de CO_2 dans l'atmosphère terrestre et le pH de l'eau de mer.

À l'aide d'analyses géochimiques sur la roche totale et de cartes de distribution des éléments par XRF, des divergences dans l'abondance des éléments traces entre le MRS et le sédiment encaissant ont été observées. Les lamines de voiles bactériens contiennent de nombreux minéraux lourds composés de Ti et Zr qui sont syngénétiquement enrichis en TE. Les différences observées des teneurs en TE au sein des différents morphotypes microbiens reflètent des variations globales et locales du régime hydrodynamique et de l'apport sédimentaire. De plus, la distribution des éléments chalcophiles dans les structures bactériennes contenant de la pyrite met en évidence un enrichissement au cours de la diagenèse précoce de la même manière que celui constaté dans les microbialites modernes. Dans nos échantillons étudiés, l'enrichissement biocontrôlé des métaux comme indiqué par l'absence d'un ratio CE/S plus élevé dans la MRS n'est pas avéré. Les variations apparentes de la concentration des CE entre les MRS et le sédiment encaissant indiquent simplement une production importante de sulfures qui fut imposée localement par un taux élevé de réduction des sulfates. Ces résultats géochimiques soulignent les distinctions des TE de la roche totale entre les MRS et le sédiment encaissant. Il est probable que des changements des conditions environnementales aient masqué les signaux biologiques. Par conséquent les données des TE de la roche totale doivent être utilisées avec précaution afin de mettre en évidence la biogénicité des structures fossilisées.

Une attention particulière a été accordée à la détermination de la composition isotopique du carbone et de l'azote en association avec des données du redox local de l'eau de mer. Les isotopes du carbone et de l'azote révèlent de légères différences entre les MRS et le sédiment encaissant. Toutefois, il est peu probable que celles-ci caractérisent de manière distincte des populations microbiennes différentes. La géochimie du carbone organique étaye l’idée que de multiples niveaux trophiques sont impliqués dans le cycle du C_{org} d'origine photosynthétique, incluant la phototrophie, l'hétérotrophie et la méthanotrophie. Les facies bactériens et sédimentaires montrent des valeurs isotopiques bien expliquées par la fixation de l'azote. Compte tenu de la composition en N des black shales, cela apporte une preuve tangible de la présence d'un modeste réservoir nitrique dans la Formation du FB supérieur. Ce dernier a probablement été modulé par la structure redox de l'océan. Cette famine azotée aurait été transitoire en raison d’un fort taux de dénitrification probablement lié à la chimiocline dans les sédiments sous-jacents (Membre du FB_1 supérieur) et d’un cycle aérobique azoté pleinement opérationnel dans les sédiments sus-jacents (Formation du FC inférieur). L'abondance d'éléments nutritifs dans les eaux de surface juste en aval d’un système d'upwelling aurait permis aux diazotrophes de suivre le rythme en réapprovisionnant l'azote biodisponible. Il est important de noter que la présence de plusieurs voies métaboliques du C et de la réduction de l’N dans les MRS du Paléoprotérozoïque pointe vers l’occurrence de cycles biogéochimiques équivalents à ceux observés dans les voiles microbiens actuels. Ainsi, les analyses isotopiques permettent de mettre en valeur l'existence de processus microbiogéochimiques analogues, au Paléoprotérozoïque.

Ces données montrent que les MRS ont enregistré un large éventail d'informations minéralogiques et géochimiques. L'étude géobiologique est d'un intérêt considérable car elle peut fournir des indices pour identifier une vie primitive dans les roches sédimentaires plus anciennes. De plus, les interactions entre les communautés bactériennes benthiques et les macroorganismes du Membre FB_2 du Francevillien fournissent un aperçu écologique unique au moment de la première émergence d’une biosphère complexe, il y a 2,1 Ga.

Travaux futurs

En perspective à ce travail, il serait intéressant d'interpréter et de corréler des anciennes biosignatures à travers les fossiles moléculaires dans les roches étudiées. La matière organique du Francevillien est considérée comme trop mature et, par conséquent, peu d'analyses ont été effectuées. L'investigation des biomarqueurs lipidiques par spectroscopie infrarouge et chromatographie en phase gazeuse - spectrométrie de masse pourrait être d'un grand intérêt pour étudier les groupes fonctionnels organiques qui composent la matière carbonée. Par exemple, ces outils de travail servent à comprendre les interactions organominérales (Kebukawa *et al.*, 2019) ou à déchiffrer la prédominance de l'apport algaire *vs.* bactérien dans le milieu sédimentaire (*e.g.*, Pehr *et al.*, 2018; Riboulleau *et al.*, 2018). De plus, les plus anciennes traces moléculaires lipidiques qui indiquent la présence des eucaryotes ont été retrouvées dans des sédiments de ~ 820 Ma (Brocks *et al.*, 2017). Une potentielle présence des eucaryotes dans les sédiments du Gabon serait d'une grande importance dans l'histoire évolutive de la vie et permettrait de corroborer l'hypothèse d'une émergence précoce de ces organismes au Paléoprotérozoïque (*e.g.*, Gold *et al.*, 2017; Kipp *et al.*, 2018).

Les données géochimiques de la roche totale ont été utilisées dans le cadre de ce travail pour vérifier le potentiel de telles analyses dans la distinction de structures biologiques de celles non biologiques. Cependant, l'étude géochimique en relation avec la provenance (*i.e.*, origine de la source détritique) n'a pas encore été traitée. L'analyse de la provenance est une méthode pratique puisqu'elle est principalement appliquée sur des sédiments fins pour explorer leurs contextes paléotectoniques et/ou paléogéographiques (*e.g.*, McLennan *et al.*, 1983; McLennan, 1989; Armstrong-Altrin *et al.*, 2004). Cette étude permettrait de contraindre l'environnement de dépôt à grande échelle dans lequel les MRS prospérèrent. De plus, certains résultats obtenus par cette approche géochimique ont été publiés sur des échantillons provenant des formations FA (Bankole, 2015) et FB (Bankole *et al.*, 2018) du Gabon. Il serait donc intéressant de comparer les informations des différentes formations lithostratigraphiques pour mieux comprendre l'évolution de la provenance dans le sous-bassin de Franceville.

Les teneurs des CE de la roche totale dans les MRS ne montrent pas d'enrichissement biocontrôlé des métaux. Toutefois, cela pourrait s'expliquer par le fait que l'analyse de la roche totale reflète une large gamme de fractions minérales, ce qui rend les corrélations difficiles à interpréter. Les analyses par spectrométrie de masse à plasma à couplage inductif par ablation laser (LA-ICP-MS) sur la pyrite dans les MRS et les sédiments permettraient d'aboutir à un résultat plus probant. Cette approche largement utilisée montre un éventail considérable de compositions en CE (Large *et al.*, 2014; Gregory *et al.*, 2015). Ainsi, des variations du ratio CE/S entre les MRS et les roches du Francevillien, pour une même texture de pyrite, pourraient potentiellement indiquer si l'élément chalcophile est enrichi par un processus biocontrôlé ou par à un fluide secondaire.

L'analyse des isotopes du soufre pourraient être envisagés pour caractériser certains morphotypes MRS. Bien que de nombreuses données isotopiques du soufre aient été obtenues sur les organismes multicellulaires du Francevillien (El Albani *et al.*, 2010, 2014, 2019), de telles analyses sur les MRS permettraient une compréhension plus globale du cycle biogéochimique du soufre en lien avec l'ensemble du biota du Francevillien. De plus, la composition isotopique du souffre permettrait d'expliquer les différents degrés de pyritisation des MRS et d'élucider leur période de mise en place durant la séquence diagénétique. En effet, un enfouissement lent des MRS aurait permis l'accessibilité d'un large réservoir des sulfates pour la sulfato-réduction microbienne, entrainant une vaste pyritisation et des valeurs négatives du $\delta^{34}S$. Au contraire, un enfouissement rapide des MRS aurait provoqué une restriction dans l'accessibilité du réservoir sulfaté pour le processus microbien de sulfato-réduction, ce qui aurait conduit à une pyritisation limitée et des valeurs positives du $\delta^{34}S$.

REFERENCES

Ader M, Boudou J-P, Javoy M, Goffé B, Daniels E (1998) Isotope study on organic nitrogen of Westphalian anthracites from the Western Middle field of Pennsylvania (U.S.A.) and from the Bramsche Massif (Germany). *Organic Geochemistry* **29**, 315–323.

Ader M, Sansjofre P, Halverson GP, Busigny V, Trindade RIF, Kunzmann M, Nogueira ACR (2014) Ocean redox structure across the Late Neoproterozoic Oxygenation Event: A nitrogen isotope perspective. *Earth and Planetary Science Letters* **396**, 1–13.

Ader M, Thomazo C, Sansjofre P, Busigny V, Papineau D, Laffont R, Cartigny P, Halverson GP (2016) Interpretation of the nitrogen isotopic composition of Precambrian sedimentary rocks: Assumptions and perspectives. *Chemical Geology* **429**, 93–110.

Algeo TJ, Tribovillard N (2009) Environmental analysis of paleoceanographic systems based on molybdenum–uranium covariation. *Chemical Geology* **268**, 211–225.

Allwood AC, Rosing MT, Flannery DT, Hurowitz JA, Heirwegh CM (2018) Reassessing evidence of life in 3,700-million-year-old rocks of Greenland. *Nature* **563**, 241–244.

Allwood AC, Walter MR, Kamber BS, Marshall CP, Burch IW (2006) Stromatolite reef from the Early Archaean era of Australia. *Nature* **441**, 714–718.

Altermann W, Schopf JW (1995) Microfossils from the Neoarchean Campbell Group, Griqualand West Sequence of the Transvaal Supergroup, and their paleoenvironmental and evolutionary implications. *Precambrian Research* **75**, 65–90.

Amard B, Bertrand-Sarfati J (1997) Microfossils in 2000 Ma old cherty stromatolites of the Franceville Group, Gabon. *Precambrian Research* **81**, 197–221.

Anbar AD, Duan Y, Lyons TW, Arnold GL, Kendall B, Creaser RA, Kaufman AJ, Gordon GW, Scott C, Garvin J, Buick R (2007) A whiff of oxygen before the Great Oxidation Event? *Science* **317**, 1903–1906.

Anbar AD, Knoll AH (2002) Proterozoic ocean chemistry and evolution: A bioinorganic bridge? *Science* **297**, 1137–1142.

Armstrong-Altrin JS, Lee YI, Verma SP, Ramasamy S (2004) Geochemistry of sandstones from the Upper Miocene Kudankulam Formation, Southern India: Implications for provenance, weathering, and tectonic setting. *Journal of Sedimentary Research* **74**, 285–297.

Arndt N, Barnes SJ, Lesher CM (2008) *Komatiite*. Cambridge University Press, Cambridge.

Arp G, Reimer A, Reitner J (1999) Calcification in cyanobacterial biofilms of alkaline salt lakes. *European Journal of Phycology* **34**, 393–403.

Arp G, Reimer A, Reitner J (2003) Microbialite formation in seawater of increased alkalinity, Satonda Crater Lake, Indonesia. *Journal of Sedimentary Research* **73**, 105–127.

Aspler LB, Chiarenzelli JR (1998) Two Neoarchean supercontinents? Evidence from the Paleoproterozoic. *Sedimentary Geology* **120**, 75–104.

Aubineau J, El Albani A, Bekker A, Somogyi A, Bankole OM, Macchiarelli R, Meunier A, Riboulleau A, Reynaud J-Y, Konhauser KO (2019) Microbially induced potassium enrichment in Paleoproterozoic shales and implications for reverse weathering on early Earth. *Nature Communications* **10**, 2670.

Aubineau J, El Albani A, Chi Fru E, Gingras M, Batonneau Y, Buatois LA, Geffroy C, Labanowski J, Laforest C, Lemée L, Mángano MG, Meunier A, Pierson-Wickmann A-C, Recourt P, Riboulleau A, Trentesaux A, Konhauser KO (2018) Unusual microbial mat-related structural diversity 2.1 billion years ago and implications for the Francevillian biota. *Geobiology* **16**, 476–497.

Awramik S, Margulis L (1974) Definition of stromatolite. *Stromatolite Newsletter* **2**, 5.

Azziley Azzibrouck G (1986) *Sédimentologie et géochimie du Francevillien B (protérozoïque inférieur). Métallogénie des gisements de manganèse de Moanda, Gabon*.

Bachan A, Kump LR (2015) The rise of oxygen and siderite oxidation during the Lomagundi Event. *Proceedings of the National Academy of Sciences* **112**, 6562–6567.

Bailey SW (1980) Structure of layer silicates. In: *Crystal structure of clay minerals and their X-ray identification* (eds. Brindley GW, Brown G). Mineralogical Society, London, pp. 1–123.

Banerjee S, Jeevankumar S (2005) Microbially originated wrinkle structures on sandstone and their stratigraphic context: Palaeoproterozoic Koldaha Shale, central India. *Sedimentary Geology* **176**, 211–224.

Banerjee S, Sarkar S, Eriksson PG, Hu X-F, Wang Y (2014) Palaeoenvironmental and biostratigraphic implications of microbial mat-related structures: Examples from the modern Gulf of Cambay and the Precambrian Vindhyan Basin, India. *Journal of Palaeogeography* **3**, 127–144.

Banerjee S, Sarkar S, Eriksson PG, Samanta P (2010) Microbially related structures in siliciclastic sediment resembling Ediacaran fossils: Examples from India, ancient and modern. In: *Microbial Mats: Modern and Ancient Microorganisms in Stratified Systems* (eds. Seckbach J, Oren A). Springer Netherlands, Dordrecht, pp. 109–129.

Bankole OM (2015) *Diagenetic transformations and redox fluid invasion into siliciclatic FA Formation, Franceville basin (2.2-2.0 Ga), Gabon*.

Bankole OM, El Albani A, Meunier A, Gauthier-Lafaye F (2015) Textural and paleo-fluid flow control on diagenesis in the Paleoproterozoic Franceville Basin, South Eastern, Gabon. *Precambrian Research* **268**, 115–134.

Bankole OM, El Albani A, Meunier A, Pambo F, Paquette J-L, Bekker A (2018) Earth's oldest preserved K-bentonites in the *ca*. 2.1 Ga Francevillian Basin, Gabon. *American Journal of Science* **318**, 409–434.

Bankole OM, El Albani A, Meunier A, Rouxel OJ, Gauthier-Lafaye F, Bekker A (2016) Origin of red beds in the Paleoproterozoic Franceville Basin, Gabon, and implications for sandstone-hosted uranium mineralization. *American Journal of Science* **316**, 839–872.

Barghoorn ES, Tyler SA (1965) Microorganisms from the Gunflint chert. *Science* **147**, 563–577.

Bassett WA (1960) Role of hydroxyl orientation in mica alteration. *Geological Society of America Bulletin* **71**, 449–456.

Battin TJ, Kaplan LA, Newbold JD, Cheng X, Hansen C (2003) Effects of current velocity on the nascent architecture of stream microbial biofilms. *Applied and Environmental Microbiology* **69**, 5443–5452.

Bauersachs T, Schouten S, Compaoré J, Wollenzien U, Stal LJ, Sinninghe Damsteé JS (2009) Nitrogen isotopic fractionation associated with growth on dinitrogen gas and nitrate by cyanobacteria. *Limnology and Oceanography* **54**, 1403–1411.

Bazylinski DA, Frankel RB (2003) Biologically controlled mineralization in prokaryotes. *Reviews in Mineralogy and Geochemistry* **54**, 217–247.

Beam JP, Bernstein HC, Jay ZJ, Kozubal MA, Jennings R deM, Tringe SG, Inskeep WP (2016) Assembly and succession of iron oxide microbial mat communities in acidic geothermal springs. *Frontiers in Microbiology* **7**, 25.

Bebout BM, Paerl HW, Bauer JE, Canfield DE, Des Marais DJ (1994) Nitrogen cycling in microbial mat communities: The quantitative importance of N-fixation and other sources of N for primary productivity. In: *Microbial Mats Structure, Development and Environmental Significance* (eds. Stal LJ, Caumette P). Springer, Berlin, Heidelberg, pp. 265–271.

Bebout GE, Fogel ML (1992) Nitrogen-isotope compositions of metasedimentary rocks in the Catalina Schist, California: Implications for metamorphic devolatilization history. *Geochimica et Cosmochimica Acta* **56**, 2839–2849.

Bekker A (2015a) Great Oxygenation Event. In: *Encyclopedia of Astrobiology* (eds. Gargaud M, Irvine WM, Amils R, Cleaves II HJ, Pinti DL, Quintanilla JC, Rouan D, Spohn T, Tirard S, Viso M). Springer-Verlag, Berlin, Heidelberg, pp. 1009–1017.

Bekker A (2015b) Lomagundi carbon isotope excursion. In: *Encyclopedia of Astrobiology* (eds. Gargaud M, Irvine WM, Amils R, Cleaves II HJ, Pinti DL, Quintanilla JC, Rouan D, Spohn T, Tirard S, Viso M). Springer-Verlag, Berlin, Heidelberg, pp. 1399–1404.

Bekker A, Holland HD (2012) Oxygen overshoot and recovery during the early Paleoproterozoic. *Earth and Planetary Science Letters* **317–318**, 295–304.

Bekker A, Holland HD, Wang P-L, Rumble D, Stein HJ, Hannah JL, Coetzee LL, Beukes NJ (2004) Dating the rise of atmospheric oxygen. *Nature* **427**, 117–120.

Bekker A, Holmden C, Beukes NJ, Kenig F, Eglinton B, Patterson WP (2008) Fractionation between inorganic and organic carbon during the Lomagundi (2.22–2.1 Ga) carbon isotope excursion. *Earth and Planetary Science Letters* **271**, 278–291.

Bekker A, Karhu JA, Eriksson KA, Kaufman AJ (2003) Chemostratigraphy of Paleoproterozoic carbonate successions of the Wyoming craton: Tectonic forcing of biogeochemical change? *Precambrian Research* **120**, 279–325.

Bekker A, Karhu JA, Kaufman AJ (2006) Carbon isotope record for the onset of the Lomagundi carbon isotope excursion in the Great Lakes area, North America. *Precambrian Research* **148**, 145–180.

Bekker A, Slack JF, Planavsky N, Krapez B, Hofmann A, Konhauser KO, Rouxel OJ (2010) Iron Formation: The sedimentary product of a complex interplay among mantle, tectonic, oceanic, and biospheric processes. *Economic Geology* **105**, 467–508.

Bellefroid EJ, Hood A v. S, Hoffman PF, Thomas MD, Reinhard CT, Planavsky NJ (2018) Constraints on Paleoproterozoic atmospheric oxygen levels. *Proceedings of the National Academy of Sciences* **115**, 8104–8109.

Ben Fekih I, Zhang C, Li YP, Zhao Y, Alwathnani HA, Saquib Q, Rensing C, Cervantes C (2018) Distribution of arsenic resistance genes in Prokaryotes. *Frontiers in Microbiology* **9**, 2473.

Benzerara K, Skouri-Panet F, Li J, Férard C, Gugger M, Laurent T, Couradeau E, Ragon M, Cosmidis J, Menguy N, Margaret-Oliver I, Tavera R, Lopez-Garcia P, Moreira D (2014) Intracellular Ca-carbonate biomineralization is widespread in cyanobacteria. *Proceedings of the National Academy of Sciences* **111**, 10933–10938.

Berg IA, Kockelkorn D, Ramos-Vera WH, Say RF, Zarzycki J, Hügler M, Alber BE, Fuchs G (2010) Autotrophic carbon fixation in archaea. *Nature Reviews Microbiology* **8**, 447–460.

Berner RA (1984) Sedimentary pyrite formation: An update. *Geochimica et Cosmochimica Acta* **48**, 605–615.

Berner RA (2004) *The Phanerozoic Carbon Cycle: CO_2 and O_2*. Oxford University Press, Oxford.

Berner RA, Raiswel R (1983) Burial of organic carbon and pyrite sulfur in sediments over Phanerozoic time: A new theory. *Geochimica et Cosmochimica Acta* **47**, 855–682.

Bertrand-Sarfati J, Potin B (1994) Microfossiliferous cherty stromatolites in the 2000 Ma Franceville group, Gabon. *Precambrian research* **65**, 341–356.

Beukes NJ, Lowe DR (1989) Environmental control on diverse stromatolite morphologies in the 3000 Myr Pongola Supergroup, South Africa. *Sedimentology* **36**, 383–397.

Beveridge TJ, Fyfe WS (1985) Metal fixation by bacterial cell walls. *Canadian Journal of Earth Sciences* **22**, 1893–1898.

Billault V, Beaufort D, Patrier P, Petit S (2002) Crystal chemistry of Fe-sudoites from uranium deposits in the Athabasca basin (Saskatchwan, Canada). *Clays and Clay Minerals* **50**, 70–81.

Bindeman IN, Zakharov DO, Palandri J, Greber ND, Dauphas N, Retallack GJ, Hofmann A, Lackey JS, Bekker A (2018) Rapid emergence of subaerial landmasses and onset of a modern hydrologic cycle 2.5 billion years ago. *Nature* **557**, 545–548.

Blättler CL, Claire MW, Prave AR, Kirsimäe K, Higgins JA, Medvedev PV, Romashkin AE, Rychanchik DV, Zerkle AL, Paiste K, Kreitsmann T, Millar IL, Hayles JA, Bao H, Turchyn AV, Warke MR, Lepland A (2018) Two-billion-year-old evaporites capture Earth’s great oxidation. *Science* **360**, 320–323.

Bleeker W (2003) The late Archean record: a puzzle in *ca*. 35 pieces. *Lithos* **71**, 99–134.

Blumenberg M, Thiel V, Riegel W, Kah LC, Reitner J (2012) Biomarkers of black shales formed by microbial mats, Late Mesoproterozoic (1.1 Ga) Taoudeni Basin, Mauritania. *Precambrian Research* **196–197**, 113–127.

Boles JR, Franks SG (1979) Clay diagenesis in Wilcox sandstones of southwest Texas: Implications of smectite diagenesis on sandstone cementation. *Journal of Sedimentary Petrology* **49**, 55–70.

Bolhar R, Kamber BS, Moorbath S, Fedo CM, Whitehouse MJ (2004) Characterisation of early Archaean chemical sediments by trace element signatures. *Earth and Planetary Science Letters* **222**, 43–60.

Bonhomme MG, Gauthier-Lafaye F, Weber F (1982) An example of Lower Proterozoic sediments: The Francevillian in Gabon. *Precambrian Research* **18**, 87–102.

Bosak T, Bush JWM, Flynn MR, Liang B, Ono S, Petroff AP, Sim MS (2010) Formation and stability of oxygen-rich bubbles that shape photosynthetic mats. *Geobiology* **8**, 45–55.

Bosak T, Knoll AH, Petroff AP (2013) The meaning of stromatolites. *Annual Review of Earth and Planetary Sciences* **41**, 21–44.

Bosak T, Liang B, Sim MS, Petroff AP (2009) Morphological record of oxygenic photosynthesis in conical stromatolites. *Proceedings of the National Academy of Sciences* **106**, 10939–10943.

Bose S, Chafetz HS (2009) Topographic control on distribution of modern microbially induced sedimentary structures (MISS): A case study from Texas coast. *Sedimentary Geology* **213**, 136–149.

Bottjer DJ, Hagadorn JW (2007) Mat-growth features. In: *Atlas of Microbial Mat Features Preserved within the Siliciclastic Rock Record* (eds. Schieber J, Bose PK, Eriksson PG, Banerjee S, Sarkar S, Altermann W, Catuneanu O). Elsevier, Amsterdam, pp. 53–71.

Bottjer DJ, Hagadorn JW, Dornbos SQ (2000) The Cambrian substrate revolution. *GSA Today* **10**, 1–7.

Bouougri EH, Porada H (2007) Mat-related features from the terminal Ediacaran Nudaus Formation, Nama Group, Namibia. In: *Atlas of Microbial Mat Features Preserved within the Siliciclastic Rock Record* (eds. Schieber J, Bose PK, Eriksson PG, Banerjee S, Sarkar S, Altermann W, Catuneanu O). Elsevier, Amsterdam, pp. 214–222.

Bouton P, Thiéblemont D, Gouin J, Cocherie A, Guerrot C, Tegyey M, Préat A, Simo Ndounze S, Kassadou AB, Boulingui B, Ekhogha H, Moussavou M (2009a) Notice explicative de la Carte géologique de la République du Gabon à 1/200,000, feuille Franceville-Boumango, Libreville.

Bouton P, Thiéblemont D, Simo Ndounze S, Goujou JC, Kassadou AB, Walemba A, Boulingui B, Ekhogha H, Moussavou M, Lambert A, Roberts D, Deschamps Y, Préat A (2009b) Carte géologique de la République du Gabon à 1/200 000, feuille Franceville - Boumango.

Braissant O, Decho AW, Dupraz C, Glunk C, Przekop KM, Visscher PT (2007) Exopolymeric substances of sulfate-reducing bacteria: Interactions with calcium at alkaline pH and implication for formation of carbonate minerals. *Geobiology* **5**, 401–411.

Brasier A, Wacey D, Rogerson M, Guagliardo P, Saunders M, Kellner S, Mercedes-Martin R, Prior T, Taylor C, Matthews A, Reijmer J (2018) A microbial role in the construction of Mono Lake carbonate chimneys? *Geobiology* **16**, 540–555.

Brasier MD, Green OR, Jephcoat AP, Kleppe AK, van Kranendonk MJ, Lindsay JF, Steele A, Grassineau NV (2002) Questioning the evidence for Earth's oldest fossils. *Nature* **416**, 76–81.

Brasier MD, Green OR, Lindsay JF, Mcloughlin N, Steele A, Stoakes C (2005) Critical testing of Earth's oldest putative fossil assemblage from the ∼3.5Ga Apex chert, Chinaman Creek, Western Australia. *Precambrian Research* **140**, 55–102.

Brayner R, Coradin T, Beaunier P, Grenèche J-M, Djediat C, Yéprémian C, Couté A, Fiévet F (2012) Intracellular biosynthesis of superparamagnetic 2-lines ferri-hydrite nanoparticles using *Euglena gracilis* microalgae. *Colloids and Surfaces B: Biointerfaces* **93**, 20–23.

Brindley GW, Brown G (1980) *Crystal structure of clay minerals and their X-ray identification*. Mineralogical Society, London.

Brocks JJ, Buick R, Summons RE, Logan GA (2003) A reconstruction of Archean biological diversity based on molecular fossils from the 2.78 to 2.45 billion-year-old Mount Bruce Supergroup, Hamersley Basin, Western Australia. *Geochimica et Cosmochimica Acta* **67**, 4321–4335.

Brocks JJ, Jarrett AJM, Sirantoine E, Hallmann C, Hoshino Y, Liyanage T (2017) The rise of algae in Cryogenian oceans and the emergence of animals. *Nature* **548**, 578–581.

Brocks JJ, Logan GA, Buick R, Summons RE (1999) Archean molecular fossils and the early rise of eukaryotes. *Science* **285**, 1033–1036.

Brocks JJ, Love GD, Summons RE, Knoll AH, Logan GA, Bowden SA (2005) Biomarker evidence for green and purple sulphur bacteria in a stratified Palaeoproterozoic sea. *Nature* **437**, 866–870.

Bros R, Stille P, Gauthier-Lafaye F, Weber F, Clauer N (1992) Sm-Nd isotopic dating of Proterozoic clay material: An example from the Francevillian sedimentary series, Gabon. *Earth and Planetary Science Letters* **113**, 207–218.

Brown II, Bryant DA, Casamatta D, Thomas-Keprta KL, Sarkisova SA, Shen G, Graham JE, Boyd ES, Peters JW, Garrison DH, McKay DS (2010) Polyphasic characterization of a yhermotolerant siderophilic filamentous cyanobacterium that produces intracellular iron deposits. *Applied and Environmental Microbiology* **76**, 6664–6672.

Buatois LA, Mángano MG (2003) Early colonization of the deep sea: Ichnologic evidence of deep-marine benthic ecology from the Early Cambrian of northwest Argentina. *Palaios* **18**, 572–581.

Buatois LA, Mángano MG (2012) The trace-fossil record of organism-matground interactions in space and time. In: *Microbial Mats in Silicilastic Depositional Systems Through Time* (eds. Noffke N, Chafetz H). SEPM (Society for Sedimentary Geology) Special Publication, Tulsa, Oklahoma, pp. 15–28.

Buatois LA, Narbonne GM, Mángano MG, Carmona NB, Myrow P (2014) Ediacaran matground ecology persisted into the earliest Cambrian. *Nature Communications* **5**, 3544.

Buick R (1990) Microfossil recognition in Archean rocks: An appraisal of spheroids and filaments from a 3500 M.y. old chert-barite Unit at North Pole, Western Australia. *Palaios* **5**, 441–459.

Buick R (2008) When did oxygenic photosynthesis evolve? *Philosophical Transactions of the Royal Society B: Biological Sciences* **363**, 2731–2743.

Burne RV, Moore LS (1987) Microbialites: Organosedimentary deposits of benthic microbial communities. *Palaios* **2**, 241–254.

Cam N, Benzerara K, Georgelin T, Jaber M, Lambert J-F, Poinsot M, Skouri-Panet F, Moreira D, López-García P, Raimbault E, Cordier L, Jézéquel D (2018) Cyanobacterial formation of intracellular Ca-carbonates in undersaturated solutions. *Geobiology* **16**, 49–61.

Canfield DE, Des Marais DJ (1993) Biogeochemical cycles of carbon, sulfur, and free oxygen in a microbial mat. *Geochimica et Cosmochimica Acta* **57**, 3971–3984.

Canfield DE, Glazer AN, Falkowski PG (2010) The evolution and future of Earth's nitrogen cycle. *Science* **330**, 192–196.

Canfield DE, Jørgensen BB, Fossing H, Glud R, Gundersen J, Ramsing NB, Thamdrup B, Hansen JW, Nielsen LP, Hall POJ (1993) Pathways of organic carbon oxidation in three continental margin sediments. *Marine Geology* **113**, 27–40.

Canfield DE, Ngombi-Pemba L, Hammarlund EU, Bengtson S, Chaussidon M, Gauthier-Lafaye F, Meunier A, Riboulleau A, Rollion-Bard C, Rouxel O, Asael D, Pierson-Wickmann A-C, El Albani A (2013) Oxygen dynamics in the aftermath of the Great Oxidation of Earth's atmosphere. *Proceedings of the National Academy of Sciences* **110**, 16736–16741.

Canfield DE, Raiswell R, Westrich JT, Reaves CM, Berner RA (1986) The use of chromium reduction in the analysis of reduced inorganic sulfur in sediments and shales. *Chemical Geology* **54**, 149–155.

Canfield DE, Thamdrup B (1994) The production of ^{34}S-depleted sulfide during bacterial disproportionation of elemental sulfur. *Science* **266**, 1973–1975.

Capone DG, Hutchins DA (2013) Microbial biogeochemistry of coastal upwelling regimes in a changing ocean. *Nature Geoscience* **6**, 711–717.

Capone DG, Subramaniam A, Montoya JP, Voss M, Humborg C, Johansen AM, Siefert RL, Carpenter EJ (1998) An extensive bloom of the N_2-fixing cyanobacterium *Trichodesmium erythraeum* in the central Arabian Sea. *Marine Ecology Progress Series* **172**, 281–292.

Carignan J, Hild P, Mevelle G, Morel J, Yeghicheyan D (2001) Routine analyses of trace elements in geological samples using flow injection and low pressure on-line liquid chromatography coupled to ICP-MS: a study of geochemical reference materials BR, DR-N, UB-N, AN-G and GH. *Geostandards Newsletter* **25**, 187–198.

Casciotti KL (2009) Inverse kinetic isotope fractionation during bacterial nitrite oxidation. *Geochimica et Cosmochimica Acta* **73**, 2061–2076.

Casciotti KL, Sigman DM, Ward BB (2003) Linking diversity and stable isotope fractionation in ammonia-oxidizing bacteria. *Geomicrobiology Journal* **20**, 335–353.

Chandler FW (1980) *Proterozoic redbed sequences of Canada*. Geological Survey Bulletin 311.

Chang C, Hu W, Wang X, Huang K-J, Yang A, Zhang X (2019) Nitrogen isotope evidence for an oligotrophic shallow ocean during the Cambrian Stage 4. *Geochimica et Cosmochimica Acta* **257**, 49–67.

Chappaz A, Lyons TW, Gregory DD, Reinhard CT, Gill BC, Li C, Large RR (2014) Does pyrite act as an important host for molybdenum in modern and ancient euxinic sediments? *Geochimica et Cosmochimica Acta* **126**, 112–122.

Checchetto V, Segalla A, Allorent G, La Rocca N, Leanza L, Giacometti GM, Uozumi N, Finazzi G, Bergantino E, Szabo I (2012) Thylakoid potassium channel is required for efficient photosynthesis in cyanobacteria. *Proceedings of the National Academy of Sciences* **109**, 11043–11048.

Chen S-C, Sun G-X, Rosen BP, Zhang S-Y, Deng Y, Zhu B-K, Rensing C, Zhu Y-G (2017) Recurrent horizontal transfer of arsenite methyltransferase genes facilitated adaptation of life to arsenic. *Scientific Reports* **7**, 7741.

Chi Fru E, Arvestål E, Callac N, El Albani A, Kilias S, Argyraki A, Jakobsson M (2015) Arsenic stress after the Proterozoic glaciations. *Scientific Reports* **5**, 1778.

Chi Fru E, Callac N, Posth NR, Argyraki A, Ling Y-C, Ivarsson M, Broman C, Kilias SP (2018a) Arsenic and high affinity phosphate uptake gene distribution in shallow submarine hydrothermal sediments. *Biogeochemistry* **141**, 41–62.

Chi Fru E, Kilias S, Ivarsson M, Rattray JE, Gkika K, McDonald I, He Q, Broman C (2018b) Sedimentary mechanisms of a modern banded iron formation on Milos Island, Greece. *Solid Earth* **9**, 573–598.

Chi Fru E, Somogyi A, El Albani A, Medjoubi K, Aubineau J, Robbins LJ, Lalonde SV, Konhauser KO (2019) The rise of oxygen-driven arsenic cycling at *ca*. 2.48 Ga. *Geology* **47**, 243–246.

Christner BC, Priscu JC, Achberger AM, Barbante C, Carter SP, Christianson K, Michaud AB, Mikucki JA, Mitchell AC, Skidmore ML, Vick-Majors TJ, the WISSARD Science Team (2014) A microbial ecosystem beneath the West Antarctic ice sheet. *Nature* **512**, 310–313.

Chu D, Tong J, Bottjer DJ, Song H, Song H, Benton MJ, Tian L, Guo W (2017) Microbial mats in the terrestrial Lower Triassic of North China and implications for the Permian–Triassic mass extinction. *Palaeogeography, Palaeoclimatology, Palaeoecology* **474**, 214–231.

Chu D, Tong J, Song H, Benton MJ, Bottjer DJ, Song H, Tian L (2015) Early Triassic wrinkle structures on land: Stressed environments and oases for life. *Scientific Reports* **5**.

Clarkson MO, Poulton SW, Guilbaud R, Wood RA (2014) Assessing the utility of Fe/Al and Fe-speciation to record water column redox conditions in carbonate-rich sediments. *Chemical Geology* **382**, 111–122.

Cloud Jr. PE (1965) Significance of the Gunflint (Precambrian) Microflora: Photosynthetic oxygen may have had important local effects before becoming a major atmospheric gas. *Science* **148**, 27–35.

Condie KC, O'Neill C, Aster RC (2009) Evidence and implications for a widespread magmatic shutdown for 250 My on Earth. *Earth and Planetary Science Letters* **282**, 294–298.

Conrad R, Claus P, Casperb P (2010) Stable isotope fractionation during the methanogenic degradation of organic matter in the sediment of an acidic bog lake, Lake Grosse Fuchskuhle. *Limnology and Oceanography* **55**, 1932–1942.

Coplen TB, Böhlke JK, De Bievre P, Ding T, Holden N, Hopple J, Krouse H, Lamberty A, Peiser H, Revesz K (2002) Isotope-abundance variations of selected elements. *Pure and Applied Chemistry* **74**, 1987–2017.

Cortial F, Gauthier-Lafaye F, Lacrampe-Couloume G, Oberlin A, Weber F (1990) Characterization of organic matter associated with uranium deposits in the Francevillian formation of Gabon (lower proterozoic). *Organic Geochemistry* **15**, 73–85.

Costerton JW, Lewandowski Z, Caldwell DE, Korber DR, Lappin-Scott HM (1995) Microbial biofilms. *Annual review of microbiology* **49**, 711–745.

Couradeau E, Benzerara K, Gérard E, Moreira D, Bernard S, Brown Jr GE, Lopez-Garcia P (2012) An early-branching microbialite cyanobacterium forms intracellular carbonates. *Science* **336**, 459–462.

Crowe SA, Paris G, Katsev S, Jones C, Kim S-T, Zerkle AL, Nomosatryo S, Fowle DA, Adkins JF, Sessions AL, Farquhar J, Canfield DE (2014) Sulfate was a trace constituent of Archean seawater. *Science* **346**, 735–739.

Cuadros J (2017) Clay minerals interaction with microorganisms: A review. *Clay Minerals* **52**, 235–261.

Cullen WR, Reimer KJ (1989) Arsenic speciation in the environment. *Chemical reviews* **89**, 713–764.

Cutter GA, Cutter LS (2006) Biogeochemistry of arsenic and antimony in the North Pacific Ocean. *Geochemistry, Geophysics, Geosystems* **7**, Q05M08.

D'Agrella-Filho MS, Cordani UG (2017) The paleomagnetic record of the São Francisco-Congo craton. In: *São Francisco craton, tectonic genealogy of a miniature continent, Eastern Brazil* (eds. Heilbron M, Cordani UG, Alkmim FF). Springer International Publishing, Berlin, pp. 305–320.

Dalsgaard T, Thamdrup B, Canfield DE (2005) Anaerobic ammonium oxidation (anammox) in the marine environment. *Research in Microbiology* **156**, 457–464.

Davies NS, Liu AG, Gibling MR, Miller RF (2016) Resolving MISS conceptions and misconceptions: A geological approach to sedimentary surface textures generated by microbial and abiotic processes. *Earth-Science Reviews* **154**, 210–246.

De Philippis R, Sili C, Paperi R, Vincenzini M (2001) Exopolysaccharide-producing cyanobacteria and their possible exploitation: A review. *Journal of Applied Phycology* **13**, 293–299.

Decho AW (1990) Microbial exopolymer secretions in ocean environments: their role (s) in food webs and marine processes. *Oceanography and Marine Biology: An Annual Review* **28**, 73–153.

Decho AW (2000) Microbial biofilms in intertidal systems: An overview. *Continental Shelf Research* **20**, 1257–1273.

Decho AW, Visscher PT, Reid RP (2005) Production and cycling of natural microbial exopolymers (EPS) within a marine stromatolite. *Palaeogeography, Palaeoclimatology, Palaeoecology* **219**, 71–86.

Des Marais DJ (2010) Marine hypersaline *Microcoleus*-dominated cyanobacterial mats in the saltern at Guerrero Negro, Baja California Sur, Mexico: A system-level perspective. In: *Microbial Mats: Modern and Ancient Microorganisms in Stratified Systems* (eds. Seckbach J, Oren A). Springer Netherlands, Dordrecht, pp. 403–420.

Deutsch C, Sarmiento JL, Sigman DM, Gruber N, Dunne JP (2007) Spatial coupling of nitrogen inputs and losses in the ocean. *Nature* **445**, 163–167.

Djokic T, van Kranendonk MJ, Campbell KA, Walter MR, Ward CR (2017) Earliest signs of life on land preserved in *ca.* 3.5 Ga hot spring deposits. *Nature Communications* **8**, 15263.

Dodd MS, Papineau D, Grenne T, Slack JF, Rittner M, Pirajno F, O'Neil J, Little CTS (2017) Evidence for early life in Earth's oldest hydrothermal vent precipitates. *Nature* **543**, 60–64.

Doyle DA (1998) The structure of the potassium channel: Molecular basis of K^+ conduction and selectivity. *Science* **280**, 69–77.

Drits VA (1993) X-ray identification of one-layer illite varieties: Application to the study of illites around uranium deposits of Canada. *Clays and Clay Minerals* **41**, 389–398.

Drits VA, Sakharov BA, Lindgreen H, Salyn A (1997) Sequential structure transformation of illite-smectite-vermiculite during diagenesis of Upper Jurassic shales from the North Sea and Denmark. *Clay Minerals* **32**, 351–371.

Drits VA, Tchoubar C (1990) *X-ray diffraction by disordered lamellar structures: Theory and applications to microdivided silicates and carbons*. Springer-Verlag, Berlin.

Dubois M (2017) *Environnement de dépôt et processus de formation des carbonates de manganèse dans les black shales paléoprotérozoiques du Bassin de Franceville (2.1 Ga ; Gabon).*

Dubois M, Lopez M, Orberger B, Rodriguez C, Boussafir M, Dreux G, Rodrigues S, Pambo F (2015) The Mn-Carbonate Rich Black Shales of the Bangombe Plateau, Francevillian Basin, Gabon. In: *Mineral Ressources in a Sustainable World* (eds. André-Mayer AS, Cathelineau M, Muchez Ph, Pirard E, Sindern S). Presented at the Proceedings of the 13th Biennial SGA Meeting, Nancy, France, pp. 1905–1908.

Dupraz C, Reid RP, Braissant O, Decho AW, Norman RS, Visscher PT (2009) Processes of carbonate precipitation in modern microbial mats. *Earth-Science Reviews* **96**, 141–162.

Dupraz C, Visscher PT (2005) Microbial lithification in marine stromatolites and hypersaline mats. *Trends in Microbiology* **13**, 429–438.

Dutkiewicz A, George SC, Mossman DJ, Ridley J, Volk H (2007) Oil and its biomarkers associated with the Palaeoproterozoic Oklo natural fission reactors, Gabon. *Chemical Geology* **244**, 130–154.

Dyhrman S, Haley ST (2011) Arsenate resistance in the unicellular marine diazotroph *Crocosphaera watsonii*. *Frontiers in Microbiology* **2**, 214.

El Albani A, Bengtson S, Canfield DE, Bekker A, Macchiarelli R, Mazurier A, Hammarlund EU, Boulvais P, Dupuy J-J, Fontaine C, Fürsich FT, Gauthier-Lafaye F, Janvier P, Javaux E, Ossa FO, Pierson-Wickmann A-C, Riboulleau A, Sardini P, Vachard D, Whitehouse M, Meunier A (2010) Large colonial organisms with coordinated growth in oxygenated environments 2.1 Gyr ago. *Nature* **466**, 100–104.

El Albani A, Bengtson S, Canfield DE, Riboulleau A, Rollion Bard C, Macchiarelli R, Ngombi Pemba L, Hammarlund E, Meunier A, Moubiya Mouele I, Benzerara K, Bernard S, Boulvais P, Chaussidon M, Cesari C, Fontaine C, Chi-Fru E, Garcia Ruiz JM, Gauthier-Lafaye F, Mazurier A, Pierson-Wickmann AC, Rouxel O, Trentesaux A, Vecoli M, Versteegh GJM, White L, Whitehouse M, Bekker A (2014) The 2.1 Ga old Francevillian biota: Biogenicity, taphonomy and biodiversity. *PLoS ONE* **9**, e99438.

El Albani A, Mangano MG, Buatois LA, Bengtson S, Riboulleau A, Bekker A, Konhauser K, Lyons T, Rollion-Bard C, Bankole O, Lekele Baghekema SG, Meunier A, Trentesaux A, Mazurier A, Aubineau J, Laforest C, Fontaine C, Recourt P, Chi Fru E, Macchiarelli R, Reynaud JY, Gauthier-Lafaye F, Canfield DE (2019) Organism motility in an oxygenated shallow-marine environment 2.1 billion years ago. *Proceedings of the National Academy of Sciences* **116**, 3431–3436.

Epstein W (2003) The roles and regulation of potassium in bacteria. *Progress in Nucleic Acid Research and Molecular Biology* **75**, 293–320.

Eriksson PG, Sarkar S, Samanta P, Banerjee S, Porada H, Catuneanu O (2010) Paleoenvironmental context of microbial mat-related structures in siliciclastic rocks. In: *Microbial Mats: Modern and Ancient Microorganisms in Stratified Systems* (eds. Seckbach J, Oren A). Springer Netherlands, Dordrecht, pp. 71–108.

Eriksson PG, Schieber J, Bouougri EH, Gerdes G, Porada H, Banerjee S, Bose PK, Sarkar S (2007) Classification of structures left by microbial mats in their host sediments. In: *Atlas of Microbial Mat Features Preserved within the Siliciclastic Rock Record*. Elsevier, Amsterdam, pp. 39–52.

Evans DAD (2013) Reconstructing pre-Pangean supercontinents. *Geological Society of America Bulletin* **125**, 1735–1751.

Evensen N, Hamilton P, O'Nions R (1978) Rare-earth abundances in chondritic meteorites. *Geochimica et Cosmochimica Acta* **42**, 1199–1212.

Fakhraee M, Hancisse O, Canfield DE, Crowe SA, Katsev S (2019) Proterozoic seawater sulfate scarcity and the evolution of ocean–atmosphere chemistry. *Nature Geoscience* **12**, 375–380.

Falkowski PG, Fenchel T, Delong EF (2008) The microbial engines that drive Earth's biogeochemical cycles. *Science* **320**, 1034–1039.

Farquhar J, Bao H, Thiemens M (2000) Atmospheric influence of Earth's earliest sulfur cycle. *Science* **289**, 756–758.

Farquhar J, Savarino J, Airieau S, Thiemens MH (2001) Observation of wavelength-sensitive mass-independent sulfur isotope effects during SO_2 photolysis: Implications for the early atmosphere. *Journal of Geophysical Research* **106**, 32829–32839.

Farquhar J, Wu N, Canfield DE, Oduro H (2010) Connections between sulfur cycle evolution, sulfur isotopes, sediments, and base metal sulfide deposits. *Economic Geology* **105**, 509–533.

Farquhar J, Zerkle AL, Bekker A (2011) Geological constraints on the origin of oxygenic photosynthesis. *Photosynthesis Research* **107**, 11–36.

Fay P (1992) Oxygen relations of nitrogen fixation in cyanobacteria. *Microbiological Reviews* **56**, 340–373.

Fennel K, Follows M, Falkowski PG (2005) The co-evolution of the nitrogen, carbon and oxygen cycles in the Proterozoic ocean. *American Journal of Science* **305**, 526–545.

Ferrage E, Vidal O, Mosser-Ruck R, Cathelineau M, Cuadros J (2011) A reinvestigation of smectite illitization in experimental hydrothermal conditions: Results from X-ray diffraction and transmission electron microscopy. *American Mineralogist* **96**, 207–223.

Feybesse JL, Johan V, Triboulet C, Guerrot C, Mayaga-Mikolo F, Bouchot V, Eko N'dong J (1998) The West Central African belt: A model of 2.5–2.0Ga accretion and two-phase orogenic evolution. *Precambrian Research* **87**, 161–216.

Flannery DT, Allwood AC, Van Kranendonk MJ (2016) Lacustrine facies dependence of highly ^{13}C-depleted organic matter during the global age of methanotrophy. *Precambrian Research* **285**, 216–241.

Flannery DT, Walter MR (2012) Archean tufted microbial mats and the Great Oxidation Event: New insights into an ancient problem. *Australian Journal of Earth Sciences* **59**, 1–11.

Flemming H-C, Wingender J, Szewzyk U, Steinberg P, Rice SA, Kjelleberg S (2016) Biofilms: An emergent form of bacterial life. *Nature Reviews Microbiology* **14**, 563–575.

Flood BE, Bailey JV, Biddle JF (2014) Horizontal gene transfer and the rock record: Comparative genomics of phylogenetically distant bacteria that induce wrinkle structure formation in modern sediments. *Geobiology* **12**, 119–132.

Fortin D, Ferris FG, Scott SD (1998) Formation of Fe-silicates and Fe-oxides on bacterial surfaces in samples collected near hydrothermal vents on the Southern Explorer Ridge in the northeast Pacific Ocean. *American Mineralogist* **83**, 1399–1408.

Frankel RB, Bazylinski DA (2003) Biologically induced mineralization by bacteria. *Reviews in Mineralogy and Geochemistry* **54**, 95–114.

Frei R, Gaucher C, Poulton SW, Canfield DE (2009) Fluctuations in Precambrian atmospheric oxygenation recorded by chromium isotopes. *Nature* **461**, 250–253.

French KL, Hallmann C, Hope JM, Schoon PL, Zumberge JA, Hoshino Y, Peters CA, George SC, Love GD, Brocks JJ, Buick R, Summons RE (2015) Reappraisal of hydrocarbon biomarkers in Archean rocks. *Proceedings of the National Academy of Sciences* **112**, 5915–5920.

Fulton JM, Arthur MA, Freeman KH (2012) Black Sea nitrogen cycling and the preservation of phytoplankton δ^{15}N signals during the Holocene. *Global Biogeochemical Cycles* **26**, GB2030.

Gancarz AJ (1978) U-Pb age (2.05 × 10^9 years) of the Oklo uranium deposit. Presented at the The Natural Fission Reactors: Annual International Atomic Energy Agency Conference, Vienna, Austria, pp. 513–520.

Garcia-Ruiz JM, Hyde ST, Carnerup AM, van Kranendonk MJ, Welham NJ (2003) Self-assembled silica-carbonate structures and detection of ancient microfossils. *Science* **302**, 1194–1197.

Garlick WG (1988) Algal mats, load structures, and synsedimentary sufides in Revett quartzites of Montana and Idaho. *Economic Geology* **83**, 1259–1278.

Garvin J, Buick R, Anbar AD, Arnold GL, Kaufman AJ (2009) Isotopic evidence for an aerobic nitrogen cycle in the Latest Archean. *Science* **323**, 1045–1048.

Gauthier-Lafaye F (1986) *Les gisements d'uranium du Gabon et les réacteurs d'Oklo. Modèle métallogénique de gîtes à fortes teneurs du protérozoique inférieur*.

Gauthier-Lafaye F (2006) Time constraint for the occurrence of uranium deposits and natural nuclear fission reactors in the Paleoproterozoic Franceville Basin (Gabon). *Geological Society of America Memoirs* **198**, 157–167.

Gauthier-Lafaye F, Weber F (1989) The Francevillian (Lower Proterozoic) uranium ore deposits of Gabon. *Economic Geology* **84**, 2267–2285.

Gauthier-Lafaye F, Weber F (2003) Natural nuclear fission reactors: Time constraints for occurrence, and their relation to uranium and manganese deposits and to the evolution of the atmosphere. *Precambrian Research* **120**, 81–100.

Gehling JG (1999) Microbial mats in terminal Proterozoic siliciclastics: Ediacaran death masks. *Palaios* **14**, 40–57.

Gerdes G (2007) Structures left by modern microbial mats in their host sediments. In: *Atlas of Microbial Mat Features Preserved within the Siliciclastic Rock Record* (eds. Schieber J, Bose PK, Eriksson PG, Banerjee S, Sarkar S, Altermann W, Catuneanu O). Elsevier, Amsterdam, pp. 5–38.

Gerdes G, Claes M, Dunajtschik-Piewak K, Riege H, Krumbein WE, Reineck H-E (1993) Contribution of microbial mats to sedimentary surface structures. *Facies* **29**, 61.

Gerdes G, Klenke T, Noffke N (2000) Microbial signatures in peritidal siliciclastic sediments: A catalogue. *Sedimentology* **47**, 279–308.

Gerdes G, Krumbein WE, Reineck H-E (1994) Microbial mats as architects of sedimentary surface structures. In: *Biostabilization of Sediments* (eds. Krumbein WE, Paterson DM, Stal LJ). Bibliotheks und Informationsystem der Carl von Ossietzky Universität Oldenberg (BIS)-Verlag, Oldenburg, pp. 165–182.

Gingras M, Hagadorn JW, Seilacher A, Lalonde SV, Pecoits E, Petrash D, Konhauser KO (2011) Possible evolution of mobile animals in association with microbial mats. *Nature Geoscience* **4**, 372–375.

Glass JB, Wolfe-Simon F, Anbar A (2009) Coevolution of metal availability and nitrogen assimilation in cyanobacteria and algae. *Geobiology* **7**, 100–123.

Gold DA, Caron A, Fournier GP, Summons RE (2017) Paleoproterozoic sterol biosynthesis and the rise of oxygen. *Nature* **543**, 420–423.

Grantham PJ, Wakefield LL (1988) Variations in the sterane carbon number distributions of marine source rock derived crude oils through geological time. *Organic Geochemistry* **12**, 61–73.

Grathoff GH, Moore DM, Hay RL, Wemmer K (2001) Origin of illite in the lower Paleozoic of the Illinois basin: Evidence for brine migrations. *Geological Society of America Bulletin* **113**, 1092–1104.

Grazhdankin D, Gerdes G (2007) Ediacaran microbial colonies: Ediacaran microbial colonies. *Lethaia* **40**, 201–210.

Greber ND, Dauphas N, Bekker A, Ptáček MP, Bindeman IN, Hofmann A (2017) Titanium isotopic evidence for felsic crust and plate tectonics 3.5 billion years ago. *Science* **357**, 1271–1274.

Gregory DD, Large RR, Halpin JA, Baturina EL, Lyons TW, Wu S, Danyushevsky L, Sack PJ, Chappaz A, Maslennikov VV, Bull SW (2015) Trace element content of sedimentary pyrite in black shales. *Economic Geology* **110**, 1389–1410.

Gregory DD, Lyons TW, Large RR, Jiang G, Stepanov AS, Diamond CW, Figueroa MC, Olin P (2017) Whole rock and discrete pyrite geochemistry as complementary tracers of ancient ocean chemistry: An example from the Neoproterozoic Doushantuo Formation, China. *Geochimica et Cosmochimica Acta* **216**, 201–220.

Grotzinger JP, Knoll AH (1999) Stromatolites in Precambrian carbonates: Evolutionary mileposts or environmental dipsticks? *Annual Review of Earth and Planetary Sciences* **27**, 313–358.

Gruber N, Galloway JN (2008) An Earth-system perspective of the global nitrogen cycle. *Nature* **451**, 293–296.

Gumsley AP, Chamberlain KR, Bleeker W, Söderlund U, de Kock MO, Larsson ER, Bekker A (2017) Timing and tempo of the Great Oxidation Event. *Proceedings of the National Academy of Sciences* **114**, 1811–1816.

Habicht KS, Gade M, Thamdrup B, Berg P, Canfield DE (2002) Calibration of sulfate levels in the Archean ocean. *Science* **298**, 2372–2374.

Hagadorn JW, Bottjer DJ (1997) Wrinkle structures: Microbially mediated sedimentary structures common in subtidal siliciclastic settings at the Proterozoic-Phanerozoic transition. *Geology* **25**, 1047–1050.

Haines SH, van der Pluijm BA (2008) Clay quantification and Ar–Ar dating of synthetic and natural gouge: Application to the Miocene Sierra Mazatán detachment fault, Sonora, Mexico. *Journal of Structural Geology* **30**, 525–538.

Hayes JM, Freeman KH, Popp BN, Hoham CH (1990) Compound-specific isotopic analyses: A novel tool for reconstruction of ancient biogeochemical processes. *Organic Geochemistry* **16**, 1115–1128.

Hayes JM, Strauss H, Kaufman AJ (1999) The abundance of ^{13}C in marine organic matter and isotopic fractionation in the global biogeochemical cycle of carbon during the past 800 Ma. *Chemical Geology* **161**, 103–125.

He J, Hu H, Qiu W, Liu J, Liu M, Zhao C, Shi X, Xu J (2016) Community diversity and biofilm characteristic response to low temperature and low C/N ratio in a suspended carrier biofilm reactor. *Desalination and Water Treatment* **57**, 22212–22222.

Helly JJ, Levin LA (2004) Global distribution of naturally occurring marine hypoxia on continental margins. *Deep Sea Research I* **51**, 1159–1168.

Herbert RA (1999) Nitrogen cycling in coastal marine ecosystems. *FEMS Microbiology Reviews* **23**, 563–590.

Hiebert RS, Bekker A, Houlé MG, Rouxel OJ (2018) Depositional setting of the Late Archean Fe oxide- and sulfide-bearing chert and graphitic argillite in the Shaw Dome, Abitibi greenstone belt, Canada. *Precambrian Research* **311**, 98–116.

Hill C, Corcoran PL, Aranha R, Longstaffe FJ (2016) Microbially induced sedimentary structures in the Paleoproterozoic, Upper Huronian Supergroup, Canada. *Precambrian Research* **281**, 155–165.

Hoch MP, Fogel ML, Kirchman DL (1992) Isotope fractionation associated with ammonium uptake by a marine bacterium. *Limnology and Oceanography* **37**, 1447–1459.

Hoehler TM, Bebout BM, Des Marais DJ (2001) The role of microbial mats in the production of reduced gases on the early Earth. *Nature* **412**, 324–327.

Hoffman PF (2013) The Great Oxidation and a Siderian snowball Earth: MIF-S based correlation of Paleoproterozoic glacial epochs. *Chemical Geology* **362**, 143–156.

Hofmann A, Bekker A, Rouxel O, Rumble D, Master S (2009) Multiple sulphur and iron isotope composition of detrital pyrite in Archaean sedimentary rocks: A new tool for provenance analysis. *Earth and Planetary Science Letters* **286**, 436–445.

Holland HD (1984) *The chemical evolution of the atmosphere and oceans*. Princeton University Press, Princeton, NJ.

Holland HD (2002) Volcanic gases, black smokers, and the Great Oxidation Event. *Geochimica et Cosmochimica Acta* **66**, 3811–3826.

Homann M, Heubeck C, Airo A, Tice MM (2015) Morphological adaptations of 3.22 Ga-old tufted microbial mats to Archean coastal habitats (Moodies Group, Barberton Greenstone Belt, South Africa). *Precambrian Research* **266**, 47–64.

Horie K, Hidaka H, Gauthier-Lafaye F (2005) U-Pb geochronology and geochemistry of zircon from the Franceville series at Bidoudouma, Gabon. Presented at the 15th Annual Goldschmidt Conference, Moscow, United States.

Hower J, Eslinger EV, Hower ME, Perry Jr EA (1976) Mechanism of burial metamorphism of argillaceous sediment: 1. Mineralogical and chemical evidence. *Geological Society of America Bulletin* **87**, 725.

Huerta-Diaz MA, Delgadillo-Hinojosa F, Otero XL, Segovia-Zavala JA, Martin Hernandez-Ayon J, Galindo-Bect MS, Amaro-Franco E (2011) Iron and trace metals in microbial mats and underlying sediments: Results from Guerrero Negro saltern, Baja California Sur, Mexico. *Aquatic Geochemistry* **17**, 603–628.

Huerta-Diaz MA, Delgadillo-Hinojosa F, Siqueiros-Valencia A, Valdivieso-Ojeda J, Reimer JJ, Segovia-Zavala JA (2012) Millimeter-scale resolution of trace metal distributions in microbial mats from a hypersaline environment in Baja California, Mexico. *Geobiology* **10**, 531–547.

Huerta-Diaz MA, Morse JW (1992) Pyritization of trace metals in anoxic marine sediments. *Geochimica et Cosmochimica Acta* **56**, 2681–2702.

Illing CJ, Hallmann C, Miller KE, Summons RE, Strauss H (2014) Airborne hydrocarbon contamination from laboratory atmospheres. *Organic Geochemistry* **76**, 26–38.

Immenhauser A (2009) Estimating palaeo-water depth from the physical rock record. *Earth-Science Reviews* **96**, 107–139.

Iniesto M, Buscalioni ÁD, Carmen Guerrero M, Benzerara K, Moreira D, López-Archilla AI (2016) Involvement of microbial mats in early fossilization by decay delay and formation of impressions and replicas of vertebrates and invertebrates. *Scientific Reports* **6**, 25716.

Iniesto M, Villalba I, Buscalioni AD, Guerrero MC, López-Archilla AI (2017) The effect of microbial mats in the decay of Anurans with implications for understanding taphonomic processes in the fossil record. *Scientific Reports* **7**, 45160.

Inoue A, Kitagawa R (1994) Morphological characteristics of illitic clay minerals from a hydrothermal system. *American Mineralogist* **79**, 700–711.

Inoue A, Velde B, Meunier A, Touchard G (1988) Mechanism of illite formation during smectite-to-illite conversion in a hydrothermal system. *American Mineralogist* **73**, 1325–1334.

Isson TT, Planavsky NJ (2018) Reverse weathering as a long-term stabilizer of marine pH and planetary climate. *Nature* **560**, 471–475.

Jahnert RJ, Collins LB (2012) Characteristics, distribution and morphogenesis of subtidal microbial systems in Shark Bay, Australia. *Marine Geology* **303–306**, 115–136.

Jarrett AJM, Cox GM, Brocks JJ, Grosjean E, Boreham CJ, Edwards DS (2019) Microbial assemblage and palaeoenvironmental reconstruction of the 1.38 Ga Velkerri Formation, McArthur Basin, northern Australia. *Geobiology* **17**.

Javaux E, Lepot K, van Zuilen M, Melezhik V, Medvedev P (2013) Palaeoproterozoic microfossils. In: *Reading the Archive of Earth's Oxygenation.* (eds. Melezhik V, Prave AR, Hanski EJ, Fallick AE, Lepland A, Kump LR, Strauss H). Springer-Verlag, Berlin, Heidelberg, pp. 1352–1371.

Javaux EJ, Lepot K (2018) The Paleoproterozoic fossil record: Implications for the evolution of the biosphere during Earth's middle-age. *Earth-Science Reviews* **176**, 68–86.

Javaux EJ, Marshall CP, Bekker A (2010) Organic-walled microfossils in 3.2-billion-year-old shallow-marine siliciclastic deposits. *Nature* **463**, 934–938.

Johnston DT (2011) Multiple sulfur isotopes and the evolution of Earth's surface sulfur cycle. *Earth-Science Reviews* **106**, 161–183.

Johnston DT, Farquhar J, Canfield DE (2007) Sulfur isotope insights into microbial sulfate reduction: *When microbes meet models*. *Geochimica et Cosmochimica Acta* **71**, 3929–3947.

Jones B, Renaut RW, Konhauser KO (2005) Genesis of large siliceous stromatolites at Frying Pan Lake, Waimangu geothermal field, North Island, New Zealand. *Sedimentology* **52**, 1229–1252.

Jørgensen BB (2001) Space for hydrogen. *Nature* **412**, 286–289.

Jørgensen BB, Boetius A (2007) Feast and famine — microbial life in the deep-sea bed. *Nature Reviews Microbiology* **5**, 770–781.

Jungblut AD, Hawes I, Mackey TJ, Krusor M, Doran PT, Sumner DY, Eisen JA, Hillman C, Goroncy AK (2016) Microbial mat communities along an oxygen gradient in a perennially ice-covered Antarctic lake. *Applied and Environmental Microbiology* **82**, 620–630.

Kalkowsky E (1908) Oolith und Stromatolith im norddeutschen Buntsandstein. *Zeitschrift der deutschen geologischen Gesellschaft* **60**, 68–125.

Kappler A, Pasquero C, Konhauser KO, Newman DK (2005) Deposition of banded iron formations by anoxygenic phototrophic Fe(II)-oxidizing bacteria. *Geology* **33**, 865–868.

Karhu JA, Holland HD (1996) Carbon isotopes and the rise of atmospheric oxygen. *Geology* **24**, 867–870.

Karl DM, Bidigare RR, Letelier RM (2001) Long-term changes in plankton community structure and productivity in the North Pacific Subtropical Gyre: The domain shift hypothesis. *Deep-Sea Research II* **48**, 1449–1470.

Kasting JF, Siefert JL (2002) Life and the evolution of Earth's atmosphere. *Science* **296**, 1066–1068.

Kebukawa Y, Kobayashi H, Urayama N, Baden N, Kondo M, Zolensky ME, Kobayashi K (2019) Nanoscale infrared imaging analysis of carbonaceous chondrites to understand organic-mineral interactions during aqueous alteration. *Proceedings of the National Academy of Sciences* **116**, 753–758.

Kennedy MJ, Pevear DR, Hill RJ (2002) Mineral surface control of organic carbon in black shale. *Science* **295**, 657–660.

Kim J, Dong H, Seabaugh J, Newell SW, Eberl DD (2004) Role of microbes in the smectite-to-illite reaction. *Science* **303**, 830–832.

Kipp MA, Stüeken EE, Yun M, Bekker A, Buick R (2018) Pervasive aerobic nitrogen cycling in the surface ocean across the Paleoproterozoic Era. *Earth and Planetary Science Letters* **500**, 117–126.

Kirschvink JL, Gaidos EJ, Bertani LE, Beukes NJ, Gutzmer J, Maepa LN, Steinberger RE (2000) Paleoproterozoic snowball Earth: Extreme climatic and geochemical global change and its biological consequences. *Proceedings of the National Academy of Sciences* **97**, 1400–1405.

Knauth LP (1998) Salinity history of the Earth's early ocean. *Nature* **395**, 554–555.

Knauth LP (2005) Temperature and salinity history of the Precambrian ocean: Implications for the course of microbial evolution. *Palaeogeography, Palaeoclimatology, Palaeoecology* **219**, 53–69.

Knoll AH, Strother PK, Rossi S (1988) Distribution and diagenesis of microfossils from the Lower Proterozoic Duck Creek Dolomite, Western Australia. *Precambrian Research* **38**, 257–279.

Koehler MC, Stüeken EE, Kipp MA, Buick R, Knoll AH (2017) Spatial and temporal trends in Precambrian nitrogen cycling: A Mesoproterozoic offshore nitrate minimum. *Geochimica et Cosmochimica Acta* **198**, 315–337.

Konhauser KO (1997) Bacterial iron biomineralisation in nature. *FEMS Microbiology Reviews* **20**, 315–326.

Konhauser KO (1998) Diversity of bacterial iron mineralization. *Earth-Science Reviews* **43**, 91–121.

Konhauser KO, Ferris FG (1996) Diversity of iron and silica precipitation by microbial mats in hydrothermal waters, Iceland: Implications for Precambrian iron formations. *Geology* **4**, 323–326.

Konhauser KO, Lalonde SV, Planavsky NJ, Pecoits E, Lyons TW, Mojzsis SJ, Rouxel OJ, Barley ME, Rosìere C, Fralick PW, Kump LR, Bekker A (2011) Aerobic bacterial pyrite oxidation and acid rock drainage during the Great Oxidation Event. *Nature* **478**, 369–373.

Konhauser KO, Pecoits E, Lalonde SV, Papineau D, Nisbet EG, Barley ME, Arndt NT, Zahnle K, Kamber BS (2009) Oceanic nickel depletion and a methanogen famine before the Great Oxidation Event. *Nature* **458**, 750–753.

Konhauser KO, Urrutia MM (1999) Bacterial clay authigenesis: A common biogeochemical process. *Chemical Geology* **161**, 399–413.

Kouketsu Y, Mizukami T, Mori H, Endo S, Aoya M, Hara H, Nakamura D, Wallis S (2014) A new approach to develop the Raman carbonaceous material geothermometer for low-grade metamorphism using peak width. *Island Arc* **23**, 33–50.

Kovalchuk O, Owttrim GW, Konhauser KO, Gingras MK (2017) Desiccation cracks in siliciclastic deposits: Microbial mat-related compared to abiotic sedimentary origin. *Sedimentary Geology* **347**, 67–78.

Krumbein WE, Brehm U, Gerdes G, Gorbushina AA, Levit G, Palinska KA (2003) Biofilm, biodictyon, biomat microbialites, oolites, stomatolies - geophysiology, global mechanism, parahistology. In: *Fossil and Recent Biofilms: A Natural History of Life on Earth* (eds. Krumbein WE, Paterson DM, Zavarzin GA). Kluwer Academic Publishers, Dordrecht, pp. 1–27.

Kumai M (1976) Identification of nuclei and concentrations of chemical species in snow crystals sampled at the South Pole. *Journal of the Atmospheric Sciences* **33**, 833–841.

Kump LR, Junium C, Arthur MA, Brasier A, Fallick A, Melezhik V, Lepland A, Crne AE, Luo G (2011) Isotopic evidence for massive oxidation of organic matter following the Great Oxidation Event. *Science* **334**, 1694–1696.

Lanson B, Sakharov BA, Claret F, Drits VA (2009) Diagenetic smectite-to-illite transition in clay-rich sediments: A reappraisal of X-Ray diffraction results using the multi-specimen method. *American Journal of Science* **309**, 476–516.

Large RR, Danyushevsky L, Hollit C, Maslennikov V, Meffre S, Gilbert S, Bull S, Scott R, Emsbo P, Thomas H, Singh B, Foster J (2009) Gold and trace element zonation in pyrite using a laser imaging technique: Implications for the timing of gold in orogenic and carlin-style sediment-hosted deposits. *Economic Geology* **104**, 635–668.

Large RR, Gregory DD, Steadman JA, Tomkins AG, Lounejeva E, Danyushevsky LV, Halpin JA, Maslennikov V, Sack PJ, Mukherjee I, Berry R, Hickman A (2015) Gold in the oceans through time. *Earth and Planetary Science Letters* **428**, 139–150.

Large RR, Halpin JA, Danyushevsky LV, Maslennikov VV, Bull SW, Long JA, Gregory DD, Lounejeva E, Lyons TW, Sack PJ, McGoldrick PJ, Calver CR (2014) Trace element content of sedimentary pyrite as a new proxy for deep-time ocean–atmosphere evolution. *Earth and Planetary Science Letters* **389**, 209–220.

Large RR, Mukherjee I, Zhukova I, Corkrey R, Stepanov A, Danyushevsky LV (2018) Role of upper-most crustal composition in the evolution of the Precambrian ocean–atmosphere system. *Earth and Planetary Science Letters* **487**, 44–53.

Leider A, Schumacher TC, Hallmann C (2016) Enhanced procedural blank control for organic geochemical studies of critical sample material. *Geobiology* **14**, 469–482.

Lekele Baghekema SG (2017) *Études multi-proxies et multi-scalaires des roches siliceuses (cherts) du bassin de Franceville (2,1 Ga) : origine et processus de formation*.

Lekele Baghekema SG, Lepot K, Riboulleau A, Fadel A, Trentesaux A, El Albani A (2017) Nanoscale analysis of preservation of *ca*. 2.1 Ga old Francevillian microfossils, Gabon. *Precambrian Research* **301**, 1–18.

Lepot K, Addad A, Knoll AH, Wang J, Troadec D, Béché A, Javaux EJ (2017) Iron minerals within specific microfossil morphospecies of the 1.88 Ga Gunflint Formation. *Nature Communications* **8**, 14890.

Lepot K, Benzerara K, Brown Jr GE, Philippot P (2008) Microbially influenced formation of 2,724-million-year-old stromatolites. *Nature Geoscience* **1**, 118–121.

Lepot K, Benzerara K, Rividi N, Cotte M, Brown Jr GE, Philippot P (2009) Organic matter heterogeneities in 2.72Ga stromatolites: Alteration versus preservation by sulfur incorporation. *Geochimica et Cosmochimica Acta* **73**, 6579–6599.

Li Y, Cai J, Song M, Ji J, Bao Y (2016) Influence of organic matter on smectite illitization: A comparison between red and dark mudstones from the Dongying Depression, China. *American Mineralogist* **101**, 134–145.

Li YH, Schoonmaker J (2003) Chemical composition and mineralogy of marine sediments. In: *Treatise on Geochemistry, Vol. 7: Sediments, Diagenesis, and Sedimentary Rocks* (ed. Mackenzie FT). Elsevier, Oxford, pp. 1–35.

Lindsay JF, Brasier MD, McLoughlin N, Green OR, Fogel M, Steele A, Mertzman SA (2005) The problem of deep carbon—An Archean paradox. *Precambrian Research* **143**, 1–22.

Linol B, de Wit MJ, Guillocheau F, Robin C, Dauteuil O (2015) Multiphase Phanerozoic subsidence and uplift history recorded in the Congo Basin: A complex successor basin. In:

Geology and Resource Potential of the Congo Basin. Springer, Berlin, Heidelberg, pp. 213–227.

Lovley DR, Klug MJ (1983) Sulfate reducers can outcompete methanogens at freshwater sulfate concentrations. *Applied and Environmental Microbiology* **45**, 187–192.

Lowe DR (1994) Abiological origin of described stromatolites older than 3.2 Ga. *Geology* **22**, 387–390.

Luo G, Junium CK, Izon G, Ono S, Beukes NJ, Algeo TJ, Cui Y, Xie S, Summons RE (2018) Nitrogen fixation sustained productivity in the wake of the Palaeoproterozoic Great Oxygenation Event. *Nature Communications* **9**, 978.

Luo G, Ono S, Beukes NJ, Wang DT, Xie S, Summons RE (2016) Rapid oxygenation of Earth's atmosphere 2.33 billion years ago. *Science Advances* **2**, e1600134.

Lydmark P, Lind M, Sörensson F, Hermansson M (2006) Vertical distribution of nitrifying populations in bacterial biofilms from a full-scale nitrifying trickling filter. *Environmental Microbiology* **8**, 2036–2049.

Lyons TW, Reinhard CT, Planavsky NJ (2014) The rise of oxygen in Earth's early ocean and atmosphere. *Nature* **506**, 307–315.

Lyons TW, Severmann S (2006) A critical look at iron paleoredox proxies: New insights from modern euxinic marine basins. *Geochimica et Cosmochimica Acta* **70**, 5698–5722.

Mackenzie FT, Garrels RM (1966) Chemical mass balance between rivers and oceans. *American Journal of Science* **264**, 507–525.

Marin-Carbonne J, Remusat L, Sforna MC, Thomazo C, Cartigny P, Philippot P (2018) Sulfur isotope's signal of nanopyrites enclosed in 2.7 Ga stromatolitic organic remains reveal microbial sulfate reduction. *Geobiology* **16**, 121–138.

Mariotti G, Pruss SB, Perron JT, Bosak T (2014) Microbial shaping of sedimentary wrinkle structures. *Nature Geoscience* **7**, 736–740.

Martin AP, Condon DJ, Prave AR, Lepland A (2013) A review of temporal constraints for the Palaeoproterozoic large, positive carbonate carbon isotope excursion (the Lomagundi–Jatuli Event). *Earth-Science Reviews* **127**, 242–261.

Marty B, Avice G, Bekaert DV, Broadley MW (2018) Salinity of the Archaean oceans from analysis of fluid inclusions in quartz. *Comptes Rendus Geoscience* **350**, 154–163.

Mata SA, Bottjer DJ (2009) The paleoenvironmental distribution of Phanerozoic wrinkle structures. *Earth-Science Reviews* **96**, 181–195.

Matsushita M, Hiramatsu F, Kobayashi N, Ozawa T, Yamazaki Y, Matsuyama T (2004) Colony formation in bacteria: Experiments and modeling. *Biofilms* **1**, 305–317.

Maynard JB (2010) The chemistry of manganese ores through time: A signal of increasing diversity of Earth-surface environments. *Economic Geology* **105**, 535–552.

McLennan SM (1989) Rare earth elements in sedimentary rocks: Influence of provenance and sedimentary processes. *Reviews in Mineralogy and Geochemistry* **21**, 169–200.

McLennan SM (2001) Relationships between the trace element composition of sedimentary rocks and upper continental crust: Trace element composition and upper continental crust. *Geochemistry, Geophysics, Geosystems* **2**, 2000GC000109.

McLennan SM, Taylor SR, Eriksson KA (1983) Geochemistry of Archean shales from the Pilbara Supergroup, Western Australia. *Geochimica et Cosmochimica Acta* **47**, 1211–1222.

McMahon WJ, Davies NS (2018) Evolution of alluvial mudrock forced by early land plants. *Science* **359**, 1022–1024.

McNevin DB, Badger MR, Whitney SM, von Caemmerer GG, Tcherkez GG, Farquhar GD (2007) Differences in carbon isotope discrimination of three variants of D-ribulose-1,5-

bisphosphate carboxylase/oxygenase reflect differences in their catalytic mechanisms. *Journal of Biological Chemistry* **282**, 36068–36076.

Medjoubi K, Leclercq N, Langlois F, Buteau A, Lé S, Poirier S, Mercère P, Sforna MC, Kewish CM, Somogyi A (2013) Development of fast, simultaneous and multi-technique scanning hard X-ray microscopy at Synchrotron Soleil. *Journal of Synchrotron Radiation* **20**, 293–299.

Melezhik VA, Fallick AE, Rychanchik DV, Kuznetsov AB (2005) Palaeoproterozoic evaporites in Fennoscandia: Implications for seawater sulphate, the rise of atmospheric oxygen and local amplification of the $\delta^{13}C$ excursion. *Terra Nova* **17**, 141–148.

Meunier A, Velde B (2004) *Illite. Origins, evolution and metamorphism*. Springer-Verlag, Berlin, Heidelberg.

Meyer M, Xiao S, Gill BC, Schiffbauer JD, Chen Z, Zhou C, Yuan X (2014) Interactions between Ediacaran animals and microbial mats: Insights from Lamonte trevallis, a new trace fossil from the Dengying Formation of South China. *Palaeogeography, Palaeoclimatology, Palaeoecology* **396**, 62–74.

Michalopoulos P, Aller RC (1995) Rapid clay mineral formation in Amazon delta sediments: Reverse weathering and oceanic elemental cycles. *Science* **270**, 614–617.

Mills DB, Ward LM, Jones C, Sweeten B, Forth M, Treusch AH, Canfield DE (2014) Oxygen requirements of the earliest animals. *Proceedings of the National Academy of Sciences* **111**, 4168–4172.

Mojzsis SJ, Arrhenius G, McKeegan KD, Harrison TM, Nutman AP, Friend CRL (1996) Evidence for life on Earth before 3,800 million years ago. *Nature* **384**, 55–59.

Moore DM, Reynolds Jr RC (1997) *X-ray diffraction and the identification and analysis of clay minerals*. Oxford University Press, New York.

Moore EK, Jelen BI, Giovannelli D, Raanan H, Falkowski PG (2017) Metal availability and the expanding network of microbial metabolisms in the Archaean eon. *Nature Geoscience* **10**, 629–636.

Mossman DJ, Gauthier-Lafaye F, Jackson SE (2001) Carbonaceous substances associated with the Paleoproterozoic natural nuclear fission reactors of Oklo, Gabon: Paragenesis, thermal maturation and carbon isotopic and trace element compositions. *Precambrian research* **106**, 135–148.

Mouélé IM, Dudoignon P, El Albani A, Meunier A, Boulvais P, Gauthier-Lafaye F, Paquette J-L, Martin H, Cuney M (2014) 2.9–1.9 Ga paleoalterations of Archean granitic basement of the Franceville basin (Gabon). *Journal of African Earth Sciences* **97**, 244–260.

Moussavou M, Edou-Minko A (2006) Contribution à l'histoire thermo-tectonique précambrienne du complexe annulaire de N'goutou par la géochimie et la géochronologie U/Pb sur minéraux accessoires (Bassin Francevillien d'Okondja, Gabon). *Africa Geoscience Review* **13**, 53–61.

Moyen J-F, Martin H (2012) Forty years of TTG research. *Lithos* **148**, 312–336.

Mulkidjanian AY, Bychkov AY, Dibrova DV, Galperin MY, Koonin EV (2012) Origin of first cells at terrestrial, anoxic geothermal fields. *Proceedings of the National Academy of Sciences* **109**, E821–E830.

Müller PJ (1977) C/N ratios in Pacific deep-sea sediments: Effect of inorganic ammonium and organic nitrogen compounds sorbed by clays. *Geochimica et Cosmochimica Acta* **41**, 765–776.

Nabhan S, Wiedenbeck M, Milke R, Heubeck C (2016) Biogenic overgrowth on detrital pyrite in *ca.* 3.2 Ga Archean paleosols. *Geology* **44**, 763–766.

Nachtegaal M, Scheidegger AM, Dähn R, Chateigner D, Furrer G (2005) Immobilization of Ni by Al-modified montmorillonite: A novel uptake mechanism. *Geochimica et Cosmochimica Acta* **69**, 4211–4225.

Nadeau PH, Wilson MJ, McHardy WJ, Tait JM (1985) The conversion of smectite to illite during diagenesis: Evidence from some illitic clays from bentonites and sandstones. *Mineralogical Magazine* **49**, 393–400.

Nagy B, Gauthier-Lafaye F, Holliger P, Mossman DJ, Leventhal JS, Rigali MJ (1993) Role of organic matter in the Proterozoic Oklo natural fission reactors, Gabon, Africa. *Geology* **21**, 655–658.

Newman SA, Klepac-Ceraj V, Mariotti G, Pruss SB, Watson N, Bosak T (2017) Experimental fossilization of mat-forming cyanobacteria in coarse-grained siliciclastic sediments. *Geobiology* **15**, 484–498.

Newman SA, Mariotti G, Pruss S, Bosak T (2016) Insights into cyanobacterial fossilization in Ediacaran siliciclastic environments. *Geology* **44**, 579–582.

Ngombi Pemba L (2014) *Géochimie et minéralogie des formations argileuses (2.2 – 2.0 Ga) du bassin de Franceville au Gabon : fluctuations de l'oxygène atmosphérique, chimie des océans et diagenèse au Paléoprotérozoïque*.

Ngombi-Pemba L, El Albani A, Meunier A, Grauby O, Gauthier-Lafaye F (2014) From detrital heritage to diagenetic transformations, the message of clay minerals contained within shales of the Palaeoproterozoic Francevillian basin (Gabon). *Precambrian Research* **255**, 63–76.

Nguyen K, Love GD, Zumberge JA, Kelly AE, Owens JD, Rohrssen MK, Bates SM, Cai C, Lyons TW (2019) Absence of biomarker evidence for early eukaryotic life from the Mesoproterozoic Roper Group: Searching across a marine redox gradient in mid-Proterozoic habitability. *Geobiology* **17**, 247–260.

Nier AO, Gulbransen EA (1939) Variations in the relative abundance of the carbon isotopes. *Journal of the American Chemical Society* **61**, 697–698.

Nisbet EG, Sleep NH (2001) The habitat and nature of early life. *Nature* **409**, 1083–1091.

Noffke N (2009) The criteria for the biogeneicity of microbially induced sedimentary structures (MISS) in Archean and younger, sandy deposits. *Earth-Science Reviews* **96**, 173–180.

Noffke N (2010) *Geobiology*. Springer, Berlin, Heidelberg.

Noffke N, Beukes N, Bower D, Hazen RM, Swift DJP (2008) An actualistic perspective into Archean worlds - (cyano-)bacterially induced sedimentary structures in the siliciclastic Nhlazatse Section, 2.9 Ga Pongola Supergroup, South Africa. *Geobiology* **6**, 5–20.

Noffke N, Christian D, Wacey D, Hazen RM (2013) Microbially induced sedimentary structures recording an ancient ecosystem in the *ca.* 3.48 billion-year-old Dresser Formation, Pilbara, Western Australia. *Astrobiology* **13**, 1103–1124.

Noffke N, Gerdes G, Klenke T, Krumbein WE (1996) Microbially induced sedimentary structures—examples from modern sediments of siliciclastic tidal flats. *Zentralblatt für Geologie und Paläontologie Teil* **1**, 307–316.

Noffke N, Gerdes G, Klenke T, Krumbein WE (1997) A microscopic sedimentary succession of graded sand and microbial mats in modern siliciclastic tidal flats. *Sedimentary Geology* **110**, 1–6.

Noffke N, Gerdes G, Klenke T, Krumbein WE (2001) Microbially induced sedimentary structures–A new category within the classification of primary sedimentary structures: Perpectives. *Journal of Sedimentary Research* **71**, 649–656.

Noffke N, Knoll AH, Grotzinger JP (2002) Sedimentary controls on the formation and preservation of microbial mats in siliciclastic deposits: A case study from the Upper Neoproterozoic Nama Group, Namibia. *Palaios* **17**, 533–544.

Notholt AJG (1980) Economic phosphatic sediments: Mode of occurence and stratigraphical distribution. *Journal of the Geological Society* **137**, 793–805.

Nutman AP, Bennett VC, Friend CRL, van Kranendonk MJ, Chivas AR (2016) Rapid emergence of life shown by discovery of 3,700-million-year-old microbial structures. *Nature* **537**, 535–538.

Och LM, Shields-Zhou GA (2012) The Neoproterozoic oxygenation event: Environmental perturbations and biogeochemical cycling. *Earth-Science Reviews* **110**, 26–57.

Ochiai E-I (1983) Copper and the biological evolution. *Biosystems* **16**, 81–86.

Okabe S, Hiratia K, Ozawa Y, Watanabe Y (1996) Spatial microbial distributions of nitrifiers and heterotrophs in mixed-population biofilms. *Biotechnology and Bioengineering* **50**, 24–35.

Onanga Mavotchy N (2016) *Études des paléomilieux paléoprotérozoïques (2.1-2.0 Ga) : La Formation FB du bassin de Franceville au Gabon*.

O'Reilly SE, Watkins J, Furukawa Y (2005) Secondary mineral formation associated with respiration of nontronite, NAu-1 by iron reducing bacteria. *Geochemical Transactions* **6**, 67–78.

Ortega-Morales BO, Santiago-García J, Chan-Bacab M, Moppert X, Miranda-Tello E, Fardeau M-L, Carrero J, Bartolo-Pérez P, Valadéz-González A, Guezennec J (2007) Characterization of extracellular polymers synthesized by tropical intertidal biofilm bacteria. *Journal of Applied Microbiology* **102**, 254–264.

Ossa Ossa F (2010) *Etude multi-approches du bassin sédimentaire paléoprotérozoïque (2. 1-2. 4 Ga) de Franceville au Gabon: Les environnements sédimentaires et l'impact des paléocirculations de fluides*.

Ossa Ossa F, Eickmann B, Hofmann A, Planavsky NJ, Asael D, Pambo F, Bekker A (2018) Two-step deoxygenation at the end of the Paleoproterozoic Lomagundi Event. *Earth and Planetary Science Letters* **486**, 70–83.

Ossa Ossa F, El Albani A, Hofmann A, Bekker A, Gauthier-Lafaye F, Pambo F, Meunier A, Fontaine C, Boulvais P, Pierson-Wickmann A-C, Cavalazzi B, Macchiarelli R (2013) Exceptional preservation of expandable clay minerals in the *ca*. 2.1 Ga black shales of the Francevillian basin, Gabon and its implication for atmospheric oxygen accumulation. *Chemical Geology* **362**, 181–192.

Ossa Ossa F, Hofmann A, Spangenberg JE, Poulton SW, Stüeken EE, Schoenberg R, Eickmann B, Wille M, Butler M, Bekker A (2019) Limited oxygen production in the Mesoarchean ocean. *Proceedings of the National Academy of Sciences* **116**, 6647–6652.

Pace A (2016) *Structures et processus de minéralisation et de diagenèse des tapis microbiens actuels en domaines hypersalins continental et marin*.

Pace A, Bourillot R, Bouton A, Vennin E, Galaup S, Bundeleva I, Patrier P, Dupraz C, Thomazo C, Sansjofre P, Yokoyama Y, Franceschi M, Anguy Y, Pigot L, Virgone A, Visscher PT (2016) Microbial and diagenetic steps leading to the mineralisation of Great Salt Lake microbialites. *Scientific Reports* **6**, 31495.

Paerl HW, Bebout BM, Currin CA, Fitzpatrick MW, Pinckney JL (1994) Nitrogen fixation dynamics in microbial mats. In: *Microbial mats Structure, Development and Environmental Significance* (eds. Stal LJ, Caumette P). Springer, Berlin, Heidelberg, pp. 325–337.

Papineau D (2010) Global biogeochemical changes at both ends of the Proterozoic: Insights from phosphorites. *Astrobiology* **10**, 165–181.

Parize O, Feybesse J-L, Guillocheau F, Mulder T (2013) Were the 2.1-Gyr fossil colonial organisms discovered in the Francevillian basin (Palaeoproterozoic, Gabon) buried by turbidites? *Comptes Rendus Geoscience* **345**, 101–110.

Partin CA, Bekker A, Planavsky NJ, Scott CT, Gill BC, Li C, Podkovyrov V, Maslov A, Konhauser KO, Lalonde SV, Love GD, Poulton SW, Lyons TW (2013a) Large-scale fluctuations in Precambrian atmospheric and oceanic oxygen levels from the record of U in shales. *Earth and Planetary Science Letters* **369–370**, 284–293.

Partin CA, Lalonde SV, Planavsky NJ, Bekker A, Rouxel OJ, Lyons TW, Konhauser KO (2013b) Uranium in iron formations and the rise of atmospheric oxygen. *Chemical Geology* **362**, 82–90.

Pecoits E, Gingras MK, Barley ME, Kappler A, Posth NR, Konhauser KO (2009) Petrography and geochemistry of the Dales Gorge banded iron formation: Paragenetic sequence, source and implications for palaeo-ocean chemistry. *Precambrian Research* **172**, 163–187.

Pecoits E, Konhauser KO, Aubet NR, Heaman LM, Veroslavsky G, Stern RA, Gingras MK (2012) Bilaterian burrows and grazing behavior at >585 million years ago. *Science* **336**, 1693–1696.

Pehr K, Love GD, Kuznetsov A, Podkovyrov V, Junium CK, Shumlyanskyy L, Sokur T, Bekker A (2018) Ediacara biota flourished in oligotrophic and bacterially dominated marine environments across Baltica. *Nature Communications* **9**, 1807.

Perry Jr EA, Hower J (1970) Burial diagenesis in Gulf Coast pelitic sediments. *Clays and Clay Minerals* **18**, 165–177.

Perry T, Klepac-Ceraj V, Zhang XV, McNamara CJ, Polz MF, Martin ST, Berke N, Mitchell R (2005) Binding of harvested nacterial exopolymers to the surface of calcite. *Environmental Science & Technology* **39**, 8770–8775.

Petrash DA, Lalonde SV, González-Arismendi G, Gordon RA, Méndez JA, Gingras MK, Konhauser KO (2015) Can Mn–S redox cycling drive sedimentary dolomite formation? A hypothesis. *Chemical Geology* **404**, 27–40.

Pflüger F (1999) Matground structures and redox facies. *Palaios* **14**, 25–39.

Philippot P, Ávila JN, Killingsworth BA, Tessalina S, Baton F, Caquineau T, Muller E, Pecoits E, Cartigny P, Lalonde SV, Ireland TR, Thomazo C, van Kranendonk MJ, Busigny V (2018) Globally asynchronous sulphur isotope signals require re-definition of the Great Oxidation Event. *Nature Communications* **9**, 2245.

Planavsky NJ, Asael D, Hofmann A, Reinhard CT, Lalonde SV, Knudsen A, Wang X, Ossa Ossa F, Pecoits E, Smith AJB, Beukes NJ, Bekker A, Johnson TM, Konhauser KO, Lyons TW, Rouxel OJ (2014a) Evidence for oxygenic photosynthesis half a billion years before the Great Oxidation Event. *Nature Geoscience* **7**, 283–286.

Planavsky NJ, Bekker A, Hofmann A, Owens JD, Lyons TW (2012) Sulfur record of rising and falling marine oxygen and sulfate levels during the Lomagundi event. *Proceedings of the National Academy of Sciences* **109**, 18300–18305.

Planavsky NJ, Bekker A, Rouxel OJ, Kamber B, Hofmann A, Knudsen A, Lyons TW (2010) Rare earth element and yttrium compositions of Archean and Paleoproterozoic Fe formations revisited: New perspectives on the significance and mechanisms of deposition. *Geochimica et Cosmochimica Acta* **74**, 6387–6405.

Planavsky NJ, McGoldrick P, Scott CT, Li C, Reinhard CT, Kelly AE, Chu X, Bekker A, Love GD, Lyons TW (2011) Widespread iron-rich conditions in the mid-Proterozoic ocean. *Nature* **477**, 448–451.

Planavsky NJ, Reinhard CT, Wang X, Thomson D, McGoldrick P, Rainbird RH, Johnson T, Fischer WW, Lyons TW (2014b) Low mid-Proterozoic atmospheric oxygen levels and the delayed rise of animals. *Science* **346**, 635–638.

Planavsky NJ, Slack JF, Cannon WF, O'Connell B, Isson TT, Asael D, Jackson JC, Hardisty DS, Lyons TW, Bekker A (2018) Evidence for episodic oxygenation in a weakly redox-buffered deep mid-Proterozoic ocean. *Chemical Geology* **483**, 581–594.

Playter T, Konhauser KO, Owttrim G, Hodgson C, Warchola T, Mloszewska AM, Sutherland B, Bekker A, Zonneveld J-P, Pemberton SG, Gingras M (2017) Microbe-clay interactions as a mechanism for the preservation of organic matter and trace metal biosignatures in black shales. *Chemical Geology* **459**, 75–90.

Pombo F (2004) *Conditions de formation des carbonates de manganèse protérozosoïques et analyse minéralogique et géochimique des minerais à bioxydes de manganèse associés dans le gisement de Moanda (Sud-Est, Gabon).*

Pope MC, Grotzinger JP, Schreiber BC (2000) Evaporitic subtidal stromatolites produced by *in situ* precipitation: Textures, facies associations, and temporal significance. *Journal of Sedimentary Research* **70**, 1139–1151.

Porada H, Bouougri EH (2007) Wrinkle structures—a critical review. In: *Atlas of Microbial Mat Features Preserved within the Siliciclastic Rock Record* (eds. Schieber J, Bose PK, Eriksson PG, Banerjee S, Sarkar S, Altermann W, Catuneanu O). Elsevier, Amsterdam, pp. 135–144.

Porada H, Bouougri EH, Ghergut J (2007) Hydraulic conditions and mat-related structures in tidal flats and coastal sabkhas. In: *Atlas of Microbial Mat Features Preserved within the Siliciclastic Rock Record* (eds. Schieber J, Bose PK, Eriksson PG, Banerjee S, Sarkar S, Altermann W, Catuneanu O). Elsevier, Amsterdam, pp. 258–265.

Porada H, Ghergut J, Bouougri EH (2008) Kinneyia-type wrinkle structures - Critical review and model of formation. *Palaios* **23**, 65–77.

Pósfai M, Cziner K, Márton E, Márton P, Buseck PR, Frankel RRB, Bazylinski DA (2001) Crystal-size distributions and possible biogenic origin of Fe sulfides. *European Journal of Mineralogy* **13**, 691–703.

Poulton SW, Canfield DE (2005) Development of a sequential extraction procedure for iron: Implications for iron partitioning in continentally derived particulates. *Chemical Geology* **214**, 209–221.

Poulton SW, Canfield DE (2011) Ferruginous conditions: A dominant feature of the ocean through Earth's history. *Elements* **7**, 107–112.

Poulton SW, Raiswell R (2002) The low-temperature geochemical cycle of iron: From continental fluxes to marine sediment deposition. *American Journal of Science* **302**, 774–805.

Préat A, Bouton P, Thiéblemont D, Prian J-P, Ndounze SS, Delpomdor F (2011) Paleoproterozoic high δ^{13}C dolomites from the Lastoursville and Franceville basins (SE Gabon): Stratigraphic and synsedimentary subsidence implications. *Precambrian Research* **189**, 212–228.

Qu Y, Črne AE, Lepland A, van Zuilen MA (2012) Methanotrophy in a Paleoproterozoic oil field ecosystem, Zaonega Formation, Karelia, Russia. *Geobiology* **10**, 467–478.

Quandt L, Gottschalk G, Ziegler H, Stichler W (1977) Isotope discrimination by photosynthetic bacteria. *FEMS Microbiology Letters* **1**, 125–128.

R Core Team (2018) *A language and environment for statistical computing.* Vienna, Austria.

Raiswell R, Hardisty DS, Lyons TW, Canfield DE, Owens JD, Planavsky NJ, Poulton SW, Reinhard CT (2018) The iron paleoredox proxies: A guide to the pitfalls, problems and proper practice. *American Journal of Science* **318**, 491–526.

Rasmussen B, Buick R (1999) Redox state of the Archean atmosphere: Evidence from detrital heavy minerals in ca. 3250–2750 Ma sandstones from the Pilbara craton, Australia. *Geology* **27**, 115–118.

Redfield AC, Ketchum BJ, Richards FA (1963) The influence of organisms on the composition of seawater. In: *The sea* (ed. Hill MN). John Wiley and Sons, New York, pp. 26–77.

Reineck H-E, Singh IB (1980) *Depositional Sedimentary Environments*. Springer, Berlin, Heidelberg.

Reinhard CT, Lyons TW, Rouxel O, Asael D, Dauphas N, Kump LR (2013a) Iron speciation and isotope perspectives on Palaeoproterozoic water column chemistry. In: *Reading the Archive of Earth's Oxygenation Volume 3: Global Events and the Fennoscandian Arctic Russia-Drilling Early Earth Project* (eds. Melezhik VA, Kump LR, Fallick AE, Strauss H, Hanski EJ, Prave AR, Lepland A). Frontiers, pp. 1483–1492.

Reinhard CT, Planavsky NJ, Gill BC, Ozaki K, Robbins LJ, Lyons TW, Fischer WW, Wang C, Cole DB, Konhauser KO (2017) Evolution of the global phosphorus cycle. *Nature* **541**, 386–389.

Reinhard CT, Planavsky NJ, Robbins LJ, Partin CA, Gill BC, Lalonde SV, Bekker A, Konhauser KO, Lyons TW (2013b) Proterozoic ocean redox and biogeochemical stasis. *Proceedings of the National Academy of Sciences* **110**, 5357–5362.

Reyes K, Gonzalez NI, Stewart J, Ospino F, Nguyen D, Cho DT, Ghahremani N, Spear JR, Johnson HA (2013) Surface orientation affects the direction of cone growth by *Leptolyngbya sp.* strain C1, a likely architect of coniform structures Octopus Spring (Yellowstone National Park). *Applied and Environmental Microbiology* **79**, 1302–1308.

Reynaud J-Y, Trentesaux A, El Albani A, Aubineau J, Ngombi-Pemba L, Guiyeligou G, Bouton P, Gauthier-Lafaye F, Weber F (2017) Depositional setting of the 2.1 Ga Francevillian macrobiota (Gabon): Rapid mud settling in a shallow basin swept by high-density sand flows. *Sedimentology* **65**, 670–701.

Reynolds Jr RC, Reynolds III RC (1996) *NEWMOD for Windows. The calculation of one-dimensional X-ray diffraction patterns of mixed-layered clay minerals*. 8 Brook Road, Hanover, New Hampshire.

Riboulleau A, Spina A, Vecoli M, Riquier L, Quijada M, Tribovillard N, Averbuch O (2018) Organic matter deposition in the Ghadames Basin (Libya) during the Late Devonian—A multidisciplinary approach. *Palaeogeography, Palaeoclimatology, Palaeoecology* **497**, 37–51.

Richert L, Golubic S, Le Guédès R, Ratiskol J, Payri C, Guezennec J (2005) Characterization of exopolysaccharides produced by cyanobacteria isolated from Polynesian microbial mats. *Current Microbiology* **51**, 379–384.

Ridge PG, Zhang Y, Gladyshev VN (2008) Comparative genomic analyses of copper transporters and cuproproteomes reveal evolutionary dynamics of copper utilization and its link to oxygen. *PLoS ONE* **3**, e1378.

Riding R (2000) Microbial carbonates: The geological record of calcified bacterial-algal mats and biofilms. *Sedimentology* **47**, 179–214.

Riding R (2011) The Nature of Stromatolites: 3,500 Million Years of History and a Century of Research. In: *Advances in Stromatolite Geobiology* (eds. Reitner J, Quéric N-V, Arp G). Springer, Berlin, Heidelberg, pp. 29–74.

Robbins LJ, Lalonde SV, Planavsky NJ, Partin CA, Reinhard CT, Kendall B, Scott C, Hardisty DS, Gill BC, Alessi DS, Dupont CL, Saito MA, Crowe SA, Poulton SW, Bekker A, Lyons TW, Konhauser KO (2016) Trace elements at the intersection of marine biological and geochemical evolution. *Earth-Science Reviews* **163**, 323–348.

Robinson RS, Kienast M, Luiza Albuquerque A, Altabet M, Contreras S, De Pol Holz R, Dubois N, Francois R, Galbraith E, Hsu T-C, Ivanochko T, Jaccard S, Kao S-J, Kiefer T, Kienast S, Lehmann M, Martinez P, McCarthy M, Möbius J, Pedersen T, Quan TM, Ryabenko E, Schmittner A, Schneider R, Schneider-Mor A, Shigemitsu M, Sinclair D, Somes C, Studer A, Thunell R, Yang J-Y (2012) A review of nitrogen isotopic alteration in marine sediments. *Paleoceanography* **27**, PA4203.

Rogers JJW, Santosh M (2002) Configuration of Columbia, a Mesoproterozoic Supercontinent. *Gondwana Research* **5**, 5–22.

Rosing MT (1999) ^{13}C depleted carbon microparticles in >3700-Ma sea-floor sedimentary rocks from West Greenland. *Science* **283**, 674–676.

Runnegar BN, Fedonkin MA (1992) Proterozoic metazoan body fossils. In: *The Proterozoic Biosphere: A Multidisciplinary Study* (eds. Schopf JW, Klein C). Cambridge University Press, Cambridge, pp. 369–388.

Sagemann J, Bale SJ, Briggs DE, Parkes RJ (1999) Controls on the formation of authigenic minerals in association with decaying organic matter: An experimental approach. *Geochimica et Cosmochimica Acta* **63**, 1083–1095.

Sallstedt T, Bengtson S, Broman C, Crill PM, Canfield DE (2018) Evidence of oxygenic phototrophy in ancient phosphatic stromatolites from the Paleoproterozoic Vindhyan and Aravalli Supergroups, India. *Geobiology* **16**, 139–159.

Sancho-Tomás M, Somogyi A, Medjoubi K, Bergamaschi A, Visscher PT, van Driessche AES, Gérard E, Farias ME, Contreras M, Philippot P (2018) Distribution, redox state and (bio)geochemical implications of arsenic in present day microbialites of Laguna Brava, Salar de Atacama. *Chemical Geology* **490**, 13–21.

Sano Y, Pillinger CT (1990) Nitrogen isotopes and N_2/Ar ratios in chests: An attempt to measure time evolution of atmospheric 6^{15}N value. *Geochemical Journal* **24**, 315–325.

Sarkar S, Banerjee S, Samanta P, Chakraborty N, Chakraborty PP, Mukhopadhyay S, Singh AK (2014) Microbial mat records in siliciclastic rocks: Examples from four Indian Proterozoic basins and their modern equivalents in Gulf of Cambay. *Journal of Asian Earth Sciences* **91**, 362–377.

Sarkar S, Banerjee S, Samanta P, Jeevankumar S (2006) Microbial mat-induced sedimentary structures in siliciclastic sediments: Examples from the 1.6 Ga Chorhat Sandstone, Vindhyan Supergroup, MP, India. *Journal of Earth System Science* **115**, 49–60.

Sarkar S, Bose P, Samanta P, Sengupta P, Eriksson P (2008) Microbial mat mediated structures in the Ediacaran Sonia Sandstone, Rajasthan, India, and their implications for Proterozoic sedimentation. *Precambrian Research* **162**, 248–263.

Sarkar S, Choudhuri A, Mandal S, Eriksson PG (2016) Microbial mat-related structures shared by both siliciclastic and carbonate formations. *Journal of Palaeogeography* **5**, 278–291.

Satkoski AM, Beukes NJ, Li W, Beard BL, Johnson CM (2015) A redox-stratified ocean 3.2 billion years ago. *Earth and Planetary Science Letters* **430**, 43–53.

Sawaki Y, Moussavou M, Sato T, Suzuki K, Ligna C, Asanuma H, Sakata S, Obayashi H, Hirata T, Edou-Minko A (2017) Chronological constraints on the Paleoproterozoic Francevillian Group in Gabon. *Geoscience Frontiers* **8**, 397–407.

Schidlowski M (1987) Application of stable carbon isotopes to early biochemical evolution on Earth. *Annual Review of Earth Planetary Sciences* **15**, 47–72.

Schidlowski M (1988) A 3,800-million-year isotopic record of life from carbon in sedimentary rocks. *Nature* **333**, 313–318.

Schidlowski M (2001) Carbon isotopes as biogeochemical recorders of life over 3.8 Ga of Earth history: Evolution of a concept. *Precambrian Research* **106**, 117–134.

Schidlowski M, Appel PWU, Eichmann R, Junge CE (1979) Carbon isotope geochemistry of the 3.7 x 10^9-yr-old Isua sediments, West Greenland: Implications for the Archaean carbon and oxygen cycles. *Geochimica et Cosmochimica Acta* **43**, 189–199.

Schidlowski M, Eichmann R, Junge CE (1976) Carbon isotope geochemistry of the Precambrian Lomagundi carbonate province, Rhodesia. *Geochimica et Cosmochimica Acta* **40**, 449–455.

Schieber J (1998) Possible indicators of microbial mat deposits in shales and sandstones: Examples from the Mid-Proterozoic Belt Supergroup, Montana, U.S.A. *Sedimentary Geology* **120**, 105–124.

Schieber J (1999) Microbial mats in terrigenous clastics: The challenge of identification in the rock record. *Palaios* **14**, 3–12.

Schieber J (2007) *Atlas of microbial mat features preserved within the siliciclastic rock record*. Elsevier, Amsterdam; New York.

Schiffbauer J, Wallace A, Hunter Jr J, Kowalewski M, Bodnar R, Xiao S (2012) Thermally-induced structural and chemical alteration of organic-walled microfossils: An experimental approach to understanding fossil preservation in metasediments. *Geobiology* **10**, 402–423.

Schirrmeister BE, Sanchez-Baracaldo P, Wacey D (2016) Cyanobacterial evolution during the Precambrian. *International Journal of Astrobiology* **15**, 187–204.

Schmitt R, Smith R, Olehy D (1964) Rare-earth, yttrium and scandium abundances in meteoritic and terrestrial matter—II. *Geochimica et Cosmochimica Acta* **28**, 67–86.

Schoepp-Cothenet B, van Lis R, Atteia A, Baymann F, Capowiez L, Ducluzeau A-L, Duval S, ten Brink F, Russell MJ, Nitschke W (2013) On the universal core of bioenergetics. *Biochimica et Biophysica Acta (BBA) - Bioenergetics* **1827**, 79–93.

Schopf JW (1993) Microfossils of the Early Archean Apex Chert: new evidence of the antiquity of life. *Science* **260**, 640–646.

Schopf JW, Kitajima K, Spicuzza MJ, Kudryavtsev AB, Valley JW (2018) SIMS analyses of the oldest known assemblage of microfossils document their taxon-correlated carbon isotope compositions. *Proceedings of the National Academy of Sciences* **115**, 53–58.

Schopf JW, Kudryavtsev AB, Agresti DG, Wdowiak TJ, Czaja AD (2002) Laser–Raman imagery of Earth's earliest fossils. *Nature* **416**, 73–76.

Schopf JW, Kudryavtsev AB, Czaja AD, Tripathi AB (2007) Evidence of Archean life: Stromatolites and microfossils. *Precambrian Research* **158**, 141–155.

Schröder S, Bekker A, Beukes NJ, Strauss H, van Niekerk HS (2008) Rise in seawater sulphate concentration associated with the Paleoproterozoic positive carbon isotope excursion: Evidence from sulphate evaporites in the ∼2.2–2.1 Gyr shallow-marine Lucknow Formation, South Africa. *Terra Nova* **20**, 108–117.

Schwark L, Frimmel A (2004) Chemostratigraphy of the Posidonia Black Shale, SW-Germany II. Assessment of extent and persistence of photic-zone anoxia using aryl isoprenoid distributions. *Chemical Geology* **206**, 231–248.

Scott C, Lyons TW (2012) Contrasting molybdenum cycling and isotopic properties in euxinic versus non-euxinic sediments and sedimentary rocks: Refining the paleoproxies. *Chemical Geology* **324–325**, 19–27.

Seilacher A, Pflüger F (1994) From biomats to benthic agriculture: A biohistoric revolution. In: *Biostabilization of sediments* (eds. Krumbein WE, Paterson DM, Stal LJ). Bibliotheks und

Informationsystem der Carl von Ossietzky Universität Oldenberg: (BIS)-Verlag, Oldenburg, pp. 97–105.

Semikhatov M, Gebelein C, Cloud P, Awramik S, Benmore W (1979) Stromatolite morphogenesis—progress and problems. *Canadian Journal of Earth Sciences* **16**, 992–1015.

Sforna MC, Daye M, Philippot P, Somogyi A van, Zuilen MA, Medjoubi K, Gérard E, Jamme F, Dupraz C, Braissant O, Glunk C, Visscher PT (2017) Patterns of metal distribution in hypersaline microbialites during early diagenesis: Implications for the fossil record. *Geobiology* **15**, 259–279.

Sforna MC, Philippot P, Somogyi A, van Zuilen MA, Medjoubi K, Schoepp-Cothenet B, Nitschke W, Visscher PT (2014) Evidence for arsenic metabolism and cycling by microorganisms 2.7 billion years ago. *Nature Geoscience* **7**, 811–815.

Shcolnick S, Summerfield TC, Reytman L, Sherman LA, Keren N (2009) The mechanism of iron homeostasis in the unicellular Cyanobacterium *Synechocystis* sp. PCC 6803 and its relationship to oxidative stress. *Plant physiology* **150**, 2045–2056.

Sheldon ND (2012) Microbially induced sedimentary structures in the *ca.* 1100 Ma terrestrial midcontinent rift of North America. In: *Microbial Mats in Silicilastic Depositional Systems Through Time* (eds. Noffke N, Chafetz HS). SEPM (Society for Sedimentary Geology) Special Publication, Tulsa, Oklahoma, pp. 153–162.

Shen Y, Buick R, Canfield DE (2001) Isotopic evidence for microbial sulphate reduction in the Early Archean era. *Nature* **410**, 77–81.

Shepard RN, Sumner DY (2010) Undirected motility of filamentous cyanobacteria produces reticulate mats: Motility produces reticulate mats. *Geobiology* **8**, 179–190.

Sigman DM, Karsh KL, Casciotti KL (2009) Ocean process tracers: Nitrogen isotopes in the ocean. In: *Encyclopedia of ocean sciences* (eds. Steele JH, Turekian K, Thorpe S). Academic, London, pp. 40–54.

Sim MS, Liang B, Petroff AP, Evans A, Klepac-Ceraj V, Flannery DT, Walter MR, Bosak T (2012) Oxygen-dependent morphogenesis of modern clumped photosynthetic mats and implications for the Archean stromatolite record. *Geosciences* **2**, 235–259.

Simpson EL, Heness E, Bumby A, Eriksson PG, Eriksson KA, Hilbert-Wolf HL, Linnevelt S, Malenda HF, Modungwa T, Okafor OJ (2013) Evidence for 2.0 Ga continental microbial mats in a paleodesert setting. *Precambrian Research* **237**, 36–50.

Slotznick SP, Winston D, Webb SM, Kirschvink JL, Fischer WW (2016) Iron mineralogy and redox conditions during deposition of the mid-Proterozoic Appekunny Formation, Belt Supergroup, Glacier National Park. In: *Belt Basin: Window to Mesoproterozoic Earth* (eds. MacLean JS, Sears JW). pp. 221–242.

Smirnov AV, Evans DAD, Ernst RE, Söderlund U, Li Z-X (2013) Trading partners: Tectonic ancestry of southern Africa and western Australia, in Archean supercratons Vaalbara and Zimgarn. *Precambrian Research* **224**, 11–22.

Soares GG, van Kranendonk MJ, Belousova E, Thomson S (2019) Phosphogenesis in the immediate aftermath of the Great Oxidation Event: Evidence from the Turee Creek Group, Western Australia. *Precambrian Research* **320**, 193–212.

Sohm JA, Webb EA, Capone DG (2011) Emerging patterns of marine nitrogen fixation. *Nature Reviews Microbiology* **9**, 499–508.

Somogyi A, Medjoubi K, Baranton G, Le Roux V, Ribbens M, Polack F, Philippot P, Samama J-P (2015) Optical design and multi-length-scale scanning spectro-microscopy possibilities at the Nanoscopium beamline of Synchrotron Soleil. *Journal of Synchrotron Radiation* **22**, 1118–1129.

Spear N, Holland HD, Garcia-Veígas J, Lowenstein TK, Giegengack R, Peters H (2014) Analyses of fluid inclusions in Neoproterozoic marine halite provide oldest measurement of seawater chemistry. *Geology* **42**, 103–106.

Sperling EA, Halverson GP, Knoll AH, Macdonald FA, Johnston DT (2013) A basin redox transect at the dawn of animal life. *Earth and Planetary Science Letters* **371–372**, 143–155.

Środoń J (1984) Mixed-layer illite-smectite in low-temperature diagenesis: Data from the Miocene of the Carpathian Foredeep. *Clay Minerals* **19**, 205–215.

Środoń J, Eberl DD (1984) Illite. In: *Review in Mineralogy vol. 13, Micas* (ed. Bailey SW). Mineralogical Society of America, Washington DC, pp. 495–544.

Stal LJ (2001) Coastal microbial mats: The physiology of a small-scale ecosystem. *South African Journal of Botany* **67**, 399–410.

Stal LJ, Moezelaar R (1997) Fermentation in cyanobacteria. *FEMS Microbiology Reviews* **21**, 179–211.

Stolz JF, Botkin DB, Dastoor MN (1989) The integral biosphere. In: *Global ecology: towards a science of the biosphere* (eds. Rambler M, Margulis L, Fester R). Academic Press, Boston, pp. 31–50.

Strother PK, Tobin K (1987) Observations on the genus *Huroniospora barghoorn*: Implications for paleoecology of the Gunflint microbiota. *Precambrian Research* **36**, 323–333.

Stüeken EE (2013) A test of the nitrogen-limitation hypothesis for retarded eukaryote radiation: Nitrogen isotopes across a Mesoproterozoic basinal profile. *Geochimica et Cosmochimica Acta* **120**, 121–139.

Stüeken EE, Buick R, Anbar AD (2015b) Selenium isotopes support free O_2 in the latest Archean. *Geology* **43**, 259–262.

Stüeken EE, Buick R, Anderson RE, Baross JA, Planavsky NJ, Lyons TW (2017) Environmental niches and metabolic diversity in Neoarchean lakes. *Geobiology* **15**, 767–783.

Stüeken EE, Buick R, Guy BM, Koehler MC (2015a) Isotopic evidence for biological nitrogen fixation by molybdenum-nitrogenase from 3.2 Gyr. *Nature* **520**, 666–669.

Stüeken EE, Kipp MA, Koehler MC, Buick R (2016) The evolution of Earth's biogeochemical nitrogen cycle. *Earth-Science Reviews* **160**, 220–239.

Suarez C, Piculell M, Modin O, Langenheder S, Persson F, Hermansson M (2019) Thickness determines microbial community structure and function in nitrifying biofilms via deterministic assembly. *Scientific Reports* **9**, 5110.

Summons RE, Bradley AS, Jahnke LL, Waldbauer JR (2006) Steroids, triterpenoids and molecular oxygen. *Philosophical Transactions of the Royal Society B: Biological Sciences* **361**, 951–968.

Sumner DY, Grotzinger JP (2004) Implications for Neoarchaean ocean chemistry from primary carbonate mineralogy of the Campbellrand-Malmani Platform, South Africa. *Sedimentology* **51**, 1273–1299.

Sumner DY, Hawes I, Mackey TJ, Jungblut AD, Doran PT (2015) Antarctic microbial mats: A modern analog for Archean lacustrine oxygen oases. *Geology* **43**, 887–890.

Suosaari EP, Reid RP, Playford PE, Foster JS, Stolz JF, Casaburi G, Hagan PD, Chirayath V, Macintyre IG, Planavsky NJ, Eberli GP (2016) New multi-scale perspectives on the stromatolites of Shark Bay, Western Australia. *Scientific Reports* **6**, 20557.

Sutherland IW (2001) The biofilm matrix – an immobilized but dynamic microbial environment. *Trends in Microbiology* **9**, 222–227.

Taj RJ, Aref MAM, Schreiber BC (2014) The influence of microbial mats on the formation of sand volcanoes and mounds in the Red Sea coastal plain, south Jeddah, Saudi Arabia. *Sedimentary Geology* **311**, 60–74.

Taylor SR, McLennan SM (1985) *The continental crust: Its composition and evolution*. Blackwell Scientific Puplications, Oxford.

Taylor SR, McLennan SM (2001) Chemical composition and element distribution in the Earth’s Crust. In: *Encyclopedia of Physical Science and Technology* (ed. Roberts AM). Academic Press, New York, pp. 697–719.

Thiéblemont D, Bouton P, Préat A, Goujou J-C, Tegyey M, Weber F, Ebang Obiang M, Joron JL, Treuil M (2014) Transition from alkaline to calc-alkaline volcanism during evolution of the Paleoproterozoic Francevillian basin of eastern Gabon (Western Central Africa). *Journal of African Earth Sciences* **99**, 215–227.

Thiéblemont D, Castaing C, Billa M, Bouton P, Préat A (2009) Notice explicative de la carte géologique et des ressources minérales de la République gabonaise à 1/1,000,000.

Thomas K, Herminghaus S, Porada H, Goehring L (2013) Formation of Kinneyia *via* shear-induced instabilities in microbial mats. *Philosophical Transactions of the Royal Society A: Mathematical, Physical and Engineering Sciences* **371**, 20120362–20120362.

Thomazo C, Nisbet EG, Grassineau NV, Peters M, Strauss H (2013) Multiple sulfur and carbon isotope composition of sediments from the Belingwe Greenstone Belt (Zimbabwe): A biogenic methane regulation on mass independent fractionation of sulfur during the Neoarchean? *Geochimica et Cosmochimica Acta* **121**, 120–138.

Thunell RC, Sigman DM, Muller-Karger F, Astor Y, Varela R (2004) Nitrogen isotope dynamics of the Cariaco Basin, Venezuela. *Global Biogeochemical Cycles* **18**, GB3001.

Tice MM (2009) Environmental controls on photosynthetic microbial mat distribution and morphogenesis on a 3.42 Ga clastic-starved platform. *Astrobiology* **9**, 989–1000.

Tice MM, Lowe DR (2004) Photosynthetic microbial mats in the 3,416-Myr-old ocean. *Nature* **431**, 549–552.

Tice MM, Lowe DR (2006a) The origin of carbonaceous matter in pre-3.0 Ga greenstone terrains: A review and new evidence from the 3.42 Ga Buck Reef Chert. *Earth-Science Reviews* **76**, 259–300.

Tice MM, Lowe DR (2006b) Hydrogen-based carbon fixation in the earliest known photosynthetic organisms. *Geology* **34**, 37–40.

Tribovillard N, Algeo TJ, Lyons T, Riboulleau A (2006) Trace metals as paleoredox and paleoproductivity proxies: An update. *Chemical Geology* **232**, 12–32.

Trichet J, Défarge C (1995) Non-biologically supported organomineralization. *Bulletin de l’Institut Océanographique (Monaco) Numéro Spécial* **14**, 203–236.

Trudinger PA, Chambers LA, Smith JW (1985) Low-temperature sulphate reduction: Biological versus abiological. *Canadian Journal of Earth Sciences* **22**, 1910–1918.

Tsikos H, Moore JM (1997) Petrography and geochemistry of the Paleoproterozoic Hotazel iron-formation, Kalahari manganese field, South Africa: Implications for Precambrian manganese metallogenesis. *Economic Geology* **92**, 87–97.

Turner P (1980) *Continental red beds*. Elsevier, Amsterdam.

Tyrrell T (1999) The relative infuences of nitrogen and phosphorus on oceanic primary production. *Nature* **400**, 525–531.

van Zuilen MA, Lepland A, Arrhenius G (2002) Reassessing the evidence for the earliest traces of life. *Nature* **418**, 627–630.

Veblen DR, Gutherie Jr GD, Livi KJT, Reynolds Jr RC (1990) High-resolution transmission electron microscopy and electron diffraction of mixed-layer illite/smectite: Experimental results. *Clays and Clay Minerals* **38**, 1–13.

Velde B, Lanson B (1993) Comparison of I/S transformation and maturity of organic matter at elevated temperatures. *Clays and Clay Minerals* **41**, 178–183.

Velde B, Meunier A (2008) *The Origin of Clay Minerals in Soils and Weathered Rocks*. Springer-Verlag, Berlin.

Velde B, Suzuki T, Nicot E (1986) Pressure-temperature-composition of illite/smectite mixed-layer minerals: Niger delta mudstones and other examples. *Clays and Clay Minerals* **34**, 435–441.

Visscher PT, Stolz JF (2005) Microbial mats as bioreactors: Populations, processes, and products. *Palaeogeography, Palaeoclimatology, Palaeoecology* **219**, 87–100.

Vorhies JS, Gaines RR (2009) Microbial dissolution of clay minerals as a source of iron and silica in marine sediments. *Nature Geoscience* **2**, 221–225.

Wacey D (2009) *Early life on earth: a practical guide*. Springer, Dordrecht.

Wacey D, Saunders M, Roberts M, Menon S, Green L, Kong C, Culwick T, Strother P, Brasier MD (2014) Enhanced cellular preservation by clay minerals in 1 billion-year-old lakes. *Scientific Reports* **4**, 5841.

Walcott CD (1914) Cambrian Geology and Palaeontology III, No. 2. Precambrian, Algonkian algal flora. *Smithsonian Miscellaneous Collections* **64**, 77–156.

Waldbauer JR, Sherman LS, Sumner DY, Summons RE (2009) Late Archean molecular fossils from the Transvaal Supergroup record the antiquity of microbial diversity and aerobiosis. *Precambrian Research* **169**, 28–47.

Walter M, Buick R, Dunlop J (1980) Stromatolites 3,400–3,500 Myr old from the North pole area, Western Australia. *Nature* **284**, 443–445.

Walter MR, Goode DT, Hall WDM (1976) Microfossils from a newly discovered Precambrian stromatolitic iron formation in Western Australia. *Nature* **261**, 221–223.

Weber F (1968) *Une série précambrienne du Gabon : le Francevillien. Sédimentologie, géochimie, relations avec les gîtes minéraux associés*.

Weber F, Gauthier-Lafaye F (2013) No proof from carbon isotopes in the Francevillian (Gabon) and Onega (Fennoscandian shield) basins of a global oxidation event at 1980–2090 Ma following the Great Oxidation Event (GOE). *Comptes Rendus Geoscience* **345**, 28–35.

Weber F, Gauthier-Lafaye F, Whitechurch H, Ulrich M, El Albani A (2016) The 2-Ga Eburnean Orogeny in Gabon and the opening of the Francevillian intracratonic basins: A review. *Comptes Rendus Geoscience* **348**, 572–586.

Webster-Brown JG, Webster KS (2007) Trace metals in cyanobacterial mats, phytoplankton and sediments of the Lake Vanda region, Antarctica. *Antarctic Science* **19**, 311–319.

Weiershäuser L, Spooner ETC (2005) Seafloor hydrothermal fluids, Ben Nevis area, Abitibi Greenstone Belt: Implications for Archean (~2.7Ga) seawater properties. *Precambrian Research* **138**, 89–123.

Westall F, Campbell KA, Bréhéret JG, Foucher F, Gautret P, Hubert A, Sorieul S, Grassineau N, Guido DM (2015) Archean (3.33 Ga) microbe-sediment systems were diverse and flourished in a hydrothermal context. *Geology* **43**, 615–618.

Westbroek P, Buddemeier B, Coleman M, Kok D, Fautin D, Stal L (1994) Strategies for the study of climate forcing by calcification. *Bulletin de l'Institut Océanographique (Monaco) Numéro Special* **14**, 203–236.

Whitney G, Velde B (1993) Changes in particle morphology during illitization: An experimental study. *Clays and Clay Minerals* **41**, 209–218.

Wilkinson JF, Duguid JP, Edmunds PN (1954) The distribution of polysaccharide production in *Aerobacter* and *Escherichia* strains and its relation to antigenic character. *Journal of General Microbiology* **11**, 59–72.

Williams RJP, Da Silva JF (2006) *The chemistry of evolution: The development of our ecosystem*. Elsevier, Amsterdam.

Williams RJP, Fraústo da Silva JJR (2002) The Involvement of Molybdenum in Life. *Biochemical and Biophysical Research Communications* **292**, 293–299.

Wilmeth DT, Corsetti FA, Beukes NJ, Awramik SM, Petryshyn V, Spear JR, Celestian AJ (2019) Neoarchean (2.7 Ga) lacustrine stromatolite deposits in the Hartbeesfontein Basin, Ventersdorp Supergroup, South Africa: Implications for oxygen oases. *Precambrian Research* **320**, 291–302.

Wilmeth DT, Dornbos SQ, Isbell JL, Czaja AD (2014) Putative domal microbial structures in fluvial siliciclastic facies of the Mesoproterozoic (1.09 Ga) Copper Harbor Conglomerate, Upper Peninsula of Michigan, USA. *Geobiology* **12**, 99–108.

Woebken D, Burow LC, Behnam F, Mayali X, Schintlmeister A, Fleming ED, Prufert-Bebout L, Singer SW, López Cortés A, Hoehler TM, Pett-Ridge J, Spormann AM, Wagner M, Weber PK, Bebout BM (2015) Revisiting N_2 fixation in Guerrero Negro intertidal microbial mats with a functional single-cell approach. *The ISME Journal* **9**, 485–496.

Yang H, Chen Z-Q, Fang Y (2017) Microbially induced sedimentary structures from the 1.64 Ga Chuanlinggou Formation, Jixian, North China. *Palaeogeography, Palaeoclimatology, Palaeoecology* **474**, 7–25.

Yun Z (1984) A Gunflint type of microfossil assemblage from early Proterozoic stromatolitic cherts in China. *Nature* **309**, 547–549.

Zerkle AL, House CH, Brantley SL (2005) Biogeochemical signatures through time as inferred from whole microbial genomes. *American Journal of Science* **305**, 467–502.

Zerkle AL, Junium CK, Canfield DE, House CH (2008) Production of ^{15}N-depleted biomass during cyanobacterial N_2-fixation at high Fe concentrations. *Journal of Geophysical Research* **113**, G03014.

Zerkle AL, Poulton SW, Newton RJ, Mettam C, Claire MW, Bekker A, Junium CK (2017) Onset of the aerobic nitrogen cycle during the Great Oxidation Event. *Nature* **542**, 465–467.

Zhang G, Kim J, Dong H, Sommer AJ (2007) Microbial effects in promoting the smectite to illite reaction: Role of organic matter intercalated in the interlayer. *American Mineralogist* **92**, 1401–1410.

Zhang W, Ding W, Li Y-X, Tam C, Bougouffa S, Wang R, Pei B, Chiang H, Leung P, Lu Y, Sun J, Fu H, Bajic VB, Liu H, Webster NS, Qian P-Y (2019) Marine biofilms constitute a bank of hidden microbial diversity and functional potential. *Nature Communications* **10**, 517.

Zhang X, Sigman DM, Morel FMM, Kraepiel AML (2014) Nitrogen isotope fractionation by alternative nitrogenases and past ocean anoxia. *Proceedings of the National Academy of Sciences* **111**, 4782–4787.

Zhao G, Cawood PA, Wilde SA, Sun M (2002) Review of global 2.1–1.8 Ga orogens: implications for a pre-Rodinia supercontinent. *Earth-Science Reviews* **59**, 125–162.

APPENDIX

Appendix 1: Additional flat pyritized microbial mats.

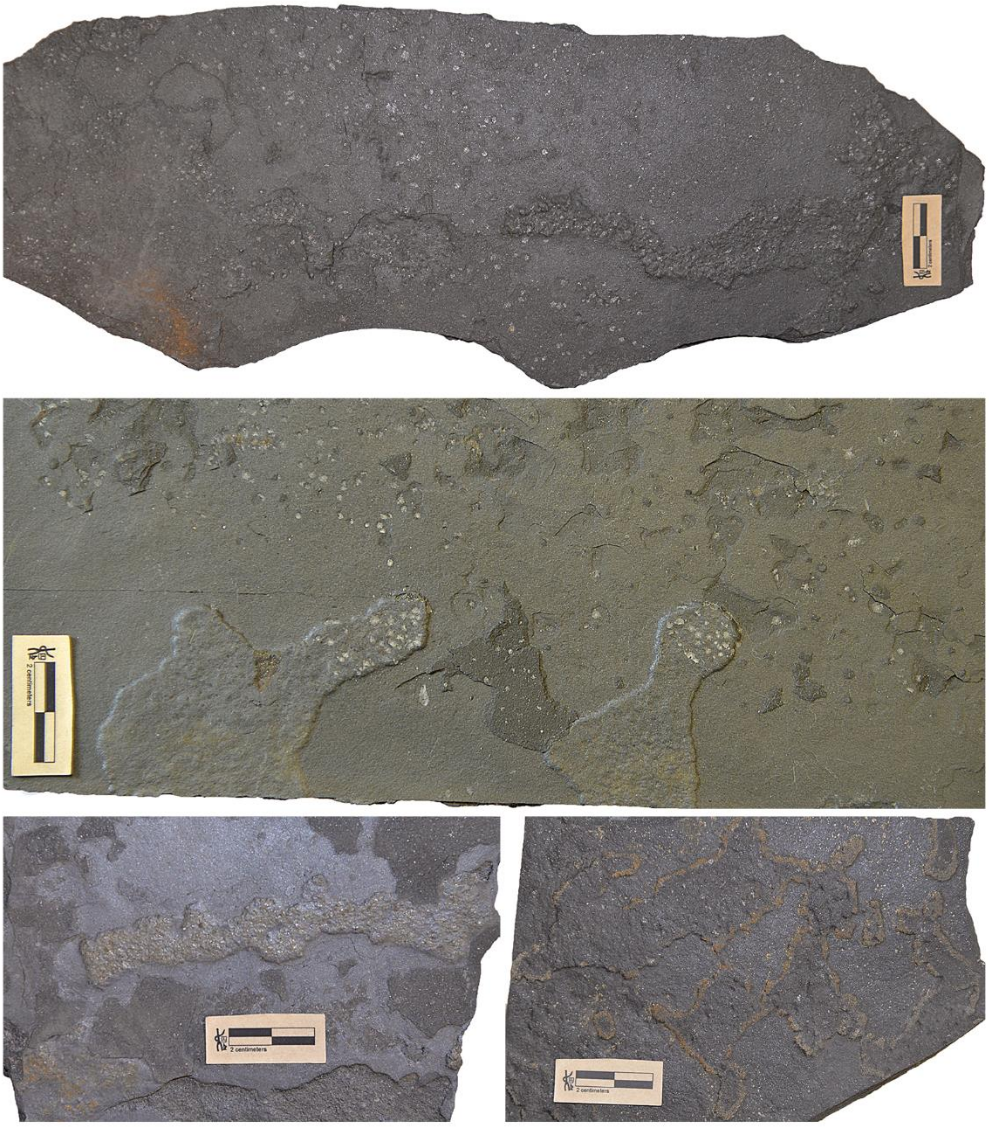

Appendix 2: EDS elemental maps of bulges of reticulate patterns in cross-section perpendicular to bedding plane. BSE and composite elemental maps. Note the wavy-crinkly laminae with a large amount of embedded heavy minerals.

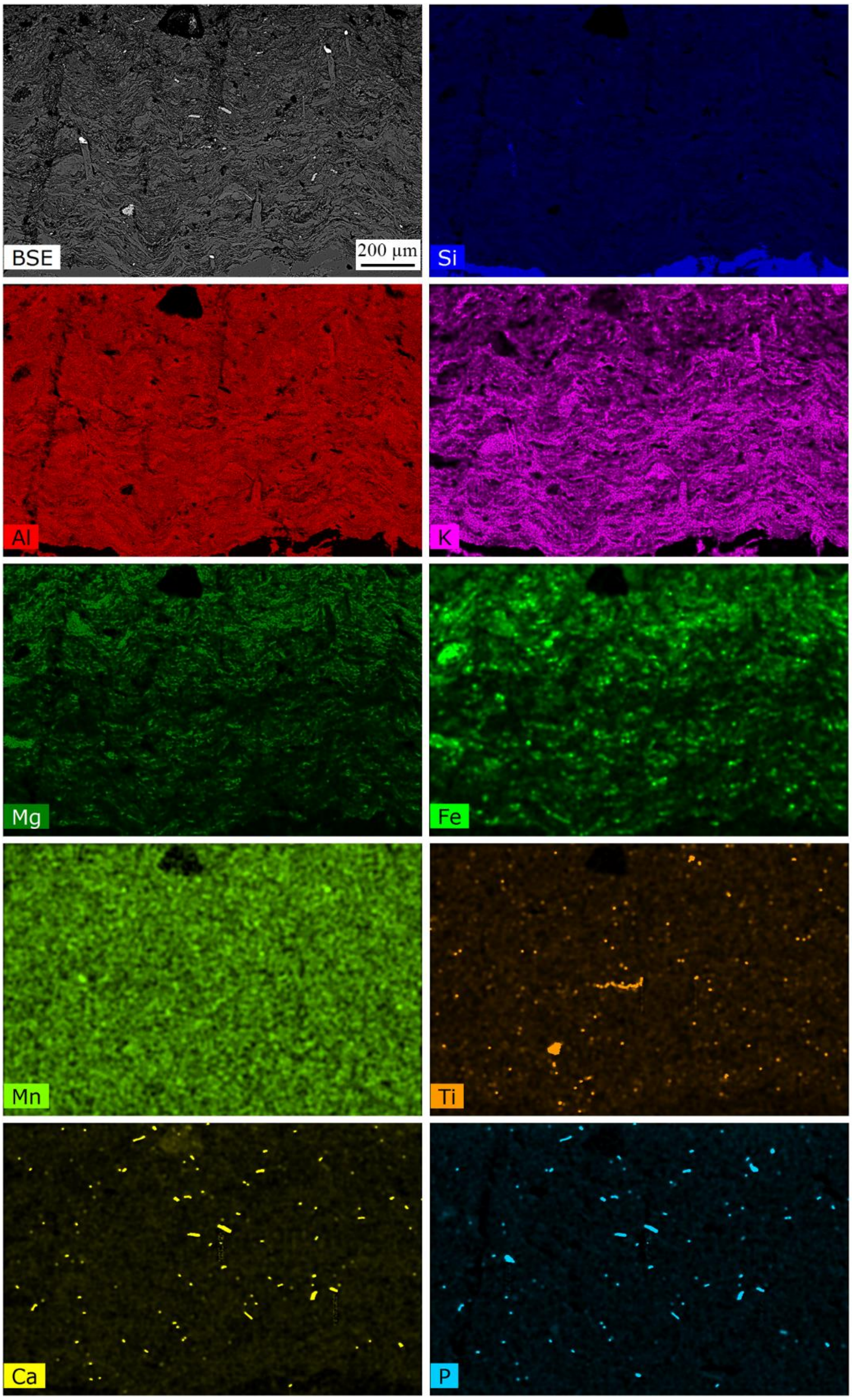

Appendix 3: Representative structural formulae of clays from microbial mats studied with EDS. EST, “elephant-skin” texture; PTMM, putative tufted microbial mat; WS, wrinkle structure; LP, linear pattern.

Samples	Si	Al^{IV}	Al^{VI}	Al_{Tot}	Mg	Fe	Ti	Mn	K	Na	Ca	∑ Oct	Int
EST	2.78	1.22	1.58	2.8	0.73	0.11	0	0	0.33	0.13	0	2.42	0.47
	3.13	0.87	1.69	2.56	0.15	0.12	0.02	0	0.71	0.15	0	1.98	0.86
	2.89	1.11	1.47	2.58	0.33	0.05	0	0	0.47	0.18	0	1.84	0.65
	3.13	0.87	1.91	2.78	0.11	0	0	0	0.74	0.1	0	2.02	0.84
	2.88	1.12	1.6	2.72	0.52	0.17	0	0	0.52	0.11	0	2.29	0.63
	3.11	0.89	1.94	2.83	0.09	0	0	0	0.79	0.1	0	2.03	0.89
	2.63	1.37	1.17	2.54	0.72	0	0.26	0	0.26	0.17	0	2.15	0.43
PTMM	3.54	0.46	1.79	2.25	0.06	0.04	0	0	0.65	0.06	0	1.89	0.71
	3.41	0.59	1.88	2.47	0.1	0	0	0	0.69	0.07	0	1.98	0.76
	3.34	0.66	1.76	2.41	0.15	0.04	0	0	0.71	0.09	0.03	1.95	0.87
	3.46	0.54	1.69	2.23	0.28	0.06	0	0	0.55	0.09	0	2.02	0.64
	3.61	0.39	1.8	2.19	0.14	0	0	0	0.47	0.17	0	1.94	0.64
	3.35	0.65	1.6	2.25	0.3	0.09	0.01	0.02	0.58	0.12	0.03	2.02	0.73
	3.16	0.84	1.77	2.61	0.14	0.04	0.02	0.02	0.48	0.29	0.04	1.98	0.8
	3.06	0.94	1.56	2.5	0.16	0.25	0.02	0.01	0.86	0.07	0.01	2	0.94
	2.98	1.02	1.83	2.85	0.08	0.04	0.01	0.01	0.89	0.03	0.04	1.98	0.95
	3.03	0.97	1.79	2.76	0.12	0.04	0.01	0.02	0.75	0.11	0.04	1.98	0.9
	3.1	0.9	1.83	2.72	0.1	0.04	0.02	0.02	0.39	0.35	0.03	2	0.77
PWWS	3.17	0.83	1.39	2.22	0.46	0.4	0	0	0.41	0.12	0	2.25	0.53
	3.44	0.56	1.66	2.21	0.3	0.13	0	0	0.45	0.14	0	2.09	0.59
	3.56	0.44	1.67	2.11	0.24	0.1	0	0	0.53	0.09	0	2.02	0.62
	3.38	0.62	1.27	1.89	0.53	0.4	0.03	0	0.34	0.09	0	2.23	0.43
	3.17	0.83	1.91	2.75	0.12	0	0	0	0.75	0.1	0	2.03	0.85
	3.82	0.18	1.77	1.94	0.15	0	0	0	0.5	0.08	0	1.92	0.57
	3.1	0.9	1.76	2.66	0.18	0.07	0.01	0.02	0.62	0.14	0.02	2.03	0.78
	3.04	0.96	1.5	2.46	0.17	0.23	0.07	0.02	0.79	0.09	0.02	1.99	0.89
	3.18	0.82	1.62	2.44	0.32	0.15	0.01	0.02	0.47	0.18	0.02	2.12	0.68
	3.07	0.93	1.39	2.32	0.48	0.3	0.02	0.03	0.55	0.08	0.01	2.22	0.65
	2.97	1.03	1.39	2.42	0.47	0.31	0.04	0.03	0.53	0.13	0.02	2.24	0.67
LP	3.19	0.81	1.85	2.66	2.38	1.64	0.12	0	0.1	0.18	0	5.99	0.28
	3.31	0.69	2.12	2.81	2.48	1.98	0	0	0.02	0.06	0	6.57	0.08
	3.41	0.59	2.25	2.83	2.37	1.64	0.12	0	0.15	0.07	0	6.37	0.22

3.06	0.94	2.48	3.42	1.98	2.07	0	0	0.2	0.08	0	6.53	0.28
2.95	1.05	1.5	2.56	0.41	0.29	0.03	0	0.65	0.09	0	2.23	0.74
3.08	0.92	1.88	2.8	0.08	0.06	0	0	0.77	0.18	0	2.02	0.95
3.19	0.81	1.82	2.62	0.1	0.06	0	0	0.86	0.05	0	1.98	0.91
3.11	0.89	0.99	1.88	0.43	0.54	0.09	0.05	0.44	0.05	0.06	2.1	0.55
3.72	0.28	1.44	1.72	0.12	0.1	0.11	0.03	0.48	0.12	0.03	1.8	0.63

Appendix 4: Organic elemental analyses (carbon and sulfur) on five microbial mats and their host sediments from the FB_2 Formation. EST, “elephant-skin” texture; DB, domal buildup; PWWS, parallel wavy wrinkle structure.

Samples	Mass (mg)	%C	%S
EST_mat	10.63	8.62	0.25
EST_host rock	16.62	0.58	0.05
DB_mat	15.32	0.53	22.16
DB_host rock	13.24	4.59	0.22
PWWS_mat	10.37	1.69	0.00
PWWS_host rock	14.17	2.2	0.00
sample4_mat	16.08	1.86	0.06
sample4_host rock	17.53	1.77	0.09
sample5_mat	12.58	1.25	0.54
sample5_host rock	13.18	2.11	0.11

Appendix 5: Photographs of mat-layer structures found in literature. (**A**) Analogous 'elephant-skin' texture from modern lower supratidal, Bahar Alouane, southern Tunisia. Modified after photo published in Gerdes (2007). (**B**) Fossil reticulate pattern on bedding plane of siliciclastic beds from the Archaean Tumbiana Formation, Australia. Modified after photo published in Flannery & Walter (2012). (**C**) A 2.0 billion-years-old tufted microbial mat from Makgabeng Formation, South Africa. Modified after photo published in Simpson *et al*. (2013). (**D**) Analogue clustered low mound-like structures with *Protichnites* trackways on bedding surface of quartz arenites from the Late Cambrian, Elk Mound Group, USA. Modified after photo published in Bottjer & Hagadorn (2007). (**E**) Modern analogous 'fairy rings' on soft muddy sediments from Bretagne salterns, France. Modified after photo published in Grazhdankin & Gerdes (2007). (**F**) Ancient example of outward-convex, spindle-shaped discoidal structures with concentric rings from the Mesoproterozoic, Sonia Sandstone, India. Modified after photo published in Sarkar *et al*. (2014). (**G**) Modern discoidal microbial colony on tidal flat from the Gulf of Cambay, India. Modified after photo published in Banerjee *et al*. (2014). Lens cap diameter: 6 cm. (**H**) Analogue discoidal microbial colony on bedding plane of sandstones from the Precambrian Vindhyan Supergroup, India. Modified after photo published in Banerjee *et al*. (2014).

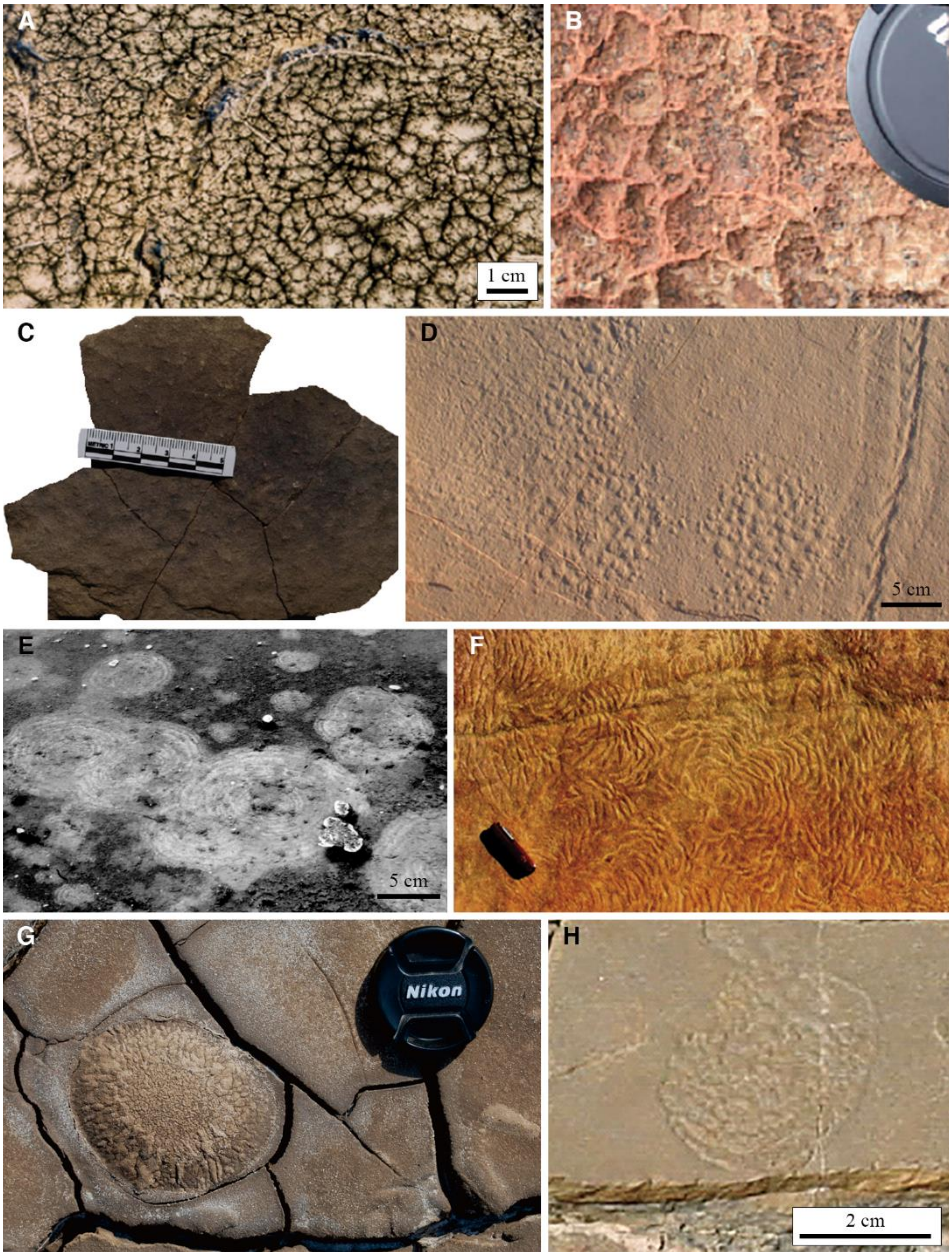

Appendix 6: Photographs of mat-related structures found in literature. (**A**) Modern example of submerged wrinkle marks from Redfish Bay, Texas. Modified after photo published in Hagadorn & Bottjer (1997). (**B**) Patches of wrinkle marks on bedding surface of fine-grained sandstones from the Early Cambrian, Chapel Island Formation, Canada. Modified after photo published in Buatois *et al*. (2014). (**C**) Parallel wavy wrinkle structures reproduced in wave tank experiments using microbial aggregates. Modified after photo published in Mariotti et al. (2014). (**D**) Analogous parallel wavy wrinkle structures on bedding plane of mudstones from the Early Cambrian, Northwest Argentina. Modified after photo published in Buatois & Mángano (2003). (**E**) Minute “Kinneyia” structures formed with microbial aggregates in wave tank experiments. Modified after photo published in Mariotti *et al*. (2014). (**F**) Ancient analogue “Kinneyia” structures on bedding surface of siltstones from the Cambrian, Oeland, Sweden. Modified after photo published in Porada & Bouougri (2007). (**G**) Linear features from modern tidal flats of Bhar Alouane, southern Tunisia. Modified after photo published in Porada & Bouougri (2007). (**H**) Putative linear patterns on bedding surface of fine-grained quartzites from the Neoproterozoic Katanga Supergroup, Zambia. Modified after photo published in Porada & Bouougri (2007).

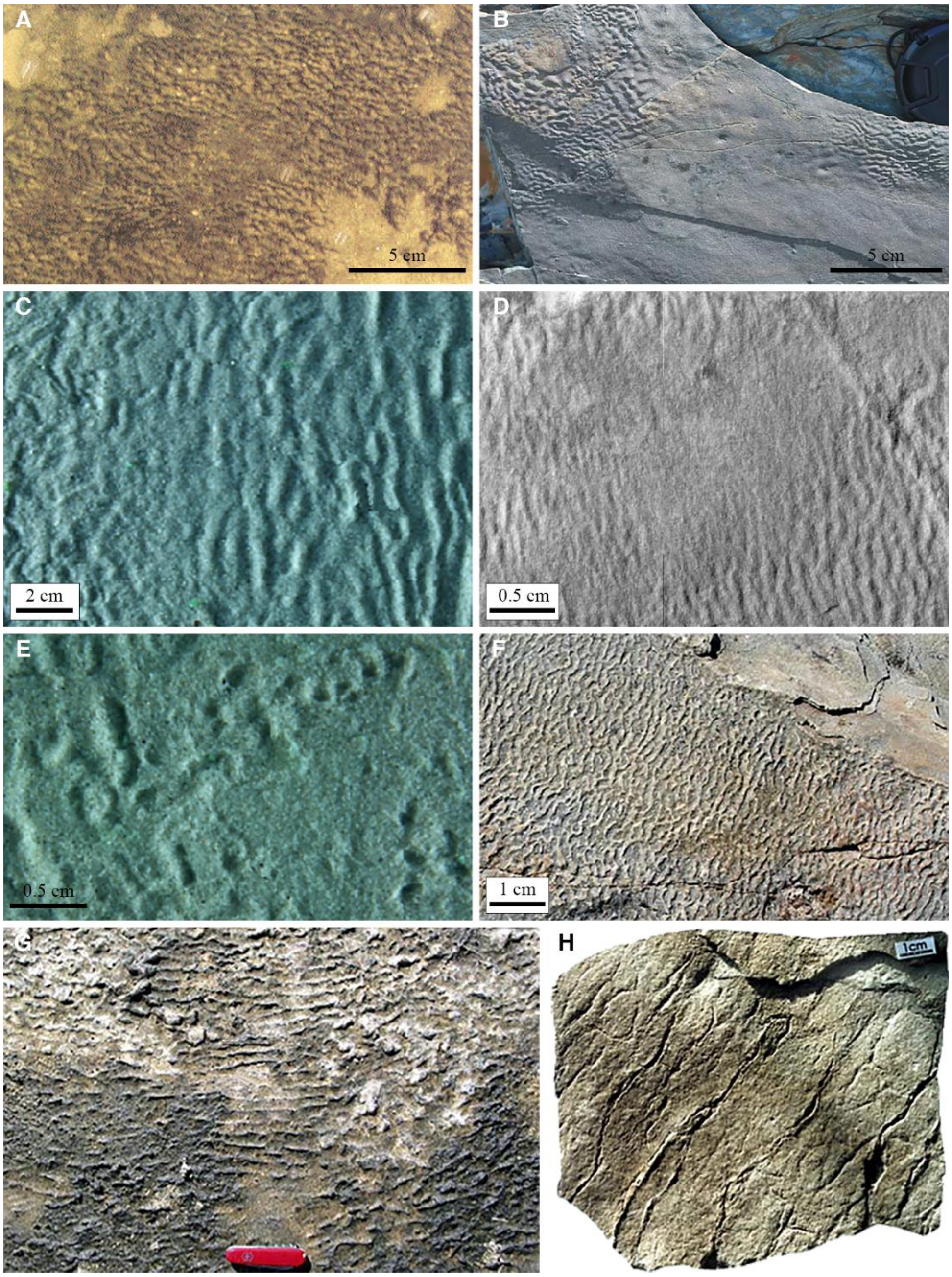

Appendix 7: Lithostratigraphic columns for the Francevillian basin. (**A**) Lithostratigraphy of the Palaeoproterozoic Francevillian Series that comprises four sedimentary formations. (**B**) Composite stratigraphic section of the FB_2 Member in the studied area. It consists of the 15 m-thick coarse-grained sandstone conformably underlying the 5 m-thick black shale sequence ([1]Horie *et al*., 2005; [2]Bros *et al*., 1992; [3]Gancarz, 1978; [4]Mouélé *et al*., 2014; [5]Gauthier-Lafaye & Weber, 2003).

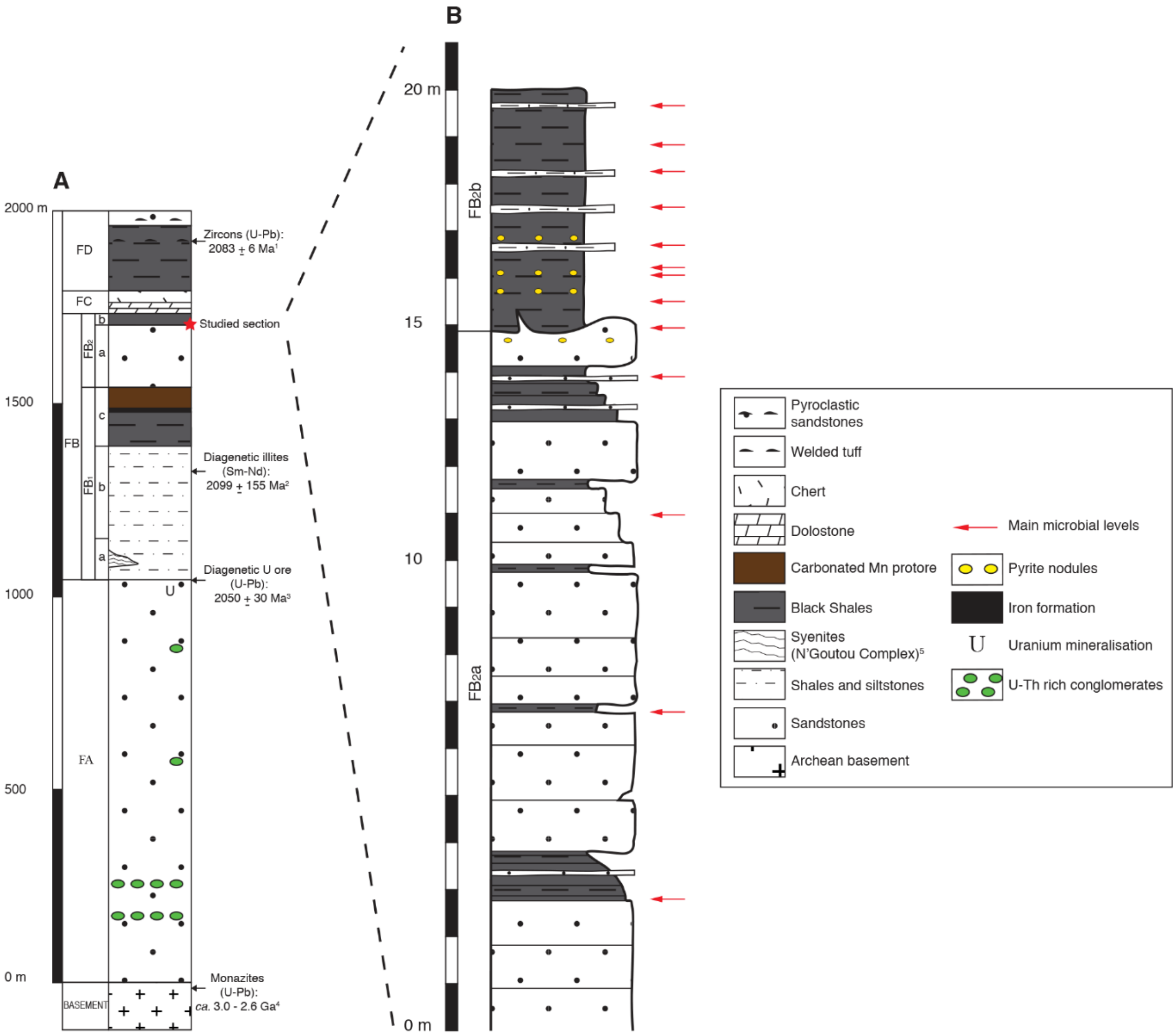

Appendix 8: Microbial mat laminae and their host sediments. (**A**) A µm-thick mat-related structure preserved as wrinkle on the top of the sandstone bed. (**B**) Polished slab section of A. (**C**) Pyritized microbial mat from the black shale facies. (**D**) SEM imaging of C. Note extensively developed euhedral pyrite, making difficult to separate black shale from pyritized mat structures. (**E**) SEM image of a thinly laminated mat from the top of the sandstone bed. Note the microtexture of mat laminae. Blue, yellow, and green arrows point to the thin biofilm layers, macrofossil (El Albani *et al*., 2010, 2014), and heavy minerals, respectively.

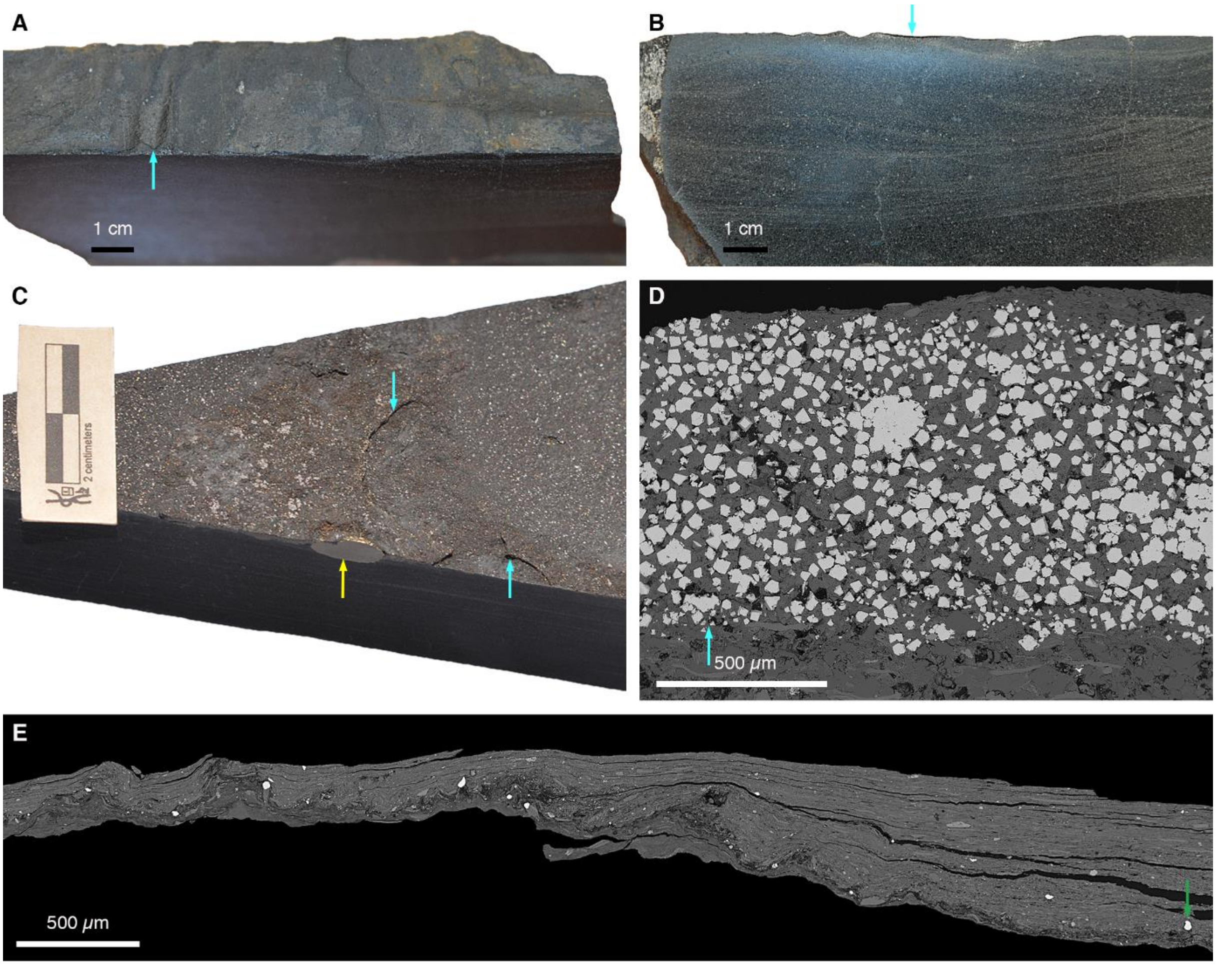

Appendix 9: Petrography, SEM, and EDX of bubble-like features in cross-section perpendicular to the bedding plane. Back-scattered electron (BSE) and composite (Si, Al, Ti, Mg, and Fe) elemental maps show mineral composition of circular structures within the MRS. The cone-like structure mainly consists of Al- and Mg-rich clays.

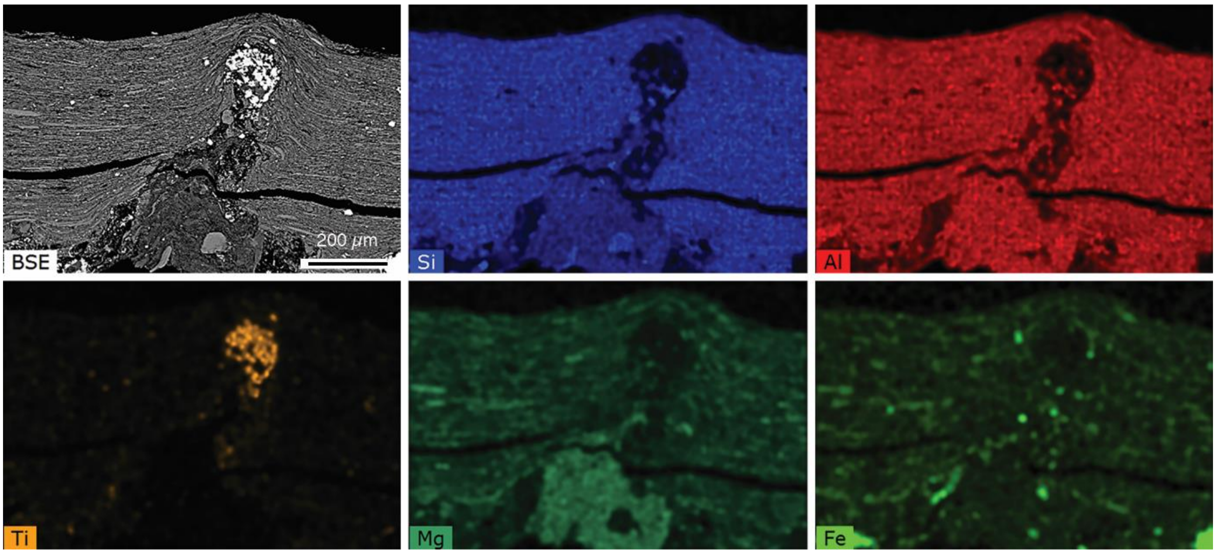

Appendix 10: Whole-rock geochemical data of major elements and carbon.

Formation	Lithology	Sample ID	Depth m	SiO_2 %	Al_2O_3 %	Fe_2O_3 %	MnO %	MgO %	CaO %	Na_2O %	K_2O %	TiO_2 %	P_2O_5 %	S_{tot} wt%	C_{tot} wt%	C_{org}* wt%
FB2b	Pyritized	FPS_s5-mat	1,3	23.2	10.1	38.4	0.1	1.35	0.59	0.19	1.88	0.14	BDL	29.37	0.69	0.56
	MRS	DB_s4-mat	2,9	32.87	9.71	29.74	0.16	1.63	1.27	0.17	1.81	0.18	BDL	22.02	3.12	2.85
		FPS_s4-mat	3,7	21.23	8.26	41.49	0.09	1.81	0.81	0.14	1.34	0.12	BDL	24.81	0.77	0.59
		FPS_s3-mat	3,8	26.69	9.62	35.26	0.12	1.87	0.86	0.19	1.62	0.15	BDL	28.45	1.36	1.18
		DB_s3-mat	4	24.17	10.5	29.86	0.08	1.44	0.85	0.19	1.97	0.15	BDL	26.9	0.53	0.35
		DB_s2-mat	4	27.84	11.83	20.82	0.07	1.44	0.51	0.21	2.28	0.2	BDL	23.88	X	X
		FR_s1-mat	4	51.3	15.74	10.33	0.24	2.43	2.08	0.31	3.04	0.34	BDL	6.46	3.52	3.08
	Black	WS_s1-sed	0,3	58.93	16.69	3.69	0.49	3.43	2.26	0.34	2.95	0.33	BDL	0.09	2.2	1.72
	shales	KS_s1-sed	1	61.85	15.14	3.81	0.23	3.02	2.07	0.3	2.83	0.42	0.2	0.09	2.91	2.47
		FPS_s5-sed	1,3	56.35	16.72	2.39	0.47	3.03	2.65	0.34	3.16	0.39	0.16	0.22	4.98	4.41
		AFBSO-12	1,4	62.88	18.65	3.44	0.07	1.96	0.37	0.39	3.63	0.41	0.17	X	X	X
		MLS_s7-sed	1,9	61.55	13.22	6.99	0.22	4.77	2.24	0.22	1.57	0.37	BDL	0.32	2.11	1.63
		AFBSO-9	2,5	54.74	12.06	6.5	0.74	5.55	5.21	0.23	1.47	0.32	0.12	X	3.8	2.68
		DB_s4-sed	2,9	58.09	17.07	2.81	0.44	3.06	2.67	0.33	3.32	0.39	0.13	0.13	3.83	3.26
		AFBSO-7	3,5	77.68	13.28	0.35	BDL	0.53	BDL	0.21	2.84	0.29	BDL	X	2.47	2.47
		FPS_s4-sed	3,7	57.81	18.6	2.2	0.26	2.74	2.07	0.35	3.73	0.39	0.16	0.16	2.62	2.18
		FPS_s3-sed	3,8	57.66	16.08	2.34	0.31	2.99	2.59	0.36	2.95	0.38	0.16	0.17	5.04	4.48
		AFBSO-6	3,9	66.18	12.04	8.87	0.11	3.09	0.24	0.22	1.35	0.26	0.15	X	3.64	3.59
		DB_s2-sed	4	56.11	17.85	2.15	0.3	2.87	2.24	0.36	3.59	0.39	BDL	0.16	4.59	4.11
		FR_s1-sed	4	58.3	18.86	2.36	0.24	2.86	2.18	0.38	3.79	0.4	0.14	0.2	2.73	2.26
		MLS_s8-sed	4,5	54.3	20.73	3.87	0.48	3.1	2.1	0.39	4.3	0.44	BDL	1.02	1.86	1.41
		MLS_s9-sed	4,5	56.29	19.14	3.02	0.37	2.99	2.09	0.37	3.87	0.41	BDL	0.34	1.77	1.32
FB2a	Non-pyritized	MLS_s1-mat	5	33.74	22.58	13.1	0.32	4.13	1.01	0.36	4.17	2.77	0.56	4.16	5.84	5.63
		LP_s3-mat	5	41.35	27.69	5.03	0.1	3.5	0.34	0.59	5.34	1.91	0.34	0.19	3.74	3.67
	MRS	MLS_s2-mat	5	33.09	23.3	9.45	0.1	4.12	0.43	0.28	4.04	3.39	0.36	3.08	9.69	9.6
		MLS_s3-mat	5	38.3	20.66	13.32	0.16	4.45	0.79	0.29	3.46	2.34	0.65	2.61	4.44	4.27
		MLS_s4-mat	5	35.62	23.78	5.69	0.11	4.35	0.68	0.28	4.44	3.21	0.51	0.36	10.59	10.44
		MLS_s5-mat	5	35.56	24.54	6.41	0.09	4.67	0.6	0.29	4.29	3.13	0.49	0.42	9	8.87
		EST_s3-mat	5	31.67	27.89	3.47	0.03	5.62	0.03	0.4	2.78	0.37	0.1	0.36	16.97	16.96
		EST_s4-mat	5	31.66	28.67	4.25	0.05	6.76	0.03	0.33	2.3	0.23	0.05	0.29	X	X
		MLS_s3-mat	9	44.31	31.77	2.48	0.03	2.9	0.16	0.49	5.74	0.87	0.12	0.84	1.6	1.57
		EST_s1-mat	13,2	36.27	31	2.72	0.01	5.57	0.1	0.5	3.56	0.36	0.02	0.17	11.09	11.07
		EST_s2-mat	13,2	38.54	31.4	2.48	0.02	4.03	0.2	0.63	5.01	0.33	0.17	0.15	X	X
	Sandstones	MLS_s1-sed	5	89.24	4.66	0.97	0.11	0.96	0.65	0.1	0.6	0.03	BDL	X	0.45	0.31
		LP_s3-sed	5	93.65	2.46	0.66	0.07	0.63	0.6	0.04	0.32	BDL	BDL	X	0.52	0.39
		MLS_s2-sed	5	89.25	3.21	0.79	0.27	1.17	1.22	0.16	0.27	0.03	BDL	X	0.83	0.57

AFBSO-3	5	96.83	0.95	0.08	0.01	0.08	BDL	*0.01*	0.08	0.02	BDL	X	0.36	0.36
LP_s2-sed	6	95.03	2.08	0.56	0.01	0.39	0.06	0.04	0.19	0.02	0.03	X	0.31	0.3
MLS_s3-sed	9	94.48	2.85	0.68	0.03	0.58	BDL	0.03	0.21	0.04	BDL	X	0.42	0.42
EST_s1-sed	13,2	94.74	1.99	0.57	BDL	0.2	BDL	*0.01*	0.28	BDL	BDL	0.02	0.58	0.58
EST_s2-sed	13,2	95.98	1.47	0.63	BDL	0.17	0.07	0.02	0.18	0.02	0.07	X	X	X

FPS: flat pyritized mat; LP: linear pattern; DB: domal buildup; WS: wrinkle structure; KS: “kinneyia” structure; MLS: mat-layer structure; FR: “fairy-ring” structure; EST: “elephant-skin” texture (Aubineau *et al.*, 2018).

BLD: below detection limit. Italicized numbers reflect samples where half or more of the analyses were below detection limits for that element.

Organic carbon is calculated as follow: $C_{org} \approx C_{tot} – (12*CaO/56)$; $C_{org} = C_{tot}$ when CaO contents < BLD.

X: Not analyzed

Appendix 11: Pairwise comparisons between all pairs of groups.

	Pyritized MRS (FB2b)	Black shales (FB2b)	Non-pyritized MRS (FB2a)	Sandstones (FB2a)
Pyritized MRS (FB2b)	-			
Black shales (FB2b)	**0.008**	-		
Non-pyritized MRS (FB2a)	**$8.0*10^{-05}$**	**$4.9*10^{-10}$**	-	
Sandstones (FB2a)	**$3.0*10^{-08}$**	**$2.9*10^{-06}$**	**$1.0*10^{-14}$**	-

p-value are given. Bold p-value (< 0.05) are significant.

Appendix 12: Cross plots of selected major elements. (**A**) SiO_2 *vs*. Al_2O_3. (**B**), K_2O *vs*. Al_2O_3. (**C**), K_2O *vs*. Na_2O. (**D**), MgO *vs*. Al_2O_3.

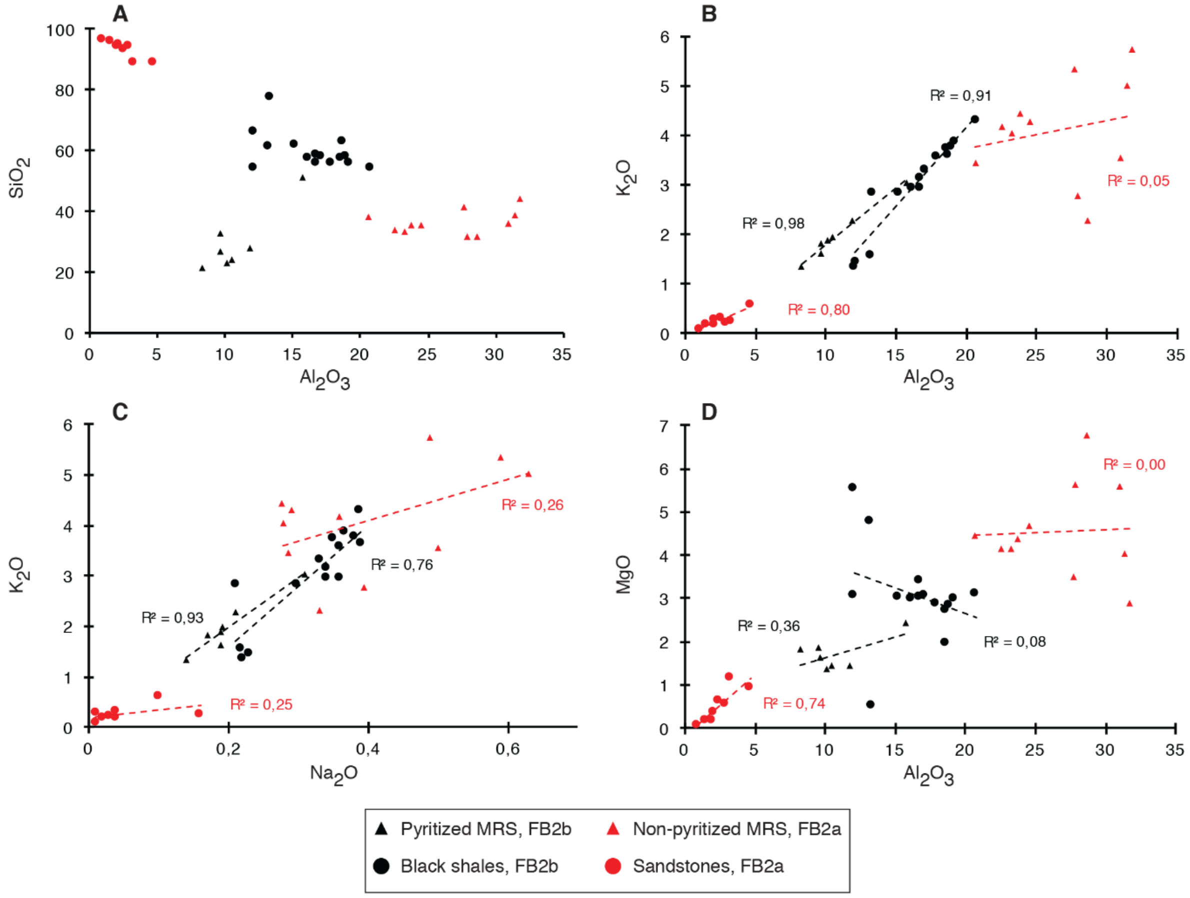

Appendix 13: XRD patterns of representative randomly oriented powders. (**A**) Non-pyritized microbial mats. (**B**) Sandstones. (**C**) Pyritized biofilms. (**D**) Black shales. [Chlorite (Ch); Mixed-layer (ML); Illite/mica (I/M); Quartz (Q); Anatase (An); Florencite (Fl); Di-tri-octahedral chlorite (Ch) (Billault *et al.*, 2002); Gypsum (Gy); Pyrite (Py); Dolomite (Do); Rhodochrosite (Rh)].

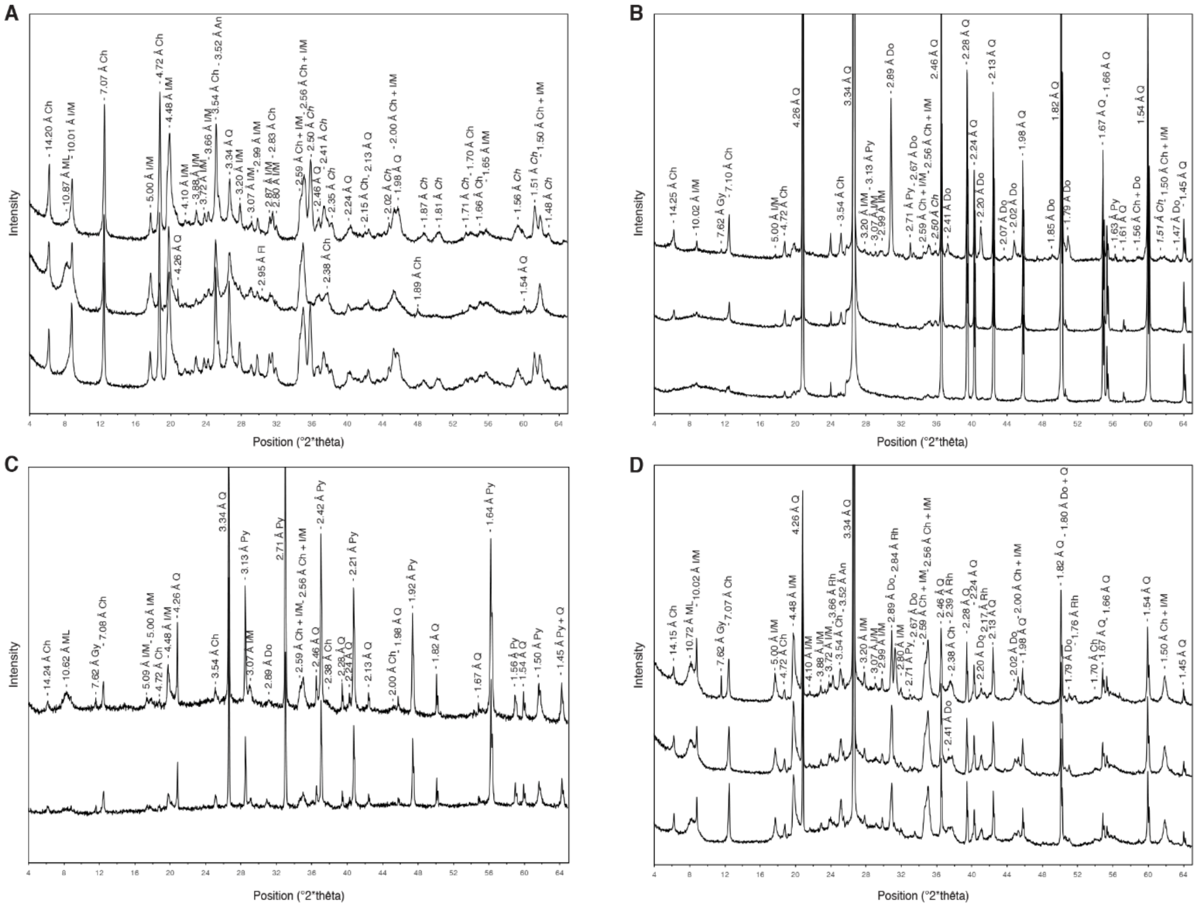

Appendix 14: XRD patterns of representative oriented <2 µm clay fraction after air-dried treatment (black lines) and glycolation (red lines). (**A**) Non-pyritized microbial mats. (**B**) Sandstones. (**C**) Pyritized biofilms. The weak signature of short-range ordered I-S MLMs likely indicates contamination from the underlying host sediment. (**D**) Black shales. [Green areas correspond to long-range ordered (R3) I-S MLMs; Blue areas represent the randomly ordered (R0) I-S MLMs; Chlorite (Ch); Mixed-layer (ML); Illite/mica (I/M); Kaolinite (K); Quartz (Q); Barite (Ba); Calcite (Ca); Gypsum (Gy)].

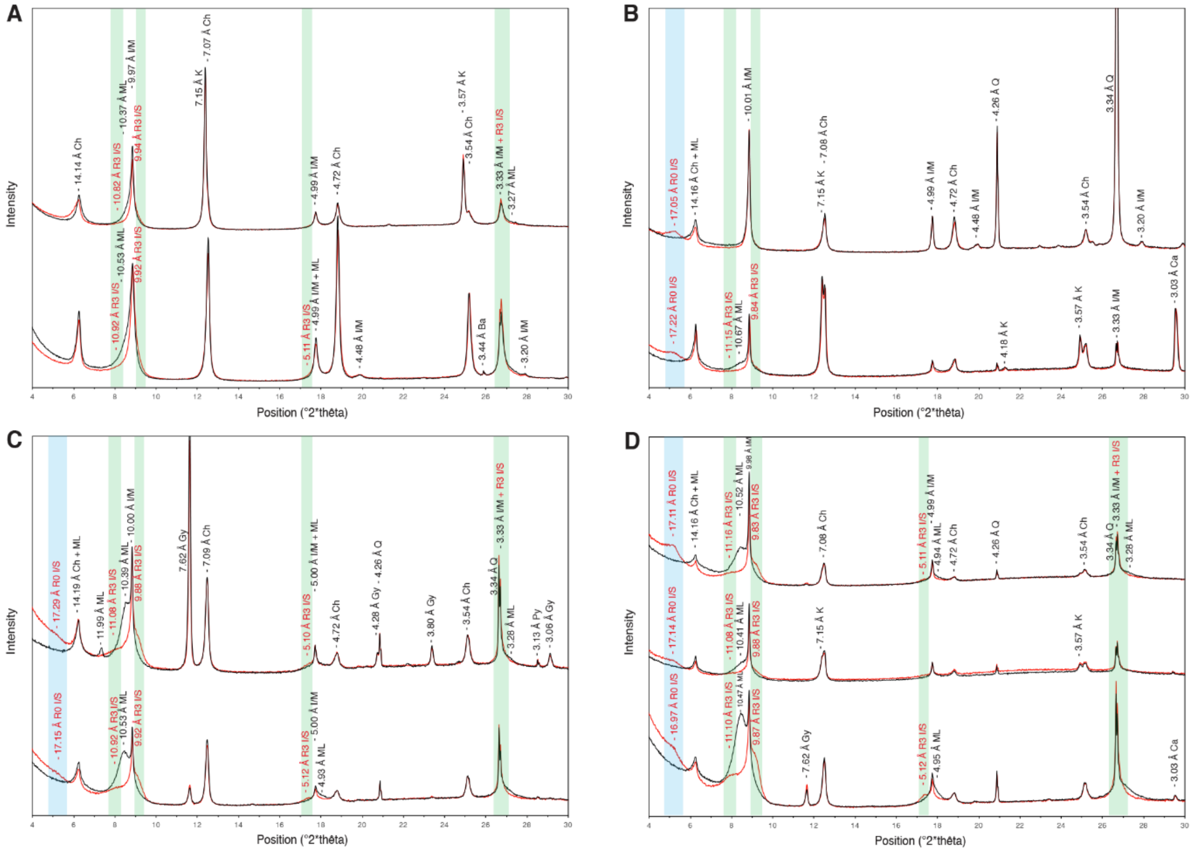

Appendix 15: XRD patterns of randomly oriented powders (<2 µm clay fraction) for the MRS and host sediment are shown at the top and bottom, respectively. The *hkl* diffraction peaks are typical of illite polytypes with $2M_1$ and $1M_t$ polytypes, representing detrital and diagenetic illites, respectively.

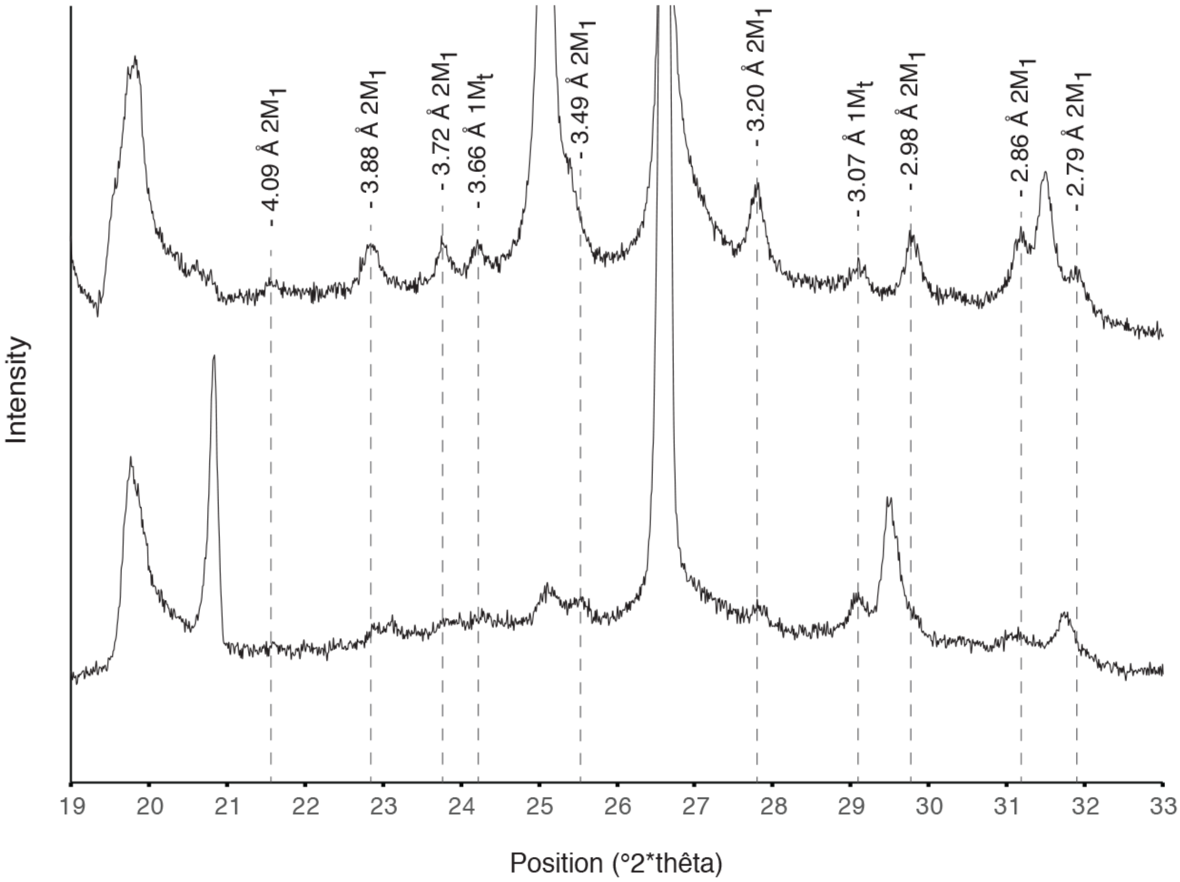

Appendix 16: Experimental (crosses) and modeled (lines) XRD profiles of selected Ca-saturated MRS samples. Contribution of different minerals to the profiles is indicated. (**A**) After air-dried preparation. (**B**) After ethylene-glycol saturation.

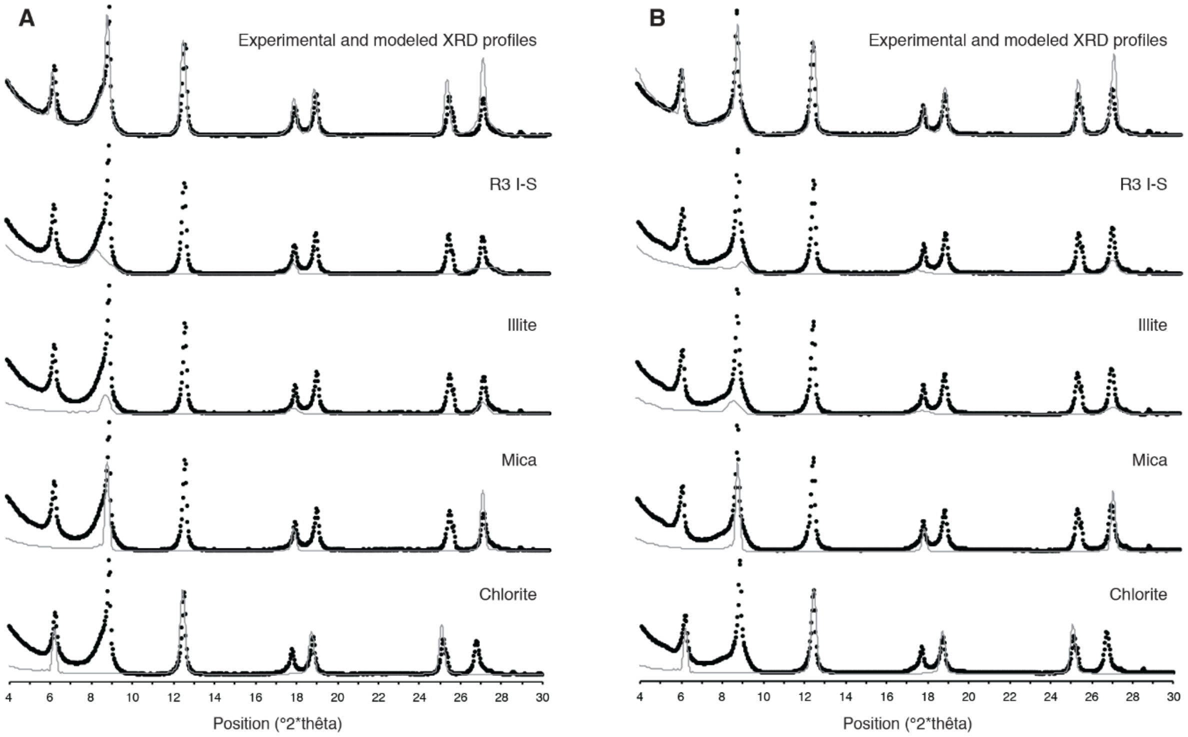

Appendix 17: Experimental (crosses) and modeled (lines) XRD profiles of Ca-saturated host sediments. Contribution of different minerals to the profiles is indicated. (**A**) After air-dried preparation. (**B**) After ethylene-glycol saturation.

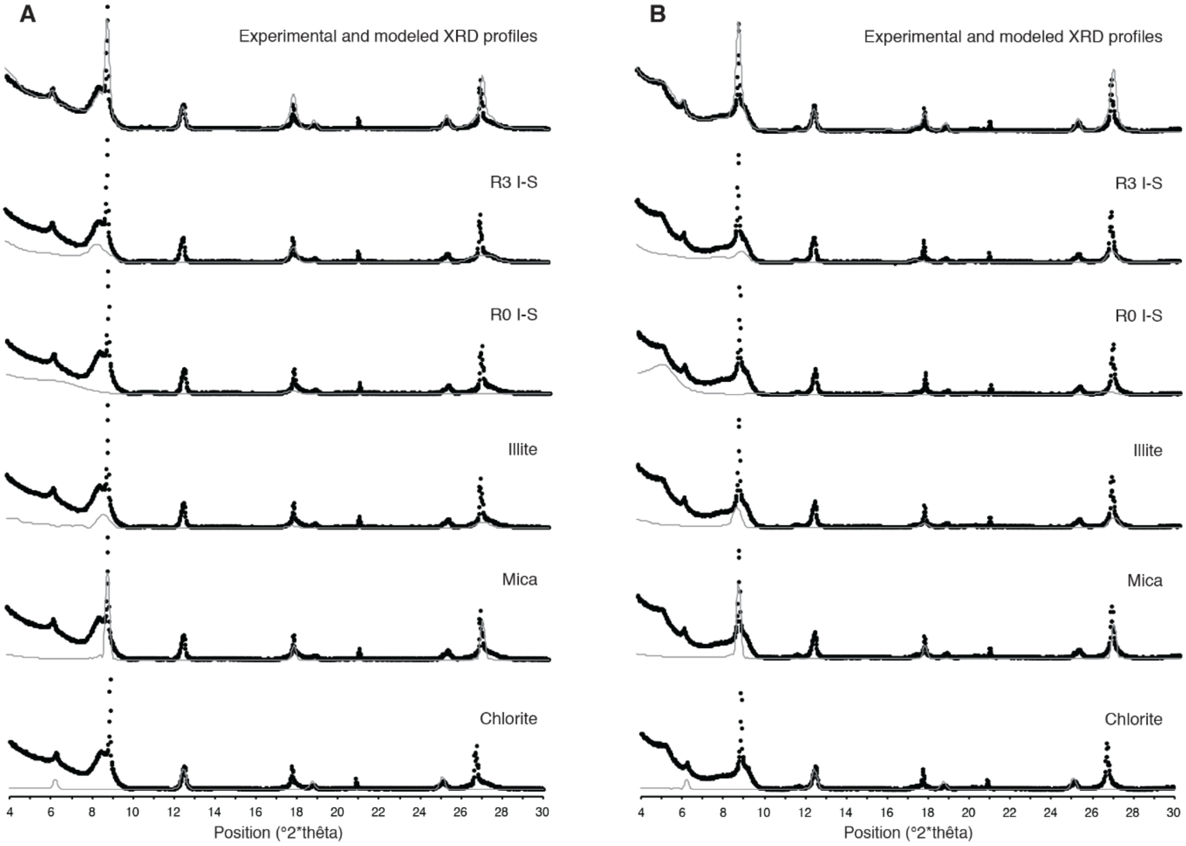

Appendix 18: Structural parameters from the simulation of experimental XRD patterns of Ca-saturated samples after air-dried treatment and glycolation.

Samples	Chlorite		Mica		Illite		Random MLM				Ordered MLM			
	Rel. Ab. (%)	N	Rel. Ab. (%)	N	Rel. Ab. (%)	N	Rel. Ab. (%)	N	Layer Prop. (%) I/S	R	Rel. Ab. (%)	N	Layer Prop. (%) I/S	R
MRS	22	14-40	40	10-25	15	4-19 (AD) 5-12 (EG)	-	-	-	-	23	10-25 (AD) 4-19 (EG)	92/8 90/10	3
					22		**-**	**-**	**-**	**-**	**34**			
Sediment	13	12-25	31	22-38	22	7-11 (AD) 5-19 (EG)	13	4-10	35/65	0	21	11-20 (AD) 11-16 (EG)	91/9 (AD) 88/12 (EG)	3

Rel. Ab., relative abundance; N, number of layers in coherent scattering domain with a lognormal distribution; Layer Prop., layer proportion in the I-S MLM; R, Reichweite parameter; AD, air dry; EG; ethylene-glycol.

We cannot compare the initial results at constant volume due to changes in the reactivity of diagenetic clay fraction, which is indicated by the concentrated detrital fraction (mica + chlorite, 62%) in the MRS relative to the sediments (44%). Therefore, bold relative abundances correspond to the calculated diagenetic fraction where the proportions of insoluble detrital components in the MRS are considered unchanged relative to the sediments (*i.e.*, 44%). The transformation from R0 to R3 I-S MLM as well as intense dissolution in the MRS represent the reactive clay fraction.

Appendix 19: Transmission-electron images of illite minerals. (**A**-**C**) Lath-shaped crystals from MRS. (**D**-**F**) Hexagonal-shaped crystals observed in MRS. (**G**-**H**) Lathlike and tiny lath-shaped crystals from host sediments. The inset with Selected Area Electron Diffraction (SAED) pattern shows a hexagonal structure typical of phyllosilicates in (*hk*0) reflection.

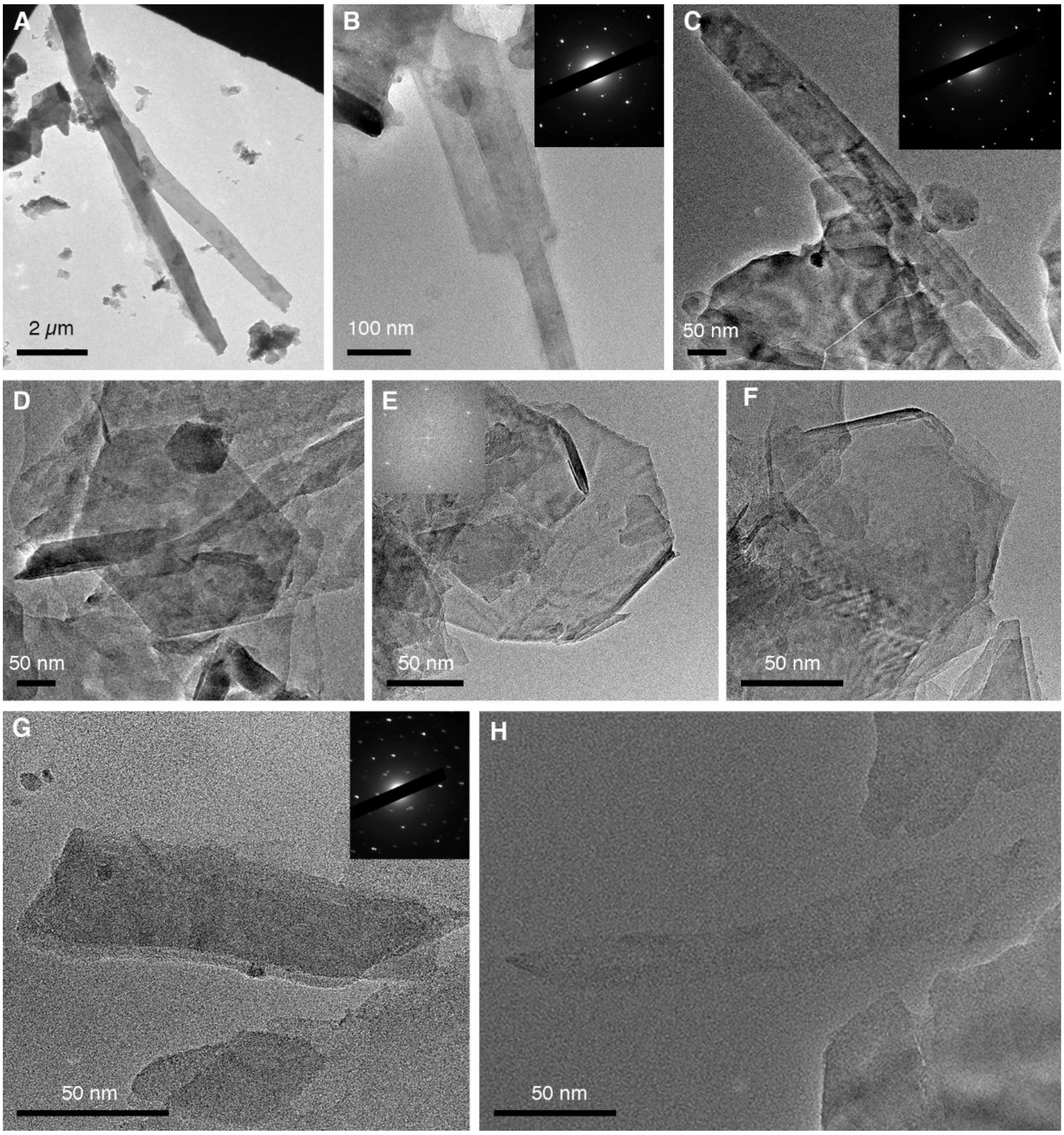

Appendix 20: Whole-rock composition of major and minor elements and enrichment factors (EF) of Ti, As, Ni, and Zr.

Formation	Lithology	Sample ID	Height m	S_T wt%	Si wt%	Al wt%	Fe wt%	Mn wt%	Mg wt%	Ca wt%	Na wt%	K wt%	Ti wt%	P wt%	EF_{Ti}	As ppm	Ba ppm	Bi ppm	Cd ppm	Co ppm
FB2b	Pyritized MRS	FPS_s5-mat	18.7	29.4	10.8	5.35	26.9	0.08	0.81	0.42	0.14	1.56	0.08	*0.02*	0.27	179	755	4.24	0.64	253
		DB_s4-mat	17.1	22	15.3	5.14	20.8	0.12	0.98	0.91	0.13	1.5	0.11	*0.02*	0.36	110	693	5.76	0.29	326
		FPS_s4-mat	16.3	24.8	9.91	4.37	29	0.07	1.09	0.58	0.1	1.11	0.07	*0.02*	0.28	112	527	4.01	0.21	193
		FPS_s3-mat	16.2	28.5	12.5	5.09	24.7	0.09	1.12	0.61	0.14	1.34	0.09	*0.02*	0.3	146	681	2.71	*0.05*	144
		DB_s2-mat	16	23.9	13	6.26	14.6	0.06	0.87	0.36	0.16	1.89	0.12	*0.02*	0.32	58.4	984	*0.05*	*0.05*	133
		DB_s3-mat	16	26.9	11.3	5.56	20.9	0.06	0.86	0.61	0.14	1.63	0.09	*0.02*	0.28	100	885	0.22	*0.1*	99.4
		FR_s1-mat	16	6.46	23.9	8.33	7.23	0.19	1.46	1.49	0.23	2.52	0.2	*0.02*	0.42	*0.8*	1234	0.25	0.57	4,713
	Black shales	WS_s1-sed	19.7	0.09	27.5	8.83	2.58	0.38	2.06	1.61	0.25	2.45	0.2	*0.02*	0.38	0.36	1132	0.11	0.23	5.35
		KS_s1-sed	19	0.09	28.9	8.02	2.67	0.18	1.81	1.48	0.22	2.35	0.25	0.09	0.53	1.41	1137	0.15	0.11	6.67
		FPS_s5-sed	18.7	0.22	26.3	8.85	1.67	0.37	1.82	1.89	0.25	2.63	0.23	0.07	0.45	*0.8*	1231	0.2	0.52	4.17
		AFBSO-12	18.6	N.D.	29.3	9.87	2.41	0.05	1.18	0.26	0.29	3.01	0.25	0.07	0.43	10.9	1505	0.31	0.34	8.89
		MLS_s7-sed	18.1	0.32	28.7	7	4.89	0.17	2.86	1.6	0.16	1.31	0.22	*0.02*	0.55	2.06	648	0.15	0.12	12.9
		AFBSO-9	17.5	N.D.	25.6	6.38	4.55	0.57	3.33	3.72	0.17	1.22	0.19	0.05	0.52	6.99	651	0.16	0.39	20.1
		DB_s4-sed	17.1	0.13	27.1	9.04	1.96	0.34	1.84	1.9	0.25	2.75	0.23	0.06	0.44	*0.8*	1294	0.21	0.42	4.18
		AFBSO-7	16.5	N.D.	36.3	7.03	0.25	0.01	0.32	*0.01*	0.16	2.36	0.17	*0.02*	0.42	2.94	1204	0.19	0.19	0.91
		FPS_s4-sed	16.3	0.16	30.9	6.37	6.21	0.09	1.85	0.17	0.16	1.12	0.16	0.07	0.41	*0.8*	1482	0.59	0.66	5.06
		FPS_s3-sed	16.2	0.17	27	9.85	1.54	0.2	1.64	1.48	0.26	3.1	0.24	0.07	0.46	*0.8*	1125	0.18	0.8	3.94
		AFBSO-6	16.1	N.D.	26.9	8.51	1.64	0.24	1.79	1.85	0.27	2.45	0.23	0.07	0.42	13.2	588	0.24	0.54	49.9
		DB_s2-sed	16	0.16	26.2	9.45	1.5	0.23	1.72	1.6	0.26	2.98	0.24	*0.02*	0.43	0.81	1319	0.09	0.15	3.43
		FR_s1-sed	16	0.2	27.2	9.98	1.65	0.19	1.72	1.55	0.28	3.14	0.24	0.06	0.41	*0.8*	1448	0.32	0.27	5.3
		MLS_s8-sed	15.5	1.02	25.3	11	2.71	0.37	1.86	1.5	0.29	3.57	0.27	*0.02*	0.41	53.1	1634	1.35	4.48	38.3
		MLS_s9-sed	15.5	0.34	26.3	10.1	2.12	0.28	1.8	1.5	0.27	3.21	0.25	*0.02*	0.42	13.2	1468 0	0.31	0.82	12.8
FB2a	Pyrite-poor MRS	MLS_s1-mat	15	4.16	15.8	12	9.17	0.25	2.48	0.72	0.26	3.46	1.66	0.24	2.39	50.8	1539	1.52	2.61	45.9
		LP_s3-mat	15	0.19	19.3	14.7	3.52	0.08	2.1	0.24	0.44	4.43	1.14	0.15	1.34	6.78	2035	0.86	0.65	5.15
		MLS_s2-mat	15	3.08	15.4	12.3	6.61	0.08	2.47	0.31	0.21	3.36	2.03	0.16	2.83	28	1409	2.33	3.35	48.4
		MLS_s3-mat	15	2.61	17.9	10.9	9.33	0.12	2.67	0.57	0.21	2.87	1.4	0.28	2.2	54.5	1225	1.43	1.84	32.2
		MLS_s4-mat	15	0.36	16.6	12.6	3.98	0.08	2.61	0.49	0.21	3.68	1.92	0.22	2.62	7.71	1512	1.39	2.54	15.8
		MLS_s5-mat	15	0.42	16.6	13	4.48	0.07	2.8	0.43	0.22	3.56	1.88	0.21	2.48	17.8	1488	1.64	2.59	13.2
		EST_s3-mat	15	0.36	14.8	14.8	2.43	0.03	3.37	0.02	0.29	2.31	0.22	0.04	0.26	2.33	1454	0.4	0.14	4.59
		EST_s4-mat	15	0.29	14.8	15.2	2.97	0.04	4.06	0.02	0.25	1.91	0.14	*0.02*	0.16	3.31	1204	0.28	0.12	5.38
		MLS_s3-mat	11	0.84	20.7	16.8	1.74	0.02	1.74	0.12	0.36	4.76	0.52	0.05	0.53	1.05	2543	0.41	0.11	5.83
		EST_s1-mat	6.9	0.17	16.9	16.4	1.9	0.01	3.34	0.07	0.37	2.96	0.2	*0.02*	0.21	1.56	2351	0.53	0.17	2.5
		EST_s2-mat	6.9	0.15	18	16.6	1.74	0.01	2.42	0.15	0.46	4.16	0.2	0.07	0.2	1.36	3253	0.34	0.16	1.76
	Sandstones	MLS_s1-sed	15	N.D.	41.7	2.47	0.68	0.09	0.58	0.47	0.08	0.5	0.02	*0.02*	0.13	1.9	281	0.18	0.27	2.7
		LP_s3-sed	15	N.D.	43.7	1.3	0.46	0.05	0.38	0.43	0.03	0.26	*0.01*	*0.02*	*0.08*	*0.8*	145	*0.05*	*0.05*	1.45
		MLS_s2-sed	15	N.D.	41.7	1.7	0.56	0.21	0.7	0.87	0.12	0.22	0.02	*0.02*	0.16	*0.8*	126	*0.05*	*0.05*	1.71
		LP_s2-sed	14	N.D.	44.4	1.1	0.39	0.01	0.24	0.04	0.03	0.16	*0.01*	0.01	0.2	1.01	95	*0.02*	0.04	0.73
		MLS_s3-sed	11	N.D.	44.1	1.51	0.47	0.02	0.35	*0.01*	0.02	0.18	0.02	*0.02*	0.26	0.7	98	*0.02*	0.03	1.39
		EST_s1-sed	6.9	0.02	44.2	1.05	0.4	*0.01*	0.12	*0.01*	*0.01*	0.24	*0.01*	*0.02*	*0.1*	1.14	121	0.08	*0.05*	0.49
		EST_s2-sed	6.9	N.D.	44.8	0.78	0.44	*0.01*	0.1	0.05	0.02	0.15	*0.01*	0.03	0.24	1.35	83	*0.02*	*0.05*	0.5

Appendix 20 (Cont.):

Formation	Lithology	Sample ID	Height m	Cr ppm	Cs ppm	Cu ppm	Hf ppm	Mo ppm	Nb ppm	Ni ppm	Pb ppm	Rb ppm	Sb ppm	Sn ppm	Sr ppm	Ta ppm	Th ppm	U ppm	V ppm	W ppm	Zn ppm	Zr ppm	EF_{As}	EF_{Ni}	EF_{Zr}
FB2b	Pyritized MRS	FPS_s5-mat	18.7	*2.5*	5.23	148	0.63	11.4	1.64	739	71.5	59.7	10.7	0.75	36.3	0.13	4.24	0.29	30.2	*0.75*	41.1	22	22.7	23.7	0.21
		DB_s4-mat	17.1	11	4.63	192	2.51	19.8	2.39	589	91.3	57	10.9	0.75	43.2	0.22	6.03	0.62	30.3	*0.75*	37.1	100	14.5	19.7	0.95
		FPS_s4-mat	16.3	*2.5*	4	82.2	0.72	13.9	1.47	588	42.7	43.8	5.42	0.75	27.6	0.11	3.7	0.3	23.5	*0.75*	61	26	17.3	23.1	0.29
		FPS_s3-mat	16.2	*2.5*	4.55	100	1.29	10.2	1.86	547	56.4	52.7	6.89	0.75	36.4	0.14	4.64	0.36	30.7	*0.75*	63.2	49	19.5	18.5	0.47
		DB_s2-mat	16	21.9	6.7	77	0.72	9.91	2.3	369	28.7	76.2	7.08	0.75	41.6	0.17	6.11	0.45	36.1	1.15	40.6	25	6.31	10.1	0.2
		DB_s3-mat	16	15.1	5.72	25.6	0.68	16.6	1.89	177	30.7	65.3	12.2	2.09	38.5	0.14	4.8	0.52	34.8	1.83	69.5	26	12.2	5.45	0.23
		FR_s1-mat	16	19.2	9.14	106	4.88	*0.25*	4.7	32.9	16.6	98.6	0.53	*0.75*	79.1	0.46	11.6	1,095	41.7	*0.75*	72.2	185	0.07	0.68	1.09
	Black shales	WS_s1-sed	19.7	37	7.95	40.1	3.53	*0.25*	4.14	48.9	5.11	95.2	0.19	0.75	74.2	0.38	10	0.83	43	1.31	102	135	0.03	0.95	0.75
		KS_s1-sed	19	41.7	9	56.1	5.56	*0.25*	5.65	52.1	8.45	105	0.3	1.23	94.2	0.52	16	1.32	38.7	2.08	82.3	210	0.12	1.12	1.29
		FPS_s5-sed	18.7	31.6	9.38	53.1	5.86	*0.25*	5.27	29	9.13	105	0.24	1.88	87.6	0.48	13.1	1.32	48.3	*0.75*	67.1	225	0.06	0.56	1.25
		AFBSO-12	18.6	54.8	11.1	56.6	5.58	0.76	5.91	60.7	10.8	125	0.54	1.28	86.3	0.53	14.4	1.21	53	1.66	93.9	220	0.75	1.06	1.09
		MLS_s7-sed	18.1	36.2	5.3	44.1	5.62	*0.25*	4.5	76	8.15	54.7	0.29	2.74	48	0.37	8.87	0.91	36.5	1.28	97.9	219	0.2	1.86	1.53
		AFBSO-9	17.5	40.6	5.53	34.6	6.76	0.76	4.61	83.2	13.4	53.9	0.83	1.31	70	0.42	10.8	1.08	32.4	1.01	151	265	0.74	2.24	2.04
		DB_s4-sed	17.1	36.3	8.54	58	5.07	0.25	5.63	42.6	15.1	108	0.26	1.94	91.6	0.53	13.5	1.24	49.5	1.78	65.6	197	0.06	0.81	1.07
		AFBSO-7	16.5	42.5	6.04	5.06	5.23	0.63	4.06	19.5	9.71	95.8	0.47	1.48	71	0.31	8.01	1.03	34.5	0.74	37	214	0.28	0.48	1.5
		FPS_s4-sed	16.3	33.8	10.7	51.9	5.03	*0.25*	5.53	33.9	12.3	126	0.28	1.63	85.9	0.47	13.5	1.25	50	1.71	53.9	192	0.05	0.59	0.96
		FPS_s3-sed	16.2	29.6	8.6	62.1	5.9	0.85	5.13	26.2	9.36	95.8	0.24	1.79	85.6	0.46	12	1.28	45.4	*0.75*	62.3	230	0.06	0.53	1.33
		AFBSO-6	16.1	30.2	4.4	28.2	7.2	0.72	3.56	115	34.2	47.1	1.38	0.99	49.7	0.35	9.47	1.02	29.1	0.88	169	293	1.4	3.1	2.26
		DB_s2-sed	16	47.7	10.6	57.6	5.48	*0.25*	5.28	30.6	5.42	120	0.27	0.75	85.1	0.5	14.5	1.32	57.5	1.6	65.2	209	0.06	0.56	1.08
		FR_s1-sed	16	33.2	11	57	4.65	*0.25*	5.33	33.5	18.2	124	0.25	4.15	84	0.47	12.8	1.24	50.7	1.64	54.2	180	0.05	0.58	0.88
		MLS_s8-sed	15.5	49.2	11.9	18.8	1.88	3.3	5.36	113	21.3	140	2.28	0.75	88.3	0.41	12.8	1.11	54.4	1.81	1475	67	3.28	1.76	0.3
		MLS_s9-sed	15.5	48.3	10.6	63	3.91	0.93	5.23	58.7	10	127	0.69	0.75	89	0.46	13.6	1.13	49.3	1.81	319	148	0.88	1	0.62
FB2a	Pyrite-poor MRS	MLS_s1-mat	15	196	12.3	209	45.7	4.76	39.3	229	97.6	148	7.95	9.4	295	3.71	77.9	8.54	96.4	8.75	306	1695	2.88	3.29	6.95
		LP_s3-mat	15	174	22.8	32.7	14.8	0.84	26.7	65.7	31.9	191	1.35	6.7	246	2.34	54.1	5.02	107	6.9	74.5	526	0.31	0.77	1.76
		MLS_s2-mat	15	230	11.8	156	79.2	3.66	47.9	224	72.4	145	5.47	4.56	323	4.35	111	10.2	91.7	9.52	195	2899	1.54	3.12	11.5
		MLS_s3-mat	15	149	11.6	115	44.9	4.63	31.6	167	96.2	124	7.36	3.14	243	2.99	65	8.28	84.6	7.03	144	1730	3.37	2.63	7.76
		MLS_s4-mat	15	208	13.3	121	57.1	1.44	44.5	134	33.5	167	1.47	3.45	346	4.05	99.5	8.92	93.9	8.69	180	2067	0.41	1.83	8.05
		MLS_s5-mat	15	194	13.1	64.2	65	2.29	43.5	119	42.3	155	2.5	3.5	321	4.09	96.9	9.2	99.9	8.43	113	2301	0.92	1.58	8.69
		EST_s3-mat	15	50.2	3.03	12.9	25.5	0.85	4.82	75.9	9.39	92.4	0.2	0.59	93.5	0.48	15.6	3.19	82.7	2.06	70.8	819	0.11	0.88	2.72
		EST_s4-mat	15	42.7	2.44	13.6	19.4	0.63	3.07	102	7.45	78.6	0.23	0.91	67.7	0.29	10.1	2.42	76.2	1.13	82.4	627	0.15	1.15	2.02
		MLS_s3-mat	11	87.8	17.7	22	16.6	*0.25*	11.7	69.9	19.6	194	0.32	2.31	207	1.04	27.3	2.92	77.1	1.83	45.3	524	0.04	0.71	1.53
		EST_s1-mat	6.9	36.9	4.14	8.04	25.9	*0.25*	4.52	133	2.86	111	0.21	0.23	105	0.41	16.6	3.95	78.8	1.38	77.2	996	0.06	1.39	2.98
		EST_s2-mat	6.9	36.6	5.1	7.41	25.9	0.57	4.59	95	2.68	176	0.17	3.5	136	0.43	16.7	3.51	75.5	2.01	61	833	0.06	0.98	2.46
	Sandstones	MLS_s1-sed	15	*2.5*	0.63	9.88	1.28	*0.25*	0.38	16	10.7	18.5	0.23	1.62	17.7	0.04	1.07	0.21	9.04	*0.75*	34.2	51	0.52	1.12	1.02
		LP_s3-sed	15	*2.5*	0.42	*2.5*	0.69	*0.25*	0.19	*5*	5.53	10.1	0.14	0.75	13.5	0.02	0.72	0.16	4.88	*0.75*	*5*	28	0.39	0.66	1.06
		MLS_s2-sed	15	*2.5*	0.41	*2.5*	1.46	*0.25*	0.43	*5*	4.39	8.7	0.15	0.75	14.9	0.04	1.01	0.2	6.23	*0.75*	17.8	59	0.3	0.5	1.69
		LP_s2-sed	14	3.92	0.42	1	1.94	*0.25*	0.28	7.42	2.56	6.71	0.13	0.48	9.35	0.03	0.64	0.2	4.36	*0.4*	14.9	78	0.62	1.15	3.46
		MLS_s3-sed	11	5.57	0.46	8.58	2.09	*0.25*	0.48	14.4	2.23	7.61	0.09	0.32	11.7	0.05	1.73	0.27	4.93	*0.4*	20.3	84	0.31	1.63	2.72
		EST_s1-sed	6.9	3.53	0.34	*2.5*	0.86	*0.25*	0.26	8.8	1	9.75	0.08	0.75	7.55	0.03	0.75	0.21	3.38	*0.75*	11.5	36	1.17	1.43	1.69
		EST_s2-sed	6.9	9.62	0.18	8.45	1.15	0.8	0.23	10.8	1.21	6.29	0.08	4.12	7.88	0.02	0.8	0.34	2.64	*0.4*	19.8	45	0.73	2.37	2.81

FPS: flat pyritized structure; LP: linear pattern; DB: domal buildup; WS: wrinkle structure; KS: “kinneyia” structure; MLS: mat-layer structure; FR: “fairy-ring” structure; EST: “elephant-skin” texture as previously described by Aubineau *et al*. (2018).

Italicized numbers refer to samples for which half or more of the data were below detection limit. The detection limit is calculated as 6 times the standard deviation of the mean on 100 measurements of blanks.

N.D. = not determined.

Appendix 21: Bulk-rock data of rare earth elements and calculated Eu anomaly and REE ratios

Formation	Lithology	Sample ID	Height m	La ppm	Ce ppm	Pr ppm	Nd ppm	Sm ppm	Eu ppm	Gd ppm	Tb ppm	Dy ppm	Y ppm	Ho ppm	Er ppm	Tm ppm	Yb ppm	Lu ppm	∑LREE ppm	∑HREE ppm	REE_T ppm	Eu/Eu*	Y/Ho	$Pr/Yb_{(SN)}$
FB2b	Pyritized MRS	FPS_s5-mat	18.7	11.1	20.4	2.13	7.49	1.22	0.26	0.86	0.12	0.52	2.43	0.1	0.23	0.03	0.17	0.03	42.39	2.06	44.7	1.24	25.32	3.95
		DB_s4-mat	17.1	17.2	32.3	3.46	12.3	2.11	0.47	1.48	0.2	1.06	4.22	0.2	0.53	0.08	0.48	0.08	67.35	4.09	71.9	1.3	29.85	2.33
		FPS_s4-mat	16.3	10.2	19	2.08	7.33	1.22	0.31	0.95	0.13	0.62	3.32	0.1	0.26	0.03	0.19	0.03	39.8	2.31	42.4	1.45	31.88	3.5
		FPS_s3-mat	16.2	13.3	24.7	2.64	9.06	1.47	0.35	1.09	0.14	0.74	5.97	0.13	0.35	0.05	0.28	0.04	51.2	2.84	54.4	1.36	31.51	2.98
		DB_s2-mat	16	16.5	30.2	3.24	11.2	1.84	0.42	1.41	0.16	0.85	4.52	0.15	0.35	N.D.	0.26	0.04	62.96	3.22	66.6	1.34	30.74	3.99
		DB_s3-mat	16	12.4	23.1	2.47	8.88	1.45	0.33	1.05	0.13	0.7	3.69	0.12	0.29	0.04	0.21	0.03	48.32	2.57	51.2	1.32	29.97	3.72
		FR_s1-mat	16	37.4	69.4	7.49	26.2	4.18	0.96	2.99	0.38	2.09	11.6	0.38	1.04	0.14	0.86	0.13	144.7	8	153.6	1.35	30.79	2.8
FB2b	Black shales	WS_s1-sed	19.7	30.1	57	6.24	22.2	3.61	0.84	2.6	0.33	1.78	10.2	0.34	0.86	0.11	0.73	0.11	119.1	6.86	126.8	1.36	30.33	2.74
		KS_s1-sed	19	52.8	97.1	10.3	35.5	5.39	1.21	3.65	0.45	2.46	13.9	0.47	1.21	0.17	1.08	0.16	200.9	9.64	211.8	1.35	29.69	3.05
		FPS_s5-sed	18.7	39.6	73.8	7.87	27.6	4.35	1	3.14	0.41	2.24	13.8	0.44	1.14	0.16	1.03	0.16	153.2	8.71	162.9	1.34	31.66	2.46
		AFBSO-12	18.6	43.4	80.4	8.7	30.6	4.91	1.08	3.51	0.45	2.44	14.3	0.43	1.2	0.16	1.06	0.16	168	9.41	178.5	1.29	33.41	2.63
		MLS_s7-sed	18.1	20.5	39.4	4.4	16.2	2.99	0.78	2.48	0.35	1.95	11.3	0.37	0.96	0.13	0.85	0.13	83.48	7.22	91.5	1.43	30.56	1.65
		AFBSO-9	17.5	23.5	44.3	4.91	18.2	3.22	0.83	2.57	0.37	2.12	13.8	0.4	1.14	0.16	1.09	0.17	94.05	8.01	102.9	1.41	34.45	1.45
		DB_s4-sed	17.1	39.4	73.9	8.02	28.1	4.47	1	3.22	0.39	2.17	12.8	0.41	1.09	0.15	0.98	0.16	153.8	8.58	163.4	1.32	31.09	2.62
		AFBSO-7	16.5	27	49.7	5.41	19	3.31	0.76	2.56	0.32	1.7	9.27	0.3	0.77	0.11	0.68	0.11	104.3	6.54	111.6	1.33	31.32	2.56
		FPS_s4-sed	16.3	40.2	74.2	8.04	28	4.64	1.03	3.37	0.43	2.34	13.6	0.43	1.12	0.15	1	0.15	155	9	165.1	1.3	31.44	2.58
		FPS_s3-sed	16.2	37.1	69.5	7.44	26.1	4.24	0.95	3.07	0.41	2.26	14.3	0.44	1.16	0.16	1.05	0.16	144.4	8.71	154.1	1.3	32.75	2.28
		AFBSO-6	16.1	27.1	52	5.69	20.6	3.71	0.95	2.88	0.39	2.16	13.2	0.4	1.09	0.16	1.04	0.16	109.1	8.28	118.3	1.44	33.33	1.76
		DB_s2-sed	16	41.9	76.9	8.24	28.5	4.52	1.03	3.2	0.41	2.32	14.3	0.45	1.19	0.16	1.08	0.16	160.1	8.96	170.1	1.34	31.68	2.46
		FR_s1-sed	16	40.1	74.3	8.07	28	4.72	1.05	3.39	0.41	2.17	12.8	0.42	1.06	0.14	0.93	0.14	155.1	8.66	164.8	1.32	30.43	2.79
		MLS_s8-sed	15.5	35.9	66.2	7.15	25.4	4.2	0.98	3.09	0.39	1.96	10.5	0.35	0.85	0.1	0.65	0.09	138.9	7.49	147.3	1.36	29.75	3.54
		MLS_s9-sed	15.5	39.2	72.7	7.82	27.6	4.46	1.02	3.19	0.4	2.15	12.3	0.4	1.04	0.14	0.88	0.13	151.8	8.33	161.2	1.35	30.4	2.85
FB2a	Pyrite-poor MRS	MLS_s1-mat	15	218	361	36.3	117	14.7	3.34	10.1	1.28	7.32	55.4	1.6	4.73	0.71	4.98	0.82	746.8	31.57	781.7	1.35	34.57	2.34
		LP_s3-mat	15	178	295	29	89.4	11	2.29	7.01	0.81	4.54	30.1	0.94	2.78	0.42	2.86	0.44	602.7	19.79	624.8	1.29	32.18	3.25
		MLS_s2-mat	15	292	499	53	185	16.8	3.12	9.92	1.38	8.62	62.2	1.95	6.25	1.02	7.1	1.17	1045	37.4	1086	1.12	31.85	2.39
		MLS_s3-mat	15	195	330	33.9	111	13.9	3.12	9.54	1.19	7.06	51.5	1.5	4.36	0.67	4.61	0.74	683.5	29.68	716.3	1.33	34.3	2.35
		MLS_s4-mat	15	303	508	52.4	170	17.1	3.41	10.9	1.38	8.19	58.8	1.78	5.54	0.87	6.11	1	1050	35.78	1089	1.21	33.08	2.75
		MLS_s5-mat	15	279	461	47.2	157	16.6	3.32	10.3	1.31	8	59.3	1.74	5.5	0.89	6.31	1.04	960.1	35.05	998.5	1.22	34.18	2.4
		EST_s3-mat	15	30.6	55.7	5.93	21.9	4	1.1	2.83	0.41	2.78	22.2	0.64	1.89	0.29	2.09	0.34	118.2	11.27	130.5	1.57	34.76	0.91
		EST_s4-mat	15	18.5	34.4	3.86	14.8	2.73	0.76	2.21	0.35	2.34	19	0.53	1.52	0.23	1.56	0.25	74.31	8.97	84	1.48	36.01	0.79
		MLS_s3-mat	11	79.3	140	15.3	54.5	9.1	2.2	6.73	0.82	4.18	20.6	0.75	1.9	0.28	1.96	0.3	298.3	16.93	317.4	1.42	27.46	2.49
		EST_s1-mat	6.9	21.1	39.2	4.4	17.1	3.32	0.86	2.25	0.36	2.47	20.1	0.58	1.84	0.29	2.14	0.35	85.14	10.28	96.3	1.45	34.38	0.66
		EST_s2-mat	6.9	19.4	36.1	4.07	16.3	3.39	0.87	2.56	0.39	2.5	17.9	0.56	1.63	0.26	1.87	0.31	79.17	10.07	90.1	1.42	31.93	0.7
FB2a	Sandstones	MLS_s1-sed	15	3.65	7.52	0.92	3.92	1.02	0.33	0.99	0.13	0.73	4.54	0.13	0.3	0.03	0.2	0.03	17.03	2.54	19.9	1.73	34.38	1.48
		LP_s3-sed	15	2.48	5.54	0.72	3.16	0.74	0.22	0.7	0.09	0.48	2.75	0.09	0.19	0.02	0.12	0.02	12.63	1.7	14.5	1.6	30.88	1.87
		MLS_s2-sed	15	3.53	7.01	0.81	3.2	0.71	0.18	0.59	0.08	0.44	2.82	0.09	0.22	0.03	0.18	0.03	15.26	1.66	17.1	1.43	31.3	1.4
		LP_s2-sed	14	1.93	4.23	0.42	1.67	0.35	0.11	0.32	0.05	0.27	1.93	0.06	0.15	0.02	0.16	0.03	8.6	1.05	9.8	1.6	33.79	0.86
		MLS_s3-sed	11	3.27	6.41	0.76	2.92	0.55	0.14	0.43	0.06	0.32	2.08	0.06	0.18	0.03	0.19	0.03	13.91	1.3	15.4	1.45	33.35	1.29
		EST_s1-sed	6.8	2.09	4.28	0.48	1.76	0.44	0.13	0.48	0.07	0.37	2.08	0.07	0.15	0.02	0.12	0.02	9.05	1.29	10.5	1.43	30.93	1.31
		EST_s2-sed	6.9	1.76	3.54	0.4	1.53	0.39	0.11	0.42	0.06	0.38	2.21	0.08	0.18	0.03	0.16	0.02	7.62	1.33	9.1	1.42	29.46	0.8

FPS: flat pyritized structure; LP: linear pattern; DB: domal buildup; WS: wrinkle structure; KS: “kinneyia” structure; MLS: mat-layer structure; FR: “fairy-ring” structure; EST: “elephant-skin” texture as previously described by Aubineau *et al*. (2018).

∑LREE refers to the sum of REE from La to Sm.

∑HREE refers to the sum of REE from Gd to Lu.

REE_T includes all REE.

Eu/Eu* refers to Eu anomaly calculated as follow: $Eu_{(SN)}/(0.66*Sm_{(SN)}+0.33*Tb_{(SN)})$

N.D. = not determined

Appendix 22: Petrography, SEM, and EDX of a poorly pyritized MRS in cross-section perpendicular to the bedding plane. Back-scattered electron (BSE) and composite (Al, Si, O, Mg, K, Fe, Ti, and Zr) elemental maps show mineral composition of the poorly pyritized MRS. A number of Ti- and Zr-rich heavy mineral crystals are embedded within these mats.

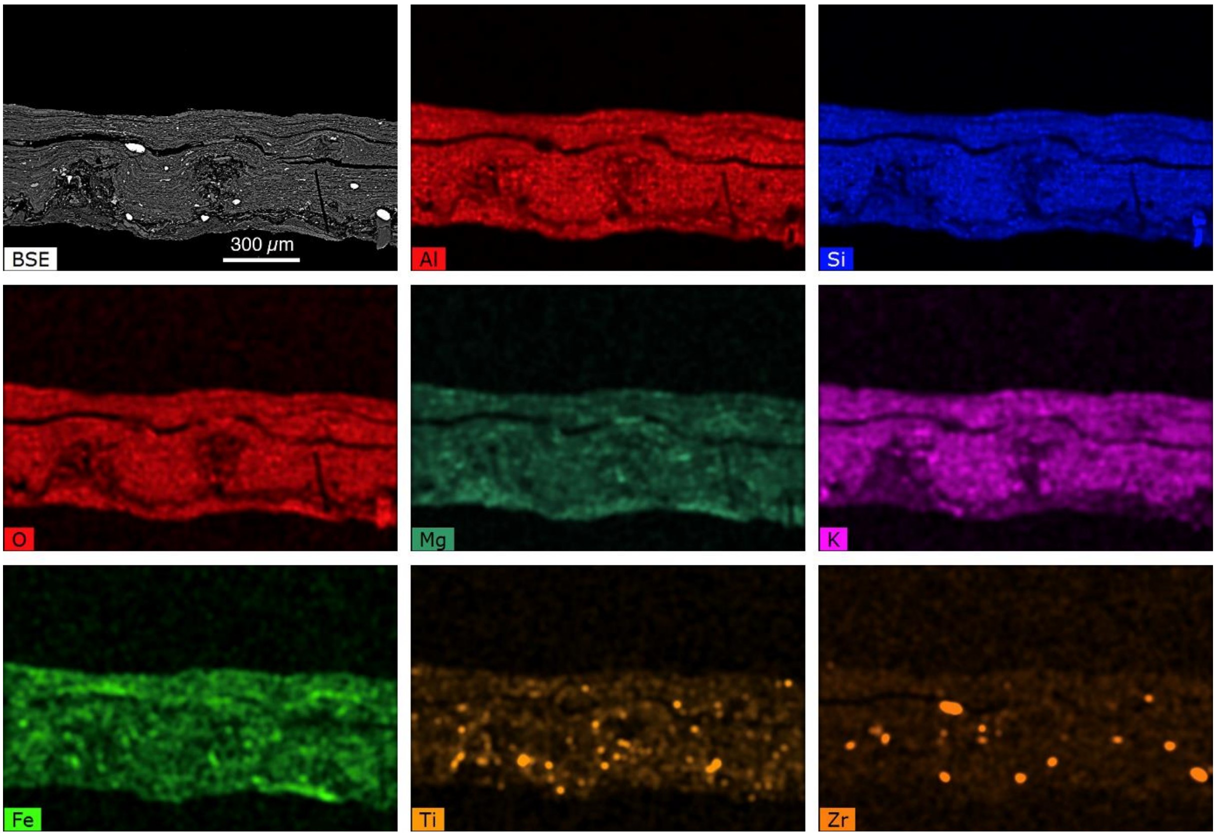

Appendix 23: SEM image of poorly pyritized MRS in secondary electron (left) and BSE (right) modes. Pyrite-rich layers observed at the bottom of MRS are highly variable in thickness. Inset box shows numerous and tiny sub-euhedral to euhedral pyrite crystals.

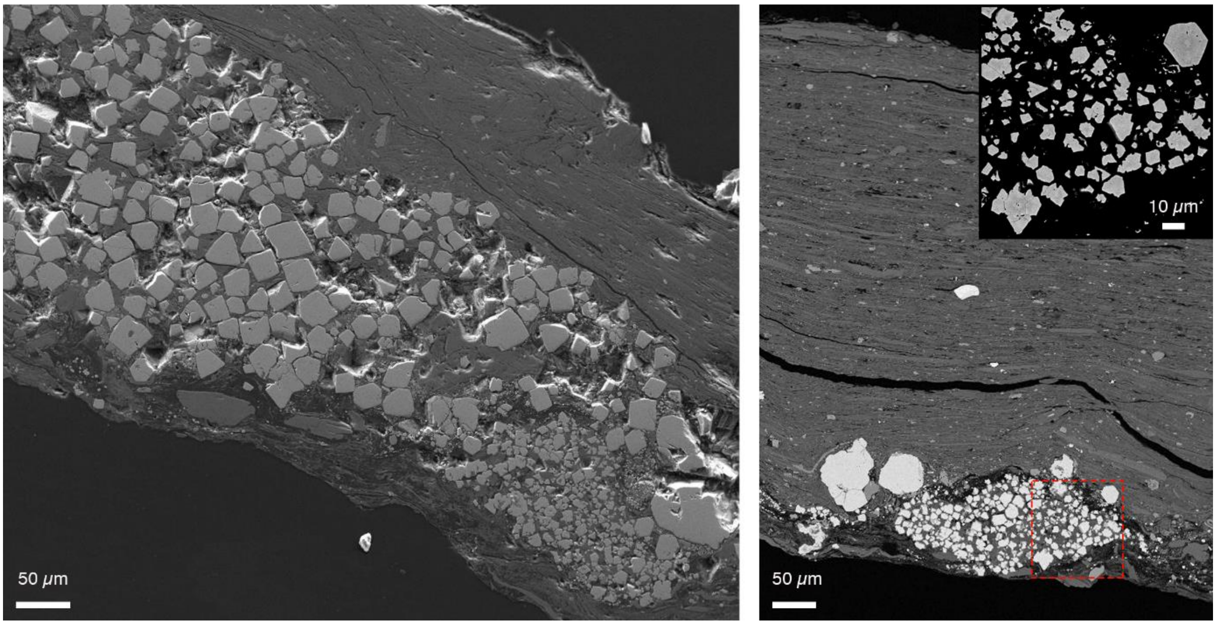

Appendix 24: Weight of each principal component.

	eigenvalue	variance %	cumulative variance %
PC1	14.12	54.32	54.32
PC2	6.35	24.44	78.76
PC3	1.87	7.18	85.94
PC4	1.36	5.22	91.15
PC5	0.73	2.82	93.98
PC6	0.47	1.8	95.78
PC7	0.34	1.32	97.1
PC8	0.24	0.92	98.02
PC9	0.15	0.58	98.6
PC10	0.11	0.43	99.04
PC11	0.09	0.33	99.37
PC12	0.05	0.17	99.54
PC13	0.03	0.13	99.68
PC14	0.02	0.09	99.77
PC15	0.02	0.07	99.84
PC16	0.01	0.06	99.9
PC17	0.01	0.04	99.94
PC18	0.01	0.02	99.96
PC19	0	0.01	99.98
PC20	0	0.01	99.99
PC21	0	0.01	99.99
PC22	0	0	100
PC23	0	0	100
PC24	0	0	100
PC25	0	0	100
PC26	0	0	100

Appendix 25: Stratigraphic profile with enrichment factor (EF) of selected immobile and chalcophile elements within host sediments. EF is relative to the average shale (Ti, Zr, and Ni concentrations for the average shale are from Taylor & McLennan (2001), and As concentration for the average shale is from Li & Schoonmaker (2003)), and calculated as $(X/Al)_{sample}/(X/Al)_{average\ shales}$, where X stands for element concentration.

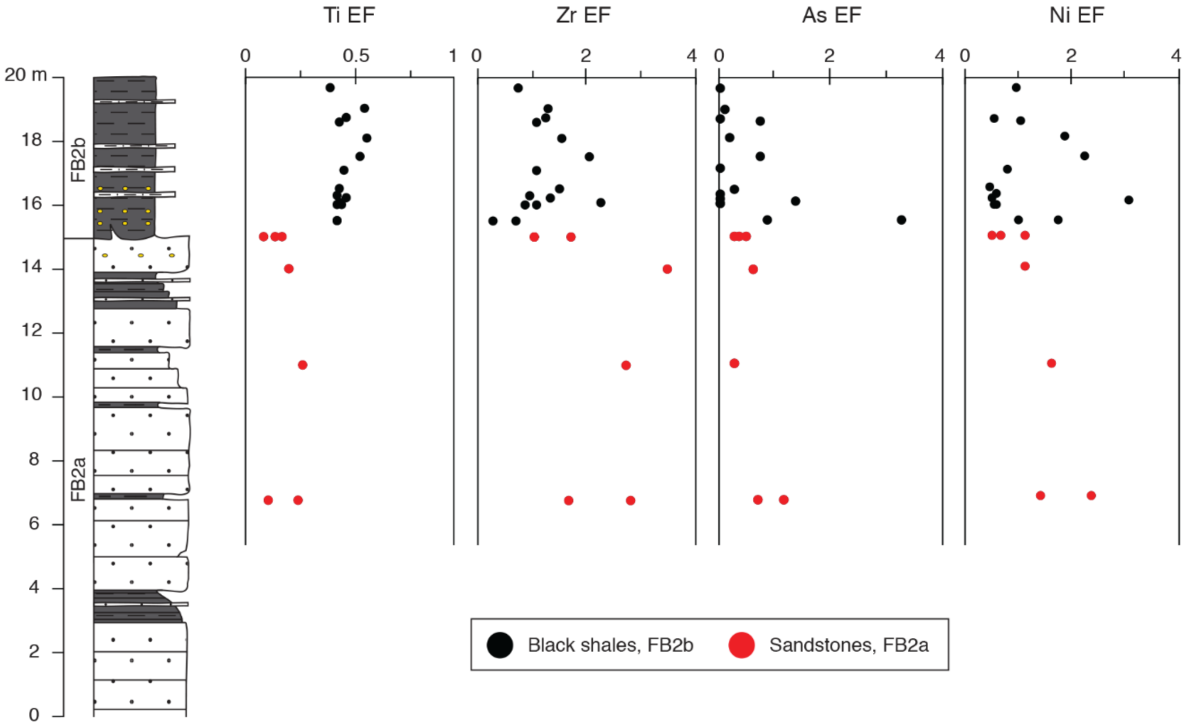

Appendix 26: Cross plot of total organic carbon versus total nitrogen for MRS and host sediments. Dotted lines show the C/N bulk ratios of 5 and 100. The C/N values of modern phytoplanktonic biomass range from 4 to 10 (Gruber & Galloway, 2008; Ader *et al*., 2016). Remineralization of biomass in the water column and during diagenesis can increase the C/N ratios.

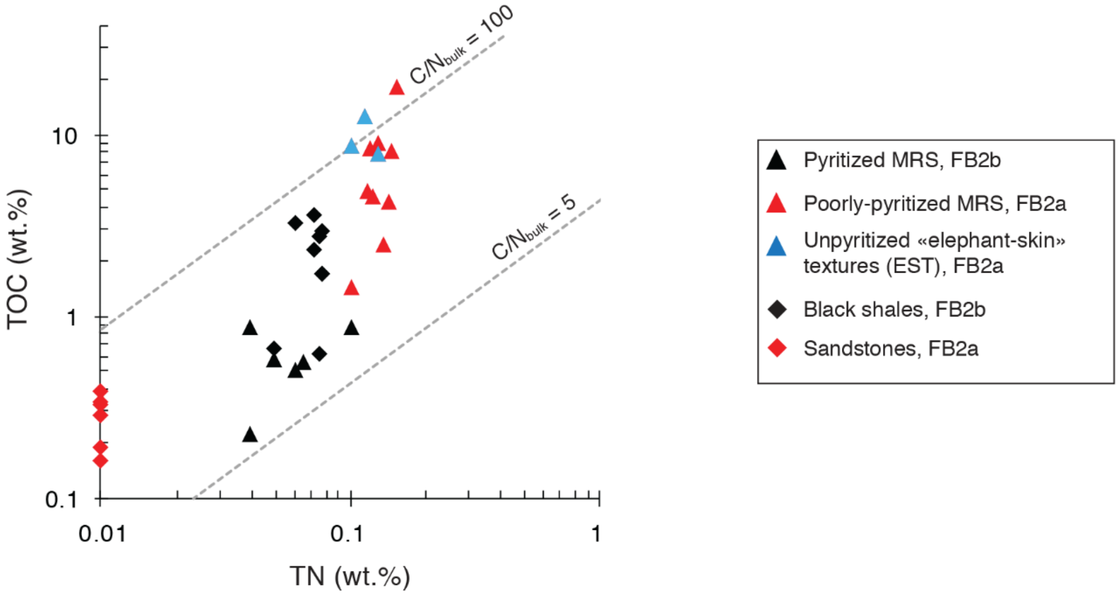

Appendix 27: Cross plot assessments of data fidelity. (**A**) Geochemical data for all bulk-rock measurements from the FB$_2$ Member. (**B**) Cross plots of K contents with TN and $\delta^{15}N_{bulk}$.

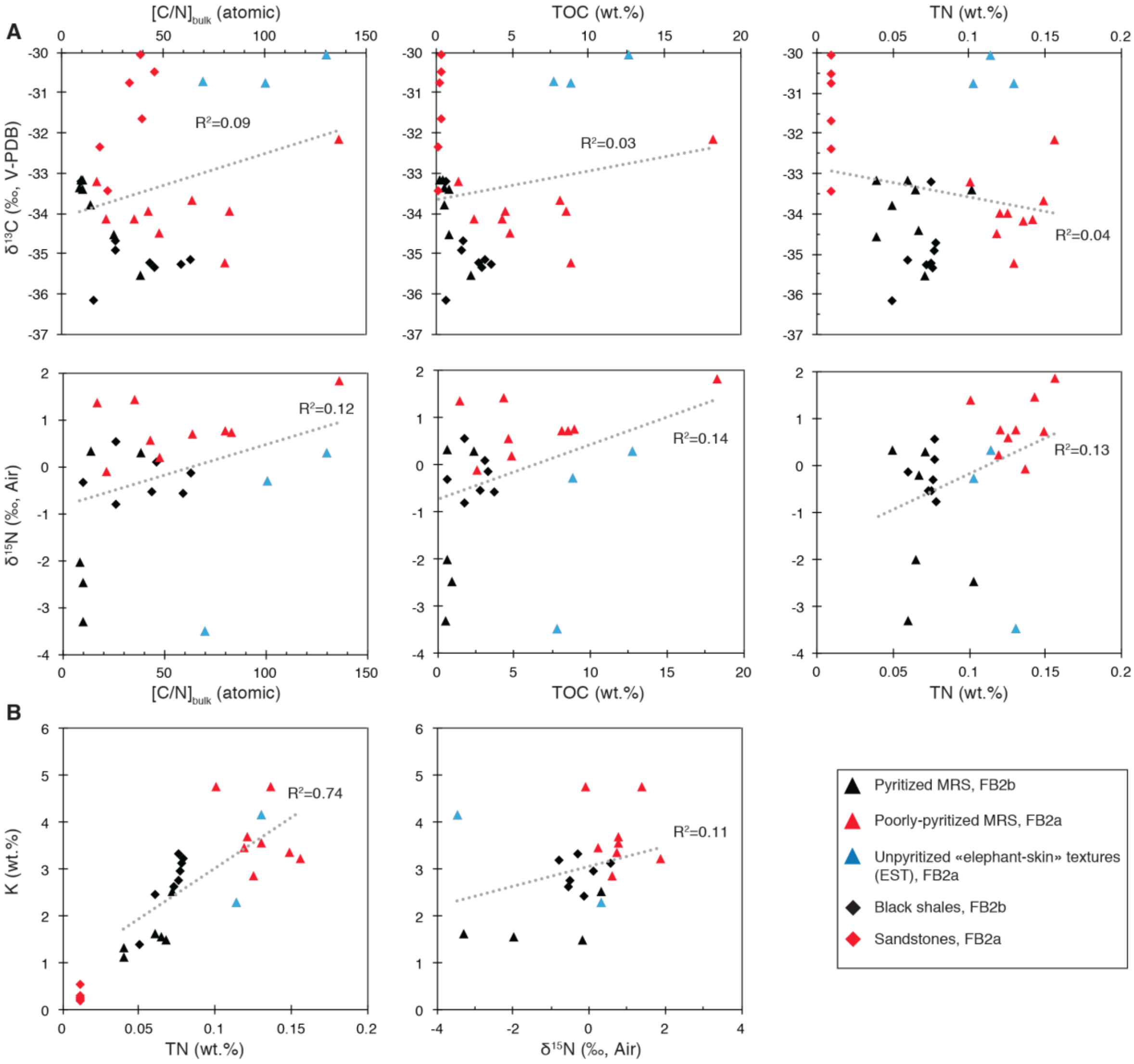

Appendix 28: Cross plot of bulk sulfur concentration and TOC for black shale samples from the FB_2 Member. Adapted from Berner & Raiswel (1983).

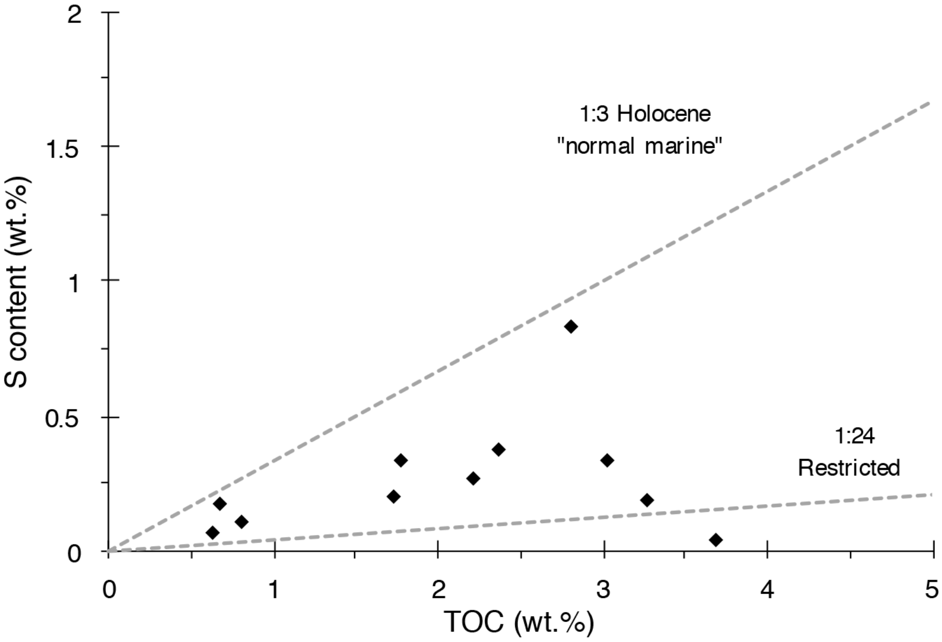

Associated works

1. Sedimentological and stratigraphic approach combined with a palaeobiological study in the Francevillian basin

SEDIMENTOLOGY the journal of the International Association of Sedimentologists IAS

Sedimentology (2017) doi: 10.1111/sed.12398

Depositional setting of the 2·1 Ga Francevillian macrobiota (Gabon): Rapid mud settling in a shallow basin swept by high-density sand flows

JEAN-YVES REYNAUD*, ALAIN TRENTESAUX*, ABDERRAZAK EL ALBANI†, JÉRÉMIE AUBINEAU†, LAURISS NGOMBI-PEMBA‡, GRACE GUIYELIGOU†, PASCAL BOUTON§, FRANÇOIS GAUTHIER-LAFAYE¶ and FRANCIS WEBER¶
**Univ. Lille, CNRS, Univ. Littoral Côte d'Opale, UMR 8187, LOG, Laboratoire d'Océanologie et de Géosciences, F-59000 Lille, France*
(E-mail: jean-yves.reynaud@univ-lille1.fr)
†Univ. Poitiers, CNRS, UMR 7285, IC2MP, F-86073 Poitiers, France
‡Département de Géologie, Faculté des Sciences, Université des Sciences et Techniques de Masuku, Franceville, Gabon
§OOLITE, 102 La Bournaire, 44690 Monnières, France
¶CNRS, UMR 7517, LhyGeS, F-67084 Strasbourg, France

ABSTRACT

The depositional setting of the 2·1 Ga fill of the Franceville Basin of Gabon is important for understanding the habitat (energy and availability of light and oxygen) and taphonomy of recently discovered early macro-organisms buried in black shales in Unit FB. The available data bearing on the stratigraphy and sedimentology of Unit FB provide new insight into processes acting on the palaeo-sea floor. The shales are interpreted to have formed as fluid mud deposits interstratified with structureless sands. The latter (Poubara sandstones) were emplaced during a forced regression during the terminal infill of fault-bounded sub-basins following a stage characterized by a ferruginous to anoxic water column. The structureless sandstones were deposited from high-density gravity currents along with a locally strong bottom oscillation of the water column. Tuft structures preserved in cyanobacterial mats, together with the position of the macro-organisms at the top of the sandstone beds within associated black shales, point to a water depth of less than 80 m. The relative sea-level fall that drove deposition of the Poubara sandstones controlled the rise of a phototrophic ecosystem and also possibly favoured the supply of oxygen and nutrients via density flows.

Keywords Black shales, cyanobacteria, dense flows, fossils, Franceville Basin, Palaeoproterozoic, turbidites.

INTRODUCTION

The Francevillian Basin of Gabon has been studied extensively due to its economic importance, given the presence of uranium and manganese ores (Baud, 1954; Weber, 1968; Gauthier-Lafaye, 1986; Gauthier-Lafaye & Weber, 2003). The basin fill provides an exceptional framework for studying the facies, mineralogy and geochemistry of the deposits of the Early Proterozoic, because the basin has undergone only minor tectonic deformation and metamorphic transformation over 2 Ga since it formed. Interest in the Francevillian Basin and its depositional history has recently been reignited by the discovery of a well-organized complex macrobiota in 2·1 Ga old deposits, pre-dating by 1 Ga the rise of eukaryotic life (El Albani *et al.*, 2010, 2014, 2016). These deposits are composed of a pyrite-rich sandstone and black shale unit – the

1

Poubara sandstones – that overlie a black shale unit which hosts the manganese ores. The underlying black shales formed during the Lomagundi event (Karhu & Holland, 1996), a time of high production and burial of organic matter following the Great Oxidation Event (GOE: 2·4 to 2·3 Ga; Holland, 1994, 2006).

The depositional setting of the Poubara sandstones and associated black shales, particularly in terms of the constraints placed on the energy and availability of light and oxygen, is important for understanding the habitat and evolutionary processes giving rise to the Francevillian macro-organisms. In the Phanerozoic, most black shales reflect low oxygenation of bottom waters, a situation that is common in deep water basins with stratified water columns (for example, the Jurassic North Sea, Pliocene Eastern Mediterranean and Modern Caribbean Sea: Sageman *et al.*, 2003; Tyson, 2005) and also in shallower waters within confined epicontinental basins (e.g. Tribovillard *et al.*, 1999). It is likely that, due to a low atmospheric oxygen pressure (maximum 20% of present-day during the GOE: Lyons *et al.*, 2014), only shallow waters were oxygenated at the time of deposition of the Francevillian black shales. On the other hand, black shales can also form due to a high rate of burial of organic-rich sediments, as is the case on upwelling-influenced margins (see extensive discussion in Tyson, 2005). Arguments on the rate of deposition and water depth are therefore crucial to improve current understanding of these fascinating fossils.

The aim of this paper was to synthesize available sedimentological data and new field and core observations bearing on the stratigraphic and sedimentary evolution of the FB Basin, with a particular focus on the Poubara sandstones and the black shales hosting the macrofossils. A revised stratigraphic and depositional model is developed based upon 35 cores, and detailed logs and facies analyses from six outcrop sections, including the one where the macrofossils were discovered. The implications of these findings for the biota are then discussed.

FRANCEVILLIAN BASIN CONTEXT

Stratigraphy

The Palaeoproterozoic Francevillian series lie within the Congo craton, a little deformed Archean tectonic block surrounded by orogenic belts ranging from the Early Proterozoic to Panafrican in age (Fig. 1A). A synthesis of the geodynamic evolution of these series is given by Weber *et al.* (2016). The Francevillian deposits are best preserved in the Booué, Franceville and Okondja basins (Fig. 1B). Hundreds of cores have been recovered from the Franceville Basin, as a consequence of manganese and uranium ore prospecting. However, only a part of this large database has been available for scientific study, mostly in unpublished PhD theses and internal reports. Five stratigraphic units are classically reported, following Weber (1968). Units FA and FC/FD are continuous across the Francevillian basins, while Unit FB is restricted to the main, fault-bounded depocentres (Fig. 1B).

Unit FA

This unit rests paraconformably on the pre-Eburnean basement. It is composed of >1000 m of detrital sediments sourced from the basement. The facies record an upward evolution from fluvial braided quartz arenite and conglomerate (Haubensack, 1981; Bankole *et al.*, 2015), to deltaic sandstones and finally to shallow-marine, tidal to wave-influenced sandstones and shales (Deynoux & Duringer, 1992; Pambo *et al.*, 2006). Sediment dispersal in the fluvial system was mostly to the south-east.

Unit FB

This unit, that is the focus of the current study, is localized within north-west/south-east fault-controlled corridors that provided accommodation and controlled the facies distribution and post-depositional deformation (Azziley-Azzibrouck, 1986; Gauthier-Lafaye, 1986; Pambo *et al.*, 2006; Bouton *et al.*, 2009). It is >1000 m thick in the centre of the Franceville Basin and mostly composed of black shales with interbedded debris flows (dolomitic olistolites with chert and shaly turbidite fragments) and dolomitic and silty/sandstone beds. The macrofossils have been found at the top of this unit (see below).

Unit FC

A thin, 10 to 50 m thick chert unit overlying dolomitized evaporites, stromatolites, oncolytic rudstones and possible volcanic tuffs (Weber, 1968; Bertrand-Sarfati & Potin, 1994; Amard & Bertrand-Sarfati, 1997; Préat *et al.*, 2011). This unit is basinwide where it has not been eroded and it oversteps Unit FB. The cherts are a diagenetic replacement of sulphates and dolomites by silica, probably of volcanic or hydrothermal

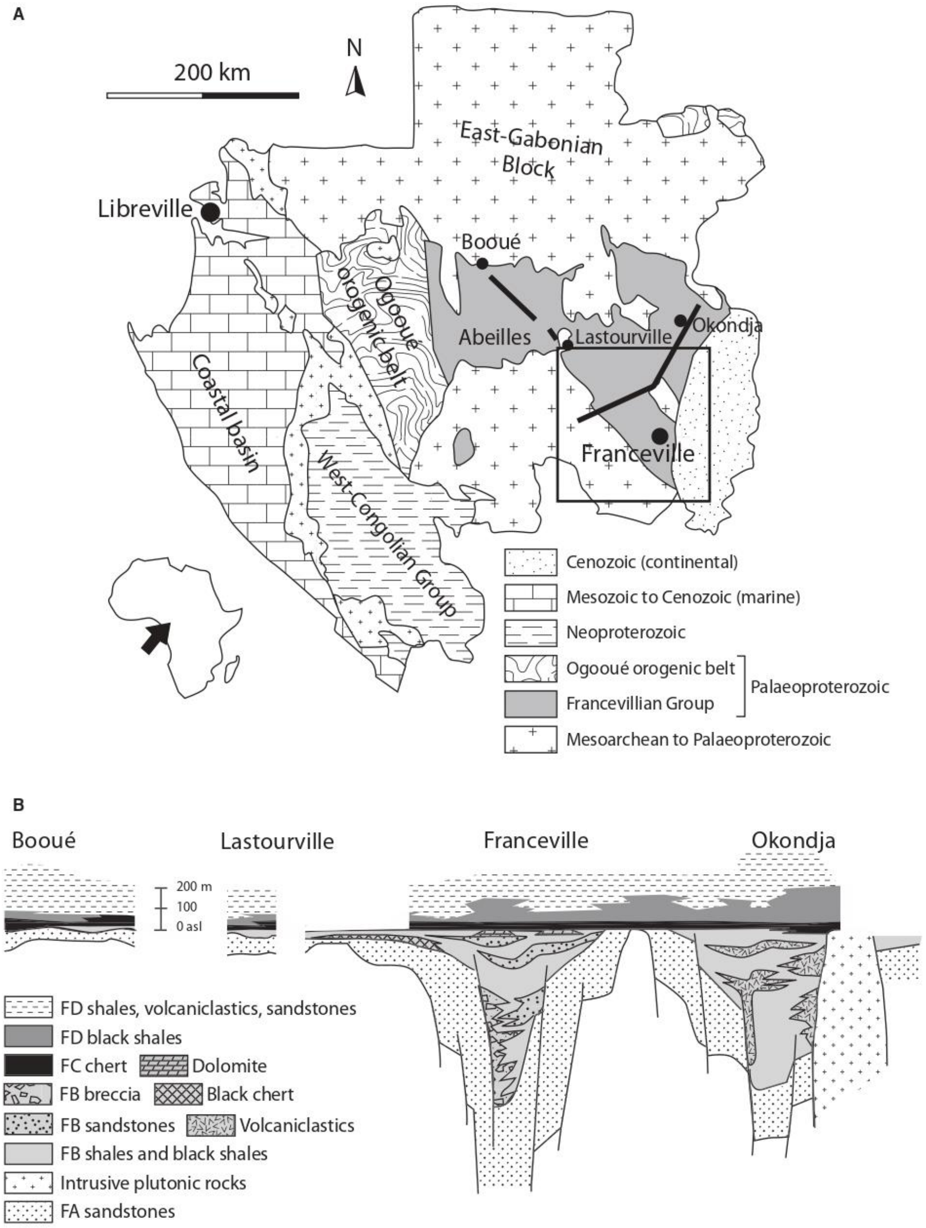

Fig. 1. (A) Simplified geological map of Gabon, showing the Palaeoproterozoic Francevillian basins. Inset frame: map in Fig. 4. Modified after Préat *et al.* (2011). (B) Cross-sections across the Francevillian basins (simplified after Bouton *et al.*, 2009). Note the fault-controlled subsidence of the Unit FB Basin, and also the datum of Unit FC as a correlation track.

origin (Préat *et al.*, 2011). The sulphate shows micro-chickenwire structure and the stromatolites exhibit teepees and collapse breccias that indicate a coastal sabkha environment (Bouton *et al.*, 2009; Préat *et al.*, 2011).

Unit FD

This unit comprises up to 400 m of black marine shales with high (up to 10%) total organic carbon (TOC) (Canfield *et al.*, 2013; Ngombi-Pemba, 2014), interbedded with pyroclastic rocks (containing isolated shards of devitrified glass) produced by subaerial fallout from explosive calc-alkaline volcanoes that become increasingly acidic towards the top of the formation (Thiéblemont *et al.*, 2014). Similar to Unit FC, this formation oversteps the FB sub-basins and has a relatively uniform thickness.

Unit FE

This unit is made up of 400 m of sandstones at Mount N'Gouadi in the Okondja Basin. These are coarse and arkosic with local conglomerate beds and pervasive cross-bedding and are interpreted as continental piedmont deposits (Bouton *et al.*, 2009).

Geodynamic evolution

Several radiometric ages are available to constrain the chronology of the Franceville Basin (see review in Weber *et al.*, 2016). The N'goutou Complex that was emplaced within Unit FB sediments yields ages ranging from 2143 ± 141 Ma (Bonhomme *et al.*, 1982) to 2027 ± 55 Ma (Moussavou & Edou-Minko, 2006). Smectites recording an early stage of Unit FB shale diagenesis yielded Sm–Nd ages at 2099 ± 115 Ma and 2036 ± 70 Ma (Bros *et al.*, 1992; Stille *et al.*, 1993). The most reliable ^{207}Pb/^{206}Pb zircon ages from Unit FD tuffaceous sandstones have yielded an age of 2021 ± 18 Ma (Bouton *et al.*, 2009).

Structural models of the basin (Gauthier-Lafaye, 1986; Feybesse *et al.*, 1998) have recently been reviewed by Weber *et al.* (2016), who integrated the available radiometric ages and the geochemistry of magmatic events to suggest a general tectonostratigraphic evolution for the Francevillian basins. According to these authors: (i) Unit FA corresponds to a rift basin following the doming of pre-Eburnean migmatites at 2·4 Ga; (ii) Unit FB records depocentres within a north–south-trending, sinistral strike-slip shear zone induced by inversion of the earlier rift system in transpression and coeval with the onset of the Eburnean orogeny; (iii) Units FC and FD record a change to a foreland regime during the Eburnean, with enlargement of the area of deposition and overstep of earlier faults with related acid, calc-alkaline, orogenic magmatism; and (iv) Unit FE is considered a post-orogenic, molasse-type deposit.

It is likely that the routing of sediments may have changed in response to these tectonic stages. While palaeocurrents measured from the bedforms and flute casts vary from one basin to another (Bouton *et al.*, 2009), Unit FA fluvial sediments were mainly sourced from the north-west (Haubensack, 1981; Mulder *et al.*, 2013), whereas sediments were routed from south-west to north-east during the onset of the Unit FB sub-basins (Weber, 1968; Mulder *et al.*, 2013; Parize *et al.*, 2013). A north-west gradient is also consistent with the orientation of slump folds and decollement faults in Unit FB (Pambo *et al.*, 2006; Ndongo *et al.*, 2016).

OVERVIEW OF UNIT FB

Weber (1968) defined a summary stratigraphic succession for Unit FB based upon facies assemblages that is still used in many publications. However, recently, this scheme has been questioned by Parize *et al.* (2013) and Mulder *et al.* (2013), who present a model where facies previously attributed to different stratigraphic units pass laterally to one another. Also, the stratigraphic unit boundaries may vary from author to author, depending on the facies interpretation (Fig. 2). This article follows (with minor changes) the facies typology defined by Azziley-Azzibrouck (1986), and the stratigraphic terminology of Weber (1968) (Fig. 3). The stratigraphic units are mapped as in Gauthier-Lafaye (1986), with minor modifications to take into account the revision of Bouton *et al.* (2009) and the present study (Fig. 4).

Facies review

Green shales

These correspond to greenish (biotite and chlorite–illite rich) silty to sandy shales with local siderite cement (Azziley-Azzibrouck, 1986). It shows current ripples with flasers and larger-scale dunes and bars interpreted as a foreshore environment. The green shales, mostly planar bedded, exhibit small wave ripples and graded

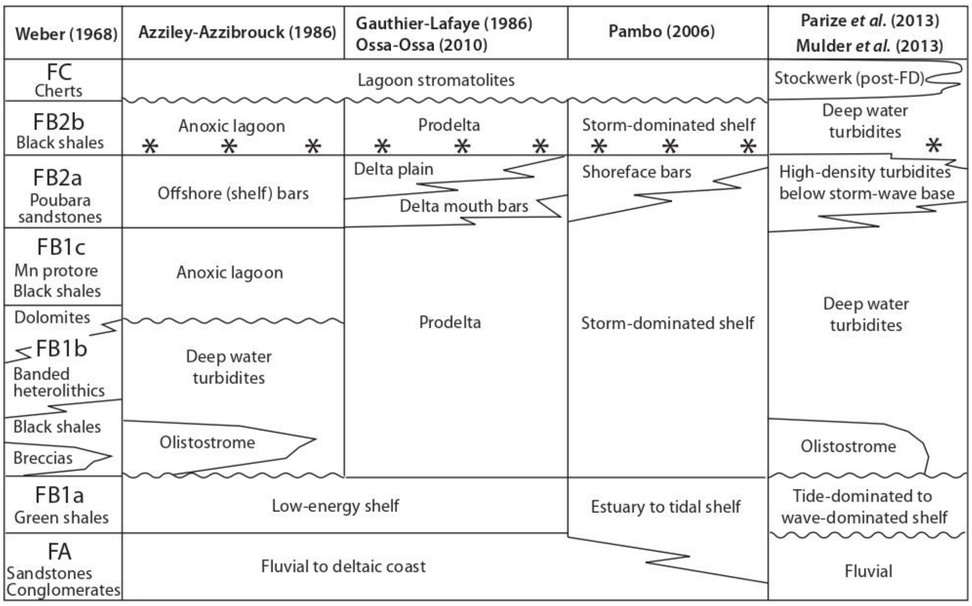

Fig. 2. Compared stratigraphic models of the FA to FC Francevillian succession in the Franceville Basin, compiled from several authors. The star line at the bottom of sub-unit FB2b indicates the stratigraphic location of the macrofossil ore described by El Albani *et al.* (2014).

beds indicative of storm-dominated shelf deposits (Deynoux & Duringer, 1992).

Black shales

Referred to as 'ampelites' by Weber (1968), they are composed of laminated silt-sized quartz and feldspar grains, together with illite, chlorite, illite/smectite (IS) clays, diagenetic carbonates of Ca–Mg–Mn–Fe, pyrite, apatite and organic matter. Carbonates (mostly dolomite) were formed during early diagenesis and are concentrated in the coarser laminae (Ngombi-Pemba, 2014). Pyrite forms disseminated automorphic crystals in the matrix. Pyrite is consistently associated with organic matter. The black shales have been interpreted as deposits ranging from a lagoonal (Azziley-Azzibrouck, 1986) to a distal turbiditic setting below storm-wave base (Parize *et al.*, 2013). Because the macrobiota have been discovered in the black shales, additional details concerning this facies are provided later in this article.

Dolomites

These locally have a banded pattern and preserve primary structure including stromatolites and intraformational breccias consistent with a locally intertidal environment (Azziley-Azzibrouck, 1986; Préat *et al.*, 2011; Fig. 5E). Dolomite is also present as a diagenetic component, forming continuous, laminated or nodular beds interbedded with banded heterolithics or black shales, particularly in the central parts of the basin. Dolomite nodules in the black shales formed around pyrite-rich layers during early diagenesis under increasingly anoxic conditions (Onanga-Mavotchi *et al.*, 2016).

Banded heterolithics

These are composed of layers of greyish shale alternating rhythmically from laminae to the bed scale with layers of light-grey siltstone cemented by dolomite (Figs 5E, 6B and C). Dolomitization occurred mostly during early diagenesis (Onanga-Mavotchi, 2016). The siltstones are characterized by flames, convoluted laminae or load features (Figs 5G, 5J and 6C), and small-scale synsedimentary faults (Fig. 5I; see also Azziley-Azzibrouck, 1986). Bedload traction is inferred, forming ripples at the top of the siltstone beds (Fig. 5F), and locally hummocky

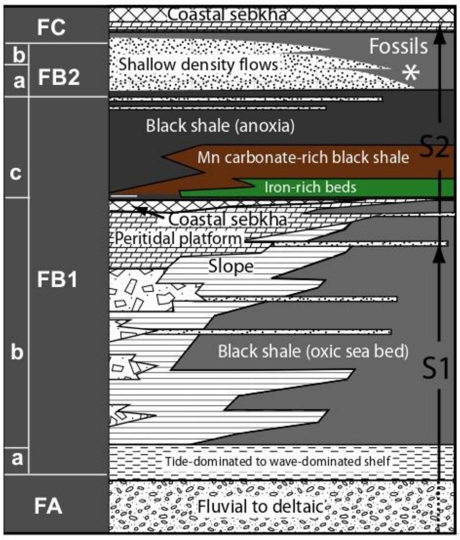

Fig. 3. Stratigraphic organization of Unit FB deposits in the Franceville Basin retained for this work. Schematic view of the spatial variability of the lithofacies, based upon correlations of the referenced cores and outcrops (Fig. 4). Basinward is towards the right. The dolomite facies can pass from stromatolites (lagoon) to black shales (basin). S1 and S2 refer to the depositional sequences interpreted in this contribution (see text for explanation).

cross-stratification (HCS) (Figs 5G and 6D). Larger-scale bed disruption and dip changes seen in cores indicate slumping of this facies (Fig. 5J), with an upward increase in the thickness of the slides through sub-unit FB1b. Small-scale shear folds and decollements are also observed (Fig. 5H). According to Azziley-Azzibrouck (1986), the banded heterolithics correspond to gravity flows on a submarine slope where mud settled out from suspension. The abundant load features at the bottom of the thicker silt layers suggest that the background mud formed a soupy ground. This is consistent with the numerous dewatering features preserved in this facies. Normal faults and slumps are consistent with mass wasting and gravity flows on more consolidated parts of a muddy slope.

Breccias

The breccias form up to several metre-thick beds interstratified within black shales or banded heterolithics. These breccias rework Archean rocks, together with Unit FA sandstones, Unit FB shales, stromatolithic cherts and oolitic dolomites; they are cemented by chalcedony or dolomite, with a locally high bitumen content (Weber, 1968; Bouton *et al.*, 2009), and are interpreted as deep water submarine canyon-fill or basin-floor olistostrome deposits (Weber, 1968; Azziley-Azzibrouck, 1986).

Poubara sandstones

These form a succession of dark coloured, generally structureless beds first described by Weber (1968). The sandstones are characterized by subrounded quartz grains with a uniform grain size of 300 μm, and a variable amount of plagioclase feldspar and micas, rare carbonate cement, and mica-derived clay minerals (illite, late diagenesis: Ngombi-Pemba *et al.*, 2014). The remaining porosity is infilled by micro-aggregates of pyrite and amorphous bitumen. In some places, conglomerate beds containing basement pebbles are interstratified (Miyama mounts), or found at the sole of large-scale channels or erosional gutters (Weber, 1968; Azziley-Azzibrouck, 1986; Parize *et al.*, 2013). The Poubara sandstones have been interpreted in very diverse ways (Fig. 7), ranging from coastal barriers (Ossa-Ossa, 2010) to proximal turbidites emplaced below storm-wave base (Parize *et al.*, 2013). The Poubara sandstones must be distinguished from sandstone beds interstratified with black shales or banded heterolithics. The latter are less well-sorted, commonly rippled and cemented by dolomite. Some of those beds are depositional, with upward water escape features (dishes and flames, cf. Fig. 5A), and may correspond to the distal fringe of breccias

Fig. 4. Geological map of the Franceville Basin, with location of the data used in this paper. Black circles refer to cores. The cores with a white label are displayed in Fig. 8. The MVG5 and MVG6 cores are too close to MVG4 to be displayed at this scale. The studied outcrops are Moanda railway station (RS: 1·4975°S, 13·2522°E), Moulendé quarry (Mou: 1·6285°S, 13·4655°E), Lekouba quarry (Lko: 1·6410°S, 13·5013°E), Mengué quarries (MvgA: 1·7276°S, 13·4776°E; MvgB: 1·6880°S, 13·4363°E), Gangolo quarry (Gan: 1·4133°S, 13·1983°E) and Lékédi River (Lek, accessed from location 1·4221°S, 13·2449°E). Structural framework and unit contours modified from Weber (1968), Gauthier-Lafaye (1986) and Bouton *et al.* (2009).

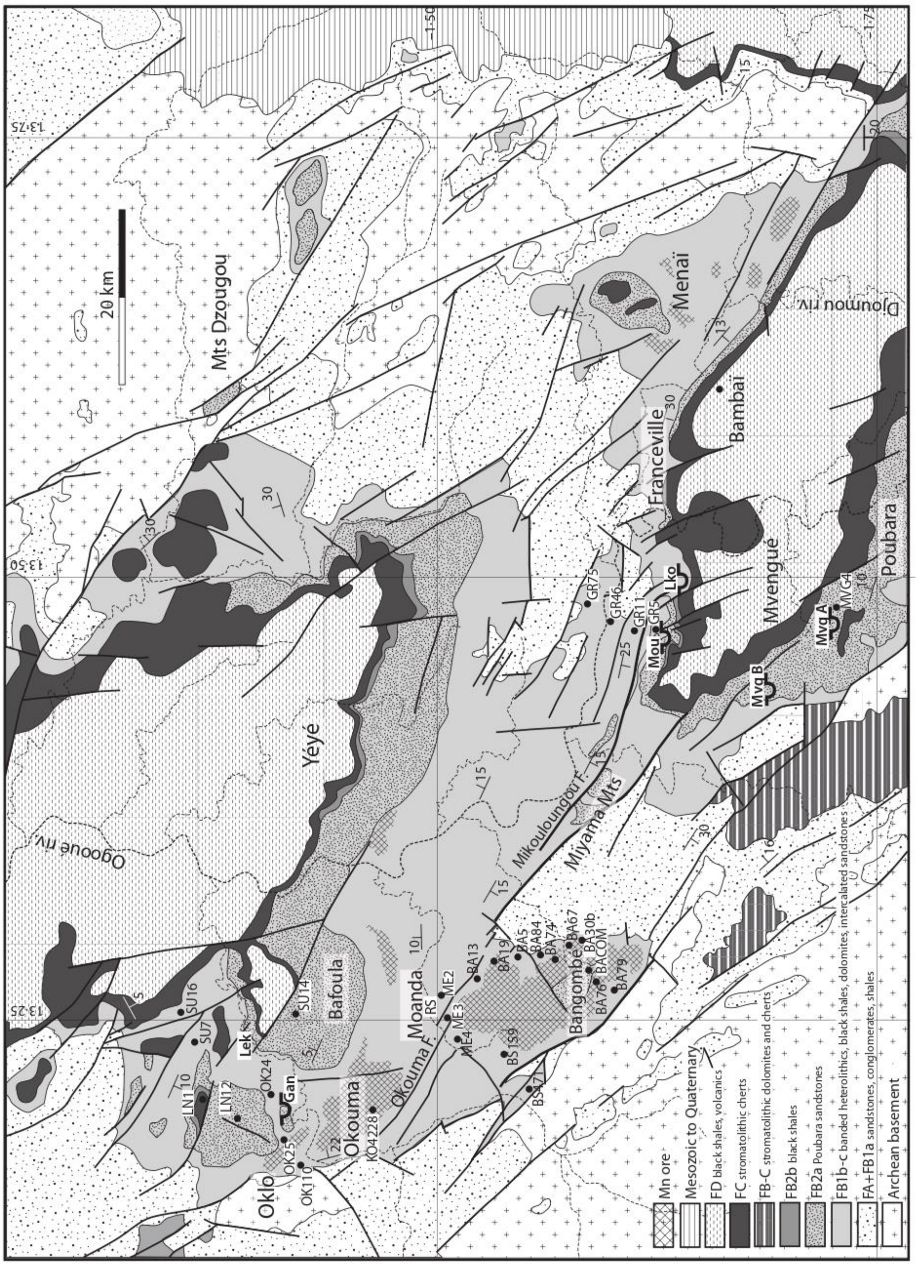
Mts Dzougou
20 km
13·25
13·50
1·50
1·75
Menaï
Djoumou riv.
Bambaï
Franceville
Lko
Mvengué
Poubara
Mvg A
MVG4
Mvg B
Mou
GR75
GR46
GR11
GR5
Yéyé
Ogooué riv.
Mikouloungou F.
Miyama Mts
Bangombé
BA67
BA30b
BACOM
BA79
BA78
BA74
BA84
BA5
BA19
BA13
Moanda
RS
ME2
ME3
ME4
BS159
BS47
Okouma F.
Okouma
KO4228
Bafoula
SU14
SU16
SU7
Lek
OK24
Gan
LN110
LN12
OK25
OK110
Oklo
Mn ore
Mesozoic to Quaternary
FD black shales, volcanics
FC stromatolithic cherts
FB-C stromatolithic dolomites and cherts
FB2b black shales
FB2a Poubara sandstones
FB1b-c banded heterolithics, black shales, dolomites, intercalated sandstones
FA+FB1a sandstones, conglomerates, shales
Archean basement

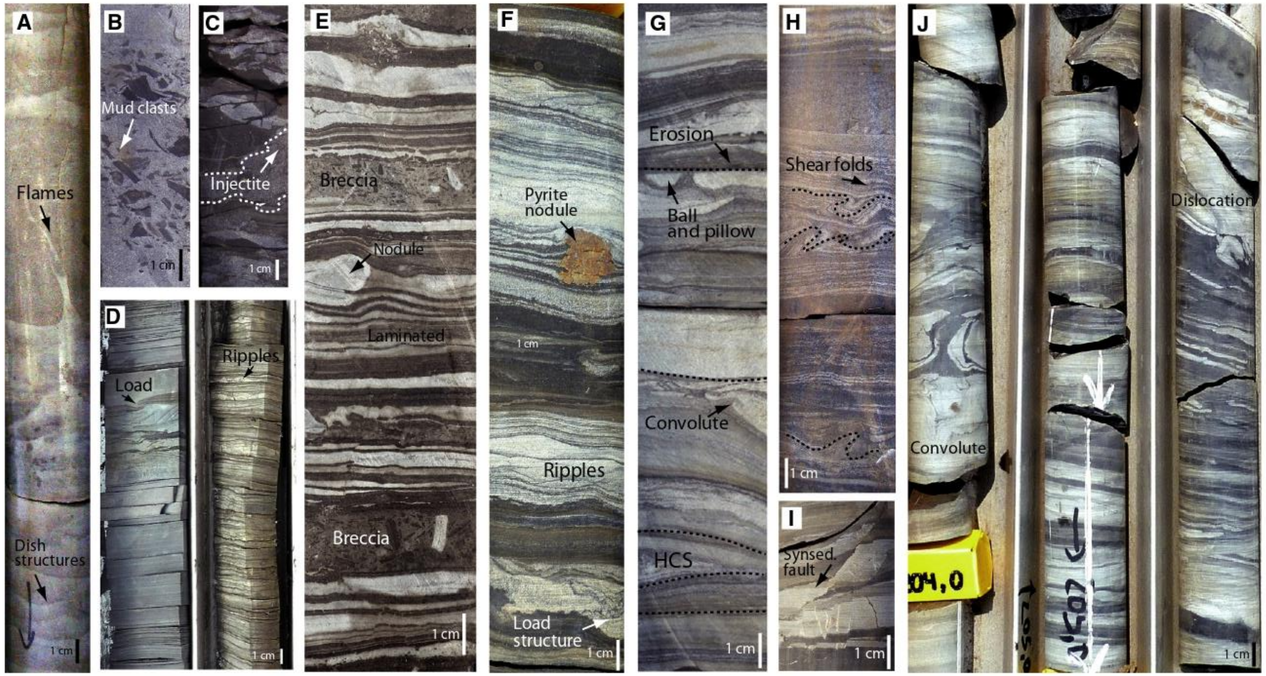

Fig. 5. Some facies of Unit FB in cores. Sub-unit FB1c: (A) Sandstone bed with water escape features interstratified in the black shales below the sub-unit FB2a Poubara sandstones (38 m in MVG4). (B) Rip-up clasts of black shale in the Poubara sandstones (28 m in MVG5, vicinity of MVG4). (C) Deformed and injected sandstone beds in the black shales at the base of the Poubara sandstones (20 m in MVG5). (D) Aspect of black shales in core. Note the rippled sand beds and the liquefaction features in some intervals (37 m in KO65035). Sub-unit FB1b: (E) Laminated dolomite (stromatolites) and interbedded breccias close to FB1c boundary (58 m in KO65035). Typical aspects of banded heterolithics: (F) rhythmic beds of shale and dolomitic siltstone, locally rippled (white layers; 259 m in KO42028). (G) Erosion and HCS in thicker beds levels (91 m in KO42039). (H) Folded beds. Note the flat laminae below and above (40 m in MVG6). (I) Synsedimentary fault (95 m in KO65035). (J) Large-scale dislocation and liquefaction features associated with slumping (204 m in KO42028).

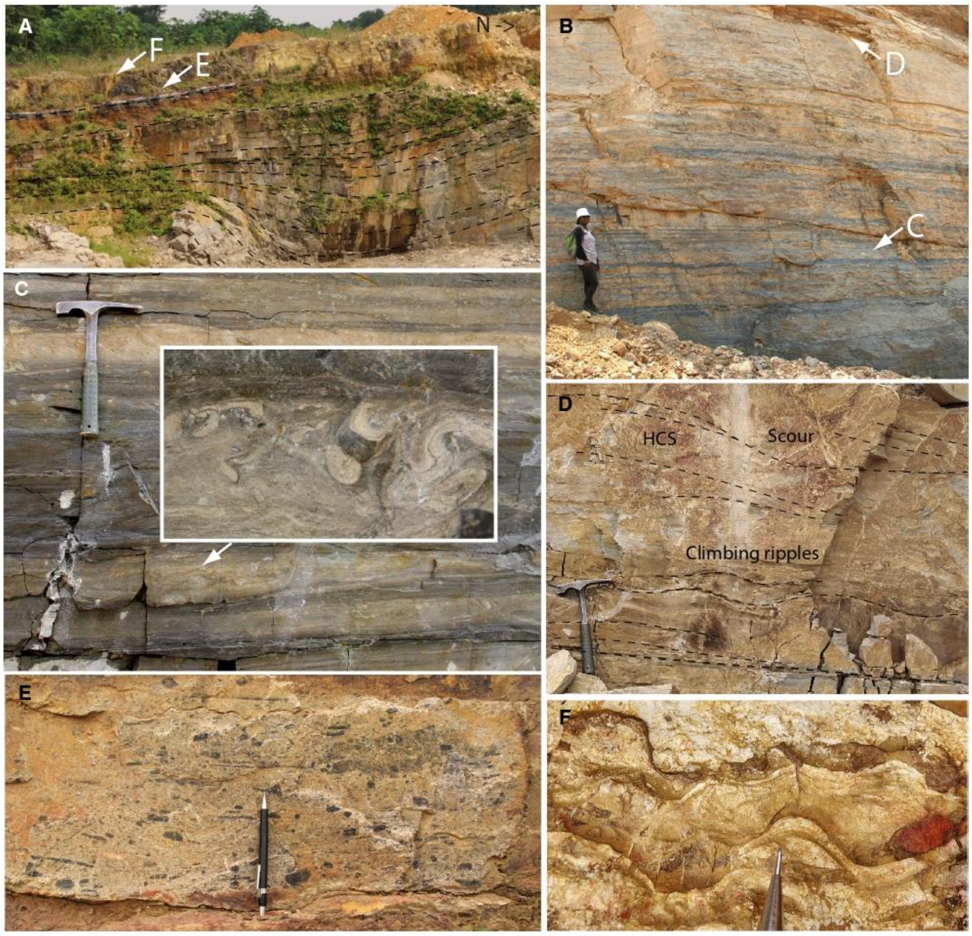

Fig. 6. Features of Lekouba quarry (cf. Fig. 4 for location). (A) Syndepositional fold within the banded heterolithics. 'E' and 'F' refer to the location of chert and breccia shown in panels (E) and (F). (B) Banded heterolithics (note the upward coarsening and upward thickening, from dominant shale in grey to dominant dolomitic sandy siltstone in yellow). Person for scale is *ca* 1·8 m tall. (C) Details of the banded heterolithics. Note the local convolute lamination of the dolomitic beds (inset frame). (D) Typical succession of structures in the uppermost beds below the breccia. Hammer for scale is 27 cm long. (E) Silicified breccia with black chert clasts. Pen for scale is 15 cm long. (F) Stromatolites at the top of the breccia.

(Azziley-Azzibrouck, 1986). Other beds, by contrast, correspond to injectites cross-cutting the primary bedding (Dubois, 2017; Fig. 5C).

Stratigraphic units

- *Sub-unit FB1a* is entirely composed of green shales that are not found in other units. This sub-unit, about 50 m thick, is relatively isopachous and has a conformable base with the underlying FA unit. The lowermost facies are transitional with the fluvial and deltaic deposits forming the top of Unit FA.
- *Sub-unit FB1b* is the thickest (locally over 1 km) and with maximum lateral changes in facies and thickness. It is characterized by the

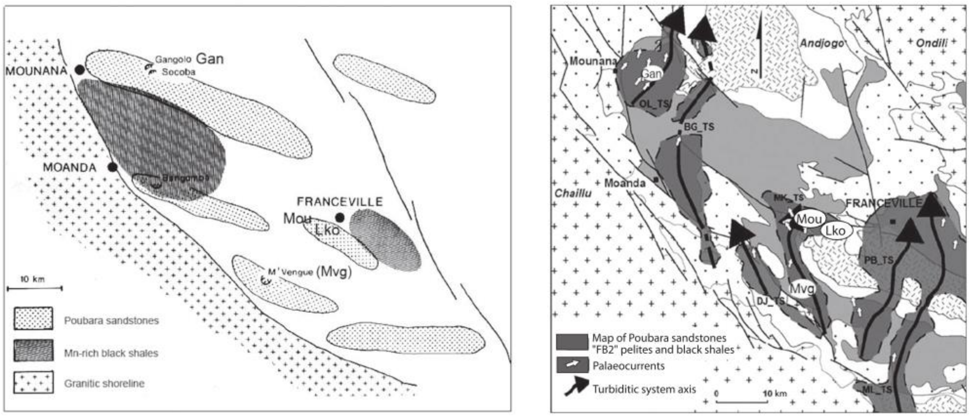

Fig. 7. Contrasted interpretations in the literature of the Poubara sandstone bodies based on different inferred geometries. Left: storm-built ridges (modified from Azziley-Azzibrouck, 1986). Right: turbiditic lobes (modified from Parize *et al.*, 2013). Mou: Moulendé; Gan: Gangolo; Lko: Lekouba; Mvg: Mvengué.

banded heterolithics, interbedded at all scales with black shales, which are ubiquitous, and, more scarcely, with dolomites or breccias. Several levels of breccias and conglomerates are preserved in this unit at the basin borders where Archean rocks are exposed. Dolomites are abundant at onlap to intrabasinal highs, and extend basinward towards the top of the unit. The black shales in FB1b have a lower TOC than those in FB1c and FB2b.

- *Sub-unit FB1c*, up to 50 m thick, is characterized by black shales with a high amount of TOC (up to 11%; Cortial *et al.*, 1990; Ngombi-Pemba, 2014), and almost no feldspar, in contrast to black shales in other units. Trace elements indicate anoxic conditions at the sea bed and possibly in the water column (Canfield *et al.*, 2013). Boghead and shungite layers are present in places (Azziley-Azzibrouck, 1986). The lower part of this unit also locally contains an iron-rich interval up to 10 m thick, well-developed at Okouma (Fig. 4). This interval comprises laminated and brecciated Fe-rich carbonates, locally silicified and pyritized, interstratified with pyrite-rich black shales (Fig. 5E). Above this interval, the bulk FB1c has Mn-rich carbonates in the matrix, forming the Mn ore at Moanda (Pambo, 2004). The black shales also exhibit dolomite or pyrite nodules that locally amalgamate to form nodular beds.
- *Sub-unit FB2a*, up to 100 m thick at the borders of the basin, is characterized by the Poubara sandstones (Weber, 1968), interstratified with thin beds of black shales (see below detailed outcrops).
- *Sub-unit FB2b* corresponds to an up to 50 m thick unit of black shales, called Djoumou shales by Weber (1968). This deposit is indicative of a return to dysoxic to oxic conditions (Canfield *et al.*, 2013).

UNIT FB STRATIGRAPHY UPDATED

Subsurface correlations

A total of 35 core logs reported from the literature and/or revisited and documented in the COMILOG core repository at Moanda have been used to re-evaluate the Unit FB stratigraphy in the subsurface (Fig. 8). Using the cores, a revised model of the basin-fill architecture is proposed (Fig. 9). Sub-unit FB1b deposits vary laterally in lithology and thickness over short distances (a few hundreds of metres, the shortest distance between drilling wells). This is because they were emplaced during a stage of fault-controlled subsidence following the initial Unit FA to FB1a transgression, with deposition occurring in elongated sub-basins separated by submerged highs (Azziley-Azzibrouck, 1986).

The top of FB1a is interpreted as a drowning surface and is therefore used as a datum for correlation (Fig. 8). The top of FB1b is interpreted as a sequence boundary with local emergence, as

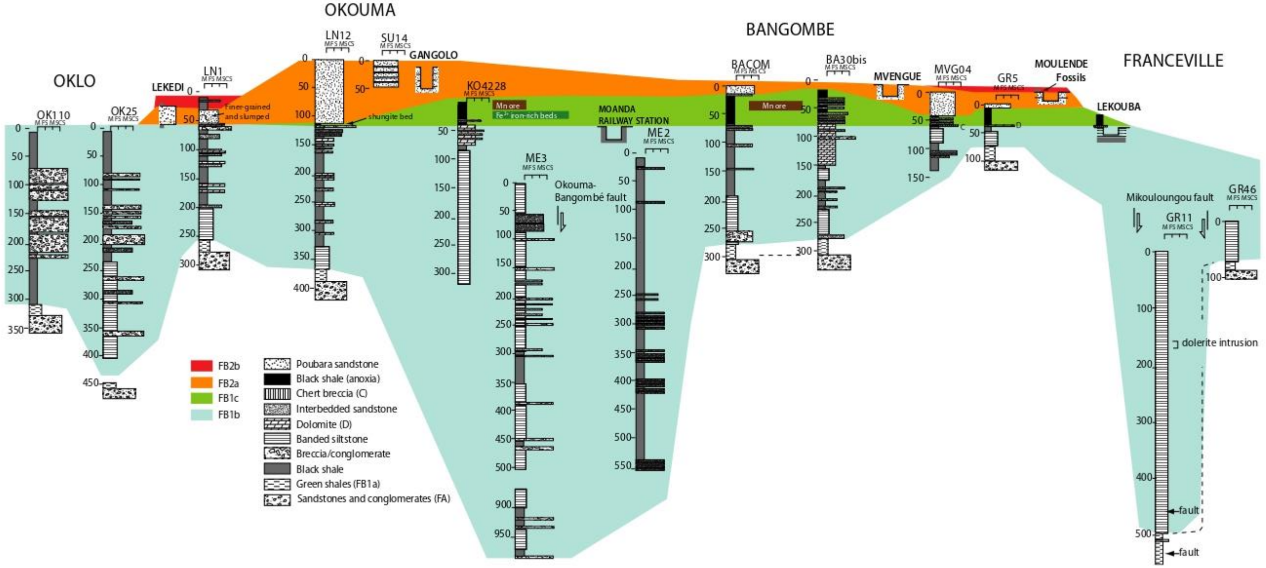

Fig. 8. Tentative core correlation across the FB deposits of the Franceville Basin. See locations in Fig. 4. The horizontalized datum is the FB1b/c boundary, corresponding to a transgressive surface. Quarry or field outcrops have been added close to the nearby cores, and at the approximate corresponding stratigraphic elevation. See text for explanations.

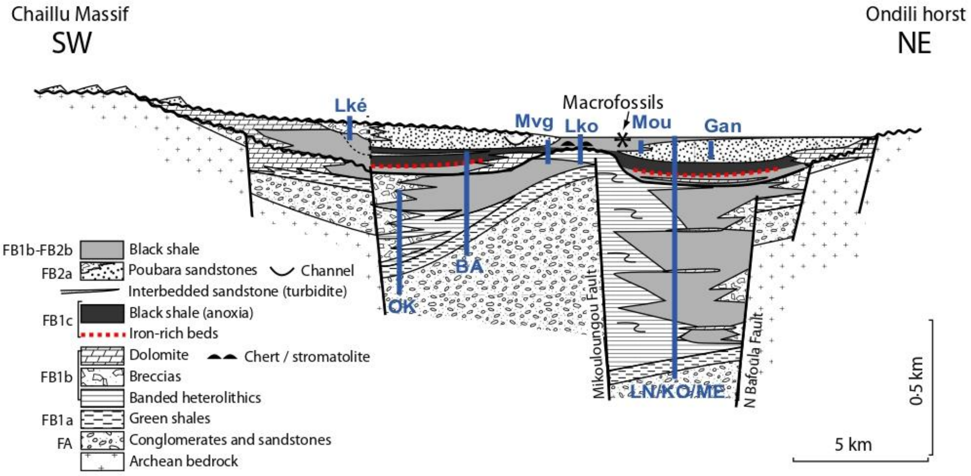

Fig. 9. Synthetic cross-section of the Franceville FB Basin based upon outcrops and cores, and figuring out the interpreted facies relationships. North-west and south-east sites are projected in blue at approximate equivalent location (in map see Fig. 4). The Poubara sandstone bodies might infill residual fault-bounded minibasins by the end of the final FB regression.

shown in the Lekouba quarry. This outcrop comprises a northward verging, synsedimentary fold (Fig. 6A) that developed within thickening-up and coarsening-up banded heterolithics, dominated at the top by mostly dolomitic beds (Fig. 6B to D). The banded heterolithics are abruptly truncated by a metre-thick black chert breccia with ghosts of dolomite clasts (Fig. 6E), capped by stromatolithic beds (Fig. 6F). A similar chert breccia, relatively rare at basin scale, is found at almost the same position near Mounana (Bouton *et al.*, 2009) and in the MVG4 core, and might correspond to a dolomite bed in core GR5 (Fig. 8). Based upon carbon, sulphur and iron isotopes, and trace metals and rare earth elements, Ngombi-Pemba (2014) and Canfield *et al.* (2013) suggest that a ferruginous sea floor existed during deposition of the iron-rich beds in FB1c, and show generalized anoxic conditions during deposition of this sub-unit. These authors conclude that FB1c should correspond to a generalized transgression. A third stratigraphic marker allowing long-distance correlations is the sharp base of the FB2a Poubara sandstones, which is interpreted as a basal surface of forced regression. FB2a is present only at the top of a few of the cores, suggesting that it is a unique unit (Donot & Weber, 1968a,b; Weber, 1968) rather than multiple bodies interstratified within the black shales, as suggested by Bouton *et al.* (2009).

The facies reported in the cores form packages ranging from <1 m to several hundreds of metres in thickness. The black shales form the intervals between all other facies and therefore constitute the background sedimentation throughout Unit FB above the green shales. In most cores, FB1b starts with banded heterolithics, which indicates an abrupt drowning and sustained tectonically controlled slope. The breccias, which are interpreted to be contemporaneous with the banded heterolithics, are restricted to areas close to onlaps against the Archean basement. In the hangingwall of the main intrabasinal faults, the banded heterolithics dominate the FB1b succession. Away from these faults, they interfinger basinward with black shales. The dolomitic intervals, which are mostly present close to the non-faulted margins of the basin (for example, to the south-west: Bangombé, Mvengué), increase upward through sub-unit FB1b. Compared to FB1b, which comprises most of the FB Basin infill, sub-units FB1c and FB2 are thinner, suggesting a decline in fault activity and associated subsidence. Towards the top of FB1c, there is a return to interstratified sandstone beds which are very similar to the overlying FB2a Poubara sandstones.

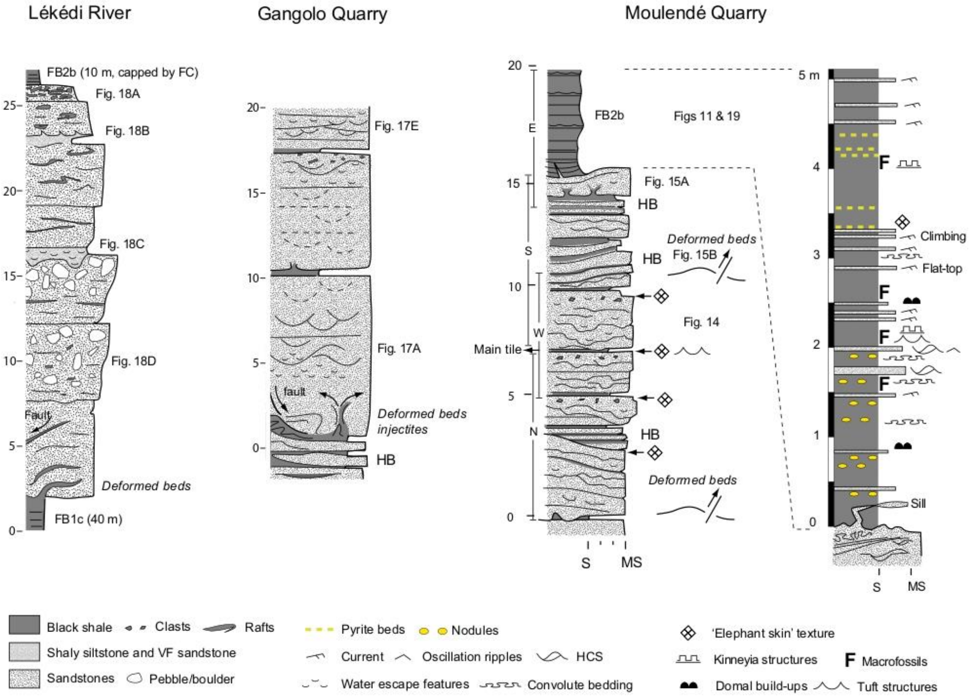

Fig. 10. Outcrop sections of sub-unit FB2 (see locations in Fig. 4). In the Gangolo quarry, detailed observations were made in the 0 to 5 m and 15 to 20 m intervals. The synthetic log of Moulendé is based upon a detailed mapping and correlation of the walls and tiles of the quarry (east, west, north and south). HB: heterolithic bedsets. F: macrofossils described in El Albani *et al*. (2010). The fossil cyanobacteria indicating a shallow water depth correspond to the tuft structures (Fig. 19E and F).

Large-scale geometry of the Poubara sandstones

The Poubara sandstones progressively pinch out basinward from Mvengué to Lekouba, where the remainder of the FB succession above the FB1b/c boundary is composed of black shales. The hypothesis of an erosional unconformity truncating the FB2a basinward can be ruled out because Unit FC is found at almost the same elevation above the chert reference bed at Moulendé and Lekouba. The contact between sub-units FB2a and FB2b is well-exposed in Moulendé quarry and is non-erosional. An interfingering contact is inferred between the FB2a Poubara sandstones and the FB2b Djoumou shales. Alternatively, there may be an onlap of the Djoumou shales against the topography left by the Poubara sandstones although this onlap is thought to be less likely. The Poubara sandstones are themselves made up of packages of sandstone beds and shale intervals at several scales, as illustrated by the SU14 core, and a similar bedding pattern is present in the outcrop in the Gangolo and Moulendé quarries (Fig. 8). Along the strike, the maximum thickness of the Poubara sandstones (about 100 m) is recorded in the west, between the Okouma–Mikouloungou and North Bafoula faults (Fig. 8). The abrupt thickness change in the Poubara sandstones below the Djoumou shales across the North Bafoula fault suggests that this fault was active during deposition. There is an overall decrease in thickness of the Poubara sandstones between the Miyama mounts towards the south-east (30 m at Mikouloungou and almost zero at Franceville), together with an increase in the abundance of black shale interbeds. The

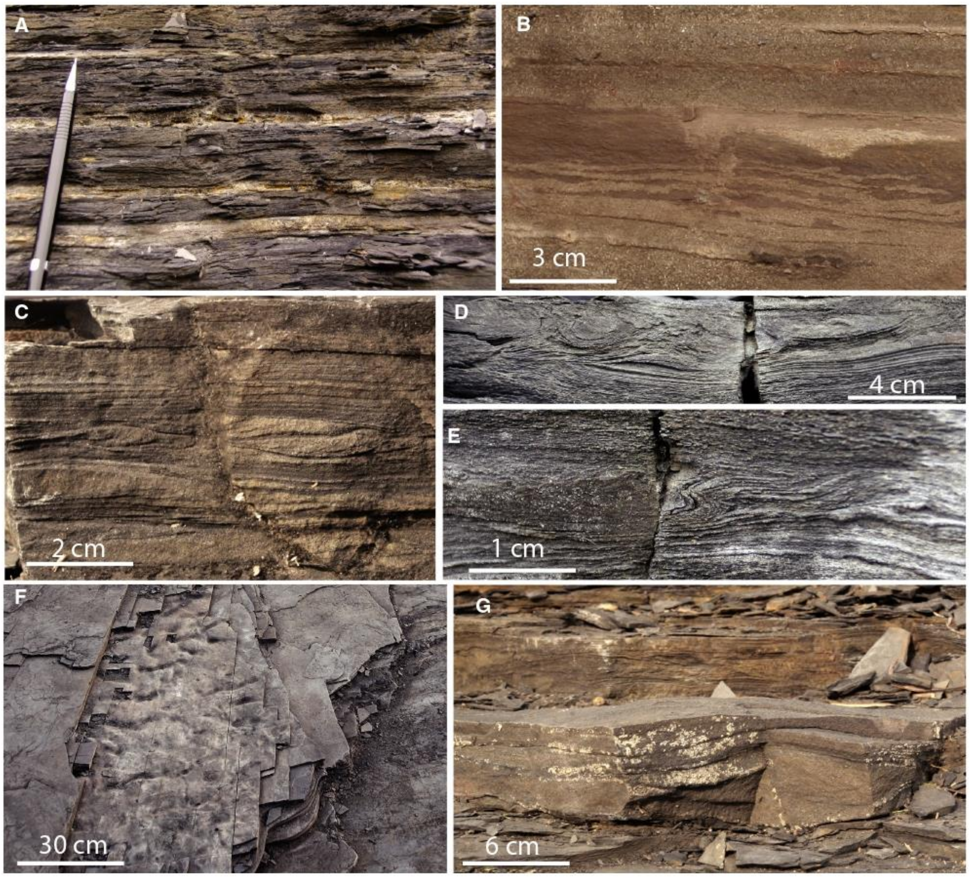

Fig. 11. Outcrop pictures of the sub-unit FB2b black shale in Moulendé quarry. (A) Sand-silt/black shale alternations forming the primary lamination. Pen for scale is 15 cm long. (B) Disrupted sand laminae within the black shale background. (C) Climbing ripples within a sandier interval. (D) and (E) load casts and convolute lamination. (F) Linguoid, flat-topped ripples. (G) Hummocky cross-stratification (HCS) structures within the thickest sand bed.

Poubara sandstones thicken up again east of Franceville (Menaï Plateau, Fig. 4). In the Franceville area, as evident at Lekouba and in the Bambaï reference core (Weber, 1968), the sandstones pass laterally to within 35 to 40 m of FB2b Djoumou shales. The Djoumou shales, where the macrofossils were discovered, is therefore a black shale pool between thicker bodies of the Poubara sandstones. These larger-scale sandy bodies might have a lobate shape.

DEPOSITIONAL SETTING OF UNIT FB: NEW RESULTS

As highlighted by Bouton *et al*. (2009) and Parize *et al*. (2013), the FB1b–FB2 black shales and sandstones are intimately interstratified at all scales, which suggests a common process and setting. This section presents further details of the studied outcrops and examples of the facies in core, providing new insight

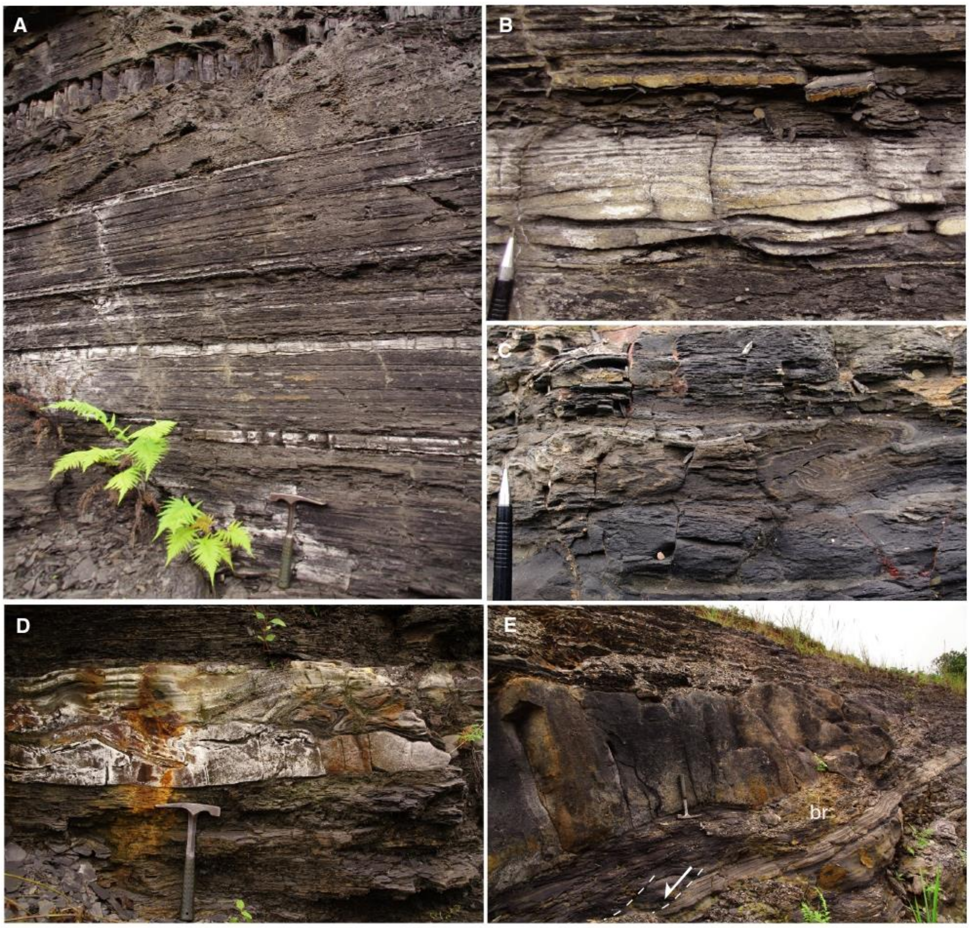

Fig. 12. Facies of sub-unit FB1b black shales at the Moanda railway station (see location in Fig. 4). (A) General aspects of the lamination. The white laminae sets are sandier (pyrite bleaching). The bed with prismatic cracks at the top of the picture is a diagenetic dolomite (nodules are found at various levels of this outcrop). Hammer for scale is 27 cm long. (B) Close-up of a sandier laminae set, with ripples at the bottom. Pen tip for scale is 2 cm long. (C) Small slump, showing shear features towards the right of the picture. (D) Interstratified sandstone, with convolute lamination and water escape features at the base, draped by planar lamination. (E) Conglomerate channel with mud breccia (br) and normal faults (arrow) in the underlying shales.

into the depositional environment, including sea floor dynamics and likely water depths. The outcrops examined are mainly quarries in Mvengué, Lekouba and Moulendé, with the 2·1 Ga macrofossils discovered in the Moulendé quarry (referred to as SOCOBA in El Albani *et al.*, 2010, 2014, 2016; Ndongo *et al.*, 2016; and KM16 in Parize *et al.*, 2013; but renamed herein after the nearby village).

Rapid mud deposition with rhythmic current pulses

New observations on the black shales

The Moulendé quarry offers a detailed section of the contact between the two FB2 sub-units (Fig. 10). There, the FB2b black shales rest conformably above the FB2a Poubara sandstones. The black shales are formed by rhythmic, millimetre to centimetre thick, fining-upward mud laminae in the clay–silt range, with intercalated beds 1 to 5 cm thick or silt/very fine sand (Fig. 11A). This facies has the same petrography as the underlying FB2a sandstone beds (Ngombi-Pemba, 2014). The very fine sandy and silty laminae are dislocated locally within the black shale (Fig. 11B). The sand stringers are composed of sets of two or three climbing ripples (Fig. 11C); they are discontinuous where the ripples are thin and starved, or continuous where thicker and, in this case, commonly associated with load casts, convoluted laminations (Fig. 11D) and basal shear structures (Fig. 11E). The ripples dominantly migrated to the east and locally exhibit a linguoid shape (Fig. 11F), or a more two-dimensional geometry. At one level, the ripples have flat tops. At another, interference oscillation ripples are observed. Small HCS are also observed in two thicker and coarser grained beds (Fig. 11G).

The Moulendé and other FB2b black shales share many features with those of the classical Moanda railway station outcrop, corresponding to the upper part of the FB1b black shales, or to their subsurface counterparts (Fig. 5D). These features are: (i) the background silty sand to mud horizontal lamination (Fig. 12A); (ii) the rippled intervals with fining-up climbing ripples grading to draping and finally to horizontal sand–mud couplets (Fig. 12B); and (iii) load features at the bottom of those sand stringers, associated with bed-shear deformation (Fig. 12C). In addition, the Moanda railway station outcrop exhibits interstratified sandstones with rip-up shale fragments and injection features at the base, capped by a planar to low-angle lamination (Fig. 12D). Finally, fining-up, gravel-rich to micro-conglomeratic beds are found as metre-thick channel or gully fills, with deformation features in the underlying black shales including small normal faults and locally a mud-clast breccia (Fig. 12E). In cores, similar deformation features of interstratified or injected and locally fluidized sand layers are found throughout the black shales, with an upward increase towards the base of the Poubara sandstones (Fig. 5C).

Interpretation

The load casts and liquefaction features found in the black shales suggest that they settled rapidly, forming a fluid mud. Interpreting a fluid mud suggests a shallow water origin. Fluid mud can form in the maximum turbidity zone of estuaries, due to flocculation of clay minerals (e.g. Nichols, 1985), but may also expand seaward of the mouth of large rivers (e.g. Kineke & Sternberg, 1995). A primary offshore origin is also reported in the literature, due to resuspension of clay particles into a nepheloid layer. Particle clumping due to mechanical stirring (mostly wave action) at the bottom of the nepheloid would cause formation and/or growth of flocs until they settle down, clearing up the nepheloid and forming a fluid mud layer to the bed (Hill, 1990; Stolzenbach *et al*., 1992). Mechanical stirring in the FB black shales is recorded by interference ripples and HCS that indicate water oscillation above the bed. Once formed, a fluid mud can flow by gravity on low-gradient shelves, under the continued action of bottom currents (e.g. Wright *et al*., 1990) or waves (e.g. Traykovski *et al*., 2000; Macquaker *et al*., 2010a). Thus, the background facies of the FB black shales could be the result of periodic resuspension by waves, bringing about fining-up laminae in black shales, as well as gravity flows of fluid muds (Ghadeer & Macquaker, 2011).

The formation of a fluid mud implies a strong stratification of water column near the bed, preventing upward diffusion of sediment (Hale & Ogston, 2015). The FB1c basin sea bed was anoxic or dysoxic most of the time, as demonstrated by Canfield *et al*. (2013), which argues in favour of water stratification. The amount of organic matter associated with clay minerals in the FB black shales facies would also enhance the formation of flocs (e.g. Macquaker *et al*., 2010b). The floc texture typical of fluid muds, as evidenced by Nishida *et al*. (2013), has not been observed so far in the FB black shales. This could be due to a very large amount of silt, which would make the sediment less cohesive. Nevertheless, specific features compare with those observed in laboratory experiments on fluid muds. Firstly, although turbulence is strongly restricted in the fluid mud layer ('plug flow' of Baas *et al*., 2009), ripples can still form at the top of the plug flow if the sediment

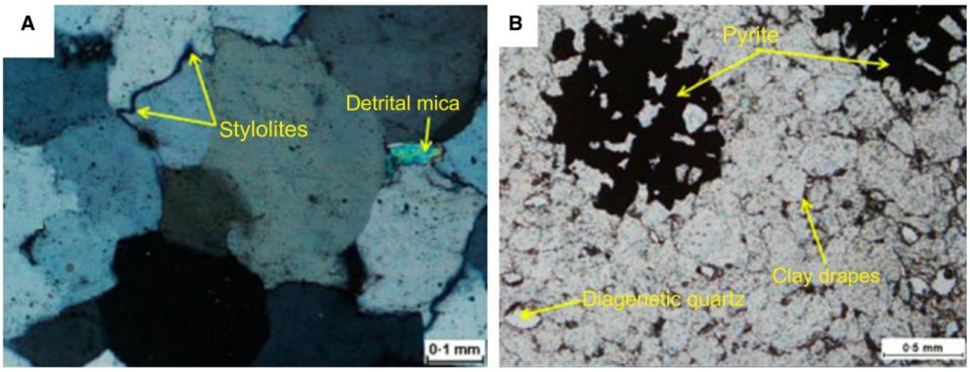

Fig. 13. Poubara sandstones of Moulendé quarry in thin section. (A) Stylolites at the detrital grain contacts. (B) Dissolved silica reprecipitates as exsolution quartz, cementing inclusions of pyrite or kerogen aggregates.

contains sand (Baas *et al.*, 2011). Thus, the rippled sands interstratified in the FB black shales could be associated with the flow of the fluid mud (and not only to resuspension events). Secondly, in the case of a turbulent flow overriding a fluid mud layer, intrabed sand and mud deposits can form, with shear structures, convolute and rip-up clasts at the bottom (Baas *et al.*, 2014). These features compare well with those observed in the black shales of the Moanda railway station.

Sand-rich density flow deposits

New observations on the Poubara sandstones

This section reports observations of the FB2a Poubara sandstones in the Moulendé, Gangolo and Mvengué quarries, and from a section close to the Lékédi River (Fig. 10).

The sandstones at Gangolo and Moulendé are dark with a high pyrite content. Thin sections show sutured quartz grains (pressure solution and overgrowth) and quartz exsolution within organic matter clasts (Fig. 13). The Mvengué sandstones have lesser amounts of matrix pyrite and organic matter and lack black shale interbeds. The Mvengué B quarry sandstones also have a higher amount of K-feldspar and lesser sorting of the quartz grains. The Moulendé sandstones are organized in overall aggradational, sheetform bedsets 1 to 2 m thick, bounded by prominent, pyritized surfaces and overlain by a decimetre-thick silty black shale interval (Fig. 14A). The bedsets are composed of >0·2 m thick sandy beds amalgamated along flat or irregular contacts, locally lined by discontinuous, millimetre-thick black shale drapes. A close-up view shows that these contacts are crenulated (Fig. 14B) or have a 'ball and pillow' geometry (Fig. 14C). Sheetform bedsets are interstratified with heterolithic bedsets, in which the sandstone beds are 0·2 to 0·5 m thick and bound by 0·05 to 0·2 m thick black shale layers. The base of sandstone beds commonly forming load structures between which the underlying mud may be laterally displaced and plastically deformed (Fig. 14D and E). The maximum degree of dislocation is found within the topmost bed beneath the transition to FB2b black shales (Fig. 15A). The thicker sandstone beds display dish structures (Fig. 16A, similar features from Gangolo and Mvengué are shown in Fig. 16B and C), and an upper surface with locally angular floating mudstone clasts (Fig. 16D; also in cores: Fig. 5B), metre-long cracks with fluidized walls (Fig. 16E), and rare planar to convoluted lamination also occur (Fig. 16G and H). A sandstone dyke and sill network sourced by the topmost bed ascends into and cuts the overlying black shales (Fig. 16F). The sheetform bedsets locally have a top surface with undulations several tens of metres in wavelength (Fig. 15A). These might locally be related to decollement folds, a feature already described by Pambo *et al.* (2006) and Ndongo *et al.* (2016). The lows on these bed tops can be infilled aggradationally by overlying deposits (Fig. 15B). Very few cross-beds are observed in the Moulendé

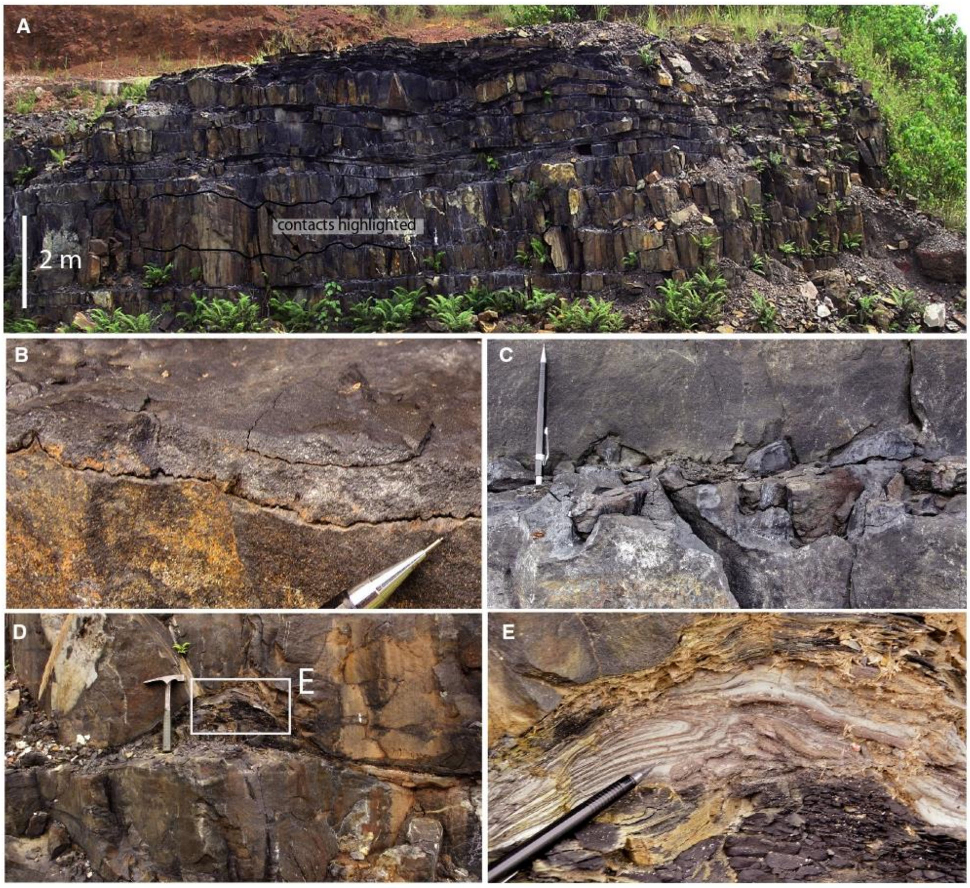

Fig. 14. Bedding and bed contacts of sub-unit FB2a Poubara sandstones in Moulendé quarry. (A) General view of the upper part of the section, with massive bedsets at the bottom, overlain by heterolithic beds, and sub-unit FB2b black shales at the top. Massive sandstone bed contacts featuring (B) stylolites and (C) ball and pillow structures. Pen for scale is 15 cm long. (D) Black shales stuffed between load casts within a massive sandstone bedset. Hammer for scale is 27 cm long. (E) Detail of the shale deformation.

quarry, apart from some HCS typically 0·2 to 0·3 m in wavelength, in the topmost bedset beneath the FB2b black shales (Fig. 17B).

The Gangolo quarry exhibits a 30 m thick succession of similar sandstones to those observed at Moulendé, organized in three tabular units, each about 10 m thick, and bounded by 0·2 to 1·0 m thick black shale intervals. As at Moulendé, the sandstone bed stacks are aggradational and composed of amalgamated beds in packages 0·5 to 3·0 m thick. The succession shows an overall fining-up and thinning-up trend (the upper unit being similar to the sheet-form bedsets with heterolithic bedset intervals as in Moulendé). The basal unit rests on black shales (probably the lower contact of FB2, as in the nearby LN12 core, see Fig. 8), showing numerous reverse faults with plastic deformation and brecciated zones injected by mud. Despite abundant dish structures, large-scale

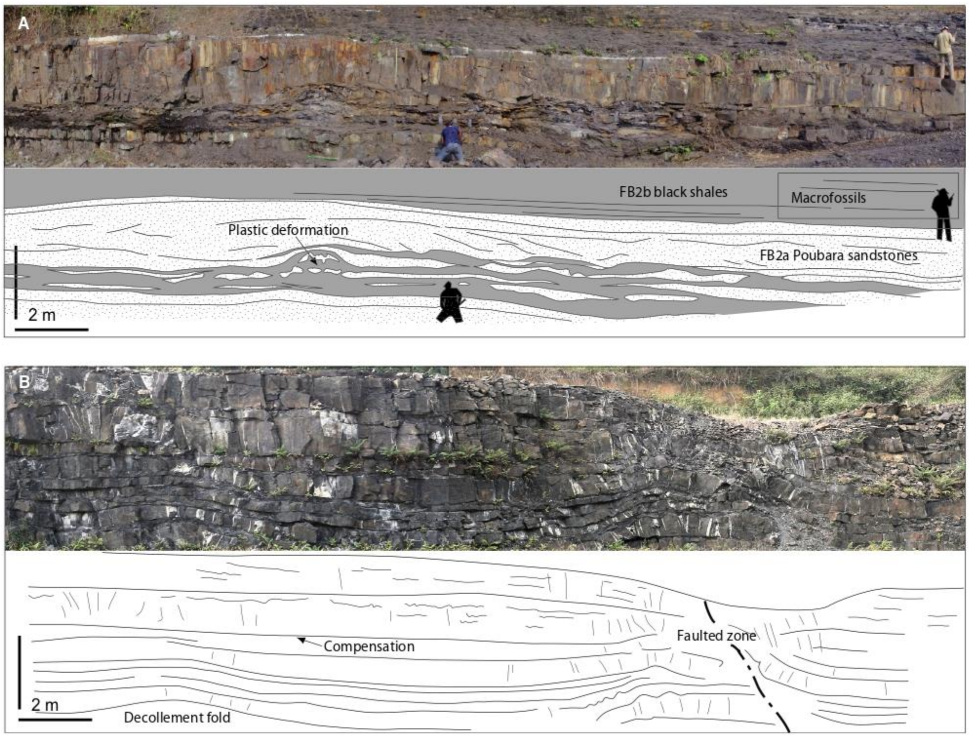

Fig. 15. Details of the bedding geometry of sub-unit FB2a Poubara sandstones in Moulendé quarry. (A) Large-scale plastic deformation at the bottom of the uppermost bedset. (B) Decollement, synsedimentary fold and fault at 10 m (see Fig. 10). The white strips correspond to tension gashes due to chemical compaction (Ndongo *et al.*, 2016).

hummocky formsets 5 to 10 m wide and up to 2 m high can be observed within the thickest sandy beds at several levels in the two lower units (Fig. 17A). The latter are buried by thick beds which are entirely traversed by dish structures, with rare floating black shale clasts up to 10 cm across. In addition, large-scale low-angle three-dimensional trough cross-bedding resembling swaley cross-stratification (SCS) or elongated but enclosed scour structures are common in the Gangolo quarry (Fig. 17E).

Two quarries in Mvengué show exposures of the Poubara sandstones (MvgA and MvgB in Fig. 4). The facies and bedding is similar to that in the Moulendé and Gangolo quarries. The Mvengué A quarry exhibits the upper 10 m of the sandstone succession observed in the nearby MVG cores, with numerous dish structures. Large-scale trough cross-bedding and hummocky bedforms similar to those in Gangolo are preserved in the MvgB section (Fig. 17C). In addition, the Mvengué B quarry exhibits a 15 m deep erosion surface probably corresponding to the south-east border of a large scour or channel wall (Fig. 17D). This surface is floored by a shale-pebble lag, and onlapped by tabular beds 0·5 to 1·0 m thick, similar to those below it and without any systematic upward trend. Locally, flute casts indicate a flow towards the north-east. Rare outcrops show conglomerates associated with the Poubara sandstones; these are mostly located in the western part of the basin.

The exposure in the Lékédi River corresponds to the upper section of the LN1 core (Fig. 8). Although poorly preserved due to weathering, the deposit shows significant differences

Fig. 16. Liquefaction or pseudo-liquefaction features in sub-unit FB2a Poubara sandstones in Moulendé quarry except (B) Gangolo and (C) Mvengué A. (A) to (C) Dish structures. Hammer head (10 cm long) and coin (2 cm diameter) for scale. (D) Floating mud clasts at the top of a massive sandstone bed (top view). (E) Liquefaction and extrusion of sand along a crack of a massive sandstone bed (top view). (F) Folded sandstone dyke at the FB2a/FB2b contact. (G) Top view of the uppermost sandstone bed below the black shales (convolute lamination). (H) In the same bed, planar lamination is preserved beneath the convolute laminae.

compared with the other studied sites (Fig. 18). These include the presence of subangular to sub-rounded, gravel-size clasts of quartz and other lithologies derived from Archean basement. The bedding is crude, forming 2 to 5 m thick bedsets locally bounded by sandstones showing subtle liquefaction (loads, flames and dishes; Fig. 18B and C). Internal stratification planes are locally highlighted by mud drapes. The outsized clasts floating within this facies are composed of: (i) black shales, ranging from sparse mud chips to folded, lift-up rafts several metres across; and (ii) pebble to boulder-sized sub-rounded blocks derived from the Archean basement (Fig. 18D). These fragments are randomly dispersed in the matrix, except in one bedset where boulders are concentrated at the top (Fig. 10). The bottom of the section (above FB1 black shales) shows the same kind of plastic deformation as before, with mud injection as

Fig. 17. Current-related structures in sub-unit FB2a Poubara sandstones. (A) Mega hummocky cross-stratification (HCS) (massive bedsets in the lower part of the section exposed in Gangolo quarry). (B) HCS (uppermost massive bedset in Moulendé quarry). (C) Flat-based and wavy-top bed in Mvengué B quarry. (D) Large-scale erosion surface in Mvengué B quarry (possibly a channel bank). (E) Trough cross-bedding interpreted as swaley cross-stratification (SCS) in Gangolo quarry (uppermost part of the section). Note the pervasive flames in the lower part of the outcrop. People (*ca* 1·8 m tall) and hammer (27 cm long) for scale.

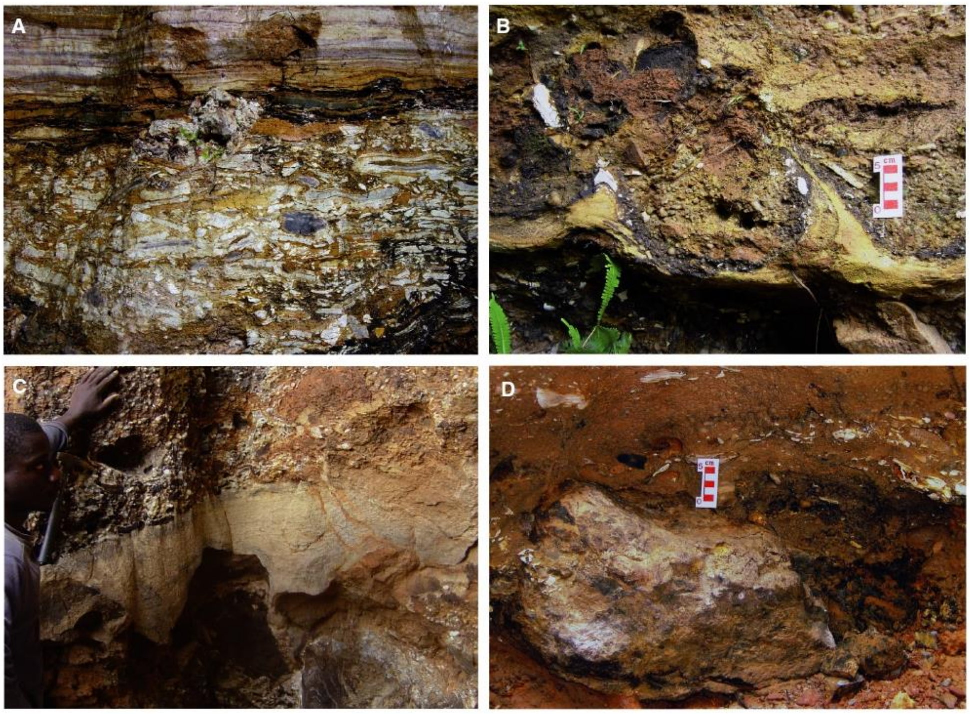

Fig. 18. Conglomeratic facies in sub-unit FB2a Poubara sandstones, Lékédi River section (see Figs. 4 and 10). (A) Mud debrite at the top of the unit. The breccia section is 60 cm thick. (B) Sand flames at the bottom of a gravelly litharenite with floating mud clasts. (C) Interstratified sandstone with dish structures. Hammer for scale is 27 cm long. (D) Boulder reworked from Unit FA. Note the floating mud chips in the gravelly litharenitic matrix.

at Gangolo. The upper part of the section exhibits an increase in black shale clasts, ending up with an almost pure debrite of black shale at the contact with the FB2b black shales (Fig. 18A).

Interpretation

The high matrix content of pyrite and organic matter in the Moulendé and Gangolo sandstones is typical of the Poubara sandstones described by Weber (1968). As for the black shales, sulphate reduction took place within the sediment and consumed organic matter. The very low amount (Quarry A) to near absence (Quarry B) of pyrite and organic matter in the Mvengué sandstones cannot be the result of weathering (oxidation) because the porosity was cemented early (Onanga-Mavotchi, 2016). The locally crenulated contacts are interpreted as stylolites, which is consistent with the quartz dissolution and overgrowth features in the pyrite-rich sandstones at Moulendé and Gangolo. The absence of such features in the Mvengué B sandstones suggests that alkalinity may have been less in this area closer to the border of the Unit FB sub-basin. The K-feldspar preserved in the Mvengué B quarry sandstones reflects a source in Archean granites or Unit FA sandstones, as well as potentially a syn-FB volcaniclastic source. This component would have been dissolved by the more alkaline waters at the other more distal sites. The proximality of Mvengué B compared to Moulendé is also supported by the north-eastward flow, as indicated by the flute casts and is also consistent with the already mentioned basinward thinning of the Poubara sandstones.

Following Parize *et al.* (2013), the Poubara sandstones in the Moulendé, Gangolo and Mvengué quarries are interpreted to have been deposited by sand-rich, concentrated density flows (Mulder & Alexander, 2001; Talling *et al.*, 2012a). The related deposits are referred to as high-density turbidites (Kuenen, 1951), sandy debris flows (Shanmugam, 1996), slurry flows (Lowe & Guy, 2000) or dense flows (Mutti *et al.*, 2003). Density flows can be formed from the concentration of sustained, hyperpycnal river flows, but also liquefaction and failure of submarine slopes (Nardin *et al.*, 1979; Talling *et al.*, 2012b). The related deposits resemble the S2 and S3 facies of the Lowe (1982) sequence or the F8 facies of Mutti (1992). The flows had no time to mix with ambient water and to evolve towards low-density turbidites before deposition of most of the sediment load, which may be why there is no grading between sandstones and the overlying black shales. The Mvengué B quarry includes a 15 m deep channel that was plugged aggradationally with little facies variation.

The grain-size homogeneity and general absence of lamination in the sandstone beds reflect the *en masse* freezing of the density flows (Baas, 2004), but might also be a consequence of the destructuration of the sediment through dewatering, as evidenced by the pervasive dish structures (Hurst & Cronin, 2001), the injectites and possibly sand volcanoes. The undulated top surface of structureless beds in Moulendé and Mvengué also might be a product of large-scale liquefaction (Stow & Johansson, 2000). Alternatively, the dish structures could be the result of upward migration and precipitation of silica exsolved during early diagenesis, consistent with the occurrence of stylolites at bed boundaries.

The internal irregular bed boundaries may correspond to scouring at the bottom of dense flows (e.g. Mutti, 1992). These scours sourced the rip-up black shale clasts. The formset preservation of the several metres large HCS indicates a relatively high instantaneous depositional rate, together with a strong near-bed oscillation of the flow. This is common in lower shoreface deposits, other evidence of which is lacking in the Poubara sandstones. The overall planar and aggradational bedding extending over tens of metres makes the interpretation of the large-scale HCS as shoreface bedforms unlikely. Basilici *et al.* (2012) describe large HCS as storm-induced bedforms in deeper shelf settings. Morsilli & Pomar (2012) reviewed the origin of HCS and showed that it can form in a wide range of settings, ranging from fluvial to deep water, and those authors suggested that large-scale HCS could be formed as the result of internal waves. In even deeper water, the related oscillation could be generated by Helmholtz waves formed at the top of density flows (Prave & Duke, 1990; Mulder *et al.*, 2009).

The scarcity of conglomerate beds in the Poubara sandstones suggests either that sediment was sorted upstream or that the source was mostly devoid of gravel-grade sediment. The Lékédi section, close to the western border of the basin, argues in favour of the former hypothesis. The matrix-supported fabric and the internal shear features in these beds are consistent with density flows. The topmost debrite in the Lékédi section may have been sourced from the wall of a submarine conduit for density flows, implying that the flow was entrenched into FB1 black shales.

Bacterial mats

Above the Poubara sandstones, at the base of the Djoumou shales which contain the macro-organisms discovered by El Albani *et al.* (2010; Fig. 19A), bacterial mats are present in the Moulendé quarry (Figs 10 and 19). Raman analyses confirm their carbon-rich composition, as compared to the enclosing facies (Aubineau, 2016). Dome-like features or vertical bump-like structures (Simpson *et al.*, 2013, cf. fig. 12) are found at the top of the sandstone beds embedded in the black shales (Fig. 19B), as well as microripples interpreted as *Kinneyia* structures (Hagadorn & Bottjer, 1997, 1999) (Fig. 19C). The top surface of the thickest sandstone beds interstratified in the black shales or within the underlying Poubara sandstones also exhibits 'elephant skin' textures (Runnegar & Fedonkin, 1992) with locally honeycomb networks (Fig. 19D). Reticulate surfaces are restricted to the shallowest parts of the marine basins (Bose & Chafetz, 2009; Noffke *et al.*, 2013; Banerjee *et al.*, 2014), and this may be caused by phototactic responses of cyanobacteria growth (Gerdes *et al.*, 2000). Motile filaments may promote gliding and tangling of the mat (Shepard & Sumner, 2010). Importantly, tuft filamentous structures similar to those formed by cyanobacteria in modern environments (Gerdes *et al.*, 2000; and Gerdes, 2007; Bose & Chafetz, 2009; Taj *et al.*, 2014; Sumner *et al.*, 2016) are found either

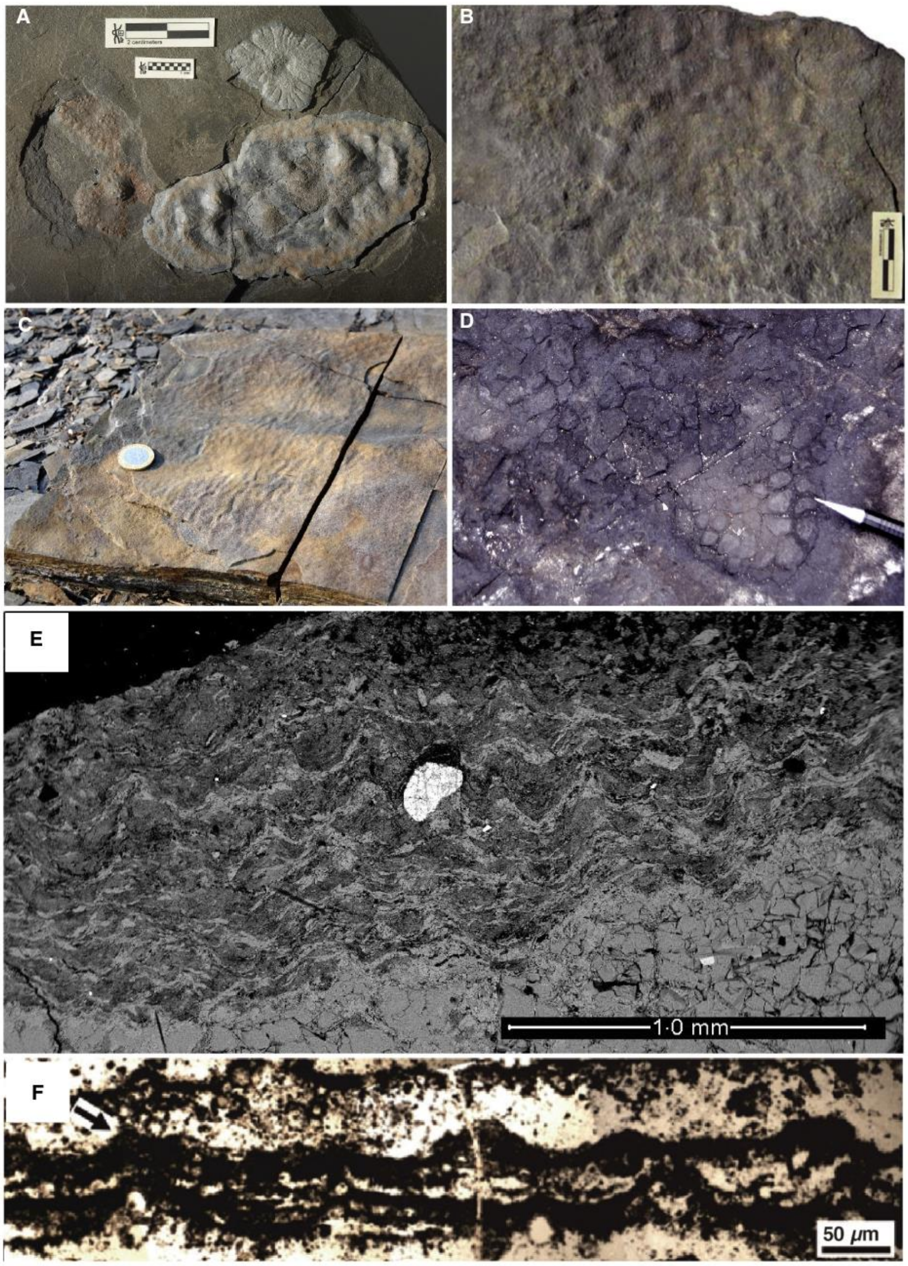
A
B
C
D
E
1·0 mm
F
50 μm

within the mat (Fig. 19E) or at the ridge junctions of the elephant skin textures or reticulate patterns. These tuft structures are thought to by typical of cyanobacteria in the Archean rock record, where they are often associated with evaporitic tidal flat settings (Fig. 19F; Flannery & Walter, 2012; Noffke *et al.*, 2013; Homann *et al.*, 2015).

So far, modern occurrences of tufts and tuft-related structures have been assigned to oxygen-producing photosynthetic bacteria (Walter *et al.*, 1972; Bosak *et al.*, 2009, 2012; Reyes *et al.*, 2013; Jungblut *et al.*, 2016; Sumner *et al.*, 2016). In the Francevillian mats, some void clusters could be related to photosynthetic, degassing structures similar to those illustrated by Eriksson *et al.* (2007a). A shallow-marine setting is most likely, given the setting of modern examples of tufted cyanobacterial mats, although continental examples are known, ranging from hot springs (e.g. Walter *et al.*, 1972) to subglacial lakes (e.g. Jungblut *et al.*, 2016). The common point is that cyanobacteria forming tuft-related structures are always found in the upper part of the oxic zone where light irradiance is highest. Reticulate patterns and putative tuft-like structures have been recognized in filamentous sulphur-oxidizing bacteria (Flood *et al.*, 2014), which can be present in the deep sea. However, owing to genomic comparisons, these phenotypic features are caused by horizontal gene transfers with cyanobacteria (Flood *et al.*, 2014). In the Archean and Palaeoproterozoic, it is therefore likely that only cyanobacteria could generate tufted mats.

Evidence for bacterial activity has already been identified in the FB and FC deposits by Azziley-Azzibrouck (1986), Cortial *et al.* (1990) and Dubois *et al.* (2015). The identification, for the first time, of cyanobacterial tuft structures in FB2 suggests a shallow water depth. However, no roll-up or desiccation structures have been found, indicative of emergence (Schieber, 1999; Eriksson *et al.*, 2007b, figs. 4c and 14 to 19; Simpson *et al.*, 2013). The maximum depth of development of cyanobacteria photosynthesis would be around 80 m (Kuwahara *et al.*, 2000). Because clear waters were probably rare in the mud-rich setting of the FB Basin, the depth of formation of the cyanobacterial mats was probably shallower than this limit. The intimate interlamination of these mats and the macrofossils excludes that the latter could be emplaced below storm-wave base, as suggested by Parize *et al.* (2013). The macrofossils are probably part of the same benthic ecological system as the bacterial mats and would therefore have lived close to the shoreline.

DISCUSSION

The facies and sub-unit stratigraphic correlation linking subsurface and outcrop suggests subdivision of Unit FB into two main sequences (Fig. 3). The lower one (S1) is dominated by submarine slope deposits infilling the subsiding FB sub-basins and is capped by a maximum regression surface (marked by stromatolites) with evidence for emergence on topographic highs. The upper sequence (S2) comprises a transgressive tract dominated by iron-rich dolomites and black shales, and a regressive tract marked by the return of interstratified sandstone beds. The Poubara sandstones are interpreted as a forced regressive, lowstand tract. The Djoumou shales would belong to the same lowstand tract, possibly amalgamated with a transgressive tract; they are capped by the FC unconformity, which is the sequence boundary terminating the FB Basin.

With the exception of the submergent sabkha environments, all of the marine deposits were formed by density flows. In FB1b, the interfingering of the banded heterolithics and black shales shows, as first suggested by Parize *et al.* (2013), that the almost rhythmic flow events in the two facies probably have a common origin and that the black shales would record the distal fringe of these events. The rhythmicity in the banded heterolithics may be the expression of autocyclic flow transformations, as in hybrid beds (Haughton *et al.*, 2009). This observation

Fig. 19. Some fossils from Moulendé quarry (see Fig. 13 for location in the section). (A) Specimen of macro-organisms similar to those described by El Albani *et al.* (2010). Random microbial domes (B) and *Kinneyia* (C) at the top of sand stringers of sub-unit FB2b black shales. Note the ripples in (C). Coin for scale is 2 cm in diameter. (D) Elephant skin textures with honeycomb networks (main tile of the quarry, see Fig. 10). Pen tip for scale is 2 cm long. (E) Scanning electron microscope (SEM) image of filamentous tuft structures preserved at the bottom of the mat with elephant skin texture shown in (D). (F) For comparison with (E), tufted biolaminae of the 3·48 Ga Dresser Formation, Pilbara, Australia (Noffke *et al.*, 2013).

supports the interpretation of the banded heterolithics as a submarine slope fan dominated by dense gravity flows (Azziley-Azzibrouck, 1986). The Poubara sandstones are also interstratified with the black shales but their previous interpretation has entailed a range of settings, and these are now considered in more detail in the light of the new observations presented above.

Previous interpretations

Most early interpretations favoured a shallow water to shelf setting for both the black shales and the Poubara sandstones. Azziley-Azzibrouck (1986) assigned the FB1c black shales to a lagoonal setting and the Poubara sandstones to storm ridges or coastal barriers orientated parallel to the basin margin (Fig. 7). However, the geological map shown in Fig. 4 shows that the ridges illustrated in Fig. 7 are parallel to the trace of the hinges of the Mvengué and Yéyé synclines, suggesting that Azziley-Azzibrouck (1986) may not have taken into account these folds when reconstructing the palaeogeography. The ridges may be outcrops of the same laterally extensive sub-unit repeated by folding. In addition, a sand ridge interpretation is inconsistent with the absence of pervasive cross-stratification and the lack of the typical large-scale lateral accretion structures expected for such bodies in storm-dominated or tide-dominated shelves (Swift *et al.*, 1991; Suter, 2006; Reynaud & Dalrymple, 2012). A shallow water interpretation was also proposed for the black shales by Ossa-Ossa (2010) who regarded the rippled sand stringers and the millimetric sand/silt/shale packages as lenticular and flaser bedding that are common in intertidal mud flats or mixed flats. However, there is no evidence, neither in the cores nor any of the outcrops, for other diagnostic criteria of tidal flat deposition (mud couplets, tidal cyclicity, bidirectionality and asymmetry of currents) or emersion (mud cracks). The only shallow-marine facies found is the dolomitic stromatolites and breccias beneath the sequence boundaries. Pambo (2004) interpreted the Poubara sandstone as storm-dominated deposits based on the presence of HCS, erosional scours and gutter casts. However, although HCS is classically associated with the lower shoreface, it has also been found in deep sea turbidites (Mulder *et al.*, 2009) and is only indicative of a strong near-bed water oscillation.

In contrast, all of the features of the Poubara sandstones and interstratified black shales are common in turbidites. This interpretation was followed by Bouton *et al.* (2009) and Parize *et al.* (2013) who attributed the Poubara sandstones to turbiditic lobes in deep water. Parize *et al.* (2013) provided a facies model for the Poubara sandstones in which there is a range of proximal, high-density turbidites with erosional bases or traction carpets (their PF3 and PF4, corresponding to the Poubara sandstones) to distal deposits, thinner and gradually more conformable and interbedded with the black shales (PF2 to PF1). Because of the absence of complete 'Bouma turbidites' (i.e. grading upward to the black shale), Parize *et al.* (2013) inferred repeated bypass of sand at the top of the Poubara sandstone beds, the finer sand and silt fraction being deposited as lower-density turbidites in more distal areas of the basin, following the classic Mutti (1992) model. However, no clear evidence of erosion or traction carpets was found at the top of the sandstone beds, which could be interpreted as bypass surfaces. Instead, the top of sandstone beds, where preserved from dewatering, might be abandonment surfaces mantled by bacterial mats.

Shallow water density flows

Reconciling the diverse past interpretations of the Unit FB deposits is critical to better understanding the macrobiota and its early Archean habitat. Following Bouton *et al.* (2009) and Parize *et al.* (2013), it seems reasonable that the FB2 Poubara sandstones and black shales were deposited in the same general setting because they are interstratified; as they both contain cyanobacterial mats, this favours a shallow water setting. This is also consistent with the presence of the linguoid and interference ripples at the level where the macrofossils and the cyanobacterial mats were found in Moulendé quarry (Fig. 10). These small bedforms are common on (although are not restricted to) intertidal flats. In a recent review of lamination in shelf mudstones, Schieber (2016) indicated that hyperpycnal flows could produce silt laminae of the kind found in the FB black shales. It is therefore possible that the coarser fraction in the black shales has not bypassed up-dip Poubara sandstone beds. Furthermore, repeated bypass may be more difficult in shallow waters where turbulent flows cannot expand vertically.

The presence of the cyanobacteria implies that water depths were <80 m, and significantly less than the >200 m proposed by Parize *et al.* (2013), based on the absence of wave-related features or storm beds in the Poubara sandstones. In such shallow waters, the absence of wave deposits in the Poubara sandstones could be explained by the relative isolation of the Franceville Basin on account of the fault-controlled setting. Prior to the development of the fault-controlled sub-basins, coastal to shelf facies with the influence of tides and waves are well-expressed in the FB1a green shales. Subsequently, connections with the open ocean may have been limited by the presence of tectonic sills, and the waves and tides could have been damped seaward of the areas of FB1c–FB2 deposition. In addition, the presence of a standing fluid mud layer may have damped currents at the sea bed (see Introduction in Winterwerp *et al.*, 2012). The aggradational high-density turbidites were thus emplaced in a confined, shallow water enclosed basin (Stow & Johansson, 2000). The water depth was probably deeper but still shelfal during transgressions associated with the two sequences, promoting anoxia in FB1c, and allowing regression (in the absence of significant fault activity) to drive emergence by the end of sequences. The stromatolites of Unit FC, however, cannot be confidently associated with the regression that is recorded by the second sequence of the FB Basin, because the FB/FC unconformity truncates all deposits below FC. However, the stromatolites at the FB1b/c boundary, by contrast, confidently indicate that emersion was achieved by the end of regression above the FB1b deposits, including the black shales. In Okouma cores (Fig. 5E), dolomitic stromatolites at this sequence boundary share many similarities with cyanobacterial microbialites typical of lagoonal environments, locally evaporitic (Trichet *et al.*, 2001; Noffke *et al.*, 2003; Oliveri *et al.*, 2009). Considering their lateral passing to black shales in the basin, a coastal to shelf setting for all of Unit FB is likely.

The density flows may have been sourced by river floods or mass wasting of delta fronts (cf. Stow & Johansson, 2000; Mutti *et al.*, 2003). In the absence of soil on land, Precambrian fluvial systems were mostly unconfined streams forming sheetflood sands and therefore not very efficient at sorting sediment (Davies & Gibling, 2010). This contrasts with the homogenous grain size of the Poubara sandstones throughout the basin. Sorting may have been achieved during transport by turbidity currents (e.g. Smith, 2004) but if water depths were shallow, transport distances are likely to have been relatively short. The sand supplied to the density flows could have been reworked from an already well-sorted stock and in this case the depositional setting can be shallow. Parize *et al.* (2007) suggested that the source of the Albian sands of the Vocontian Basin, south-east France, should have been initially sorted and accumulated by waves close to the shelf edge before being dispersed to deeper water. In the Francevillian example, a more likely and widespread stock could have been aeolian sands. Aeolian sediments were likely to be present in the continental areas surrounding the FB Basin (sourced by large exposures of FA sandstones). The 300 μm grain size of the Poubara sandstones is compatible with an aeolian origin. Similar reworking of aeolian dunes in a coastal setting has been linked to the deposition of structureless sands in shallow-marine areas of the Jurassic Western Interior Basin of North America (Eschner & Kocurek, 1986).

Environmental controls on the biota

Whereas bacteriomorphous structures are recognized in FB1c (Dubois, 2017), the biota diversity is higher in FB2 in Moulendé quarry where cyanobacteria and macro-organisms are found within the same depositional setting. This is consistent with a change to less anoxic conditions from FB1c to FB2 (Canfield *et al.*, 2013) which, in turn, is consistent with a decrease in water depth. The geochronological data imply that Unit FB coincided with the Lomagundi Event (Schidlowski *et al.*, 1976; Melezhik *et al.*, 2007), the first stage of high production and burial of organic carbon in the ocean (Bekker & Holland, 2012) following the rise of cyanobacteria and start of photosynthetic release of free oxygen in the shallow ocean (Kirschvink & Kopp, 2008). However, the position of the chemocline is uncertain. It is possible that only the surface waters were oxygenated and the rest of the water column was anoxic during FB1c (Ngombi-Pemba, 2014; Canfield *et al.*, 2013). Thus, the basin-scale, forced regression that led to deposition of the Poubara sandstones would have exposed large areas of the sea floor to oxic conditions. Also, the sea-level fall may have permitted light to reach the sea bed, promoting cyanobacteria blooms and that drove local oxygen production. These combined changes would have generated favourable conditions for the development of macro-organisms. The density flows could also have delivered additional oxygen and the nutrients necessary to fuel the ecosystem.

The delicate, sub-millimetre bacterial mats preserved at the top of the Poubara sandstone beds in Moulendé quarry suggest that, although the deposition rate was high during the flow events, energy remained low the rest of the time. The mats were rapidly buried by episodic deposition marine snow, forcing the bacteria-based benthic ecosystem to continually re-establish itself. This pulsed sedimentary regime stressed the ecosystem and may have been important from an evolutionary perspective. Aller *et al.* (2010) note that hydrodynamic reworking of muds in deltas and estuaries are efficient biogeochemical reactors with cycling of redox conditions and stages of cell metabolic processes. This reworking mixes contrasting genetic materials, promoting lateral gene transfer and related evolution jumps. This could apply to the evolution of the 2·1 Ga Franceville macrofossils as well. The regressive context with semi-isolated sub-basins may also have favoured endemism and therefore boosted selection.

CONCLUSIONS

A re-analysis of existing data together with new map, core and outcrop observations of the Francevillian Basin provides new insight into the depositional setting of Unit FB from which 2·1 Ga macrofossils have been recently recovered.

The Franceville FB Basin records two main depositional sequences, capped by emergent facies with stromatolites. The first sequence infills actively subsiding, fault-bounded sub-basins and is dominated by gravity-driven slope deposits that interfinger with black shales (FB1b). The second sequence records a decline in fault activity and a transgression followed by anoxia (FB1c: iron-rich transgressive systems tract and high total organic carbon black shales in the high-stand systems tract). A subsequent forced regressive system tract shows a return to suboxic conditions (FB2 and includes the Poubara sandstones). The macrofossils have been found in this sequence close to the maximum regressive surface within a section of the FB2b Djoumou shales located between two large bodies of FB2a Poubara sandstone. The top FB sequence boundary is a subaerial unconformity overlain by silicified stromatolithic breccias (FC).

The Poubara sandstones are composed of high-density sediment gravity flow deposits, forming largely structureless to dewatered beds interstratified with black shales. The black shales correspond with fluid muds formed at the bottom of nepheloid layers. Large-scale hummocky cross-stratification (HCS) is found locally in the Poubara sandstones and is possibly linked to near-bed flow transformation rather than surface wave oscillations. The absence of true storm beds in the Poubara sandstones suggests a sheltered setting, favoured by the configuration of the FB fault-bounded sub-basins. The upper surface of the Poubara sandstone beneath the Djoumou shales hosting the macrofossils is covered by bacterial mats with tuft structures indicative of cyanobacteria; this indicates water depths of <80 m and a shelfal setting.

The biota probably evolved in the last fluid mud ‘pool’ of the FB Basin, just before its emergence. A fall in relative sea-level increased light availability and triggered the cyanobacteria-based ecosystem. Density flows may have introduced nutrients and possibly additional oxygen that were required for larger, multicellular organisms to grow.

ACKNOWLEDGEMENTS

This work was funded by the following partners in Gabon: National Center for Scientific Research of Gabon (CENAREST); Ministry of Education, Research and Culture; Ministry of Mines, Oil, Energy and Hydraulic Resources; General Direction of Mines and Geology; Sylvia Bongo Foundation; National Parks Agency; COMILOG-Company, French Embassy at Libreville, and French Institute of Gabon, French Ministry of Foreign Affairs. For information and scientific discussion, we thank L. White, F. Idiata, P. Mouguiama, F. Pambo and N. Tribovillard. For assistance, we acknowledge C. Laforest, Ph. Recourt and L. White. In France, we acknowledge the French CNRS-INSU, FEDER Poitou-Charentes, the University of Poitiers and the Région Poitou-Charentes for financial support. The authors warmly thank Nigel Mountney and Peter Haughton for their help in writing and improving the successive manuscripts, and an anonymous reviewer for his or her constructive comments. They also thank

Elaine Richardson for her careful final editing of the text.

REFERENCES

Aller, J.Y., **Aller, R.C.**, **Kempf, P.F.**, **Chistoserdov, A.Y.** and **Madrid, V.M.** (2010) Fluidized muds: a novel setting for the generation of biosphere diversity through geologic time. *Geobiology*, **8**, 169–178.

Amard, B. and **Bertrand-Sarfati, J.** (1997) Microfossils in 2000 Ma old cherty stromatolites of the Franceville Group, Gabon. *Precambrian Res.*, **81**, 197–221.

Aubineau, J. (2016) The structural diversity of 2.1 Ga-old microbial mats and their environmental interpretation from the Francevillian series (Gabon). Unpublished MSc memoir, University of Lille, 63 pp.

Azziley-Azzibrouck, G. (1986) Sédimentologie et géochimie du Francevillien B (Protérozoïque inférieur), métallogénie des gisements de manganèse de Moanda. Unpublished PhD, ULP, Strasbourg, 210 pp.

Baas, J.H. (2004) Conditions for formation of massive turbiditic sandstones by primary depositional processes. *Sed. Geol.*, **166**, 293–310.

Baas, J.H., **Best, J.L.**, **Peakall, J.** and **Wang, M.** (2009) A phase diagram for turbulent, transitional, and laminar clay suspension flows. *J. Sed. Res.*, **79**, 162–183.

Baas, J.H., **Best, J.L.** and **Peakall, J.** (2011) Depositional processes, bedform development and hybrid bed formation in rapidly decelerated cohesive (mud-sand) sediment flows. *Sedimentology*, **58**, 1953–1987.

Baas, J.H., **Manica, R.**, **Puhl, E.**, **Verhagen, I.** and **Borges, A.O.** (2014) Processes and products of turbidity currents entering soft muddy substrates. *Geology*, **42**, 371–374.

Banerjee, S., **Sarkar, S.**, **Eriksson, P.G.** and **Hu, X.F.** (2014) Palaeoenvironmental and biostratigraphic implications of microbial mat-related structures: examples from the modern Gulf of Cambay and the Precambrian. *J. Paleogeogr.*, **3**, 127–144.

Bankole, O.M., **El Albani, A.**, **Meunier, A.** and **Gauthier-Lafaye, F.** (2015) Textural and paleo-fluid flow control on diagenesis in the Paleoproterozoic Franceville Basin, South Eastern, Gabon. *Precambrian Res.*, **268**, 115–134.

Basilici, G., **de Luca, P.H.V.** and **Poiré, D.G.** (2012) Hummocky cross-stratification-like structures and combined-flow ripples in the Punta Negra Formation (Lower-Middle Devonian, Argentine Precordillera): a turbiditic deep-water or storm-dominated prodelta inner-shelf system? *Sed. Geol.*, **267–268**, 73–92.

Baud, L. (1954) Carte géologique de reconnaissance à l'échelle du 1/500 000: Franceville-Est, SA33 NO E-12. Gouvernement général de l'Afrique équatoriale française, Carte géologique de reconnaissance de l'Afrique équatoriale française. 34 pp.

Bekker, A. and **Holland, H.D.** (2012) Oxygen overshoot and recovery during the early Paleoproterozoic. *Earth Planet. Sci. Lett.*, **317–318**, 95–304.

Bertrand-Sarfati, J. and **Potin, B.** (1994) Microfossiliferous cherty stromatolites in the 2000 Ma Franceville Group, Gabon. *Precambrian Res.*, **65**, 341–356.

Bonhomme, M.G., **Gauthier-Lafaye, F.** and **Weber, F.** (1982) An example of lower proterozoic sediments: the Francevillian in Gabon. *Precambrian Res.*, **18**, 87–102.

Bosak, T., **Liang, B.**, **Sim, M.S.** and **Petroff, A.P.** (2009) Morphological record of oxygenic photosynthesis in conical stromatolites. *PNAS*, **106**, 10939–10943.

Bosak, T., **Liang, B.**, **Wu, T.D.**, **Templer, S.P.**, **Evans, A.**, **Vali, H.**, **Guerquin-Kern, J.-L.**, **Klepac-Ceraj, V.**, **Sim, M.S.** and **Mui, J.** (2012) Cyanobacterial diversity and activity in modern conical microbialites. *Geobiology*, **10**, 384–401.

Bose, S. and **Chafetz, H.S.** (2009) Topographic control on distribution of modern microbially induced sedimentary structures (MISS): a case study from Texas coast. *Sed. Geol.*, **213**, 136–149.

Bouton, P., **Thiéblemont, D.**, **Gouin, J.**, **Cocherie, A.**, **Guerrot, C.**, **Tegyey, M.**, **Préat, A.**, **Simo Ndounze, S.** and **Moussavou, M.** (2009) Notice explicative de la Carte géologique de la République du Gabon à 1/200 000, feuille Franceville-Boumango. Editions DGMC – Ministère des Mines, du Pétrole, des Hydrocarbures, Libreville, 79 pp.

Bros, R., **Stille, P.**, **Gauthier-Lafaye, F.**, **Weber, F.** and **Clauer, N.** (1992) Sm-Nd isotopic dating of Proterozoic clay material; an example from the Francevillian sedimentary series, Gabon. *Earth Planet. Sci. Lett.*, **113**, 207–218.

Canfield, D.E., **Ngombi-Pemba, L.**, **Hammarlund, E.U.**, **Bengtson, S.**, **Chaussidon, M.**, **Gauthier-Lafaye, F.**, **Meunier, A.**, **Riboulleau, A.**, **Rollion-Bard, C.**, **Rouxel, O.**, **Asael, D.**, **Pierson-Wickmann, A.-C.** and **El Albani, A.** (2013) Oxygen dynamics in the aftermath of the Great Oxidation of Earth's atmosphere. *PNAS*, **110**, 16736–16741.

Cortial, F., **Gauthier-Lafaye, F.**, **Oberlin, A.**, **Lacrampe-Couloume, G.** and **Weber, F.** (1990) Characterization of organic matter associated with uranium deposits in the Francevillian Formation of Gabon (Lower Proterozoic). *Organ. Geochem.*, **15**, 73–85.

Davies, N.S. and **Gibling, M.R.** (2010) Cambrian to Devonian evolution of alluvial systems: the sedimentological impact of the earliest land plants. *Earth-Sci. Rev.*, **98**, 171–200.

Deynoux, M. and **Duringer, P.** (1992) Etude sédimentologique du gisement d'uranium d'Oklo - Okelobondo. Protérozoïque inférieur du bassin de Franceville, Gabon. Rapport interne, CGS-ULP, 35 pp.

Donot, M. and **Weber, F.** (1968a) Carte géologique de reconnaissance au 1/500.000, feuille Franceville-Est avec notice explicative. Première édition. Ministère des Mines du Gabon et BRGM, 43 pp.

Donot, M. and **Weber, F.** (1968b) Carte géologique de reconnaissance au 1/500.000, feuille Franceville-Ouest avec notice explicative. Première édition. Ministère des Mines du Gabon et BRGM, 55 pp.

Dubois, M. (2017) Environnement de dépôt et processus de formation des carbonates de manganèse dans les black shales paléoprotérozoïques du bassin de Franceville (2,1 Ga); Gabon. Unpublished PhD thesis, University of Montpellier, 332 pp.

Dubois, M., **Lopez, M.**, **Orberger, B.**, **Rodriguez, C.**, **Boussafir, M.**, **Dreux, G.**, **Rodrigues, S.** and **Pambo, F.** (2015) The Mn-Carbonate Rich Black Shales of the Bangombe Plateau, Francevillian Basin, Gabon. In: *Mineral Resources in a Sustainable World* (Eds A.S. André-Mayer, M. Cathelineau, Ph. Muchez, E. Pirard and S. Sindern), Proceedings of the 13th Biennial SGA Meeting, 24–27 August 2015, Nancy, France, p.p. 1905–1908.

El Albani, A., **Bengton, S.**, **Canfield, D.E.**, **Bekker, A.**, **Miacchiarelli, R.**, **Mazurier, A.**, **Hammarlund, E.U.**, **Boulvais, P.**, **Dupuy, J.J.**, **Fontaine, C.**, **Fürsi, F.T.**, **Gauther-Lafaye, F.**, **Janvier, P.**, **Javaux, E.**, **Ossa-Ossa, F.**, **Pierson-**

Wickmann, A.C., **Riboulleau, A.**, **Sardini, P.**, **Vachard, D.**, **Whitehouse, M.** and **Meunier, A.** (2010) Large colonial organisms with coordinated growth in oxygenated environments 2.1 billion years ago. *Nature*, **466**, 100–104.

El Albani, A., **Bengtson, S.**, **Canfield, D.E.**, **Riboulleau, A.**, **Rollion Bard, C.**, **Macchiarelli, R.**, **Ngombi Pemba, L.**, **Hammarlund, E.**, **Meunier, A.**, **Moubiya Mouele, I.**, **Benzerara, K.**, **Bernard, S.**, **Boulvais, P.**, **Chaussidon, M.**, **Cesari, C.**, **Fontaine, C.**, **Chi-Fru, E.**, **Garcia Ruiz, J.-M.**, **Gauthier-Lafaye, F.**, **Mazurier, A.**, **Pierson-Wickmann, A.-C.**, **Rouxel, O.**, **Trentesaux, A.**, **Vecoli, M.**, **Versteegh, G.**, **White, L.**, **Whitehouse, M.** and **Bekker, A.** (2014) The 2.1 Ga old francevillian biota biogenicity, taphonomy and biodiversity. *PLoS ONE*, **9**, e99438.

El Albani, A., **Macchiarelli, R.** and **Meunier, A.** (2016) *Aux origines de la vie: Une nouvelle histoire de l'évolution.* Dunod, Paris, 217 pp.

Eriksson, P.G., **Schieber, J.**, **Bouougri, E.**, **Gerdes, G.**, **Porada, H.**, **Banerjee, S.**, **Bose, P.K.** and **Sarkar, S.** (2007a) Classification of structures left by microbial mats in their host sediments. In: *Atlas of Microbial mat Features Preserved Within the Clastic Rock Record* (Eds J. Schieber, P.K. Bose, P.G. Eriksson, S. Banerjee, S. Sarkar, W. Altermann and O. Catuneanu), pp. 39–52. Atlas in Geosciences 2. Elsevier, Amsterdam.

Eriksson, P.G., **Porada, H.**, **Banerjee, S.**, **Bouougri, E.**, **Sarkar, S.** and **Bumby, A.J.** (2007b) Mat-destruction features. In: *Atlas of Microbial mat Features Preserved Within the Clastic Rock Record* (Eds J. Schieber, P.K. Bose, P.G. Eriksson, S. Banerjee, S. Sarkar, W. Altermann and O. Catuneanu), pp. 76–105. Elsevier, Amsterdam.

Eschner, T. and **Kocurek, G.** (1986) Marine destruction of eolian sand seas: origin of mass flows (Entrada, Utah). *J. Sed. Petrol.*, **56**, 401–411.

Feybesse, J.-L., **Johan, V.**, **Triboulet, C.**, **Guerrot, C.**, **Mayaga-Mikolo, F.**, **Bouchot, V.** and **Eko Ndong, J.** (1998) The West Central African belt: a model of 2.5–2.0 Ga accretion and two-phase orogenic evolution. *Precambrian Res.*, **87**, 161–216.

Flannery, D.T. and **Walter, M.R.** (2012) Archean tufted microbial mats and the Great Oxidation Event: new insights into an ancient problem. *Aust. J. Earth Sci.*, **59**, 1–11.

Flood, B.E., **Bailey, J.V.** and **Biddle, J.F.** (2014) Horizontal gene transfer and the rock record: comparative genomics of phylogenetically distant bacteria that induce wrinkle structure formation in modern sediments. *Geobiology*, **12**, 119–132.

Gauthier-Lafaye, F. (1986) Les gisements d'uranium du Gabon et les réacteurs d'Oklo : modèle métallogénique de gîtes à fortes teneurs du Protérozoïque inférieur. Sciences Géologiques, Strasbourg, Mémoire 78, 206 pp.

Gauthier-Lafaye, F. and **Weber, F.** (2003) Natural nuclear fission reactors: time constraints for occurrence, and their relation to uranium and manganese deposits and to the evolution of the atmosphere. *Precambrian Res.*, **120**, 81–100.

Gerdes, G. (2007) Structures left by modern microbial mats in their host sediments. In: *Atlas of Microbial mat Features Preserved within the Clastic Rock Record* (Eds J. Schieber, P.K. Bose, P.G. Eriksson, S. Banerjee, S. Sarkar, W. Altermann and O. Catuneanu), pp. 5–38. Elsevier, Amsterdam.

Gerdes, G., **Klenke, T.** and **Noffke, N.** (2000) Microbial signatures in peritidal siliciclastic sediments: a catalogue. *Sedimentology*, **47**, 279–308.

Ghadeer, S.G. and **Macquaker, J.H.S.** (2011) Sediment transport processes in an ancient mud-dominated succession: a comparison of processes operating in marine offshore settings and anoxic basinal environments. *J. Geol. Soc. London*, **168**, 1121–1132.

Hagadorn, J.W. and **Bottjer, D.J.** (1997) Wrinkle structures: microbially mediated sedimentary structures common in subtidal siliciclastic settings at the Proterozoic – Phanerozoic transition. *Geology*, **25**, 1047–1050.

Hagadorn, J.W. and **Bottjer, D.J.** (1999) Restriction of a late Neoproterozoic biotope; suspect-microbial structures and trace fossils at the Vendian-Cambrian transition. *Palaios*, **14**, 73–85.

Hale, R.P. and **Ogston, A.S.** (2015) In situ observations of wave-supported fluid-mud generation and deposition on an active continental margin. *J. Geophys. Res. Earth Surface*, **120**, 2357–2373.

Haubensack, C. (1981) Environnement des grès protérozoïques et des indices uranifères du secteur Kiéné dans le bassin de Franceville (République gabonaise): aspects sédimentologiques et géochimiques. Unpublished PhD thesis. Univ. Strasbourg, 105 pp.

Haughton, P., **Davis, C.**, **McCaffrey, W.** and **Barker, S.** (2009) Hybrid sediment gravity flow deposits – Classification, origin and significance. *Mar. Petrol. Geol.*, **26**, 1900–1918.

Hill, P.S. (1990) The potential role of large, fast-sinking particles in clearing nepheloid layers. *Philos. Trans. R. Soc. Lond. Ser. A*, **331**, 103–117.

Holland, H.D. (1994) Early Proterozoic atmospheric change. In: *Early Life on Earth*(Ed. S. Bengston), pp. 237–244. Columbia Univ Press, New York.

Holland, H.D. (2006) The oxygenation of the atmosphere and oceans. *Philos. Trans. R. Soc. Lond., Ser. B*, **361**, 903–915.

Homann, M., **Heubeck, C.**, **Airo, A.** and **Tice, M.M.** (2015) Morphological adaptations of 3.22 Ga-old tufted microbial mats to Archean coastal habitats (Moodies Group, Barberton Greenstone Belt, South Africa). *Precambrian Res.*, **266**, 47–64.

Hurst, A. and **Cronin, B.T.** (2001) The origin of consolidation laminae and dish structures in some deep-water sandstones. *J. Sed. Res.*, **71**, 136–143.

Jungblut, A.D., **Hawes, I.**, **Mackey, T.J.**, **Krusor, M.**, **Doran, P.T.**, **Sumner, D.Y.**, **Eisen, J.A.**, **Hillman, C.** and **Goroncy, A.** (2016) Microbial Mat Communities along an Oxygen Gradient in a Perennially Ice-Covered Antarctic Lake. *Appl. Environ. Microbiol.*, **82**, 620–630.

Karhu, J.A. and **Holland, H.D.** (1996) Carbon isotopes and the rise of atmospheric oxygen. *Geology*, **24**, 867–870.

Kineke, G.C. and **Sternberg, R.W.** (1995) Distribution of fluid muds on the Amazon continental shelf. *Mar. Geol.*, **125**, 193–233.

Kirschvink, J.L. and **Kopp, R.E.** (2008) Palaeoproterozoic ice houses and the evolution of oxygen-mediating enzymes: the case for a late origin of photosystem II. *Philos. Trans. R. Soc. Lond., Ser. B*, **363**, 2755–2765.

Kuenen, P.H. (1951) Properties of turbidity currents of high density. *SEPM Spec. Publ.*, **2**, 14–33.

Kuwahara, V.S., **Toda, T.**, **Hamasaki, K.**, **Kikuchi, T.** and **Taguchi, S.** (2000) Variability in the relative penetration of ultraviolet radiation to photosynthetically available radiation in temperate coastal waters, Japan. *J. Oceanogr.*, **56**, 399–408.

Lowe, D.R. (1982) Sediment gravity flows; II, Depositional models with special reference to the deposits of high-density turbidity currents. *J. Sed. Res.*, **52**, 279–297.

Lowe, D.R. and **Guy, M.** (2000) Slurry-flow deposits in the Britannia Formation (Lower Cretaceous), North Sea: a new perspective on the turbidity current and debris flow problem. *Sedimentology*, **47**, 31–70.

Lyons, T.W., **Reinhard, C.T.** and **Planavsky, N.J.** (2014) The rise of oxygen in Earth's early ocean and atmosphere. *Nature*, **506**, 307–315.

Macquaker, J.H.S., **Bentley, S.J.** and **Bohacs, K.M.** (2010a) Wave-enhanced sediment-gravity flows and mud dispersal across continental shelves: reappraising sediment transport processes operating in ancient mudstone successions. *Geology*, **38**, 947–950.

Macquaker, J.H.S., **Keller, M.A.** and **Davies, S.J.** (2010b) Algal blooms and « marine snow »: mechanisms that enhance preservation of organic carbon in ancient fine-grained sediments. *J. Sed. Res.*, **80**, 934–942.

Melezhik, V.A., **Huhma, H.**, **Condon, D.J.**, **Fallick, A.E.** and **Whitehouse, M.J.** (2007) Temporal constraints on the Paleoproterozoic Lomagundi-Jatuli carbon isotopic event. *Geology*, **35**, 655–658.

Morsilli, M. and **Pomar, L.** (2012) Internal waves vs. surface storm waves: a review on the origin of hummocky cross-stratification. *Terra Nova*, **24**, 273–282.

Moussavou, M. and **Edou-Minko, A.** (2006) Contribution à l'histoire thermo-tectonique précambrienne du complexe annulaire de N'goutou par la géochimie et la géochronologie U/Pb sur minéraux accessoires (Bassin Francevillien d'Okondja, Gabon). Bassins africains - Biogéosciences et environnement. *Afr. Geosci. Rev.*, **13**, 53–62.

Mulder, T. and **Alexander, J.** (2001) The physical character of subaqueous sedimentary density flows and their deposits. *Sedimentology*, **48**, 269–299.

Mulder, T., **Razin, P.** and **Faugères, J.-C.** (2009) Hummocky cross-stratification-like structures in deep sea turbidites: Upper Cretaceous Basque basins (Western Pyrenees, France). *Sedimentology*, **56**, 997–1015.

Mulder, T., **Feybesse, J.-L.**, **Guillocheau, F.** and **Parize, O.** (2013) Contexte tectono-sédimentaire du bassin de Franceville (Gabon). 14e Congrès français de sédimentologie, livre des résumés. *ASF Publ.*, **73**, 294.

Mutti, E. (1992) *Turbidite Sandstones*, p. 275. Instituto di Geologia Universita di Parma & AGIP, Parma, Italy.

Mutti, E., **Tinterri, R.**, **Benevelli, G.**, **Biase, D.D.** and **Cavanna, G.** (2003) Deltaic, mixed and turbidite sedimentation of ancient foreland basins. *Mar. Petrol. Geol.*, **20**, 733–755.

Nardin, T.R., **Hein, F.J.**, **Gorsline, D.S.** and **Edwards, B.D.** (1979) A review of mass movement processes, sediment and acoustic characteristics, and contrasts in slope and base-of-slope systems versus canyon-fan-basin floor systems. *SEPM Spec. Publ.*, **27**, 61–73.

Ndongo, A., **Guiraud, M.**, **Vennin, E.**, **Mbina, M.**, **Buonchristiani, J.-F.**, **Thomazo, C.** and **Flotté, N.** (2016) Control of fluid-pressure on early deformation structures in the Paleoproterozoic extensional Franceville Basin (SE Gabon). *Precambrian Res.*, **277**, 1–25.

Ngombi-Pemba, L. (2014) Géochimie et minéralogie des formations argileuses (2.2-2.0 Ga) du bassin de Franceville au Gabon : fluctuations de l'oxygène atmosphérique, chimie des océans et diagenèse au Paléoprotérozoïque. Unpublished PhD, Université de Poitiers, 268 pp.

Ngombi-Pemba, L., **El Albani, A.**, **Meunier, A.**, **Grauby, O.** and **Gauthier-Lafaye, F.** (2014) From detrital heritage to diagenetic transformations, the message of clay minerals contained within shales of the Palaeoproterozoic Francevillian basin (Gabon). *Precambrian Res.*, **255**, 63–76.

Nichols, M.M. (1985) Fluid mud accumulation process in an estuary. *Geo. Mar. Lett.*, **4**, 171–176.

Nishida, N., **Ito, M.**, **Inoue, A.** and **Takizawa, S.** (2013) Clay fabric of fluid-mud deposits from laboratory and field observations; potential application to the stratigraphic record. *Mar. Geol.*, **33**, 71–78.

Noffke, N., **Gerdes, G.** and **Klenke, T.** (2003) Benthic cyanobacteria and their influence on the sedimentary dynamics of peritidal depositional systems (siliciclastic, evaporitic salty, and evaporitic carbonatic). *Earth Sci. Rev.*, **62**, 163–176.

Noffke, N., **Christian, D.**, **Wacey, D.** and **Hazen, R.M.** (2013) Microbially induced sedimentary structures recording an ancient ecosystem in the ca.3.48 billion-year-old dresser formation, Pilbara, Western Australia. *Astrobiology*, **13**, 1103–1124.

Oliveri, E., **Neri, R.**, **Bellanca, A.** and **Riding, R.** (2009) Carbonate stromatolites from a Messinian hypersaline setting in the Caltanissetta Basin, Sicily: petrographic evidence of microbial activity and related stable isotope and rare earth element signatures. *Sedimentology*, **57**, 142–161.

Onanga-Mavotchi, N. (2016) Etude des paléomilieux paléoprotérozoïques (2,1-2,2 Ga) : la formation FB du bassin de Franceville au Gabon. Unpublished PhD, University of Poitiers, 244 pp.

Onanga-Mavotchi, N., **El Albani, A.**, **Trentesaux, A.**, **Fontaine, C.**, **Pierson-Wickmann, A.-C.**, **Boulvais, P.**, **Riboulleau, A.**, **Ngombi-Pemba, L.**, **Pambo, F.** and **Gauthier-Lafaye, F.** (2016) The Role of the Early diagenetic dolomitic concretions in the preservation of the 2.1 Ga paeolenvironmental signal: Paleoproterozoic of the Franceville Basin, Gabon. *C.R. Geosci.*, **348**, 609–618.

Ossa-Ossa, F. (2010) Etude multi-approches du bassin sédimentaire paléoprotérozoïque (2.1-2.4 Ga) de Franceville au Gabon : les environnements sédimentaires et l'impact des paléocirculations de fluides. Unpublished PhD, Université de Poitiers, 299 pp.

Pambo, F. (2004) Conditions de formation des carbonates de manganèse protérozoïques et analyse minéralogique et géochimique des minerais à bioxydes de manganèse associés dans le gisement de Moanda (Sud-Est, Gabon). Unpublished PhD, Université de Bourgogne, 274 pp.

Pambo, F., **Guiraud, M.**, **Quesne, D.**, **Gauthier-Lafaye, F.**, **Azziley-Azzibrouck, G.** and **Lang, J.** (2006) The Proterozoic Franceville Basin (S.E. Gabon): an example of interaction between marine sedimentation and extensional faulting. *Afr. Geosci. Rev.*, **13**, 77–106.

Parize, O., **Beaudoin, B.**, **Champanhet, J.-M.**, **Fries, G.**, **Imbert, P.**, **Labourdette, R.**, **Paternoster, B.**, **Rubino, J.-L.** and **Schneider, F.** (2007) A methodological approach to clastic injectites: From field analysis to seismic modeling - Examples of the Vocontian Aptian and Albian injectites (southeast France). In: *Sand Injectites: Implications for Hydrocarbon Exploration and Production* (Eds A. Hurst and J. Cartwright), *AAPG Memoir*, **87**, 173–183.

Parize, O., **Feybesse, J.-L.**, **Guillocheau, F.** and **Mulder, T.** (2013) Were the 2.1-Gyr fossil colonial organisms discovered in the Francevillian basin (Palaeoproterozoic, Gabon) buried by turbidites?. *C.R. Geosci.*, **345**, 101–110.

Prave, A.R. and **Duke, W.L.** (1990) Small-scale hummocky cross-stratification in turbidites: a form of antidune stratification? *Sedimentology*, **37**, 531–539.

Préat, A., **Bouton, P.**, **Thiéblemont, D.**, **Prian, J.-P.**, **Ndounze, S.S.** and **Delpomdor, F.** (2011) Paleoproterozoic high $\delta 13C$ dolomites from the Lastoursville and Franceville basins

(SE Gabon): stratigraphic and synsedimentary subsidence implications. *Precambrian Res.*, **189**, 212–228.

Reyes, K., **Gonzalez, N.I.**, **Stewart, J.**, **Ospino, F.**, **Nguyen, D.**, **Cho, D.T.**, **Ghahremani, N.**, **Spear, J.R.** and **Johnson, H.A.** (2013) Surface Orientation Affects the Direction of Cone Growth by Leptolyngbya sp. Strain C1, a Likely Architect of Coniform Structures Octopus Spring (Yellowstone National Park). *Appl. Environ. Microbiol.*, **79**, 1302–1308.

Reynaud, J.-Y. and **Dalrymple, R.W.** (2012) Shallow-marine tidal deposits. In: *Principles of Tidal Sedimentology* (Eds R.A. Davis and R.W. Dalrymple), pp. 335–369. Springer.

Runnegar, B.N. and **Fedonkin, M.A.** (1992) Proterozoic metazoan body fossils. In: *The Proterozoic Biosphere: A Multidisciplinary Study* (Eds J.W. Schopf and C. Klein), pp. 369–388. Cambridge University Press, Cambridge.

Sageman, B.A., **Murphy, A.E.**, **Werne, J.P.**, **Ver Straeten, C.A.**, **Hollander, D.J.** and **Lyons, T.W.** (2003) A tale of shales: the relative roles of production, decomposition, and dilution in the accumulation of organic-rich strata, Middle– Upper Devonian, Appalachian basin. *Chem. Geol.*, **195**, 229–273.

Schidlowski, M., **Eichmann, R.** and **Junge, C.E.** (1976) Carbon isotope geochemistry of the Precambrian Lomagundi carbonate province, Rhodesia. *Geochim. Cosmochim. Acta*, **40**, 449–455.

Schieber, J. (1999) Microbial mats in terrigenous clastics: the challenge of identification in the rock record. *Palaios*, **14**, 3–13.

Schieber, J. (2016) Mud re-distribution in epicontinental basins - Exploring likely processes. *Mar. Petrol. Geol.*, **71**, 119–133.

Shanmugam, G. (1996) High-density turbidity currents: are they sandy debris flows? *J. Sed. Res.*, **66**, 2–10.

Shepard, R.N. and **Sumner, D.Y.** (2010) Undirected motility of filamentous cyanobacteria produces reticulate mats. *Geobiology*, **8**, 179–190.

Simpson, E.L., **Heness, E.**, **Bumby, A.**, **Eriksson, P.G.**, **Eriksson, K.A.**, **Hilbert-Wolf, H.L.**, **Linnevelt, S.**, **Fitzgerald Malenda, H.**, **Modungwa, T.** and **Okafor, O.J.** (2013) Evidence for 2.0Ga continental microbial mats in a paleodesert setting, 1–15. *Precambrian Res.*, **237**, 36–50.

Smith, R. (2004). Silled sub-basins to connected tortuous corridors: sediment distribution systems on topographically complex sub-aqueous slopes. In: *Confined Turbidite Systems* (Eds S.A. Lomas and P. Joseph), *Geol. Soc. Spec. Publ.*, **222**, 23–43.

Stille, P., **Gauthier-Lafaye, F.** and **Bros, R.** (1993) The Neodymium isotope system as a tool for petroleum exploration. *Geochim. Cosmochim. Acta*, **57**, 4521–4525.

Stolzenbach, K.D., **Newman, K.A.** and **Wong, C.S.** (1992) Aggregation of fine particles at the sediment-water interface. *J. Geophys. Res C Oceans*, **97**, 17889–17898.

Stow, D.A. and **Johansson, M.** (2000) Deep-water massive sands: nature, origin and hydrocarbon implications. *Mar. Petrol. Geol.*, **17**, 145–174.

Sumner, D.Y., **Jungblut, A.D.**, **Hawes, I.**, **Andersen, D.T.**, **Mackey, T.J.** and **Wall, K.** (2016) Growth of elaborate microbial pinnacles in Lake Vanda, Antarctica. *Geobiology*, **14**, 556–574.

Suter, J.R. (2006) Facies models revisited; clastic shelves. In: *Facies Models Revisited* (Eds H.W. Posamentier and R.G. Walker), *SEPM Spec. Publ.*, **84**, 339–397.

Swift, D., **Oertel, G.**, **Tillman, R.** and **Thorne, J.** (1991) Shelf sand and sandstone bodies; geometry, facies and sequence stratigraphy. *IAS Spec. Publ.*, **14**, 532.

Taj, R.J., **Aref, M.A.M.** and **Schreiber, B.C.** (2014) The influence of microbial mats on the formation of sand volcanoes and mounds in the Red Sea coastal plain, south Jeddah, Saudi Arabia. *Sed. Geol.*, **311**, 60–74.

Talling, P.J., **Masson, D.G.**, **Sumner, E.J.** and **Malgesini, G.** (2012a) Subaqueous sediment density flows; depositional processes and deposit types. *Sedimentology*, **59**, 1937–2003.

Talling, P.J., **Malgesini, G.** and **Felletti, F.** (2012b) Can liquefied debris flows deposit clean sand over large areas of sea floor? Field evidence from the Marnoso-arenacea Formation, Italian Apennines. *Sedimentology*, **60**, 720–762.

Thiéblemont, D., **Bouton, P.**, **Préat, A.**, **Goujou, J.-C.**, **Tegyey, M.**, **Weber, F.** and **Treuil, M.** (2014) Transition from alkaline to calc-alkaline volcanism during evolution of the Paleoproterozoic Francevillian basin of eastern Gabon (Western Central Africa). *J. Afr. Earth Sci.*, **99**, 215–227.

Traykovski, P., **Geyer, W.R.**, **Irish, J.D.** and **Lynch, J.F.** (2000) The role of wave-induced density-driven fluid mud flows for cross-shelf transport on the Eel River continental shelf. *Cont. Shelf Res.*, **20**, 2113–2140.

Tribovillard, N., **Trichet, J.**, **Défarge, C.** and **Trentesaux, A.** (1999) Jurassic lagoonal environments and quasi-abiotic platy limestone accumulation: microbial interventions. *Sedimentology*, **46**, 1183–1197.

Trichet, J., **Défarge, C.**, **Tribble, J.** and **Tribble, G.** (2001) Christmas Island lagoonal lakes, models for the deposition of carbonate–evaporite–organic laminated sediments. *Sed. Geol.*, **140**, 177–189.

Tyson, R.V. (2005) The "Productivity versus Preservation" controversy: cause, flaws, and resolution. In: *The Deposition of Organic-Carbon-Rich Sediments: Models, Mechanisms, and Consequences* (Ed. N.B. Harris), *SEPM Spec. Publ.*, **82**, 17–33.

Walter, M.R., **Bauld, J.** and **Brock, T.D.** (1972) Siliceous algal and bacterial stromatolites in hot spring and geyser effluents of Yellowstone national park. *Science*, **178**, 402–405.

Weber, F. (1968) Une série précambrienne du Gabon : le Francevillien. Sédimentologie, géochimie, relations avec les gîtes minéraux. Mémoire du Service de Cartographie Géologique d'Alsace Lorraine 28, 328 pp.

Weber, F., **Gauthier-Lafaye, F.**, **Whitechurch, H.**, **Ulrich, M.** and **El Albani, A.** (2016) Continental collision during the 2 Ga Eburnean Orogeny in Gabon and opening of the Francevillian intracratonic basins: a review. *C.R. Geosci.*, **348**, 572–586.

Winterwerp, J.C., **de Boer, G.J.**, **Greeuw, G.** and **van Maren, D.S.** (2012) Mud-induced wave damping and wave-induced liquefaction. *Coast. Eng.*, **64**, 102–112.

Wright, L.D., **Wiseman, W.J., Jr**, **Yang, Z.S.**, **Bornhold, B.D.**, **Keller, K.H.**, **Prior, D.B.** and **Suhayda, J.N.** (1990) Processes of marine dispersal and deposition of suspended silts off the modern mouth of the Huanghe (Yellow River). *Cont. Shelf Res.*, **10**, 1–40.

Manuscript received 8 December 2016; revision accepted 27 June 2017

2. Spatial organization between the MRS and multicellular organisms in the studied area

Organism motility in an oxygenated shallow-marine environment 2.1 billion years ago

Abderrazak El Albani[a,1], M. Gabriela Mangano[b], Luis A. Buatois[b], Stefan Bengtson[c], Armelle Riboulleau[d], Andrey Bekker[e], Kurt Konhauser[f], Timothy Lyons[e], Claire Rollion-Bard[g], Olabode Bankole[a], Stellina Gwenaelle Lekele Baghekema[a], Alain Meunier[a], Alain Trentesaux[d], Arnaud Mazurier[a], Jeremie Aubineau[a], Claude Laforest[a], Claude Fontaine[a], Philippe Recourt[d], Ernest Chi Fru[h], Roberto Macchiarelli[i,j], Jean Yves Reynaud[d], François Gauthier-Lafaye[k], and Donald E. Canfield[l,1]

[a]Unité Mixte de Recherche (UMR), Centre National de la Recherche Scientifique (CNRS), IC2MP 7285, University of Poitiers, 86073 Poitiers, France; [b]Department of Geological Sciences, University of Saskatchewan, Saskatoon, SK S7N 5A5, Canada; [c]Department of Palaeobiology, Swedish Museum of Natural History, SE-104 05 Stockholm, Sweden; [d]UMR 8187 Laboratoire d'Océanologie et de Géosciences, CNRS, University of Lille, Université du Littoral-Côte-d'Opale, 59655 Villeneuve d'Ascq, France; [e]Department of Earth Sciences, University of California, Riverside, CA 92521; [f]Department of Earth and Atmospheric Sciences, University of Alberta, Edmonton, AB, T6G 2E3, Canada; [g]Institut de Physique du Globe de Paris, Sorbonne Paris Cité, Université Paris Diderot, UMR 7154 CNRS, F-75005 Paris, France; [h]Geomicrobiology/Biogeochemistry, School of Earth and Ocean Sciences, Cardiff University, CF10 3AT Cardiff, United Kingdom; [i]Unité de Formation Géosciences, Université de Poitiers, 86073 Poitiers, France; [j]UMR 7194 CNRS, Muséum National d'Histoire Naturelle, Paris, France; [k]Laboratoire d'Hydrologie et de Géochimie de Strasbourg, UMR 7517 CNRS, 67084, Université de Strasbourg, France; and [l]Department of Biology, Nordic Center for Earth Evolution, DK-5230 Odense M, Denmark

Contributed by Donald E. Canfield, December 22, 2018 (sent for review September 11, 2018; reviewed by Phoebe A. Cohen and Marc Laflamme)

Evidence for macroscopic life in the Paleoproterozoic Era comes from 1.8 billion-year-old (Ga) compression fossils [Han TM, Runnegar B (1992) *Science* 257:232–235; Knoll et al. (2006) *Philos Trans R Soc Lond B* 361:1023–1038], Stirling biota [Bengtson S et al. (2007) *Paleobiology* 33:351–381], and large colonial organisms exhibiting signs of coordinated growth from the 2.1-Ga Francevillian series, Gabon. Here we report on pyritized string-shaped structures from the Francevillian Basin. Combined microscopic, microtomographic, geochemical, and sedimentologic analyses provide evidence for biogenicity, and syngenicity and suggest that the structures underwent fossilization during early diagenesis close to the sediment–water interface. The string-shaped structures are up to 6 mm across and extend up to 170 mm through the strata. Morphological and 3D tomographic reconstructions suggest that the producer may have been a multicellular or syncytial organism able to migrate laterally and vertically to reach food resources. A possible modern analog is the aggregation of amoeboid cells into a migratory slug phase in cellular slime molds at times of starvation. This unique ecologic window established in an oxygenated, shallow-marine environment represents an exceptional record of the biosphere following the crucial changes that occurred in the atmosphere and ocean in the aftermath of the great oxidation event (GOE).

motility | Paleoproterozoic Era | oxygenation | Francevillian

The exquisitely preserved sediments of the Francevillian Series B (FB) Formation from southeastern Gabon were deposited in an oxygenated (1, 2) offshore to offshore-transition environment at 2,100 ± 30 million years ago (Ma) (3, 4). The deposits pass upwards into shallow water, stromatolitic dolostones, and dolomitic cherts of the Francevillian C (FC) Formation (*SI Appendix*, Figs. S1 and S2), recording a regression (1, 2). The specimens for this study were collected from black, silty shale intercalated with siltstone to very fine-grained sandstone in the FB_2 Member of the FB Formation (*SI Appendix*, Figs. S1 and S2).

The black, silty shales preserve millimeter-sized, diverse string-shaped structures (Figs. 1 and 2), most of which are pyritized. These structures occur throughout the member; however, they are most abundant in the basal-most meter on the bedding plane (Fig. 1 and *SI Appendix*, Fig. S1*C*). Microbially induced sedimentary structures prevail in the interbedded sandstone and silty sandstone layers (*SI Appendix*, *Supplementary Information Text 1* and Fig. S3) and are commonly present in the vicinity of the string structures (Fig. 1 *E*, *F*, *I*, and *J*).

More than 80 specimens from several fossiliferous horizons were studied using X-ray microcomputed tomography (micro-CT) (Fig. 2, *SI Appendix*, Figs. S4–S7, and Movies S1–S4). The analysis reveals the presence of string-shaped structures within the strata (Fig. 2, *SI Appendix*, Figs. S4–S7, and Movies S1–S5). Some of these structures occur close to pyritized laminae lenses extending over several centimeters (Fig. 2 *C*–*F* and Movies S1–S3), suggesting an association with organic-rich mats where microbial sulfate reduction was enhanced (Fig. 2 *C*–*F* and *SI Appendix*, Figs. S3 and S5–S7). In one case, a sheetlike structure with a distinct boundary forms an apparent continuity with an equally distinct string (Fig. 3). Strings are mostly parallel to the bedding plane and, when observed in vertical cross sections (Fig. 2 *C*–*F*, *SI Appendix*, Fig. S6, and Movies S1 and S2), display an elliptic to rounded section, flattened parallel to the bedding (Fig. 4 *C* and *E* and *SI Appendix*, Fig. S6). They appear to have only a minor impact on the original sedimentary fabric with the laminae generally bending around

Significance

The 2.1 billion-year-old sedimentary strata contain exquisitely preserved fossils that provide an ecologic snapshot of the biota inhabiting an oxygenated shallow-marine environment. Most striking are the pyritized string-shaped structures, which suggest that the producer have been a multicellular or syncytial organism able to migrate laterally and vertically to reach for food resources. A modern analogue is the aggregation of amoeboid cells into a migratory slug phase in modern cellular slime molds during time of food starvation. While it remains uncertain whether the amoeboidlike organisms represent a failed experiment or a prelude to subsequent evolutionary innovations, they add to the growing record of comparatively complex life forms that existed more than a billion years before animals emerged in the late Neoproterozoic.

Author contributions: A.E.A. and D.E.C. designed research; A.E.A., M.G.M., L.A.B., S.B., A.R., A.B., K.K., T.L., and D.E.C. performed research; A.E.A., M.G.M., L.A.B., S.B., A.R., A.B., K.K., T.L., C.R.-B., O.B., S.G.L.B., A. Meunier, A.T., A. Mazurier, J.A., C.L., C.F., P.R., E.C.F., R.M., J.Y.R., and D.E.C. analyzed data; A.E.A., M.G.M., L.A.B., S.B., A.R., A.B., K.K., T.L., C.R.-B., A. Meunier, F.G.-L., and D.E.C. wrote the paper; and O.B., S.G.L.B., A.T., J.A., and C.L. contributed to the fieldwork.

Reviewers: P.A.C., Williams College; and M.L., University of Toronto Mississauga.

The authors declare no conflict of interest.

[1]To whom correspondence may be addressed. Email: abder.albani@univ-poitiers.fr or dec@biology.sdu.dk.

This article contains supporting information online at www.pnas.org/lookup/suppl/doi:10.1073/pnas.1815721116/-/DCSupplemental.

www.pnas.org/cgi/doi/10.1073/pnas.1815721116

PNAS Latest Articles | 1 of 6

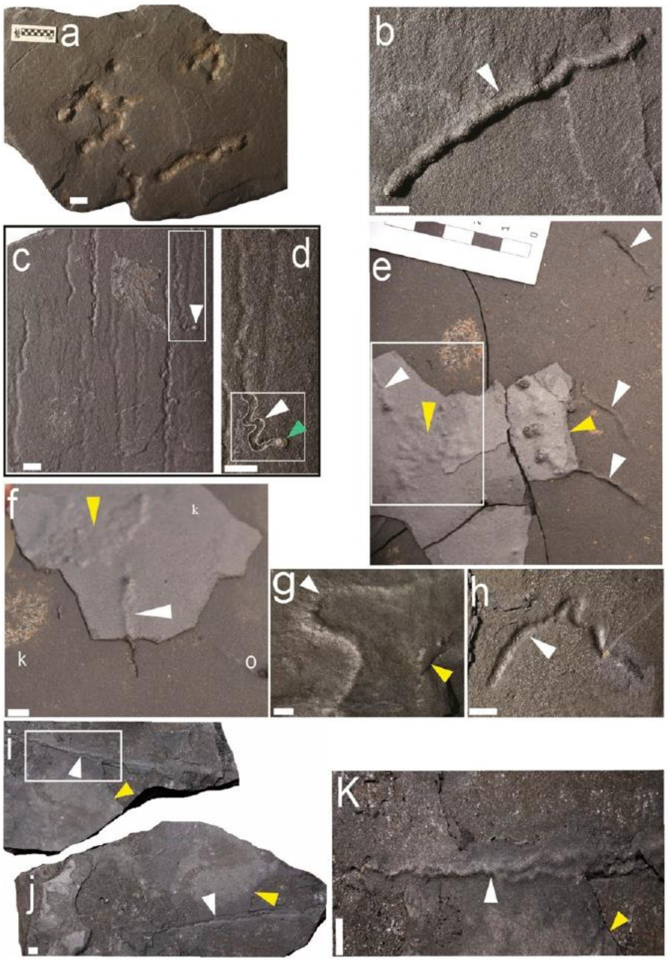

Fig. 1. Reflected-light photographs of pyritized string-shaped specimens from the Francevillian Series, Gabon. White and yellow arrows point to string-shaped specimens and microbial mats, respectively. (*A*) Slab displaying several straight specimens with straight to convoluted strings. (*B*–*I*) Sinuous strings. (*C*) Straight or slightly contorted strings; frame denotes specimen in *D*. (*D*) Enlarged part of *C*, contour of trace marked in white within frame. Note the termination of the trace showing a small pyrite globule (green arrow). (*E*) Slab displaying several subparallel specimens in the vicinity of bacterial mats. Note that the relief increase at the surface of the sediment from right to left for each specimen; frame denotes specimen in *F*. (*F*) Enlarged part of *E*, white arrow shows the detail of the trajectory of specimen under the fine clay laminae toward the bacterial mats (yellow arrow). (*I* and *J*) Part and counterpart of twinned contorted strings, parting from each other at upper white arrow; box denotes specimen in *K*. (*K*) Enlarged part of *J*; note the contorted strings and braided aspect. (Scale bars: 1 cm.)

these structures consistent with their early formation (Fig. 2*I*, *SI Appendix*, Figs. S6 and S7, and Movies S1 and S2). Specifically, the features indicate compaction of soft, fine-grained sediment around a relatively rigid object and show that the strings were in place and mineralized when the sediments were still compacting (Fig. 2*I*). Detrital phyllosilicate particles are parallel to bedding and aligned along the perimeter of the strings (Fig. 4). This relationship confirms precompactional formation of pyrite within the string structures resulting in local rearrangement of sediment grains during compaction. Combined SEM-back-scattered electron (BSE) imaging and energy-dispersive X-ray spectrometry (EDX) analyses also indicate contrasting textures and mineralogical compositions within and outside the strings (Fig. 4 *E* and *F*). Very few detrital minerals (e.g., quartz) are scattered within the pyrite strings, while authigenic illite and chlorite grains show signs of free growth within the pore spaces (Fig. 4 *E*–*G*).

The strings have a straight to sinuous shape (Figs. 1 and 2 and *SI Appendix*, Figs. S4–S8) and a maximum length of 170 mm. The simplest specimens are horizontal, unbranched, with straight (Figs. 1 *A* and *B* and 2 *A* and *B*, *SI Appendix*, Fig. S6, and Movie S3) to sinuous shapes (Fig. 1 *C*–*K*, *SI Appendix*, Figs. S6–S8, and Movies S1 and S2). They are 1–6 mm wide, with a relatively

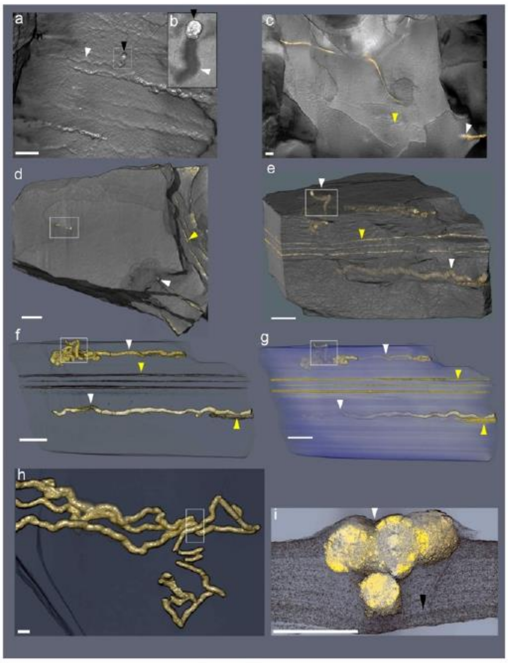

Fig. 2. Micro-CT-based reconstructions of string-shaped structures from the Francevillian Series, Gabon. White and yellow arrows point to string-shaped specimens and microbial mats, respectively. (*A*) Volume rendering showing the external surface of straight structures. *Inset* (*B*) shows enlargement of string ending with a pyrite crystal (black arrows). Same specimen as in Fig. 1 *D* and *E*. (*C*) External surface volume rendering showing weakly sinuous string. (*D*) External surface volume rendering, frame denotes the position of subvertical tubes. (*E*) External volume transparencies of the same specimen as in *D*, lateral view showing the string-shaped specimens inside the host rock. Frame denotes the position of subvertical tubes. (*F* and *G*) External volume transparencies of the same sample as in *D* and *E* at different heights in the sample. (*H*) Twinned contorted strings; box denotes portion (cross-section) figured in *I*. (*I*) Virtual cross-section of contorted strings, black arrow points to the precompactional deformation of silty shale laminae. (Scale bars: 1 cm.)

constant diameter along the structures (Fig. 2 *C*–*H* and Movie S3). A rounded termination is typically observed at the end of the structures (Figs. 1 and 2*A*), but one specimen ends with a spheroidal pyrite concretion showing a similar size to the string structure (Figs. 1 *C* and *D* and 2*A*, *Inset*). Specimens may develop a short, low-wavelength sinuosity and angular bends (Fig. 1 *D*, *C*, *I*, and *J*). In some cases, there are two or more parallel strings (Fig. 1 *C*, *D*, *I*, and *J*) that may intertwine and display a contorted helicoid shape, in places involving several strings in a braided pattern (Figs. 1 *I* and *J* and 2 *G* and *H*, *SI Appendix*, Fig. S4, and Movie S4). X-ray micro-CT and petrographic microscopy reveal that these string-shaped structures also intersect the stratification (Fig. 2*E*, *SI Appendix*, Figs. S7 and S8, and Movie S2). Strings might traverse silty-shale laminae and continue along at other levels, with angles of penetration ranging from 12° to 85° (Figs. 2 *D*–*F* and 4*E*, *SI Appendix*, Figs. S5*C* and S8, and Movies S1 and S2).

The pyritized string structures are present in sediment deposited under oxygenated bottom-water conditions (1, 5). This is consistent with the observation that selective pyritization preferably occurs in oxic, organic-lean sediments, because localized organic enrichments favor the needed chemical gradients. The pyrite structures display highly negative δ^{34}S values (−31‰ to −21‰; *SI Appendix*, Figs. S9 and S10 and Table S1), which are in the range of the lightest values for sedimentary pyrite deposited before the late Neoproterozoic Era (6, 7). Considering a δ^{34}S value of ∼15‰ for seawater sulfate at 2.1 Ga (6, 8–11), the low δ^{34}S values of the string-shaped structures indicate early diagenetic pyrite formation from sulfide generated by sulfate-reducing microorganisms close to the sediment–water interface from a relatively large seawater sulfate pool (12–14). Consistent with this observation, recent results suggest that concentration of sulfate in seawater may have been unusually high at this time, much higher than levels present immediately before and after this period of the Paleoproterozoic Era (12, 13).

The morphological patterns of the string-shaped structures and their relationship with the host sediment are very similar to those of burrows preserved through selective pyritization of mucus (14, 15), suggesting that the Francevillian structures may also be the result of early pyritization of a mucus strand. Nonetheless, it is critical to explore first the possibility of an abiogenic origin for the morphologies by making comparison with abiotic structures. Detailed comparison with syneresis cracks and pyrite precipitated from migrating fluids (*SI Appendix*, *Supplementary Information Text 2*, Fig. S11, and Table S2) indicates that the mineralogy, 3D morphology, texture, and sulfur isotope composition of the Francevillian string-shaped structures are markedly different from these abiogenic structures.

The pyritic strings described herein may sometimes look similar to other elongated body fossils in the Gabon biota, particularly where secondary pyritization has affected the morphology. Lobate body fossils previously reported from these beds in places may have a narrow, taillike appendix that in well-preserved specimens shows a flat cross-sectional profile and the same pattern of radiating fabric and transverse folding characteristic of the main body (14, 15). In heavily pyritized specimens, these primary features are obscured, resulting in featureless rods. These fossils resemble the specimen in Fig. 3 (see, e.g., figures 4C and D, 5, and 6E and F in ref. 5), but are usually coarser and display the typical fabric of the lobate fossils. Another fossil that may have similarity to string-shaped structures is a hitherto undescribed body fossil forming a network of interconnected rings, where the walls are expressed as thin pyritic strands along the bedding plane (*SI Appendix*, *Supplementary Information Text 3* and Fig. S12). Short fragments of this fossil missing the

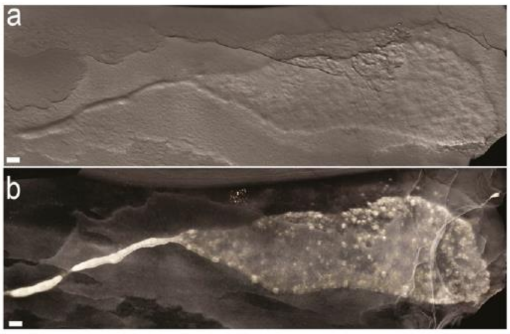

Fig. 3. (*A* and *B*) Volume rendering showing continuity between sheet and string morphologies in a single specimen. (Scale bars: 1 cm.)

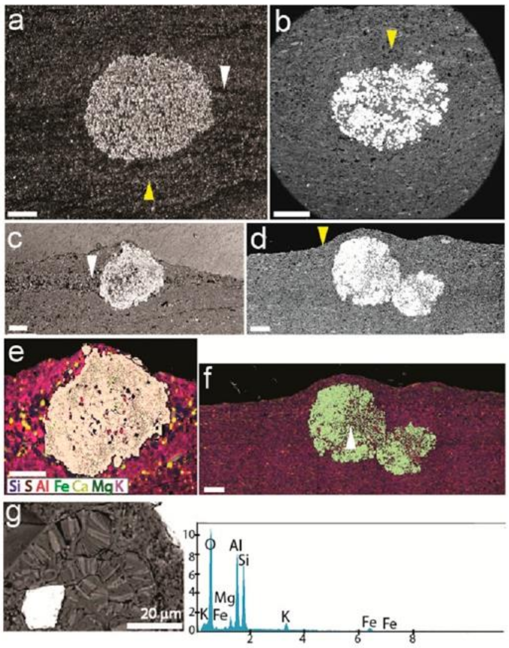

Fig. 4. Petrography with SEM and EDX of pyritized string-shaped structures from the Francevillian Series, Gabon. (*A* and *C*) Sediment laminae, white arrow, intersected by pyritic strings. Laminae bending around the pyrite string confirm precompactional formation, yellow arrow. (*B* and *D*) Bending of sediment layers, yellow arrows, around pyritic strings. (*E* and *F*) Element mapping of sections in *C* and *D*, showing mineralogical composition of the strings and embedding sediment. White arrow indicates the area of elemental point analyses (*G*). (Scale bars: 1 cm.) (*G*) Elemental points analysis indicate the presence of K, Mg, and Fe, which confirm the presence of illite and chlorite, respectively. The picture (*Left*) shows authigenic illite and chlorite grains and free growth of these minerals within the pore spaces.

branching points may be mistaken for the string structures on the bedding plane.

Experimental work (16) has shown that an oscillatory flow may interact with centimeter microbial aggregates, resulting in the formation on the sediment surface of elongate structures that may vaguely resemble the Francevillian string-shaped structures. However, the latter shows clear evidence of emplacement within the sediment. In addition, formation of the Francevillian Series B below the fair-weather wave base is inconsistent with continuous wave agitation.

A pyritized string of organic matter may represent the body of a filamentous organism or it may be the remnants of an organic tube or a mucus strand constructed by a motile organism. Among filamentous organisms, the closest living analogs to the Francevillian straight-to-sinuous structures are sulfur-oxidizing bacteria, such as *Thioploca* and *Beggiatoa*. These occur as horizontally to vertically oriented sheathed filaments or filament bundles in sediment, thriving at the interface between a weakly oxic sediment–water interface and underlying reducing sediments (17, 18). Individual filaments generally have a diameter of a few to tens of micrometers, although giant *Beggiatoa* filaments may reach nearly 200 µm in diameter (18). Sheathed *Thioploca* filaments bundles with up to 500-µm diameter have been recorded (17). The mucus sheaths of these sulfur-oxidizing bacteria allow filaments to migrate in the sediment between the surficial and the deeper portions (17). Importantly, these microbial structures are much smaller than ours. Phanerozoic pyritized organic trails and burrows of dimensions comparable to those of the Francevillian structures are commonly ascribed to animals (15, 19), but networks of pyritic filaments less than 1 mm in diameter have been interpreted as bacterial or fungal in origin (15).

Other than length differences, the distinction between pyritized tubes and trace fossils is subtle, but the latter can also be recognized by being massive and locally branching and through their incorporation of extraneous material (19–22). The Francevillian structures reported herein conform to this pattern and thereby resemble traces left by motile organisms, rather than individual filaments of bacteria or sheaths/tubes. They are somewhat reminiscent of simple straight forms resembling grazing trails in Ediacaran sedimentary successions, commonly in association with microbial mats (23–26). However, unlike these Ediacaran trails, the Francevillian structures have rounded terminations and occasional bulbous elements. Moreover, characteristic levees formed by sediment pushing on both sides, crucial in ascertaining the locomotory origin of some of the Ediacaran trace fossils, are absent in the Francevillian structures. In addition, a metazoan origin would not be supported by evidence from molecular clocks and the fossil record, which suggest a much younger origin for animals at ~650 Mya (23, 24).

Although the Francevillian specimens tend to be oriented parallel to bedding, they are occasionally oblique to subvertical in orientation, crossing up to 1.5 cm of sediment and locally disturbing primary laminations. These relationships can be taken as evidence for movement within the sediment, consistent with the absence of levees, which form in association with trails at the sediment–water interface, or even as tool marks produced by microbial aggregates moving under oscillating flow regimes (25). Given the inconsistencies with traces produced by animals or with sheaths enveloping motile bacteria, an alternative interpretation should be sought to explain their generation. Production by a microbial organism seems highly unlikely due to the lack of empirical evidence that such organism can produce megascopic infaunal trace fossils. There is no easy explanation, owing to morphologic simplicity of the structures and their great age, but a possible analog for the formation of these structures involves cellular slime molds, a group within Mycetozoa referred to as Dictyosteliida (27–29). These organisms, as illustrated by *Dictyostelium discoideum* and *D. polycephalum*, spend most of their life cycle as individual amoebae feeding on bacteria, but when food becomes scarce, single cells may aggregate to form a multicellular organism, referred to as "a slug," which subsequently moves on and within the sediment in search of a place for sporulation (29–32). During their aggregation stage, slime molds display behavior that is remarkably similar to that of simple animals (29).

The overall morphology of the Francevillian structures suggests an organism that was able to aggregate and migrate in a similar fashion to that of cellular slime molds, leaving a mucus trail behind. The occasional continuity between sheet and string morphology (Fig. 3) is particularly suggestive of this kind of behavior. The slug phase of cellular slime molds can develop differences in speed, with faster anterior relative to the posterior portion of the aggregate, resulting in a narrow isthmus between the anterior and posterior parts (33). The bulbous elements and the globular morphology of some of the string structures may have resulted from this movement pattern. Since metazoan trace fossils essentially reflect the maximum width of the producer, burrows tend to display constant diameter, but this is not necessarily the case with locomotive structures produced by mobile cell aggregates. The broken and crenulated appearance of some strings (Fig. 2 *E*–*G*) is consistent with slugs crossing over each other, resulting in the grafting of tips onto the slug as has been observed in cellular slime molds during aggregation (33). In some cases, the tips of two slugs going in the same direction may fuse, producing a larger one. The tip of the aggregate may also split into two in a process known as twinning (33). In addition, parallel orientation of some structures may reflect parallel movement of the aggregates, as has been commonly observed in modern dictyostelid slugs that move along environmental gradients (30). The morphologic variability and intergradation of forms observed in the Francevillian structures (Fig. 1), in particular the transfiguration between sheets and strings (Fig. 3), as well as grafting and twinning of strings (Figs. 1 *I* and *J* and 2 *G* and *H* and *SI Appendix*, Fig. S4), suggest locomotion of cell aggregates rather than organisms having a distinct body shape and the presence of an interactive sensorial system that reflects deliberate behavior.

Structures consisting of pairs of ridges preserved in positive hyporelief in *Myxomitodes* of the 2.0–1.8 Ga Stirling biota have been interpreted as mucus-supported trails of syncytial or multicellular organisms comparable to dictyostelid slime molds (31). The Francevillian structures, which are up to ∼300 million years older than the Stirling biota, contrast with *Myxomitodes* in their shape and dimensions. Again, the Francevillian features were formed within the sediment as indicated by their oblique and subvertical orientations to sediment lamination and in association with matgrounds (Fig. 2 *C–G*), whereas *Myxomitodes* is exclusively parallel to the bedding and interpreted as having been formed at the sediment–water interface (31).

Regardless of the difficulties in distinguishing between body and trace fossils, the interpretation of the Francevillian structures as those produced by organisms comparable in behavior to cellular slime molds is consistent with their morphologic variability and mode of occurrence. The stimulus to become multicellular for dictyostelids is the lack of food (29–32).

Thus, the aggregative stage of slime molds could take place when all available organic material has been consumed. The Francevillian structures tend to occur next to matgrounds (Fig. 2 *C–F*), which are abundant and regularly spaced vertically. A plausible ecosystem structure includes a community of single (nonaggregated), amoebalike organisms thriving on buried microbial mats, but aggregating during times of starvation to move within the sediment to reach another mat at a different level. This mode of existence is consistent with movement guided by chemotaxis, which has been documented in modern dictyostelid slugs (33, 34). Slime molds have been observed to move vertically through sediment layers that are up to 7 cm thick (29, 30), showing the capability to penetrate the substrate in a way analogous to a muscular organism. This pattern is consistent with the localized vertical displacement revealed by the Francevillian structures. In addition, very shallow matgrounds could have enhanced oxygen concentrations creating oases rich in oxygen within the sediment at depths shallow enough to still receive light (32) (*SI Appendix*, *Supplementary Information Text 1*). Modern studies have shown that during the day, concentrations of oxygen within biomats can be up to 4 times higher than in the oxygen-stressed overlying water column, highlighting the role of biomats as both oxygen and food resource during the Precambrian (32).

However, there are two significant differences between the Francevillian structures and those formed by modern slime molds. First, slime molds live in soils, not in marine sediment (33). In open-marine environments, the chemical gradients that are necessary for the amoeboid cells to aggregate are not observed at the surface of sediments, but frequently develop within the sediment as a result of microbial activity and sediment permeability. This argument is strong in rejecting a slime-mold interpretation in the case of the surface trace *Myxomitodes* (31). Unlike *Myxomitodes*, the Francevillian structures were formed within a fine-grained and overall undisturbed sediment, where the development of chemical gradients was favored. Second, the width of modern slime-mold slugs is up to 0.2 mm, significantly smaller than that of the structures documented here. Importantly, we are not suggesting that the Francevillian structures were produced by slime molds, although the size and complexity of the fossils suggest that the organism may have been a eukaryote. We rather advocate an analogous situation wherein amoebalike organisms with the capability to aggregate in a similar fashion could have been responsible for producing these complex structures. The restriction of modern dictyostelids to soils does not rule out the possibility that amoebalike organisms may have been able to evolve the trait of aggregation in marine environments below the sediment–water interface, particularly in microbially bound sediments.

The timing of origin of eukaryotes and its potential link to the GOE has been the focus of intense debate (35–37). Integration of genomic and fossil evidence suggests that eukaryotes emerged ∼1.84 Ga ago, therefore postdating the GOE (37) and the Francevillian structures, which correspond in age to the end of the Lomagundi Event (∼2.22–2.06 Ga). This event represents the largest global positive C isotope excursion in Earth's history, which is recorded in the FB and FC formations of the Francevillian Series (2). This excursion is thought to reflect a time of relatively high oxygen content in the atmosphere and ocean relative to the time intervals immediately before and after (38). Regardless of the ∼300 My discrepancy between the Francevillian and the proposed timing for origin of eukaryotes, it is reasonable to assume that such an increase in oxygenation may have promoted evolutionary innovations, such as those recorded by the Gabonese biota and associated ecosystems (1, 39).

The Lomagundi Event may have ended up with a dramatic deoxygenation after which seawater O_2 levels remained near or below the lower limit necessary for complex life to survive until the late Neoproterozoic (40). In addition to this broad temporal relationship with an oxygen increase, the FB and FC formations were deposited in nearshore to offshore environments that allowed widespread development of microbial mats (*SI Appendix*, Fig. S3). These shallow-water, oxygen and food-rich conditions within the photic zone were instrumental for the establishment of an ecosystem able to harbor more advanced forms of life, including organisms that could migrate. The fossiliferous Francevillian strata were ultimately preserved in essentially undeformed and nonmetamorphosed strata (41). These special conditions underscore the uniqueness of the Francevillian biota, although it cannot be entirely excluded that our occurrence is related more to favorable taphonomic conditions than to environmental or evolutionary drivers/patterns. While it remains uncertain whether the Francevillian string-shaped structures represent a failed experiment or a prelude to subsequent evolutionary innovations, they add to the growing record of comparatively more complex life forms that colonized shallow-marine environments more than a billion years before animals emerged in the late Neoproterozoic.

Methods

Textural relationships between the pyritized string-shaped structures and the silty shale matrix embedding the structures were assessed on polished slab sections with a ZEISS Discovery V8 stereoscope combined with AxioCam ERc 5s microscope camera. SEM was carried out on a JEOL 5600 LV equipped with an Oxford EDX for mineralogical analyses.

The micro-CT analysis of the samples was run on an RX-solutions EasyTom XL Duo equipment, which has one micro- and one nanofocus (LaB6 filament) Hamamatsu X-ray sources coupled to a Varian PaxScan 2520DX flat panel. Reconstructions were done with the XAct software (RX-solutions) with a classical filtered back projection algorithm and reduction of beam hardening artifact. Virtual sections, 3D rendering, and videos were performed with Avizo Fire v.9.2 (FEI).

Values of $\delta^{34}S$ were measured with secondary ion mass spectrometry (SIMS) using a Cameca IMS1270 and 1280 at Centre de Recherches Pétrographiques et Géochimiques facility (Nancy, France). The sulfur isotope compositions were measured using a 20-µm Cs^+ primary beam of ~2–5 nA. Sulfur isotopes were measured in a multicollection mode using two off-axis Faraday cups (L′2 and H1). The gains of the Faraday cups were intercalibrated at the beginning of the analytical session and their offsets were determined before each analysis during the presputtering (300 s). Typical ion intensities of 3×10^9 counts per second were obtained on $^{32}S^-$, so that an internal error better than ±0.1‰ can be reached. Instrumental mass fractionation and external reproducibility were determined by multiple measurements of the in-house reference material Pyr3B ($\delta^{34}S = +1.41$‰). The external reproducibility ranges between 0.05 and 0.40‰ (1 sigma) depending on the analytical session.

ACKNOWLEDGMENTS. For information and scientific discussion, we thank, P.-D. Mouguiama, F. D. Idiata, L. White, J. C. Baloche, R. Oslisly, F. Weber, A. Chirazi, F. Pambo, Idalina Moubiya Mouélé, and J. L. Albert. For assistance, we acknowledge C. Lebailly, Ph. Jalladeau, D. Autain, and S. Riffaut and the administrative staff of the University of Poitiers. We appreciate assistance from the Gabonese government, Centre National Pour la Recherche Scientifique & Technique du Gabon (CENAREST), General Direction of Mines and Geology of Gabon, Sylvia Bongo Ondimba Foundation, Agence Nationale des Parcs Nationaux du Gabon, University of Masuku, COMILOG and SOCOBA Companies, French Embassy at Libreville, Institut Français du Gabon, Le Centre National de la Recherche Scientifique (CNRS), and La Région Nouvelle Aquitaine for their supports. The authors acknowledge the support from RX-Solutions (Industrial X-Ray Tomography company), the Trace Analysis for Chemical, Earth and Environmental Sciences (TrACEES) platform from the Melbourne Collaborative Infrastructure Research Program at the University of Melbourne and P′ Institute UPR 3346 from Poitiers University.

1. El Albani A, et al. (2010) Large colonial organisms with coordinated growth in oxygenated environments 2.1 Gyr ago. *Nature* 466:100–104.
2. Canfield DE, et al. (2013) Oxygen dynamics in the aftermath of the Great Oxidation of Earth's atmosphere. *Proc Natl Acad Sci USA* 110:16736–16741.
3. Bros R, Stille P, Gauthier-Lafaye F, Weber F, Clauer N (1992) Sm-Nd isotopic dating of Proterozoic clay material: An example from the Francevillian sedimentary series, Gabon. *Earth Planet Sci Lett* 113:207–218.
4. Horie K, Hidaka H, Gauthier-Lafaye F (2005) U-Pb geochronology and geochemistry of zircon from the Franceville series at Bidoudouma, Gabon. *Geochim Cosmochim Acta* 69:A11.
5. El Albani A, et al. (2014) The 2.1 Ga old Francevillian biota: Biogenicity, taphonomy and biodiversity. *PLoS One* 9:e99438.
6. Canfield DE, Farquhar J (2009) Animal evolution, bioturbation, and the sulfate concentration of the oceans. *Proc Natl Acad Sci USA* 106:8123–8127.
7. Zhelezinskaia I, Kaufman AJ, Farquhar J, Cliff J (2014) Large sulfur isotope fractionations associated with Neoarchean microbial sulfate reduction. *Science* 346:742–744.
8. Guo Q, et al. (2009) Reconstructing Earth's surface oxidation across the Archean-Proterozoic transition. *Geology* 37:399–402.
9. Canfield DE (2001) Isotope fractionation by natural populations of sulfate-reducing bacteria. *Geochim Cosmochim Acta* 65:1117–1124.
10. Habicht KS, Gade M, Thamdrup B, Berg P, Canfield DE (2002) Calibration of sulfate levels in the archean ocean. *Science* 298:2372–2374.
11. Johnston DT, Farquhar J, Canfield DE (2007) Sulfur isotope insights into microbial sulfate reduction: When microbes meet models. *Geochim Cosmochim Acta* 71:3929–3947.
12. Planavsky NJ, Bekker A, Hofmann A, Owens JD, Lyons TW (2012) Sulfur record of rising and falling marine oxygen and sulfate levels during the Lomagundi event. *Proc Natl Acad Sci USA* 109:18300–18305.
13. Scott C, et al. (2014) Pyrite multiple-sulfur isotope evidence for rapid expansion and contraction of the early Paleoproterozoic seawater sulfate reservoir. *Earth Planet Sci Lett* 389:95–104.
14. Schieber J (2002) The role of an organic slime matrix in the formation of pyritized burrow trails and pyrite concretions. *Palaios* 17:104–109.
15. Virtasalo JJ, Löwemark L, Papunen H, Kotilainen AT, Whitehouse MJ (2010) Pyritic and baritic burrows and microbial filaments in postglacial lacustrine clays in the northern Baltic Sea. *J Geol Soc London* 167:1185–1198.
16. Mariotti G, Pruss SB, Ai X, Perron JT, Bosak T (2016) Microbial origin of early animal trace fossils? *J Sediment Res* 86:287–293.
17. Jørgensen BB, Gallardo VA (1999) *Thioploca* spp.: Filamentous sulfur bacteria with nitrate vacuoles. *FEMS Microbiol Ecol* 28:301–313.
18. Larkin J, Henk MC, Aharon P (1994) *Beggiatoa* in microbial mats at hydrocarbon vents in the Gulf of Mexico and Warm Mineral Springs, Florida. *Geo Mar Lett* 14:97–103.
19. Thomsen E, Vorren TO (1984) Pyritization of tubes and burrows from Late Pleistocene continental shelf sediments off North Norway. *Sedimentology* 31:481–492.
20. Seilacher A, Buatois LA, Mángano MG (2005) Trace fossils in the Ediacaran–Cambrian transition: Behavioral diversification, ecological turnover and environmental shift. *Palaeogeogr Palaeoclimatol Palaeoecol* 227:323–356.
21. Jensen S, Droser ML, Gehling JG (2006) A critical look at the Ediacaran trace fossil record. *Neoproterozoic Geobiology and Paleobiology*, eds Xiao S, Kaufman AJ (Springer, Dordrecht, The Netherlands), pp 115–157.
22. Buatois LA, Mángano MG (2016) Ediacaran ecosystems and the dawn of animals. *The Trace-Fossil Record of Major Evolutionary Events: Volume 1: Precambrian and Paleozoic*, eds Mángano MG, Buatois LA (Springer, Dordrecht, The Netherlands), pp 27–72.
23. Cunningham JA, Liu AG, Bengtson S, Donoghue PCJ (2017) The origin of animals: Can molecular clocks and the fossil record be reconciled? *BioEssays* 39:1–12.
24. Love GD, et al. (2009) Fossil steroids record the appearance of Demospongiae during the Cryogenian period. *Nature* 457:718–721.
25. Mariotti G, Pruss SB, Perron JT, Bosak T (2016) Microbial shaping of sedimentary wrinkle structures. *Nat Geosci* 7:736–740.
26. Hagiwara H (1991) A new species and some new records of dictyostelid cellular slime molds from Oman. *Bull Natl Sci Mus Tokyo Ser B* 17:109–121.
27. Wallraff E, Wallraff HG (1997) Migration and bidirectional phototaxis in *Dictyostelium discoideum* slugs lacking the actin cross-linking 120 kDa gelation factor. *J Exp Biol* 200:3213–3220.
28. Sternfeld J, O'Mara R (2005) Aerial migration of the Dictyostelium slug. *Dev Growth Differ* 47:49–58.
29. Bonner JT (2006) Migration in *Dictyostelium polycephalum*. *Mycologia* 98:260–264.
30. Bonner JT, Lamont DS (2005) Behavior of cellular slime molds in the soil. *Mycologia* 97:178–184.
31. Bengtson S, Rasmussen B, Krapež B (2007) The Paleoproterozoic megascopic Stirling biota. *Paleobiology* 33:351–381.
32. Gingras M, et al. (2011) Possible evolution of mobile animals in association with microbial mats. *Nat Geosci* 4:372–375.
33. Kessin RH (2001) *Dictyostelium: Evolution, Cell Biology, and the Development of Multicellularity* (Cambridge Univ Press, Cambridge, United Kingdom).
34. Bonner JT (2009) *The Social Amoebae: The Biology of Cellular Slime Molds* (Princeton Univ Press).
35. Schirrmeister BE, de Vos JM, Antonelli A, Bagheri HC (2013) Evolution of multicellularity coincided with increased diversification of cyanobacteria and the Great Oxidation Event. *Proc Natl Acad Sci USA* 110:1791–1796.
36. Knoll AH, Nowak MA (2017) The timetable of evolution. *Sci Adv* 3:e1603076.
37. Betts HC, et al. (2018) Integrated genomic and fossil evidence illuminates life's early evolution and eukaryote origin. *Nat Ecol Evol* 2:1556–1562.
38. Lyons TW, Reinhard CT, Planavsky NJ (2014) The rise of oxygen in Earth's early ocean and atmosphere. *Nature* 506:307–315.
39. Aubineau J, et al. (2018) Unusual microbial mat-related structural diversity at 2.1 billion years old and implications for the Francevillian biota. *Geobiology* 16:476–497.
40. Planavsky NJ, et al. (2014) Earth history. Low mid-Proterozoic atmospheric oxygen levels and the delayed rise of animals. *Science* 346:635–638.
41. Gauthier-Lafaye F, Weber F (2003) Natural nuclear fission reactors: Time constraints for occurrence, and their relation to uranium and manganese deposits and to the evolution of the atmosphere. *Precambrian Res* 120:81–100.

3. Implications of the rise of arsenic cycling in the Francevillian Series

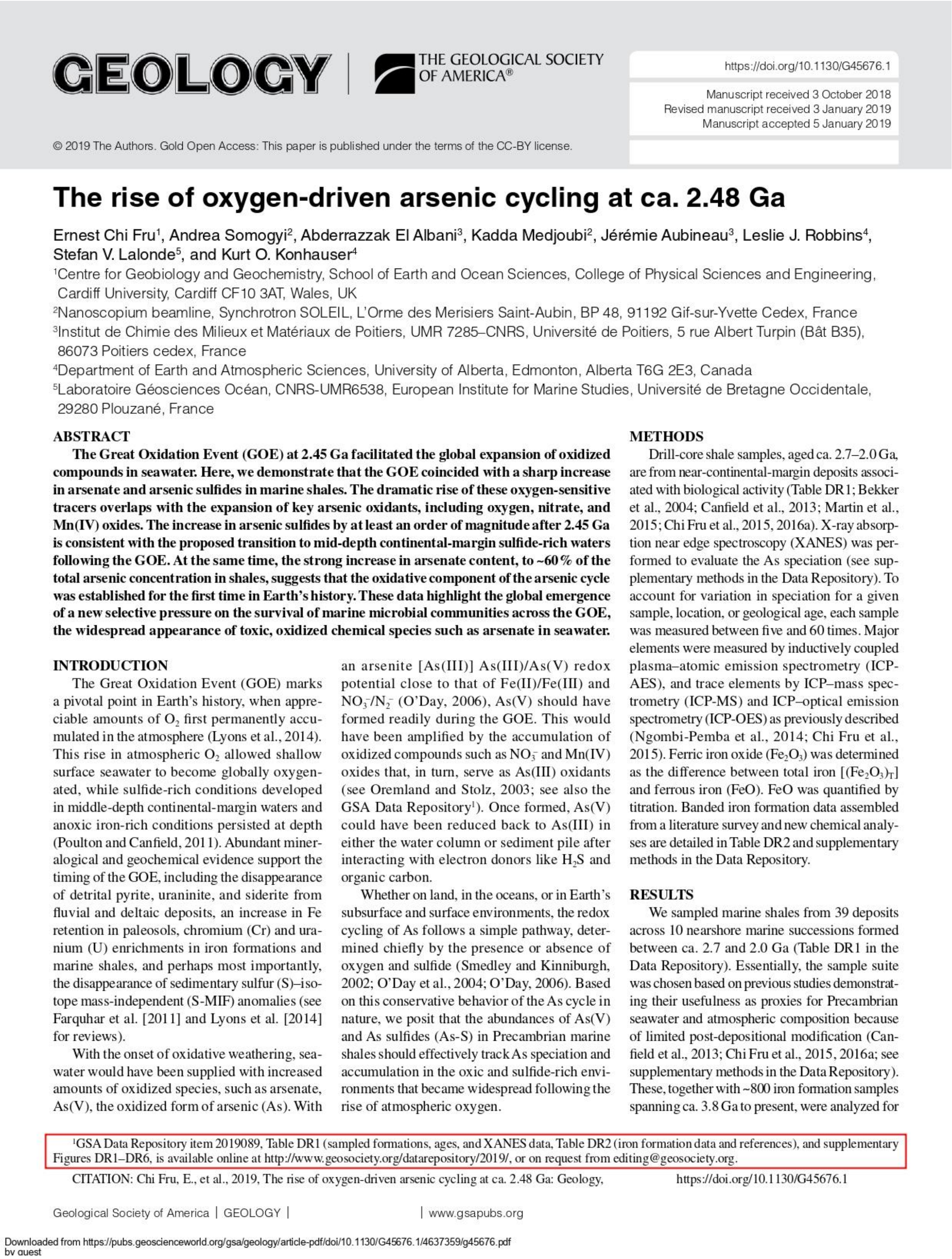

GEOLOGY | THE GEOLOGICAL SOCIETY OF AMERICA®

https://doi.org/10.1130/G45676.1

Manuscript received 3 October 2018
Revised manuscript received 3 January 2019
Manuscript accepted 5 January 2019

The rise of oxygen-driven arsenic cycling at ca. 2.48 Ga

Ernest Chi Fru[1], Andrea Somogyi[2], Abderrazzak El Albani[3], Kadda Medjoubi[2], Jérémie Aubineau[3], Leslie J. Robbins[4], Stefan V. Lalonde[5], and Kurt O. Konhauser[4]

[1]Centre for Geobiology and Geochemistry, School of Earth and Ocean Sciences, College of Physical Sciences and Engineering, Cardiff University, Cardiff CF10 3AT, Wales, UK
[2]Nanoscopium beamline, Synchrotron SOLEIL, L'Orme des Merisiers Saint-Aubin, BP 48, 91192 Gif-sur-Yvette Cedex, France
[3]Institut de Chimie des Milieux et Matériaux de Poitiers, UMR 7285–CNRS, Université de Poitiers, 5 rue Albert Turpin (Bât B35), 86073 Poitiers cedex, France
[4]Department of Earth and Atmospheric Sciences, University of Alberta, Edmonton, Alberta T6G 2E3, Canada
[5]Laboratoire Géosciences Océan, CNRS-UMR6538, European Institute for Marine Studies, Université de Bretagne Occidentale, 29280 Plouzané, France

ABSTRACT

The Great Oxidation Event (GOE) at 2.45 Ga facilitated the global expansion of oxidized compounds in seawater. Here, we demonstrate that the GOE coincided with a sharp increase in arsenate and arsenic sulfides in marine shales. The dramatic rise of these oxygen-sensitive tracers overlaps with the expansion of key arsenic oxidants, including oxygen, nitrate, and Mn(IV) oxides. The increase in arsenic sulfides by at least an order of magnitude after 2.45 Ga is consistent with the proposed transition to mid-depth continental-margin sulfide-rich waters following the GOE. At the same time, the strong increase in arsenate content, to ~60% of the total arsenic concentration in shales, suggests that the oxidative component of the arsenic cycle was established for the first time in Earth's history. These data highlight the global emergence of a new selective pressure on the survival of marine microbial communities across the GOE, the widespread appearance of toxic, oxidized chemical species such as arsenate in seawater.

INTRODUCTION

The Great Oxidation Event (GOE) marks a pivotal point in Earth's history, when appreciable amounts of O_2 first permanently accumulated in the atmosphere (Lyons et al., 2014). This rise in atmospheric O_2 allowed shallow surface seawater to become globally oxygenated, while sulfide-rich conditions developed in middle-depth continental-margin waters and anoxic iron-rich conditions persisted at depth (Poulton and Canfield, 2011). Abundant mineralogical and geochemical evidence support the timing of the GOE, including the disappearance of detrital pyrite, uraninite, and siderite from fluvial and deltaic deposits, an increase in Fe retention in paleosols, chromium (Cr) and uranium (U) enrichments in iron formations and marine shales, and perhaps most importantly, the disappearance of sedimentary sulfur (S)–isotope mass-independent (S-MIF) anomalies (see Farquhar et al. [2011] and Lyons et al. [2014] for reviews).

With the onset of oxidative weathering, seawater would have been supplied with increased amounts of oxidized species, such as arsenate, As(V), the oxidized form of arsenic (As). With an arsenite [As(III)] As(III)/As(V) redox potential close to that of Fe(II)/Fe(III) and NO_3^-/N_2^- (O'Day, 2006), As(V) should have formed readily during the GOE. This would have been amplified by the accumulation of oxidized compounds such as NO_3^- and Mn(IV) oxides that, in turn, serve as As(III) oxidants (see Oremland and Stolz, 2003; see also the GSA Data Repository[1]). Once formed, As(V) could have been reduced back to As(III) in either the water column or sediment pile after interacting with electron donors like H_2S and organic carbon.

Whether on land, in the oceans, or in Earth's subsurface and surface environments, the redox cycling of As follows a simple pathway, determined chiefly by the presence or absence of oxygen and sulfide (Smedley and Kinniburgh, 2002; O'Day et al., 2004; O'Day, 2006). Based on this conservative behavior of the As cycle in nature, we posit that the abundances of As(V) and As sulfides (As-S) in Precambrian marine shales should effectively track As speciation and accumulation in the oxic and sulfide-rich environments that became widespread following the rise of atmospheric oxygen.

METHODS

Drill-core shale samples, aged ca. 2.7–2.0 Ga, are from near-continental-margin deposits associated with biological activity (Table DR1; Bekker et al., 2004; Canfield et al., 2013; Martin et al., 2015; Chi Fru et al., 2015, 2016a). X-ray absorption near edge spectroscopy (XANES) was performed to evaluate the As speciation (see supplementary methods in the Data Repository). To account for variation in speciation for a given sample, location, or geological age, each sample was measured between five and 60 times. Major elements were measured by inductively coupled plasma–atomic emission spectrometry (ICP-AES), and trace elements by ICP–mass spectrometry (ICP-MS) and ICP–optical emission spectrometry (ICP-OES) as previously described (Ngombi-Pemba et al., 2014; Chi Fru et al., 2015). Ferric iron oxide (Fe_2O_3) was determined as the difference between total iron [$(Fe_2O_3)_T$] and ferrous iron (FeO). FeO was quantified by titration. Banded iron formation data assembled from a literature survey and new chemical analyses are detailed in Table DR2 and supplementary methods in the Data Repository.

RESULTS

We sampled marine shales from 39 deposits across 10 nearshore marine successions formed between ca. 2.7 and 2.0 Ga (Table DR1 in the Data Repository). Essentially, the sample suite was chosen based on previous studies demonstrating their usefulness as proxies for Precambrian seawater and atmospheric composition because of limited post-depositional modification (Canfield et al., 2013; Chi Fru et al., 2015, 2016a; see supplementary methods in the Data Repository). These, together with ~800 iron formation samples spanning ca. 3.8 Ga to present, were analyzed for

[1]GSA Data Repository item 2019089, Table DR1 (sampled formations, ages, and XANES data, Table DR2 (iron formation data and references), and supplementary Figures DR1–DR6, is available online at http://www.geosociety.org/datarepository/2019/, or on request from editing@geosociety.org.

CITATION: Chi Fru, E., et al., 2019, The rise of oxygen-driven arsenic cycling at ca. 2.48 Ga: Geology, https://doi.org/10.1130/G45676.1

As, Ti, and Fe content (Table DR2). The oxidation state of As and associated elements in shale minerals was examined by X-ray absorption near edge spectroscopy (XANES) (Fig. DR1 in the Data Repository) and X-ray fluorescence (Fig. DR2), respectively. After we excluded potential X-ray–induced oxidation of reduced As(III) species to As(V), and As(V) reduction during XANES analysis, our data revealed the following:

(1) Early Paleoproterozoic shale As/Fe ratios are mostly within the Neoarchean range, rising from a minimum of ~1.0×10^{-6} at the Archean-Proterozoic boundary to a maximum of 4.0 at ca. 2.0 Ga (Fig. 1A).

(2) With the exception of one sample, As(III) was exclusively below the XANES detection limit (Table DR1), implying that <15% of total As might be present as As(III). XANES spectra exhibit two prominent peaks in the 11.8695–11.8705 keV range, corresponding to As-S and As(V) species (Fig. DR1).

(3) The gradual increase in total As content in marine sediments across the GOE is mainly due to As-S and As(V) enrichment (Figs. 1B–1C).

(4) As-S and As(V) enrichment begins at 2.48 Ga, intensifying in the 2.32 Ga Timeball Hill Formation, South Africa (Fig. 1C), consistent with previously reported Cr and U enrichments in iron formations (Konhauser et al., 2011; Partin et al., 2013).

(5) As/Ti ratios in iron formations coincide with an increase in the oxidative supply of As from land to the oceans at the GOE (Fig. 2A). A lack of strong variability in As/Fe ratios across the GOE transition (Fig. 2B) suggests that the size of the Fe pool was not a major determinant of sediment As concentration and speciation trends at this time.

(6) In the Francevillian shales, Gabon, bulk As concentrations >50 ppm increase with rising Fe-oxide content (Fig. DR3A). However, there is a generally weak correlation between Fe-oxide and As concentration across the Francevillian Series. This is most prominent when As is <50 ppm (Fig. DR3A), along with a correlation between Mo and As in the sulfide-rich FD formation of the Francevillian Series (Figs. DR4 and DR5). This suggests that the rise of near–continental margin sulfidic conditions across the GOE was a critical factor controlling sediment As content and oxidation state.

(7) Some Precambrian pyrite-specific As enrichments are significant (Large et al., 2014; Gregory et al., 2015), but may not represent bulk shale As concentrations (Figs. DR3B and DR3C).

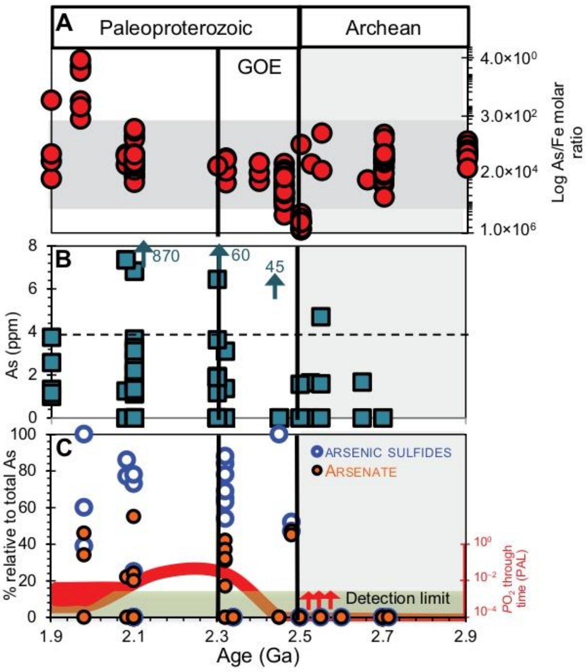

Figure 1. Secular sedimentary arsenic (As) dynamics across Archean-Proterozoic boundary. A: Bulk As/Fe ratio trends (see Chi Fru et al. [2015] for data description). Horizontal shading indicates range of Archean values. B: Bulk average As content in shales across sampled interval measured by inductively coupled plasma–optical emission spectrometry. Arrows are maximum X-ray fluorescence values (see Methods in text and Table DR1 [see footnote 1]). C: X-ray absorption near edge spectroscopy (XANES) data showing distribution of As species in shales. Red trace line shows atmospheric oxygenation dynamics relative to present atmospheric level (PAL), according to Lyons et al. (2014). Red arrows show whiffs of O_2 according to Anbar et al. (2007). Green shading indicates XANES detection limit, which is 15% total As content; data below detection limit are statistically uncertain and are rounded down to zero for graphical display. GOE—Great Oxidation Event.

DISCUSSION

The similar range of As/Fe ratios recorded during the early Paleoproterozoic relative to the Archean in both shales and iron formations suggests that the rise of As(V) and As-S species across the GOE cannot be explained by rapid fluctuations in the sedimentary Fe reservoir (see the Data Repository). Instead we suggest that this change is linked to the intensification of oxidative weathering of a felsic and/or As-S–rich continental crust (Konhauser et al., 2011; Large et al., 2018; see the Data Repository for details), containing up to 1500 ppm of As (Henke, 2009). The peak in As/Ti ratios in iron formations at ca. 2.48 Ga is consistent with a contemporaneous spike in Cr/Ti ratios, interpreted to reflect the onset of terrestrial aerobic sulfide oxidation (Konhauser et al., 2011). The muted GOE iron formation As/Fe signal, relative to Archean ratios, and the knife-sharp rise in the As/Ti trend across the GOE (Fig. 2A) may be related to Snowball Earth glaciations influencing continental As supply patterns (Chi Fru et al., 2015). This hypothesis is supported by the suppression of As/Fe and As/Ti ratios in Neoproterozoic iron formations (Figs. 2A and 2B; Table DR2) that are a product of submarine hydrothermal activity and a result of ice sheets restricting sediment supply and promoting water-column anoxia (Hoffman et al., 1998; see the Data Repository).

Under anoxic conditions, As and S chemistry becomes coupled, such that sulfide production scales with As-S deposition (O'Day et al., 2004; Data Repository). Arsenic sulfides, however, can be oxidized to As(V) in O_2-rich conditions (e.g., the case of arsenopyrite in Reaction 1).

$$4FeAsS + 13O_2 + 6H_2O \rightarrow 4H_3As_4 + 4FeSO_4. \quad (1)$$

In addition, the formation of As(V) only occurs when relevant As(III) oxidants (e.g., O_2, MnO_2, NO_3^-) are available (Oremland and Stolz, 2003; see the Data Repository). Electron donors are required to regenerate As(III) from As(V), and as today, microbes catalyze both the oxidative and reductive reactions (Oremland and Stolz, 2003). As(V) accumulation, therefore, occurs when production rates are greater than consumption rates, likely explaining the observed rise of As(V) in the data:

Anoxygenic photosynthetic and anoxic NO_3^--dependent chemoautotrophic oxidation of As(III) have been proposed as the most viable mechanisms by which appreciable Archean As(V) production could have occurred (Oremland and Stolz, 2003; Sforna et al., 2014). If these processes were prominent over As(V) reduction,

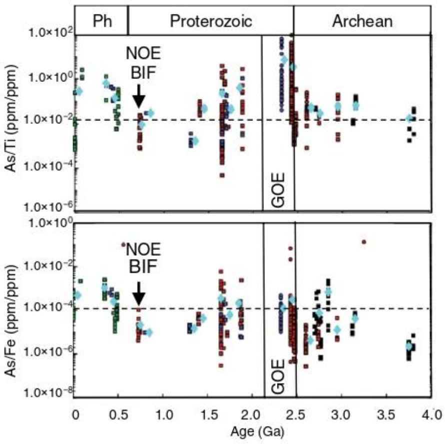

Figure 2. Distribution of As in iron formations (IFs), spread through Earth's history. A: As/Ti ratio. B: As/Fe ratio. Red symbols are Superior-type IFs; black, Algoma-type IFs; blue, ironstones; and green, Phanerozoic hydrothermal iron sediments. Squares represent bulk sample digestions; circles, laser ablation analyses. Light blue diamonds show 100 m.y. time-binned averages, plotted in middle of each bin (e.g., 2.4–2.5 Ga, plotted at 2.45 Ga). Two bins, plotted at 3.25 Ga and 0.55 Ga, were excluded from As/Fe plot as they were represented by single sample each. Ph—Phanerozoic; GOE—Great Oxidation Event.

a strong sedimentary As(V) signal would be expected. Our data, however, suggest that anoxic As(III) oxidation of Archean crust was limited, relative to that of post-GOE deposits. To this end, there is a significant increase in As(V) in the 2.32 Ga Timeball Hill Formation, suggesting that As(V) production outpaced consumption, compared to the period before. Further, the prevalence of As-S coincides with significant pyrite deposition in Timeball Hill black shales (Bekker et al., 2004). The strength and reproducibility of the As-S and As(V) signals (Fig. 1C) are consistent with the oxidation of terrestrial minerals containing reduced As to produce soluble As(V) that was then transported to the oceans during the GOE.

In addition to being a strong As(III) oxidant, O_2, as it accumulated in the atmosphere, would have initiated the generation of additional As(III) oxidants, including Mn(IV) oxides and NO_3^- (Oremland and Stolz, 2003; Roy, 2006; Zerkle et al., 2017). As expected, the elevated As-S content in shales coincides with the suggested expansion of microbial reduction of sulfate, coincident with the GOE (Kah et al., 2004; Poulton and Canfield, 2011; Planavsky et al., 2012). Neither diagenesis nor the photochemical oxidation of As are likely to have significantly affected our interpretation (see the Data Repository).

Major biogeochemical As cycling pathways in the anoxic Archean oceans are proposed to have been distinct from those operating in the redox-stratified Paleoproterozoic seawater column (Figs. 3A and 3B). Accordingly, the oxidative supply of As(V) from land promotes the large-scale uptake of As(V) through phosphate transporters by marine phytoplankton. This is followed by intracellular As(V) reduction via cytoplasmic As(V)-reductases and the extrusion of As(III) by membrane transporters (Fig. 3C) (Dyhrman and Haley, 2011; Wurl et al., 2013, 2015; Yan et al., 2014; Sánchez-Riego et al., 2014; Saunders and Rocap, 2016). The conversion of As(V) to As(III) minimizes phosphate loss, as physicochemical similarities between As(V) and phosphate complicates differentiation by the cell. Not surprisingly, As(V) displays nutrient-like behavior in the modern oxidized ocean, with a rapid increase in the thermocline and near-constant concentration at depth (Cutter and Cutter, 2006; Wurl et al., 2013, 2015). The shuttling of As(V) into, and As(III) out of, the cell followed by rapid re-oxidation back to As(V) limits As sedimentation and increases seawater residence time (Henke, 2009). This thermodynamic disequilibrium accounts for up to 20% of inorganic As in the oxygenated surface ocean being present as As(III) (Cutter et al., 2001; Cutter and Cutter, 2006; Wurl et al., 2013, 2015; Fig. 3D).

Importantly, some oxidized compounds mobilized for the first time during the GOE would have been toxic for microbes that had evolved in their absence under dominantly anoxic marine conditions. Arsenate, for instance, is toxic to all three domains of life down to the nanomolar range and its concentration displays a strong inverse relationship with marine primary production, particularly because of the interference of As(V) with phosphate metabolism (see Smedley and Kinniburgh, 2002; Dyhrman and Haley, 2011; see the Data Repository). Methylated arsenicals, implicated in the adaptation of early life to As-rich environments (Chen et al., 2017) and linked to As detoxification, contain ≥35% of As in the photic zone (Cutter et al., 2001; Cutter and Cutter, 2006; Wurl et al., 2013, 2015). This biological processing of As, plus sulfide and Fe(III)-(oxyhydr)oxide mineralization, would have influenced the distribution of As resistance, As-based metabolisms, and biological phosphate uptake in extant biota (see the Data Repository for a discussion on implications for biological arsenic cycling and phosphate uptake). It has also been suggested that the large-scale deposition of iron formations at the Archean-Paleoproterozoic transition facilitated the preferential incorporation of phosphorus (P) over As(V) into Fe(III) (oxyhydr)oxides. This

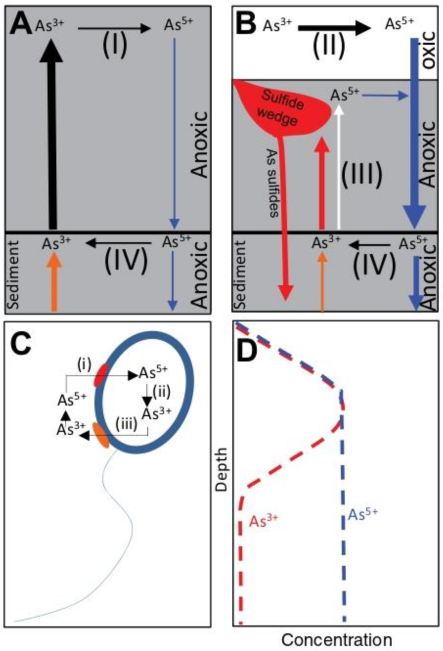

Figure 3. Conceptual models of principal marine arsenic (As) cycling pathways. A: Proposed Archean As cycle. B: Proposed Paleoproterozoic As cycle. (I)—potential predominant anoxygenic photosynthetic oxidation of As(III) to As(V) in unstratified Archean oceans with low sulfide content; (II)—potential elevation of As(III) oxidation to As(V) in Great Oxidation Event (GOE) redox stratified oceans, coupled to rise in seawater oxygen, Mn-oxide, and sulfate content; (III)—potential decrease in As-dependent anoxygenic photoautotrophy and increase in chemoautotrophic nitrate-dependent oxidation of As(III) to As(V) after GOE; (IV)—As(III) regeneration by anaerobic dissimilatory As(V) reduction with organic matter. White, blue, red, and orange arrows represent As(III) regenerated in sediments and water column through anaerobic As(V) reduction, As(V) production by As(III) oxidation, As-sulfide formation pathways, and hydrothermal As(III) release, respectively. Arrow size represents hypothesized size of pool for each As species reaction pathway. C: A microbial cell performing As(V) detoxification: (i)—phosphate transporter (red); (ii)—cytoplasmic As(V) reduction to As(III); (iii)—extrusion of As(III) through As(III) efflux pump (orange). D: Conceptual model depicting behavior of As(III) and As(V) in modern fully oxygenated ocean (Cutter et al., 2001; Maher and Butler, 1988).

would have led to a simultaneous buildup of As(V) and depletion of P in seawater that would have negatively impacted marine primary productivity (Chi Fru et al., 2016b; Hemmingsson et al., 2018).

The rise in As-S and As(V) appears some 30 m.y. before the loss of S-MIF, providing compelling evidence that the GOE was protracted rather than instantaneous. This rise in marine As-S and As(V) across the Archean-Proterozoic boundary overlaps with the expansion of major As oxidants during the GOE. We propose that this radical change enabled the expansion of a global As cycle reminiscent of the modern, and is related to the onset of abundant As-S and As(V) species in sulfidic and oxygenated environments, respectively. The emergence and impact of these toxic species have yet to be considered despite this knowledge forming a critical prerequisite for understanding how life adapted to the new redox landscape that emerged with the GOE.

ACKNOWLEDGMENTS

The European Research Council (ERC) Seventh Framework (F7) program funded this work (grant 336092). Support is acknowledged from the Centre National de la Recherche Scientifique , la Région Nouvelle Aquitaine and Gabonese, Centre Nationale pour la Recherche Scientifique et Technique (CENAREST). We thank Aivo Lepland for black shale samples from the Zaonega Formation (Russia).

REFERENCES CITED

Anbar, A.D., et al., 2007, A whiff of oxygen before the Great Oxidation Event?: Science, v. 317, p. 1903–1906, https://doi.org/10.1126/science.1140325.

Bekker, A., Holland, H.D., Wang, P.-L., Rumble, D., Stein, H.J., Hannah, J.L., Coetzee, L.L., and Beukes, N.J., 2004, Dating the rise of atmospheric oxygen: Nature, v. 427, p. 117–120, https://doi.org/10.1038/nature02260.

Canfield, D.E., et al., 2013, Oxygen dynamics in the aftermath of the Great Oxidation of Earth's atmosphere: Proceedings of the National Academy of Sciences of the United States of America, v. 110, p. 16,736–16,741, https://doi.org/10.1073/pnas.1315570110.

Chi Fru, E., Arvestål, E., Callac, N., El Albani, A., Kilias, S., Argyraki, A., and Jakobsson, M., 2015, Arsenic stress after the Proterozoic glaciations: Scientific Reports, v. 5, 17789, https://doi.org/10.1038/srep17789.

Chi Fru, E., Rodríguez, N.P., Partin, C.A., Lalonde, S.V., Andersson, P., Weiss, D.J., El Albani, A., Rodushkin, I., and Konhauser, K.O., 2016a, Cu isotopes in marine black shales record the Great Oxidation Event: Proceedings of the National Academy of Sciences of the United States of America, v. 113, p. 4941–4946, https://doi.org/10.1073/pnas.1523544113.

Chi Fru, E., Hemmingsson, C., Holm, M., Chiu, B., and Iñiguez, E., 2016b, Arsenic-induced phosphate limitation under experimental Early Proterozoic oceanic conditions: Earth and Planetary Science Letters, v. 434, p. 52–63, https://doi.org/10.1016/j.epsl.2015.11.009.

Chen, S.-C., Sun, G.-X., Rosen, B.P., Zhang, S.-Y., Deng, Y., Zhu, B.-K., Rensing, C., and Zhu, Y., 2017, Recurrent horizontal transfer of arsenite methyltransferase genes facilitated adaptation of life to arsenic: Scientific Reports, v. 7, 7741, https://doi.org/10.1038/s41598-017-08313-2.

Cutter, G.A., and Cutter, L.S., 2006, Biogeochemistry of arsenic and antimony in the North Pacific Ocean: Geochemistry Geophysics Geosystems, v. 7, Q05M08, https://doi.org/10.1029/2005GC001159.

Cutter, G.A., Cutter, L.S., Featherstone, A.M., and Lohrenz, S.E., 2001, Antimony and arsenic biogeochemistry in the western Atlantic Ocean: Deep-Sea Research Part II: Topical Studies in Oceanography, v. 48, p. 2895–2915, https://doi.org/10.1016/S0967-0645(01)00023-6.

Dyhrman, S.T., and Haley, S.T., 2011, Arsenate resistance in the unicellular marine diazotroph *Crocosphaera watsonii*: Frontiers in Microbiology, v. 2, 214, https://doi.org/10.3389/fmicb.2011.00214.

Farquhar, J., Zerkle, A.L., and Bekker, A., 2011, Geological constraints on the origin of oxygenic photosynthesis: Photosynthesis Research, v. 107, p. 11–36, https://doi.org/10.1007/s11120-010-9594-0.

Gregory, D., et al., 2015, Trace element content of sedimentary pyrite in black shales: Economic Geology and the Bulletin of the Society of Economic Geologists, v. 110, p. 1389–1410, https://doi.org/10.2113/econgeo.110.6.1389.

Hemmingsson, C., Pitcain, I.K., and Chi Fru, E., 2018, Evaluation of uptake mechanisms of phosphate by Fe(III) (oxyhydr)oxides in early Proterozoic oceanic conditions: Environmental Chemistry, v. 15, p. 18–28, https://doi.org/10.1071/EN17124.

Henke, K.V., ed., 2009, Arsenic: Environmental Chemistry, Health Threats and Waste Treatment: West Sussex, UK, John Wiley and Sons, 588 p., https://doi.org/10.1002/9780470741122.

Hoffman, P.F., Kaufman, A.J., Halverson, G.P., and Schrag, D.P., 1998, The Neoproterozoic snowball Earth: Science, v. 281, p. 1342–1346, https://doi.org/10.1126/science.281.5381.1342.

Kah, C.L., Lyons, T.W., and Frank, T.D., 2004, Low marine sulphate and protracted oxygenation of the Proterozoic biosphere: Nature, v. 431, p. 834–838, https://doi.org/10.1038/nature02974.

Konhauser, K.O., et al., 2011, Aerobic bacterial pyrite oxidation and acid rock drainage during the Great Oxidation Event: Nature, v. 478, p. 369–373, https://doi.org/10.1038/nature10511.

Large, R., et al., 2014, Trace element content of sedimentary pyrite as a new proxy for deep-time ocean-atmosphere evolution: Earth and Planetary Science Letters, v. 389, p. 209–220, https://doi.org/10.1016/j.epsl.2013.12.020.

Large, P.R., Mukherjee, I., Zhukova, I., Cockrey, R., Stepanov, A., and Danyushevsky, L.V., 2018, Role of upper-most crustal composition in the evolution of the Precambrian ocean-atmosphere system: Earth and Planetary Science Letters, v. 487, p. 44–53, https://doi.org/10.1016/j.epsl.2018.01.019.

Lyons, T.W., Reinhard, C.T., and Planavsky, N.J., 2014, The rise of oxygen in Earth's early ocean and atmosphere: Nature, v. 506, p. 307–315, https://doi.org/10.1038/nature13068.

Maher, W., and Butler, E., 1988, Arsenic in the marine environment: Applied Organic Chemistry, v. 2, p. 191–214, https://doi.org/10.1002/aoc.590020302.

Martin, A.P., Prave, A.R., Condon, D.J., Lepland, A., Fallick, A.E., Romashkin, A.E., Medvedev, P.V., and Rychanchik, D.V., 2015, Multiple Palaeoproterozoic carbon burial episodes and excursions: Earth and Planetary Science Letters, v. 424, p. 226–236, https://doi.org/10.1016/j.epsl.2015.05.023.

Ngombi-Pemba, L., El Albani, A., Meunier, A., Grauby, O., and Gauthier-Lafaye, F., 2014, From detrital heritage to diagenetic transformations, the message of clay minerals contained within shales of the Palaeoproterozoic Francevillian basin (Gabon): Precambrian Research, v. 255, p. 63–76, https://doi.org/10.1016/j.precamres.2014.09.016.

O'Day, P.A., 2006, Chemistry and mineralogy of arsenic: Elements, v. 2, p. 77–83, https://doi.org/10.2113/gselements.2.2.77.

O'Day, P.A., Vlassopoulos, D., Root, R., and Rivera, N., 2004, The influence of sulfur and iron on dissolved arsenic concentrations in the shallow subsurface under changing redox conditions: Proceedings of the National Academy of Sciences of the United States of America, v. 101, p. 13,703–13,708, https://doi.org/10.1073/pnas.0402775101.

Oremland, R.S., and Stolz, J.F., 2003, The ecology of arsenic: Science, v. 300, p. 939–944, https://doi.org/10.1126/science.1081903.

Partin, C.A., Lalonde, S.V., Planavsky, N.J., Bekker, A., Rouxel, O.J., Lyons, T.W., and Konhauser, K.O., 2013, Uranium in iron formations and the rise of atmospheric oxygen: Chemical Geology, v. 362, p. 82–90, https://doi.org/10.1016/j.chemgeo.2013.09.005.

Planavsky, N.J., Bekker, A., Hofmann, A., Owens, J.D., and Lyons, T.W., 2012, Sulfur record of rising and falling marine oxygen and sulfate levels during the Lomagundi event: Proceedings of the National Academy of Sciences of the United States of America, v. 109, p. 18,300–18,305, https://doi.org/10.1073/pnas.1120387109.

Poulton, S.W., and Canfield, D.E., 2011, Ferruginous conditions: A dominant feature of the ocean through Earth's history: Elements, v. 7, p. 107–112, https://doi.org/10.2113/gselements.7.2.107.

Roy, S., 2006, Sedimentary manganese metallogenesis in response to the evolution of the Earth system: Earth-Science Reviews, v. 77, p. 273–305, https://doi.org/10.1016/j.earscirev.2006.03.004.

Sánchez-Riego, A.M., López-Maury, L., and Florencio, F.J., 2014, Genomic responses to arsenic in the cyanobacterium *Synechocystis* sp. PCC 6803: PLoS One, v. 9, e96826, https://doi.org/10.1371/journal.pone.0096826.

Saunders, J.K., and Rocap, G., 2016, Genomic potential for arsenic efflux and methylation varies among global *Prochlorococcus* populations: The ISME Journal, v. 10, p. 197–209, https://doi.org/10.1038/ismej.2015.85.

Sforna, M.C., Philippot, P., Somogyi, A., van Zuilen, M.A., Medjoubi, K., Schoepp-Cathenet, B., Nitschke, W., and Visscher, P.T., 2014, Evidence for arsenic metabolism and cycling by microorganisms 2.7 billion years ago: Nature Geoscience, v. 7, p. 811–815, https://doi.org/10.1038/ngeo2276.

Smedley, P.L., and Kinniburgh, D.G., 2002, A review of the source, behaviour and distribution of arsenic in natural waters: Applied Geochemistry, v. 17, p. 517–568, https://doi.org/10.1016/S0883-2927(02)00018-5.

Wurl, O., Zimmer, L., and Cutter, G.A., 2013, Arsenic and phosphorus biogeochemistry in the ocean: Arsenic species as proxies for P-limitation: Limnology and Oceanography, v. 58, p. 729–740, https://doi.org/10.4319/lo.2013.58.2.0729.

Wurl, O., Shelley, R.U., Landing, W.M., and Cutter, G.A., 2015, Biogeochemistry of dissolved arsenic in the temperate to tropical North Atlantic Ocean: Deep-Sea Research Part II: Topical Studies in Oceanography, v. 116, p. 240–250, https://doi.org/10.1016/j.dsr2.2014.11.008.

Yan, C., Wang, Z., and Luo, Z., 2014, Arsenic efflux from *Microcystis aeroginosa* under different phosphate regimes: PLoS One, v. 9, e116099, https://doi.org/10.1371/journal.pone.0116099.

Zerkle, A.L., Poulton, S.W., Newton, R.J., Mettam, C., Claire, M.W., Bekker, A., and Junium, C.K., 2017, Onset of the aerobic nitrogen cycle after the Great Oxidation Event: Nature, v. 542, p. 465–467, https://doi.org/10.1038/nature20826.

Printed in USA